

Research-based exploration of deep groundwater within the eastern limb of the Bushveld Igneous Complex for hydrogeological characterisation and potential future water resource identification

Final Report

Report
to the Water Research Commission

by

Allwright AJ¹, de Lange S², Lubbe R², Mbonambi L², Vivier K³ and Witthuser KT⁴

¹Department of Earth Sciences, Stellenbosch University, Stellenbosch, South Africa

² Institute for Groundwater Studies, University of the Free State, Bloemfontein, South Africa

³ Artesium Consulting Services (Pty) Ltd; Artesium SA (Pty) Ltd

⁴ Delta-H Water Systems Modelling PTY Ltd

WRC report no. 3200/1/25

ISBN 978-0-6392-0706-3

May 2025



This is the final report of WRC project no. C2022/2023-00812.

DISCLAIMER

This report has been reviewed by the Water Research Commission (WRC) and approved for publication. Approval does not signify that the contents necessarily reflect the views and policies of the WRC, nor does mention of trade names or commercial products constitute endorsement or recommendation for use.

EXECUTIVE SUMMARY

This Water Research Commission (WRC) project was initiated to investigate deep groundwater systems within the eastern limb of the Bushveld Igneous Complex (BIC), leveraging opportunities provided by the Bushveld Complex Drilling Project (BVDP). While the original plan included drilling two deep boreholes, the project ultimately focused on a single borehole, which facilitated data collection from a depth of 950 m within this project timeframe. The project aimed to characterise deep fractured aquifers, assess groundwater chemistry and isotopic signatures, and refine the regional hydrogeological conceptual model.

The study confirmed the presence of deep fracture-controlled aquifers, with groundwater inflows observed between 800 m and 950 m, highlighting the role of structural controls in groundwater movement at depth. Hydrochemical and isotopic analyses revealed a transition from Ca-Mg-HCO₃ facies at shallower depths to Na-Cl facies at greater depths, indicating increased mineralisation and long residence times with limited modern recharge. From the analysed water quality information, there appears to be two distinct systems, a shallow and deeper system. The difference in water quality could confirm the assumption made in the western limb that shallow aquifers are generally not linked to deeper aquifers (> 300 mbgl).

Hydraulic testing demonstrated permeability variations, with higher hydraulic conductivity within fracture zones, particularly in pyroxenite and chromitite layers. Geophysical logging provided further evidence of structurally controlled groundwater flow, with borehole imaging revealing interconnected faults and dykes acting as potential conduits. Unexpected drilling observations, including cementing failures and the emergence of anomalous dark, odorous fluids, raised questions about fluid migration processes and potential deep-seated geochemical reactions. The detection of methane and other dissolved gases suggests possible abiogenic gas sources or geothermal interactions.

The findings from this WRC project indicate that deep groundwater systems within the Bushveld Igneous Complex (BIC) could serve as a resource for industrial and mining applications, particularly in regions where surface water is scarce. Additionally, the elevated temperatures and gas anomalies suggest geothermal energy potential, warranting further investigation. However, one of the key challenges encountered during this study was the influence of drilling fluids during sampling, which introduced complexities in the hydrochemical and isotopic analyses. Despite this challenge, valuable hydrogeological information was successfully collected, demonstrating the potential for deep groundwater research in the BIC.

Typically, exploration boreholes in mining environments are closed or cemented immediately after drilling for safety and operational considerations. However, an important outcome of this research is that this borehole has been advocated to remain open to allow for continued deep groundwater investigations, particularly for advanced groundwater dating using noble gas isotopes. The plan is to allow the borehole to rest for a period post-drilling to ensure that hydrogeological conditions stabilise, eliminating the influence of drilling fluids and additional source water. Further research funding will be sought to facilitate detailed post-drilling sampling and hydrogeochemical analyses, allowing for a more accurate characterisation of the deep groundwater system without drilling-related interference.

This research provides the first detailed hydrogeological characterisation of deep groundwater in the Bushveld Igneous Complex, forming the basis for a revised hydrogeological conceptual model that integrates geological, geophysical, and hydrogeochemical insights. Future work should focus on refining these findings through continued monitoring, targeted hydraulic testing, and geochemical studies, supporting water resource management, geothermal energy exploration, and broader geological modelling efforts in South Africa.

ACKNOWLEDGEMENTS

The Water Research Commission is acknowledged for the funding of this project, of which none of this work would have been possible.

The following members of the reference group are thanked for their guidance during the project and for their peer review of the final report:

- Mr Yazeed Van Wyk (Water Research Commission: Chairperson)
- Prof Louis van Rooy (University of Pretoria)
- Dr Gideon Steyl (ACT Williams)
- Prof Thokozani Kanyerere (University of the Western Cape)
- Dr Johanita Kotze (Anglo America)

A special word of thanks is extended to the following:

- The ICDP-funded Bushveld Drilling Project (BVDP) for facilitating the water research aspects on the BVDP drill hole, including the steering committee: Prof Susan Webb, Mr Stuart Hill, Prof Freddie Roelofse, Prof Robert Trumbull, Mr Thulani Maupa, Prof Lew Ashwal, and Prof Reiner Klemm. Special thank you to technical staff at the drill site, Kwena Mathopa and Katlego Tlaila.
- Dr Lore-Mari Deysel and the Institute for Groundwater Studies Laboratory for collaborating on the water quality analysis on collected water samples with drilling fluids.
- Dr Janine Colling and Prof Chris Harris from the BIOGRIP Laboratories for collaborating on the analysis on collected water samples with drilling fluids for stable water isotopes.
- Marius Smit and Lorinda Rust for support services at the Institute for Groundwater Studies (University of the Free State)

CONTENTS

EXECUTIVE SUMMARY	iii
ACKNOWLEDGEMENTS	iv
CONTENTS	v
LIST OF FIGURES	ix
LIST OF TABLES.....	xv
1 INTRODUCTION	1
1.1 PROJECT AIMS	3
1.2 SCOPE AND LIMITATIONS	3
2 BUSHVELD COMPLEX (BC)	4
2.1 INTRODUCTION	4
2.2 GEOLOGY	5
2.2.1 Rustenburg Layered Suite	5
2.2.2 Lebowa Granite Suite	6
2.2.3 Rashoop Granophyre Suite	6
2.2.4 Rooiberg Group.....	6
2.2.5 Eastern Limb	7
2.3 MINING	12
2.3.1 Eastern Limb	12
2.4 GROUNDWATER	22
2.4.1 Alluvial aquifers	22
2.4.2 Weathered bedrock aquifers.....	22
2.4.3 Fractured bedrock aquifers	23
2.4.4 Eastern Limb	24
3 GROUNDWATER DATABASE OVERVIEW FOR THE EASTERN LIMB BUSHVELD COMPLEX....	27
3.1 OVERVIEW.....	27
3.2 BOREHOLE DATA ANALYSIS.....	28
3.2.1 Borehole Depths	28
3.2.2 Water Strike Depths	28
3.2.3 Blow Yields.....	33
3.2.4 Groundwater Levels	35
3.2.4.1 Groundwater flow direction.....	35
3.2.4.2 Groundwater Level Trends	36
3.3 HYDRAULIC CHARACTERISTICS	42
3.3.1 Geology	43
3.3.2 Lineaments.....	46
3.3.3 Drainage.....	49
3.3.4 Topography and slope	52
3.3.5 Borehole Depth	53
3.3.6 Summary.....	53
3.4 HYDROCHEMICAL CHARACTERISTICS	55
3.4.1 Hydrogeochemical classification.....	55

3.4.2	Hydrogeochemical processes controlling groundwater chemistry	62
3.5	GROUNDWATER RECHARGE AND GROUNDWATER ABSTRACTIONS	68
3.5.1	Groundwater Recharge Estimation	68
3.5.2	Groundwater Abstractions	69
3.6	HYDROGEOLOGICAL CONCEPTUAL MODEL.....	73
3.6.1	Hydrostratigraphy of the eastern limb of the Bushveld Igneous Complex.....	73
3.6.2	Hydrogeological Properties.....	73
3.6.3	Hydrochemistry and Groundwater Flow	74
3.7	SUMMARY AND DISCUSSION	77
3.7.1	Groundwater Level Trend Analysis	77
3.7.2	Hydraulic characteristics	78
3.7.3	Hydrogeochemical Characteristics	79
3.8	GROUNDWATER FLOW AND RECHARGE	80
3.8.1	Limitations of the investigation	81
4	DEEP SCIENTIFIC DRILLING.....	83
4.1	INTRODUCTION	83
4.2	DATA COLLECTION DURING DRILLING	83
4.2.1	Hydrogeological data	83
4.2.2	Online gas analyser (OLGA).....	86
4.3	GEOPHYSICAL LOGGING AND SAMPLING SURVEYS.....	88
4.3.1	Electrical resistivity.....	88
4.3.2	Spectral Gamma Ray (SGR)	91
4.3.3	Acoustic / Sonic.....	92
4.3.4	Dipmeter.....	94
4.3.5	Magnetic susceptibility	95
4.3.6	Mud logging (mud parameter).....	96
4.3.7	Borehole imaging	97
4.3.8	Vertical Seismic Profile (VSP).....	99
4.3.9	Fluid sampling	99
4.3.10	Borehole Magnetic Resonance (BMR)	100
4.3.11	Flow meter	102
4.3.12	Water quality	104
4.3.13	Suites of geophysical surveys.....	105
4.4	HYDRAULIC TESTING.....	108
4.4.1	Fluid production test (Packer pumping test)	108
4.4.2	Flowing Fluid Electrical Conductivity (FFEC) logging	111
4.4.3	Combination of FFEC and packer pumping testing	112
5	BVDP BOREHOLE DRILLING AND METHODOLOGY	114
5.1	INTRODUCTION	114
5.2	DRILL SITE	114
5.3	PRE-DRILLING	118
5.3.1	Drilling	118
5.3.2	Geology – core processing	118
5.3.3	Water sampling	118
5.3.4	Gas analysis.....	119
5.3.5	Microbiological sampling	119
5.4	BOREHOLE DESIGN	119
5.5	DRILLING AND SAMPLING WORKFLOW ON SITE	121
5.5.1	Geological core workflow	121

5.5.2	Fluid sampling workflow	122
5.5.2.1	Information from drillers	122
5.5.2.2	Monitoring and sampling circulating drill fluids	122
5.5.2.3	Drilling fluid sampling protocol	123
5.5.3	Online gas workflow	123
5.5.3.1	Degasser/separator	125
5.5.3.2	miniRUEDI equipment	127
5.5.4	Microbiological workflow	129
5.5.4.1	Sampling procedure	129
5.6	PHASED SURVEYING AND SAMPLING	133
5.7	GEOPHYSICAL SURVEYING	133
5.7.1	Tools	133
5.7.2	Methodology	133
5.8	FLUID SAMPLING	134
5.8.1	Phase 1 (350 m) and Phase 2 (800 m)	134
5.8.2	Phase 3 (End of Hole - EOH)	135
5.8.2.1	Equipment and preparation	135
5.8.2.2	Sampling procedure	135
5.9	HYDRAULIC TESTING	135
5.9.1	Procedure – SWIPS Operation (HydroGeo Services – phase 2)	136
6	BVDP BOREHOLE DRILLING RESULTS	137
6.1	LITHOLOGICAL LOGS	137
6.2	GEOPHYSICAL SURVEYS	140
6.2.1	Structure log summary	140
6.2.2	Hydrological log	141
6.2.3	Borehole Radar	145
6.3	PHASE 1 WATER SAMPLING AND PRELIMINARY RESULTS	150
6.3.1	Water quality	154
6.3.2	Stable water isotopes	157
6.4	PHASE 2 WATER SAMPLING AND PRELIMINARY RESULTS	161
6.4.1	Water quality	164
6.4.2	Stable water isotope	169
6.5	DRILLING FLUID SAMPLING AND PRELIMINARY ANALYSIS	173
6.6	HYDRAULIC TESTING	183
6.6.1	Methodology and field report	183
6.6.2	Results	184
6.7	ONLINE GAS ANALYSIS	188
6.7.1	Configuration	189
6.7.2	Standard operating procedure	189
6.8	SUMMARY	192
7	DEEP GROUNDWATER INSIGHTS FROM BVDP BOREHOLE	195
7.1	OVERVIEW	195
7.2	GEOLOGICAL AND STRUCTURAL CONTEXT	195
7.3	HYDROLOGICAL FINDINGS	195
7.4	HYDROGEOLOGICAL IMPLICATIONS	196
7.5	CONCEPTUALISING DEEP GROUNDWATER IN THE BUSHVELD	197
7.6	LONG-TERM INVESTIGATIONS AND FUTURE POTENTIAL	198
7.7	POTENTIAL FOR FUTURE WATER SUPPLY	198

8	CONCLUSIONS AND RECOMMENDATIONS	200
8.1	HYDROGEOLOGICAL AND STRUCTURAL INSIGHTS	200
8.2	HYDROCHEMICAL AND ISOTOPIC EVOLUTION	200
8.3	DRILLING CHALLENGES AND BOREHOLE MANAGEMENT	201
8.4	IMPLICATIONS FOR WATER RESOURCE DEVELOPMENT AND GEOTHERMAL POTENTIAL ..	201
8.5	RECOMMENDATIONS.....	201
9	REFERENCES	203
	Appendix A.....	a

LIST OF FIGURES

Figure 1 Location of the drilled hole, BVDP, within the Rustenburg Layered Suite on the eastern limb of the Bushveld Igneous Complex. Borehole is located within the central section of the Eastern Limb between the Wonderkop fault and Steelpoort lineament.	2
Figure 2 Geology of the Bushveld Igneous Complex (Scoon and Viljoen, 2019). Eastern Limb divided into northern and southern sectors by Scoon and Viljoen (2019) in this map, but others have divided the Eastern Limb into an upper western section, central section and southern section (Figure 5).....	4
Figure 3 Generalised stratigraphic column for the eastern limb of the Rustenburg Layered Suite showing zones, lithologies, reefs, and marker layers and relationship to the overlying felsic Bushveld lithologies and the underlying Transvaal Supergroup (Scoon and Viljoen, 2019).....	5
Figure 4 Rooiberg stratigraphy and section indicating the relationship with the underlying Pretoria Group (Transvaal Supergroup), and the intrusions of the Rustenburg Layered Suite and Lebowa Granite Suite (Lenhardt et al., 2017).	8
Figure 5 Generalised geological map of the Eastern Limb of the Bushveld Complex, showing the three sectors depicted by Rose et al. (2012) and Seabrook (2005) (Rose et al., 2012). Western Sector above the Wonderkop Fault; Central Sector between the Wonderkop Fault and Steelpoort Lineament to the south; Southern Sector below the Steelpoort Lineament.	9
Figure 6 Simplified geological cross-section from Kgolokoslakasi to Jagdlust, showing the irregular floor of the RLS in the northern sector (characterised by Scoon and Viljoen (2019)), also depicted as the central sector of the eastern limb by Rose et al. (2012) (Scoon and Viljoen, 2019). Section line indicated on Figure 7.....	10
Figure 7 Geological map of the eastern limb of the Bushveld Complex, showing the sectors by Scoon and Viljoen (2019) and the section line from Kgolokoslakasi to Olifants River (Scoon and Viljoen, 2019).....	11
Figure 8 Mineral deposits that are mostly mined in the Bushveld Igneous Complex (Council for Geoscience, 2000).....	13
Figure 9 Locality Map of operating - and historic mines as well as proposed exploration projects in the eastern limb of the Bushveld Igneous Complex	14
Figure 10 Operational and mothballed mines in the eastern limb of the Bushveld Igneous Complex (SFA (Oxford), 2022)	21
Figure 11 Simplified hydrogeological conceptual model of the Bushveld Complex illustrating the pyroxenite aquifer (Gebrekristos and Cheshire, 2012)	24
Figure 12 Geological Map of the study area, the eastern limb of Bushveld Igneous Complex, showing its location with reference to towns and cities. Approximate location of the BVDP borehole is indicated as a black star.	27
Figure 13 Distribution of boreholes across the study area	30
Figure 14 Borehole depth frequency for boreholes within the Bushveld Igneous Complex, according to the different lithostratigraphic divisions in the study area.....	31
Figure 15 Depth to water strike frequency for boreholes within the eastern limb of the Bushveld Igneous Complex. The primary and secondary water strikes zones identified are marked with solid and dashed boxes, respectively.	32
Figure 16 Borehole blow yield frequency for the eastern limb of the Bushveld Igneous Complex from the collected groundwater database.....	33
Figure 17 Blow yield variation with depth, according to average blow yield for the specific depth intervals. .	35
Figure 18 Groundwater level and flow direction map for the study area.....	37
Figure 19 Correlation analysis between groundwater levels (mamsl) and elevation	38
Figure 20 Groundwater level time-series data for the groundwater level monitoring boreholes in the study area: boreholes (a) M01-2432, (b) M02-3612, (c) M06-1064, (d) M06-1551, (e) M06-1613, (f) M28-0062, (g) MP17-00031.	41
Figure 21 Frequency histograms and cumulative distribution of transmissivity (m ² /day) for the study area..	42

Figure 22 Transmissivity variation across the study area in relation to the geology	44
Figure 23 Cumulative distribution of transmissivity (m ² /day) of boreholes in relation to stratigraphic units in the study area	45
Figure 24 Cumulative distribution of transmissivity (m ² /day) of boreholes located within 250 m of lithological contacts and boreholes located at distance more than 250 m from lithological contacts	46
Figure 25 Structural geology map of the eastern limb of the Bushveld Igneous Complex showing the spatial distribution of borehole and their varying transmissivity values	47
Figure 26 Cumulative distribution of transmissivity (m ² /day) of boreholes in relation to the borehole's proximity to lineaments, cumulative frequency curves for boreholes within 300 m distance to lineament and boreholes located more than 300 m away from lineaments.....	48
Figure 27 Cumulative distribution of transmissivity (m ² /day) of boreholes in the study area relative to the lineament density.....	49
Figure 28 (a) Lineament density map, (b) drainage density map, (c) topography map and (d) slope map of the study area	50
Figure 29 Cumulative distribution of transmissivity (m ² /day) of boreholes in the study area relation to the borehole's proximity to perennial rivers	51
Figure 30 Cumulative distribution of transmissivity (m ² /day) of boreholes relative to the drainage density of study area	51
Figure 31 Cumulative distribution of transmissivity (m ² /day) of boreholes relative to the elevation classes..	52
Figure 32 Cumulative distribution of transmissivity (m ² /day) of boreholes relative to the slope classes in the study area	53
Figure 33 Spatial distribution of the hydrochemical groups across the eastern limb of the Bushveld Igneous Complex, identified by the HCA.....	56
Figure 34 Piper Diagram showing Rustenburg Layered Suite, hydrochemical group based on HCA	60
Figure 35 Piper Diagram showing Raseop Granophyre Suite hydrochemistry dataset, hydrochemical group based on HCA	61
Figure 36 Piper Diagram displaying Lebowa Granite Suite hydrochemistry dataset, hydrochemical group based on HCA	61
Figure 37 Gibb's diagrams displaying the mechanism of controlling groundwater quality in the eastern limb of the Bushveld Igneous Complex, for the different lithostratigraphic divisions; (a) Rustenburg Layered Suite (b) Raseop Granophyre Suite and (c) Lebowa Granite Suite	63
Figure 38 Bivariate plot (Ca + Mg) vs. (HCO ₃ +SO ₄) for (a) Rustenburg Layer Suite (b) Raseop Granophyre Suite and (c) Lebowa Granite Suite.....	65
Figure 39 Bivariate plots showing Na/Cl vs EC for (a) Rustenburg Layer Suite (b) Raseop Granophyre Suite and (c) Lebowa Granite Suite.....	67
Figure 40 Annual groundwater recharge map for the eastern limb of the Bushveld Igneous Complex, estimated using the Chloride Mass Balance method.	70
Figure 41 Recharge map displaying the recharge percentage of the mean annual precipitation in the eastern limb of the BIC	71
Figure 42 Volumes of overall registered groundwater use in the eastern limb of the Bushveld Igneous Complex, over the years.	72
Figure 43 Hydrogeological conceptual model of the eastern limb of the Bushveld Igneous Complex based on the publicly available groundwater information mainly focused on traditional shallow groundwater resources	76
Figure 44 Illustration of an example of online gas analysis results. Compressed mud gas log of the KTB main hole displaying only the most prominent CH ₄ (ppmv) and He (ppmv) shows	86
Figure 45 Illustration of the Online Gas Analysis (OLGA) setup and details of analyses performed (GFZ and ICDP, 2020)	87
Figure 46 The response of resistivity logs in formations with various fluids (Glover, 2014a)	89
Figure 47 The response of resistivity logs for different formation water salinities (Glover, 2014a).....	89

Figure 48 Typical resistivity log response in a sand/shale sequence (Glover, 2014a)	90
Figure 49 An example of a DLL log, showing separation of the LLs and LLd, and from the MSFL, indicating the presence of a permeable formation with hydrocarbons (gas in this case in a formation of about 15% porosity) (Glover, 2014a)	90
Figure 50 An example to illustrate the freshwater/saltwater interface in the Cuxhaven borehole in northern Germany in resistivity logs (DLL). DLLs: shallow dual laterolog; DLLd: deep dual laterolog; GR: gamma-ray log (Wonik, 2007).	91
Figure 51 An example of a typical spectral gamma ray log (Glover, 2014b)	92
Figure 52 Typical responses of a sonic (acoustic) log (Glover, 2014c)	93
Figure 53 Stratigraphic core description displayed with dipmeter log to illustrate the analysis of facies and transport direction (Luchtel, 1999, as cited in Doveton, 2017)	94
Figure 54 Example acoustic image of the depth interval 203.8 - 207.5 m in the Fürstenwald borehole near Kassel, Germany as recorded by Wonik (2007). GR: gamma-ray log; CAL: Caliper log; True	95
Figure 55 An example of a magnetic susceptibility log (MSUS) illustrating systematic variations associated with lava facies flow packages and boundaries (Jerram et al., 2019)	96
Figure 56 Example of a composite image of the <i>Triple Combo</i> Open Hole Log and Mud Log. Core points are identified to the right of the log tracks. The first track contains a colour filled natural gamma ray curve. Warmer colours (yellow) indicate reservoir intervals (sandstones). Cooler colours (green/blue) indicate confining units (mudstones). The third track shows Neutron and Density porosity curves. The Density Porosity Curve is filled (yellow) when Density Porosity is > 20% (Koperna, 2020).	97
Figure 57 Borehole imaging illustration by Jerram et al. (2019). (a) Simplified schematic displaying the four-arm Caliper response to common borehole conditions; (b) basics of televiewer imaging of borehole features; (c) example of some of these features from the PTA2 borehole televiewer data.	98
Figure 58 Track 1: Depth in meters; Track 2: Borehole geometry; Track 3: Resistivity; Track 4: NMR relaxation time distribution; Track 5: NMR determined porosity; Track 6: Mineralogy (Dlubac et al., 2013)	101
Figure 59 An example flowmeter log (Track 5 borehole flow) and background geophysical logs for well JPG-1, June 1999, Jefferson Proving Ground, Indiana (Wilson et al., 2001)	102
Figure 60 An example heat-pulse flowmeter log from a borehole in fractured-rock aquifer. Flow was measured under ambient (left) and pumping (right) conditions. Arrows indicate interpreted direction of flow, as fluid moves from zones of higher head to lower head (USGS, 2016).	103
Figure 61 An impeller flowmeter log in an exploratory borehole conducted by Cogswell (2022) which indicates a rapid downhole flow of water from the alluvial gravels to the underlying fractured limestone (Cogswell, 2022)	104
Figure 62 Multi-parameter logging in borehole P12 on July 15, 1997 under natural conditions (no pumping) and under pumping (Schürch and Vuataz, 2002)	105
Figure 63 An example of a suite of hypothetical geophysical borehole log responses to various altered and fractured crystalline rocks (ERG and CERl, 1993)	106
Figure 64 An example of traditional geophysical logs for a borehole in crystalline rocks (foliated granite schist (Paillet, 1994))	107
Figure 65 Illustration of packer test assemblies, a) single packer test-open borehole; b) double packer test-open borehole; c) double packer test wireline assembly (Royle, 2002; Yihdego, 2017)	109
Figure 66 Four categories of hydraulic tests commonly applied to packer tests in fractured rock (Quinn et al., 2012)	110
Figure 67 Illustration of the FFEC logging method. The borehole is first flushed with low-salinity fluid, water level of well is lowered to induce flow into borehole along permeable fractures, and conductivity log is run to identify regions with increased salinity corresponding to inflow zones. Q represents the pump flow rate, $A(FEC)$ is the change in electrical conductivity at time intervals t , q is the inflow rate, and C is the salinity of the formation water associated with each flow zone (Tsang et al., 2016).	112
Figure 68 Location of the borehole on the Marula Mine lease area within the eastern limb of the Bushveld Igneous Complex (BIC)	115
Figure 69 Borehole is located north-east from the Marula Mine operations area.	115

Figure 70 Positions of the three vertical boreholes are shown, with lines indicating the sections of stratigraphy they intersect with the location on the eastern limb of the BIC and location within the Clapham compartment of the central section of the eastern limb (Wilson, 2015).	116
Figure 71 Stratigraphy of the Lower and Marginal Zones of the Bushveld Igneous Complex and BUS from the combined profiles derived from the drill cores CH1, CH6 and CH7 is called the Clapham section (Wilson, 2015).	117
Figure 72 Borehole drilling and design, consisting of three phases, showing the Bushveld Complex lithologies and the underlying Transvaal Supergroup (*not to scale).	120
Figure 73 Illustration of the circulating drilling fluid around a drill that gas from the surrounding formations dissolve into (ICDP, 2024)	124
Figure 74 Illustration of the surface circulation system where the degassing unit is placed in the “Possum belly” (ICDP, 2024).	125
Figure 75 Photos of the A) degasser/gas-water separator, B) photo of the degasser/gas-water-separator installed at the BVDP drill site within the circulating drilling mud system on surface, C) water safety valve installed on site, and D) closeup of gas line safety valve with water levels visible in the outer and inner tubes	126
Figure 76 Schematic overview (top) and photo (bottom) of the miniRUEDI mass-spectrometer system (see also Table 18): 6-port inlet selector valve (S), capillary (C), inlet valve (V), quadrupole mass spectrometer (QMS), turbomolecular pump (TP), and diaphragm pump (DP). The inlet selector valve and the quadrupole mass spectrometer are controlled by a computer. The photo shows the miniRUEDI mounted in a wheeled hardshell suitcase for transport and protection (Brennwald, et al., 2016)....	127
Figure 77 Tracer procedures at the drill site, depicting the addition of the tracer to the drill mud and periodic sampling of the drill fluid. For safety, it is recommended to wear gloves during this sampling.	131
Figure 78 Core sampling procedure at the drill site, illustrating breaking 1 m core intervals from drill rig into sections for two separate processes and storage	132
Figure 79 Simplified lithological log showing changes in lithology over the complete current depth of the BVDP hole	139
Figure 80 Depth of open fractures and major open joint/fractures identified from geophysical logging	140
Figure 81 Total dissolved Salts (TDS) calculated from measured fluid electrical conductivity from geophysical log	141
Figure 82 Fluid temperature measured from geophysical logging	142
Figure 83 Hydrology log presented from the geophysical logging, including fluid electrical conductivity (EC) and fluid temperature with depth along with the calliper and flowmeter measurements	145
Figure 84 Borehole radar results from a depth of 0 to 260 mbgl, showing the general lithological log	146
Figure 85 Borehole radar results from a depth of 160 to 430 mbgl, showing the general lithological log	147
Figure 86 Borehole radar results from a depth of 420 to 680 mbgl, showing the general lithological log	148
Figure 87 Borehole radar results from a depth of 680 to 940 mbgl, showing the general lithological log	149
Figure 88 Raw geophysical data preview for the purpose of selecting depths for fluid sampling (depth from 0 to 47 mbgl) showing sample 1 depth at 46 mbgl.	151
Figure 89 Raw geophysical data preview for the purpose of selecting depths for fluid sampling (depth from 46 to 109 mbgl) showing sample 2 depth at 62.5 mbgl, sample 3 at 75.5 mbgl and sample 4 at 110 mbgl.	152
Figure 90 Raw geophysical data preview for the purpose of selecting depths for fluid sampling (depth from 266 to 352 mbgl) showing sample 5 depth at 272 mbgl and sample 6 at 292 mbgl.	153
Figure 91 Piper diagram of the phase 1 groundwater samples	156
Figure 92 STIFF diagrams of the phase 1 groundwater samples.	156
Figure 93 Schoeller diagram of the phase 1 groundwater samples.	157
Figure 94 Filtering process for sample processed for isotope analysis	157

Figure 95 Delta plot of the phase 1 samples with GMWL on a global scale showing the location of the samples with respect to larger context, namely low latitude geography plotting with enriched overall isotopes	160
Figure 96 Delta plot of the phase 1 samples on a local scale showing the variation in isotope signatures with depth	160
Figure 97 Illustration of the deviation between Deuterium excess for each sample	161
Figure 98 Raw geophysical data preview from phase 2 survey, for the purpose of selecting depths for fluid sampling (depth from 0 to 370 mbgl) showing sample 7 at a depth at 362 mbgl. Solid casing installed in phase 1 is noted to a depth of 350 mbgl	162
Figure 99 Raw geophysical data preview from phase 2 survey, for the purpose of selecting depths for fluid sampling (depth from 360 to 840 mbgl) showing sample 8 to 13 at a depth 383, 389, 450, 575, 623, 650 and 695 mbgl, respectively.	163
Figure 100 Raw geophysical data preview from phase 2 survey, for the purpose of selecting depths for fluid sampling (depth from 800 to 950 mbgl) showing sample 14 to 16 at a depth 815, 885 and 935 mbgl, respectively.	164
Figure 101 Piper diagram of the phase 2 groundwater samples.....	165
Figure 102 Durov diagram of the phase 2 groundwater samples.	168
Figure 103 STIFF diagrams of the phase 2 groundwater samples.	168
Figure 104 Schoeller diagram of the phase 2 groundwater samples.	169
Figure 105 Illustration of which samples were flagged as having trace amounts of potential contamination (orange: both runs indicated contamination; grey: one of two runs indicated contamination (either trace and then clean, or clean and then trace detected; green: both runs were clean)	170
Figure 106 Zones of samples based on Picarro indication of degree of trace organic contaminants that might affect isotopes results (orange: both runs indicated contamination; grey: one of two runs indicated contamination (either trace and then clean, or clean and then trace detected; green: both runs were clean)	171
Figure 107 Delta plot of phase 1 and 2 samples on a local scale showing the variation in isotope signatures with depth. Labels denote sample number and depth at which sample was collected. Samples 1 – 6 form Phase 1 and samples 7 – 16 and source form Phase 2. The source sample is the surface clean water supply used to flush the hole.	172
Figure 108 "BVDP- Drilling Fluid Sampling Protocol" locations.	174
Figure 109 Piper diagram of the drilling fluid samples from 10 July 2024.....	177
Figure 110 Durov diagram of the drilling fluid samples of 10 July 2024.....	177
Figure 111 STIFF diagram of the drilling fluid samples of 10 July 2024.	178
Figure 112 Schoeller diagram of the drilling fluid samples of 10 July 2024.	178
Figure 113 Piper diagram of the drilling fluid samples of 16 July 2024.....	179
Figure 114 Durov diagram of the drilling fluid samples of 16 July 2024.....	179
Figure 115 STIFF diagrams of the drilling fluid samples of 16 July 2024.	180
Figure 116 Schoeller diagram of the drilling fluid samples of 16 July 2024.	180
Figure 117 Piper diagram of the drilling fluid samples of 23 July 2024.....	181
Figure 118 Durov diagram of the drilling fluid samples of 23 July 2024.....	181
Figure 119 STIFF diagrams of the drilling fluid samples of 23 July 2024.	182
Figure 120 Schoeller diagram of the drilling fluid samples of 23 July 2024.	182
Figure 121 Hydraulic packer testing setup with HQ SWiPS System.....	184
Figure 122 Plot of estimated hydraulic conductivity from each packer test conducted.....	185
Figure 123 Correlation of hydraulic conductivity (K in m/d) against depth and results from the packer testing to the geophysical structural log and geological log details. General lithology is indicated behind the depth scale with predominantly pyroxenite of the upper and lower Critical Zone.	186

Figure 124 Components of the KivuRUEDI.....	189
Figure 125 System equilibration (upper) and peak procedure (lower).	191
Figure 126 Analysis set label.....	191
Figure 127 Example of an analysis sequence.....	192
Figure 128 Visual representation of the information collected and analysed on the borehole in this report, with the downhole TDS profile and zones of drilling fluid contamination identified from the stable isotopes added to the packer testing results analysis with geological features noted as possible locations for groundwater flow along with downhole geophysical structure information (depth major open fractures were identified)	194
Figure 129 Re-drilled cement after an attempt to cure cement in the hole at depth (1 150 m to 1 270 m <i>*where lamprophyre dyke was intersected</i>); cement core shows distinct places where flow prevented curing (left); anomalous fluid sampled (right)	196
Figure 130 Updated hydrogeological conceptual model of the eastern limb of the Bushveld Igneous Complex including the insights from the deep drilling project hole up to a depth of 1 450 mbgl along with simplified geological log, hydrological log and photos of broken lamprophyre core at 1420 mbgl. .	199

LIST OF TABLES

Table 2 Historic mine information in the eastern limb of the Bushveld Igneous Complex (DMR, 2022; Fourie et al., 2020).....	15
Table 3. Operating mine information in the Easter Limb on the Bushveld Igneous Complex (DMR, 2022; Fourie et al., 2020; ASSORE, 2016; Anglo American Platinum, 2014; Ivanhoe Mines, 2022; Marula, 2018; Burger et al., 2016; Du Toit and Scholes, 2018; Ramushu et al., 2018; Mining Data Solution Online, 2022; Sibanye-Stillwater, 2020)	15
Table 4 Proposed exploration projects in the eastern limb of the Bushveld Igneous Complex (DMS, 2022; Sibanye-Stillwater, 2020).....	18
Table 5 Borehole data analysis statistical summary according to the stratigraphic units in the study area ...	29
Table 6 Statistical summary of blow yield data for the eastern limb of the BIC from the collected groundwater database	34
Table 7 Groundwater level trend statistical analysis results, including the rainfall Sen's Slope Estimator for the corresponding water level monitoring period. Statistically significant decreasing trends, according to the computed Mann-Kendall test are denoted by ↓ (decreasing) symbol and rainfall with significant trends are signalled by Sen's slope estimator values in bold text.	38
Table 8 Statistical summary of transmissivity value for the eastern limb of the Bushveld Igneous Complex .	42
Table 9 Descriptive statistics for transmissivity according to the lithostratigraphic divisions of the BIC	43
Table 10 Statistical analysis of transmissivity values relative to various factors. Geometric mean transmissivity values used to assess and compare the influence of the factors on the permeability of the eastern limb of the BIC	54
Table 11 Table showing varimax rotated R-mode PCA loadings matrix.....	58
Table 12 Table showing the various MAP used to estimate the groundwater recharge by CMB method and the average recharge for different areas in the study area, relative to the nearest weather station	69
Table 13 Registered groundwater use in the eastern limb of the Bushveld Igneous Complex (WARMS, 2023)	72
Table 14 Mean hydrogeological characteristic of each lithostratigraphic unit of the eastern limb of the Bushveld Igneous Complex.....	75
Table 15 Overview of the steps of borehole drilling supervision from a hydrogeological perspective, including the responsibilities of the driller and of the supervisor, with the essential data to be collected at each step (SADC-GMI et al., 2019).....	84
Table 16 Borehole/rock parameters to be assessed by the planned geophysical logging and sampling surveys on the new drill holes (Webb, 2019)	88
Table 17 List of tectonic, sedimentary and diagenetic features typically identified on borehole images (Gaillot et al., 2007)	98
Table 18 Parts list for the miniRUEDI, depicted in Figure 76 (Brennwald, et al., 2016)	127
Table 19 Phase 1 groundwater sampling results.	155
Table 20 Key Differences in Handling Organic Contaminants	158
Table 21 Calculated Deuterium excess (dD) on the phase 1 samples from the IRMS and IGR for comparison with the deviation between the measurements	159
Table 22 Phase 2 groundwater sampling results.	166

Table 23 Drilling fluid sample analysis results.....	175
Table 24 Summary of the 12 hydraulic packer testing conducted over the Phase section of the hole	185
Table 25 Hydraulic test number, estimated hydraulic conductivity (K) and associated comments from the geological log approximately at the corresponding depth	187

1 INTRODUCTION

Water is central to human development, and groundwater forms a vital component, supplying approximately 50% of all drinking water worldwide (Velis et al., 2017; Smith et al., 2016). With climate change leading to more frequent and intense weather patterns, the strategic importance of groundwater for global water security is expected to increase (Grönwall and Danert, 2020; Foster and MacDonald, 2014).

The National Water Security Framework for South Africa (2020) highlights the need to diversify water sources, with a focus on alternative supplies that can support socio-economic development (Nepfumbada and Seetal, 2020). Deep groundwater is considered a potential alternative water source, particularly when supported by advanced engineering methods (Gude, 2018). Additionally, managed aquifer recharge (MAR) can play a role in integrated water resource management, offering a lower evaporation-loss storage option (Dillon and Arshad, 2016). However, there is limited knowledge about South Africa's deep aquifer systems, mainly due to the high costs of deep drilling and the lack of hydrogeological data collection in mining exploration. Furthermore, mining companies are often reluctant to publicly share hydrogeological information, limiting the availability of data. To address these knowledge gaps, research-based drilling is required to improve the understanding of deep groundwater systems.

This Water Research Commission (WRC) project, in collaboration with the Bushveld Complex Drilling Project (BVDP), provided a unique opportunity to explore deep groundwater within the Bushveld Igneous Complex (BIC). The research focused on drilling a single borehole (BVDP-2), which was successfully completed to a final depth of 950 m. While the original plan anticipated drilling to $\pm 2,500$ m, this borehole still provided valuable hydrogeological insights into the fractured aquifer systems of the region. The borehole, located within the Rustenburg Layered Suite of the eastern limb of the BIC, allowed for the collection of crucial hydrogeochemical, isotopic, and structural data to enhance the understanding of groundwater flow and deep aquifer potential (Figure 1).

In deep crystalline rock environments, groundwater is typically confined to fractures, faults, and veins produced by brittle deformation. Within the central section of the eastern limb of the BIC, major NNE-striking dykes and WNW-striking dykes have been identified as potential groundwater-bearing zones (Basson, 2019; Stoch et al., 2020). These structures are situated between the Wonderkop Splay/Stofpoort Fault and the Steelpoort/Dwarsrivier Fault, which define the central structural framework of the region. While groundwater has been encountered at depth in some parts of the BIC, other areas remain largely unexplored (Titus et al., 2009a; Gebrekristos and Cheshire, 2012; Dalasile and Abiye, 2018). The depth to which unweathered, fractured aquifers extend remains uncertain, and previous studies have emphasized the lack of deep borehole data as a major constraint in understanding regional groundwater systems (Titus et al., 2009a; Fourie et al., 2020).

This research successfully advanced knowledge of deep groundwater in the Bushveld Complex by confirming the presence of fracture-controlled aquifers, hydrogeochemical evolution with depth, and structurally influenced flow paths. The findings from this 950 m borehole contribute to a revised hydrogeological conceptual model and provide a foundation for future studies on groundwater availability, geothermal potential, and long-term sustainability of deep aquifers in the region.

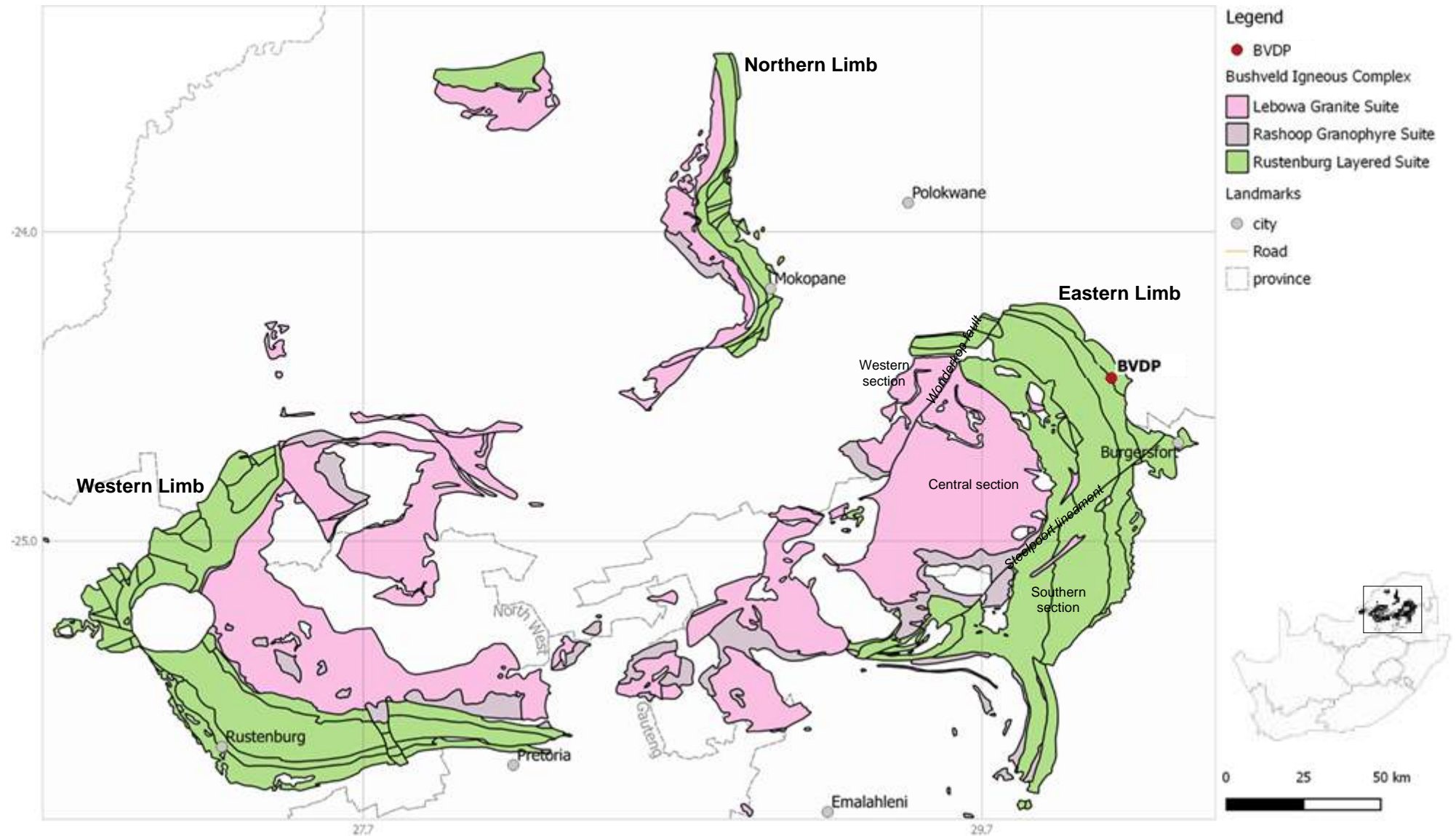


Figure 1 Location of the drilled hole, BVDP, within the Rustenburg Layered Suite on the eastern limb of the Bushveld Igneous Complex. Borehole is located within the central section of the Eastern Limb between the Wonderkop fault and Steelpoort lineament.

1.1 PROJECT AIMS

The following are the aims of the project:

1. To ensure the opportunity to collect hydrogeological information from the deep BVDP boreholes is utilised.
2. Develop new knowledge on the understanding of natural water supply potential through the collection of new data on deep groundwater systems in the Bushveld Igneous Complex.
3. Stimulate local expertise in deep borehole drilling and data collection for researchers and students, drawing on the opportunity to collaborate with an international ICDP team.
4. Facilitate the generation of research-based information to serve the academic community in terms of postgraduate studies and publications.

The collected data aims to support numerous scientific research, including the identification and characterisation of the deep groundwater system; investigation of groundwater quality and possible reactions taking place; interconnectivity of upper weathered and deep fractured aquifers; and determining the geothermal energy potential. Additionally, a number of other research disciplines would be stimulated by the data collected, including deep natural gas and deep biosphere (microbiology).

A specific scientific hypothesis undertaken will be the depth to which fractures are found and whether the presence of fractures translates to the occurrence of groundwater. Furthermore, whether chemical precipitation within fractures is a factor to either assist or hinder groundwater movement. By means of down-hole geophysical logging and in-hole geohydrological tests, the depth-dependent hydraulic conductivity and its relation to fracture density and orientation can be determined. Temperature gradient and fluid flow rates in the boreholes will help assess the potential for groundwater extraction and geothermal energy production.

1.2 SCOPE AND LIMITATIONS

The groundwater database considered for the eastern limb of the bushveld complex is limited to publicly available data because navigating the NDA process required for the mining/industry data was challenging to include this information. However, it is considered to add to the conceptual understanding. The BVDP borehole has not yet reached its final depth and this more insights into the even deeper groundwater system (> 1.2 km) will still be achieved at a later stage.

2 BUSHVELD COMPLEX (BC)

2.1 INTRODUCTION

The Bushveld Igneous Complex is a Paleoproterozoic (2.06 Ga) mafic to ultra-mafic layered sequence, which comprises of pyroxenite, norite and anorthosite assemblages. The complex intruded the northern section of the Transvaal Supergroup. It extends across the Limpopo, North West, Mpumalanga and Gauteng Provinces in South Africa. It covers an area of 65 000 km² and has a vertical thickness of approximately 8 km (Cawthorn et al., 2006). Present-day outcrops of the BIC occur as lobes, known as the Northern, Eastern and Western limbs (Figure 2).

The stratigraphic sequence of the BIC is mainly divided into the underlying Rustenburg Layered Suite and the overlying felsic Bushveld Granite; the Roshoop Granophyre Suite and Lebowa Suite (Jones, 2018) (Figure 3). The igneous complex hosts the world's largest platinum-group elements (PGE), chromium and vanadium reserves (Viljoen and Chürmann, 1998).

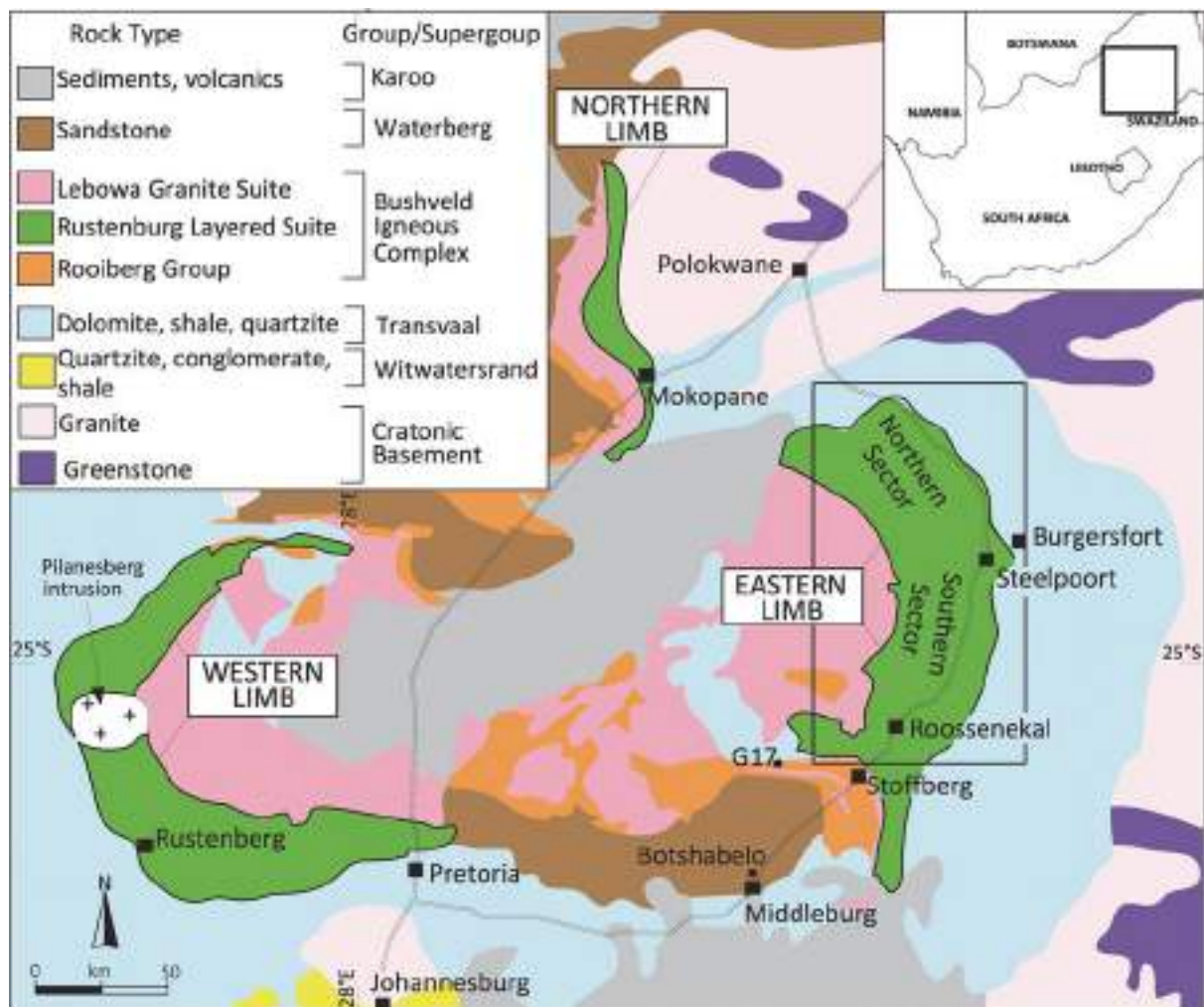


Figure 2 Geology of the Bushveld Igneous Complex (Scoon and Viljoen, 2019). Eastern Limb divided into northern and southern sectors by Scoon and Viljoen (2019) in this map, but others have divided the Eastern Limb into an upper western section, central section and southern section (Figure 5)

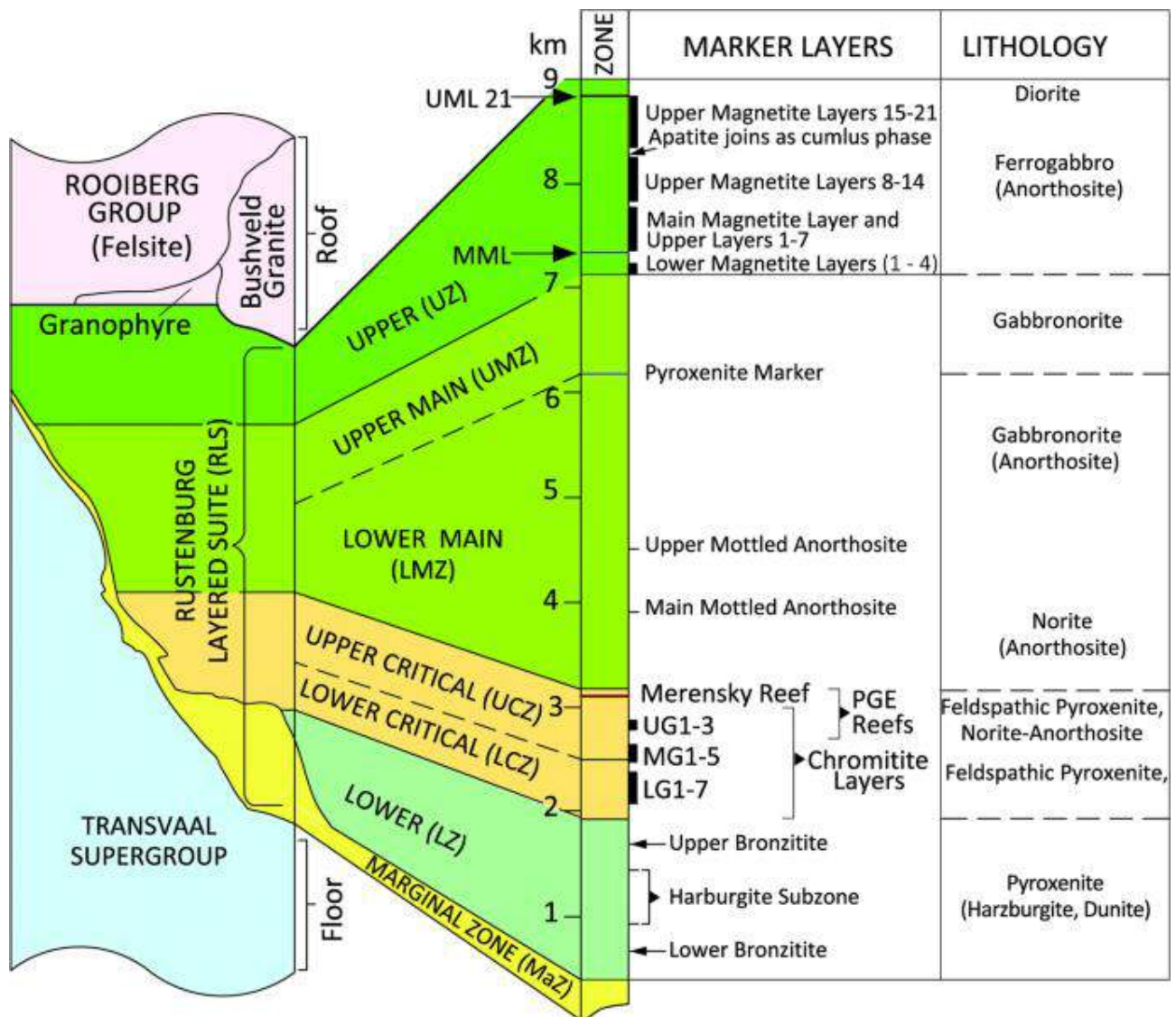


Figure 3 Generalised stratigraphic column for the eastern limb of the Rustenburg Layered Suite showing zones, lithologies, reefs, and marker layers and relationship to the overlying felsic Bushveld lithologies and the underlying Transvaal Supergroup (Scoen and Viljoen, 2019)

2.2 GEOLOGY

2.2.1 Rustenburg Layered Suite

The ultra-mafic Rustenburg Layered Suite (RLS) formed from a series of intrusions. It is subdivided into five zones, based on lithological and geochemical parameters. The zones are the Marginal Zone, Lower Zone, Critical Zone, Main Zone and Upper Zone (Figure 3).

Marginal Zone

The lowest zone of the Rustenburg Layered Suite is the Marginal Zone (MaZ). It primarily consists of norite with minor pyroxenite (Cawthorn et al., 2006). The thickness of this unit varies from zero to hundreds of meters and it is not continuous throughout the suite (Kinnaid, 2005). The zone does not contain material of economic interest (Viljoen and Chürmann, 1998).

Lower Zone

The overlying Lower Zone is comprised of pyroxenite, harzburgites and dunites (Viljoen and Chürmann, 1998). Three subzones are typically identified within the Lower Zone, namely an upper and lower bronzitite subzone (hard layers of orthopyroxenite) with a center harzburgites subzone (less resistant layers of olivine-rich rocks) (Scoon and Viljoen, 2019).

Critical Zone

The Critical Zone is characterised by layers of cyclic chromitite, pyroxenite, norite and anorthosite (Cawthorn et al., 2006). The unit has a lateral thickness of up to 1 500 m (Kinnaird, 2005). The Lower Critical Zone contains LG1 – LG7 and MG1 – MG2 seams (Scoon and Viljoen, 2019). The Upper Critical Zone contains the MG3 – MG5 chromitite layers, UG1 – UG3 seams and the Merensky Reef. The world's largest platinum reserves occur in the Critical Zone, in well-defined layers in the Merensky Reef and UG2. The uppermost unit of the Critical Zone, the Merensky Reefs and Bastard Cyclic Units, mark the transition to the Main Zone (Cawthorn et al., 2006; Scoon and Viljoen, 2019).

Main Zone

The Main Zone comprises of thick units of norite and gabbronorite (Cawthorn et al., 2006). The norites graded upwards into gabbronorites (Viljoen and Chürmann, 1998). The zone includes several mottled anorthosite layers in the lower part and two third into the unit appears a distinctive pyroxenite layer characterised by oikocryst, called the Pyroxenite Marker (Viljoen and Chürmann, 1998). The Pyroxenite Marker is used to subdivide the Main Zone into upper and lower zones (Scoon and Viljoen, 2019). The main zone is > 3 000 m thick and forms approximately half of the RLS (Kinnaird, 2005).

Upper Zone

The base boundary of the Upper Zone is defined by the presence of well-defined magnetite layers of varying thickness (Cawthorn et al., 2006) above the Pyroxenite Marker (Viljoen and Chürmann, 1998). The magnetite layers occur in four groups, namely the Lower layers (1 – 4); Main Magnetite Layer (MML) and Upper layers (1 – 7); Upper layers (8 – 14) and Upper layers (15 – 21) (Scoon and Viljoen, 2019). Vanadium reserves are associated with magnetite layers and the reserves extracted from the East and West limbs of the BIC (Viljoen and Chürmann, 1998). The Main Magnetite Layer (2 m) that is of economic significance, occurs as the fourth layer from the bottom of the Upper Zone and has been strip-mined in the eastern limb over many kilometers (Kinnaird, 2005; Scoon and Viljoen, 2019).

2.2.2 Lebowa Granite Suite

The Lebowa Granite Suite occurs within the inner curve of the west and east limbs of the BIC (Figure 2). It consists of a series of sill-like intrusions that are chemically composed of alkali feldspar, quartz and minor mafic minerals. The principal granite types are Nebo Granites, Makhutso, Klipkloof, Bobbejaankop and Verena Granites (Cawthorn et al., 2006).

2.2.3 Rashoop Granophyre Suite

The Rashoop Granophyre Suite mainly occurs between the Lebowa Granites and overlying the Rooiberg Group (Figure 3). The granophyric rocks represent an acid phase of the Bushveld Complex and are classified as magmatic and metamorphic type. Majority of the granophyric rocks are similar in chemical composition to the uppermost rhyolitic unit of the Rooiberg Group (Cawthorn *et al.*, 2006).

2.2.4 Rooiberg Group

The Rooiberg Group is stratigraphically associated with the Transvaal Supergroup, yet it is petrogenetically linked with the Bushveld Large Igneous Province, including the Bushveld Complex (Lenhardt et al., 2017).

Felsic and some minor basic volcanic events of the Bushveld Igneous Province are persevered in the Rooiberg Group, which has a maximum thickness of 400 m (Cawthorn et al., 2006).

It comprises of four formations, namely Dullstroom, Damwal, Kwaggasnek and Schrikkloof Formations (Figure 4). The three intrusive suites of the Bushveld Complex (RLS, Lebowa Granite Suite and Rashoop Granophyre Suite) disrupt the stratigraphy of the Rooiberg Group. The lowermost Dullstroom Formation of the Rooiberg Group lies unconformably over the Pretoria Group lithology and its lowest section is beneath the Bushveld lithologies. The overlying three formations of the Rooiberg Group and the upper sections of the Dullstroom Formation were detached by the RLS and form the roof of the BIC (Figure 4) (Lenhardt et al., 2017).

The Loskop Formation of the Transvaal Supergroup overlies the Rooiberg Group unconformably, consisting of red shale intercalated with conglomerate in the lower part and impure quartzite in the upper part (Figure 4) (~ 1 100 m) (Lenhardt et al., 2017).

2.2.5 Eastern Limb

The eastern limb of the BIC is separated into three sectors, namely the western, central and southern sector (Seabrook, 2005; Rose, et al., 2011). The division along the limb occurred due to major structural features, faults. The western and central sector are divided by the Wonderkop and Stofpoort faults. The central sector is located above the NE Steelpoort fault, while the southern sector is below (Seabrook, 2005; Rose, et al., 2011) (Figure 5). There are distinct differences in the lithostratigraphy of each sector, more so with placement of the Lower Zone and the Critical Zone along with its chromitites (Scoons and Teigler, 1995).

Southern sector

The Lower Zone is absent throughout the southern sector. The Lower Critical Zone is thin and discrete while the overlying Upper Critical Zone is thinner however well developed and continuous (Scoons and Teigler, 1995). The LG chromitites are either thin or absent, MG chromitites are thick and continuous and the UG chromitites are thick (Scoons and Teigler, 1995). The outcrops in the southern sector show mafic layers dipping at 10 - 15° and intrusions of NNE and WNW striking dykes (Seabrook, 2005). The breakup of Gondwana resulted in the present-day faults, associated fractures and subvertical dyke, trending in the same direction (Sami, 2009).

Western sector

In comparison to the central and southern sector of the eastern limb, the western sector has been relatively poorly studied. The Critical Zone in this sector has an approximate thickness of 250 m, which is thinner in contrast to the central and southern sectors, which have a thickness of 1 500 and 600 m, respectively. West to the Wonderkop fault, there is a significant increase in the dip of the strata. The western sector dips approximately 50 - 60° (Seabrook, 2005).

Central sector

The central sector is the most researched sector of the Eastern limb (Scoons and Teigler, 1995). It dips at approximately 10°, however increases up to 45° northwards, in the Olifants River area (Seabrook, 2005). Unlike in the southern and western sector, the lower zone of the RLS is present and has trough-like features (Seabrook, 2005), which further divide the central sector into three compartments at Olifants River, Clapham and Burgersfort-Winterveld (Figure 5). The Lower Zone is persevered within the trough-like depressions, created by the dome structures of the floor of the complex (Clarke et al., 2009). The Critical Zone is well persevered with thick and contains well-developed LG chromitites, thin and discrete MG chromitites and thin continuous UG chromitites (Scoons and Teigler, 1995).

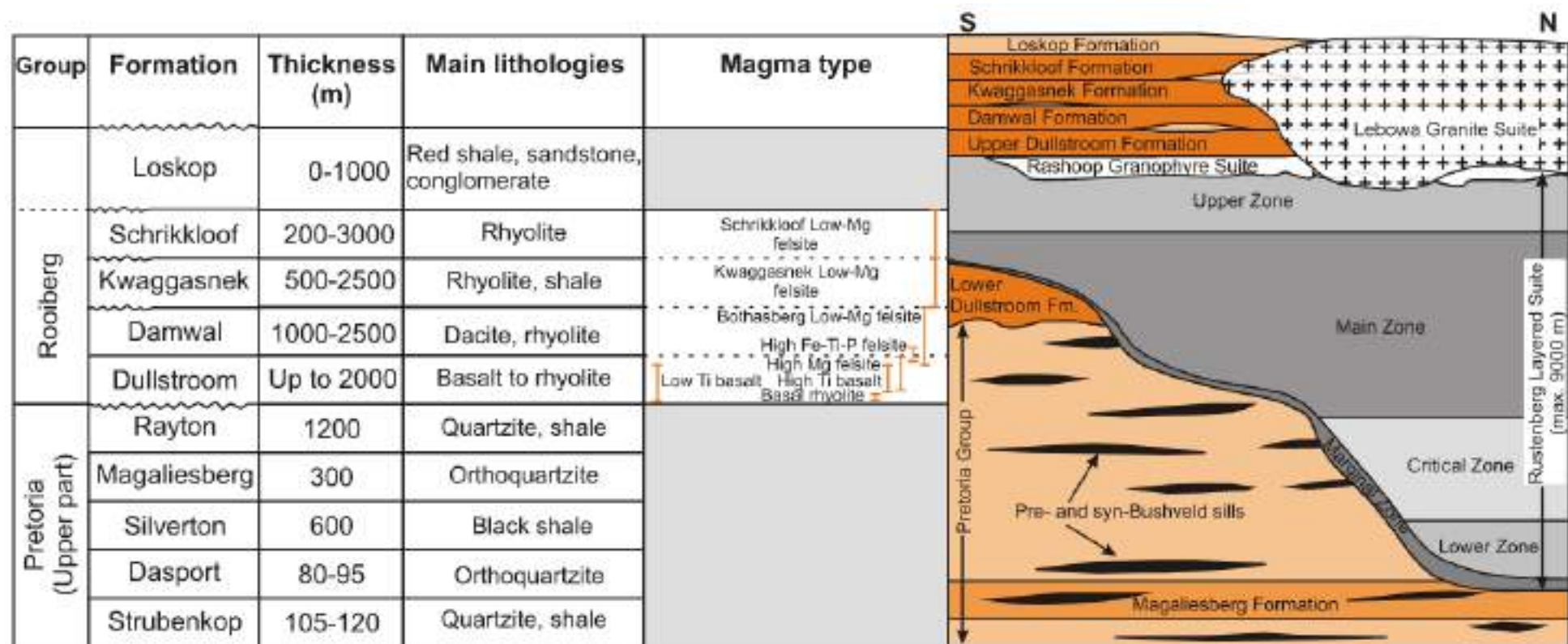


Figure 4 Rooiberg stratigraphy and section indicating the relationship with the underlying Pretoria Group (Transvaal Supergroup), and the intrusions of the Rustenberg Layered Suite and Lebowa Granite Suite (Lenhardt et al., 2017).

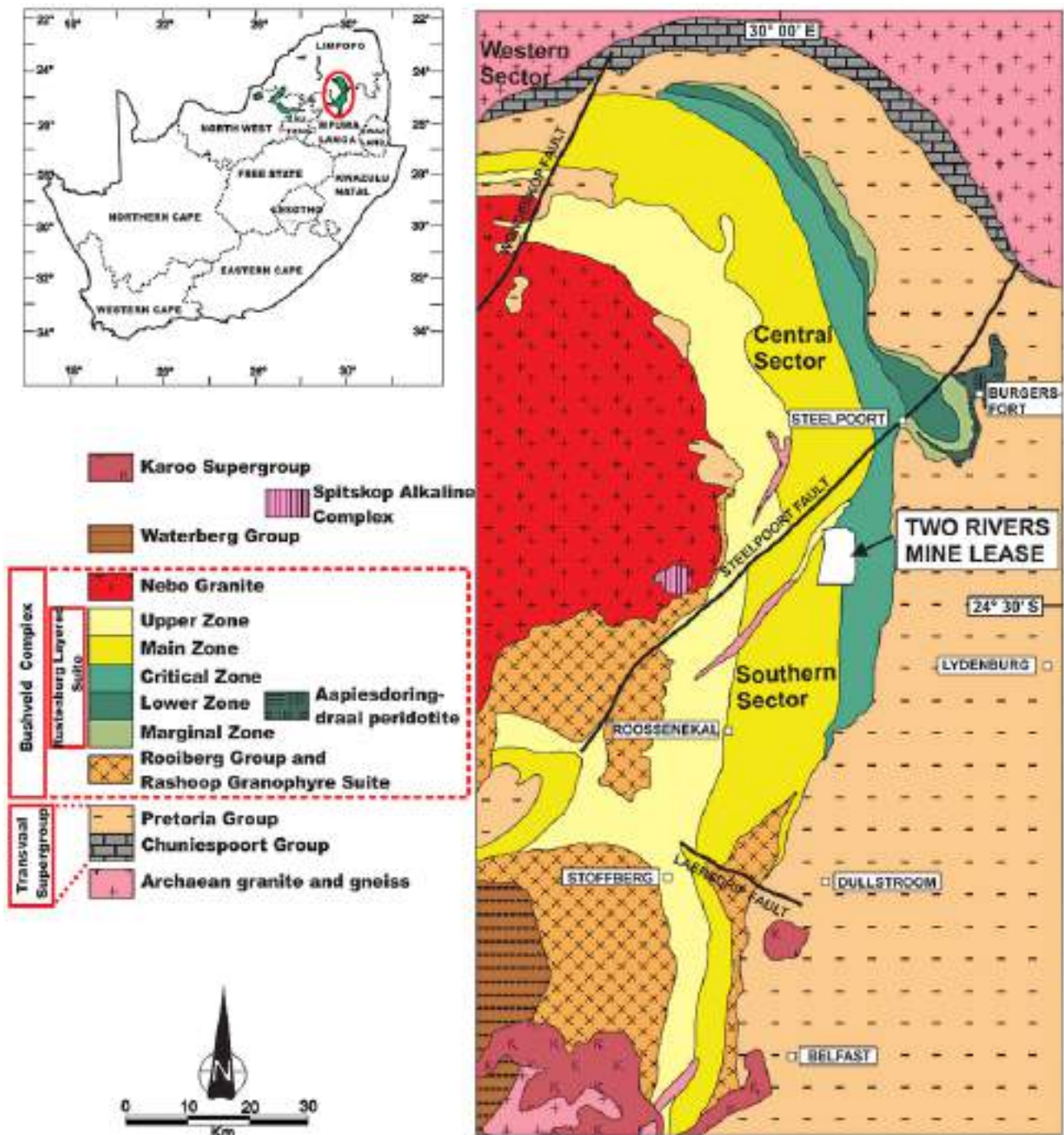


Figure 5 Generalised geological map of the Eastern Limb of the Bushveld Complex, showing the three sectors depicted by Rose et al. (2012) and Seabrook (2005) (Rose et al., 2012). Western Sector above the Wonderkop Fault; Central Sector between the Wonderkop Fault and Steelpoort Lineament to the south; Southern Sector below the Steelpoort Lineament.

The tabular mafic igneous rocks dip at shallow angles to the W or SW in the Eastern Limb of the BIC (Scoon and Viljoen, 2019) (Figure 6). A prominent feature in the north eastern part of the Bushveld Complex are domes comprising of Transvaal Supergroup metasediments, which underwent high-grade metamorphism. The anticlinal structures formed in the Transvaal floor rocks are due to diapirism prompted by pressure stresses from gravitational load and heat from the Bushveld magma (Scoon, 2002). The dome structures are typically NW-SE orientated (Clarke et al., 2009) and mainly occur along the regional lineament, the boundary areas of the Eastern Limb (Scoon, 2002), the Wonderkop and Steelpoort faults. The domes may protrude beyond the Lower Zone.

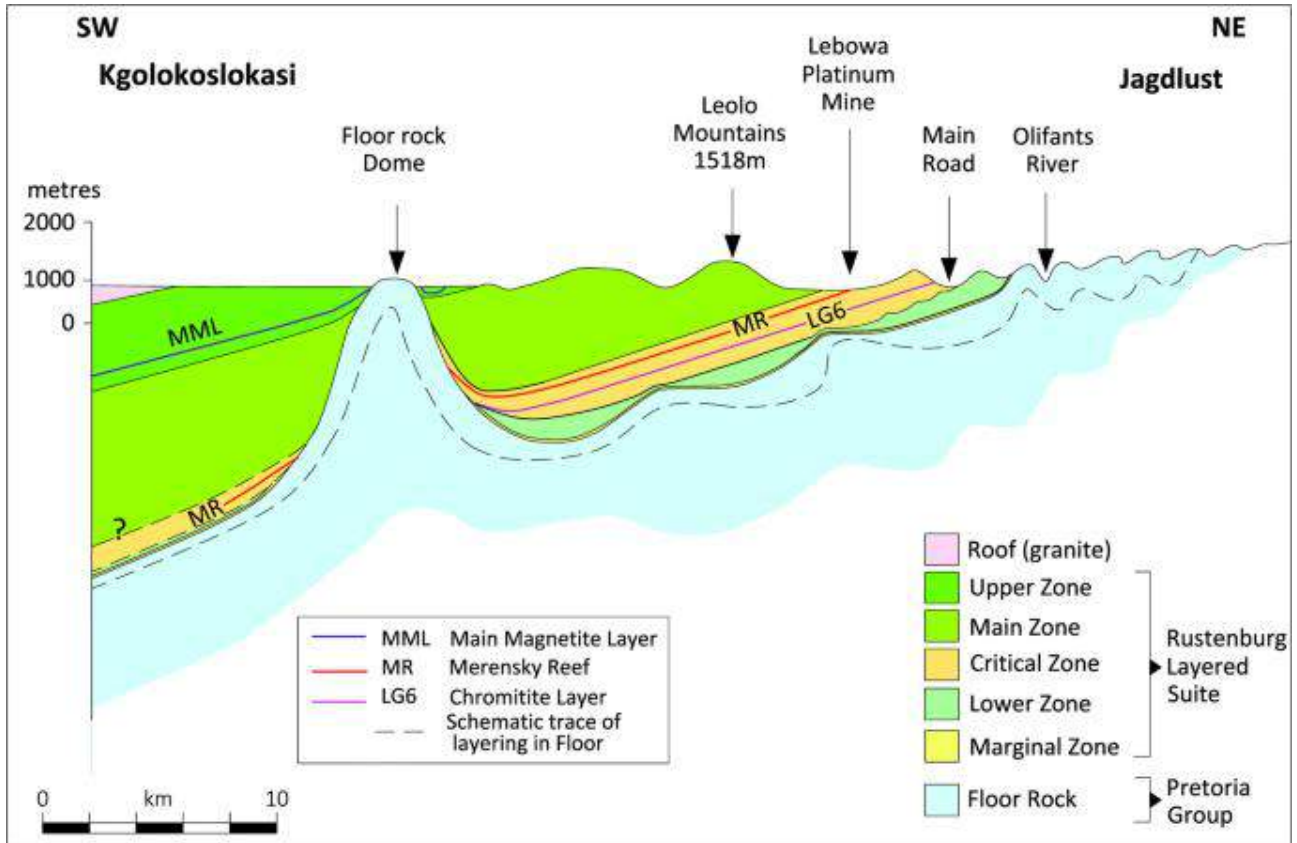


Figure 6 Simplified geological cross-section from Kgolokoslakasi to Jagdlust, showing the irregular floor of the RLS in the northern sector (characterised by Scoon and Viljoen (2019)), also depicted as the central sector of the eastern limb by Rose et al. (2012) (Scoon and Viljoen, 2019). Section line indicated on Figure 7.

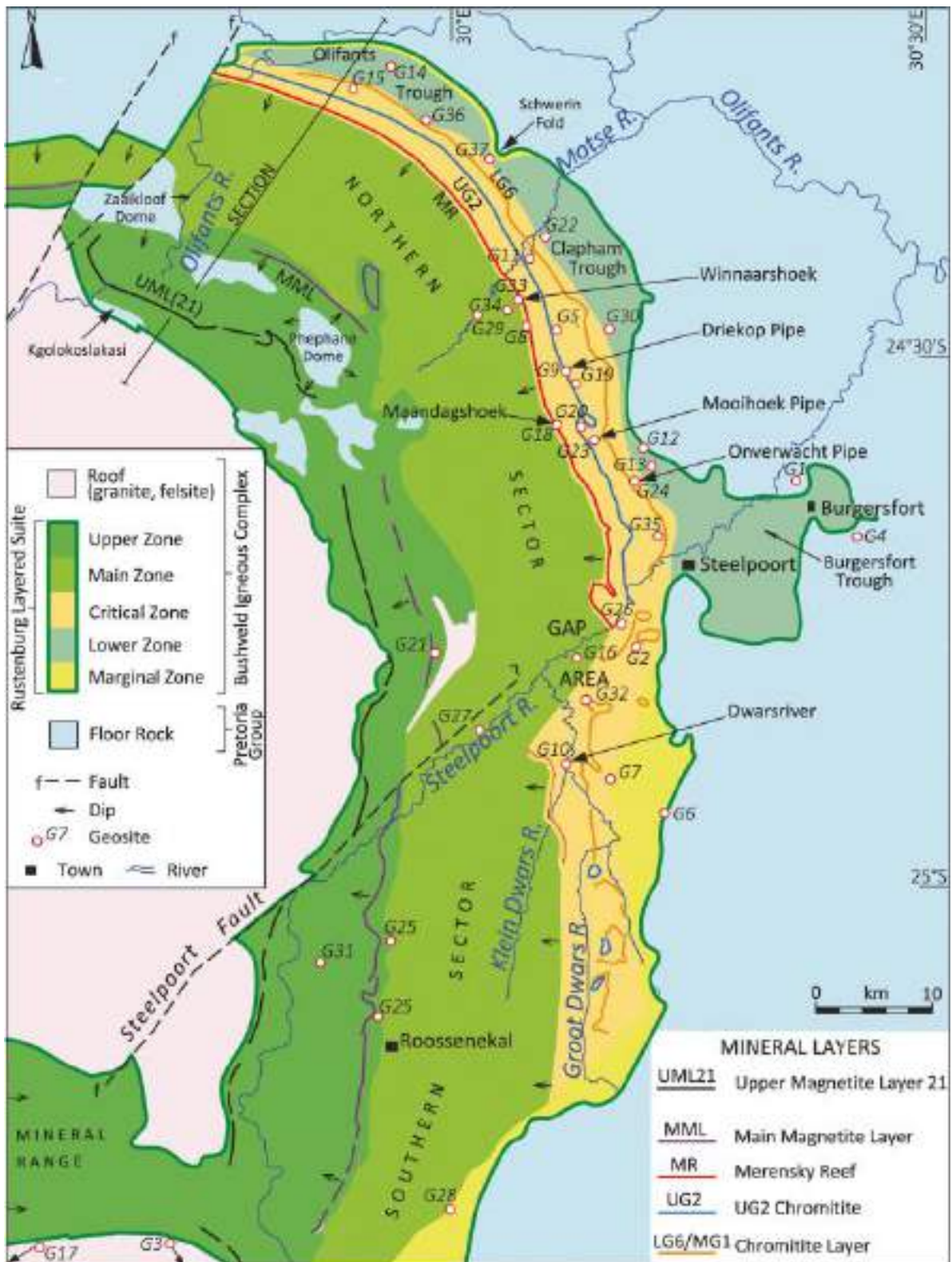


Figure 7 Geological map of the eastern limb of the Bushveld Complex, showing the sectors by Scoon and Viljoen (2019) and the section line from Kgolokoslakasi to Olifants River (Scoon and Viljoen, 2019)

2.3 MINING

More than half of the world's platinum, vanadium and chromium is produced by South Africa's Bushveld Igneous Complex. The minerals that are mostly mined in the Bushveld Igneous Complex are chromite found within chromitite layers in areas of Steelpoort and Rustenburg; magnetite and vanadium found within magnetite layers near Brits and Roossenekal; platinum, related metals and gold found within the Merensky Reef and UG2 near Steelpoort (Figure 8) (McCarthy and Rubidge, 2005).

The Upper Zone of the Bushveld Igneous Complex contain titanium magnetite, where the lower layers are rich in vanadium and the upper layers are rich in titanium. The Critical Zone of the Bushveld Igneous Complex contain important mineral layers such as chromitite and platinum group elements (PGE) which are contained in the UG2 layer and in the Merensky Reef (Scoons and Viljoen, 2016).

Additionally, dimension stone is mined from quarries in the Bushveld Igneous Complex near Belfast and Rustenburg to use as grave stones and building material. Andalusite is mined near Zeerust, Thabazimbi and Steelpoort to use in manufacturing of bricks for lining of furnaces (McCarthy and Rubidge, 2005).

When mining of the Bushveld Igneous Complex first commenced, mining was undertaken on small-scale in the eastern limb but was soon halted due to the lack of resource availability, such as water, in comparison to the Rustenburg area on the western limb. By the 1990's, mining was undertaken from Brits to Thabazimbi, along the arc of the western limb of the Bushveld Igneous Complex. However, UG2 was not mined initially as suitable technology and techniques were not available to extract the platinum (McCarthy and Rubidge, 2005). Mining of UG2 was only undertaken since the 1970's as technology and mining techniques emerged with an increase in demand of platinum and associated metals which lead to the development of new mines in the eastern limb of the Bushveld Igneous Complex (McCarthy and Rubidge, 2005).

2.3.1 Eastern Limb

The eastern limb of the Bushveld Igneous Complex was intruded by zones of ultramafic-mafic rocks which are known as the Upper Zone, Main Zone, Critical Zone, Lower Zone and Marginal Zone (Scoons and Viljoen, 2016). From these zones, the Upper – and Critical Zones are mostly mined for their respective mineralized layers (Scoons and Viljoen, 2016). These mineralized layers contain some of the most sought-after ores which are mined by various chrome and platinum mines in the eastern limb of the Bushveld Igneous Complex (Scoons and Viljoen, 2016) as illustrated in Figure 9 and listed in Table 1 (Historic mines in the eastern limb of the Bushveld Igneous Complex),

Table 2 (Operating mines in the eastern limb of the Bushveld Igneous Complex) and (Proposed Exploration projects in the eastern limb of the Bushveld Igneous Complex). Some of these mines situated in or in close proximity of the eastern limb of Bushveld Igneous Complex are discussed.

Everest platinum mine is an opencast and underground mine situated in the southern portion of the eastern limb of the Bushveld Igneous Complex, which is situated near Lydenburg, in the Mpumalanga Province. The mine and associated assets were obtained by Northam Platinum Holdings Limited in February 2015 from Aquarius Platinum South Africa (Pty) Ltd, which enabled the development of the **Booyssendal South mine** which is owned by Northam Platinum Holdings Limited (Northam Platinum Holdings Limited, 2021).

Mapochs mine is an underground mine situated west of Booyssendal South mine and Everest platinum mine and is owned by Ghofa Trading (Pty) Ltd. Dimension stone is mostly mined at the Mapochs mine (Department of Mineral Resources, 2022).

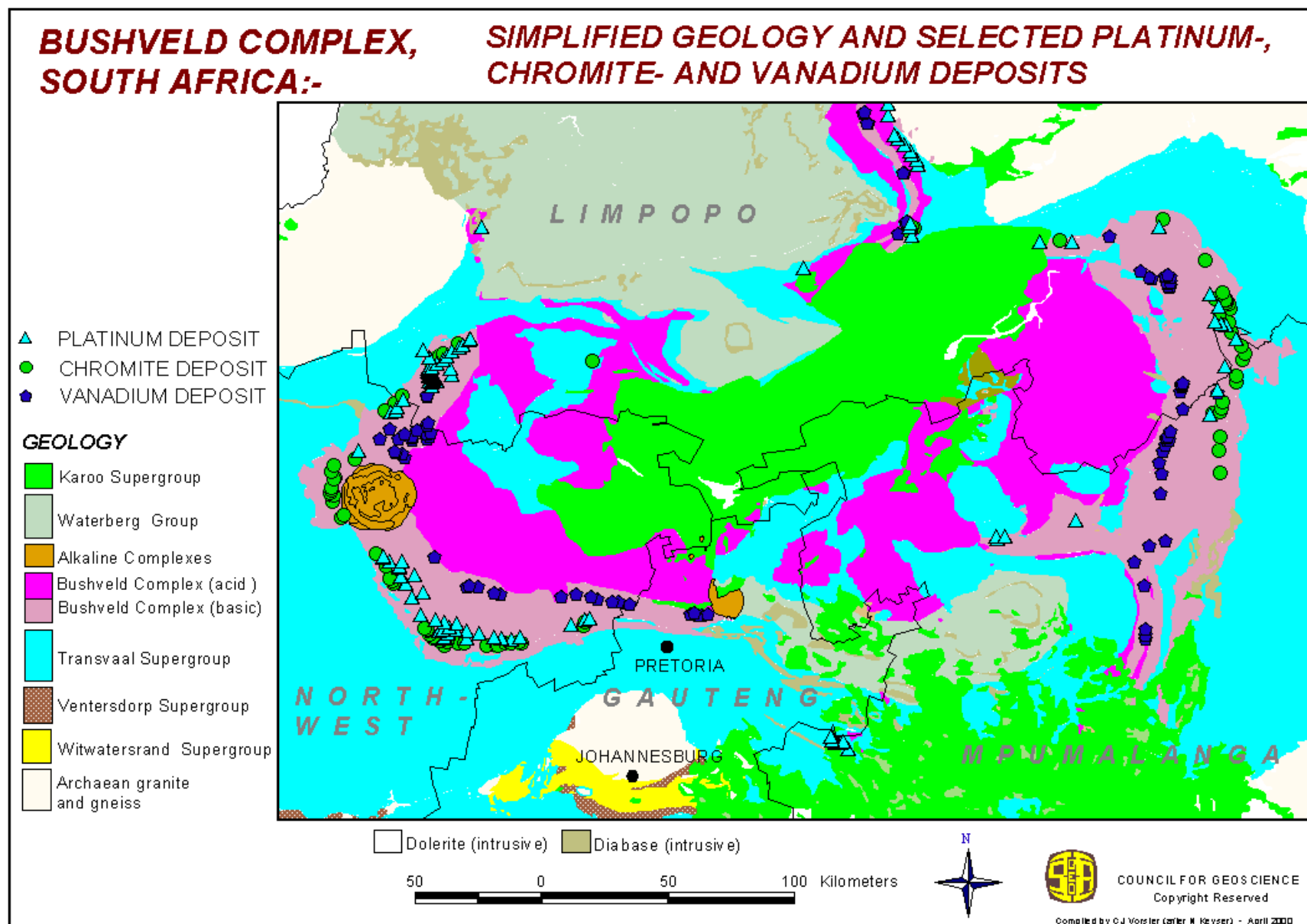


Figure 8 Mineral deposits that are mostly mined in the Bushveld Igneous Complex (Council for Geoscience, 2000)

Figure 9 Locality Map of operating - and historic mines as well as proposed exploration projects in the eastern limb of the Bushveld Igneous Complex

Table 1 Historic mine information in the eastern limb of the Bushveld Igneous Complex (DMR, 2022; Fourie et al., 2020)

Mine	Type of Mine	Depth of Mine	Mine Owner	Contact Person	Contact Details
Everest Platinum Mine	Opencast & Underground	>800 m	Previous owner - Aquarius Platinum South Africa (Pty) Ltd New owner – Northam Platinum Holdings Ltd	DS Smith (Lead competent person) & PB Beale (Company Secretary)	Mine: (014) 536 4118 / 086 590 7422 Lead competent person: damian.smith@norplats.co.za Company secretary: trish.beale@norplats.co.za

Table 2. Operating mine information in the Easter Limb on the Bushveld Igneous Complex (DMR, 2022; Fourie et al., 2020; ASSORE, 2016; Anglo American Platinum, 2014; Ivanhoe Mines, 2022; Marula, 2018; Burger et al., 2016; Du Toit and Scholes, 2018; Ramushu et al., 2018; Mining Data Solution Online, 2022; Sibanye-Stillwater, 2020)

Mine	Type of Mine	Depth of Mine	Mine Owner	Mining House	Contact Person	Contact Details
Akanani Mine	Underground		Sibanye-Stillwater as part of Lonmin transaction		Vongani Mashaba	Mine: (015) 491 8146
Annesley Andalusite Mine	Opencast		Imerys SA (Pty) Ltd			Mine: (012) 643 5880 / (012) 643 5961
Attaclay (Pty) Ltd	Opencast		Elbroc Mining Products (Pty) Ltd			Mine: (011) 392 4025 / (011) 392 4021
Blueridge Mine	Underground		Joint Venture Imbani Platinum & Sibanye-Stillwater			Mine: (014) 495 1161/ 086 669 0386
Bokoni Platinum Mines	Underground	650 m	Atlatsa Corporation & Anglo American Platinum (AAP)	Rustenburg Platinum Mines (RPM)		Mine: (051) 620 0229 / (051) 620 0196
Booyse dal Mine North	Opencast		Northam Platinum Holdings Ltd	Booyse dal Platinum (Pty)	DS Smith (Lead competent person) & PB Beale (Company secretary)	Mine: (014) 784 3200 / (014) 785 1411 Lead competent person: damian.smith@norplats.co.za Company secretary: trish.beale@norplats.co.za

Research-based deep drilling in the Bushveld Igneous Complex

Mine	Type of Mine	Depth of Mine	Mine Owner	Mining House	Contact Person	Contact Details
Booyssendal South	Mine Opencast	>800 m	Northam Platinum Holdings Ltd	Booyssendal Platinum (Pty)	DS Smith (Lead competent person) & PB Beale (Company Secretary)	Mine: (014) 784 3200 / (014) 785 1411 Lead competent person: damian.smith@norplats.co.za Company secretary: trish.beale@norplats.co.za
De Groote Boom Chrome Mine	Opencast		De Groote Boom Minerals (Pty) Ltd			Mine: 082 906 3299
Der Brochen Mine	Underground		Anglo American Platinum (AAP)	Rustenburg Platinum Mines (RPM)	Dr Gordon Smith	Gordon.smith@angloamerican.com
Dilokong Chrome Mine (Pty) Ltd	Underground		ASA Metals (Pty) Ltd			Mine: (013) 230 7600 / (013) 230 7754
Dwarsriver Chrome Mine (DCM) (Assmang Mine)	Opencast & Underground		ASSORE (Pty) Ltd		Pius Monyela	Mine: (013) 230 5300 / (013) 230 5318
Eastern Chrome Mines (Steelpoort, Doornbosch, Montrose (new name – Lannex), Tweefontein)	Underground	>1000 m	Samancor Chrome Ltd			Mine: (013) 230 7199 / (013) 230 7000 (013) 230 7103
Helena Mine	Underground		Glencore			Mine: (013) 230 6600 / (013) 230 6502
Inca Limestone Mokopane Mining	Opencast		Inca Mining (Pty) Ltd			Mine: (015) 667 0536 / (051) 667 0539
Ivanplats Limited (Pty) Ltd	Opencast	780 m	Ivanhoe (Pty) Ltd			Mine: (051) 491 0600
Klipspringer Diamond Mine	Opencast & Underground		Mwana Africa			Mine: (011) 883 9550/ (011) 883 2146
Leo Limestone	Opencast		H Pistorius & Kie (Pty) Ltd			Mine: (012) 342 1075 / (012) 342 1199
Lonmin Mine	Underground		Sibanye-Stillwater		Doreen Bogale	Mine: (014) 571 2000 /

Research-based deep drilling in the Bushveld Igneous Complex

Mine	Type of Mine	Depth of Mine	Mine Owner	Mining House	Contact Person	Contact Details
						(014) 536 4516
Magareng Mine	Opencast & Underground	750 m	Glencore			Mine: (013) 230 6600 / (013) 230 6502
Mapochs Mine	Opencast		Ghofa Trading (Pty) Ltd			Mine: 083 547 9642 / (013) 273 5000
Marula Platinum Mine	Underground	770 m	Impala Platinum Holdings Limited	Implats Holdings Company	Johan Theron (Group Executive)	Mine: (011) 731 9000/ (013) 214 6021 Group Executive: (011) 731 9013
Modikwa Mine	Platinum Underground	450 m	African Rainbow Minerals (ARM) & Anglo American Platinum (AAP)		Wimpy Britz	Mine: (013) 230 2084 / 086 661 1680
Mogalakwena Platinum Mine	Opencast	45 – 245 m	Anglo American Platinum (AAP)		Hendrik van Niekerk (Mine Manager) & Richard Cox	Mine: (015) 418 2717 / (051) 418 3101 Mine Manager: linkedin.com/in/hendrik-van-niekerk-46b7002a
Mototolo Mine	Platinum Underground	450 m	Glencore Kagiso Tiso Platinum Partnership & Anglo-American Platinum (AAP)	Rustenburg Platinum Mines (RPM)	Trevor Raymond	Mine: (013) 230 5588 / (013) 230 5588/ 082 654 8467
North Block Complex (NBC) Glisa Mine	Opencast & Underground	>60 m	Universal Coal and Energy Holdings South Africa (Pty) Ltd (UCEHSA) & Ndalamo Resources (Pty) Ltd			Mine: (010) 900 0349
Nkomati Nickel Mine	Underground		African Rainbow Minerals (ARM) & Norilsk Nicke			Mine: (013) 712 8200 / (013) 712 8300
Nkwe Platinum Mine	Opencast		Zijin Mining Group Co. Limited			Mine: (010) 591 3989
Smokey Hills (Phokatab) Platinum Mine	Underground	25 m	Phokathaba Platinum (Pty) Ltd			Mine: 079 160 1352 / (013) 230 7450
Spitsvle	Opencast		BCR Minerals (Pty) Ltd			Mine: (011) 467 5793 / 086 671 0418
Thorncliffe Mine	Underground	>500 m	Glencore	Xstrara Alloys	Larnay Friedlander (Glencore Mine Procurement)	Mine: (013) 230 6500 / (013) 230 6502

Research-based deep drilling in the Bushveld Igneous Complex

Mine	Type of Mine	Depth of Mine	Mine Owner	Mining House	Contact Person	Contact Details
					Vulela Makuni (Mine Manager)	linkedin.com/in/larnay-friedlander-67b19495
Twickenham Mine	Platinum Opencast & Underground	1181 m	Anglo American Platinum (AAP)			Mine: (013) 231 9266
Two Rivers Mine	Platinum Underground	935 m	African Rainbow Minerals (ARM) & Impala Platinum	Implats Holdings Company	JJ Joubert (General Manager)	Mine: (013) 230 2800 / 086 594 7739

Table 3 Proposed exploration projects in the eastern limb of the Bushveld Igneous Complex (DMS, 2022; Sibanye-Stillwater, 2020).

Mine	Type of Mine	Depth of Mine	Mine Owner	Contact Person	Contact Details
Ga-Phasha Project	N/A	N/A	Joint Venture between Anglo American Platinum (AAP) & Atlatza Resources Corporation		
Zondernaam Mining	Underground	N/A	Joint Venture between wholly-held subsidiary Aquarius Platinum (SA) Corporate Services (Pty) Ltd & Bakgaga Mining		

Akanani mine is situated near Mokopane, in the Limpopo Province and is technically situated in the northern limb of the Bushveld Igneous Complex but have been included as an operational platinum mine in the eastern limb as the mine is associated with the underground Lonmin mine as the ownership of the Akanani mine was obtained via the ownership of the **Lonmin mine** by Sibanye-Stillwater in 2019 (Sibanye-Stillwater, 2020). The ore is situated in the Upper Critical Zone which is approximately 750 m deep, where the P2 unit is expected to be of higher grade than the P1 unit (Sibanye-Stillwater, 2020).

Sibanye-Stillwater is the owner in a joint venture with Imbani Platinum of another opencast platinum mine on the south of the eastern limb of the Bushveld Igneous Complex known as the **Blueridge mine**. According to the SFA (Oxford), 2022, the mine is termed a mothballed mine, which indicates that physical mining has been ceased and that the mine is currently under care and maintenance until physical mining is undertaken in the future again. This was applied to the Blueridge mine due to depressed PGM prices (Sibanye-Stillwater, 2020). The term mothballed can be applied to the following mines which include Bokoni mine, Twickenham mine and Smokey Hills mine as illustrated in Figure 10.

Bokoni mine is an underground platinum mine situated in the northern portion of the eastern limb of the Bushveld Igneous Complex. The mine is owned in a joint venture by Atlantis Resources Corporation and Anglo American Platinum (AAP) (Rustenburg Platinum Mines (RPM)). Anglo American Platinum (AAP) owns

Twickenham mine which is an opencast and underground platinum mine currently under maintenance and care.

Annesley Andalusite mine is an opencast andalusite mine situated in the northern portion of the eastern limb of the Bushveld Igneous Complex, approximately north-west of the Twickenham mine. The andalusite mine is owned by Imerys SA (Pty) Ltd.

Der Brochen mine is an underground platinum mine situated on the southern portion of the eastern limb of the Bushveld Igneous Complex in close proximity to Boosyendal South mine. Der Brochen mine is owned by Anglo American Platinum (Rustenburg Platinum Mines (RPM)) and is currently in operation. Anglo American Platinum (AAP) and African Rainbow Minerals (ARM) owns **Modikwa platinum mine** in a joint venture. The underground mine is situated near Burgersfort in the Limpopo Province.

Anglo American Platinum (AAP) and Glencore Kagiso Tiso Platinum Partnership owns **Mototolo platinum underground mine**. The mine is situated in the southern portion of the eastern limb of the Bushveld Igneous Complex near Burgersfort in the Limpopo Province.

Mogalakwena platinum mine is an opencast mine situated near Mokopane in the Limpopo Province. The mine is owned by Anglo American Platinum (AAP) and is technically situated in the northern limb of the Bushveld Igneous Complex.

Ivanplats Limited (Pty) Ltd mine is an opencast platinum mine situated in the northern limb of the Bushveld Igneous Complex approximately between Mogalakwena platinum mine and Akanani mine.

Three additional mines found in close proximity of the northern limb of the Bushveld Igneous Complex are the **Klipspringer Diamond mine** which is an opencast and underground diamond mine owned by Mwana Africa; **Inca Limestone Mokopane mine** which is an opencast limestone mine owned by Inca Mining (Pty) Ltd; and, **Leo Limestone mine** which is an opencast limestone mine.

Smokey Hills mine, also known as Phokatab platinum mine, is situated near Burgersfort in the Limpopo Province. This underground mine is owned by Phokathaba Platinum (Pty) Ltd where mining is currently closed until future notice.

Two mines situated north to north-east of the Smokey Hills mine are the **Attacloy (Pty) Ltd opencast mine** and **Dilokong Chrome underground mine**. Bentonite and attapulgite are both commodities mined by the

Attaclay mine (Department of Mineral Resources, 2022). Chrome is mostly mined by the Dilokong Chrome mine (Department of Mineral Resources, 2022).

The **Nkwe platinum mine** is situated south of the Smokey Hills mine. The mine is an opencast platinum mine which is owned by Zijin Mining Group Co. Limited. African Rainbow Minerals (ARM) and Norilsk Nickel owns **Nkomati Nickel mine** which is situated south of the eastern limb of the Bushveld Igneous Complex.

North block Complex (NBC) Glisa mine is situated west of the Nkomati Nickel mine, which is south of the eastern limb of the Bushveld Igneous Complex. The mine is both an opencast and underground mine. Both coal and bituminous commodities are mined at the NBC Glisa mine (Department of Mineral Resources, 2022).

Two Rivers platinum mine is an underground mine which is situated in the southern portion of the eastern limb of the Bushveld Igneous Complex. The mine is owned in a joint venture by African Rainbow Minerals (ARM) and Impala Platinum Holdings (Implats Holdings Company).

De Groote Boom Chrome mine and **Dwarsriver Chrome mine**, also known as Assmang mine, are two mines found in close proximity to the Two Rivers platinum mine. The De Groote Boom Chrome mine is an opencast chrome mine which is owned by De Groote Boom Minerals (Pty) Ltd, whereas Dwarsriver Chrome mine is both an opencast and underground mine which is owned by ASSORE (Pty) Ltd.

Impala Platinum Holdings (Implats Holdings Company) owns an underground platinum mine situated in the northern portion of the eastern limb of the Bushveld Igneous Complex known as the **Marula platinum mine**. The UG2 Reef and Merensky Reef are both mined for platinum at the Marula mine (Marula, 2018).

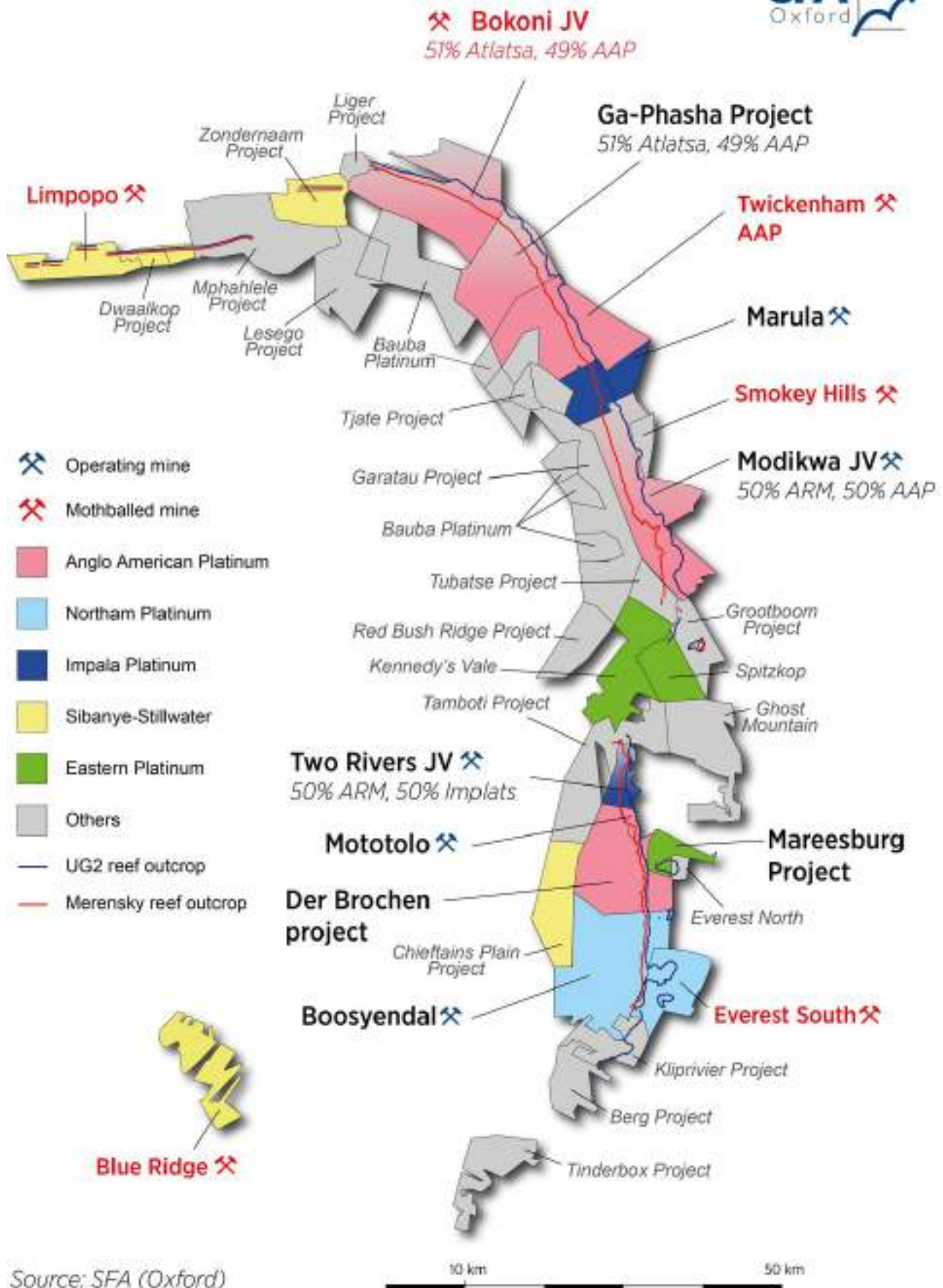
Glencore owns the **Helena mine**, **Magareng mine** and **Thorncliffe mine** which are all situated in the southern portion of the eastern limb of the Bushveld Igneous Complex in close proximity to each other in the Lydenburg district. Chrome is mostly mined at these three mines owned by Glencore (Department of Mineral Resources, 2022).

Eastern chrome mines such as Steelpoort; Doornboch; Lannex, previously known as Montrose; and Tweefontein are situated in the northern portion of the eastern limb of the Bushveld Igneous Complex. These Eastern chrome mines are owned by Samancor Chrome Ltd.

Spitsvlei mine is situated south of the Eastern chrome mines in the southern portion of the eastern limb of the Bushveld Igneous Complex in the Lydenburg district. The opencast chrome mine is owned by BCR Minerals (Pty) Ltd.

The **Ga-Phasha mining project** is owned by a joint venture between Anglo American Platinum (AAP) and Atlatla Resources Corporation. The platinum mining project adjoins Twickenham mine and Bokoni mine to the south and north respectively and is situated in the northern portion of the eastern limb of the Bushveld Igneous Complex.

The **Zondernaam mining project** is situated northwest of the eastern limb of the Bushveld Igneous Complex and is owned by a joint venture between Aquarius Platinum (SA) Corporate Services (Pty) Ltd and Bakgaga Mining. The Zondernaam mining project is currently in the early stages of exploration in the northern portion of the eastern limb of the Bushveld Igneous Complex (Sibanye-Stillwater, 2020). The two main layers that will be targeted for ore extraction will be UG2 Reef and Merensky Reef, however due to the fact that the ores do not outcrop in this area, the project is not currently being considered for development (Sibanye-Stillwater, 2020).



Source: SFA (Oxford)

Figure 10 Operational and mothballed mines in the eastern limb of the Bushveld Igneous Complex (SFA (Oxford), 2022)

2.4 GROUNDWATER

The typical aquifer system in the Bushveld Igneous Complex can be described as a shallow intergranular aquifer situated in a weathered zone which is underlain by a semi-confined deep fractured bedrock (crystalline rock) aquifer (Titus et al., 2009). Titus et al. (2009) noted that there is a possibility that the shallow weathered aquifers might be connected to alluvial river aquifers. Gebrekristos and Cheshire (2012) described three types of aquifers in the Bushveld Complex, now explicitly including alluvial aquifers in the areas of river courses with the upper weathered aquifers and underlying fractured aquifers.

Overall, groundwater in the Bushveld Igneous Complex flows through a series of interconnected fractures and the typical yield associated with currently utilised aquifers of the Bushveld Igneous Complex can be described as low to moderate with exceptions of some aquifers (Lourens, 2013; Fourie et al., 2020). Lourens (2013) reported borehole yields of less than 2 l/s for the Bushveld granites and Rooiberg Group; and borehole yields generally ranging from 0.5 to 5 l/s for the Rustenburg Layered Suite. The BIC is reported to generally have good water quality according to analysis performed by Lourens (2013).

When siting traditional (shallow) boreholes for water supply, Lourens (2013) recommends targeting the transition zone between the upper weathered aquifer and underlying composite rock; as well as the contact zone between intrusive dykes and host rock; faults with associated shear and fracture zones; and intrusive carbonite complexes. For the deeper fractured groundwater system, faults and dyke contact zones are recommended as drilling targets (Lourens, 2013).

2.4.1 Alluvial aquifers

The alluvial aquifers of the Bushveld Complex are the same as alluvial aquifers in other parts of the country, where deposited gravel, sand, silt or clay comprise the unconsolidated material of these aquifers. These aquifers are thus laterally discontinuous and localised around riverbanks and floodplains. Alluvial aquifers tend to be unconfined and high yielding when interacting directly with surface water bodies. The particle size of the unconsolidated material is the limiting factor on permeability, and clay deposits would form low-yielding areas within these aquifers. Alluvial aquifers of the Bushveld Complex are associated with an Mg-Ca-HCO₃-Cl water type according to analysis by Dalasile and Abiye (2018) (Gebrekristos and Cheshire, 2012; Dalasile and Abiye, 2018).

2.4.2 Weathered bedrock aquifers

The shallow intergranular weathered aquifers consist of a weathered overburden consisting of saprolite and saprock. This weathered overburden varies in thickness of approximately 12 – 50 m, a transmissivity that varies from low to moderate and a high storativity. The shape of the shallow aquifer is therefore determined through the degree of chemical weathering. These aquifers generally have boreholes with a yield of 0.5 l/s to 1 l/s, although some boreholes in these shallow aquifers can have a yield of 2 l/s (Titus et al., 2009; Lourens, 2013).

Shallow weathered aquifers are associated with an Mg-Ca-HCO₃ type water according to analysis performed by Titus et al. (2009). When river courses are present in the area, the alluvial material from the rivers overlies or simply replaces this weathered overburden. These shallow weathered aquifers, in combination with the alluvial aquifers, traditionally supply water for irrigational and domestic purposes in the Bushveld Igneous Complex (Titus et al., 2009).

2.4.3 Fractured bedrock aquifers

Crystalline rocks are practically impermeable without weathering or fracturing. The occurrence of groundwater and hydraulic conductivity are associated with interconnected fracture network, which are structurally controlled hence hydraulic properties are heterogeneous (Greenbaum, 1992; Titus et al., 2009).

The semi-confined deep fractured bedrock aquifer consists of anorthosite, pyroxenes and fractured norites that underlay the shallow weathered aquifer (Titus et al., 2009). According to Titus et al. (2009), the groundwater flows from the weathered overburden to the deep fractured aquifers. These deep fractured bedrock aquifers commonly have high Na-Cl water facies, which is due to the long residence time (Titus et al., 2009; Fourie et al. 2020).

The water type for samples analysed by Titus et al. (2009) from the deep mine fissure inflows were generally classified as Na-Ca-Cl or Ca-Na-Cl water types. The hydrochemical characteristics of the deep mine inflows include higher levels of total dissolved solids (TDS) – ranging from 350 – 100 mg/l. The increasing TDS content in the water is also indicative of water with a longer residence time (Titus et al., 2009).

These fractured crystalline bedrock aquifers generally have low porosity and permeability, with high hydraulic conductivities only along fractures and fracture networks (Lenkoe-Magagula, 2013). Typically, little groundwater is found in the semi-confined deeper unweather rocks of the Bushveld Igneous Complex due to the low storage capacity of the fractures and matrix associated with the deeper aquifers (Fourie et al. 2020).

The degree of weathering and fracturing of crystalline rocks varies with different mineral composition, texture and granularity which is associated with the tendency to form aquifers (Greenbaum, 1992; Gebrekristos and Cheshire, 2012). For instance, the degree of weathering UG2 pyroxenite is greater than the surrounding norites and anorthosites (Gebrekristos and Cheshire, 2012). The UG2 pyroxenite layer associated with the critical zone of the Bushveld Igneous Complex can be described as the most important aquifer associated with mining activities in the western limb. This is due to the high yield associated with the dipping pyroxenite geological unit's bedding planes and mineralogical composition which weathers more than the overlying and underlying geological units, due to preferential chemical and physical weathering conditions (Gebrekristos and Cheshire, 2012). The weathering increases the effective porosity and permeability of the pyroxenite layer, which is suitable for groundwater flow and storage (Gebrekristos and Cheshire, 2012).

On the western limb of the BIC, significant groundwater inflows into mine workings have been recorded where intersecting the UG2 pyroxenite layer through unsealed exploration boreholes or mine roof bolts penetrating the pyroxenite layer from underneath (Gebrekristos and Cheshire, 2012). The UG2 pyroxenite layer is a feldspathic pyroxenite containing a series of chromitite layers, namely UG2S (stringers), UG2L (leader) and UG2. Potential groundwater storage is within the UG2S (stringers) zone due to weathering along the chromitite and pyroxenite layers. Additionally, some potential groundwater storage in the joints overlying the UG2 pyroxenite, as well as in the UG2 pyroxenite-anorthosite contact zone and lower part of the anorthosite (Gebrekristos and Cheshire, 2012).

Gebrekristos and Cheshire (2012) developed a conceptual model to explain the groundwater inflows into underground mine workings from the UG2 pyroxenite layer (Figure 11). The conceptual model includes recharge from the surface where these layer dips upwards, with addition recharge through any potential vertical or sub-vertical fractures connecting the layer at depth to surface.

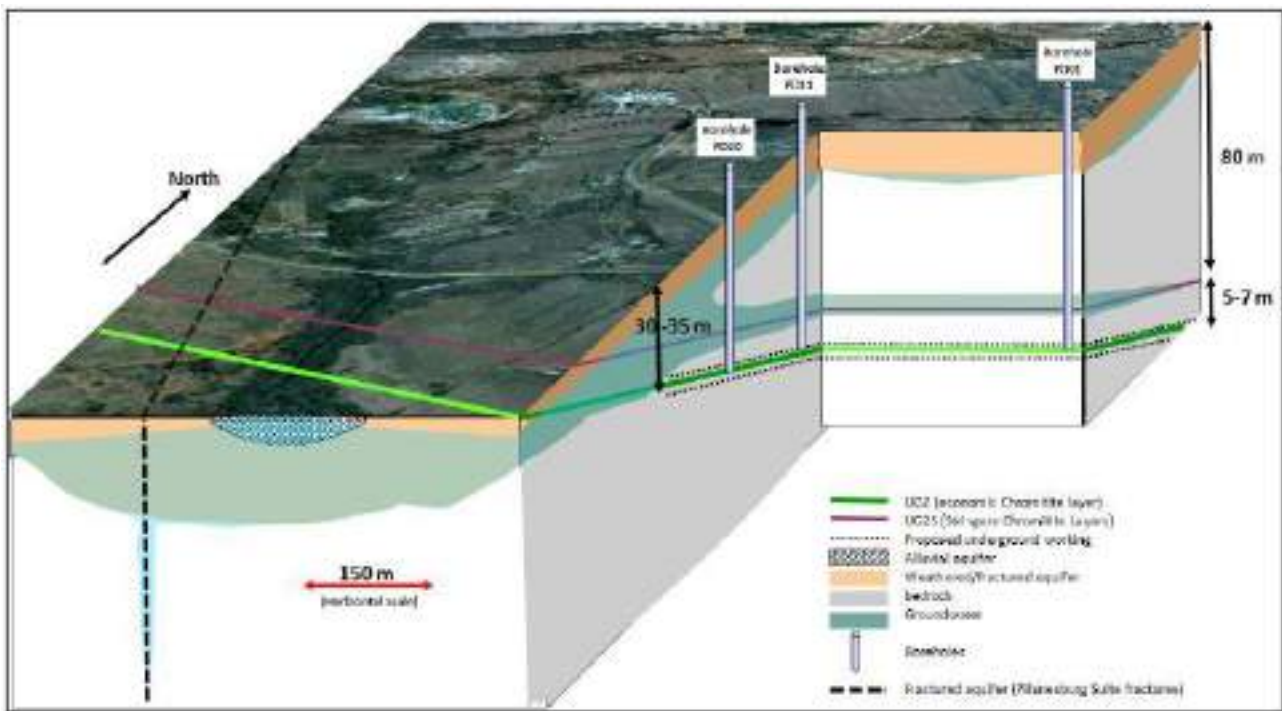


Figure 11 Simplified hydrogeological conceptual model of the Bushveld Complex illustrating the pyroxenite aquifer (Gebrekristos and Cheshire, 2012)

Gebrekristos and Cheshire (2012) characterised the hydraulic properties of the UG2 pyroxenite, in the Critical Zone of the BIC western limb. The transmissivity of the UG2 pyroxenite aquifer at 40 mbgl is $\pm 10 \text{ m}^2/\text{d}$ and at 50 mbgl is equal to $1 \text{ m}^2/\text{d}$, whereas the transmissivity at 80 mbgl in the surrounding norites and anorthosites is approximately zero. The blow yield was found to be greater in shallow depths where weathering is higher, suggesting that the hydraulic conductivity in the overburden decreases with depth and this is due to an increase in stress from the overburden (Gebrekristos and Cheshire, 2012).

2.4.4 Eastern Limb

The Eastern Limb of the Bushveld Igneous Complex is mainly underlain by the Rustenburg Layered Suite, which comprises of pyroxenite, anorthosite and norite. A statistical summary, conducted by Holland (2012), of the regional groundwater characteristics in the eastern Bushveld Complex reported the average water supply borehole depth of 68 mbgl ($n = 1847$); average water level of 13.2 mbgl ($n = 1432$); average water strike depth of 33.2 mbgl ($n = 307$); and average weathering depth of 17.3 mbgl ($n = 386$) (Holland, 2012).

Various mines in the western limb of the Bushveld Igneous Complex experience challenges associated with the groundwater such as the ingress of large volumes of groundwater infiltrating mines (Dalasile and Abiye, 2018). According to Dalasile and Abiye (2018), mines associated with the eastern limb of the Bushveld Igneous Complex seldom experience such groundwater ingress problems in comparison to groundwater in mining in the western limb. This is thought to be due to inconsistency of the hydraulic parameters associated with the Bushveld Igneous Complex due to the geological nature and degree of weathering of the aquifers (Dalasile and Abiye, 2018). This phenomenon could also be due to the fact that fracture frequency decreases with the increase of depth (Dalasile and Abiye, 2018).

Case Study – Tweefontein farm (Dalasile and Abiye, 2018)

Dalasile (2018) studied the geological features in relation to the groundwater system of Tweefontein 360KT farm, in the eastern limb of the BIC. Aquifers identified from field observations include a clayey alluvial aquifer overlying a fractured bedrock with the prominent structural features (faults, fractures and dykes) trending in a north-eastern direction. Lateral movement of groundwater in the shallow aquifer is present due to weathering and fracturing of rocks in the area (Dalasile and Abiye, 2018).

Dalasile and Abiye (2018) investigated the groundwater flow and fracture frequency between the geological features by analysing borehole core samples from the study area. The boreholes intersected dykes and a fault zone. The fracture frequency increased with depth from 0 – 40 mbgl, more so for the borehole that intersected dolerite dykes, and below 40 mbgl the fracture frequency decreased with depth. The core analysis was only limited to 80 mbgl. Dalasile and Abiye (2018) reported typical water strikes from shallow boreholes varying from dry to 16 - 30 m, and borehole yields in the area vary from 0.83 l/s to 1.38 l/s.

A horizontal borehole was drilled perpendicular to a prominent NE-striking shear zone (20 m thick) to investigate lateral connection and if the zone is water bearing. Water was not encountered in the shear zone. Even subsequent boreholes drilled in different orientations within the shear zone were not water bearing. Clay content and filling within shear zone limits vertical hydraulic conductivity (Dalasile and Abiye, 2018).

Case Study – Spitzkop (Water Geosciences Consulting, (2007)

Water Geosciences Consulting (2007) conducted an investigation into the groundwater conditions of the Spitzkop area, Steelpoort Valley in Limpopo Province. Three main aquifers were identified: shallow alluvial aquifers, weathered aquifers and fractured rock aquifers. The shallow alluvial aquifers which are associated with the Steelpoort River and its tributaries, including the Dwars River, provide groundwater storage and recharge to the underlying weathered aquifers. The deeper fractured bedrock aquifers have a low permeability and are poorly connected with the upper weathered aquifers.

Majority of the boreholes in the area yield less than about 2 l/s, however there are anomalous yields of 10 l/s or higher which are assumed to be associated with recharge from ephemeral losses. Surface and groundwater interaction occurs in the main rivers - the alluvial aquifers are in hydraulic continuity and contribute to the baseflow of the study area. The Steelpoort River is sustained by shallow groundwater flow.

Hydrochemical analysis of groundwater samples from the study area inferred the dominant water type as Mg-Ca-HCO₃. The magnesium and calcium are indicative of silicate weathering processes in the weathered aquifer and the bicarbonate-type presences young, recently recharged groundwater – these are common chemical characteristics of shallow groundwater in the BIC. The other water type found in Spitzkop area is Mg-Ca-HCO₃-SO₄, which can be attributed to an anthropogenic source of SO₄ contamination in contact with the dominant water type.

Case Study – Der Brochen Mine (WSM Leshika, 2004)

A deep aquifer drilling programme was conducted by WSM Leshika (2004) in the Der Brochen mining area, approximately 30 km SSW of Steelpoort. The groundwater exploration programme aimed to explore the occurrence of groundwater beyond the better understood upper weathered and fractured aquifers (< 50 m) of the Bushveld Complex. The investigation was motivated by an overall increasing demand for water supply by the local communities and mining operations, a need to limit groundwater inflow into the underground workings and deep-water strikes encountered in certain structures in the Nebo Granites.

The Der Brochen mining area is located in the Eastern Limb of the Bushveld complex, south of the Steelpoort fault. The area is underlain by the Critical Zone of the RLS in the east and the Main Zone west of the area. The deep drilling groundwater exploration programme targeted structural zones in the Klein-Dwars and Groot-Dwars catchment, in attempts to intersect regional flow which can occur within interconnected fractures of major fault systems, such as the St George and Helena Faults. A lineament analysis from satellite lineament data was undertaken in order to map structural zones in the area. The evaluated dominant structural set orientations were grouped into three orientational sets; the NNE to N trending main long lineament of the study area, NNE to NE direction which coincides with the Klein Dwars river fault, the dyke swarms and Steelpoort fault occur and the ENE lineament set which trend along the direction of a major lineament of regional dimension, the Thabazimbi–Murchison Lineament.

Nine boreholes were drilled between the depth of 100 – 300 m. The drilling targets were selected adjacent to high yielding boreholes, adjacent to a borehole with deepest weathering profile, intersecting lineaments, within highly fractured media in fault zones or dyke intrusions and anomalies detected from magnetic geophysical surveys. High yield water strikes were generally intersected in the alluvial aquifer or on the weather and fresh rock contact, at shallow depth. No major groundwater sources were intercepted beyond 40 mbgl. Water strike encountered below 50 mbgl were ≤ 1.0 l/sec. The deep aquifer drilling programme concluded that there are insignificant quantities of groundwater at deep depths. The findings suggested that groundwater sources in Bushveld Igneous Complex are confined to the upper weathered and fractured zone (WSM Leshika, 2004).

In contrast to the deep aquifer drilling programme findings, groundwater bearing structures were encountered at depths of 400 m in geological exploration drilling of the UG2 decline on the Der Brochen Farm. This indicates that some fractures in the Klein- and Groot-Dwars River regional fracture zone are water bearing (Services Shangani Management, 2020).

It is not clear whether the deeper fractured aquifer in the Bushveld Complex, specifically the Eastern limb, could be completely ruled out for groundwater occurrence. With the limited available and conflicting information available, the occurrence of groundwater is variable and structurally based, yet there is clearly an opportunity to further investigate the deeper fractured system. With the deep scientific drilling, complemented with mining industry, a clearer understanding of the deep fractured groundwater systems will be achieved. Additionally, the underlying Transvaal Supergroup aquifers, which typically are good yielding aquifers at surface, will be intersected at depth (> 1 km) and providing information on whether these aquifers contain groundwater would be beneficial.

3 GROUNDWATER DATABASE OVERVIEW FOR THE EASTERN LIMB BUSHVELD COMPLEX

3.1 OVERVIEW

Groundwater within the eastern limb of the Bushveld Igneous Complex is investigated, in order to develop, an integrated comprehension of the groundwater dynamics in the area – through a collation of currently available hydrogeological data and other groundwater-related data. The investigation reports on hydrogeological processes, groundwater dynamics, and hydrochemical and hydraulic parameters, which express the complexities of the structurally controlled aquifer systems and delineate the varying hydrogeological properties of each hydrostratigraphic unit.

The focus of this investigation is on the eastern limb of the Bushveld Igneous Complex, Figure 12, which has an area of approximately 10 022 km². The eastern limb underlies the Limpopo and Mpumalanga Provinces, towns within the study area include Burgersfort, Steelpoort and Magalatsana, and it is situated 44 km south of Polokwane. Geographically, the study area is located between the latitudes, 24.212222°S to 25.838333°S and longitudes, 29.190278°E to 30.407500°E. This eastern limb is within the Middle Olifants Catchment, a subdivision of the Olifants Water Management Area.

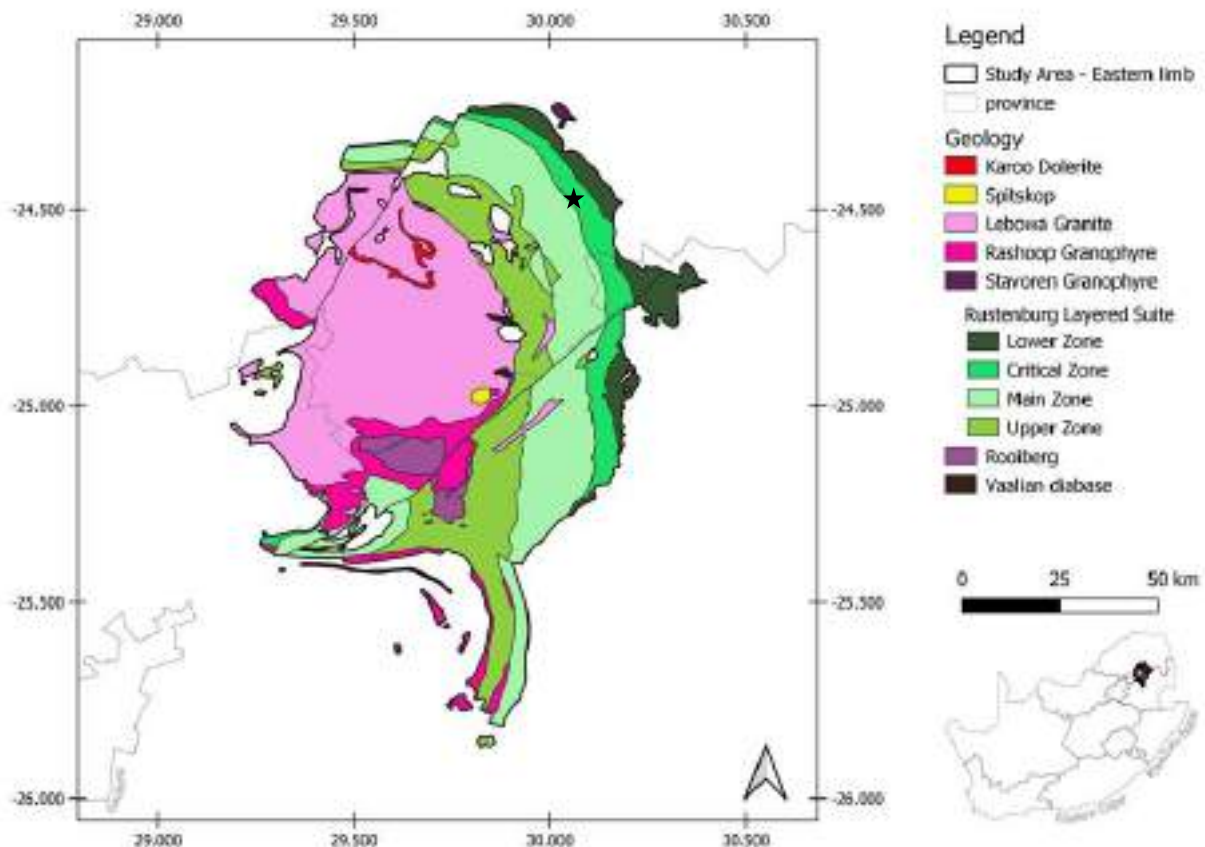


Figure 12 Geological Map of the study area, the eastern limb of Bushveld Igneous Complex, showing its location with reference to towns and cities. Approximate location of the BVDP borehole is indicated as a black star.

3.2 BOREHOLE DATA ANALYSIS

Groundwater in the investigated area was described according to groundwater data as established from drilled boreholes. Figure 13 shows the spatial distribution of the boreholes from the various databases – which consist of boreholes intended for water supply and groundwater monitoring. The borehole data analysis, which consists of borehole depths, water strike depths, blow yields and groundwater levels as recorded in the NGA and GRIP, as well as water level measurements from Hydstra database was evaluated.

An overview of the borehole data for the study area is presented in Table 4, which provides summarised characterisation of groundwater occurrence within the eastern limb relative to borehole data. The boreholes in the study area's RLS and Rashoop Granophyre Suite are drilled to an average depth of 54,3 and 55 mbgl, respectively. The average borehole depths in the Rooiberg Group and the Lebowa Granite Suite are deeper; 72, 6 and 77.3 mbgl, respectively. The depth to water strikes in the RLS are described by an average of 35 mbgl, the average Rashoop Granophyre Suite water strike depth is slightly deep at 38 mbgl. Similar to the borehole depths, the average water depths in the Rooiberg Group and the Lebowa Granite Suite, 46,1 and 50,5 mbgl, respectively, are deeper than the average water strikes of the previously mentioned lithostratigraphic units. The lowest average blow yield (0,3 l/s) measured at the intercepted water strikes in the Rooiberg Group. The average blow yields for the RLS, Rashoop Granophyre Suite and the Lebowa granites; 1.7 l/s, 1,6 and 0,8 l/s, respectively, are moderately low yields.

3.2.1 Borehole Depths

The distribution of borehole depth data in the study area was evaluated in Figure 14, which depicts the borehole depth data for each lithostratigraphic units. The borehole depths dataset for the Rooiberg Group is relatively smaller (24 boreholes), in comparison to the other stratigraphic units in the study area which have a larger surface area and consequentially have more borehole. In the Rooiberg Group, boreholes are frequently drilled to the depth of 30 -40 mbgl and 75% of the borehole are drilled less than 90 mbgl (Figure 14a).

The total number of borehole depths recorded for boreholes drilled in the Rustenburg Layered Suite tallies to 1 077 boreholes. The RLS borehole depth data in Figure 14b, shows an approximately log-normal distribution, which suggests that the frequency of boreholes drilled in this unit decreases as the depth interval increases. The highest frequency for borehole depths in the RLS occurs between the depths of 70 – 80 mbgl, where about 89% of the boreholes are below 90 mbgl.

The Rashoop Granophyre Suite borehole depth data in Figure 14c shows an approximately log-normal distribution, with 84% of the 135 recorded borehole depths less than 90%. The highest frequency in this lithostratigraphic unit is boreholes drilled to the depth of 20 – 30 mbgl. The Lebowa Granite Suite which has the second highest number of borehole depth records, 928 records. Figure 14d also shows an approximately log-normal distribution, with the highest borehole depth frequency ranging from 70 – 80 mbgl. 78% of the boreholes drilled in the Lebowa granites, less than 90 mbgl.

Majority of the recorded borehole depths are drilled in the RLS and the Lebowa Granite Suite and for both the stratigraphic units, the highest frequency of borehole depths in between 70 – 80 mbgl depth interval. Overall, the distribution of the recorded borehole depth data for the investigated area (Figure 14), indicates that the boreholes are generally drilled to depths less than 90 mbgl, which implies that sufficient groundwater is typically intercepted at shallow depths (less than 100 mbgl).

3.2.2 Water Strike Depths

Figure 15, displays the water strike depth data distribution as per lithostratigraphic units in the eastern limb of the BIC, and shows log-normal distribution for all histograms. The water strike zones in the study area are described as primary and secondary water strike zones, categorised by the highest frequency bins and the

bins with subsequently higher frequency. The water strike zones identified were determined by the depth interval with the highest frequency of water strike depths.

Table 4 Borehole data analysis statistical summary according to the stratigraphic units in the study area

		Lithostratigraphic division			
		Roiberg Group	Rustenburg Layered Suite	Rashoop Granophyre Suite	Lebowa Granite Suite
Borehole Depth (mbgl)	N	24	1077	135	928
	Min	30,8	3,5	6,0	2,4
	Mean	72,6	54,3	55,0	77,3
	Max	160,3	300,0	204,0	187,0
Water Strike Depth (mbgl)	N	22	860	119	445
	Min	12	1	6,4	3
	Mean	46,1	35,0	38,0	50,5
	Max	93	202	204	187
Blow yield (l/s)	N	22	860	119	445
	Min	0,0	0,0	0,0	0,0
	Mean	0,3	1,7	1,6	0,8
	Max	1,2	90,0	23,3	25,0
Groundwater levels (mbgl)	N	15	990	84	584
	Min	8,5	0,6	0,6	0,0
	Mean	17,5	18,6	16,5	21,7
	Max	27,4	128,0	118,0	94,9

The Rooiberg Group has a considerably lower number of recorded water strike depths; this is mainly related to the relatively smaller surface areal extent of this stratigraphic unit in the study area. The primary water strike zone is located between 20 – 30 mbgl and the secondary water strike zone is between the depth of 30 – 50 mbgl. 60% of the boreholes drilled in the Rooiberg Group encountered water with 60 mbgl (Figure 15a).

Almost 60% of the recorded water strike depths in the study area are for boreholes drilled within the Rustenburg Layered Suite. Where 85% of the water strike depth are within the first 60 mbgl. The identified primary and secondary water strike zones in the RLS, are between 10 – 30 mbgl and 30 – 40 mbgl, respectively (Figure 15b). Similarly, the primary and secondary water strike zone for the Rashoop Granophyre Suite, as determined from 119 records, are also located within the same depth zones as the RLS. In the Rashoop Granophyre Suite, the cumulative frequency suggests that 83% of the water strikes in this unit, are within 60 mbgl (Figure 15c).

In the Lebowa Granite Suite (number of water strike depths recorded are 445), the highest frequency of water strike depths is between the depth of 10 – 30 mbgl, this is recognised as the primary water strike zone. And the water strike zone identified as secondary zone, extends from the depths of 30 – 70 mbgl. 80% of the water strike depths in the Lebowa Granites are within 80 mbgl (Figure 15d).

Overall, water strike depths in the investigated area are generally encountered at shallow depths. The distribution of the water strike depth data in Figure 15 suggests that the possibility of intercepting groundwater decreases with depth. Both primary and secondary water strike zone for all lithostratigraphic units in the study area are within 70 mbgl. The water strike zones in the study area (within 70 mbgl) are shallow, and the highest borehole depth frequency is between 70 – 80 mbgl, which is also relatively within shallow depths and majority of the boreholes are drilled below 80 mbgl. This suggests that the depth to which boreholes are drilled is established by the water strikes intercepted. This implies that the water strikes encountered at shallow depths, produce sufficient and possibly sustainable yields.

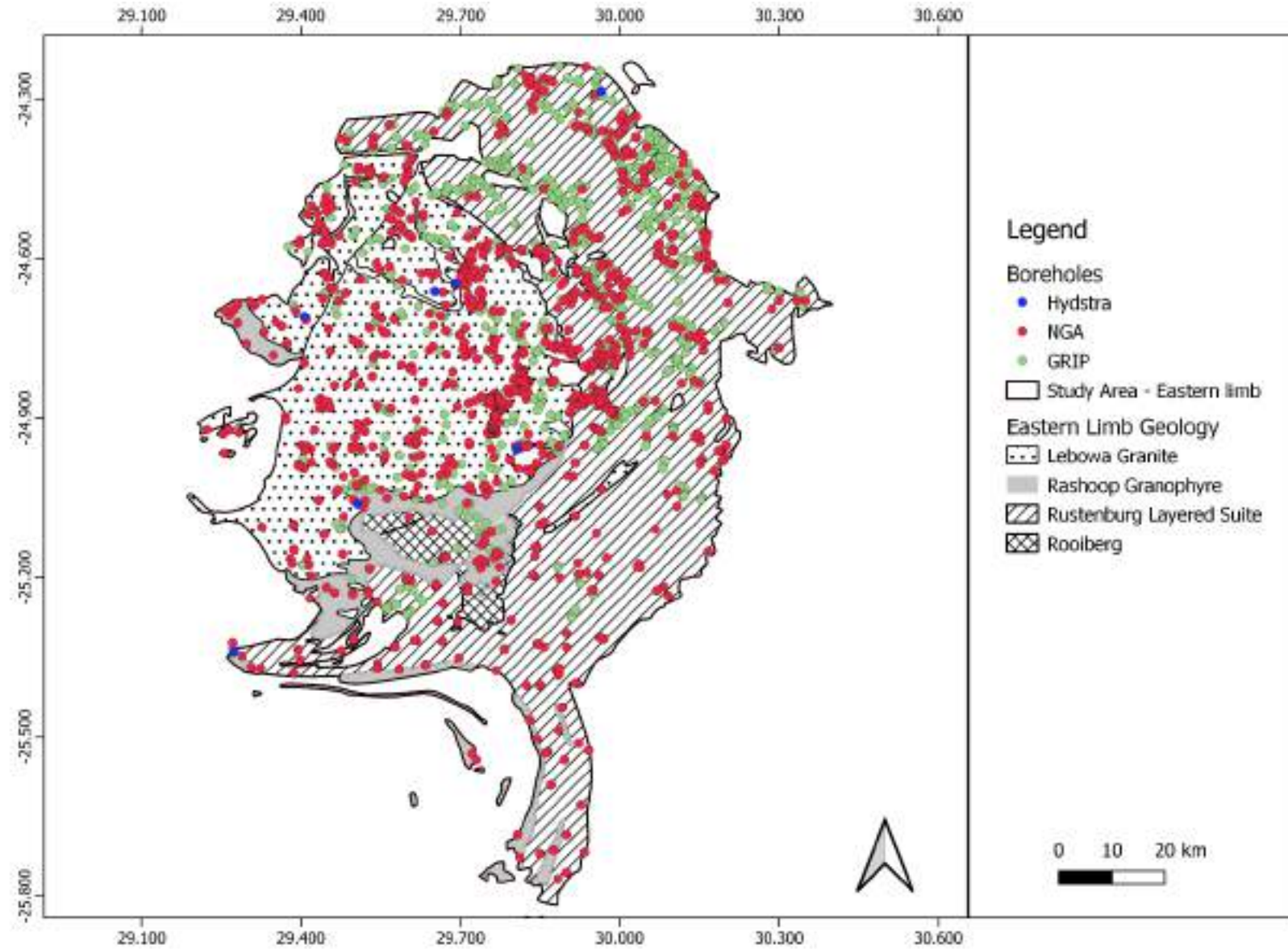


Figure 13 Distribution of boreholes across the study area

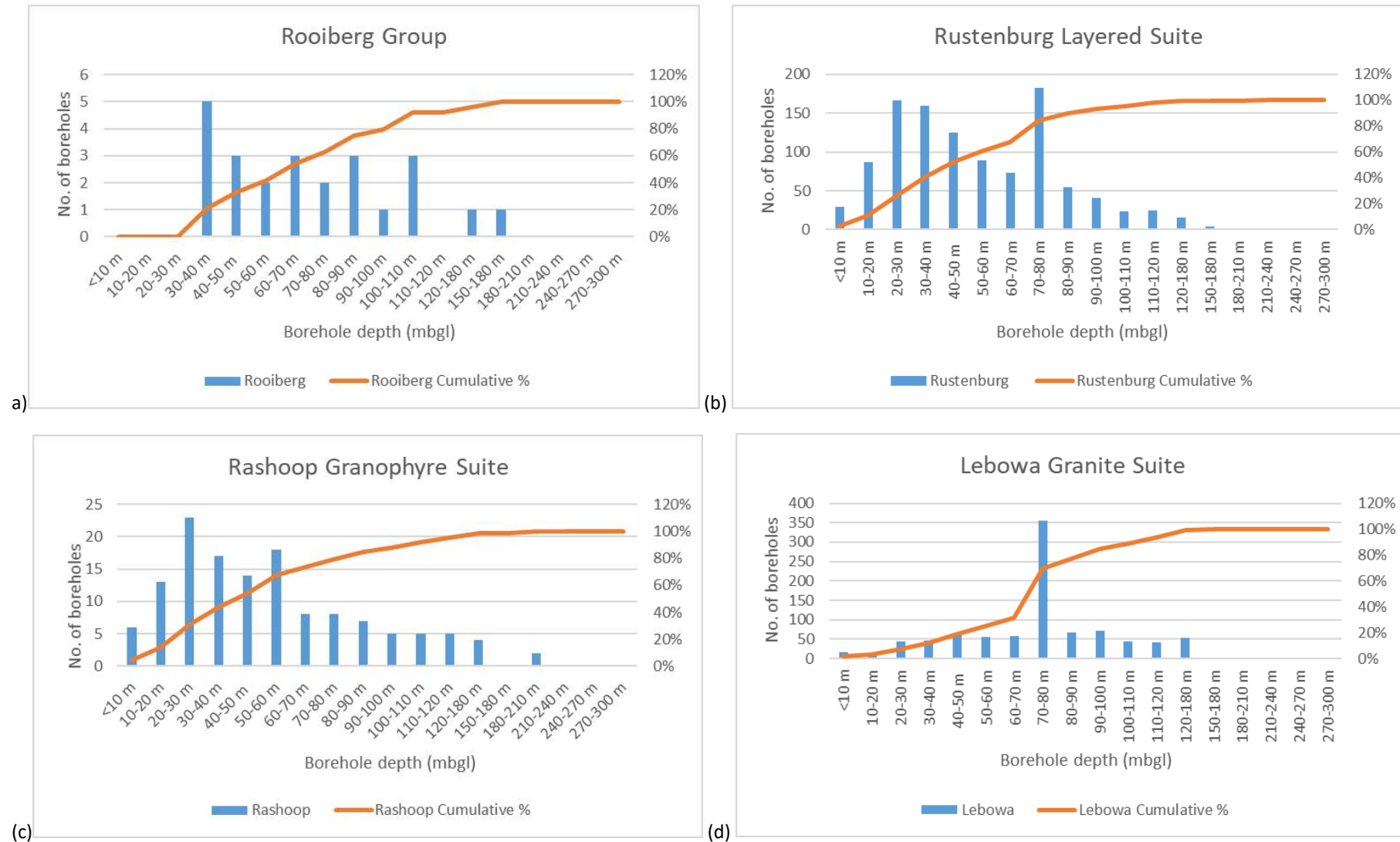


Figure 14 Borehole depth frequency for boreholes within the Bushveld Igneous Complex, according to the different lithostratigraphic divisions in the study area.

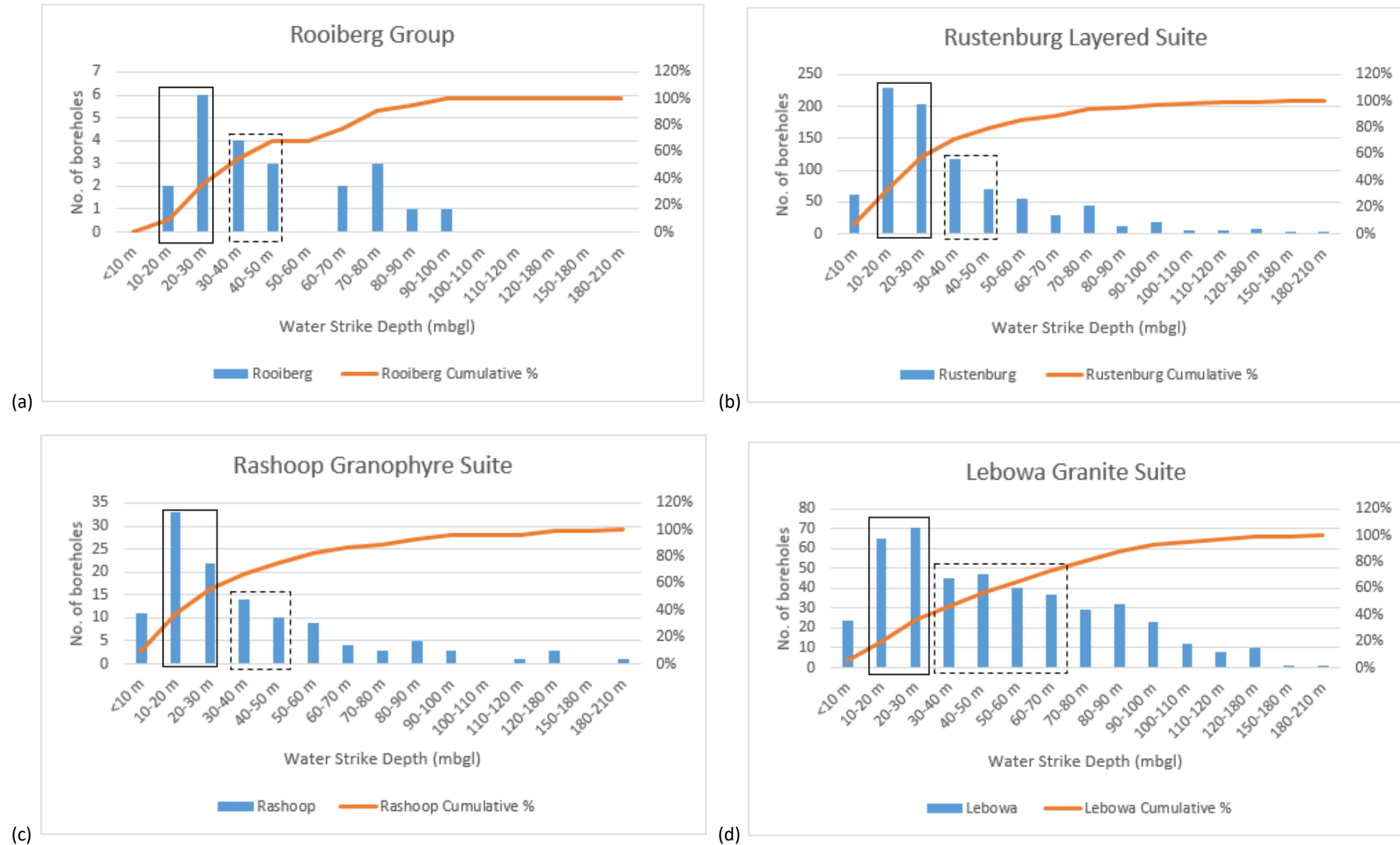


Figure 15 Depth to water strike frequency for boreholes within the eastern limb of the Bushveld Igneous Complex. The primary and secondary water strikes zones identified are marked with solid and dashed boxes, respectively.

3.2.3 Blow Yields

The blow yields for water strike depths recorded for boreholes drilled in the study area consists of 1481 records. The distribution of the blow yield data is shown in Figure 16. 42% of the blow yields, the highest frequency, ranges from 0 – 0,1 l/s. Figure 16, illustrates that the 17,9% of the blow yields are between 0,1 – 0,5 l/s, are classified as low yield boreholes, 21,6 % boreholes are moderately low yields (0,5 – 2 l/s), 12,7% are moderately high yielding and 5% of boreholes have high yields, exceeding 5 l/s.

A significant number (42, 8%) of the recorded borehole yields have very low yields, this yield bin is classified as dry to very low yielding boreholes, indicative of unsuccessful borehole drills. It should be noted that not all of the recorded water strike depths have an associated blow yield therefore the percentage of the unsuccessful borehole yield is not necessarily accurate reflection of unsuccessful boreholes drills, however, may offer a generally indication for prospects of groundwater development in the area.

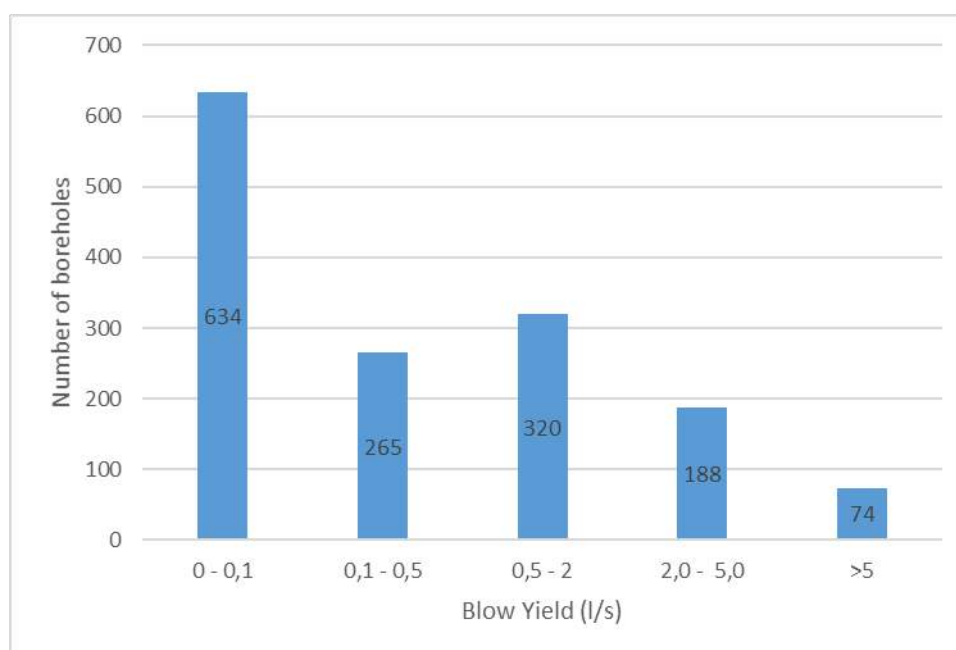


Figure 16 Borehole blow yield frequency for the eastern limb of the Bushveld Igneous Complex from the collected groundwater database

Table 5 presents a summary of the borehole yields for each of the lithostratigraphic units in the eastern limb of the BIC. For the Rooiberg Group, the blow yields are mainly within the 0 – 0,1 l/s class (bin) and none of the blow yield exceed 2 l/s. The highest number of blow yields recorded is obtained from boreholes drilled within the RLS. The RLS, Rashoop Granophyre Suite and the Lebowa Granite Suite blow yield data has similar data distribution. The dry to very low yield boreholes (0 – 0,1 l/s) have the highest frequency and the frequency of borehole yield numbers in each class decreases as the blow yield class increases, from low to high yield blow yield class. Boreholes in the Lebowa Granite Suite, have the lowest number of blow yields (3%) which exceed 5 l/s, after the Rooiberg Group. While the Rashoop Granophyre Suite boreholes have the highest number of high yielding borehole (7%), and majority of the moderately high yield boreholes are within the RLS.

Figure 17 displays the average blow yields with depth to demonstrate the variation of blow yields with depth. The average blow yield was calculated for intervals of 10 m from 0 – 120 mbgl, then the intervals increased to 30 m depth intervals. For boreholes drilled in the Rooiberg Group, the highest average blow yield (0,69 l/s) consists of water strikes encountered within the depth of 70 – 80 mg. For the primary and secondary water strike zones identified in this stratigraphic unit, the average blow yields are below 0,5 l/s. Most of the blow yield data is concentrated in the RLS and the Lebowa Granite Suite units. The general trend overserved from RLS blow yield dataset, is that the average blow yield per depth interval decreases with depth. This suggests that

generally the water intercepted, volumes of the yields for groundwater from intercepted water strikes is likely to decrease with depth.

In the primary and secondary water strike zones of the Rашoop Granophyre Suite, the average blow yield for the various depth interval in the zone range from 2 – 2,5 l/s. The highest average blow yield per depth interval in this stratigraphic is 2,39 l/s and 2,42 l/s for 20 – 30 mbgl and 30 – 40 mbgl, respectively, which falls within the depths range interpreted as the primary and secondary water strike zones. In the Lebowa Granite Suite, the average blow yields increase within the first 50 mbgl, then below that depth, the average blow yield per depth interval the decreases, with depth. The highest blow yield average in the Lebowa Granites is at the 40 – 50 mbgl depth interval which falls within the secondary water strike zone.

Typically, there is a declined in the average blow yield per depth interval, however there are significant deviations observed at deeper depths, notably at 150 – 180 mbgl and 180 – 210 mbgl for the RLS, where the calculated average blow yield is 3,6 l/s and 1,33 l/s, respectively. Since the frequency of water strikes decreases with depth (Figure 15), therefore a relatively small number contributed to these high average blow yields. The high average blow yield per depth noticed at deeper depths can be attributed to possibly localised open deep fractures at greater depths in the crystalline fractured bedrock aquifers.

Table 5 Statistical summary of blow yield data for the eastern limb of the BIC from the collected groundwater database

Lithostratigraphic Division	Blow yield (l/s)					
	No. of records	0 - 0,1	0,1 - 0,5	0,5 - 2	2,0 - 5,0	>5
Rooiberg Group	22	45%	36%	18%	0%	0%
Rustenburg Layered Suite	860	40%	17%	22%	16%	5%
Rashoop Granophyre Suite	119	38%	21%	22%	13%	7%
Lebowa Granite Suite	445	51%	19%	22%	6%	3%

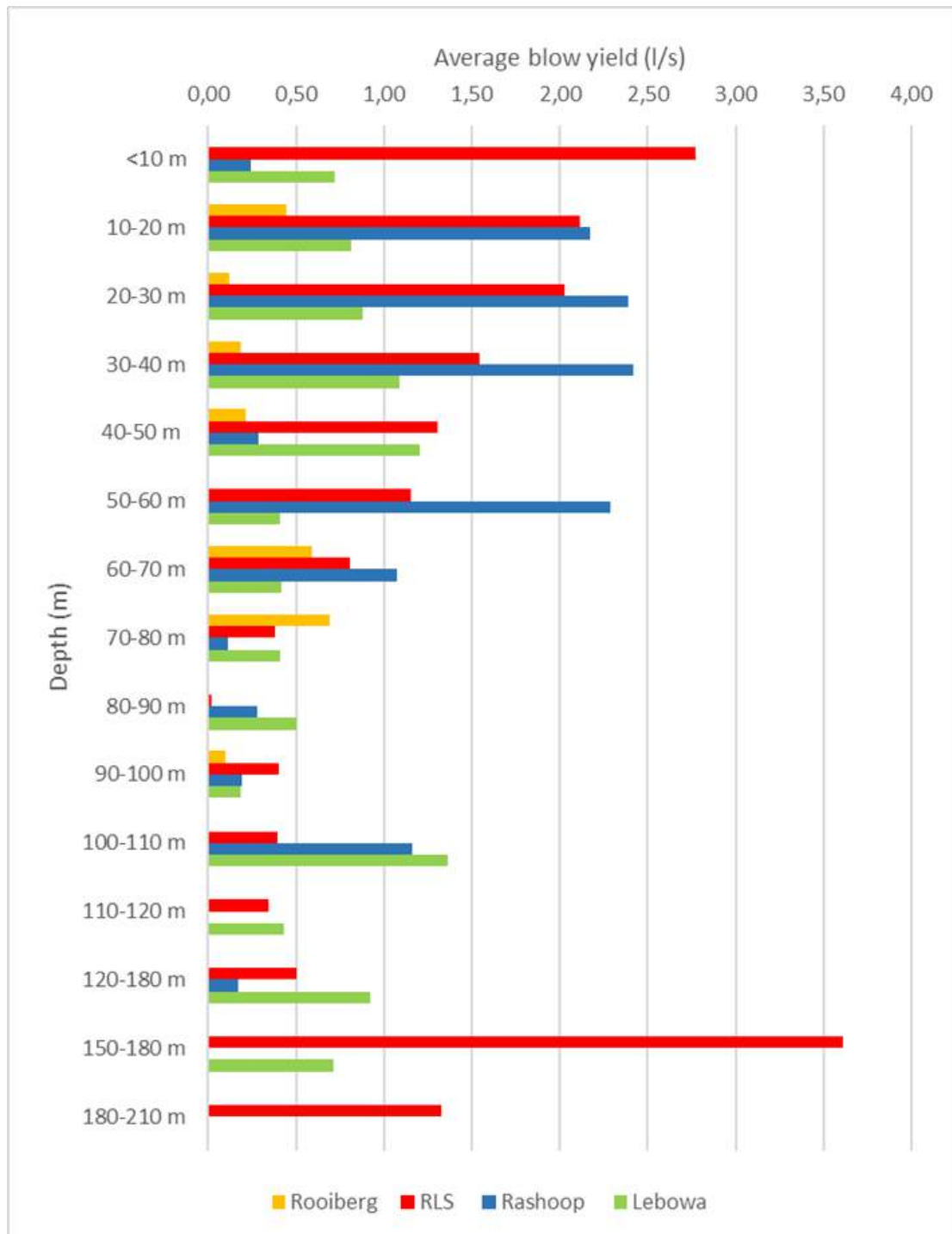


Figure 17 Blow yield variation with depth, according to average blow yield for the specific depth intervals.

3.2.4 Groundwater Levels

3.2.4.1 Groundwater flow direction

Groundwater level measurements for the study area were used to interpolate groundwater levels to compose of groundwater level contour map (Figure 18) and determine the groundwater flow direction. The recorded groundwater levels from boreholes across the study area in the investigation area, in the eastern limb of the BIC range from 0 – 128 mbgl, this indicates that the water table in some area within the investigated area is close to the ground level.

The groundwater levels measurement recorded with reference to mbgl were converted to mamsl, to understand the correlation between groundwater levels and the ground elevation. The water table determined by interpolation of groundwater levels and the resulting groundwater levels contours in Figure 18 show that the groundwater levels (mamsl) in the study area tends to follow the topography of the study area. The groundwater flows from high topographical gradients to lower gradients. The correlation between the groundwater levels and the surface elevation, evaluated in, Figure 19 indicates a strong linear relationship ($R^2 = 0,99$), which suggests that spatial variation in groundwater levels across the study area is strongly related to the changes in surface topography.

Localised groundwater flow within the regional scale study area, flows towards varying directions. The regional groundwater flows direction assumes topographical gradients. Groundwater flow direction vectors depicted in Figure 18, converge towards the main rivers in the study area, the Olifants River and the Steelpoort River, which are at lower topography which supports that groundwater generally flows from high to low elevations and suggest that groundwater flows into these water bodies.

The deepest water level in the study area are observed in the northern part of the eastern limb (Figure 18), it should be noted that this region of the study area is the RLS and mining activities are concentrated this area, therefore groundwater levels decline may also be contributed by mine dewatering.

3.2.4.2 *Groundwater Level Trends*

Groundwater level trends and water level variability were analysed using water level data from the DWS monitoring network. Groundwater level fluctuations are due to sources and sinks in the groundwater systems, which results in volumetric changes in groundwater reserves, exhibited through groundwater water level variations. There are different factors which impact water levels, these include precipitation, evapotranspiration, base flow, land use and influence of anthropogenic activities (Tladi et al., 2023).

Groundwater level time-series data from seven monitoring boreholes, located within the study were used for the groundwater level trend analysis. Boreholes which had relatively long-term monitoring data were used, the period of monitoring data analysed ranged from eleven to seventeen years. Non-parametric tests, Mann-Kendall tests and Sen's slope estimator were applied to determine trends of the water level time-series and the rate of increase or decrease (m/year), respectively. The statistical analysis was performed at a 95% confidence level. The results of the water-level time series data are presented in Table 6. The computed p -values for the Mann-Kendall test (Appendix A) were all lower than the significance level ($\alpha = 0,05$), therefore this indicated the presence of a trend in all the monitoring boreholes' time-series data. Statistically significant decreasing trends were observed, which are consistent throughout all analysed time-series data, and Figure 20 shows a graphical presentation of the time-series data with decreasing trends. The analysed groundwater levels in the eastern limb have Sen's slope which ranges from -0,095 to -0,755 m/year.

The highest decline in groundwater levels was observed in borehole M06-1064, where groundwater levels were reduced by 6,75 m during the 11-year monitoring period. The statistically significant decreasing trend is described by a Sen's slope of 0,775 m/year – which is the highest in the analysed time-series data. Rainfall trend at this borehole is also decreasing, at a rate of -26,454 mm/year, which is the highest decreasing rainfall trend observed. Decrease in rainfall, subsequently result in a decrease in recharge, and this may be the reason for the reduced groundwater levels.

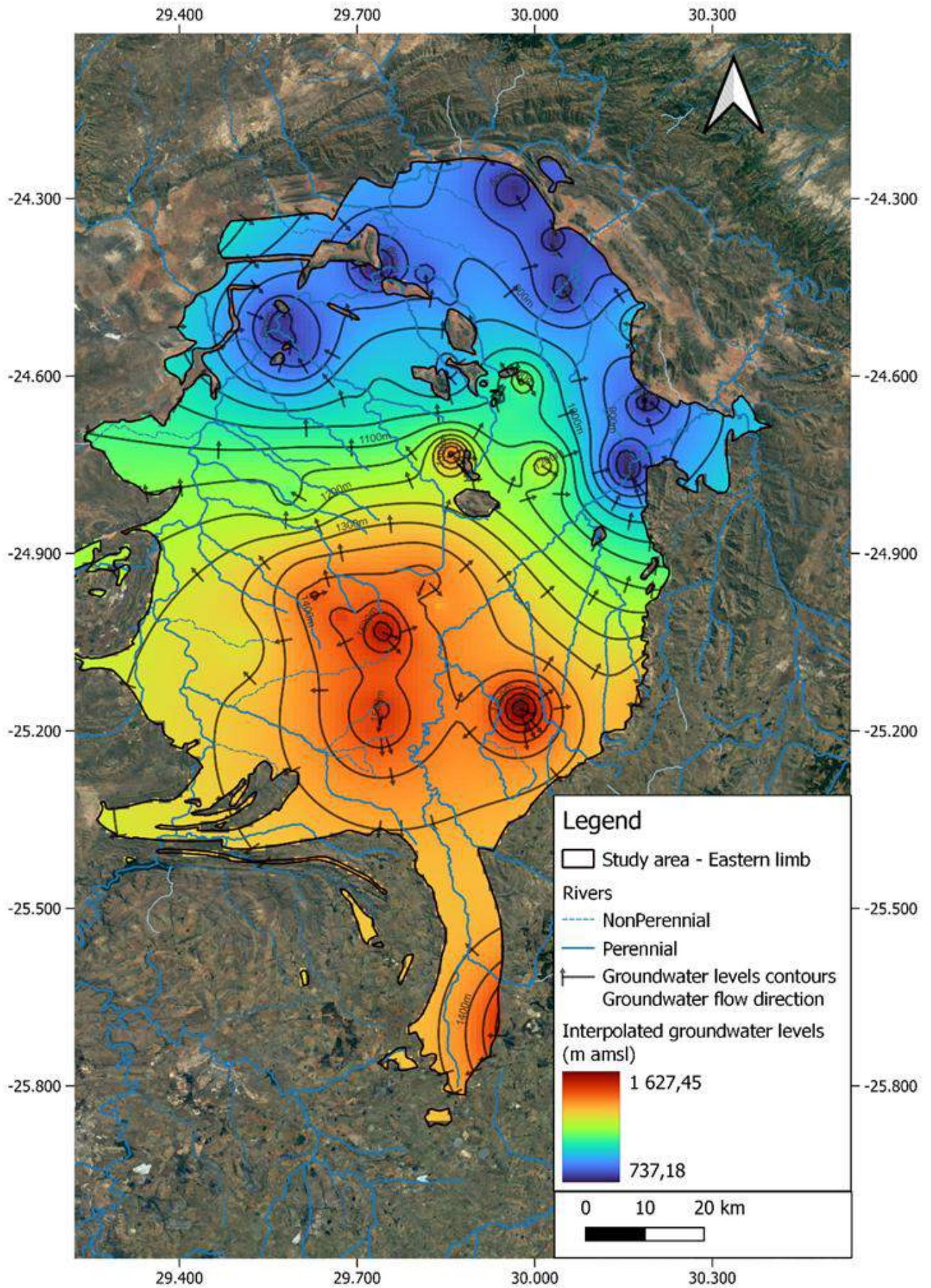


Figure 18 Groundwater level and flow direction map for the study area

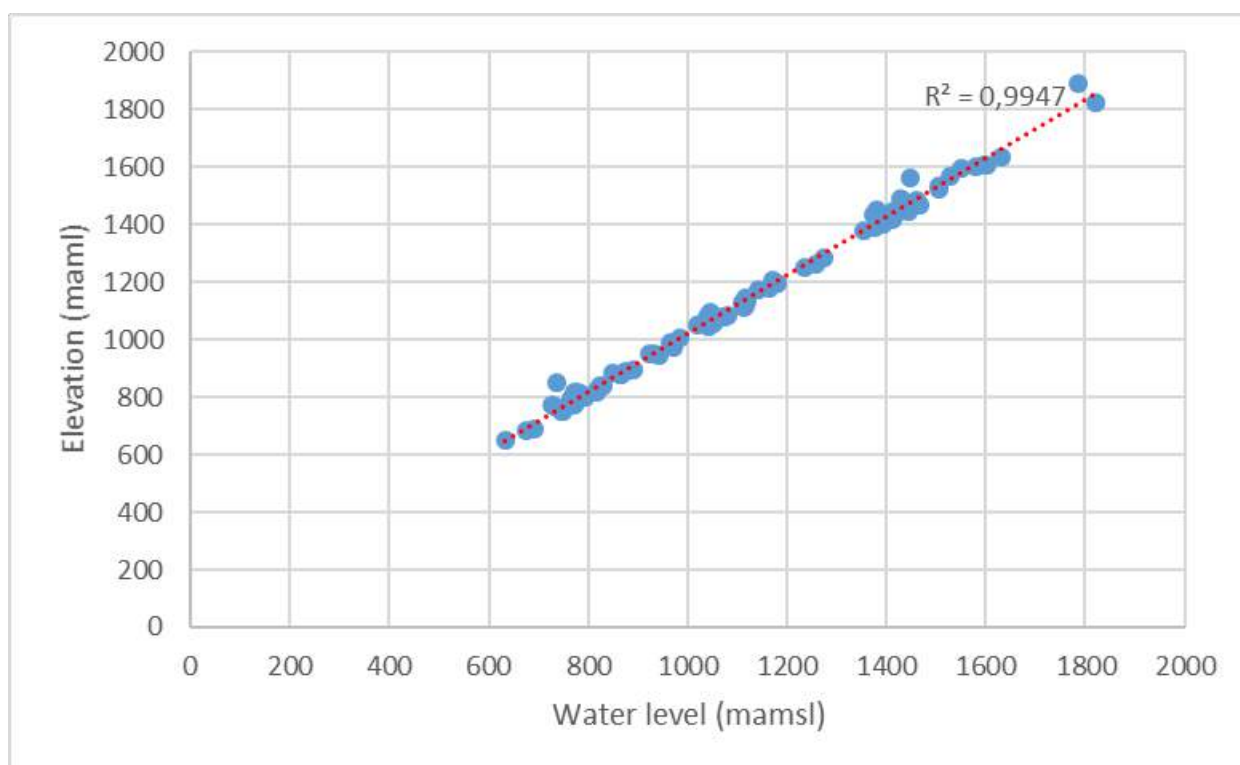


Figure 19 Correlation analysis between groundwater levels (mamsl) and elevation

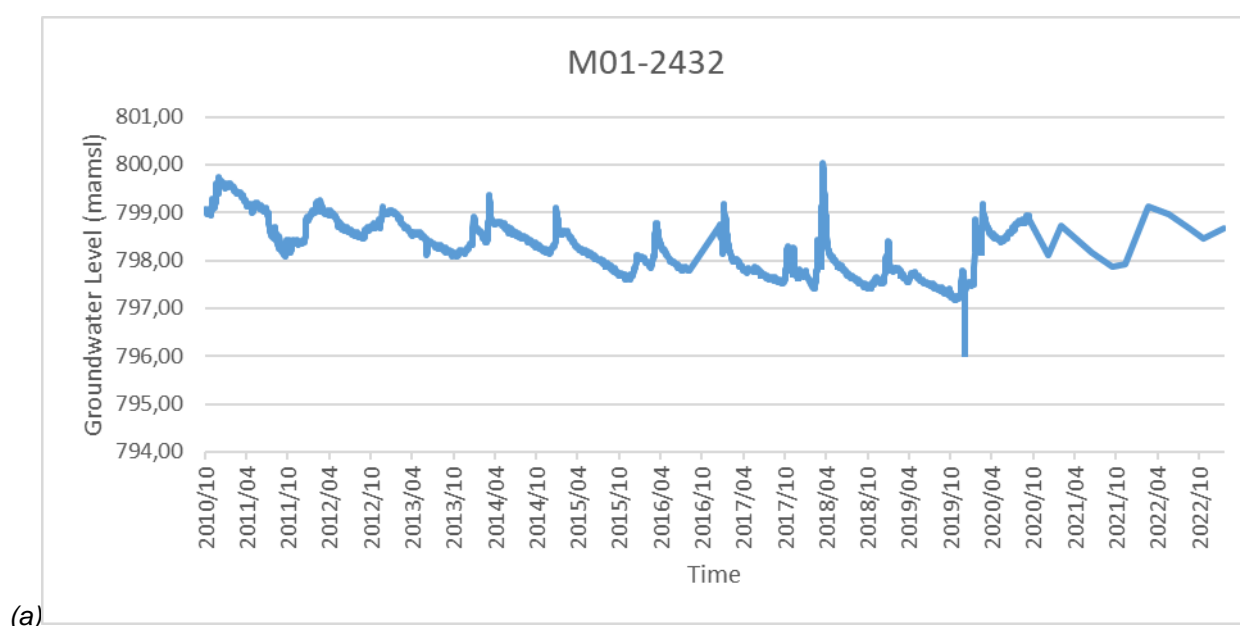
Table 6 Groundwater level trend statistical analysis results, including the rainfall Sen's Slope Estimator for the corresponding water level monitoring period. Statistically significant decreasing trends, according to the computed Mann-Kendall test are denoted by ↓ (decreasing) symbol and rainfall with significant trends are signalled by Sen's slope estimator values in bold text.

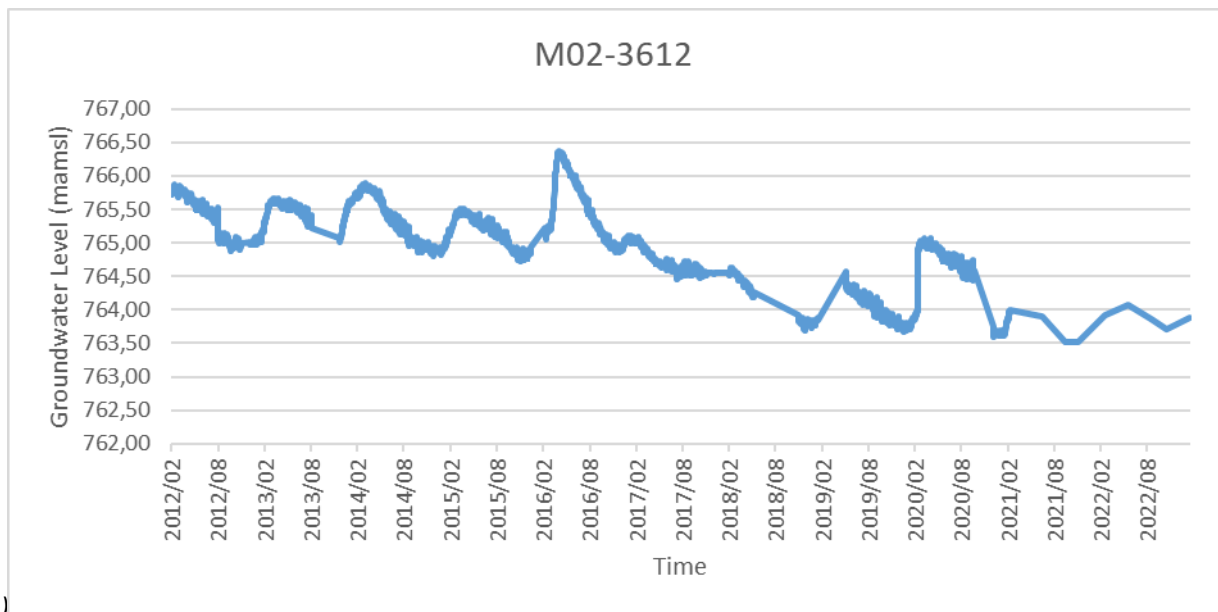
DWS ID	Latitude	Longitude	Litho-stratigraphic Division	Period of data	GWL Trend	GWL Sen's Slope Estimator (m/year)	Total change GWL	Rainfall Sen's Slope Estimator (mm/year)
M01-2432	-24,70891	29,40535	Lebowa	2010 - 2023	↓	-0,095	-0,36	-24,655
M02-3612	-24,28484	29,96515	RLS	2012 - 2023	↓	-0,173	-1,89	10,920
M06-1064	-24,64631	29,69125	Lebowa	2010 - 2021	↓	-0,755	-6,75	-26,454
M06-1551	-24,95754	29,80591	Lebowa	2009 - 2022	↓	-0,578	-6,45	-22,375
M06-1613	-24,66141	29,65162	Lebowa	2010 - 2023	↓	-0,569	-6,14	-21,554
M28-0062	-25,06145	29,50623	Lebowa	2006 - 2023	↓	-0,250	-2,21	1,788
MP17-00031	-25,3395	29,2736	RLS	2012 - 2023	↓	-0,262	-1,09	0,000

Other substantial reductions in groundwater levels are observed in boreholes M06-1551 and M06-1613, where statistically significant decreases are described by rates of change of -0,578 m/year and -0,569 m/year, respectively. The total decline of groundwater in the boreholes were 6,45 m and 6,14 m, respectively. During the monitoring period of the analysed boreholes M06-1551 and M06-1613 groundwater time-series, the rainfall at these monitoring sites show decreasing trends described by a rate of change of -22,375 mm/year and -21,554 mm/year. Decreasing rainfall trend possibly explain the reduced water levels. Borehole M06-1551 is located in a village, therefore decline in water levels are also probably attributed to water supply abstraction. Borehole M06-1613, is located within land used for agricultural activities therefore the reduced groundwater levels may also be influence by abstractions for irrigation.

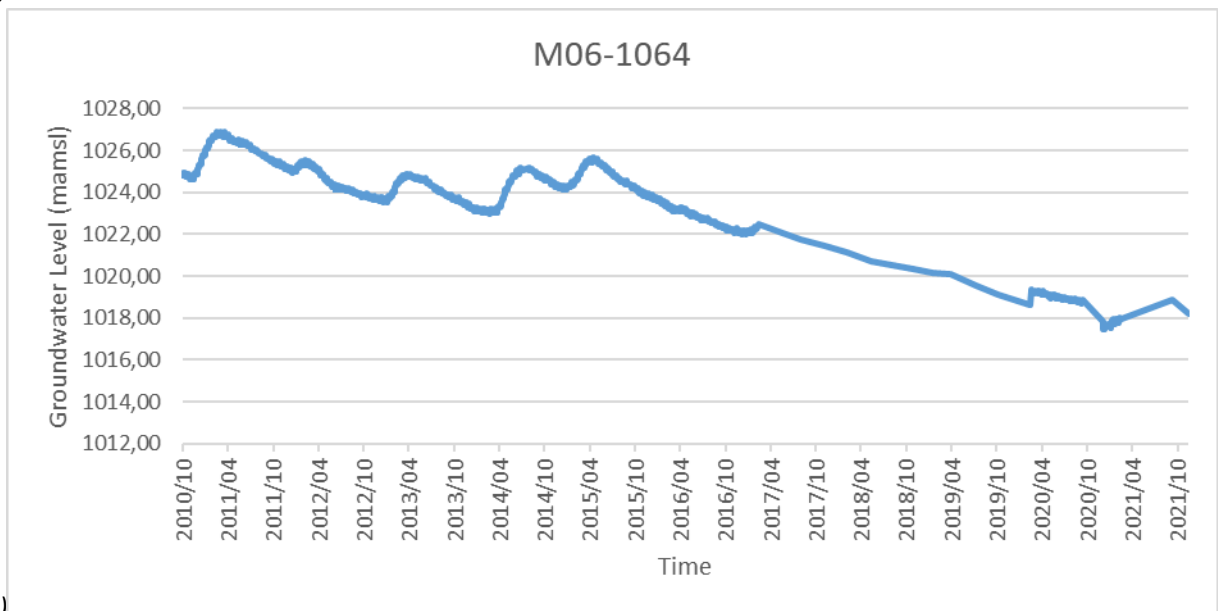
Notable reduction in water levels were also observed at boreholes M28-0062, M02-3612 and MP17-00031, which have trends decreasing at the rate of -0,250 m/year, -0,173 m/year and -0,262 m/year, respectively. The total change in groundwater over the observation period is 2,21 m, 1,89 m and 1,09 m decline, respectively. Unlike the above-mentioned boreholes, the rate of change of rainfall at monitoring boreholes M28-0062 and M02-3612 is positive; 1,788 mm/year and 10,920 mm/year respectively. While the rate of change for rainfall at MP-00031 is 0 mm/year – indicating that rainfall is relatively constant. This suggests that rainfall trends are not the predominant influence for groundwater decline at these monitoring sites. Borehole M28-0062, is located in a community setting, while MP17-00031 is in close proximity to a village. In the quaternary catchment, where borehole MP17-00031 (B32H), there are numerous of registered groundwater users, according to the WARMS database, abstractions in the quaternary catchment amount to $1,96 \times 10^6 \text{ m}^3$ annually: for agricultural irrigation and water supply. M02-3612 is located 2 km north, away from a mine in the RLS, and it is also close to Tsipeng Village. There is a concentration of registered groundwater users in the RLS, and such explains the observed decline in water levels at borehole M02-3612. In the quaternary catchment of borehole M02-3612, registered groundwater abstraction annual volumes amount to $1,09 \times 10^6 \text{ m}^3$ - main water users in the catchment are within mining. Therefore, groundwater decreasing trends in boreholes M28-0062, M02-3612 and MP17-00031, can be attributed to groundwater abstractions.

M01-2432 is the borehole with the lowest total decline in groundwater levels, water levels were reduced by 0,36 m, at a rate of -0,095 m/year. The slight decline in water levels is possibly due to decreasing trends in rainfall, which change at a rate of -24,655 mm/year. Variations in rainfall are observed in groundwater levels since rainfall is a source of natural groundwater recharge. Overall, the water level time-series data for monitoring boreholes in the study area all show statistically significant decreasing trends, which are mainly attributed to decreasing rate of change of rainfall and at other sites the reductions are probably due to groundwater abstractions, for community water supply, agricultural irrigation and mining operations.

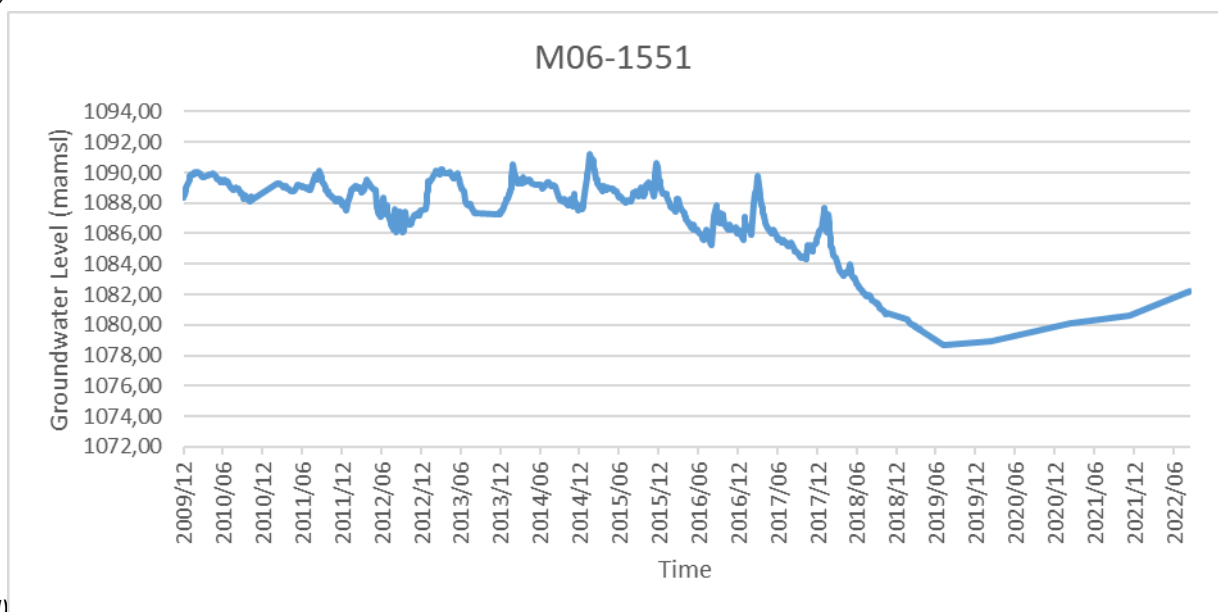




(b)



(c)



(d)

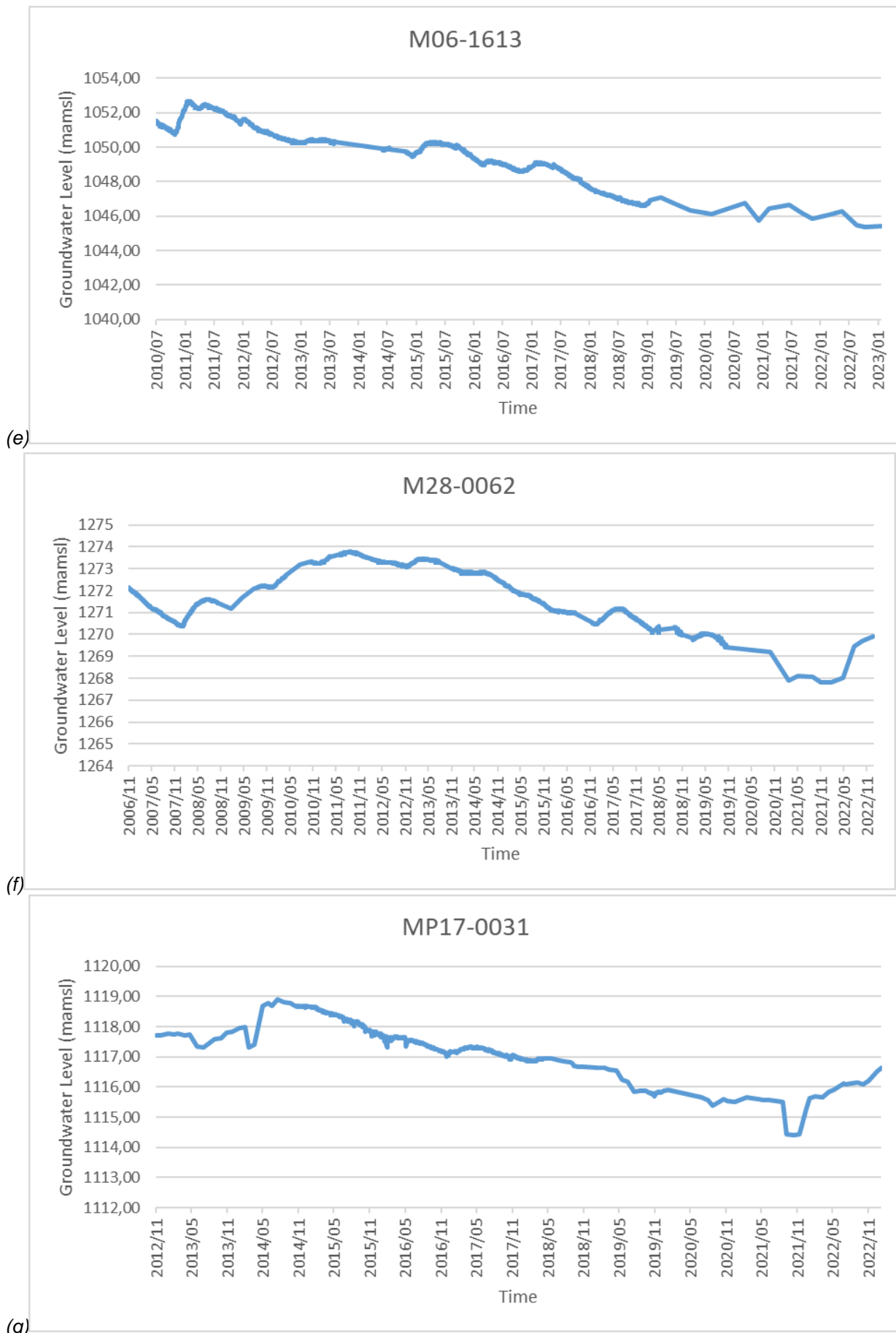


Figure 20 Groundwater level time-series data for the groundwater level monitoring boreholes in the study area: boreholes (a)M01-2432, (b) M02-3612, (c) M06-1064, (d) M06-1551, (e) M06-1613, (f) M28-0062, (g) MP17-00031.

3.3 HYDRAULIC CHARACTERISTICS

Assessment and understanding of hydraulic parameters of the area of interest is an important aspect of groundwater development and management, as hydraulic properties describe the ability of groundwater movement within an aquifer system which is also a function of borehole productivity. In this investigation, the hydraulic characterisation of the eastern limbs aquifers is based on the hydraulic parameters of the boreholes obtained from the GRIP database. The hydraulic parameters in this database, transmissivity and storativity values, were obtained from single borehole pumping test data collected and analyses as part of the GRIP. The analyses and interpretation of the step drawdown constant discharge rate test was executed in Flow Characteristics Programme for aquifer test, where transmissivity and storativity values were obtained using methods like the Copper Jacob (1935), Theis (1935) and Barker Fractal methods.

Descriptive statistics of the study area's transmissivity values are presented in Table 7. According to the statistical analyses, transmissivity in the eastern limb of the BIC ranges from 0,1 – 1500 m²/day. The average transmissivity value is 28,5 m²/day. Figure 21 depicts the frequency histogram for the transmissivity dataset of the investigated area, which shows an approximately log-normal distribution. The 0 – 1 m²/day bin has the highest frequency, and the central tendency of the data is described by the mode value of 0,3 m²/day and median value of 7 m²/day. About 78% of the transmissivity dataset has values less than the study area's average transmissivity.

Table 7 Statistical summary of transmissivity value for the eastern limb of the Bushveld Igneous Complex

Transmissivity (m ² /day)	
No. of boreholes	891
Mean	28,5
Median	7
Mode	0,3
Standard Deviation	81,7
Minimum	0,1
Maximum	1500

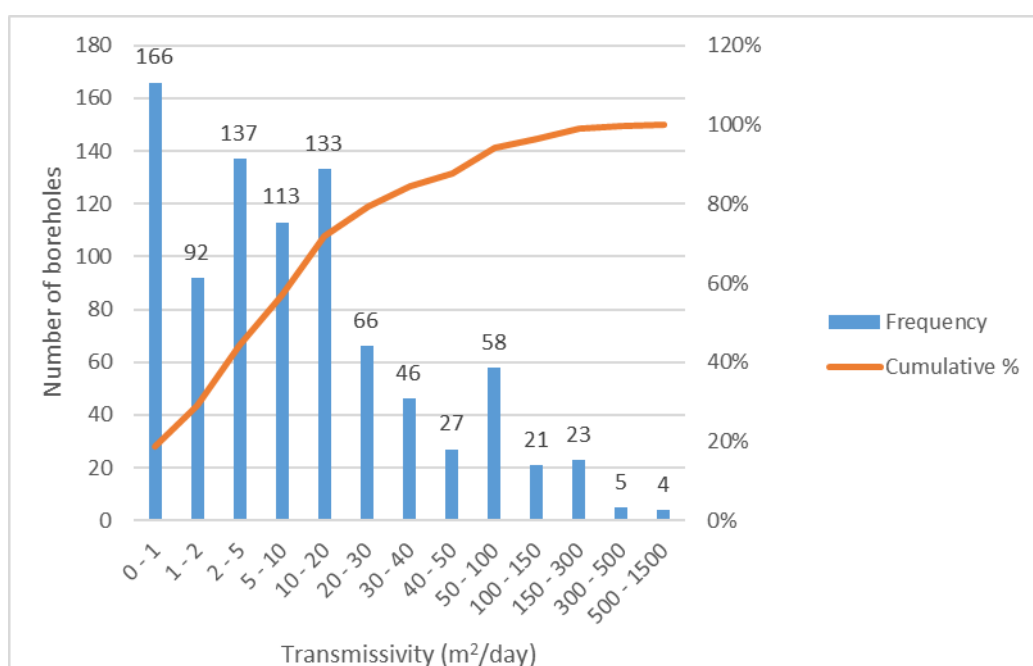


Figure 21 Frequency histograms and cumulative distribution of transmissivity (m²/day) for the study area

The transmissivity expresses the permeability of the aquifer materials, and groundwater flow within a groundwater system which is influenced by various factors. The relation between transmissivity and the following factors: geology, lineaments, drainage, topography and slope, was assessed in order to identify factors which have a significant influence transmissivity in the investigated area. In crystalline bedrock aquifers the occurrence and movement of water is mainly associated the presence of fracture and fault zones, therefore the influence between the study area's geology and lineaments, and transmissivity values was assessed. Drainage, topography and slope - which are factors related to geomorphology, which also has an influence on groundwater potential. And the borehole depth in relation to the transmissivity was evaluated.

3.3.1 Geology

The occurrence and the flow of groundwater within an aquifer is governed by the physical properties of the geological unit, therefore permeability varies across different stratigraphic units. The distribution of boreholes and their associated transmissivities, across the various geological units in the study area is displayed in Figure 22. The map depicts that transmissivity values for boreholes located in the granitic phase of the limb are generally lower than the transmissivity values of boreholes in the RLS. The statistical summary presented in Table 8, provides a comparison for how hydraulic parameters differ for each lithostratigraphic division in the study area. The presented statistics align with the displayed spatial distribution (Figure 22). The Rooiberg Group is the lithological unit with the least number of boreholes, data points and has the lowest mean transmissivity, followed by Rashoop Granophyre Suite and the Lebowa Granite Suite, respectively. While the RLS has the highest mean transmissivity, 42 m²/day – which is even greater than the mean transmissivity for the entire eastern limb (28 m²/day). Majority of the boreholes contributing to the study area's transmissivity dataset (59,4%) are located within the RLS, which hosts one of the boreholes with the highest transmissivity in the study area.

Table 8 Descriptive statistics for transmissivity according to the lithostratigraphic divisions of the BIC

Lithostratigraphic Division		Transmissivity (m ² /day)						
		No. of boreholes	Mean	Median	Mode	Standard Deviation	Min	Max
Lebowa Granite Suite		297	7,7	1,6	0,3	23,1	0,1	219,0
Rashoop Granophyre Suite		30	3,3	1,8	0,8	4,0	0,1	15,6
Rustenburg Layered Suite		530	42,3	15,0	20,0	102,0	0,2	1500,0
Rustenburg Layered Suite Subdivisions	Upper Zone	188	28,7	12,6	15,0	50,1	0,2	361,0
	Main Zone	182	42,2	16,3	20,0	97,0	0,2	852,0
	Critical Zone	82	46,5	24,7	69,0	72,1	0,4	410,0
	Lower Zone	78	71,0	17,0	35,0	191,1	0,7	1500,0
Rooiberg Group		5	2,1	3,0	-	1,6	0,2	3,6

The distribution of transmissivity data with respect to the geology was further analysed through cumulative distribution curves as shown in Figure 23, which were used to compare the cumulative frequency for transmissivity for each lithostratigraphic unit in the study area. There is a relatively wide gap between the cumulative distribution curves of the granitic and mafic units of the investigated area. In the group of units with lower transmissivity; Rooiberg Group, Rashoop Granophyre and Lebowa Granite Suite; the Lebowa Granites have relatively higher transmissivities.

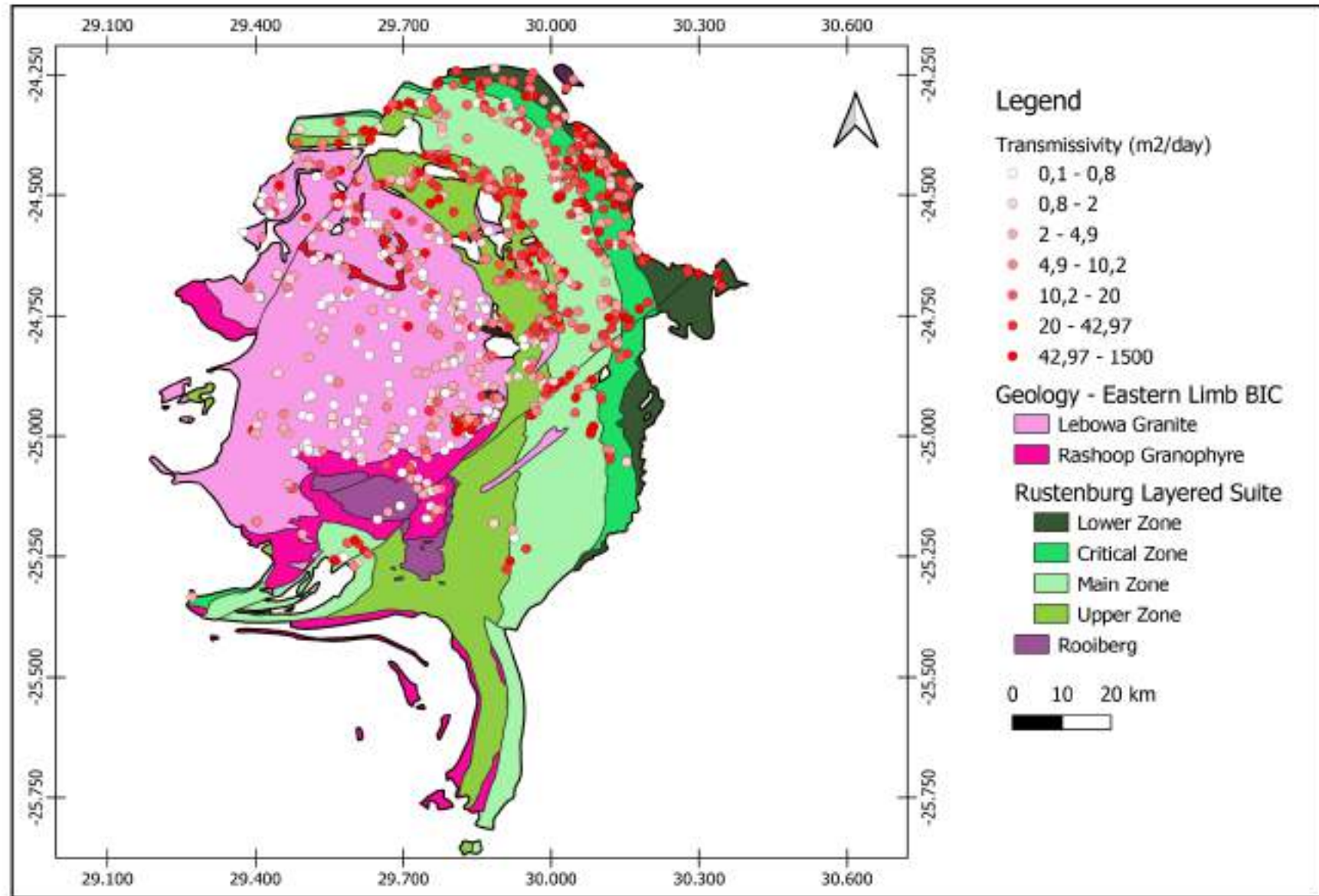


Figure 22 Transmissivity variation across the study area in relation to the geology

The data distribution for RLS is presented as per each subdivision - the most permeable lithological units in the study area are within the RLS, with 82% of the Lower Zone data less than 100 m²/day and 89% of the Critical Zone data is within 100 m²/day range. Transmissivity in the RLS increases from the Upper Zone to the Lower Zone.

Geological contact zones mark a transition in geological characteristics, and consequently a change in hydraulic properties is expected, additionally the zone may also present zones of weakness – therefore the relation between lithological contact zones was assessed. Figure 24 shows the cumulative frequency curve for transmissivities for boreholes located within 250 m of lithological contacts, compared with boreholes located positioned at a distance greater than 250 m away from the contacts. 16% of the dataset consists of boreholes within the 250 m buffer zone, therefore majority of the boreholes are not within close proximity to lithological contact zones. Figure 24 shows that 80% of the boreholes located more than 250 m away from geological contacts have transmissivity values less than 30 m²/day, while 70% of boreholes within 250 m from geological contacts have transmissivity values less than 30 m²/day. Therefore, this indicates that boreholes located within 250 m of the contacts have higher transmissivity. The geometric mean of 10 m²/day versus 6 m²/day, for boreholes within the distance of 250 m from contact and boreholes at a further distance, respectively, reveal that boreholes within closer proximity to contacts are associated with higher transmissivity. However, the Spearman's rho of -0,235 indicates that there is negative weak correlation between transmissivity and boreholes' distance to lithological contacts.

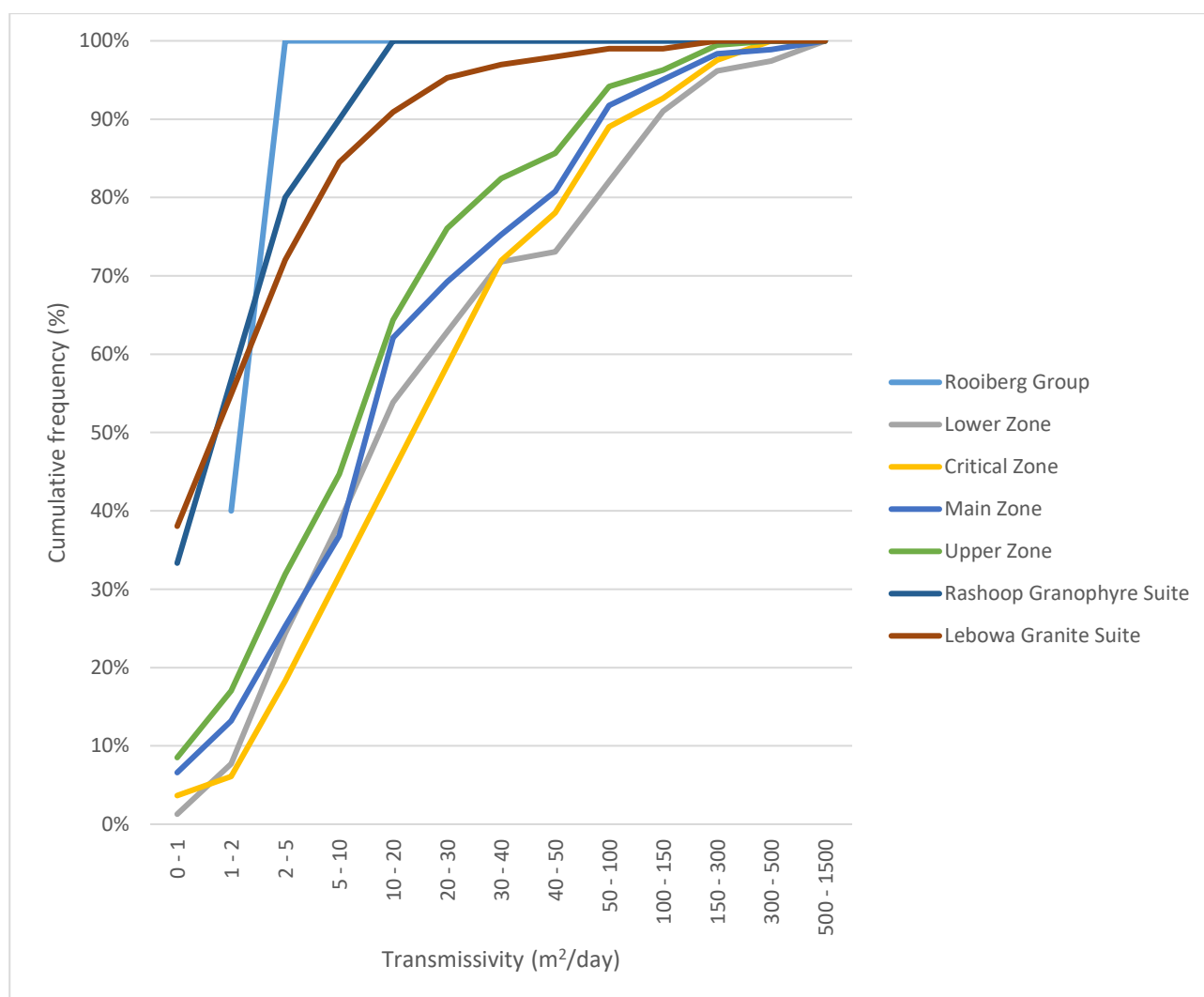


Figure 23 Cumulative distribution of transmissivity (m²/day) of boreholes in relation to stratigraphic units in the study area

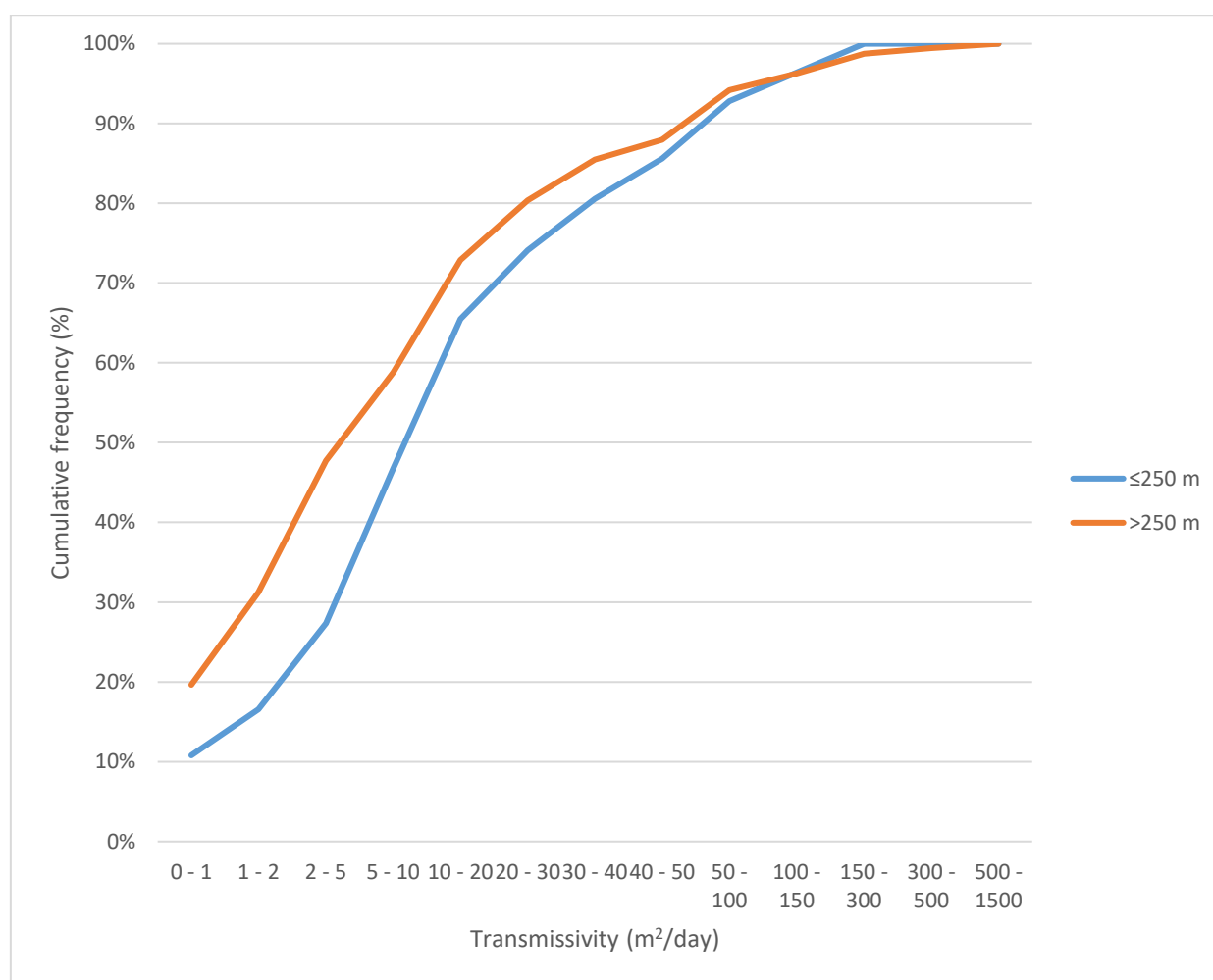


Figure 24 Cumulative distribution of transmissivity (m²/day) of boreholes located within 250 m of lithological contacts and boreholes located at distance more than 250 m from lithological contacts

3.3.2 Lineaments

The investigated area consists of crystalline rocks, therefore the development of aquifers depends on the presence of secondary features, such as fractures and faults. The structural geology map of the study area in Figure 25, modified after the 1: 1 000 000 Geological map sourced from CGS, shows the occurrence of structural features in the area, identified as faults, dykes and inferred geological lineaments, in relation to the varying transmissivity values across the eastern limb. Figure 25 depicts a concentration of geological lineaments in the north eastern part of the study, which is mainly the central sector of the RLS, and boreholes located this sector have relatively higher transmissivities.

In this investigation the structural geology map of the study area was applied for the analysis of the association between transmissivity and geological lineament structures (which specifically include dykes, faults and inferred lineaments as depicted in Figure 25). The influence of distance from lineaments on transmissivity was assessed. Figure 26 shows that approximately 77% of the transmissivity data for boreholes within 300 m from lineaments are less than 50 m²/day, whereas 88% boreholes at distance beyond 300 m from lineaments have transmissivities less than 50 m²/day. This suggests that boreholes within close proximity to geological lineaments have higher transmissivities. The geometric means which decrease from 10,18 m²/day for boreholes within 300 m of lineaments to 6,19 m²/day for boreholes at a distance >300 m, support the correlation deduced from Figure 26. The association between borehole distance to lineaments and transmissivity can also be described by Spearman's rho of -0,165, which implies that there is a correlation between the two variables, however the correlation is weak.

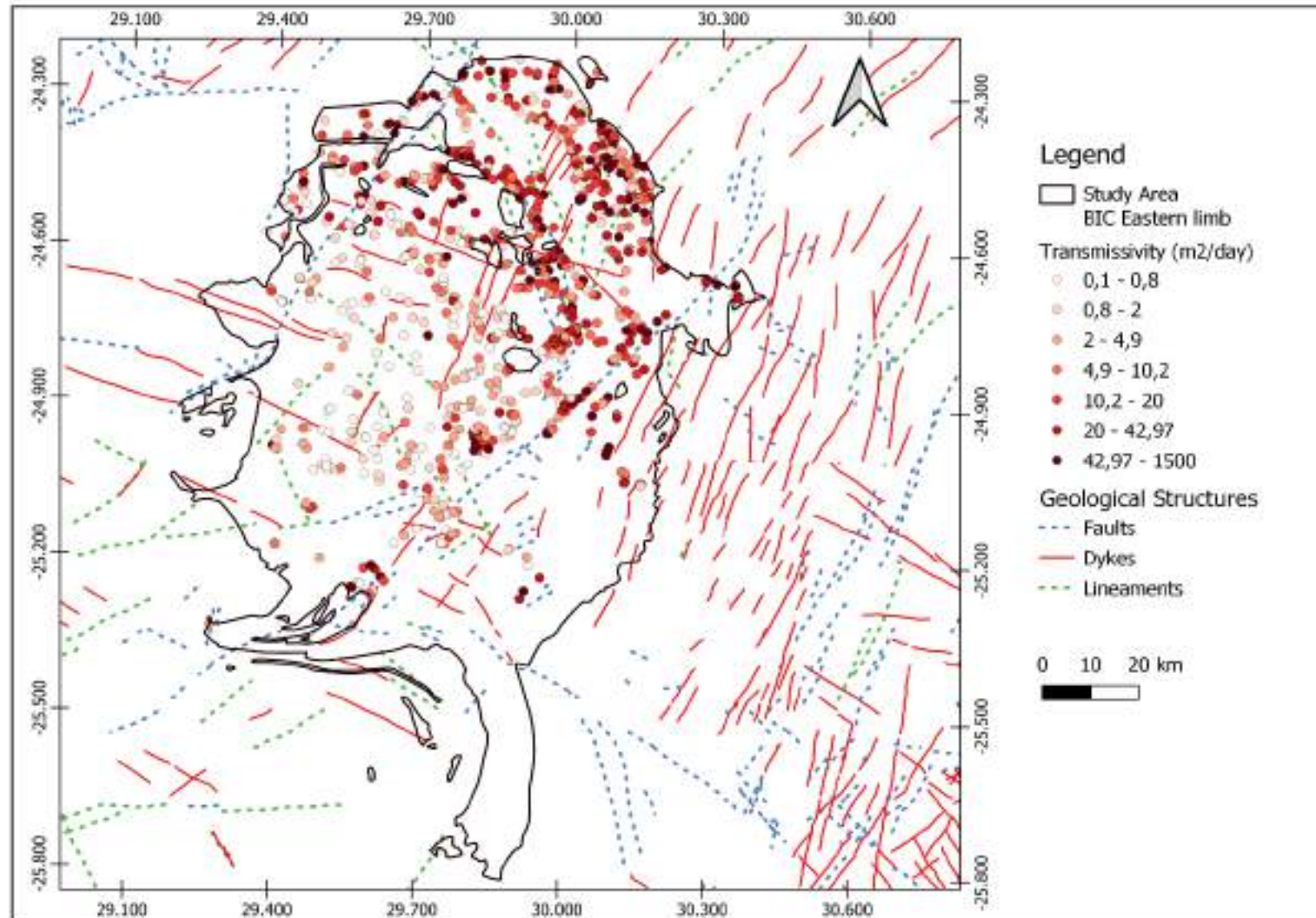


Figure 25 Structural geology map of the eastern limb of the Bushveld Igneous Complex showing the spatial distribution of borehole and their varying transmissivity values

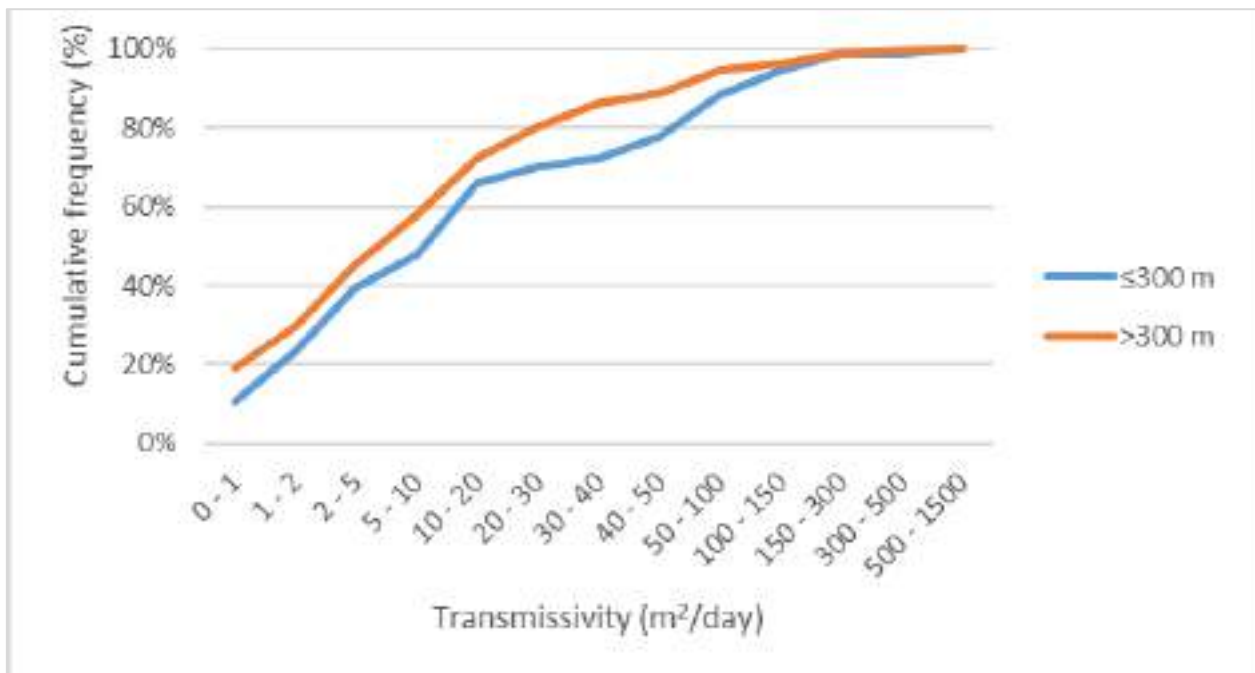


Figure 26 Cumulative distribution of transmissivity (m²/day) of boreholes in relation to the borehole's proximity to lineaments, cumulative frequency curves for boreholes within 300 m distance to lineament and boreholes located more than 300 m away from lineaments

The influence of lineament density was also assessed in Figure 27, which was based on lineament density values calculated and depicted in Figure 28a. The lineament density map shows that the maximum lineament density value for the study area is 1,81 km⁻¹, which indicates that lineament density in the area is at low level. This suggests that permeability due to lineament density, which is related to interconnection between structural discontinuities, is relatively low. For the analysis, the lineament density of the study area is categorised into four classes, where lineament density ranging 0 – 0,5 km⁻¹ is the lowest and 1,4 – 1,8 km⁻¹ is the highest density class for the study area. In Figure 27, transmissivities of boreholes were compared according to the lineament density class the boreholes are located in. The cumulative frequency curves show that boreholes within the lineament density >1,4 km⁻¹ are associated with the highest transmissivity, however only 0,35% of the transmissivity dataset is located within the highest lineament density zone. Majority of the boreholes (82,5%) are located within the 0 -0,5 km⁻¹ lineament density zone. The cumulative frequency curves show that transmissivity is lowest in this density zone.

Spearman's rho of 0,107 between transmissivity and lineament density suggests that there is a weak positive correlation between the two variables. Analysis of the transmissivity geometric mean for each lineament density class, shows that the geometric means increase as the density classes increase; 6, 04 m²/day and 16,24 m²/day represent the geometric mean transmissivity values, for the lowest and highest lineament density class, respectively. From the above analyses, a relationship between the two variables can be established, which suggests that an increase in lineament density is associated with higher hydraulic conductivity.

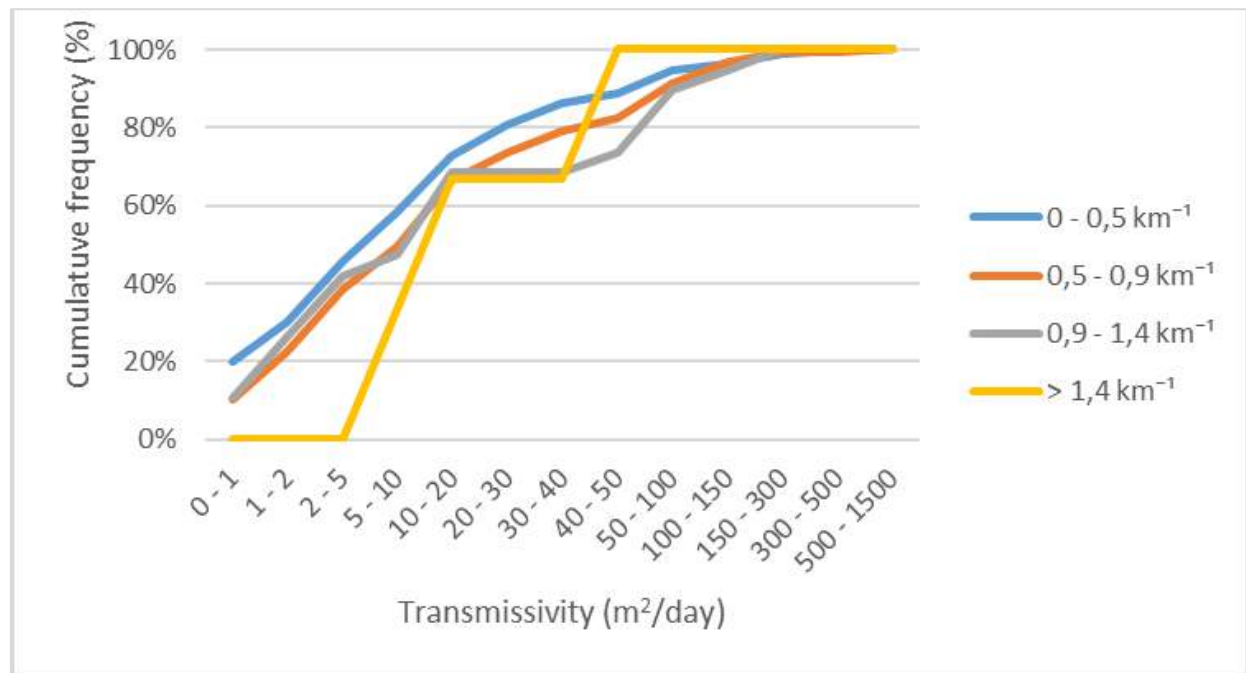
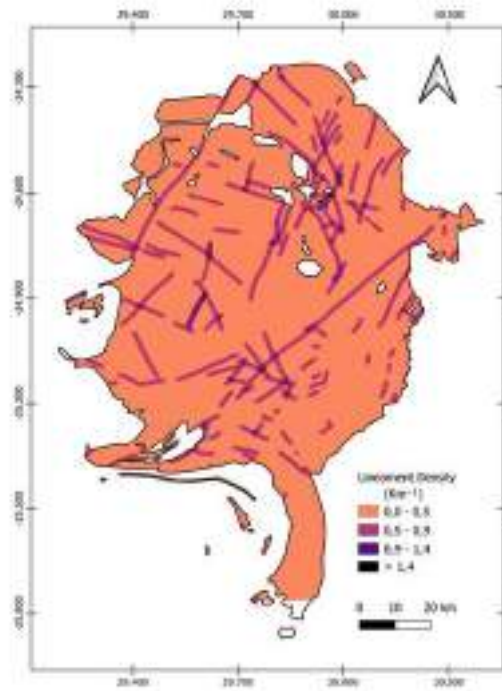


Figure 27 Cumulative distribution of transmissivity (m²/day) of boreholes in the study area relative to the lineament density

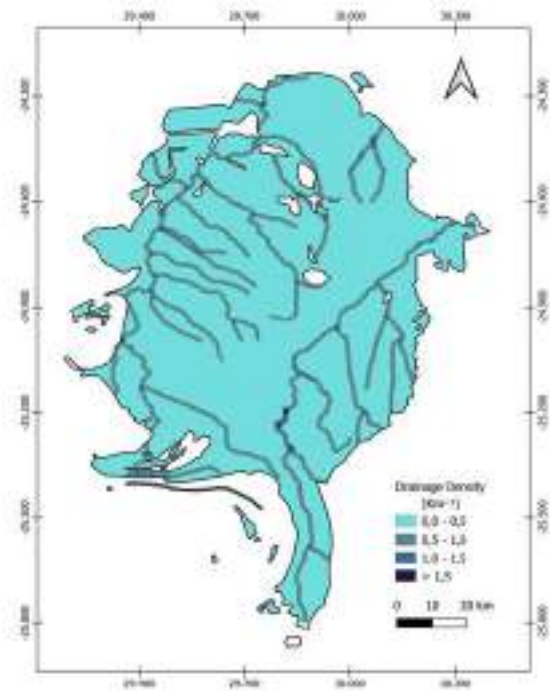
3.3.3 Drainage

In fractured aquifers, watercourse usually develop along zones of structural weakness, therefore along drainage patterns, an increase in secondary structures, discontinuities and weathering, is expected. The influence of distance of boreholes from perennial rivers on transmissivity was assessed by comparing transmissivity data of boreholes within 100 m distance from river course versus transmissivity of boreholes more than 100 m away from perennial rivers. The distribution of the transmissivity data for the different scenarios is shown in Figure 29. There is a slight variation observed in the cumulative frequency of transmissivity; 80,43% of boreholes within the 100 m buffer zone have transmissivity less than 30 m²/day, while 79,29% of boreholes outside of the buffer zone have transmissivity less than 30 m²/day. The geometric mean for boreholes within the buffer zone is 8,5 m²/day and lower for boreholes away from rivers, 6,4 m²/day. This suggest that transmissivity of boreholes within aquifers in the vicinity of rivers are generally higher than boreholes located away from rivers. The relation of these factors is also defined by Spearman's rho equal to – 0,051, which indicates that the correlation between the borehole distance from rivers and transmissivity is a very weak negative correlation.

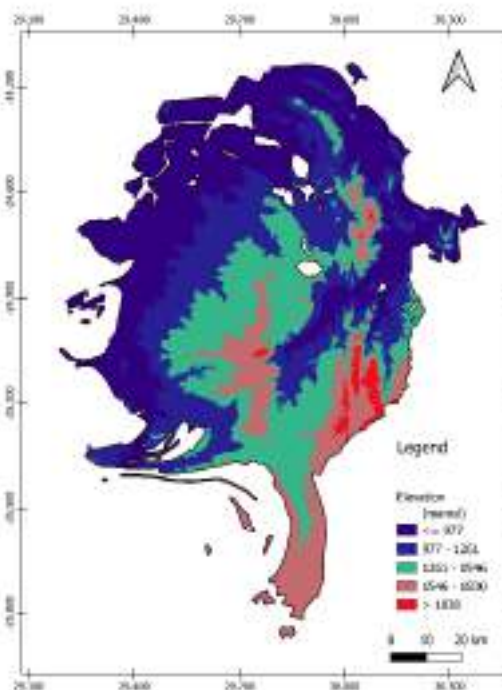
Drainage density is also another factor considered for the assessment of its relation to the study area's hydraulic properties. The drainage density measurement used for analysis of drainage density influence on transmissivity is shown in Figure 28b, and the maximum drainage density value calculated is 1,99 km⁻¹, which suggests that the study area is overall low drainage density zone. The distribution of transmissivity data in relation to the drainage density in the area is displayed in Figure 30, where the study area's drainage density is categorised into classes; with 0 – 0,5 km⁻¹ being the lowest and >1,5 km⁻¹ being the highest drainage density zone.



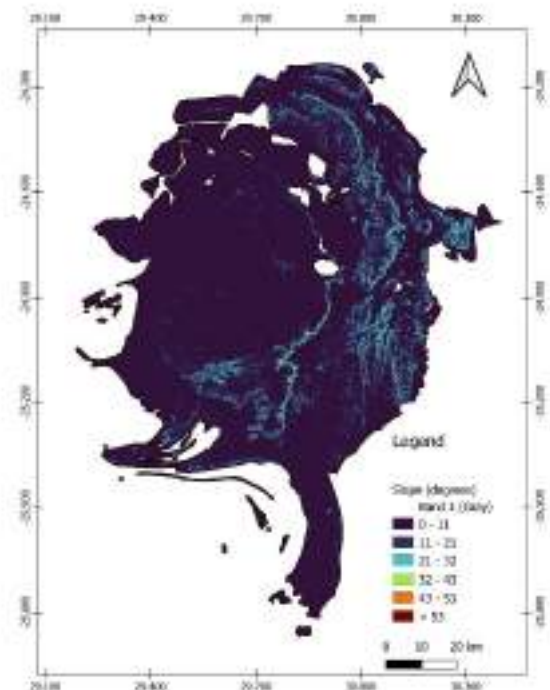
(a)



(b)



(c)



(d)

Figure 28 (a) Lineament density map, (b) drainage density map, (c) topography map and (d) slope map of the study area

The highest drainage density class covers a significant smaller area of the study area and as a result only 0,23% transmissivity data points are located in the drainage density zone, with the geometric transmissivity of 80 m²/day. Majority of the boreholes (74,4%) are located in the 0 – 0,5 km⁻¹ drainage density class, and the geometric mean for this class is 6 m²/day. This indicates that relatively higher drainage density zones are related to higher transmissivity. This relation is also observed in the cumulative frequency curves presented in Figure 30, which show that 88,91% and 50% of the lowest and highest drainage density zone, respectively, have transmissivity values less 50 m²/day. The relationship between the variables can also be described by a Spearman's rho of 0,12 which indicates a positive weak correlation.

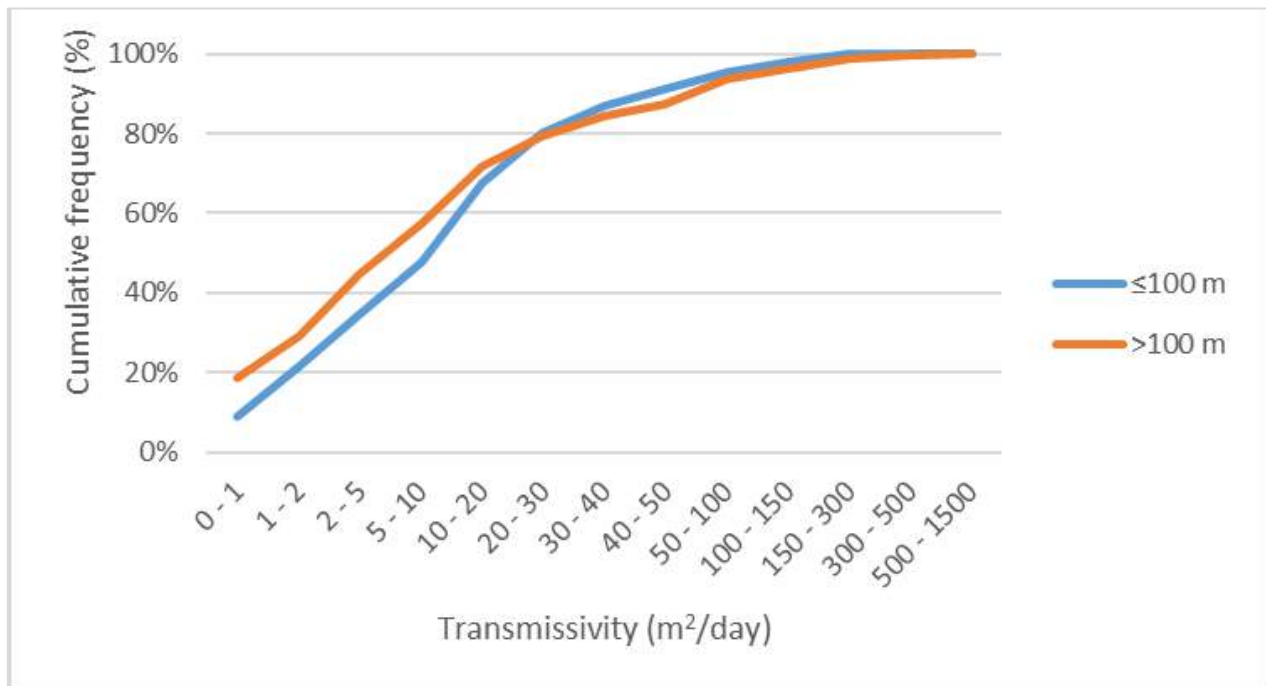


Figure 29 Cumulative distribution of transmissivity (m²/day) of boreholes in the study area relation to the borehole's proximity to perennial rivers

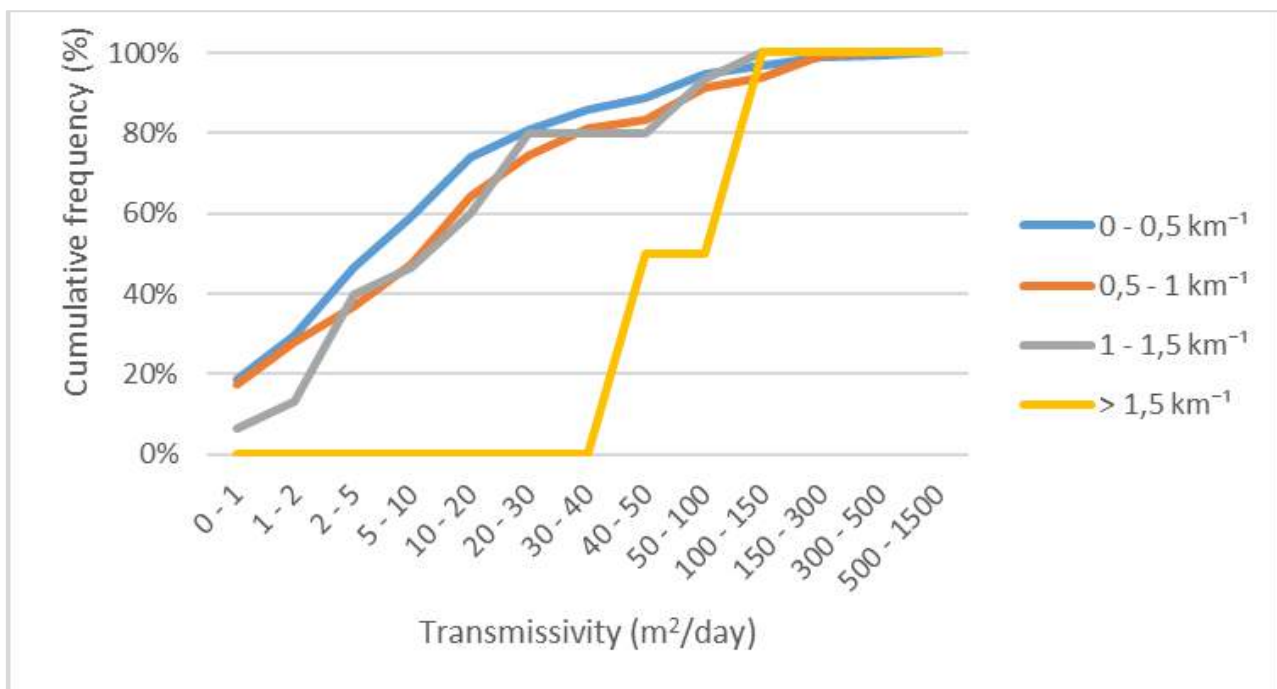


Figure 30 Cumulative distribution of transmissivity (m²/day) of boreholes relative to the drainage density of study area

3.3.4 Topography and slope

The topography and slope are geomorphological factors, and since the geomorphology of a study area also influences on hydrogeological dynamics, the factors association with groundwater was analysed. Figure 28c and Figure 28d show the elevation and slope of the study area, and the classes of each factor which were evaluated in relation to the hydraulic parameters of the investigated aquifer system.

The distribution of the transmissivity data in relation to the study area's elevation is given in Figure 31, show that lower elevation is associated with higher transmissivity. In the 1546 – 2115 mamsl elevation class which represents the highest elevation, 98,11% of the boreholes have transmissivity less than 20 m²/day, whereas 61,19% of the boreholes located in the lowest elevation class, <977 mamsl, have transmissivities less than 20 m²/day. This trend is also expressed by the transmissivity geometric means, which show a decrease from the lowest elevation class to the highest elevation class, which have geometric means of 11,21 m²/day and 2,4 m²/day, respectively. A Spearman's correlation between elevation and transmissivity of -0,367 was obtained, which implies a negative moderate correlation.

The calculated slope of the study area's terrain (Figure 28d) was categorised as 0° - 10°, 11° – 20° and >21°, which represent gentle, moderate and steep slopes, respectively. Figure 32 illustrates the analysis of transmissivity data in relation to the slope categorises, shows that 100% of boreholes position in moderate and steep slopes, have transmissivity values less than 100 m²/day, whereas 93,8% of the boreholes drilled on gentle slope terrains have transmissivity values less than 100 m²/day. Such suggests that gentles slopes are related to higher transmissivity values as compared to moderate and steep slopes. According to the analysis of geometric means, moderate slope category with a mean 14,40 m²/day, is associated with an increase in transmissivity, in contrast to gentle and steep slopes, with geometric means equal to 6,44 m²/day and 6,30 m²/day, respectively. Therefore, according to the cumulative frequency curves, higher transmissivity is generally related to gentle slopes, however according to geometric means, moderate slopes are related to higher transmissivities. Based on this variation, an association between the slope and transmissivity was not established. It is noteworthy that most (97,3%) of the boreholes are located in the gentle slope terrain. Additionally, the relation between the two variable was assessed by the Spearman's rho, which is equal to -0,129 indicating a very weak correlation.

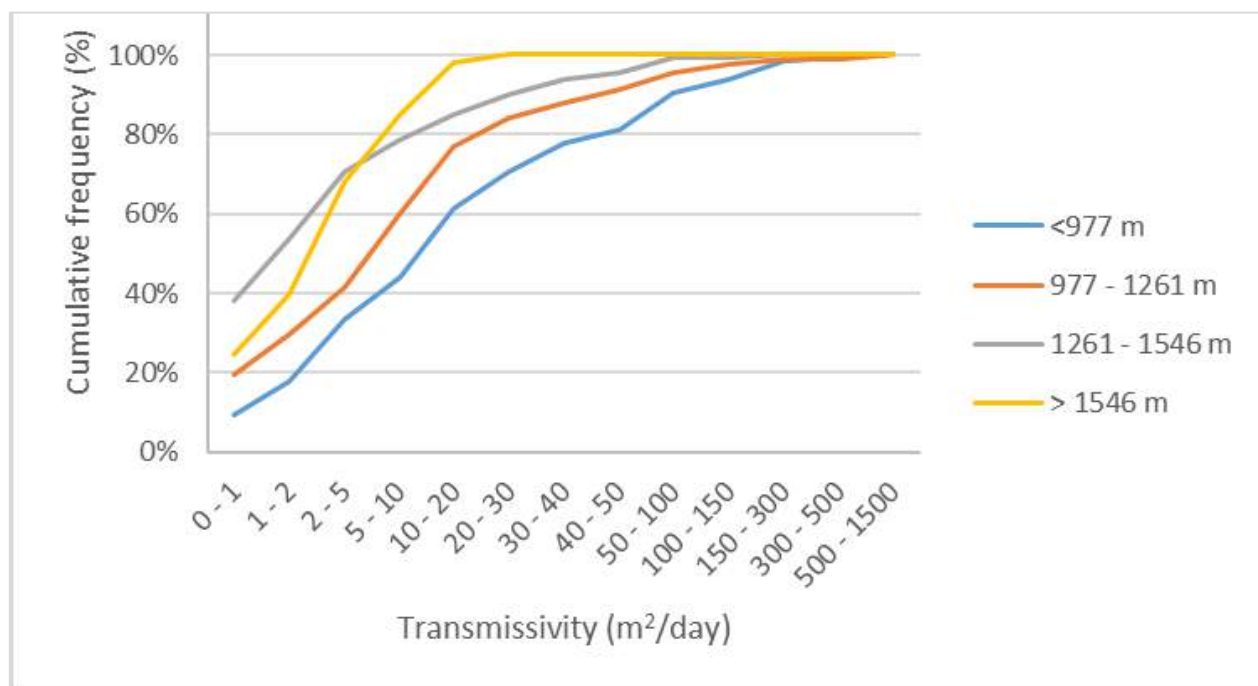


Figure 31 Cumulative distribution of transmissivity (m²/day) of boreholes relative to the elevation classes

3.3.5 Borehole Depth

Borehole depths in the investigated area range from near groundwater surface to 300 mbgl. The variation of transmissivity values in relation to borehole depths was assessed based on borehole depth intervals; < 50 mbgl, 50 – 100 mbgl, 100 – 150 mbgl and >150 mbgl. Borehole drilled to a depth less than 50 mbgl have the highest mean transmissivity (13,70 m²/day) and the lowest mean is for the borehole drilled to a depth greater than 150 mbgl (1,81 m²/day). The geometric mean transmissivity values decrease as the borehole depth increase. It should be noted that majority of the transmissivity dataset (48%) consists of boreholes drilled between 50 – 100 mbgl. And that in each borehole depth interval there are boreholes with relatively higher transmissivity values than the mean. The maximum transmissivity values are 852 m²/day, 1500 m²/day, 344,5 m²/day and 40 m²/day for the following borehole depth intervals, < 50 mbgl, 50 – 100 mbgl, 100 – 150 mbgl and >150 mbgl, respectively. This indicates a wide variability of transmissivity values even with various borehole depth interval. Based on the geometric means, there is an influence of borehole depth on transmissivity – the association suggest that transmissivity generally decreases with an increase in borehole depth. This association is also supported by the Spearman's rho value of -0,39, which implies that there is a moderate negative correlation between borehole depth and transmissivity.

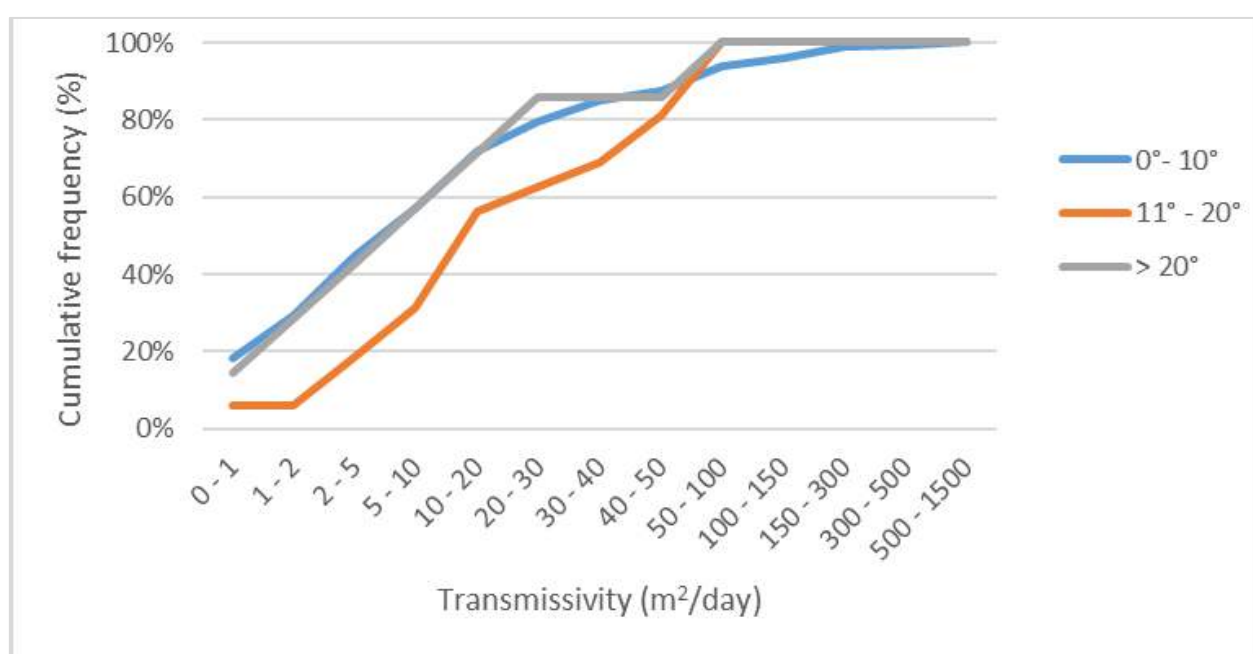


Figure 32 Cumulative distribution of transmissivity (m²/day) of boreholes relative to the slope classes in the study area

3.3.6 Summary

Hydraulic characteristics across the study area were studied in relation to how various factors influence permeability in the groundwater system of the eastern limb of the BIC. Statistical analyses were applied to determine the correlation between the transmissivity and the factors.

The RLS has the highest transmissivity compared to the other lithostratigraphic units in the study area. The lowest transmissivity is attained in the Rooiberg Group. Table 9 shows the geometric means, used to assess the variation of transmissivity in relation to different extents of each factor. Boreholes in close proximity to geological contacts are associated with higher transmissivity, the two variables have a negative correlation. Distance to lineaments and perennial rivers, in the study area, are also related to higher transmissivity. The relationship between transmissivity and lineament density as well as drainage density, showed that an increase in density is related to an increase in transmissivity, which indicates a positive correlation. There is an inverse

relation between transmissivity and factors; topography and borehole depth, which suggests that boreholes at lower elevations have higher permeability and boreholes drilled to shallow depths. In the study area, no distinct relation was determined between transmissivity and the terrain slope.

Evaluating the relationship established by geometric mean (Table 9) and data distribution analyses compared to the correlation established by bivariate analysis, the Spearman's correlation, showed that transmissivity and borehole depth have the highest correlation (-0,39), followed by topography (-0,367), while out of all the analysed factors, in the study area, transmissivity and distance to rivers have the least significant correlation (-0,051).

Table 9 Statistical analysis of transmissivity values relative to various factors. Geometric mean transmissivity values used to assess and compare the influence of the factors on the permeability of the eastern limb of the BIC

Factors	N	Geometric Mean Transmissivity (m ² /day)
Distance to Geological Contacts		
≤250 m	139	10,24
>250 m	723	6,00
Distance to Lineaments		
≤300 m	94	10,18
>300 m	768	6,20
Lineament Density		
0 - 0,5 km ⁻¹	715	6,04
0,5 - 0,9 km ⁻¹	125	9,51
0,9 - 1,4 km ⁻¹	19	9,64
> 1,4 km ⁻¹	3	16,24
Distance to Rivers		
≤100 m	46	8,50
>100 m	816	6,45
Drainage Density		
0 - 0,5 km ⁻¹	685	6,01
0,5 - 1 km ⁻¹	160	8,65
1 - 1,5 km ⁻¹	15	11,24
> 1,5 km ⁻¹	2	80,25
Elevation		
<977 m	438	11,21
977 - 1261 m	211	5,91
1261 - 1546 m	160	2,39
> 1546 m	53	2,41
Slope		
0° - 10°	839	6,45
11° - 20°	16	14,41
> 20°	7	6,31
Borehole Depth		
<50 mbgl	307	13,70
50 - 100 mbgl	427	5,43
100 - 150 mbgl	132	2,45
150 - 300 mbgl	23	1,81

3.4 HYDROCHEMICAL CHARACTERISTICS

The groundwater quality database and regional hydrogeochemical characterisation of the eastern limb Bushveld Igneous Complex is based on hydrochemical data obtained from the national groundwater quality database, Water Management System (WMS). A combination of approaches was employed; multivariate statistical analyses, traditional graphical methods and bivariate plot analyses, to identify the dominant hydrochemical facies and understand the various hydrochemical processes controlling the groundwater chemistry, for each lithostratigraphic division of the BIC.

3.4.1 Hydrogeochemical classification

Groundwater chemistry dataset for each lithostratigraphic subdivision of the BIC was clustered into hydrochemical groups, consisting of groundwater samples with similar water quality, by Hierarchical cluster analysis (HCA). The spatial distribution of the identified hydrochemical groups is illustrated in Figure 33. The mean concentrations for hydrochemical variables of each hydrochemical group is presented in **Error! Reference source not found.**

Groundwater samples from the Rustenburg Layered Suite are classified into Group 1, 2, 3 and 4, which are characterised by an increase in mineralisation, respectively. Group 1 and 2 are similar, for both groups; the dominant cation is calcium and magnesium, and the anionic concentration is enriched in bicarbonate, which is associated with recently recharged water. Group 1 and 2 comprises of the largest sample sizes, therefore these form the dominant water type in the RLS. The chemical character of groundwater changes in Group 3, the hydrochemical group is characterised by an anionic dominance of chloride ions, which shifts the water type to Ca-Mg-Cl, and this indicates that groundwater mixing has occurred. Group 4, which consist of the lowest number of samples (5), has the highest mean concentrations for all hydrochemical variables, and it is characterised as Na-Cl water type.

The increase in mineralisation from Ca-Mg-HCO₃ (Group 1 and 2) to mixed type Ca-Mg-Cl (Group 3) to Na-Cl (Groups) is due to chemical evolution of groundwater from the groundwater recharge zone, and groundwater is altered as it undergoes hydrogeochemical processes along the flow path.

The groundwater samples from Raseebie Granophyre Suite are classified into two comparable clusters, Group 5 and 6. There is a general increase in mineralisation observed from Group 5 to 6, and the dominant anion for both groups is bicarbonate and dominant cations are calcium and sodium. The water types identified in this lithology are Ca-HCO₃ and Na-HCO₃. The increasing concentration of sodium suggest that groundwater evolved from Ca-HCO₃, which is related to newly recharged water, to Na-HCO₃ as groundwater was altered by water-rock interactions.

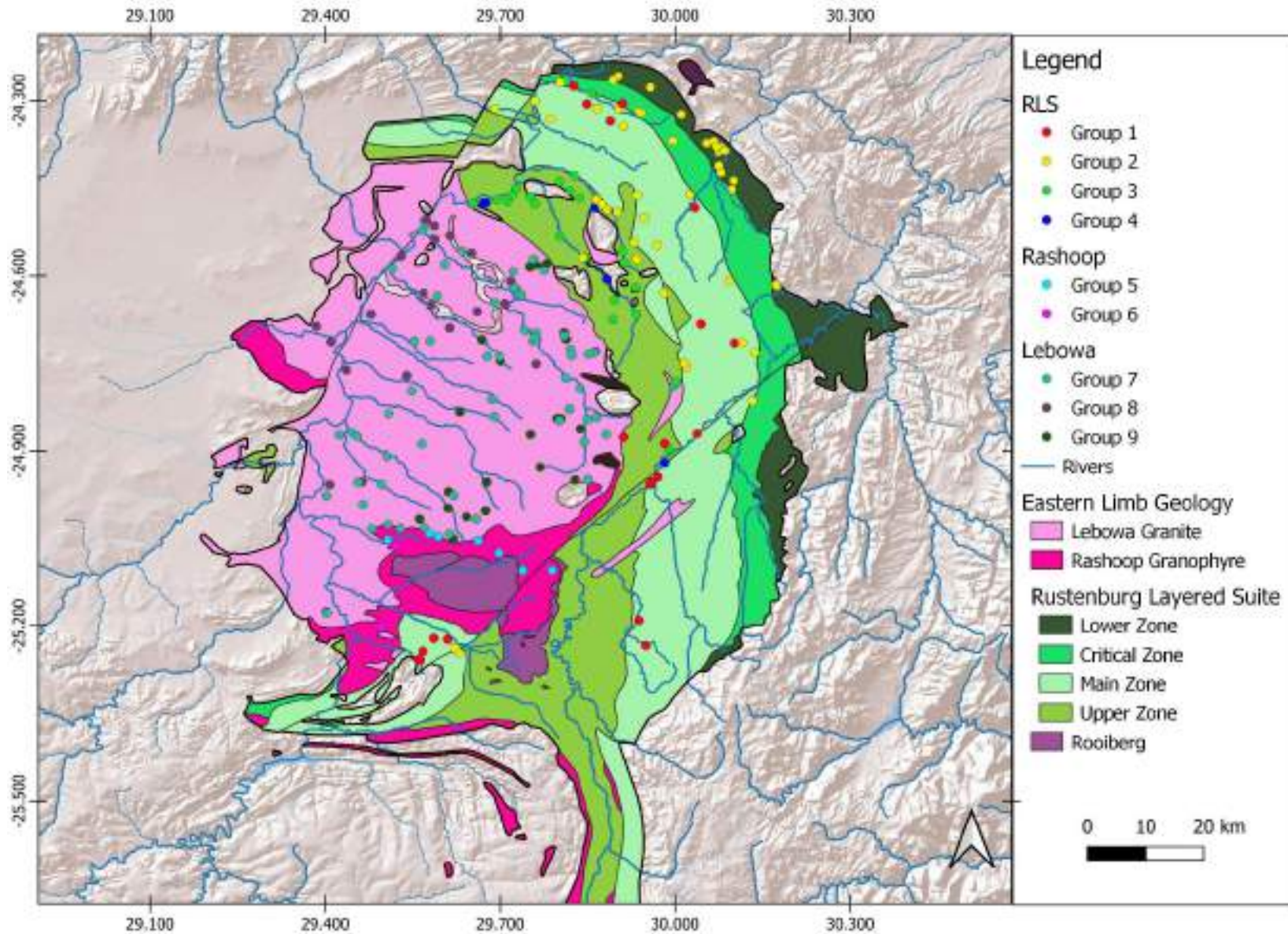


Figure 33 Spatial distribution of the hydrochemical groups across the eastern limb of the Bushveld Igneous Complex, identified by the HCA

In the Lebowa Granite Suite, hydrochemical data was clustered into Group 7, 8 and 9. Group 7 and 9 have similar chemical character, the abundant anion is HCO_3^- , and sodium and calcium are abundant cations. The mean hydrochemical variables increase in Group 8, suggesting an increase in groundwater salinity. In group 8, the anionic dominance is by chloride ions and sodium concentration increases. Therefore, based on mean concentrations of the hydrochemical variables of the hydrochemical groups, the dominant water types in the Lebowa Granite Suite, are Ca-HCO_3 , Na-HCO_3 and Na-Cl .

There is an observed trend of TDS increasing from Group 1 to 4, in the Rashedo Granophyre Suite, the TDS concentrations increase from Group 5 to 6, while in the Lebowa Granite Suite, the increase is from Group 9, 7 to 8. The groundwater in the study area has EC and TDS values, which are generally inverse to the elevation of the monitoring sites. Based on general hydrogeology principles, groundwater typically flows from recharge zones, in highland areas to discharge zones in lower elevation areas, where dissolved solids in the groundwater increase as groundwater moves through the aquifer, to discharge zones. This phenomenon is described as major ion evolution sequence, where evolutionary processes are related increased residence time along water flow paths, and also associated with increased mineralisation. Regional changes are observed as the chemical character of anions in groundwater, evolves from HCO_3^- at recharge zone to Cl^- , as an end-member of the anion evolution sequence (Freeze & Cherry, 1979). Such is observed in the investigation area, mineralisation of groundwater generally increases, in monitoring sites associated with lower elevation. And Group 4 and Group 8, are characterised by Na-Cl , which signals the end of the chemical evolutionary sequence – at this point of the sequence groundwater has evolved towards the chemical character of seawater (Freeze and Cherry, 1979).

The hydrochemical groups in the intermediate zones and discharge zones, Group 3, 4 and 8, have elevated SO_4^{2-} mean concentrations. Such can be explained by the shift of dominant anions in the chemical evolution sequence, related to mineralisation along the groundwater flow path. Intermediate areas are associated with SO_4^{2-} dominant ions, which changes to $\text{SO}_4^{2-} + \text{Cl}^- \rightarrow \text{Cl}^-$, with regional transformation from intermediate zones to recharge zones. According to knowledge of the Bushveld Igneous Complex and the land-use at the location of a few monitoring boreholes, the high concentrations of sulphates in the RLS may have been introduced into the groundwater system through possible contamination associated with sulphides from mining and mine tailings facilities.

The hydrochemical groups; 1, 2, 5, 6, 7 and 9 are classified as fresh water (0- 1000 mg/l TDS) according to the mean total dissolved solids (TDS) and groups 3, 4 and 8 with relatively higher mean TDS concentrations are classified as brackish water (1000 – 10 000 mg/l TDS). The groundwater quality for group 1, 2, 6, 7 and 9 are within the allowable standards of the South African National Standard (SANS) 241 Drinking Water Specifications. The mean concentrations of the RLS group 3 and 4, have elevated mean concentrations for EC, TDS, Mg and Cl, and additionally in Group 4, SO_4 mean concentration also exceeds the allowable limits for human consumption. In the Bushveld Granites, fluoride mean concentration for Group 5 and Group 8 are high - elevated fluoride content in groundwater from the granitic phase of the Bushveld Igneous Complex has been previously reported (Botha and Van Rooy, 2001; Lourens, 2013), this is due to groundwater interaction with granitic rocks containing fluoride minerals. Group 8, in the Lebowa Granite Suite, mean levels for sodium, chloride and fluoride, also exceed the allowable limits for drinking water.

PCA was used to identify the main hydrochemical variables controlling the groundwater quality, to infer the underlying factors controlling the hydrogeochemistry, establish probable relationships between the hydrochemical variables and hydrogeochemical processes within the groundwater system of the study area. The PCA was executed for three hydrochemical datasets for the different lithostratigraphic divisions in the BIC; Rustenburg Layered Suite, Rashedo Granophyre Suite and the Lebowa Granite Suite and the results are presented in Table 10. For all PCA performed, principal components (PC) selected for the analyses have an eigenvalue greater than one were considered for the extraction and for the analyses, hydrochemical variables with high positive loading (> 0.5) (Sergeant et al., 2016; Yidana et al., 2011) were selected, as an important contributor to the groundwater quality.

For the PCA executed for RLS, the hydrochemical data was reduced to three principal components with eigenvalues greater than one, explained by a cumulative variance of 73,94%, where PC1, PC2 and PC3 have variance of 41, 55%, 19,16% and 13,24%, respectively. The first principal component has high positive loadings for EC, TDS, Ca, Na, SO₄ and Cl hydrochemical variables. EC and TDS are a function of the ionic concentration and the temperature of the water. Calcium, sodium, sulphate and chloride are interpreted as the major ions contributing to the salinity of the groundwater. Significant loadings for EC and TDS indicate an increase in solutes in groundwater, is directly proportional to the TDS and EC, therefore higher TDS suggests longer residence and interactions between the groundwater and the geology.

Calcium and magnesium enrichment in groundwater mainly attributed to carbonate and silicate weathering (Davraz and Batur, 2021; Kumar, 2013; Wali et al., 2019) however silicate minerals are the main minerals composing the rocks of the study area, therefore significant Ca in groundwater associated with weathering of silicate minerals. The main source of sodium from the dissolution of minerals through weathering processes (Wali et al., 2019; Zakaria et al., 2021), or through influence of evapotranspiration processes, saline intrusions and (Kumar, 2013) and anthropogenic influences from infiltration of agricultural runoff and sewage (Zakaria et al., 2021). Chloride ions in groundwater are related to dissolution of soil salinity, linked to evaporation of precipitation (Masindi and Abiye, 2018) and may also be derived from anthropogenic processes (Wali et al., 2019). SO₄ in hydrogeological systems is sourced from anthropogenic activities (Masindi and Abiye, 2018; Wali et al., 2019).

Table 10 Table showing varimax rotated R-mode PCA loadings matrix

	<i>Rustenburg Layered Suite</i>			<i>Rashoop Granophyre Suite</i>			<i>Lebowa Granite Suite</i>		
<i>Parameter</i>	<i>PC1</i>	<i>PC2</i>	<i>PC3</i>	<i>PC1</i>	<i>PC2</i>	<i>PC3</i>	<i>PC1</i>	<i>PC2</i>	<i>PC3</i>
<i>pH</i>	-0,63	0,10	-0,16	0,09	0,81	0,18	0,01	0,83	0,19
<i>EC</i>	0,93	0,34	0,09	0,80	0,59	0,05	0,97	0,13	0,13
<i>TDS</i>	0,90	0,42	0,06	0,76	0,65	0,06	0,96	0,18	0,20
<i>Ca</i>	0,91	-0,12	-0,02	0,55	0,82	0,02	0,74	0,01	0,29
<i>Mg</i>	0,39	0,83	-0,07	0,91	0,06	-0,18	0,80	-0,07	0,45
<i>Na</i>	0,85	0,33	0,19	0,57	0,67	0,37	0,93	0,20	0,01
<i>K</i>	0,45	0,29	0,56	0,31	-0,70	0,12	0,13	0,13	0,61
<i>HCO₃</i>	-0,43	0,58	-0,30	0,28	0,92	0,19	0,47	0,50	0,55
<i>SO₄</i>	0,54	0,64	0,16	0,97	-0,07	-0,04	0,95	0,04	-0,05
<i>Cl</i>	0,97	0,17	0,06	0,89	0,13	-0,34	0,95	-0,02	0,07
<i>F</i>	0,18	-0,02	0,87	-0,29	0,20	0,88	0,09	0,82	-0,21
<i>NO₃</i>	0,04	0,72	-0,01	-0,02	0,13	-0,88	0,78	0,10	-0,13
<i>NH₄</i>	-0,08	-0,12	0,68	-0,08	0,34	0,54	-0,06	-0,12	0,60

The second principal component has high positive loading for Mg, HCO₃, SO₄, NO₃ variables, these major ions have significant contributions to the resulting groundwater chemistry. The dominance magnesium and bicarbonate results in Mg-HCO₃ water type, which represents recent groundwater. With reference to the geology of the study area, bicarbonate ions in groundwater are primarily are sourced form silicate weathering and another origin is through Ca-HCO₃ rainwater recharged into the groundwater system (Ahokpossi et al., 2018; Davraz and Batur, 2021; Masindi and Abiye, 2018). Sulphate and nitrate concentrations in groundwater are derived from anthropogenic influences.

The third principal component has high positive loading for the following hydrochemical variables; K, F, NH₄. This principal component explains the water-rock interaction processes and anthropogenic influences on groundwater chemistry. The occurrence of Potassium and fluoride in groundwater is sourced from rocks bearing these minerals, through water-rock interactions. NH₄ dissolved in groundwater through infiltration of

anthropogenic sources into groundwater system, such as agricultural return flows, sewage and wastewater (Masindi and Abiye, 2018).

The Rashoop Granophyre Suite groundwater samples dataset PCA results rendered three principal components with eigenvalues greater than 1, with a cumulative variance of 84,16%. The first principal component represents 35,85% of the total variance, has high positive loadings for EC, TDS, Ca, Mg, Na, SO₄ and Cl. The second principal which contains 31,33% explained by high positive loading for the following hydrochemical variables; pH, EC, TDS, Ca, Na and HCO₃. The first and second principal components explain the major ions contributing to the salinity of groundwater chemistry, which are derived from geogenic sources, through interacting of groundwater with the crystalline aquifer materials. The third principal is explained by 16,98% of the total variance, with high positive loading for F, NO₃ and NH₄, where fluoride is released from dissolution of granitic rock, as it is commonly present in granitic terrains. NO₃ and NH₄ occurrence in groundwater is derived from anthropogenic source.

From the groundwater samples dataset from the Lebowa Granite Suite reduced by PCA, three principal components with eigenvalues were retained with total variance of 75,41% composed of principal component 1, 2 and 3. The first principal component represents 50,57% of the total variance has positive loadings for the following hydrochemical variables; EC, TDS, Ca, Mg, Na, SO₄, Cl and NO₃, which are mainly released from hydrogeochemical processes, interaction of water and rocks, and the groundwater chemistry is also modified by evapotranspiration processes – while NO₃ is influenced by anthropogenic sources. The second principal component contains 13,46% of the total variance, and has high positive loadings for pH, HCO₃ and F. The third principal component explained by a variance of 11,38%, with positive loading for pH, HCO₃ and F. Bicarbonate is largely source from silicate weathering processes, and when pH is slightly alkaline, as is in the study area, it is related to anionic concentration dominated by bicarbonate.

The PCA application in this study does not necessarily enhance the hydrochemical classification determined by HCA, however it serves as a method that reduces the data and highlights the dominant hydrochemical variables responsible for the prevailing groundwater conditions, in each lithostratigraphic division. Inferences drawn from the identified main hydrochemical variables enlightened on the possible hydrochemical processes responsible for the groundwater water in each division. PCA and the HCA, provided an opportunity to also include other ions, other than main major ions and physiochemical parameter to the analysis – which is one of the methods advantages over graphical hydrochemical methods, such as Piper plots.

The application of multivariate methods in hydrochemical investigation, does not essentially directly inform on the cause, evolution and hydrochemical processes responsible for the identified main hydrochemical variables and dominant hydrochemical facies. Therefore, the hydrochemistry dataset for the investigated region was also assessed using Piper diagrams, to identify the various hydrochemical facies present, and possibly determine groundwater mixing and hydrochemical evolution processes within the eastern limb of BIC. Piper plots aided in refining and confirming the hydrochemical relationship and processes deduced from the multivariate analysis. Due to the density of the hydrochemical dataset, the groundwater samples clustering determined by HCA method were also applied to this analysis – for easy of identification and for spatial distribution reference.

The Piper diagram, Figure 34, shows that alkaline earths exceed alkalis ($\text{Ca} + \text{Mg} > \text{Na} + \text{K}$) and weak acids exceed strong acids ($\text{CO}_3 + \text{HCO}_3 > \text{SO}_4 + \text{Cl}$) in the Rustenburg Layered Suite. The dominant anion in this dataset is bicarbonate and the cation ternary diagram shows that for cations there is no dominant type. The dominant hydrochemical facies is magnesium calcium bicarbonate (Ca-Mg-HCO₃) which consists of water groundwater samples group 1 and majority of group 2 water samples. Ca-Mg-HCO₃ is related to recently recharged groundwater and is associated with the following hydrogeochemical processes; silicate weathering, reverse ion exchange (Zakaria et al., 2021). Other hydrochemical facies found in the RLS (Figure 34) are related to group 3 and 4, are mixed water types, Ca-Mg-SO₄-Cl and Ca-Na-HCO₃ and Na-Cl water type associated with relatively high mineralisation. A strong trend is observed, in dominant cations and anions, where sodium and chloride, respectively, are increasing from group 1 to group 4, which indicates that

mineralisation is progressing through the groups. This attests to the interpreted evolutionary processes and transition of hydrochemical water types, with change in elevation, of the hydrochemical groups identified by HCA.

The major ion chemistry of the Rashoop Granophyre Suite, plotted in the Piper diagram, Figure 35, shows that the cation chemistry described by sodium to mixed water type and anions are dominated by bicarbonate water type. Hydrochemical facies found in the Rashoop Granophyre Suite, are Ca-HCO_3 and Na-HCO_3 . It should be noted that there is a small number of monitoring sites in this unit, therefore only 11 samples were used to characterise the Rashoop Granophyre Suite.

Based on the Piper diagram interpretation, Figure 36, majority of the groundwater samples from Lebowa Granite Suite are characterised as weak acids which exceed strong acids ($(\text{CO}_3 + \text{HCO}_3 > \text{SO}_3 + \text{Cl})$). This is due to the bicarbonate type dominance, as reflected on the anion ternary plot (Figure 36). The cation ternary diagram shows sodium type dominance to mixed type. Therefore, the main hydrochemical facies in Lebowa Granite Suite (largely contributed by hydrochemical group 7 and 9) are Ca-HCO_3 and mixed Na-HCO_3 . Few samples in this lithostratigraphic division (mainly clustered as group 8), reflect mixed water type Ca-Mg-Cl and Na-Cl .

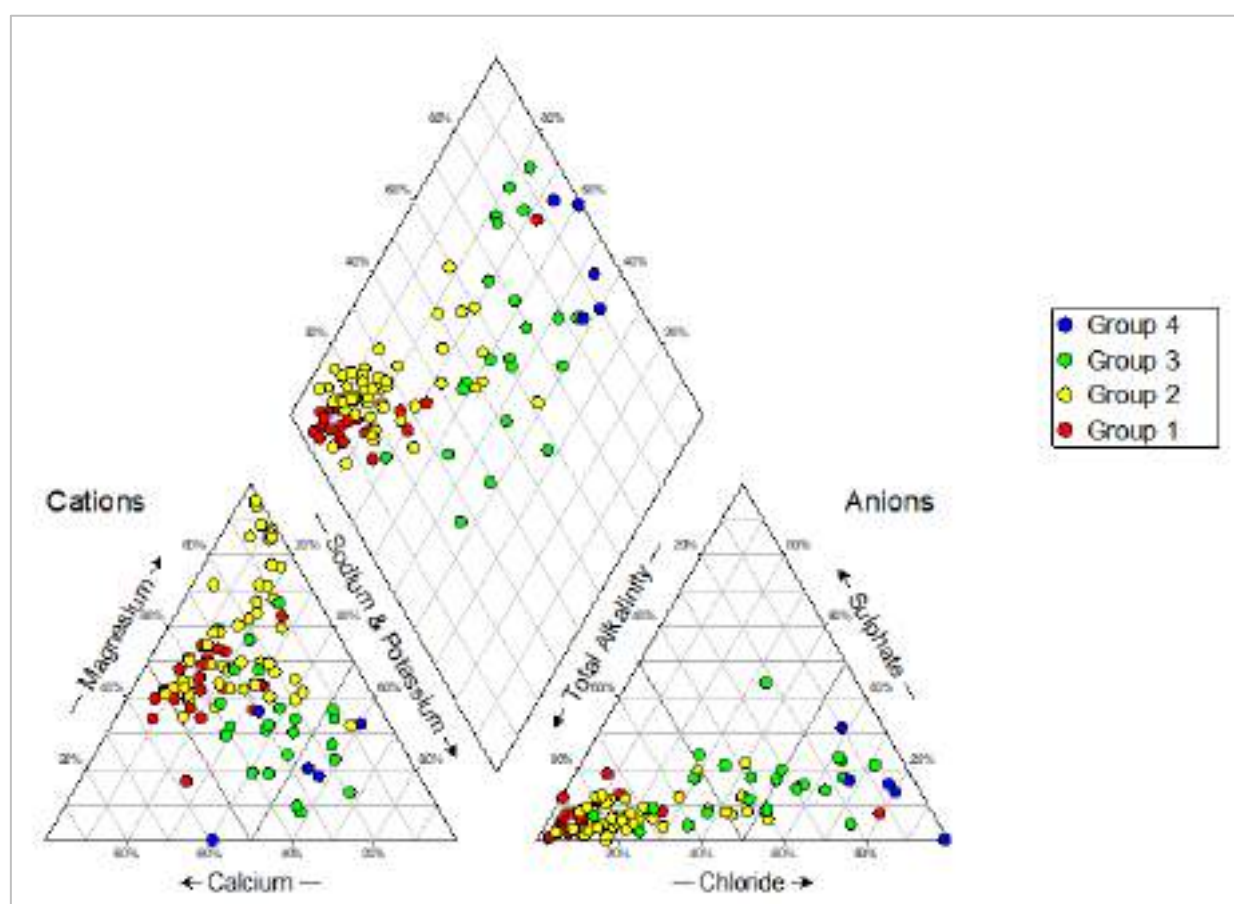


Figure 34 Piper Diagram showing Rustenburg Layered Suite, hydrochemical group based on HCA

The dominance of Ca-HCO_3 water type is related to modern groundwater, which is influenced by groundwater recharge derived from rainfall. The mixed water types and Na-Cl are attributed to hydrogeochemical processes which occur as the groundwater interacts with aquifer materials, which result in the evolution of groundwater. An increase in mineralisation suggests an increase in groundwater residence times, hence Na-Cl with highest mineralisation denotes the end of the evolutionary process. Such, corresponds with the increased concentrations of Na and Cl in group 8, recognised in the HCA, related to evolution of ions associated with lower, discharge zone water with high dissolved solids.

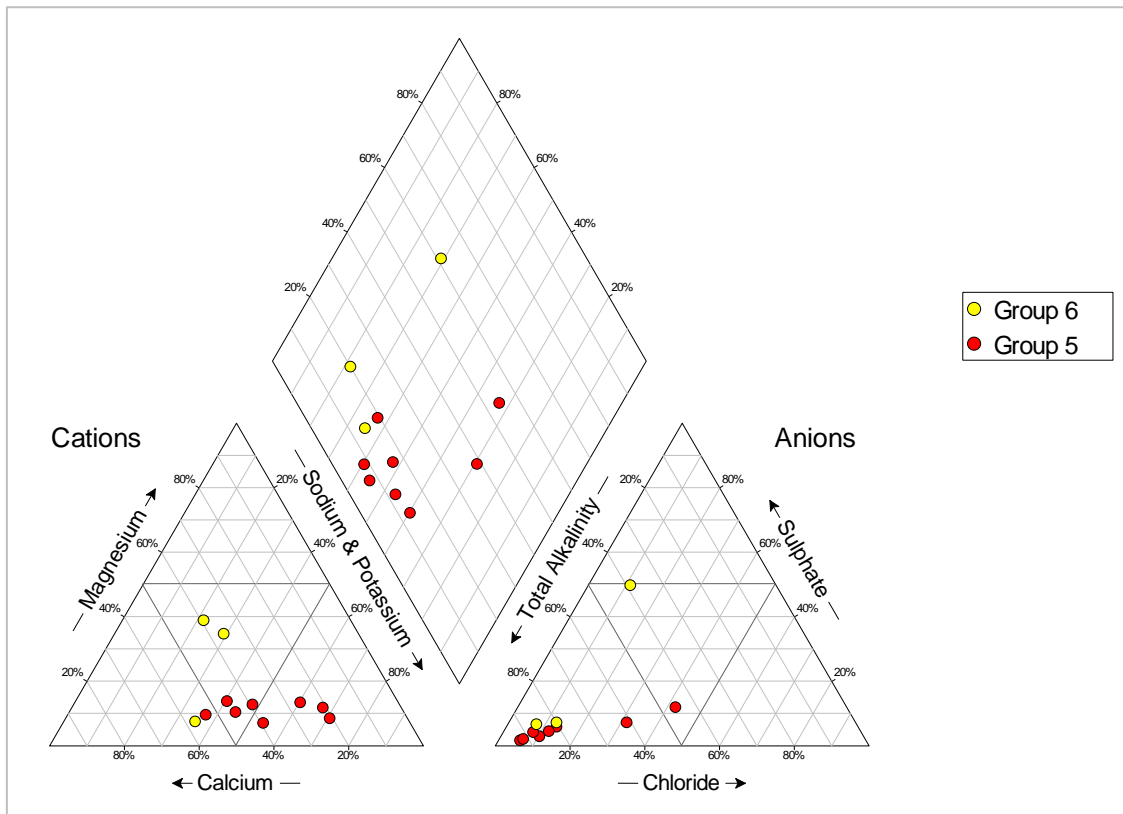


Figure 35 Piper Diagram showing Rashoop Granophyre Suite hydrochemistry dataset, hydrochemical group based on HCA

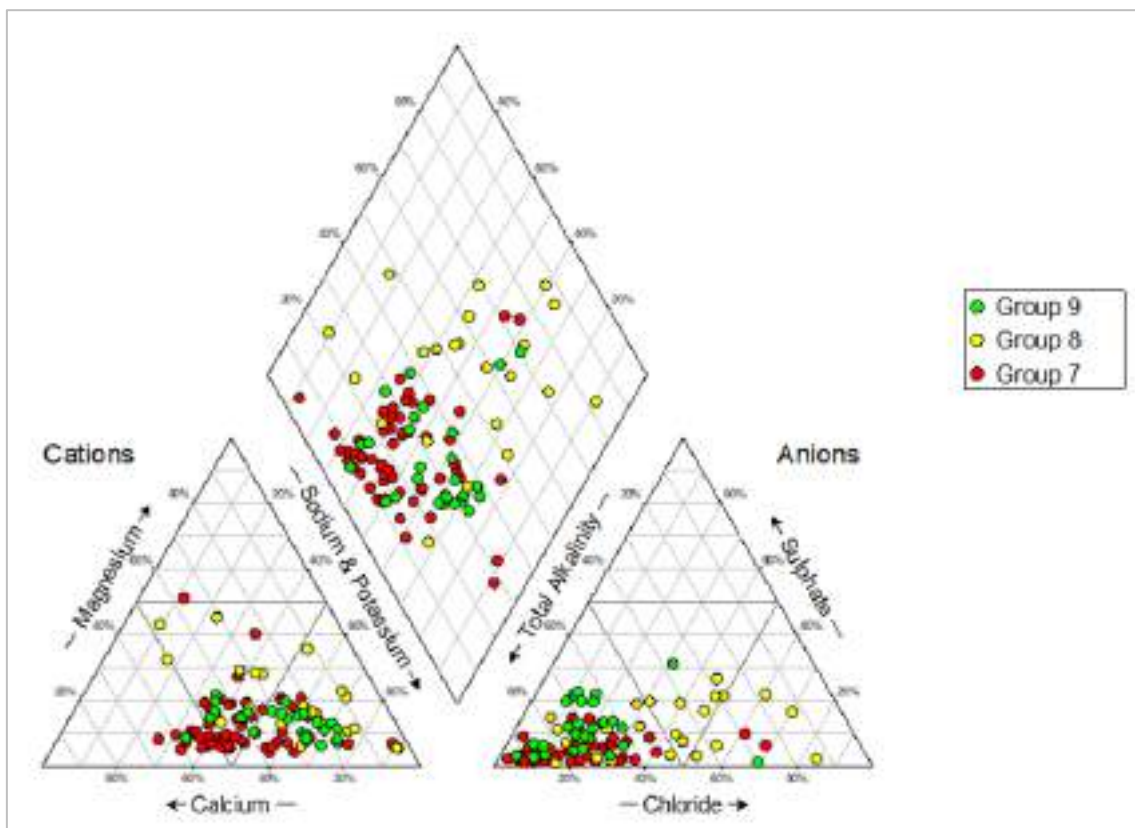


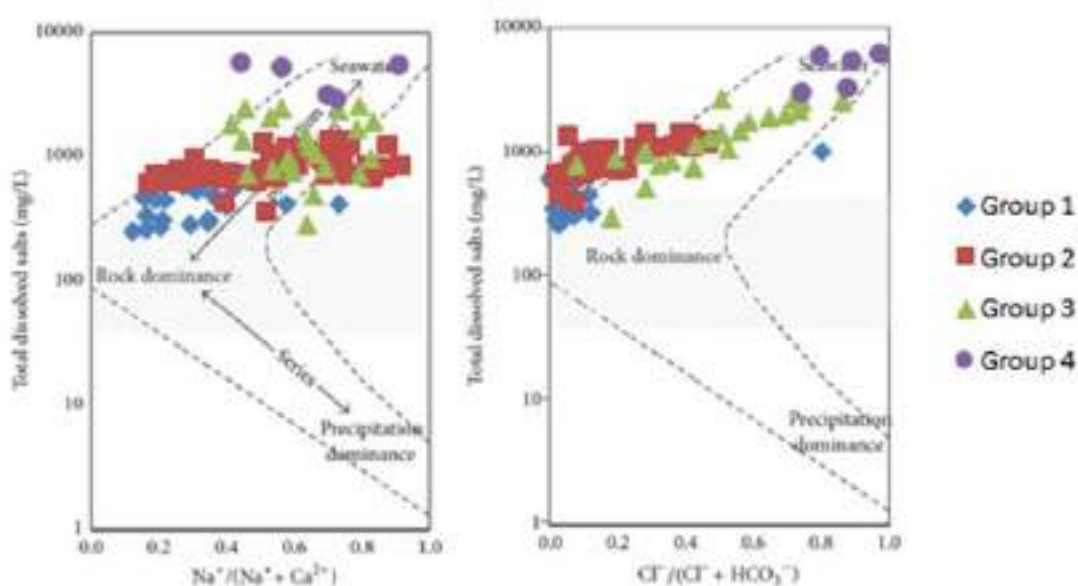
Figure 36 Piper Diagram displaying Lebowa Granite Suite hydrochemistry dataset, hydrochemical group based on HCA

3.4.2 Hydrogeochemical processes controlling groundwater chemistry

The chemical composition of groundwater from recharge is changed – the alterations are influenced by dissolution of the aquifer's rock minerals, ion exchange processes, evapotranspiration and anthropogenic influences. Hydrogeochemical processes controlling the groundwater chemistry and the hydrochemical facies in the Bushveld Igneous Complex were investigated. The Gibb's diagram, a ratio of $[\text{Na} + \text{K}] / [\text{Na} + \text{K} + \text{Ca}]$ and $[\text{Cl}] / [\text{Cl} + \text{HCO}_3]$ for cations and anions, respectively, was used to understand which natural mechanisms control the groundwater chemistry. The groundwater samples' hydrochemistry origin is described according to four fields on the Gibb's diagram, namely, evaporation dominance, evaporation-precipitation dominance, rock dominance, and precipitation dominance.

The Gibbs diagrams in Figure 37a, reveal that the RLS groundwater samples; Group 1 hydrochemistry is controlled by water-rock interactions, Group 2 and 3, plot on the evaporation-precipitation and rock dominance fields. Group 4 plots onto the evaporation dominance field, towards sea-water boundary, this is due to the high salinity content, the chemical character of these samples is close to that of seawater. Hydrochemical classification by HCA and graphical methods, noted regional changes in water types in the study area; in the RLS characterised by trends of increasing mineralisation from Group 1 to Group 4, associated with chemical evolution. The Gibbs diagram Figure 37a, also displays this increase in mineralisation, from Group 1 fresh groundwater to Group 4 with the highest TDS, and the diagram reveals that the elevated salinity is not solely attributed to prolonged water-rock interaction processes, but is also due to evapotranspiration influences, as cited in PCA interpretation.

According to Gibbs diagram, Figure 37b, the groundwater chemistry of Rashoop Granophyre Suite (Group 5 and 6) is related to rock dominance. This agrees with previous chemical characterisation, which identified that water types in this lithostratigraphic unit, are related to recently recharge water and mixed water types, associated with water-rock interactions. The Gibbs diagrams in Figure 37c, shows that hydrogeochemical processes controlling the chemistry of groundwater in the Lebowa Granite Suite, Group 7 and 9, are water-rock interactions, and hydrochemical group 8 illustrates both rock and evaporation-precipitation dominance. The influence of evapotranspiration in water chemistry of Group 8, explains the previously noted, elevated content of sodium and chloride in this hydrochemical group. None of the hydrochemical data plotted on the lower portion of the Gibbs diagrams (Figure 37), therefore this indicates that the groundwater chemistry of the BIC is predominantly controlled by evaporation and water-rock interaction processes.



(a)

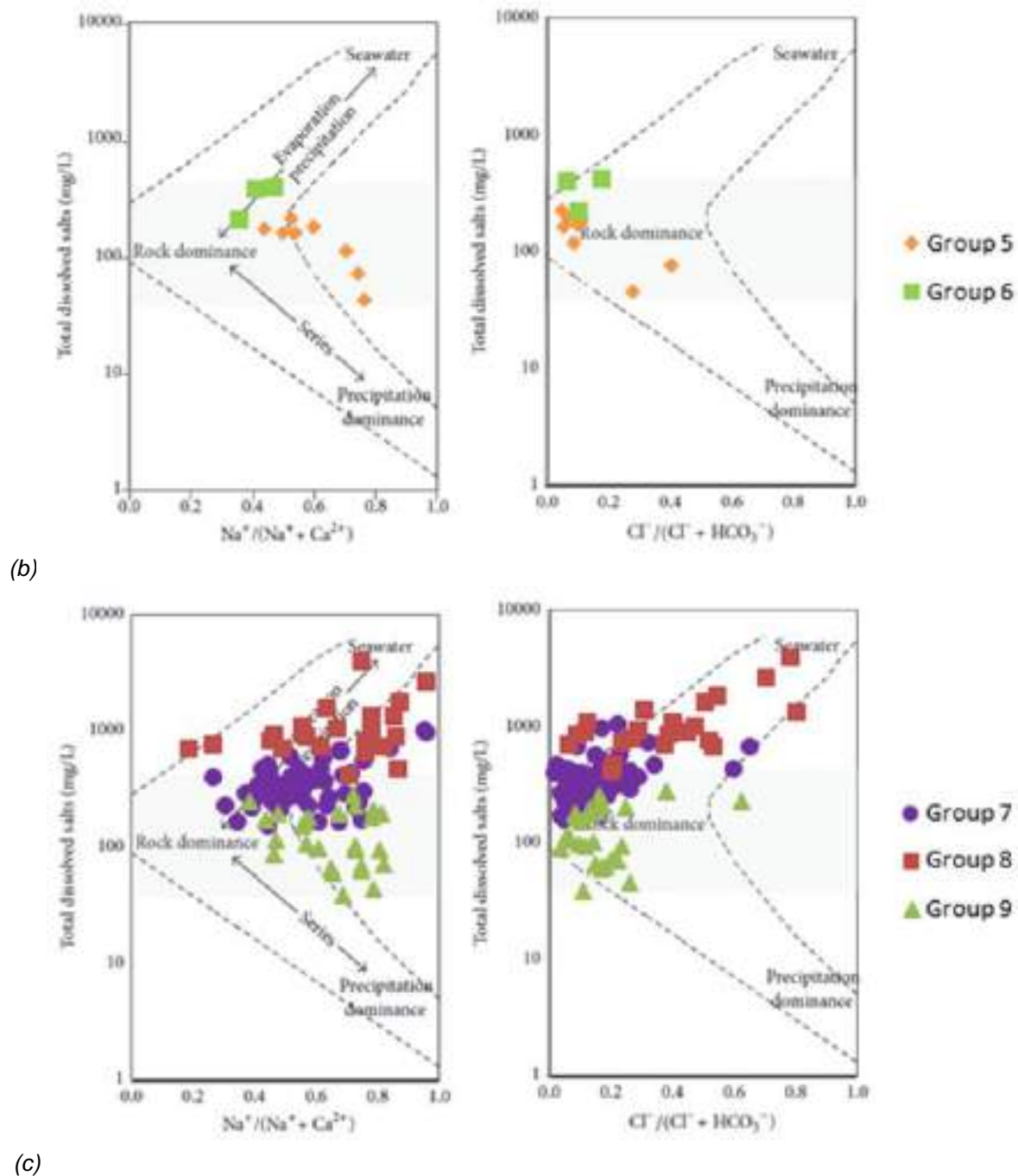


Figure 37 Gibb's diagrams displaying the mechanism of controlling groundwater quality in the eastern limb of the Bushveld Igneous Complex, for the different lithostratigraphic divisions; (a) Rustenburg Layered Suite (b) Raseop Granophyre Suite and (c) Lebowa Granite Suite

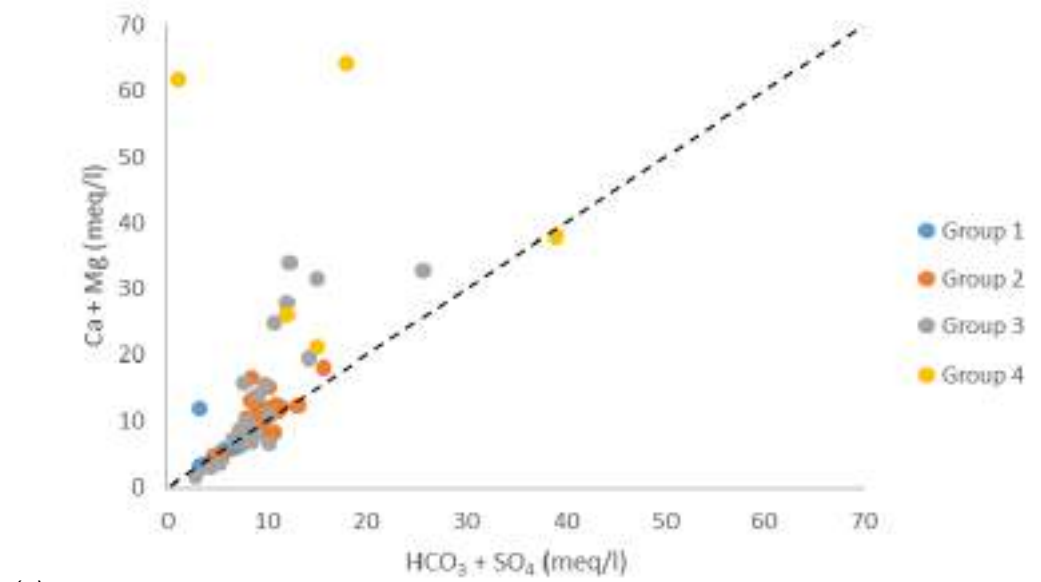
Further interpretations on water-rock interactions and hydrochemical processes were evaluated according to bivariate plot analysis and iron concentration ratios. The $\text{Ca} + \text{Mg}$ vs $\text{HCO}_3 + \text{SO}_4$ plot can be used to assess ion exchange processes control on groundwater chemistry, groundwater samples which plot on below the 1:1 equiline display ion exchange processes, and groundwater samples above the equiline are influenced by reverse ion exchange processes (Belkhiri et al., 2010; Masindi and Abiye, 2018; Rezaei et al., 2017) or evaporation processes (Rezaei et al., 2017). The $\text{Ca} + \text{Mg}$ vs $\text{HCO}_3 + \text{SO}_4$ plot is also applied to investigate the influence of silicate and carbonate weathering on groundwater quality - in the case where water samples plot along the 1:1 line, it indicates that weathering of carbonates and silicates is present (Davraz and Batur, 2021; Elango and Kannan, 2007).

The relationship between the dominant major ions in the study area's groundwater; Ca, Mg, HCO_3 , SO_4 , Na, and Cl, was evaluated by bivariate scatter plots. The Ca + Mg vs $\text{HCO}_3 + \text{SO}_4$ plots for the different lithostratigraphic divisions in the study area are presented in Figure 38. Silicate minerals are the major minerals contributing to the Bushveld Igneous Complex's geochemistry, therefore the possibility of carbonate weathering processes governing the study area's hydrogeochemistry is disqualified. Figure 38a shows that majority RLS groundwater samples plot along the equiline, therefore this indicates that the dissolution of silicate minerals, from pyroxenes, feldspars and olivine in the rock matrix, as well as ion exchange and reverse ion exchange processes, are the main water-rock interaction processes in the RLS. The few samples that plot above the aquiline indicate the presence reverse ion exchange processes.

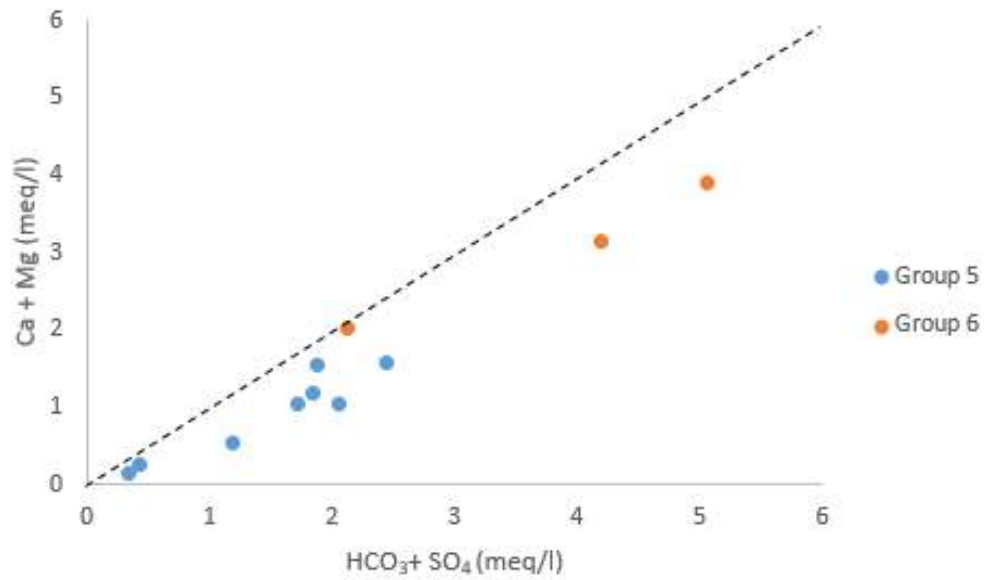
In Figure 38b, all the Rashoop Granophyre Suite groundwater samples are displayed below the equiline, which suggests that silicate weathering and ion exchange processes produced the solutes in the groundwater. Decreasing Mg^{2+} and Ca^{2+} ions in groundwater, is attributed to cation exchange processes, these ions exchange sites occupied by Na^+ and K^+ in the aquifer.

The Ca + Mg vs $\text{HCO}_3 + \text{SO}_4$ plot, Figure 38c, presenting the Lebowa Granite Suite groundwater samples, shows that majority of the samples fall below the equiline, this indicates that the dominant hydrochemical processes in this division are, weathering of silicate minerals and ion exchange processes. Some samples clustered under hydrochemical Group 8 are above the equiline, which suggests that the hydrochemistry of these groundwater samples is also influenced by reverse ion exchange processes.

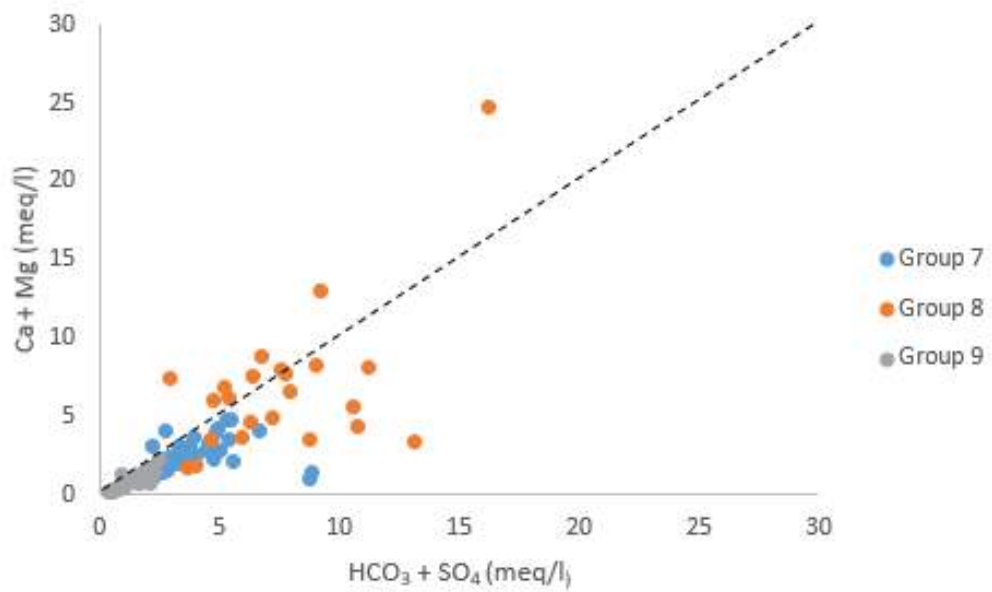
In groundwater systems, especially in semi-arid regions, evapotranspiration processes contribute to the salinity of groundwater. Soil salinity is increased by evapotranspiration, and the produced sodium and chloride ions are dissolved into groundwater during infiltration (Masindi and Abiye, 2018). Na/Cl molar ratio is used to describe the control of evapotranspiration on the groundwater salinity. In the case where, Na/Cl ratio is more than 1, it indicates that evapotranspiration is not the only hydrogeochemical processes responsible for the groundwater chemistry (Davraz and Batur, 2021). Sodium in groundwater may be sourced from various hydrogeochemical processes. When the Na/Cl ration is equal to ± 1 , the sodium and chloride in the groundwater is derived from mainly halite dissolution. Whereas, when the Na/Cl molar ratio is greater than 1, sodium is derived from silicate weathering processes and also ion exchange processes, which results in sodium concentration that exceed chloride concentrations (Davraz and Batur, 2021; Rezaei et al., 2017; Sheikhy Narany et al., 2014).



(a)



(b)



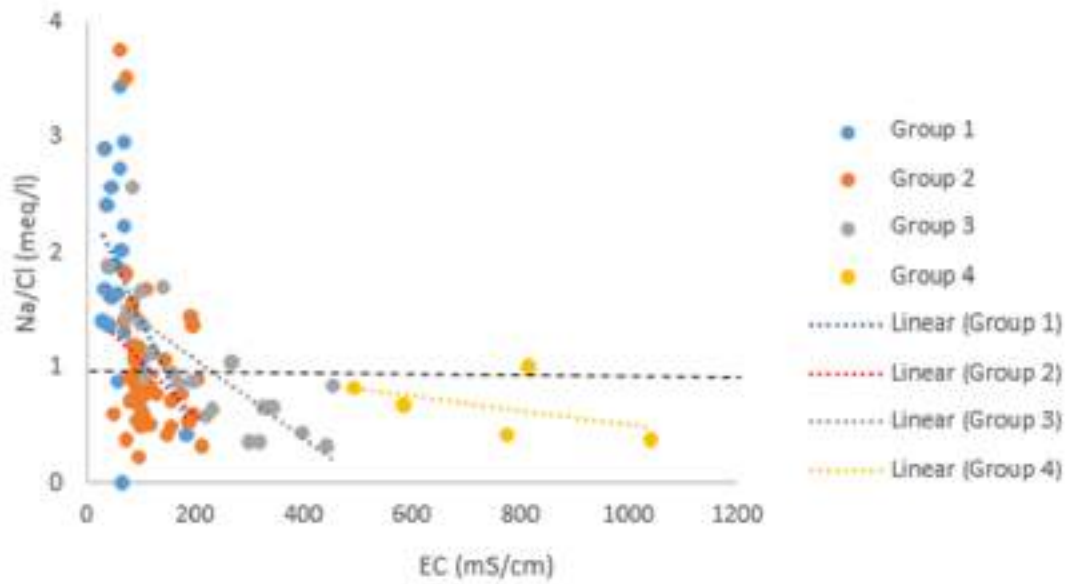
(c)

Figure 38 Bivariate plot (Ca + Mg) vs. (HCO₃+SO₄) for (a) Rustenburg Layer Suite (b) Rashooph Granophyre Suite and (c) Lebowa Granite Suite

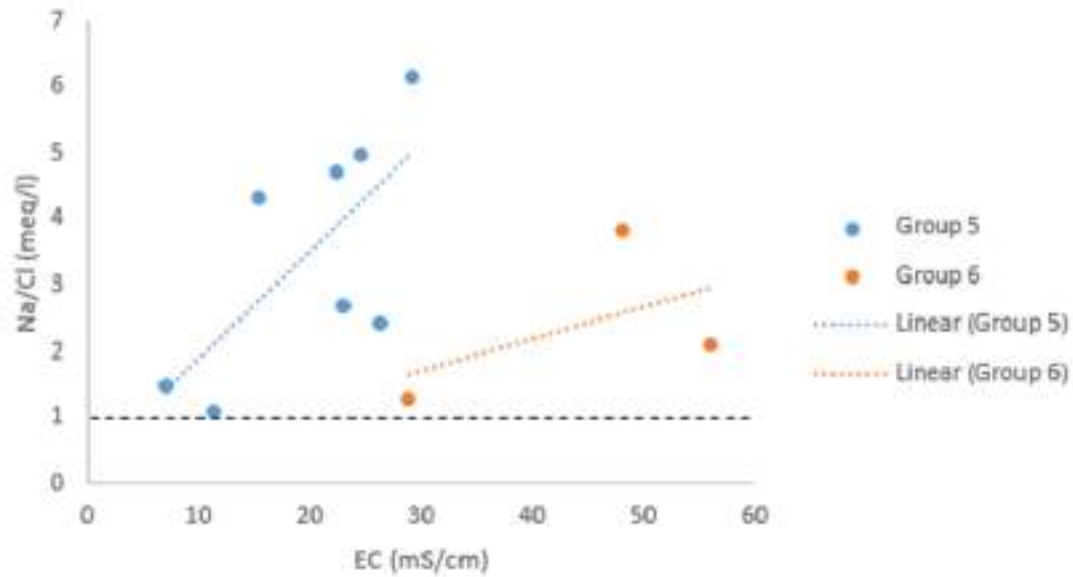
The influence of evapotranspiration on the hydrogeochemistry of investigated area is studied using Na/Cl vs EC bivariate scatter plots. Rustenburg Layered Suite hydrochemistry data in Figure 39a, plots above and below the Na/Cl equals to one reference line. This indicates that evapotranspiration processes do not solely contribute to the presence of sodium ions in groundwater. Sodium is dominantly sourced from silicate weathering and cation exchange reactions. Hydrochemical Group 1 samples mainly occur above the reference line, which signals that sodium is released from silicate weathering processes. Group 2 and 3 Na/Cl ratios range above and below the reference line, with most of samples plotting below the line, such suggests that evapotranspiration processes and reverse ion exchange process contribute to the chemistry of the samples below the line, while samples above the reference line reveal influence of silicate weathering and ion exchange processes. Similarly, Ca + Mg vs $\text{HCO}_3 + \text{SO}_4$ plot (Figure 38a) revealed that silicate weathering processes and cation exchange are the main hydrochemical processes in these groups. All Group 4 samples plot below the reference line – this indicates that evaporation processes and reverse ion processes are responsible the group's groundwater chemistry. This agrees with Gibbs diagram Figure 37a, which indicates that Group 4 water chemistry is dominated by evaporation processes, and the bivariate analysis, Ca + Mg vs $\text{HCO}_3 + \text{SO}_4$ plot (Figure 38a), which shows that reverse ion exchange process influence the chemistry of Group 4 samples.

Figure 39b, shows that groundwater samples plot above the reference line, this suggests that silicate weathering processes are the dominant source of sodium in the groundwater. This corresponds with the rock dominance, categorisation of mechanisms controlling water chemistry, based on the Gibbs plot (Figure 37b) for water samples from the Rashedo Granophyre Suite. Which was further described as silicate weathering according to the Ca + Mg vs $\text{HCO}_3 + \text{SO}_4$ plot (Figure 38b). Majority of the Lebowa Granite Suite groundwater samples plot above the reference line, Figure 39c, this indicates that the main hydrogeochemical processes contributing to the groundwater chemistry are silicate weathering processes and cation exchange. Based Ca + Mg vs $\text{HCO}_3 + \text{SO}_4$ plot (Figure 38c), the same hydrochemical processes, silicate weathering processes and cation exchange, have been interpreted as the main contributors to the groundwater chemistry of the Lebowa Granite Suite. Some Group 8 samples plot below the reference line, such shows that evapotranspiration processes influence the salinity of these groundwater samples, as well as reverse ion exchange. The mentioned is corroborated by Group 8 samples plotting on the evaporation dominance field on the Gibbs diagram, and the reverse ion exchange influences on groundwater chemistry as revealed in the bivariate plot in Figure 38c.

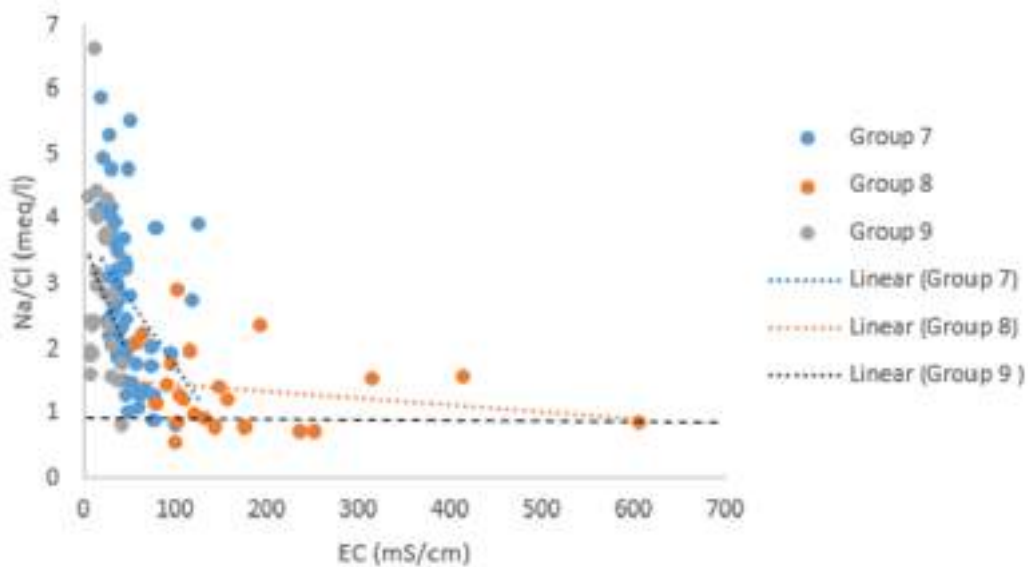
Evapotranspiration processes directly increase the amount of TDS in groundwater, therefore the influence of evapotranspiration in the salinity of groundwater can be evaluated by observing the relationship between Na/Cl and TDS or EC (which is directly proportional to TDS). A horizontal trend along Na/Cl ratio equal to 1, would indicate dominance evaporation processes. The trend lines in the Na/Cl vs EC plots, Figure 39a and Figure 39c show a decreasing trend as the EC increases, while in Figure 39b the Na/Cl ratio increases with EC. This trend also supports that the occurrence of sodium in groundwater is attributed to other hydrogeochemical processes, other than evapotranspiration influences.



(a)



(b)



(c)

Figure 39 Bivariate plots showing Na/Cl vs EC for (a) Rustenburg Layer Suite (b) Rashoop Granophyre Suite and (c) Lebowa Granite Suite

3.5 GROUNDWATER RECHARGE AND GROUNDWATER ABSTRACTIONS

3.5.1 Groundwater Recharge Estimation

The quantification of groundwater recharge is an important aspect of sustainable groundwater resource management. In this investigation, natural groundwater recharge was estimated using the Chloride Mass Balance (CMB) method. The method based on the assumption that chloride is a natural environmental tracer, and therefore the ratio of the input chloride in precipitation to the chloride content in groundwater is used to estimate rate of groundwater recharge (Xu and Beekman, 2003). This method prescribed, as a suited recharge estimation method for semi-arid to regions, such as the study area, furthermore it is a simple and cost-effective method.

The CMB method in this investigation applied point data; harmonic means of chloride concentration from 1220 monitoring boreholes time-series data, sourced from the WMS database and the concentration of chloride in rainfall (1 mg/l) obtained from a previous study by Van Wyk et al., (2012). The various mean annual precipitation (MAP) (Table 11) values, across the study area were based on rainfall data collected from weather stations within and in close proximity of the study area. The MAP values were determined by applying Thiessen polygon boundaries across the eastern limb, and the highest MAP was within the Wolkberg weather station region, followed by the Belfast weather station polygon. The chloride concentrations in the groundwater samples ranged from 1,5 mg/l to 4212 mg/l – all chloride concentrations were within the acceptable range for application of CMB methods, since none exceeded the saltwater chloride concentration of 19 000 mg/l.

The annual groundwater recharge estimates obtained from the borehole sites across the study area range from 0,14 mm/a (0,02% of MAP) to 410 mm/a (66,7% of MAP). The point data recharge estimates were interpolated to produce a groundwater recharge estimation map, as displayed in Figure 40, which shows the spatial variability of groundwater recharge. The regional groundwater recharge estimation, in Figure 41 is visualised as the percentage of MAP.

The mean groundwater recharge estimated for the study area is 32,28 mm/a which is approximately 5,7% of the MAP. The groundwater recharge maps (Figure 40 and Figure 41) show that the recharge estimated for the upper region of the study area is lower than the average recharge, and the recharge is generally higher in the lower region of the study area. In areas where the groundwater recharge is estimated to be 0 – 2,4% of the MAP, this includes recharge into RLS, Rashoop Granophyre Suite and Lebowa Granite Suite geologies, the lower recharge is associated with lower topography. Specifically, the average elevation for estimated recharge between 0 – 10 mm/a is 914 mamsl. Whereas the regions of the eastern limb with an estimated groundwater recharge greater than 100 mm/a - where about 17 % to the maximum calculated recharge percentage (66,7%) of the MAP, a relatively smaller area of the limb – it is related to higher topographical areas in the study area. The high recharge occurs in the mainly the Rooiberg Group and the RLS, Lebowa also Rashoop geological units. The regional distribution of the estimated natural groundwater through precipitation, shows a pattern that follows the topography, the recharge is higher at higher elevations, which are associated with recharge zones. The estimated recharge for the study area is further discussed, in relation to other groundwater recharge maps in the discussion chapter (chapter six).

Table 11 Table showing the various MAP used to estimate the groundwater recharge by CMB method and the average recharge for different areas in the study area, relative to the nearest weather station

Weather Station	Period of data	MAP (mm/a)	Recharge (mm/a)
Wolkberg	1999 - 2022	821,21	10,0
Belfast	2005 - 2022	642,51	45,1
Laersdrif - Police ARS	1994 - 2022	618,71	85,5
Mantrombi	1993 - 2022	582,19	55,4
Marble Hall	1995 - 2022	529,20	9,2
Oudestad	1992 - 2022	491,68	31,7
Tubatse - Agric	1996 - 2022	408,99	37,0

3.5.2 Groundwater Abstractions

Sustainable groundwater development and management requires groundwater abstraction monitoring, which should be used to ensure effective management and control of overall usage of groundwater resources. A summary table of registered groundwater users and the quantity of the groundwater abstracted in the eastern limb of the BIC, according to the WARMS database are presented in Table 12. The overall volume of groundwater abstracted from the study area is $4,08 \times 10^7 \text{ m}^3$. The dominant groundwater users are in the mining sector, which consumes 66,77% of the registered groundwater use volumes, followed by the agriculture sector, which in jointly accounts for 17,66% of the registered groundwater volume.

Sustainable groundwater development and management requires groundwater abstraction monitoring, which should be used to ensure effective management and control of overall usage of groundwater resources. A summary table of registered groundwater users and the quantity of the groundwater abstracted in the eastern limb of the BIC, according to the WARMS database are presented in Table 10. The overall volume of groundwater abstracted from the study area is $4,08 \times 10^7 \text{ m}^3$. The dominant groundwater users are in the mining sector, which consumes 66,77% of the registered groundwater use volumes, followed by the agriculture sector, which in jointly accounts for 17,66% of the registered groundwater volume.

Figure 42 shows the accumulate abstraction volumes over the past 40 years, throughout the entire eastern limb. There has been an exponential increase in volumes of groundwater use. A significant incline in the abstraction volumes occurred in the year 2011. An increase in the volume of registered groundwater abstractions occurred from 2011 to 2023, the increase amounted to $3,09 \times 10^7 \text{ m}^3$. This is a substantial increase in comparison to the $2,34 \times 10^6 \text{ m}^3$, which occurred in the previous 12-year interval (2011 -1999). This shows the use of groundwater in the region is rapidly increasing.

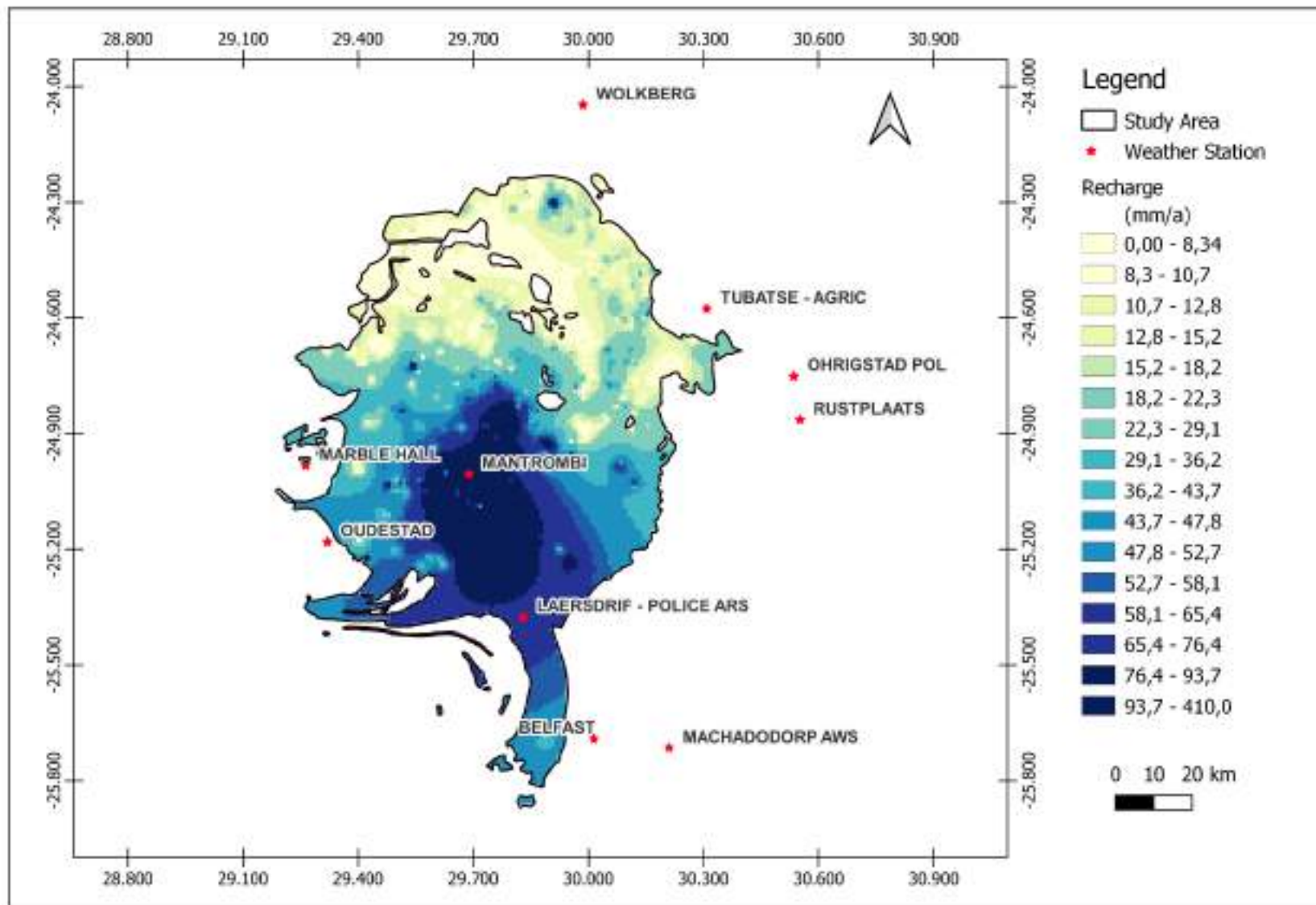


Figure 40 Annual groundwater recharge map for the eastern limb of the Bushveld Igneous Complex, estimated using the Chloride Mass Balance method.

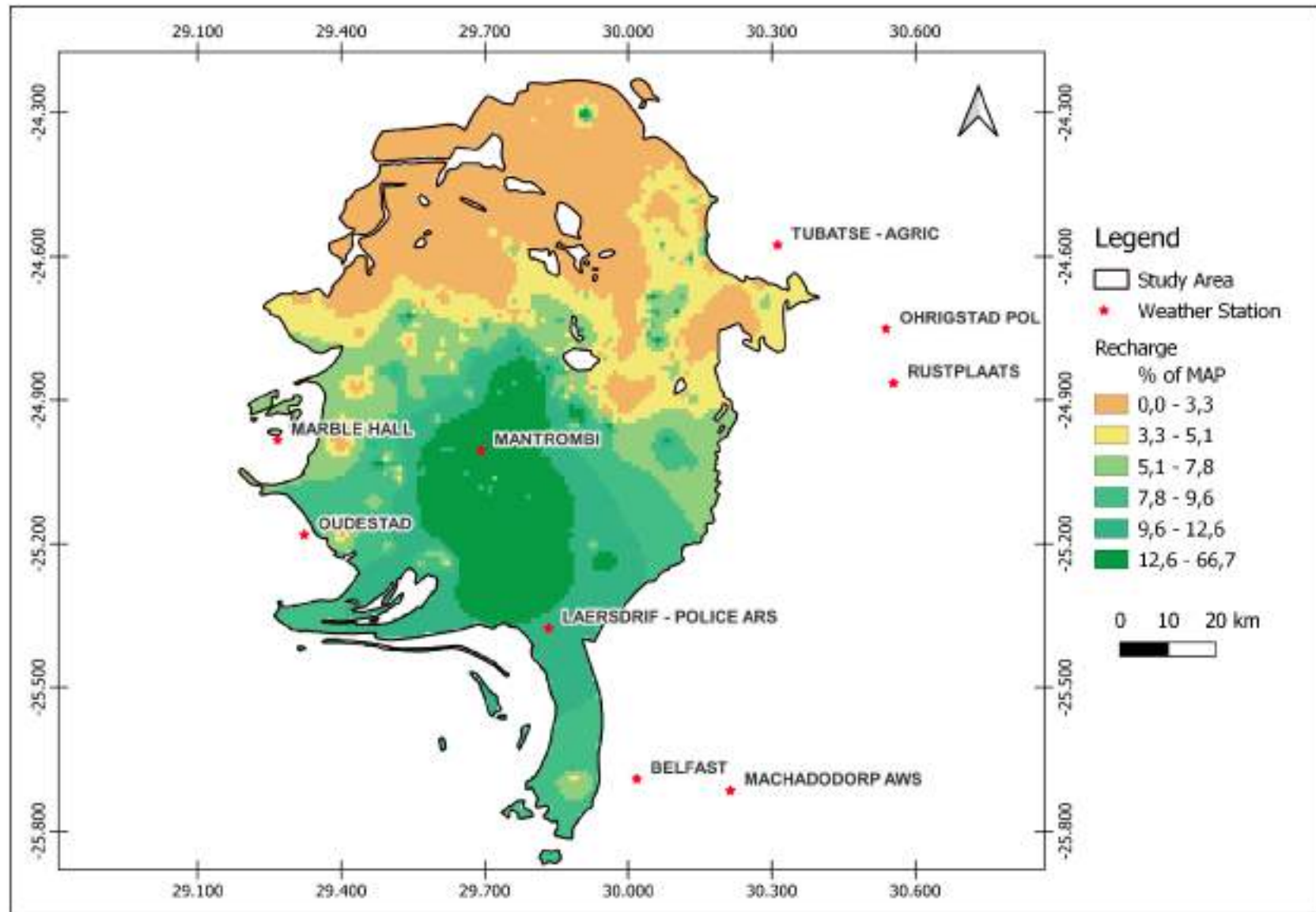
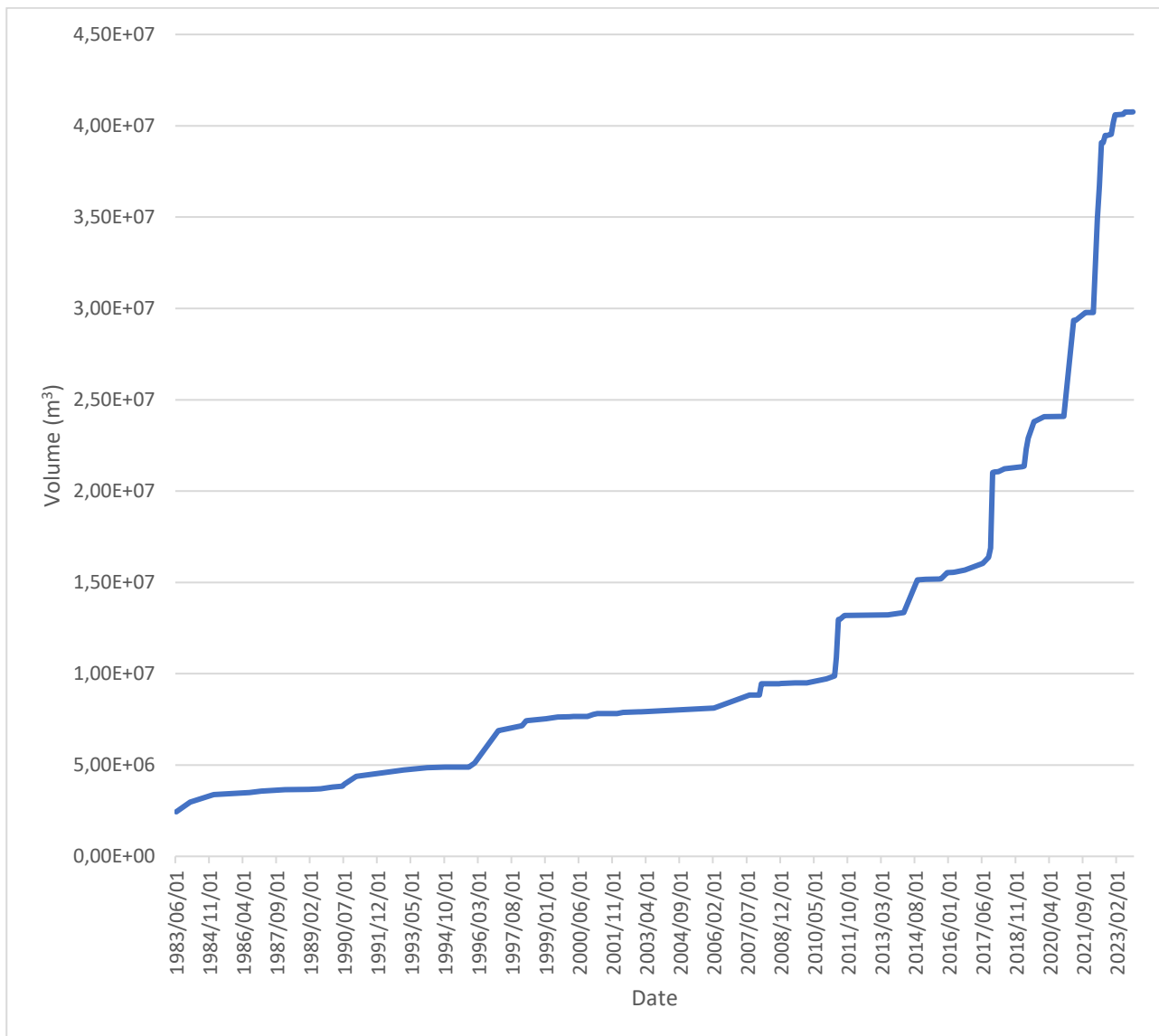


Figure 41 Recharge map displaying the recharge percentage of the mean annual precipitation in the eastern limb of the BIC

Table 12 Registered groundwater use in the eastern limb of the Bushveld Igneous Complex (WARMS, 2023)

Water Use Sector	No. of geosites	Registered Volume (m ³ /year)	% of total groundwater use water use sector
Mining	232	2,72E+07	66,77%
Agriculture: Irrigation	91	6,49E+06	15,92%
Industry (Urban)	37	4,03E+06	9,89%
Water Supply Service	33	1,92E+06	4,72%
Agriculture: Watering Livestock	18	7,09E+05	1,74%
Schedule 1	8	3,38E+05	0,83%
Industry (non-urban)	8	4,34E+04	0,11%
Urban (excluding industrial &/or domestic)	1	7,01E+03	0,02%
Power Generation	1	4,50E+01	0,00%
Total	429	4,08E+07	100,00%

**Figure 42 Volumes of overall registered groundwater use in the eastern limb of the Bushveld Igneous Complex, over the years.**

3.6 HYDROGEOLOGICAL CONCEPTUAL MODEL

The developed conceptual understanding of the groundwater system within the eastern limb of the BIC is presented. A hydrogeological conceptual model a simplified representation of the natural groundwater system of an area of interest. In this study, the conceptual model is based on the collated groundwater database and analysed geological, hydrogeological and hydrogeochemical setting (Figure 43).

3.6.1 Hydrostratigraphy of the eastern limb of the Bushveld Igneous Complex

The hydrogeological system of the eastern limb of the Bushveld Igneous Complex consists of two types of aquifers. A conceptualised hydrogeological system of the eastern limb of the Bushveld Igneous Complex comprises of a two-layered model. The upper and lower layer represents the weathered bedrock aquifer and the fractured bedrock aquifer, respectively. The study area's two-layer hydrostratigraphic units are also classified as an intergranular and fractured aquifer system according to the hydrogeological classification by Orpen (1994). Groundwater flow system in the RLS, Rashoop Granophyre Suite and the Lebowa Granite Suite; geological units of the eastern limb depend on the development of secondary porosity and secondary permeability, which are a function of the weathering intensity of the geological unit and occurrence of permeable discontinuity structures. The regional Wonderkop and Steelpoort fault systems and the associated fractures govern the secondary fractures associated with groundwater occurrence.

Groundwater occurs in the weathered overburden of varying thickness (maximum thickness of 50 m) overlying the fractured bedrock aquifers. The weathered bedrock aquifers are the primary storage unit of the aquifer system, where considerable amount of groundwater is stored due to intergranular porosity and permeability formed by micro-fractures formed by the weathered materials. In the vicinity of rivers, there are alluvial aquifers, which overlie the weathered bedrock aquifers; these aquifers are also classified as intergranular and are hydraulically connected with the weathered overburden. In fractured bedrock aquifers, groundwater is stored and flows through structural discontinuities such as fissures, fractures and joints, which act as hydraulic conduits when open or if the structures contain permeable material. The fractured unit and weathered overburden are hydraulically connected, at zones where structural discontinuities extend to the interface of the two hydrostratigraphic units.

3.6.2 Hydrogeological Properties

The weathered and fractured aquifer units are a regional conceptualisation of groundwater occurrence in the eastern limb. The hydrogeological properties varying across the different stratigraphic units in the study area (Table 13), variation in hydrogeological properties is an indication of heterogeneity which is a characteristic of the eastern limb aquifer system. The Rustenburg Layered Suite form the lithostratigraphic units, which outcrop on the eastern part of the eastern limb, its hydrogeological characteristics show the best potential in the study area for groundwater development. Overall, the RLS has an average transmissivity of 42,3 m²/day, with the Lower Zone having the highest permeability at an average of 71 m²/day. This stratigraphic unit has the highest average blow yield of 1,7 l/s and the mean water strike depth of 35 mbgl. The average depth to the water table in the RLS rocks is at 18 mbgl. The hydraulic parameters of the Rooiberg Group and the Rashoop Granophyre Suite, described by an average of 2,1 and 3,3 m²/day, indicate that these units have a relatively lower permeability. The aquifers of the Lebowa Granite Suite are characterised by an average transmissivity of 7,7 m²/day and an average blow yield of 0,8 l/s. The depth to groundwater varies across the eastern limb, the shallowest mean water level is within Rashoop Granophyre Suite, and the deepest mean water level are in the Lebowa Granite Suite, where the average water levels are 16,5 and 21,7 mbgl, respectively. Based on hydraulic properties and borehole data which indicates the typical occurrence of groundwater, the RLS offers the best potential for groundwater development, in comparison to the Lebowa Granites and the other stratigraphic units in the study area. The average water strike depth indicate that groundwater is intercepted at deeper levels in Lebowa Granite Suite (50 mbgl) as compared to the RLS (35 mbgl).

3.6.3 Hydrochemistry and Groundwater Flow

Groundwater types in the RLS vary from Ca-Mg-HCO₃, Ca-Mg-SO₄-Cl and Na-Cl, and the eastern limb granitic geological units have Ca-HCO₃, Na-HCO₃ and Na-Cl water types. The hydrogeochemical characterisation of the eastern limb suggests that there is a hydrochemical evolution from recently recharged groundwater (Ca-Mg-HCO₃ and Ca-HCO₃) to groundwater types with increased mineralisation which denote an increase in residence time along flow paths. The regional groundwater flow direction generally follows the eastern limb's topographical gradient. Groundwater flows from recharge zones at high elevation to lower elevations, groundwater direction indicates that groundwater is discharged into the main rivers of the study area, the Olifants and Steelpoort Rivers. The mean annual precipitation for eastern limb area of approximately 10 022 km² varies from 821,21 to 408,99 mm/a, and the estimated mean annual groundwater recharge ranges from 0,14 to 410 mm/a, where groundwater recharge potential is higher at recharge zones associated with the study area's high elevation zones. Groundwater abstraction volumes based on registered groundwater user quantities to 4,08 x10⁷ m³ annually.

Table 13 Mean hydrogeological characteristic of each lithostratigraphic unit of the eastern limb of the Bushveld Igneous Complex

Geology Lithostratigraphic Division		Aquifer Type	Water Level (mbgl)	Water Strike (mbgl)	Blow yield (l/s)	Hydraulic Parameters		Hydrochemical Facies
						Transmissivity (m ² /day)	Storativity	
Lebowa Granite Suite		Intergranular and Fractured Aquifers	21,7	50,5	0,8	7,7	0,008	Ca-HCO ₃ Na-HCO ₃ Na-Cl
Rashoop Granophyre Suite		Intergranular and Fractured Aquifers	16,5	38	1,6	3,3	0,002	Ca-HCO ₃ Na-HCO ₃
Rustenburg Layered Suite Subdivisions	Upper Zone	Intergranular and Fractured Aquifers	18,6	35	1,7	28,7	0,021	Ca-Mg-HCO ₃ Ca-Mg-SO ₄ -Cl Na-Cl
	Main Zone					42,2	0,033	
	Critical Zone					46,5	0,002	
	Lower Zone					71,0	0,049	
Rooiberg Group		Fractured Aquifers	17,5	46,1	0,3	2,1	0,002	-

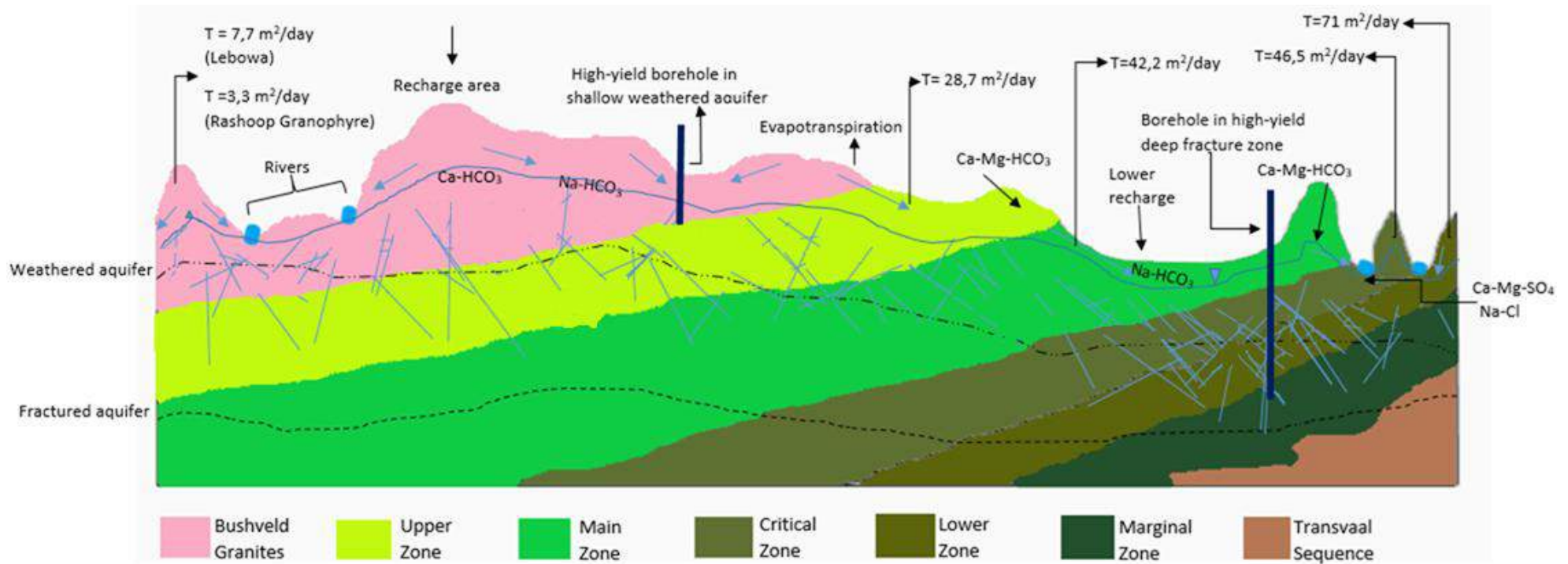


Figure 43 Hydrogeological conceptual model of the eastern limb of the Bushveld Igneous Complex based on the publicly available groundwater information mainly focused on traditional shallow groundwater resources

3.7 SUMMARY AND DISCUSSION

The deepest water supply borehole depth in the study area is in the Lebowa Granite Suite (77,3 mbgl), and the shallowest borehole depth is in the RLS (54,5 mbgl). Most of the boreholes in the study area are drilled between the depth of 70 – 80 mbgl, this indicates that borehole depths are generally drilled to shallow depths, and boreholes are associated with shallow aquifers (< 100 mbgl). There are several reasons which determine the depth of a borehole – the borehole depth can be determined by depth to which sufficient groundwater yields are obtained, and/or the borehole depth limits are also based on the driller depth, and financial constraints.

Based on averages, shallow water strike depths are related to the RLS, while the deepest water strike average is related to the Lebowa Granites. The identified primary and secondary water-strike depth zones, for the Rooiberg Group, Rashoop Granophyre Suite and RLS are within 50 mbgl. In contrast, the secondary water strike zone of the Lebowa Granite Suite extends to 70 mbgl. The deeper secondary water zone, as well as the deeper borehole depths, in the Lebowa Granite Suite, suggests that the water intercepted at these deeper water strikes is related to the open discontinuities in the fractured bedrock aquifers – since the maximum weathering depth is 50 mbgl (Titus et al., 2009). And because borehole depths and water strike depths are the same range in the Lebowa Granite Suite, it suggests that borehole depths are mainly guided by obtaining sufficient yields.

Blow yields are the initial yield estimates, quantified during the drilling process, and are the first indication of the success rate of the drilled borehole. The highest mean blow yield was obtained in the RLS (1,7 l/s), and the lowest mean blow yield is from the Rooiberg Group (0,3 l/s) and the Lebowa Granites (0,8 l/s) – suggesting that groundwater occurrence and flow is higher in the RLS.

The blow yield variation was also evaluated in relation to depth; by comparing the average blow yield per depth interval; which showed that the blow yield generally decreases with depth. This trend indicates that the likelihood of obtaining sufficient yields decreases with an increase in depth. However, there are outliers observed, where high yields at great depths (150 – 210 mbgl) are obtained, these are probably a result of deep open fractures. Such has been identified by McCaffrey (1998), where the fractures were related to mine inflows in the western limb and the deep fractures were characterised as high-yield fractures (10 l/s and 25 l/s). This suggests that there is a possibility of intercepting, high-yielding fractures at deep depths, however, the identified are anomalies. It is difficult to establish the occurrence and frequency of the deep open, water bearing fracture since there is limited available data on hydrogeological properties at deep depths, and also due to the heterogeneous nature of the BIC fractured bedrock aquifers.

The analysed borehole depth, water strike depth, blow yields and water levels, generally show a log-normal distribution, this suggests that groundwater is generally encountered at shallow depths and that blow yields are within the lower yielding classes. With that said, the data distribution also showed a wide range, which suggests that there is wide variation in the borehole properties, which corroborates the heterogeneity of the BIC, which translates to the heterogeneity of hydrogeological properties.

3.7.1 Groundwater Level Trend Analysis

Analyses of groundwater level trends is an important element of groundwater management. Statistically significant decreasing trends were observed in the groundwater levels data series of monitoring boreholes in the investigated area. The observed trends are limited to seven water level monitoring boreholes in the entire study area, in relation to the study area of approximately 10 022 km², therefore number of boreholes to determine the overall trends is relatively small.

The groundwater level decline in the study area is attributed to the identified decreasing rainfall trends, and groundwater abstraction, for various groundwater uses; community water supply, agricultural irrigation and mining water use, related to the land uses in the vicinity of the monitoring boreholes. Natural groundwater recharge is mainly derived from rainfall. Rainfall trends in the study area are both decreasing and increasing trends, however the main observed trend is decreasing, with some rainfall trends statistically defined as significant decreasing rainfall trend. This is confirmed by an analyses of climate conditions in the Olifants WMA, by Adeola et al. (2022), which reported a general decrease rainfall trend. A decrease in rainfall effectively results in a decrease groundwater recharge, hence rainfall is identified as one of the one cause for groundwater level decline in the study area. Besides rainfall decrease, land-use of an area can also impact the groundwater recharge of an area. And according to Gyamfi et al. (2016) groundwater recharge declined in the Olifants WMA is also due to land-use changes that have occurred throughout past years.

DWA (2011) and DWAF (2004), stated that agricultural activities in the region depend largely on groundwater resources, and also DWAF (2004) also noted the effects of mine dewatering on groundwater quantity, therefore this validates that groundwater abstractions by the agricultural and mining sectors contribute to groundwater level decline.

3.7.2 Hydraulic characteristics

Transmissivity variation across the study area was assessed relative to different factors, linked to the hydrogeological, geological setting and geomorphology of the eastern limb of the BIC. The factors assessed for their influence on the permeability of the aquifers, included geology, lineaments, drainage, topography and slope, as well as borehole depth. Descriptive statistics and bivariate analysis were used to establish the correlation between the transmissivity and each factor. This approach has been applied by Holland (2012), Madrucci et al. (2008), Mäkelä (2012), McFarlane et al. (1992) and Onana et al., (2017), in various regions characterised as crystalline fractured aquifer, to evaluate factors which are related to higher borehole productivity, based on either transmissivity values, specific yields or borehole yields.

The analyses of transmissivity values, in relation to the lithostratigraphic divisions in the Bushveld Igneous Complex, shows that stratigraphic units across the study have varying transmissivity, with the highest transmissivity observed in the RLS, specifically the Lower Zone. Generally, the RLS is more transmissive than the Bushveld granites. Variation in secondary permeability, is expected since, crystalline bedrock rock aquifers of different geological units, have different rocks, hence prevailing hydrogeological properties in the matrix of these aquifers depend, also depend on the level and intensity of permeable secondary features. Studies on geological influence on borehole productivity, by McFarlane et al. (1992) and Onana et al. (2017) study supports, the results of this investigation which revealed that geological changes, have an influence on the hydraulic characteristics. While, Mäkelä (2012) reported that variation of geological units in crystalline bedrock aquifers, in central Finland showed no significant influence on hydraulic parameters.

Geological contact zones are associated with higher transmissivity value, therefore the proximity to geological units has a negative correlation. The observed correlation is comparable with results from the investigation on groundwater occurrence in the basement aquifers of the Limpopo and Luvuvhu-Letaba WMA by (Dippenaar, 2008), which revealed that boreholes in geological contact zone are have higher transmissivity and are high yielding. Also, a study by Madrucci et al., (2008) agrees with these findings, because their research also related distance close proximity to geological contacts with higher borehole productivity. Overall, the establish relation between hydraulic parameters and geological contacts supports recommendations by Botha and Van Rooy (2001) and Lourens (2013); which state that geological contacts in the BIC are favourable borehole drill targets for groundwater development.

Lineament mapping for targeting geological structures, related with groundwater occurrence, such as fractures, is a widespread approach in groundwater development in fractured bedrock aquifers – and in the context of structurally controlled hydrogeological system in South African, researchers such as Sami (2009) promotes this approach. In this regional investigation, the assessment of lineament influence on the

transmissivity showed that there is negative correlation between these elements. Previous work by Holland (2012), Onana et al. (2017), Madrucci et al. (2008), and Mäkelä (2012), relates close proximity to lineaments with an increase in hydraulic parameters, which is in line with the current findings. Lineament density, which can be linked to fracture connectivity, has a positive influence on the permeability of aquifers in the study area. Although, lineament density across the study area is generally low, which signals that interconnectivity of linear geological structure in the area is low – and for structurally controlled aquifers interconnectivity is favourable for groundwater flow and occurrence. Similar to the applied analyses of lineament density association with transmissivity, by Madrucci et al., (2008), lineament density influences on borehole hydraulic parameters established the alike influence – where lineament connectivity was associated with higher parameters.

Assessment of geomorphological influences on the transmissivity, according to distance from perennial rivers and topography, revealed that high transmissivity is related to areas distance to perennial rivers and lower elevation zones. Therefore, transmissivity has a negative correlation with distance to rivers and topography. Studies by Mäkelä (2012), McFarlane et al. (1992), and Onana et al. (2017) observed the same negative correlation in crystalline bedrock rocks. Even though high borehole productivity has been related to distance close to the river course, it is important to highlight that floodplain delineation should be considered in groundwater development, since there are regulations that state that there should be no developments or construction within 1: 100 years floodline.

No particular correlation between slope and elevation was established, this was probably because most the boreholes in the study area, are located on gentle slopes – this is like due to easy of accessibility for drilling and access of the borehole to the water users. Therefore, there was not enough data available to establish a relationship. However, considering that in fractured aquifers transmissivity is a function of the secondary hydrogeological properties, and the development of fractured aquifers is structurally controlled, therefore, the terrain feature does not affect subsurface features. In hydrogeology, the slope is usually considered as factor which can influence groundwater, since infiltration of water is related to gentle slope. As a result, in groundwater potential studies, such as the study by Adesola et al. (2023), to evaluate it usually incorporated in relation to groundwater recharge.

High transmissivities are related to shallow borehole depth, and the association between the borehole depth and transmissivity is a strong negative correlation. Study by Mäkelä (2012), which reports significant negative correlation between borehole depth and hydraulic properties fractured crystalline aquifers, as well as, Douagui et al. (2019), reported that borehole depth has inverse relation with hydraulic parameters. However, Onana et al. (2017) did not establish the same correlation between borehole depth and transmissivity, in a crystalline bedrock setting, instead observed a zone which showed an increase in permeability between 40 – 70 mbgl, then transmissivity decrease. Such is also another indication of the heterogeneous nature of fractured aquifers.

The identified significant relation between the study area's borehole depths and transmissivity, can be interpreted as that secondary permeability decreases with depth – which can be associated with the decrease in likelihood to encounter water yielding fracture at deeper depths. Dalasile and Abiye (2018) conducted a small-scale investigation on fracture frequency in the eastern limb – the results revealed that for the first 40 mbgl fracture frequency increased than after fracture frequency decreased. A decrease in fracture frequency can be related to a decrease in open discontinuities, which can be the reason for the decrease in transmissivity with depth, as well as the previously mentioned decrease in average blow yield with increasing depth.

3.7.3 Hydrogeochemical Characteristics

Hydrogeochemical characterisation of the eastern limb revealed that overall, the dominant water types are calcium magnesium bicarbonate and calcium bicarbonate. Multiple approaches were applied to characterise to groundwater chemistry and determine hydrochemical processes controlling the groundwater chemistry. In the RLS, the dominant cation species found were calcium and magnesium – related to water-rock interactions with the pyroxene and olivine-rich mafic rocks and the main anion species was bicarbonate, which derived

from weathering of the dominant silicate minerals and associated with recharge through Ca-HCO₃ rainfall water type. The identified dominant water types are consistent with findings from previous studies by Ahokposi et al. (2018), Dalasile and Abiye (2018) Lencwane (2021) and Titus et al. (2009), which analysed hydrochemistry in areas, located in the other limbs of the complex.

The other water types present in the RLS, are mixed; Ca-Na-HCO₃ Ca-Mg-Cl, Ca-Mg-SO₄-Cl and Ca-Mg-SO₄-Cl, as well as minor Na-Cl water type. These water types show an increase in TDS from the dominant water types – this is indicative of chemical evolution processes; mineralisation occurs along the groundwater flow path from recharge to discharge zones. As a result, these other water types are observed in lower-lying areas, close to the rivers. Comparable trends of increasing mineralisation were also reported by Ahokposi et al. (2018) and Lencwane (2021) in other regions of the BIC.

In the granitic phase of the Bushveld Complex, similar trends of increasing mineralisation, inverse to elevation are also observed and are attributed to chemical evolution processes. In the Rashedoop Granophyre Suite, water types are Ca-HCO₃ and Na-HCO₃ are present, which signal recently recharged water and mixed water-type due to water-rock interactions, respectively. In the Lebowa Granite Suite, the prevalent water type is Ca-HCO₃ and Na-HCO₃ and minor high salinity water types; Ca-Mg-Cl and Na-Cl, which indicates an end to chemical evolution process. A regional characterisation of crystalline aquifers across Limpopo province, by Holland (2011) supports these results since similar hydrochemical facies were identified.

The main hydrochemical processes in the groundwater system, are silicate weathering and cation exchange processes. Other processes in the groundwater system that influence the groundwater composition; are evapotranspiration and reverse ion exchange processes. Due to the semi-arid to arid condition of the study area, evaporation rates are high, and this also contributes to the high levels of sodium and chloride in groundwater types related to the discharge zone. And considering the land uses in the area associated with high Na and Cl, another possible source of the noted high concentration of sodium and chloride, is from agricultural inflow. Overall, the regional hydrochemical characterisation and identify hydrochemical processes influencing the groundwater system of the eastern limb of the BIC, complement other hydrochemical investigations conducted in the northern and western regions of the Bushveld Igneous Complex at a smaller scale (Ahokposi et al., 2018; Lencwane, 2021).

Groundwater quality analysis based on the mean concentration of hydrochemical groups identified in the study area show that about 12% of the groundwater samples are classified as brackish water – indicating that EC and TDS for these samples are high. In the RLS, some of the water samples (12%) EC, TDS, Mg and Cl concentrations exceed allowable limits for drinking water according to SANS 241, while 2% of the analysed samples have SO₄ content that is above the limits. In the Lebowa Granites, some of the samples (10%) showed elevated levels of Na, Cl and F, which are not within the allowable limits for drinking water. The listed parameters mostly match with groundwater quality reported by Lourens (2013) which stated that in the BIC; chloride, fluoride, nitrate and sulphate are chemical parameters which may sometimes, exceed these limits.

3.8 GROUNDWATER FLOW AND RECHARGE

Groundwater recharge for the study area was estimated using the CMB method. Point recharge estimates used harmonic averages groundwater chloride concentrations from groundwater quality monitoring boreholes. And for the chloride concentration in rainfall a single value was used from a previous study Van Wyk et al. (2012). The concentration of chloride in rainfall is a harmonic mean, derived from regional rainfall water quality data collected over a period of seven years, and with only 19 monitoring sites – the value used is an approximate figure.

The calculated annual recharge ranged from 0,1 mm/a to 410 mm/a, equivalent to 0,02% - 66% of the MAP. Overall, the mean recharge across the study is equal to 33 mm/a (5,7% MAP). According to a National

Groundwater Recharge Map by Vetger (1995), which provides generalised recharge values at a rather wide spatial scale, the recharge ranges between 32 – 45 mm/a, therefore the calculated mean is comparable with this generalised recharge estimate. A groundwater resource assessment by the DWAF (2006), which aimed to improve national recharge estimates such as Vetger (1995), quantified summaries of groundwater recharge for each quaternary catchment. Based on DWAF (2006), which applied adjusted CMB methods, quaternary catchments within the eastern limb have recharge values which range from 9,5 – 55 mm/a (2 – 7 % of MAP). This can also be represented by an average value of 29 mm/a or 5% of MAP, which corresponds with the calculated mean recharge of 32 mm/a and 6% MAP.

There are no spatial patterns, related to geological variations, established from the constructed groundwater recharge, as expected due to aquifer properties that vary from one geological unit to the next, which consequently are likely to affect the infiltration rate of water into the saturated zone. The observed groundwater recharge variability is linked to topographical changes; where groundwater recharge values increase, with elevation. High recharge zones are identified as recharge areas and lower groundwater recharge zones, which occur by rivers are associated with discharge zones. The observed relationship between topography and recharge estimate, as well as linking the variability to the study areas' recharge and discharge zones, is supported by general hydrogeology principles of groundwater flow and occurrence (Freeze and Cherry, 1979).

Analysis of groundwater levels reveals that regional groundwater flow typically follows topographical gradients, this is consistent with the general trend, stated by DWAF (2006), of water table variability in fractured aquifers across South Africa. Regional groundwater flow tends to lower elevations areas, and the flow directions indicate that groundwater is discharged into the main drainage systems in the study area, the Olifants and Steelpoort Rivers – which can characterise surface water and groundwater interaction in the area.

3.8.1 Limitations of the investigation

The presented regional groundwater assessment is based on groundwater characterisation, by analyses of existing hydrogeological data, retrieved from the national groundwater database. Therefore, the findings of this investigation are limited to the available data within the groundwater databases.

The data from the NGA and GRIP databases applied for the borehole properties analyses and the hydraulic characteristics analyses, consists of boreholes that were drilled for groundwater supply. Therefore, the location of the boreholes is subjective to hydrogeological conditions which yield optimal water volumes, and the distribution and number of boreholes are also subject to demand and supply. At most times, scientific methods and surveys are applied to site the prime borehole location. Thus, the analyses and results presented in the investigation are susceptible to these biases. The data used from NGA and GRIP databases contains data gathered from different time periods, possible temporal effects were not regarded in the analyses. Borehole locations may be referenced incorrectly in the databases accessed, and since this investigation incorporates a desktop study and analyses by geo-processing data, incorrect coordinates may compromise the outcomes of the study.

Groundwater level monitoring boreholes in the study area are limited to only seven boreholes, therefore analysis of groundwater level trends was restricted by this limitation. More boreholes would have offered a better resolution, in terms of groundwater level conditions and water level variability in the eastern limb. For instance, in the RLS, in the areas concentrated with mining activities, there is only a single borehole which can be used to monitor the effects of mining on groundwater levels.

The hydrogeochemical characterisation of the groundwater system is based on water samples from three-year periods (2006 -2008), since more monitoring data points were collected during this period, therefore analysis provides better resolution for the spatial distribution analysis applied, to determine the dominant water types and the main hydrochemical processing controlling the water chemistry and identify the recharge and discharge zones. The use of data from a single period presents shortcomings of the investigations – since

temporal long-term and season effects were not taken into account due to data availability limitations. The number of active groundwater quality monitoring sites drastically decreased post 2008 therefore, the groundwater quality data available is limited. The available data in the groundwater quality database, and collected groundwater quality samples are infrequent, additionally, available monitoring sites do not have sufficient time-series data to analyse hydrochemical trends over long-term and seasonal time scales.

For the groundwater recharge estimation by the CMB method, a single value from literature was used for the concentration of chloride in precipitation, this presents a shortcoming since the single value homogenises the chloride input, whereas the CMB is based on the ratio of the input chloride in precipitation to the chloride content in groundwater.

4 DEEP SCIENTIFIC DRILLING

4.1 INTRODUCTION

Scientific drilling is defined as applying drilling methods developed in the hydrocarbon and mineral exploration industry to drill holes and retrieve samples of rock and fluid for scientific, not-for-profit purposes (Harms and Tobin, 2011). While deep scientific drilling is then defined as drilling for scientific research goals beyond near-surface geological and shallow groundwater exploration to depths greater than several hundred meters subsurface, through land, sea ice, or below the sea/lake floor (Harms and Tobin, 2011).

The boreholes to be drilled are geological focused and thus small diameter wireline core drilling, nonetheless as far as possible hydrogeological data collection will be facilitated and forms the focus for this discussion. Theoretical and practical background for the components to be considered are presented.

4.2 DATA COLLECTION DURING DRILLING

4.2.1 Hydrogeological data

The SADC framework for groundwater data collection and management emphasises data from boreholes siting, drilling and testing are essential for any hydrogeological borehole investigation, and attention should be given to borehole drilling data as this cannot be collected afterwards (SADC-GMI et al., 2019). Data to be collected during borehole drilling includes (SADC-GMI et al., 2019):

- Location and date;
- Borehole construction (e.g. geometry, materials, screening, pump);
- Lithological log: a record of the lithologies encountered while drilling (depth vs. type of formation, texture, colour, state of weathering);
- Penetration rates per depth;
- Depth of water strikes, permeable/preferential groundwater flow zones;
- Blow yield of each water strike;
- Quality of water from each strike (e.g. pH and EC as indicators);
- Actual borehole designs and dimensions;
- Borehole construction details – casing, screen and gravel/sand packed depth;
- Site description with photographs; and
- Drilling report

SADC-GMI et al. (2019) tabulate a detailed overview of the steps of borehole drilling supervision from a hydrogeological perspective, including the responsibilities of the driller and of the supervisor, with the essential data to be collected at each step (

Table 14). These steps of borehole drilling supervision apply for typical shallow water supply boreholes, but the same principles and data required applies for deeper boreholes.

It is thus important that the required specifications are provided to the driller in the drilling specification document (SoW), including the drilling fluid system, reticulation system, water supply and usage, cleaning of borehole, surveys to be performed and samples to be taken (if the drill rig is required). A trained hydrogeologist will be on site to supervise the drilling and to ensure hydrogeological information is collected and recorded.

Table 14 Overview of the steps of borehole drilling supervision from a hydrogeological perspective, including the responsibilities of the driller and of the supervisor, with the essential data to be collected at each step (SADC-GMI et al., 2019)

Borehole drilling supervision phases	Driller's Responsibility	Supervisor's Responsibility	Key data to be collected phase
1. Sourcing for the appropriate driller	<ul style="list-style-type: none"> Respond to request by the client 	<ul style="list-style-type: none"> Request for a first quotation from at least 3 drilling contractors for the task at hand, Use the assessment and check in step two and select the most cost effective and capable driller. 	<ul style="list-style-type: none"> Initial quotation for services of the drilling contractor for drilling, construction, development and completion
2. Pre-mobilisation	<ul style="list-style-type: none"> Raise specific questions about scope of work and contract requirements, Submit samples of materials 	<ul style="list-style-type: none"> Discuss about borehole design (use as a guide but can be modified during the drilling), Check the quality and specifications casings and screens, Check the quality and specifications of gravel/sand pack material + packers (if applicable), Assess the overall capacity of the drillers. 	<ul style="list-style-type: none"> Most cost effective and capable driller selected for appointment Indication of satisfaction with the quality of material and also capacity of the driller, if not: Make recommendations to driller for improvements, If not satisfied with material, communicate with driller and if possible, procure appropriate materials separately.
3. Mobilisation	<ul style="list-style-type: none"> Submit program of work, Avail equipment and materials for readiness inspection by drilling supervisor, Move equipment to site and materials to the site. 	<ul style="list-style-type: none"> Check the readiness of the driller; Approve drilling equipment and material, Liaise/inform community leaders about the date of the drilling a week or two prior to drilling. Guide the driller to the site (Now days GPS is used for direction) 	<ul style="list-style-type: none"> The community leaders are aware about the presence of the drilling team and have given their consent, The driller has arrived on the site and ready for the drilling,
4. Drilling	<ul style="list-style-type: none"> Position and operate the rig, Drill, construct, develop and complete the borehole according to specifications in the drilling contract, Collect drilling chip samples to a safe place for logging, and Conduct blow yield test for each water strike 	<ul style="list-style-type: none"> Monitor the drilling right set up, ensure it is oriented according project specifications, Monitor the drilling process, Measure groundwater quality after water strikes (EC and pH can provide a general indicator) + record blow yields. 	<ul style="list-style-type: none"> Date of drilling Exact location of borehole Lithology logs (normally per 1 meter of drilling depth) such as: type of formation, texture, colour, structure, state of weathering, etc. Penetration rates per 1 meter of drilling depth indicators)
5. Borehole construction	<p>According to the supervisor's specifications:</p> <ul style="list-style-type: none"> Gravel/sand pack the borehole Install casing and screen Etc. 	<ul style="list-style-type: none"> Instruct casing and screening depth as informed by observations made during in step 4 Ensure gravel pack is properly placed around the borehole at the desired depths 	<ul style="list-style-type: none"> Actual borehole designs and dimensions Borehole construction details – screen and gravel/sand packed depth Optional: Site description with photographs

Borehole drilling supervision phases	Driller's Responsibility	Supervisor's Responsibility	Key data to be collected phase
6. Development and completion	<p>According to the supervisor's specifications:</p> <ul style="list-style-type: none"> Develop the borehole, Construct sanitary seal and pad, Disinfect the hole if it is needed. 	<p>Ensure that the:</p> <ul style="list-style-type: none"> Borehole is sufficiently developed i.e. water is clear, Sanitary seal and pad properly constructed according to design specifications and to suit site conditions Borehole is sufficiently disinfected. Measure the groundwater level after completion 	<ul style="list-style-type: none"> Borehole completed, now waiting handover to the client/responsible authorities, Record of groundwater level data after completion, Record below yields and blow depths
7. Demobilisation	<ul style="list-style-type: none"> Remove all equipment and rubbish from site 	<ul style="list-style-type: none"> Ensure the drilling site is properly cleaned and restored to its former state 	<ul style="list-style-type: none"> The drilling site is now clean and restored to its former state and site ready for handover. Start compiling the drilling report
8. Documentation and handing over	<p>Submit all records to the drilling supervisor/client</p>	<ul style="list-style-type: none"> Report and handover the borehole to the client 	<p>Submit drilling report and hand over borehole to the client.</p> <ul style="list-style-type: none"> The report should document the whole borehole (s) installation processes analyse borehole data obtained in step 9 (drilling) to 11 (development & completion) and develop an initial conceptual understanding of the aquifer where the borehole has been drilled. Such initial conceptual understanding should include aspects such lithology logs, location of main flow zones (water strikes), piezometric/hydraulic heads¹, aquifer structure and type

¹ To determine accurate piezometric/hydraulic, use borehole elevation (meters above mean sea level) determined using differential GPS.

4.2.2 Online gas analyser (OLGA)

Erzinger et al. (2006) developed a real-time mud gas monitoring technique for scientific drilling in non-hydrocarbon formations to sample and study the composition of crustal gases. Continuous mud gas logging during drilling is typically done in oil and gas operations, but in deep scientific drilling this provides a means to measure gases from depths in real-time and use this information to understand deep systems. Off-site isotope studies on mud samples can also facilitate the understanding on the origin and evolution of deep-seated crustal fluids (Erzinger et al., 2006).

The experimental setup is illustrated in Figure 45. For online drilling mud gas analysis, the dissolved gas is 1) continuously extracted from returning drilling mud in an airtight gas-water separator located at the “possum belly”; 2) pumped in a field laboratory nearby the shale shakers; 3) automatically analysed for its composition (CO_2 , N_2 , H_2 , O_2 , He , Ar , CH_4 , C_2H_6 , C_3H_8 , $i/n\text{-C}_4\text{H}_{10}$, and ^{222}Rn) in real-time, and 4) automatically sampled for further studies (stable isotopes, noble gases). The outcome and results of the analysis can be applied to detect fluid-bearing horizons, shear zones, open fractures, sections of enhanced permeability and methane hydrate occurrences in the subsurface of fault zones (Erzinger et al., 2004; Wiersberg and Erzinger, 2007; 2008), volcanoes (Tretner et al., 2008), geothermal and permafrost areas (Wiersberg et al., 2005), and others. An example of continuous drilling fluid analysis in the German Continental Deep Drilling Program (KTB) borehole indicated several fluid inflow zones with increased concentrations of chloride and/or methane and/or helium (Figure 44). Off-site isotope studies on the mud gas samples can provide information to determine the origin, evolution and migration mechanisms of deep-seated fluids (Wiersberg and Erzinger, 2007). The online gas analysis results can also inform decisions on the depth at which to conduct whether rock and fluid sampling (GFZ and ICDP, 2020).

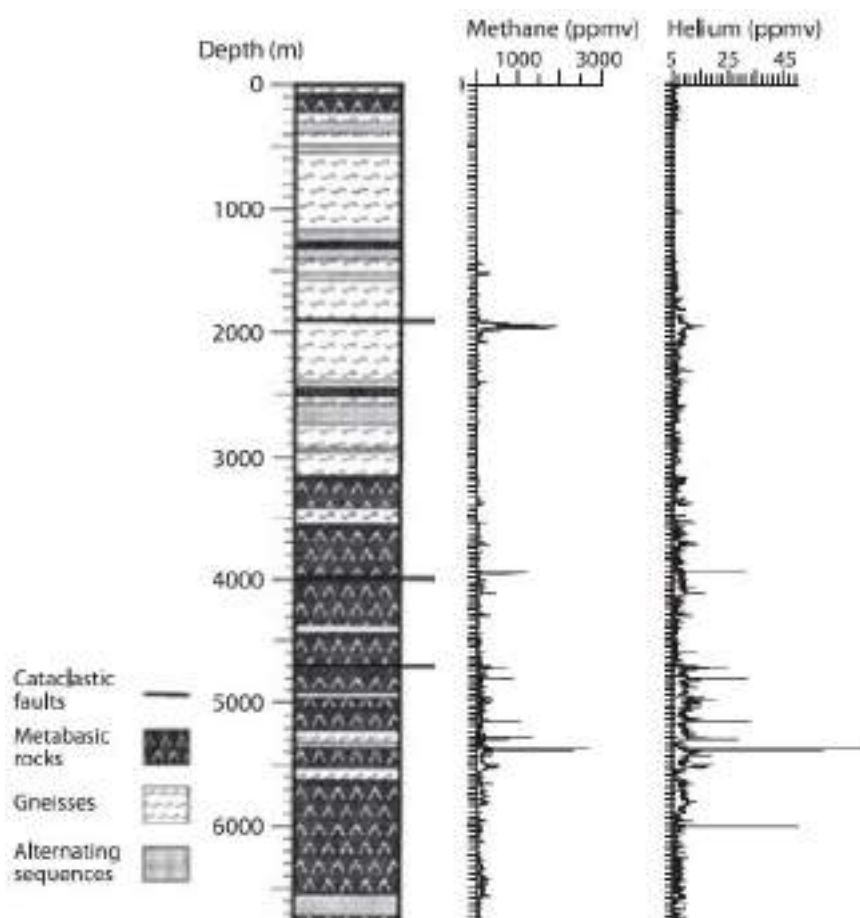


Figure 44 Illustration of an example of online gas analysis results. Compressed mud gas log of the KTB main hole displaying only the most prominent CH_4 (ppmv) and He (ppmv) shows

Online monitoring of gas from circulating drilling mud has been proven as a reliable and economical technique to obtain information on the composition and spatial distribution of gases at depth-in real time (Erzinger et al., 2006). The method has been successfully applied on several ICDP drilling projects (Erzinger et al., 2006; Tretner et al., 2008; Wiersberg and Erzinger, 2008).

Typically, the mud gas comprises of air and components that are mechanically released as the drill bit crushes the rocks during drilling, components present in the rock pore space, and gas entering the borehole, either as free gas or, more likely, dissolved in liquids (Erzinger et al., 2006). It is assumed that gases in groundwater would also be included in this description, and this project provides an opportunity to investigate this further.

The online gas analysis requires drill mud circulation to be able to perform the analysis. There are situations where the mud is lost in the drill hole and does not reach surface and thus the analysis can then not be performed. For example, in highly fractured or brecciated young volcanic rocks (high permeability).

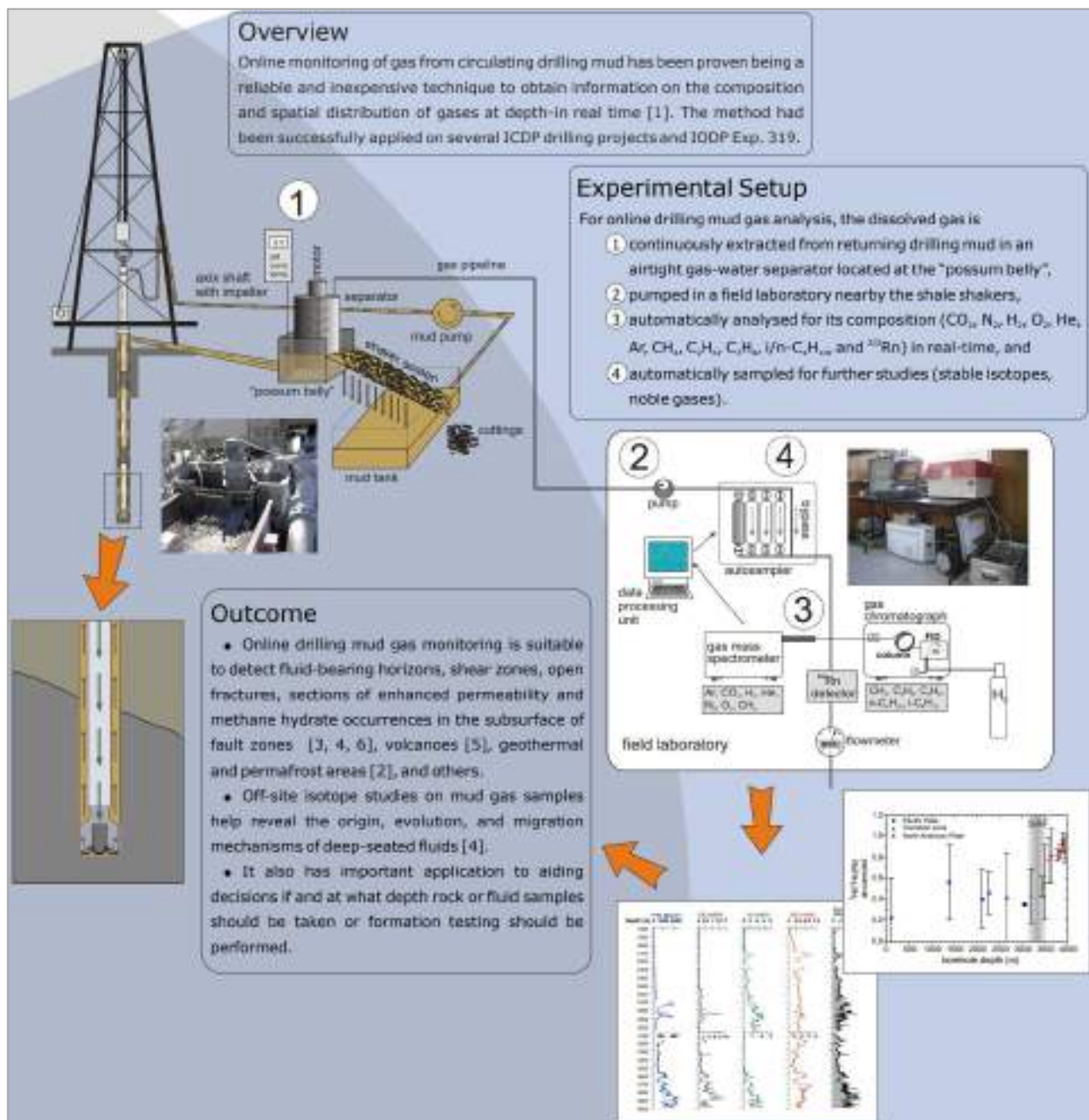


Figure 45 Illustration of the Online Gas Analysis (OLGA) setup and details of analyses performed (GFZ and ICDP, 2020)

4.3 GEOPHYSICAL LOGGING AND SAMPLING SURVEYS

Geophysical borehole logging techniques provide information on structural features and geological formations in a borehole remotely (ICRC, 2010). Down-hole wireline logging will provide continuous recording of the physical-chemical parameters of the borehole walls (Webb, 2019). The full suite of borehole / rock parameters to be assessed by geophysical logging is tabulated in Table 15 (Webb, 2019).

Table 15 Borehole/rock parameters to be assessed by the planned geophysical logging and sampling surveys on the new drill holes (Webb, 2019)

Property	Application
Electrical resistivity	porosity & salinity, hydrogeology
Magnetic susceptibility	lithology ID, constraints on layering processes
Total field magnetics	field orientation, magnetic intensity studies
Acoustic velocity (sonic log)	rock physics
VSP (geophone chain)	rock physics
Density	lithology ID, constraints on layering processes
Temperature	geothermal gradient, hydrogeology
Pressure (fluid)	hydrogeology
Porosity	lithology, rock competence, hydrogeology
Permeability	lithology, hydrogeology
Hydraulic Conductivity	hydrogeology
Gamma spectrometry	lithology, heat production studies
Borehole geometry	stress state
Borehole imaging	lithology, rock competence
Flow rates	hydrogeology
Water quality (Electrical conductivity, Oxygen and pH)	hydrogeology, microbiology

The planned geophysical logging surveys include both the traditional suite of geologically focused logs, as well as some specifically groundwater-related surveys, including the Borehole Magnetic Resonance (BMR) logging tool for hydraulic conductivity, Flow Meter tool and Water Quality probe survey. Each will be discussed here briefly.

4.3.1 Electrical resistivity

Electric logging consists of lowering a device used to measure the electric resistance of the rock layers in the downhole portion of the borehole. This is achieved by running an electric current through the rock formation and measuring the electrical resistance that the current encounters along the survey (Speight, 2019).

Resistivity logs can be used to identify formation water and the salinity of that water. If the shallow curve has low resistivity, but the medium and deep penetrating tools have a higher resistivity that is the same (they overlie each other), the formation is permeable and contains only formation water (Figure 46). If the mud filtrate resistivity is constant, the effect is greater for formations with fresh formation waters than those for saline formation waters (Figure 47).

An example electrical resistivity survey results is illustrated in Figure 48, where the typical response of an electrical tool in a sand/shale sequence is shown. Lower resistivity is recorded in the shales due to the presence of bound water in clays that are subject to surface conduction. Sandstones have higher resistivity measurements which are dependent on their porosity, pore geometry, resistivity of formation water, and water/oil/gas saturations (Glover, 2014a).

The dual laterolog (DLL) is the latest version of the laterolog. As its name implies, it is a combination of two tools and can be run in a deep penetration (LLd) and shallow penetration (LLs) mode (Glover, 2014a). An example DLL log is shown in Figure 49 showing separation of the LLs and LLd.

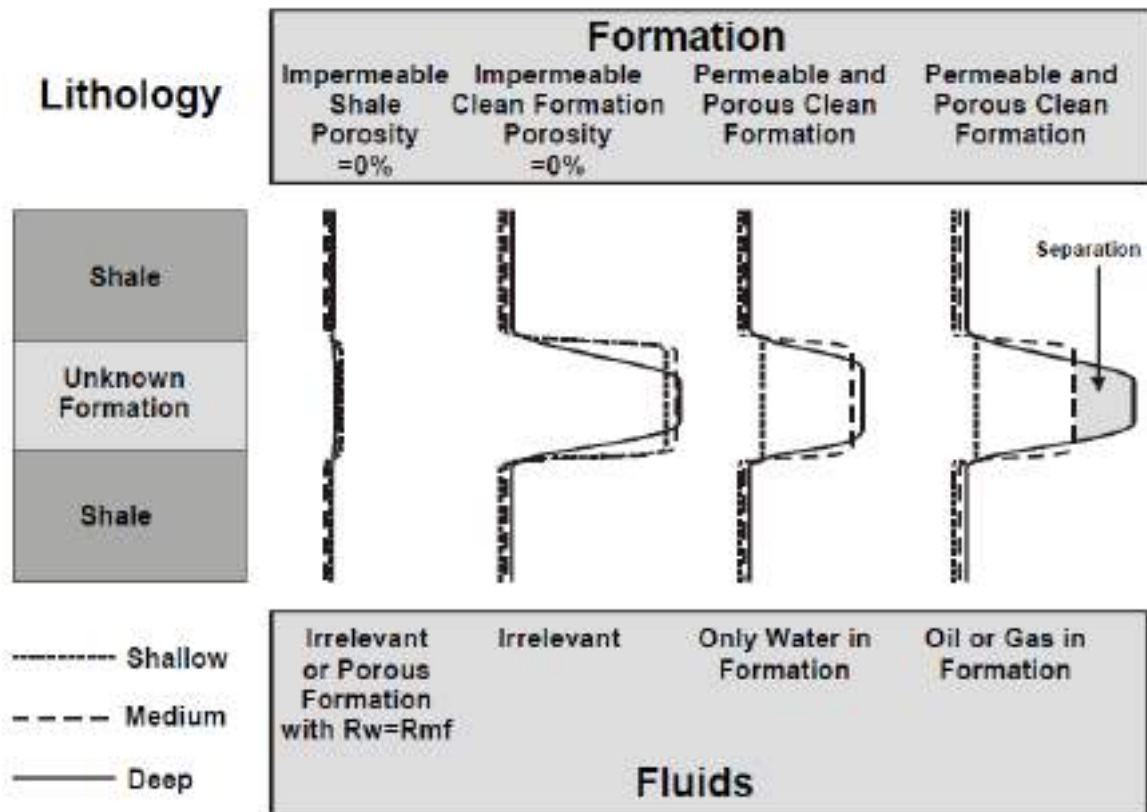


Figure 46 The response of resistivity logs in formations with various fluids (Glover, 2014a)

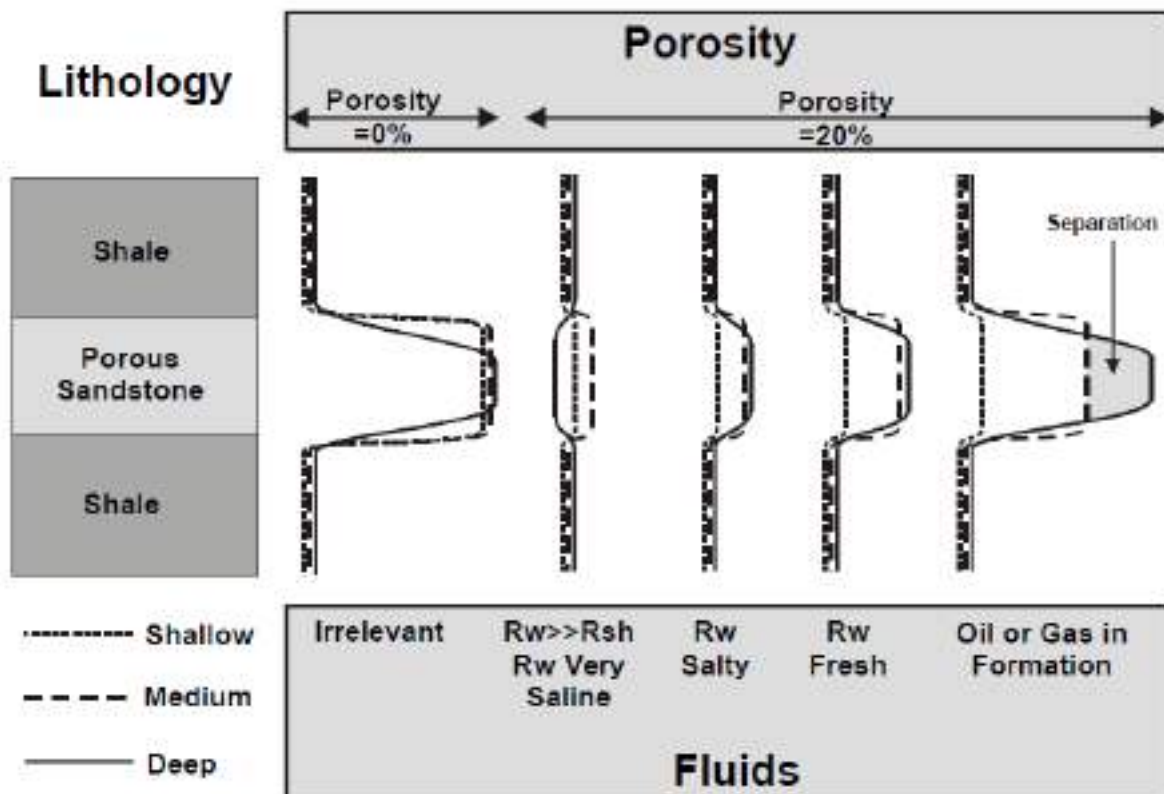


Figure 47 The response of resistivity logs for different formation water salinities (Glover, 2014a)

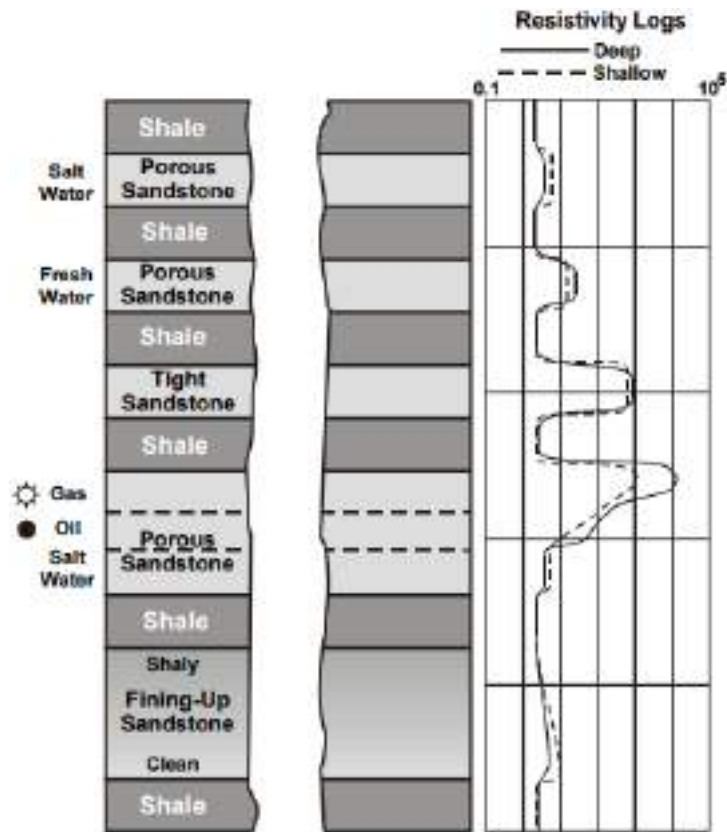


Figure 48 Typical resistivity log response in a sand/shale sequence (Glover, 2014a)

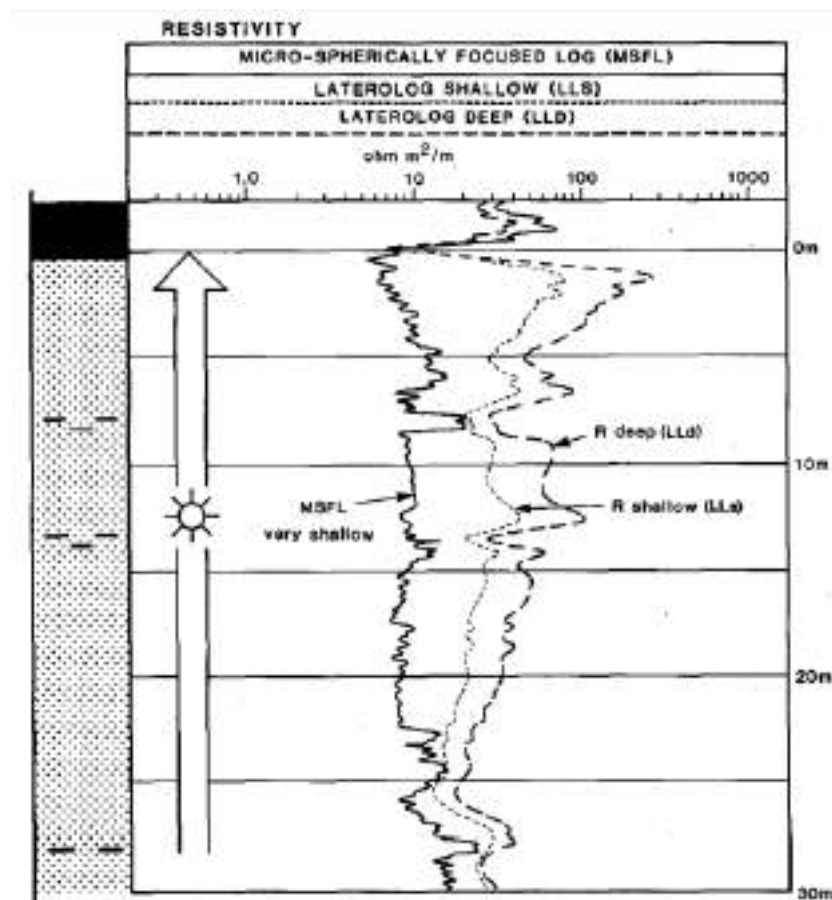


Figure 49 An example of a DLL log, showing separation of the LLs and LLd, and from the MSFL, indicating the presence of a permeable formation with hydrocarbons (gas in this case in a formation of about 15% porosity) (Glover, 2014a)

Specifically in fractured crystalline rock, resistivity is sensitive to the presence of interstitial fluids and alteration minerals (Boness and Zoback, 2004). Hydrothermal alteration of the rocks also influences the formation resistivity where the alteration minerals of different resistivities could be attributed to geothermal activity (Steingrímsson, 2011; Chan et al., 2014). Chan et al. (2014) report on geophysical logging on a deep borehole (TVD 2.4 km) which intersects 875 m of crystalline basement rocks. The electrical resistivity log showed significant lower resistivity intervals at depths greater than 1 400 m, which were correlated to the presence of brine in the fracture zones (Chan et al., 2014).

An example of electrical resistivity log of drilling fluid in a borehole illustrating the freshwater/saltwater boundary (Figure 50) (Wonik, 2007).

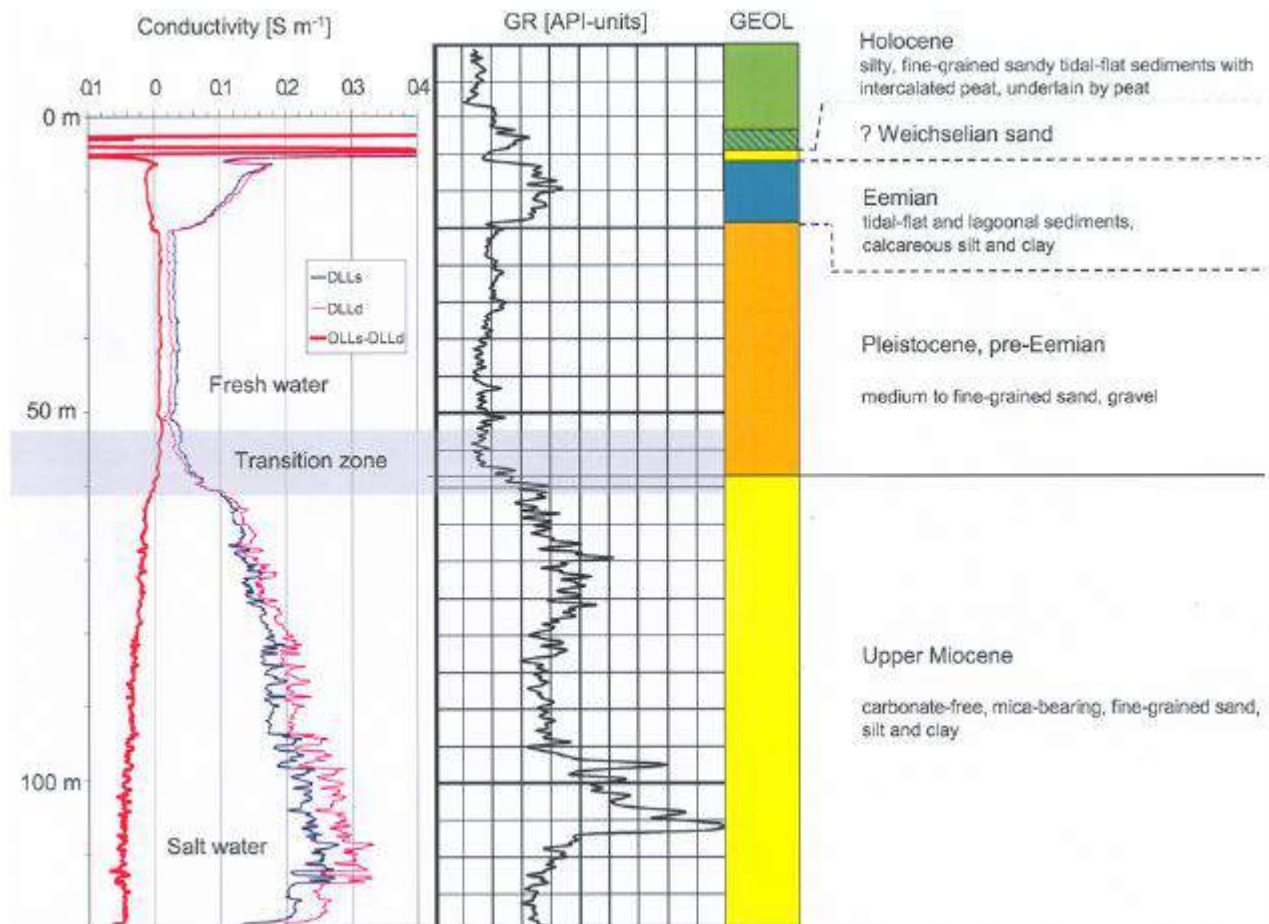


Figure 50 An example to illustrate the freshwater/saltwater interface in the Cuxhaven borehole in northern Germany in resistivity logs (DLL). DLLs: shallow dual laterolog; DLLd: deep dual laterolog; GR: gamma-ray log (Wonik, 2007).

4.3.2 Spectral Gamma Ray (SGR)

Nuclear logging includes all methods that either detect the presence of unstable isotopes or create such isotopes in the vicinity of a borehole. Gamma and neutron logs are probably the most common nuclear methods used in ground-water studies (ERG and CERI, 1993).

Spectral Gamma Ray records the amount of energy of gamma photons either on a continuous basis or at selected depths with a stationary probe. Types and amounts of radioisotopes can be measured. Allows more precise identification of lithology than gamma log; permits identification of artificial radioisotopes that might be contaminating water supplies; widely used by petroleum industry should probably be used more frequently in groundwater investigations, according to ERG and CERI (1993).

A typical spectral gamma ray log is illustrated in , where the total gamma ray log (SGR) and computed gamma ray log (CGR) are showed along with the calculated abundances associated with the radiation from the individual contributions from K^{40} (%), U^{238} (ppm) and Th^{232} (ppm) (Glover, 2014b).

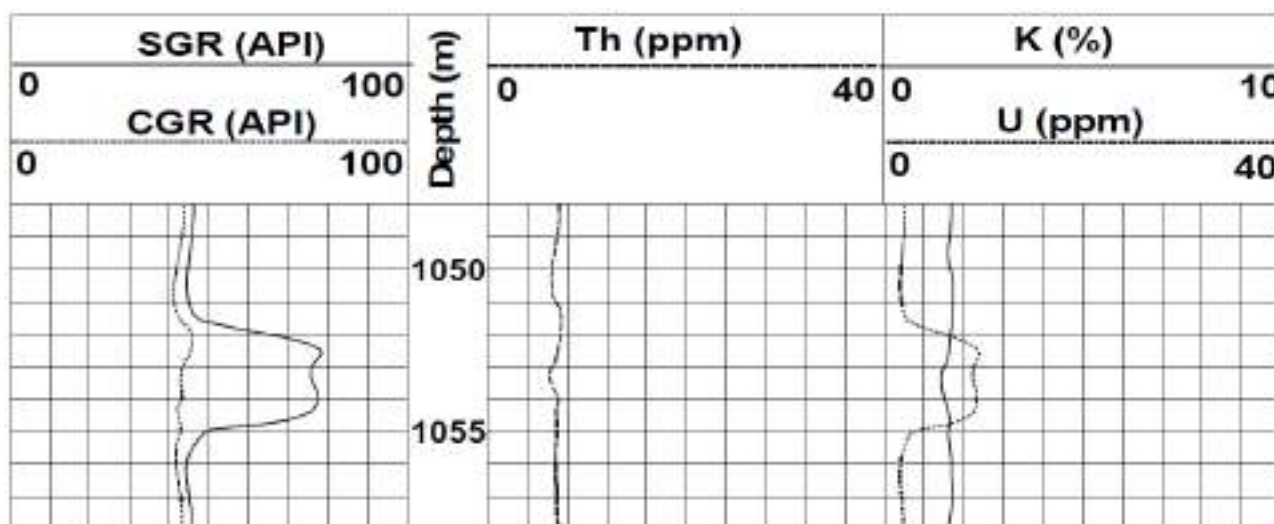


Figure 51 An example of a typical spectral gamma ray log (Glover, 2014b)

The spectral gamma ray log is especially useful for subtle lithological and compositional analysis due to the high vertical resolution of the results. Additionally, it can be used to identify igneous rocks, as in the Bushveld Complex, where values of Th and U from the spectral gamma ray log are used together with the density from the density log and the sonic wave travel time from the sonic log to identify and distinguish between igneous rocks. The SGR can also be applied to fracture detection based on the principle that uranium is soluble in reducing conditions, and dissolved uranium precipitated along fractures will cause local peaks in the uranium SGR log. It should be noted that such peaks should be confirmed with image logs because uranium peaks do not solely indicate fractures (Glover, 2014b).

4.3.3 Acoustic / Sonic

Acoustic, also known as sonic, logging is the recording of travel times of acoustic waves from one or more transmitters to receivers installed at suitable distances along a borehole probe (Agliardi et al., 2016). Acoustic logging is useful for providing information on lithology and porosity but is typically limited to consolidated materials in fluid-filled boreholes (ERG and CERI, 1993). Acoustic logging is especially valuable for characterising secondary porosity and fractures (ERG and CERI, 1993; Paillet, 1994).

An example response of a sonic (acoustic) log is illustrated in Figure 52, where changes in lithologies are sensitive, but the response is dependent on the density (compaction) of the layer. There is also a strong response to gas-filled porous units and water bearing porous zones. The sonic log can also be used to identify overpressure zones in a borehole (Glover, 2014c). Agliardi et al. (2016) conducted acoustic logging in a crystalline core complex with success, where the acoustic log effectively mirrored local heterogeneity.

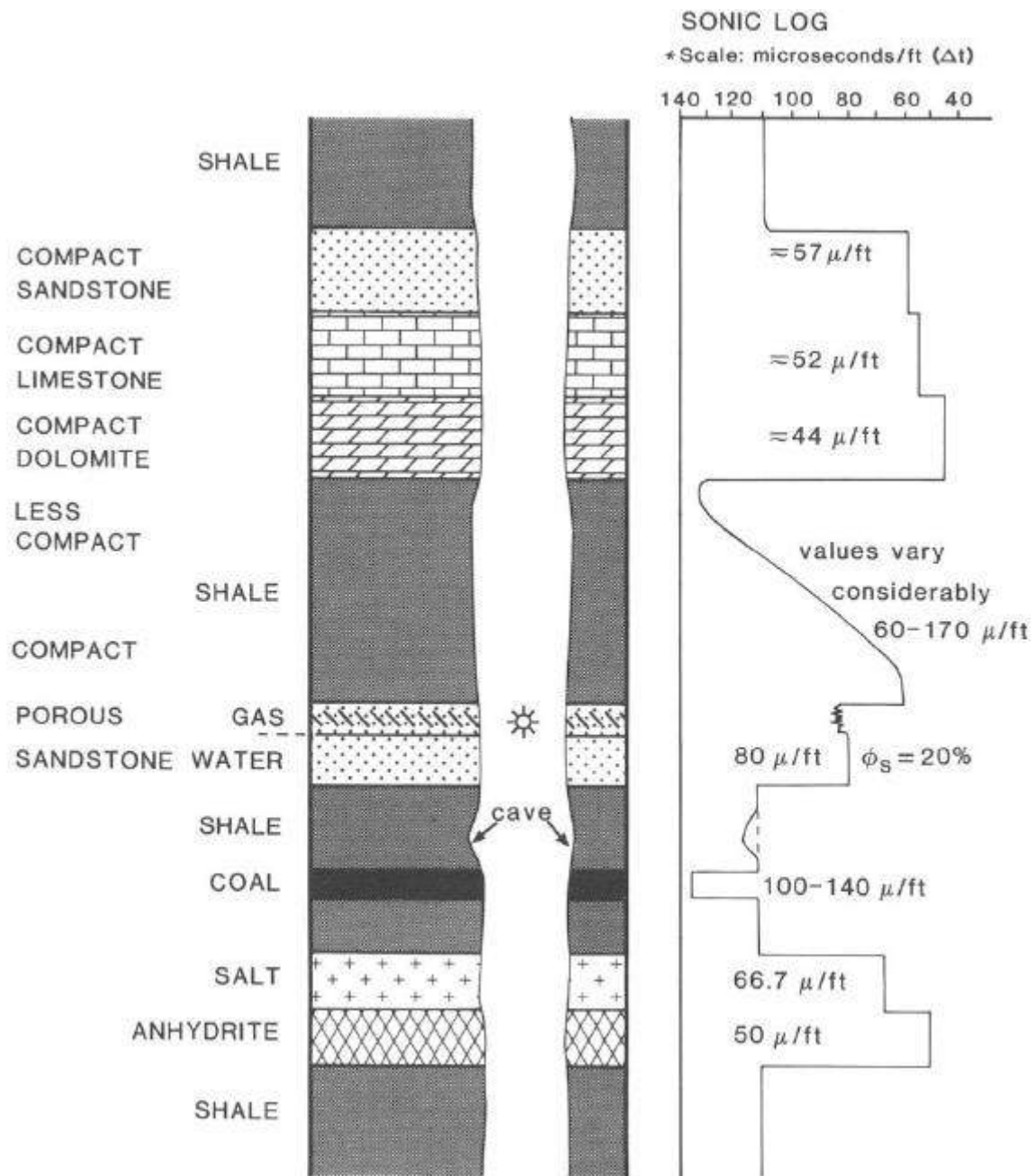


Figure 52 Typical responses of a sonic (acoustic) log (Glover, 2014c)

4.3.4 Dipmeter

A dipmeter comprises a number of wall-contact microresistivity probes (ERG and CERI, 1993). An example of a dipmeter log results is shown in Figure 53, where a core description is displayed alongside the results to illustrate the analysis of facies and transport direction (Doveton, 2017). From Figure 53, it can be seen that the upper shale layers show small dips in a westerly direction that indicates regional stratigraphic dip and a red pattern near the sandstone. The uppermost sandstone unit had been interpreted to be estuarine and tidal influence by Luchtel (1999), as cited in Doveton (2017), and explained that this is evident by the distinctive bimodal character of the dips in the tadpoles as well as the rose diagram with directions to the south-east and north-west. The middle sandstone layer consists of stacked fluvial channels with unimodal blue dip patterns of crossbeds oriented to the southeast. The lowest sandstone layer has a uniform pattern of low-angle dips to the south-south-east. The shale below the sandstone has a green pattern of shallow dips to the south-west that probably reflects regional stratigraphic dip (Doveton, 2017).

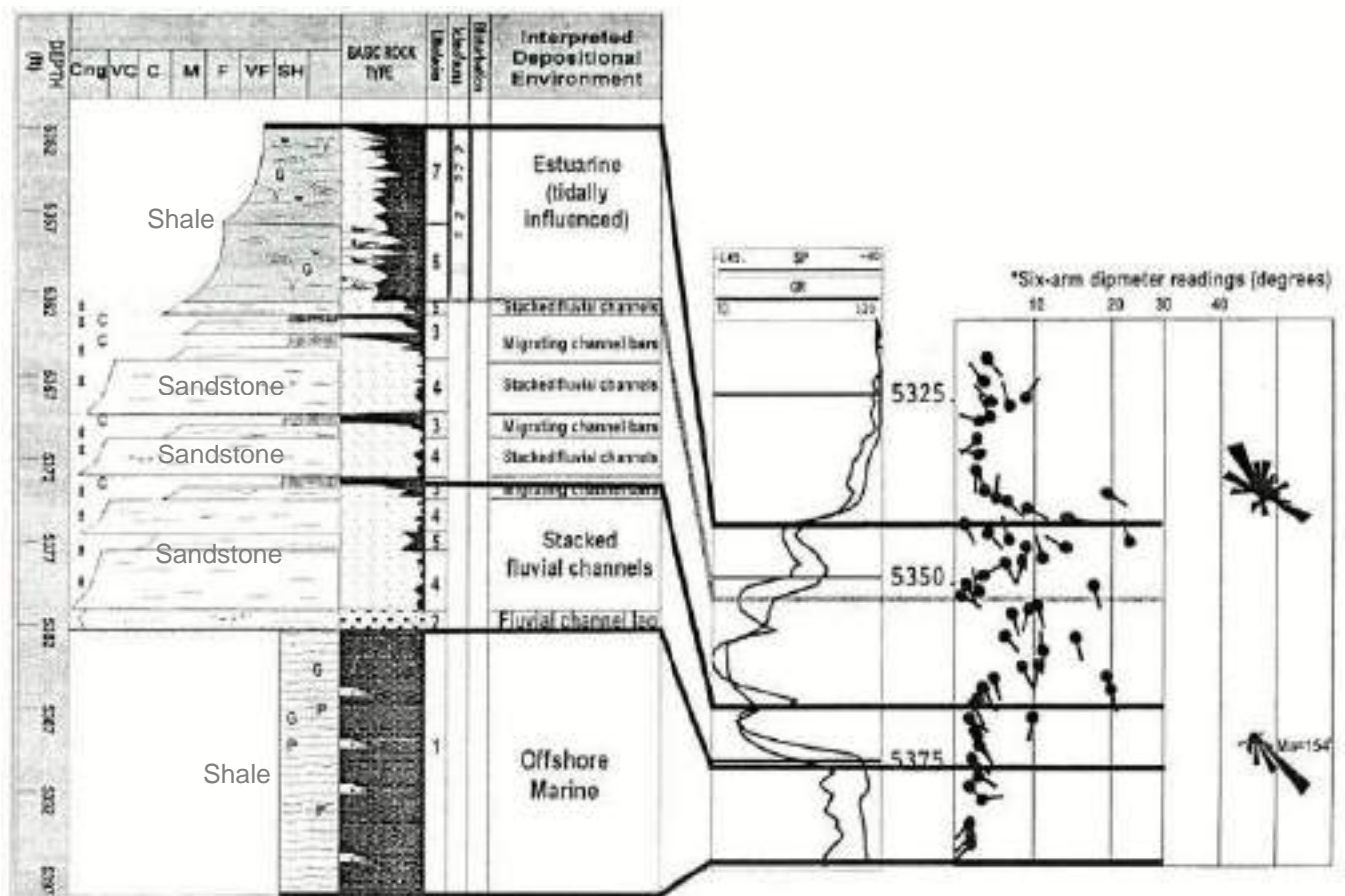


Figure 53 Stratigraphic core description displayed with dipmeter log to illustrate the analysis of facies and transport direction (Luchtel, 1999, as cited in Doveton, 2017)

The dipmeter is considered, by ERG and CERI (1993), the best instrument for gathering information on the location and orientation of primary sedimentary structures over a wide variety of hole conditions, and it provides data on the strike and dip of bedding planes also on fractures, albeit less precisely (ERG and CERI, 1993).

Dip measurements are typically used to define regional or structural dip yet can also be used to identify structural dip anomalies associated with structural deformation, i.e. faults, folds. Additionally, analysis of dipmeter logs can inform stratigraphic phenomena such as discontinuities or angular unconformities (Serra, 1983).

According to Wonik (2007), dipmeter logs are also useful for detecting fractures. Used in complement with a borehole televiewer, in the ultrasound range, can accurately determine fractures and the dip of strata. Programs are available for calculating dip angles from the data in these two methods (illustration example in Figure 54) (Wonik, 2007).

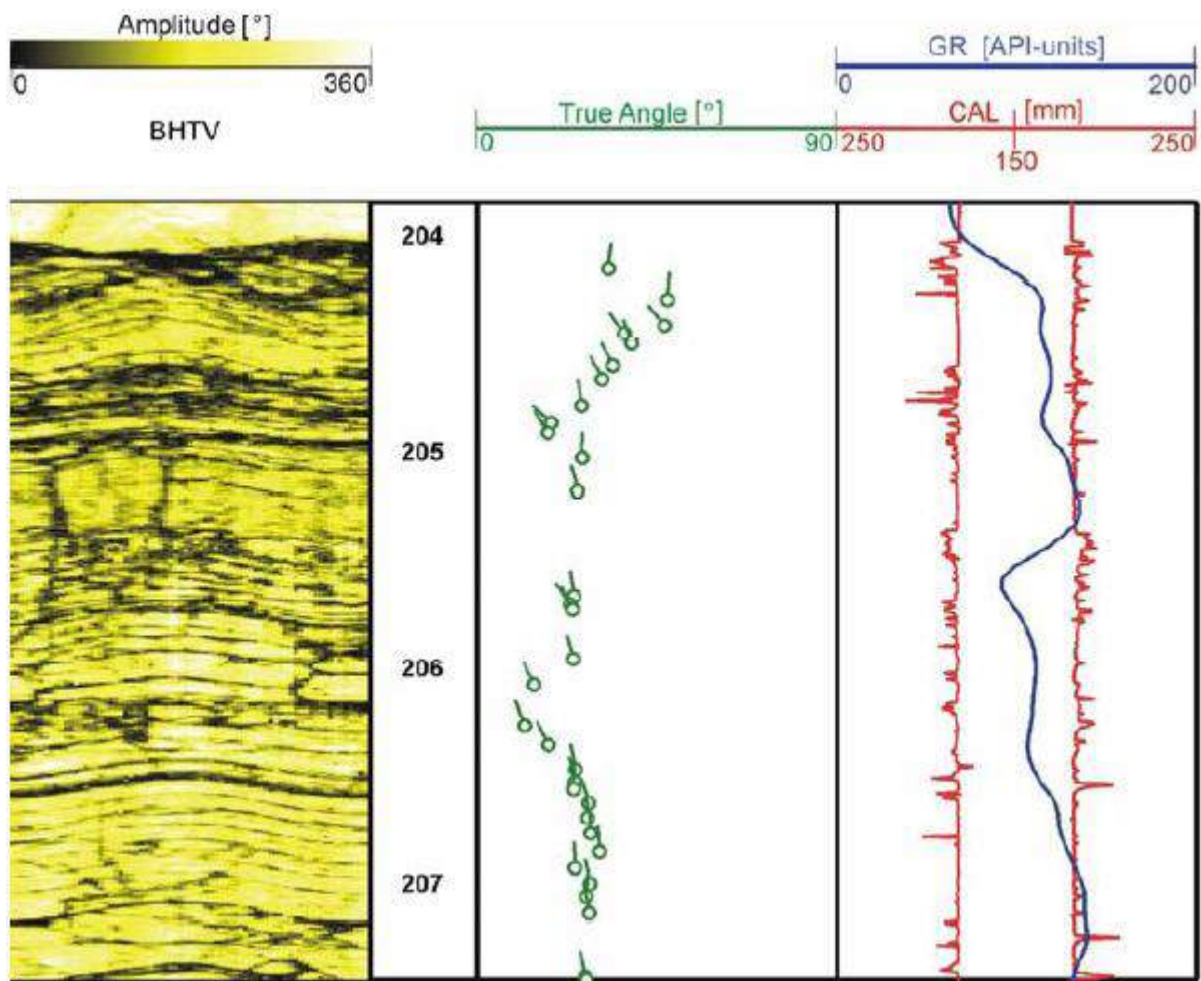


Figure 54 Example acoustic image of the depth interval 203.8 - 207.5 m in the Fürstenwald borehole near Kassel, Germany as recorded by Wonik (2007). GR: gamma-ray log; CAL: Caliper log; True Angle: direction and dip angle of fractures and other structures in the borehole wall (dipmeter) (Wonik, 2007)

4.3.5 Magnetic susceptibility

Electromagnetic well logging methods can be used in both dry wells and those containing water or drilling fluid. In contrast to electrical methods, these methods can be used in boreholes with plastic casing. The parameters electrical conductivity and susceptibility can be determined using an induction tool or a susceptibility tool, respectively. Magnetic susceptibility measures the ability of a rock formation to become magnetised in response to an applied magnetic field and gives inference to the abundance of ferromagnetic magnetic minerals within the tested rock volume. Magnetic susceptibility can be used for lithological classification, inspection of well completion and technical conditions of borehole, as well as for identifying metal scrap forced into the rock during drilling (Wonik, 2007; Jerram et al., 2019).

In rocks, magnetic susceptibility is primarily dependent on the volume percent of magnetite, and magnetite is common in igneous and metamorphic rocks (Altstatt et al., 2002; Jones and Oldenburg, 2007). An example of a magnetic susceptibility log, conducted by Jerram et al. (2019), shows a significant level of systematic

variations associated with lava facies flow packages and boundaries (Figure 55). The response is not uniform in nature but, in many instances, a sharp reduction or increase in susceptibility can be seen at or in other cases immediately prior to the facies boundaries. Planke et al. (1999) had demonstrated that flow top alteration can cause a kick in susceptibility values at the transition from lava interiors up into the crust, and the results by Jerram et al. (2019) confirm these observations in terms of magnetic susceptibility (Jerram et al., 2019).

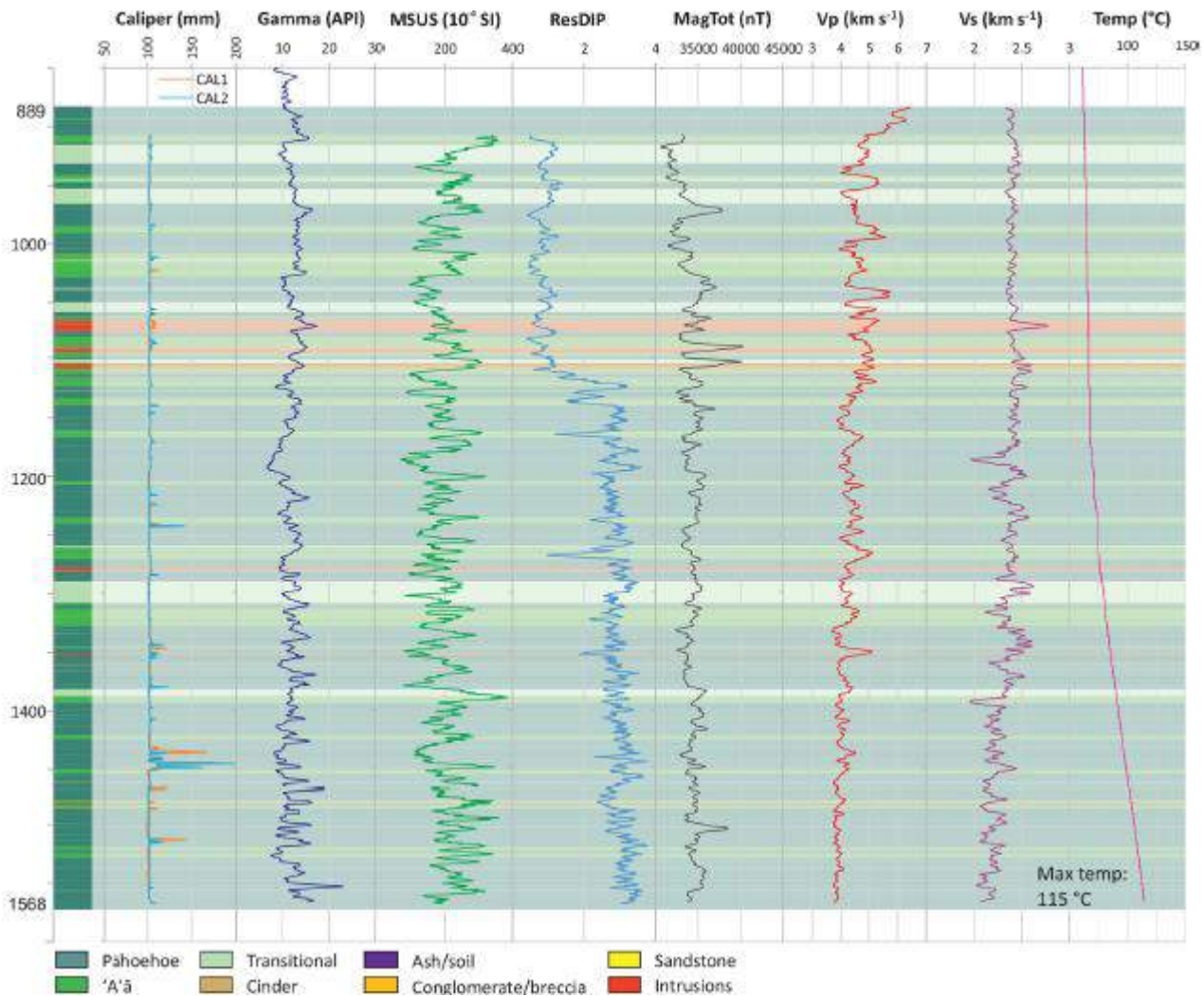


Figure 55 An example of a magnetic susceptibility log (MSUS) illustrating systematic variations associated with lava facies flow packages and boundaries (Jerram et al., 2019)

4.3.6 Mud logging (mud parameter)

Mud logging is the detailed record of examining the cuttings of rock brought to the surface by the circulating drilling medium, typically drilling mud (Koperna, 2020). Mud logging procedures can also record gas shows. Mud logs used in conjunction with geophysical borehole logs can be used to define formation tops, pick core points, evaluate potential hydrocarbon zones and assess geological risks, i.e. fault zones). Koperna (2020) makes use of the mud log in addition to a suite of *Triple Combo* geophysical logs (Figure 56). The *Triple Combo* logs contain Array Induction (Resistivity), Gamma Ray (GR), Spontaneous Potential (SP), Sonic, Differential Caliper, Formation Photoelectric Factor, Density Porosity, Neutron Porosity, and Borehole Profile log measurements (Koperna, 2020).

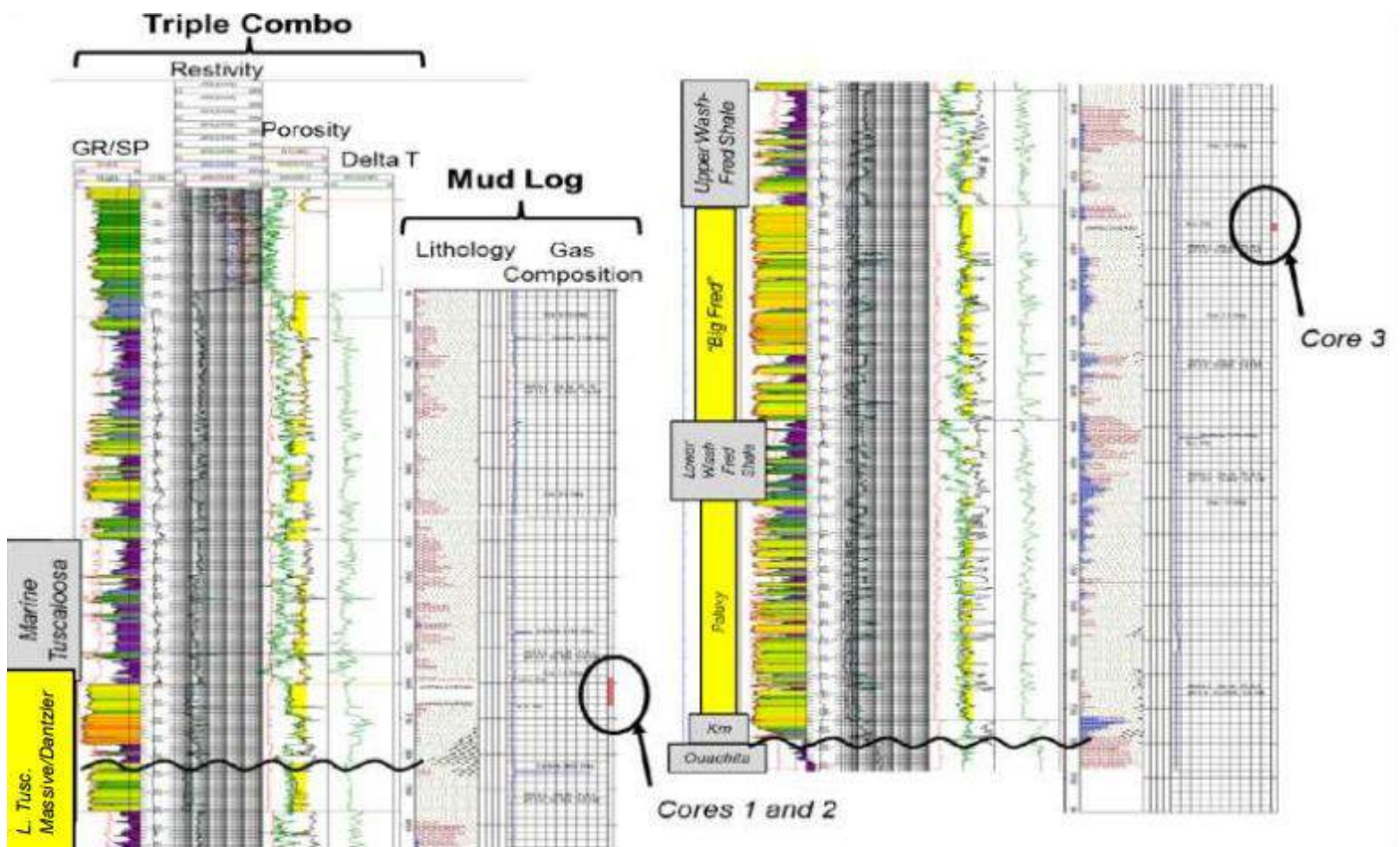


Figure 56 Example of a composite image of the *Triple Combo* Open Hole Log and Mud Log. Core points are identified to the right of the log tracks. The first track contains a colour filled natural gamma ray curve. Warmer colours (yellow) indicate reservoir intervals (sandstones). Cooler colours (green/blue) indicate confining units (mudstones). The third track shows Neutron and Density porosity curves. The Density Porosity Curve is filled (yellow) when Density Porosity is > 20% (Koperna, 2020).

4.3.7 Borehole imaging

Borehole imaging logging tools provide high-resolution images of the borehole wall. Images are created either directly, through optical technologies (photographs or video) or indirectly, through a high density of geophysical measurements (electrical resistivity, ultrasonic velocity or acoustic reflectivity) (Prensky, 1999; Kingdon et al., 2016). Acoustic (televIEWer) and electrical borehole imaging are used more extensively, due to the limitations of optical imaging, namely a separate light source and clear borehole fluid.

An example of some features illustrated in a borehole televIEWer data, as reported by Jerram et al. (2019), is shown in Figure 57. A simplified schematic displaying the four-arm Caliper response to common borehole conditions is shown, along with an overview of the basics of televIEWer imaging of borehole features and examples in borehole televIEWer data (Figure 57) (Jerram et al., 2019).

Borehole imaging can manually or (semi-) automatically identify and quantify bedding, fracture features, faults, and stratigraphic features. In addition to identifying fractures and faults, borehole imaging tools can be used in support of detailed core analysis for a variety of other applications, such as sequence stratigraphy, facies reconstruction, stratigraphy, and diagenetic analysis (Table 16) (Guillot et al., 2007).

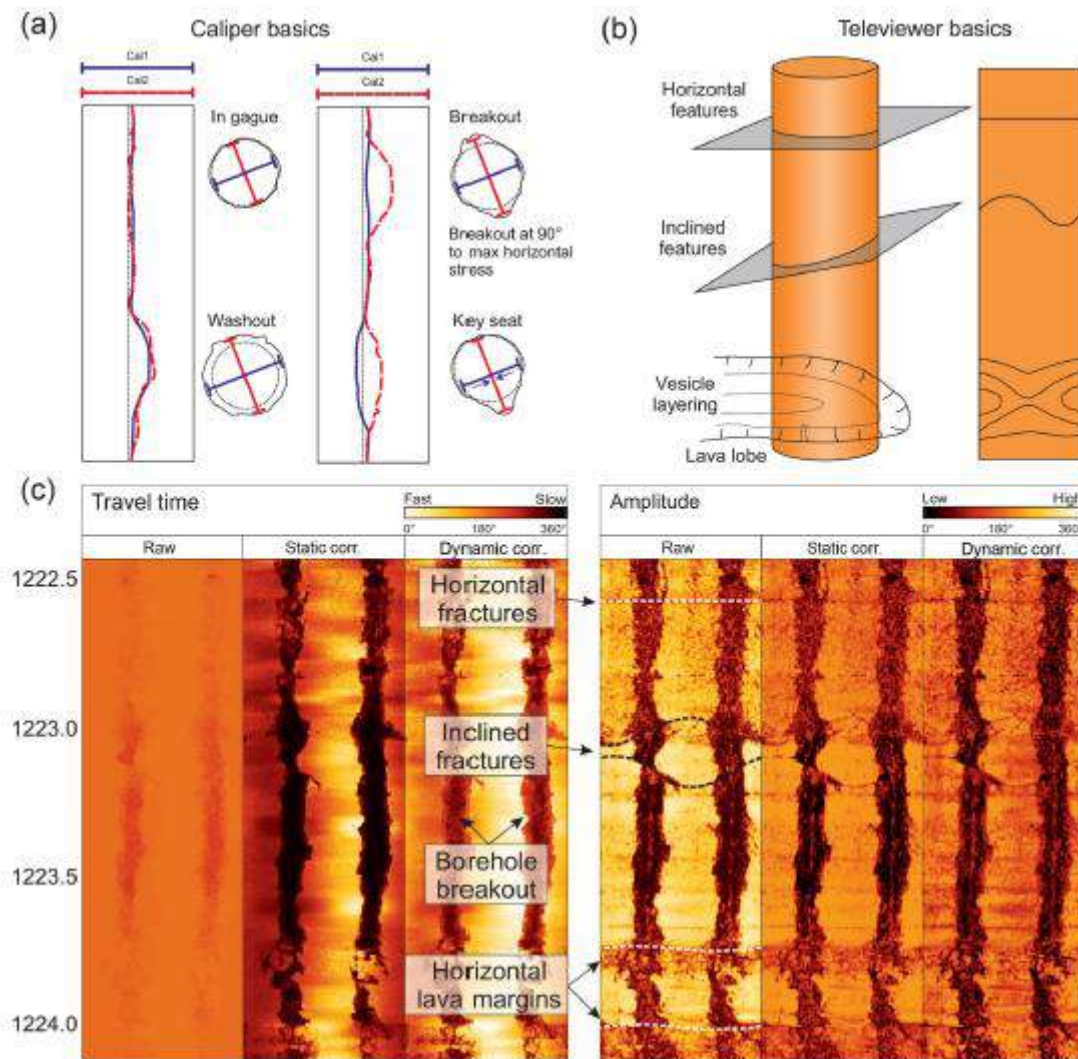


Figure 57 Borehole imaging illustration by Jerram et al. (2019). (a) Simplified schematic displaying the four-arm Caliper response to common borehole conditions; (b) basics of televiwer imaging of borehole features; (c) example of some of these features from the PTA2 borehole televiwer data.

Table 16 List of tectonic, sedimentary and diagenetic features typically identified on borehole images (Gaillot et al., 2007)

	Tectonic	Sedimentary	Diagenetic
Self-evident	Structural dip	Bedding surfaces	Stylotites (high amplitude peaks)
	Natural fractures drilling	Laminations	
	Induced fracture	Cross-bedding	
	Breakout	Grading	
	Folds	Erosional surface	
		Deformation features	
Ambiguous		Lithological changes	
	Faults	Cobbles, pebbles, Breccia	Nodular concretions
		Detrital shales, ripples	Cherts
		Bioturbation	Vugs
Needs core		Grain size/texture	
	Small fractures	Bioturbation	Stylotites (low amplitude peaks)
	Horizontal fractures	Thin lamination	
		Limestone textures	

Slimhole ATV's and optical televiewer (OTVs) provide exception azimuthal and vertical resolution, e.g. advanced logging technology televiewer: Acoustic Borehole Imager (ABI). The ABI-43 ultrasonic acoustic borehole imaging tool is planned to be used, because it is ultra-compact and state-of-the-science (Gaillot et al., 2007; READ, 2020).

4.3.8 Vertical Seismic Profile (VSP)

Vertical seismic profiles (VSPs) are small-scale seismic surveys in which geophones are lowered into a borehole to record waves traveling both down into the earth (direct waves from the surface source and down-going multiples) and back toward the surface (primary reflections and up-going multiples). VSPs contain information about the reflection and transmission properties of the earth with a coverage that depends upon the geometry of the VSP experiment and the structure near the well. Vertical seismic profiling (VSP) techniques provide a method to measure accurately the seismic velocity and lithologic structure near the borehole. However, rig standing time is a limiting factor in VSP acquisition (Stewart et al., 1984; Oristaglio, 1985; Frignet and Hartog, 2014).

Vertical seismic profiles (VSPs) are normally attained by deploying downhole seismic sensors in a borehole with wireline logging cable and then triggering a seismic source. The measurement involves recording the total up-going and down-going seismic wave fields propagating through a stratigraphic section by means of geophones clamped to the wall of a drilled well. VSPs can be applied to establish the detectability of a target horizon, i.e. porous zone. A slim line borehole geophone chain with a maximum of 17 levels (3-component geophones each) is planned to be used in the geophysical logging (Balch et al., 1982; Hardage, 1985).

Borehole seismic methods can use various surface-borehole or borehole-borehole source and geophone/hydrophone configurations. They are used primarily for stratigraphic, fracture, and geotechnical characterization. VSP can be applied to detect of lithologic boundaries, fracture detection, and even estimate permeability and hydraulic conductivity according to ERG and CERI (1993).

4.3.9 Fluid sampling

Fluid samples from deep boreholes can provide insights into subsurface physical, chemical, and biological conditions. Recovery of representative samples of subsurface fluids is required for analysis of aqueous chemistry, isotopic composition, dissolved gases, and microbial community characterisation. However, collecting these samples poses a number of challenges, from formation contamination by drilling, to maintaining integrity during recovery from depths. Not only are there substantial engineering issues in retrieval of a representative sample, but there is often the practical reality that fluid sampling is only one of numerous activities typically planned for deep boreholes (Freifeld, 2009).

A fluid sampler is an electronically controlled device that can be run on a logging cable to collect water samples at selected depths in a borehole. A formation tester is a wireline device that can be used to recover fluid samples from rocks penetrated by a borehole and to record flowing and shut-in pressure versus time (Keys, 1989).

Typically, it is referred to as fluid sampling, yet it is referring to groundwater most of the time. Sampling groundwater from exploratory boreholes can be a challenge due to the depth, remote locations, and purging requirements. Drilling fluid used during the drilling of the borehole creates a water column that needs to be purged prior to sampling in order to attain a representative sample. In deep boreholes, this can mean hundreds or thousands of litres of water that needs to be removed prior to collecting a sample. One option to avoid larger purging volumes, is to make use of packer systems to isolate specific target areas and only perform purging within that unit before sampling (BESST, 2018).

Physical and chemical properties of groundwater can be determined by 1) taking sample at specific depths, or 2) measuring in-situ properties (temperature, electrical conductivity, pH, redox potential and oxygen saturation). See section 4.3.12 for the latter option details.

4.3.10 Borehole Magnetic Resonance (BMR)

Nuclear Magnetic Logging (NML) is a procedure where protons (hydrogen nuclei) are aligned with an impressed magnetic field that is turned off, and the radiation produced by the precession of their magnetic fields about the Earth's magnetic field is measured. The measured intensity of this precession at a specified time after the impressed field is turned off is logged as free-fluid index, which is related to hydrogen in fluids that are free to move. This method is also called a Nuclear Magnetic Resonance (NMR) log (Keys, 1989). NMR is often classified as a nuclear method, but it is a magnetic method that uses the same principle as the proton precession magnetometer with the exception that the precession of protons (hydrogen atoms) in water molecules is measured in the formation after an induced magnetic field has been turned off (ERG and CERL, 1993). The details of the theory of NMR are presented by Walsh et al. (2013) and Karjalainen (2020).

NMR is a quantitative geophysical method that can be used to make in situ assessments of porosity, water content, mobile and immobile water fraction, and estimates of permeability. As a downhole logging technology (Borehole Magnetic Resonance – BMR), NMR has been widely used in the oil and gas industry, however it is only recently that NMR tools have been designed for use in small-diameter boreholes that are typically used in groundwater studies (Walsh et al., 2013; USGS, 2019). In deep boreholes, hydrogeological parameters are typically determined by the analysis of packer tests on identified zones. Laboratory core analysis can also provide hydrogeological parameters, but on small, discrete samples. On the other hand, BMR can provide a continuous log of hydrogeological properties (EGS, 2019).

The NMR log, in a fluid-bearing geologic material, the initial $S(t)$ signal amplitude is directly proportional to the water content in the excited volume, while the T_2 decay time conveys information about the pore environment. The net observed T_2 relaxation time represents the contribution of three different relaxation mechanisms acting in parallel, each with a characteristic time. The resultant BMR log produces an output of T_2 , transverse relaxation time, which is the measurement of decay of magnetisation in the transverse plane. The total integrated amplitude of the T_2 distribution reflects the volume fraction of fluid (or porosity if the sample is saturated) (Walsh et al., 2013).

Permeability (k) or hydraulic conductivity (K) can be estimated from NMR measurements by applying calculation models. For example, the generalised Schlumberger-Doll Research (SDR) equation (Equation 1) (Walsh et al., 2013).

$$k = C_{SDR} \phi_{NMR}^a T_{2ml}^b \quad \text{Equation 1}$$

where,

ϕ_{NMR}^a is the NMR-derived porosity

T_{2ml} is the logarithmic mean of the T_2 distribution

C_{SDR} , a and b are empirically determined variables

Hydraulic conductivity can then be calculated using standard equations from the calculated permeability values. However, to improve the accuracy of permeability estimates, the value of a , b , and C are commonly refined on a site- or lithology-specific basis by calibration with direct flow measurements (Walsh et al., 2013). Karjalainen (2020) investigated BMR logs in a crystalline bedrock system and found that while BMR is suitable for long drillholes in crystalline bedrock to determine the T_2 distribution, total porosity and recognising water conducting zones; the derived permeability and water content data remains uncertain without precise calibration. Karjalainen (2020) reported challenges with calibration BMR permeability values with hydraulic

packer tests due to the averaging nature of packer tests, and recommended calibration with laboratory permeability values. Vouillamoz et al., (2005) also conducted BMR surveys in crystalline basement aquifers and reported that the transmissivity could be accurately estimated from BMR data after calibration with pumping test results, yet with a mean difference of $\pm 41\%$. Vouillamoz et al., (2005) noted that the main limiting factors of BMR applied specifically in hard-rock areas are the 1D approximation in a highly heterogeneous context, the screen effect that causes deep weathered-fissured reservoirs to be poorly resolved when topped by shallow alterites reservoirs, and the suppression principle that causes deep narrow fractures to be undetectable (Vouillamoz et al., 2005). MRS is site-dependent, and modelling results show that MRS performance depends on the magnitude of the natural geomagnetic field, the electrical conductivity of rocks, the electromagnetic noise and other factors (Legchenko et al., 2002). An example of a BMR log is shown in Figure 58, from an application in an unconsolidated aquifer conducted by Dlubac et al. (2013).

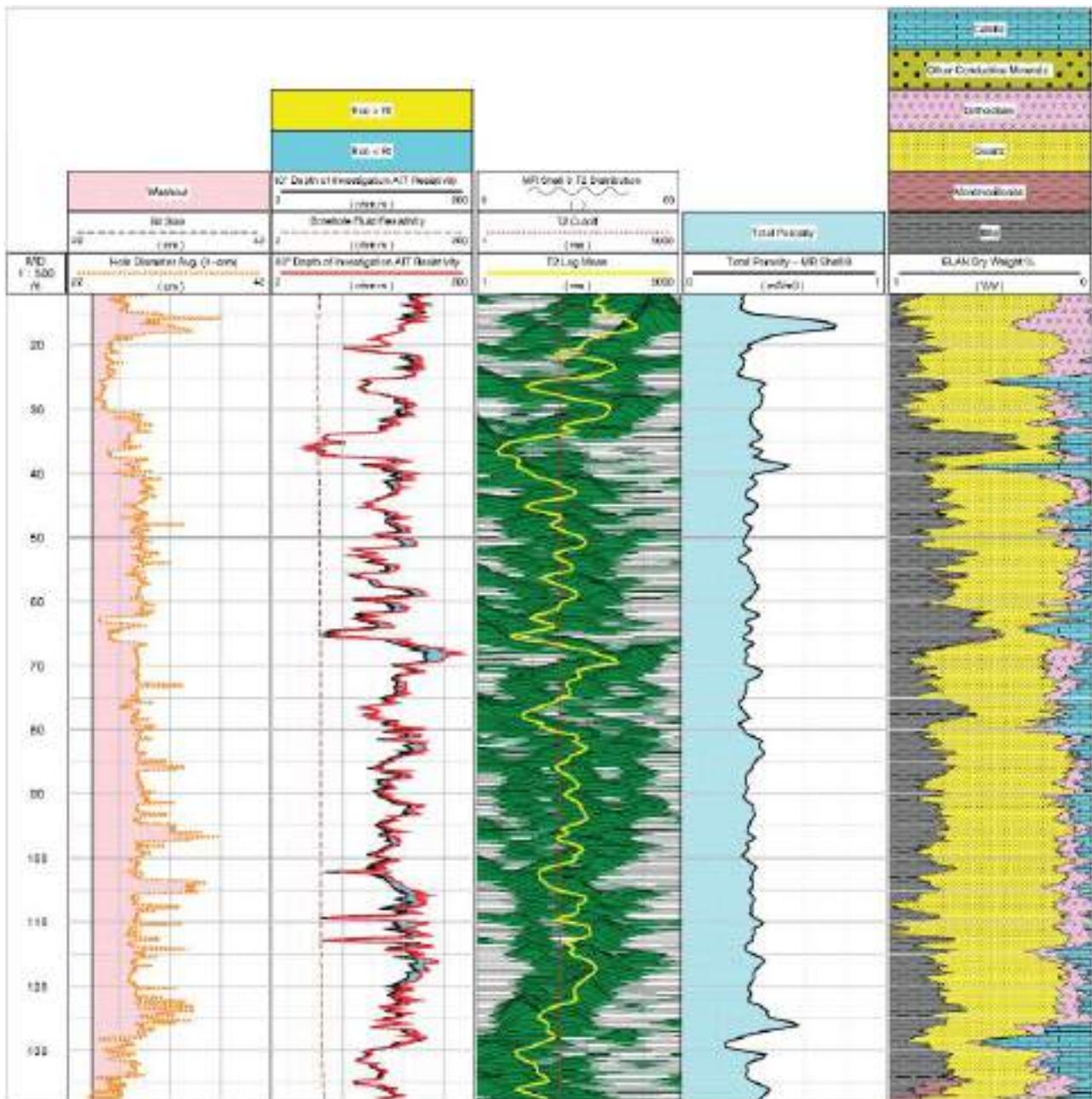


Figure 58 Track 1: Depth in meters; Track 2: Borehole geometry; Track 3: Resistivity; Track 4: NMR relaxation time distribution; Track 5: NMR determined porosity; Track 6: Mineralogy (Dlubac et al., 2013)

4.3.11 Flow meter

Borehole flowmeters, whether vertical or horizontal, can be used to identify water producing zones in an open bedrock well. Vertical flowmeter logging measures vertical movement of fluid in a borehole, while horizontal flowmeters have the additional benefit of being able to measure the direction of flow through the borehole. There are different types of flowmeters probes available to identify, measure and quantify the flow of groundwater in a borehole, namely the impeller flowmeter, heatpulse flowmeter, and electromagnetic flowmeter (Wilson et al., 2001; USGS, 2016; Cogswell, 2022).

Flowmeter data provides important insights into the local hydrogeology, including the source of groundwater flow in a borehole, zones where groundwater is being lost from a borehole, and measurement and quantification of vertical flow rates in a borehole. Groundwater-flow velocities and directions can be used to help develop and calibrate ground-water-flow models, supplement or replace natural and forced gradient tracer tests, assess intra-borehole flow, assess flow connections during cross-hole tests and, when combined with other geophysical logs, aid in the detailed interpretation of the hydrogeologic framework (Wilson et al., 2001; Cogswell, 2022).

USGS (2016) report that in fractured-rock investigations, it is important to conduct flowmeter logging under ambient and stressed conditions. Flowmeter logging conducted under pumping conditions can be used to identify transmissive fracture zones with similar ambient heads that would not be identified without stressing the aquifer. Example flowmeter logs are presented in Figure 59 and Figure 60. In Figure 59, no vertical flow under ambient conditions was recorded, but under pumping conditions indicated all inflow was produced from the upper zone and potential bedding plane (Wilson et al., 2001).

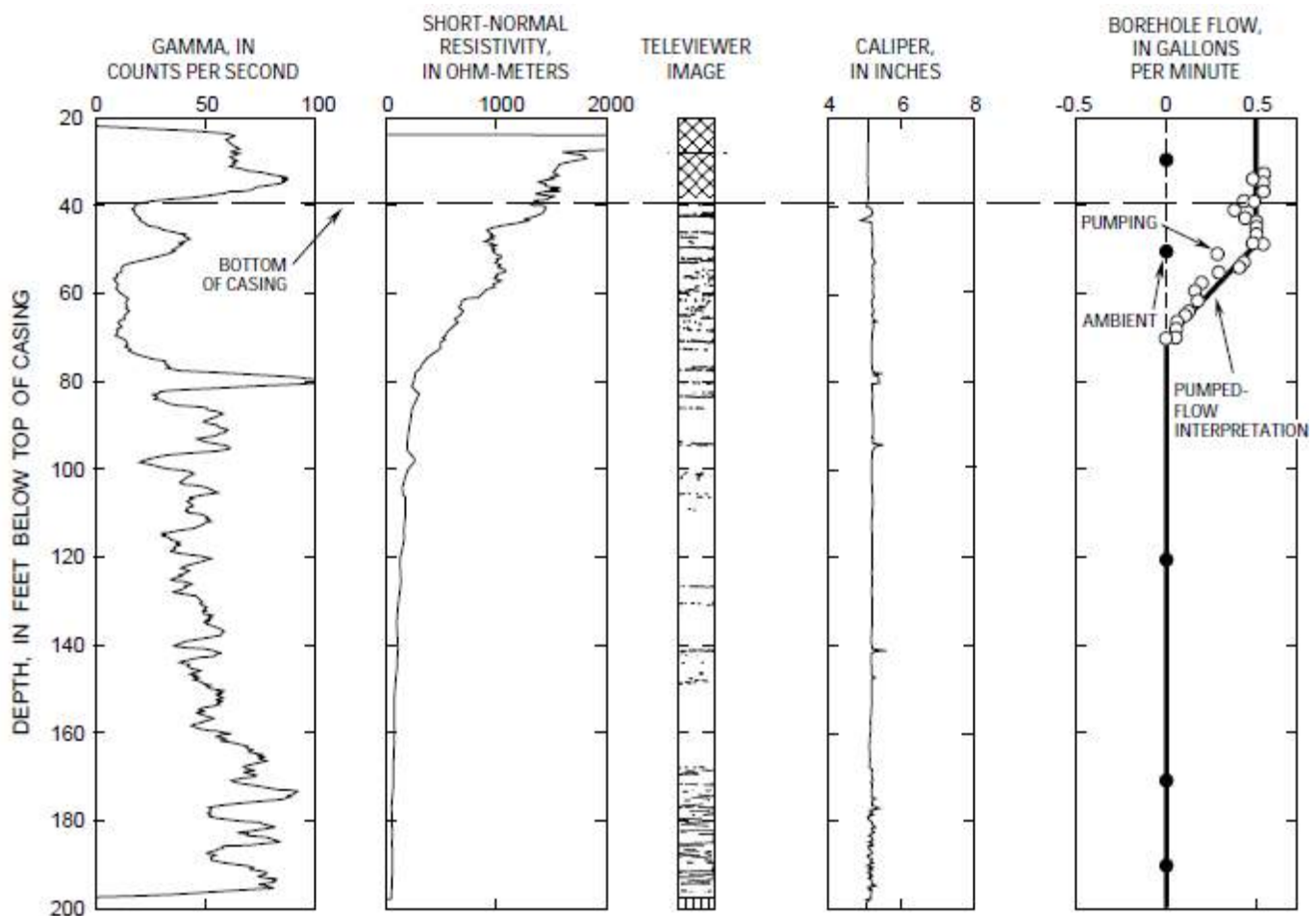


Figure 59 An example flowmeter log (Track 5 borehole flow) and background geophysical logs for well JPG-1, June 1999, Jefferson Proving Ground, Indiana (Wilson et al., 2001)

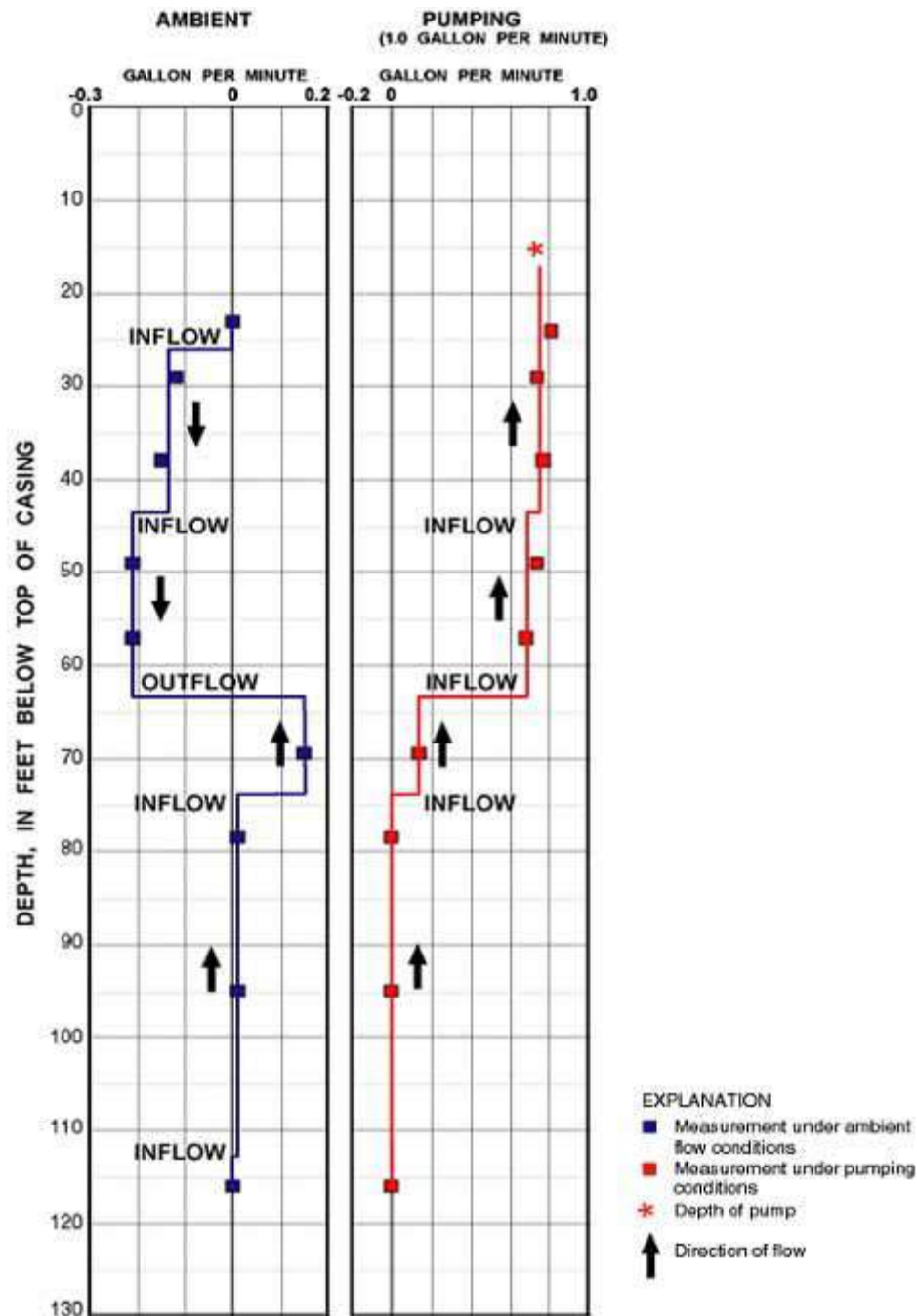


Figure 60 An example heat-pulse flowmeter log from a borehole in fractured-rock aquifer. Flow was measured under ambient (left) and pumping (right) conditions. Arrows indicate interpreted direction of flow, as fluid moves from zones of higher head to lower head (USGS, 2016).

Another example is presented in Figure 61 for an impeller flowmeter log in an exploratory borehole in the Middle East. The investigation was performed in response to the local alluvial gravel aquifer drying up. Impeller flowmeter logging indicated a rapid downhole flow of the water from the alluvial gravels to the underlying fractured limestone (Cogswell, 2022).

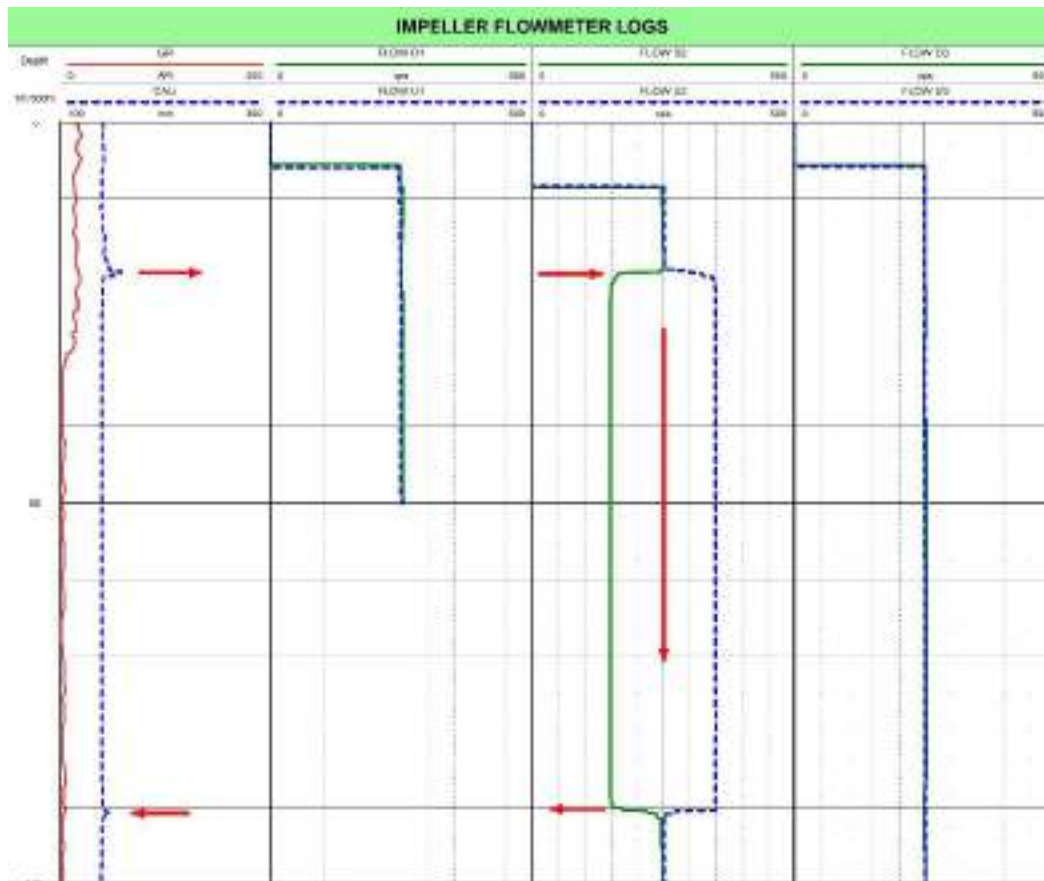


Figure 61 An impeller flowmeter log in an exploratory borehole conducted by Cogswell (2022) which indicates a rapid downhole flow of water from the alluvial gravels to the underlying fractured limestone (Cogswell, 2022)

4.3.12 Water quality

The physical and chemical properties of groundwater can be determined by 1) taking fluid samples at specific depths and sending for laboratory analysis, or 2) by measuring temperature, fluid conductivity, pH, pressure, redox potential, and degree of oxygen saturation using a multi-parameter probe. Multi-parameter hydrochemical borehole logging permits determination of the vertical evolution of the groundwater quality in the aquifer (Schürch and Vuataz, 2002; Wonik, 2007).

In a study conducted by Schürch and Vuataz (2002), a multi-parameter hydrochemical data transmitter was lowered into five shallow boreholes to measure simultaneously electrical conductivity, temperature, dissolved oxygen, redox potential, as well as pH and turbidity (Figure 62). Schürch and Vuataz (2002) found that the step in the multi-parameter logs generally coincided with lithologic boundaries and corresponded to flow zones where groundwater was moving into the borehole. The integration of geological information and multi-parameter hydrochemical logging can be helpful in identifying the heterogeneous nature of an aquifer, of the vertical distribution of its groundwater quality, and of its flow system (Schürch and Vuataz, 2002).

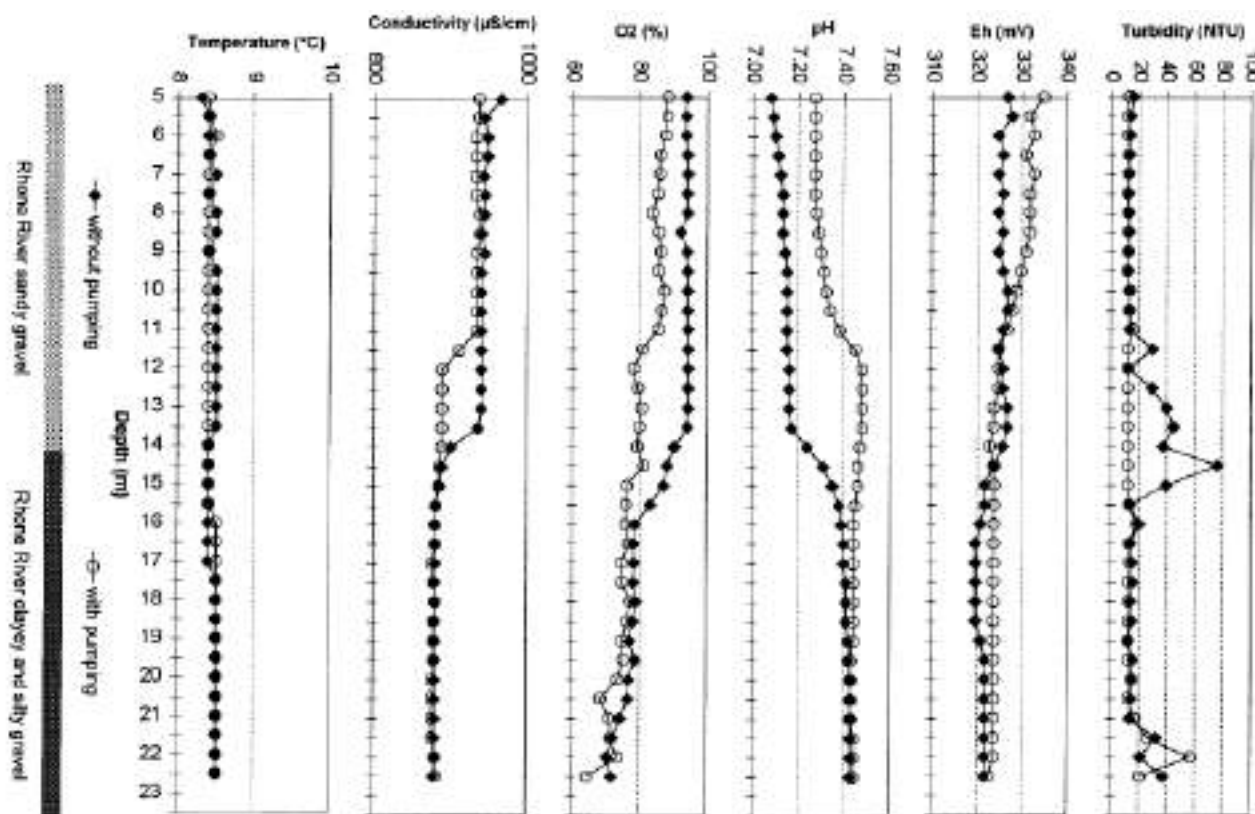


Figure 62 Multi-parameter logging in borehole P12 on July 15, 1997 under natural conditions (no pumping) and under pumping (Schürch and Vuataz, 2002)

4.3.13 Suites of geophysical surveys

Geophysical surveys are not typically performed as single logging exercises because many logs require others for interpretation, and multiple logs have synergistic relationships to provide correlating information. An example of a suite of logs for a hypothetical hole in crystalline rock is shown in Figure 63, where logs show the ability to locate fractured and altered material that may serve as preferential flow paths for groundwater (ERG and CERl, 1993). Wonik (2007) also stated that characteristic physical rock parameters, especially several in combination, can be used to determine or confirm the lithology of the rocks penetrated by the borehole. Furthermore, to maximise the benefit of a logging program, logs should be interpreted as a suite based on a thorough understanding of the principles as well as all the available background information for the area (Keys, 1989). Keys (1989) recommends that the suite of logs to be made must be based not only on study objectives, but also on knowledge of the synergistic nature of logs.

An example of how geophysical logs can be used to characterise fractures in crystalline rocks is shown in Figure 64, illustrating that the analysis is optimised when several geophysical measurements are made because the ambiguity in the interpretation is reduced. In terms of fracture characterisation, the example in Figure 64 also shows that the logs are mostly indicating effects that are indirectly related to fractures rather than giving a direct sample of the hydraulic properties of fractures. Yet, comparison of core fracture data with the logs demonstrates the effectiveness of this combination of data in the analysis. Core samples are used to identify the location of fractures, whereas logs are used to give a more representative sample of fracture properties over a volume extending away from the borehole. Geophysical logs also prove useful in identifying fractures in those intervals where core is not recovered (Paillet, 1994).

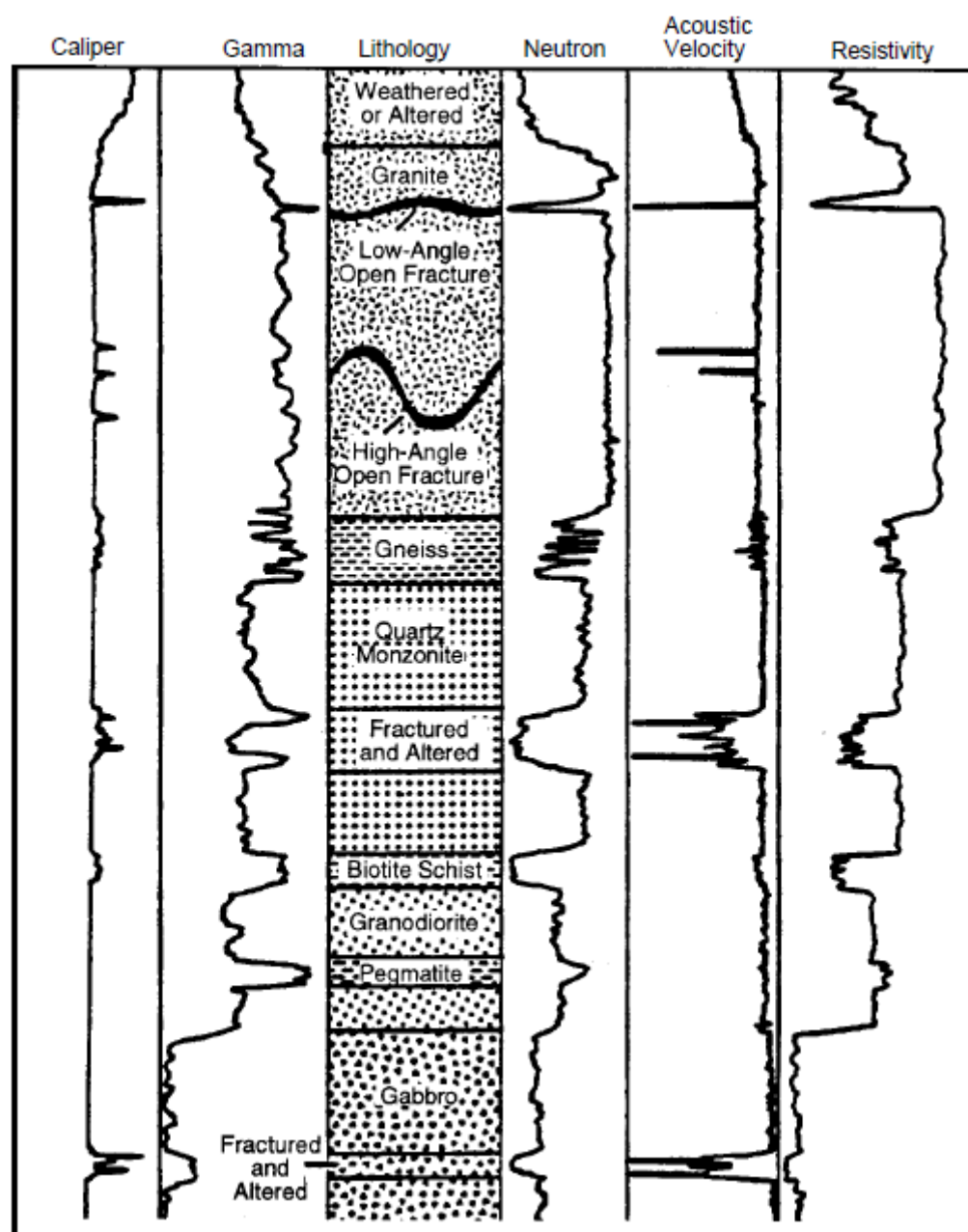


Figure 63 An example of a suite of hypothetical geophysical borehole log responses to various altered and fractured crystalline rocks (ERG and CERI, 1993)

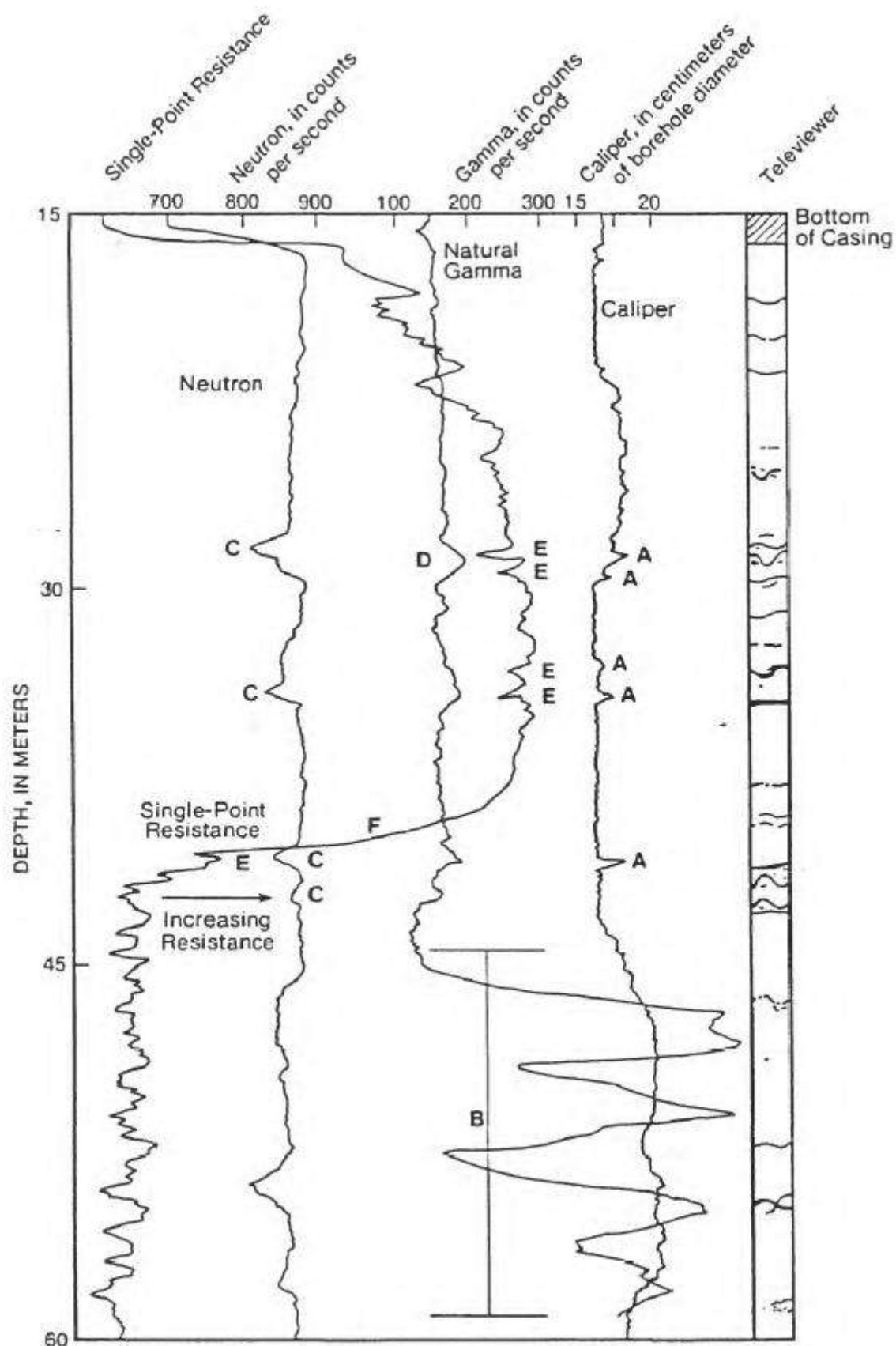


Figure 64 An example of traditional geophysical logs for a borehole in crystalline rocks (foliated granite schist (Paillet, 1994)

4.4 HYDRAULIC TESTING

Hydraulic testing aims to provide information on the spatial distribution of hydraulically conductive zones, including hydraulic transmissivities and hydraulic heads, to facilitate understanding of the hydrogeology of the deep subsurface. Additionally, temperature and water salinity or chemical characteristics of these zones complement the conceptual understanding of hydraulically conductive zones at depth, typically founded on fractures or faults (Doughty et al., 2017).

Direct data on these conductive fractures can be obtained through downhole tests in deep boreholes. For example, fluid production (pumping test) or injection tests can be conducted at selected depths in the borehole contained by two packers, and in these packer intervals fluid samples can be collected. The intervals over which to perform the tests require prior knowledge of potential hydraulically conductive zones. Borehole televiewer logging can identify fractures intercepted by the borehole but cannot differentiate between hydraulically conductive fractures. Doughty et al. (2017) report that hundreds of thousands of fractures inspected over several tens of boreholes (> 1 000 m), only 10% were characterised as open or partly open and furthermore only 2 – 3% had measurable transmissivity.

Alternatively, an effective method to specifically investigate hydraulic conductive fractures intercepted by a borehole is the Flowing Fluid Electrical Conductivity (FFEC) logging method (Tsang et al., 1990; Tsang and Doughty, 2003; Doughty and Tsang, 2005; Doughty et al., 2005; West and Odling, 2007; Doughty et al., 2013; Moir et al., 2014). FFEC are sensitive to fracture flow and efficient to deploy in the field. They classify as a flow-logging technique and also known under hydrophysical logging (Doughty et al., 2005).

4.4.1 Fluid production test (Packer pumping test)

Packer pumping tests use inflatable packers to seal the annular space between the packer pipe and the borehole wall, isolating an open interval to be evaluated, and are performed after the borehole is completed. Additional equipment includes a pump to inflate and/or deflate the packers, a sampling pump, flow meters, and pressure gauges. Because packers can be deflated, moved to other locations in the borehole, and re-inflated they can be used to conveniently determine the vertical distribution of hydraulic system parameters (Kuhlman et al., 2014).

Packer assemblies used in open boreholes and through wireline rods have different configurations, namely single packers test, double packer test, and double packer wireline assembly (Figure 65). Packer tests measure the rate of flow and/ or pressure build-up/decay in the test interval over a period of time. There are three common packer testing methods, namely 1) injection (Lugeon) tests, 2) discharge tests; and 3) shut-in recovery tests. For injection tests, water is injected at specific pressure levels and the resulting pressure is recorded when the flow has reached a quasi-steady state condition. For discharge tests, the isolated zone is pumped and water discharged from the borehole with the decay in formation pressure recorded after an equilibration period. Lastly, for the shut-in recovery tests, the tests are typically run in conjunction with a discharge test. The shut-in pressure build-up over time is monitored and recorded against the elapsed time since the discharge test, and the time since the recovery test was started (Kuhlman et al., 2014; Yihdego, 2017).

Quinn et al. (2012) classify four categories of hydraulic packer tests for fractured rock specifically, namely 1) constant-head step tests, 2) rising and falling head slug tests, 3) constant rate pumping tests carried out to near steady state, and 4) recovery tests. Each category with typical results, analysis advantages are presented in Figure 66 (Quinn et al. (2012)).

Royle (2002) presents standard operating procedures for borehole packer testing, in which the details of equipment, preparation and procedures are outlined.

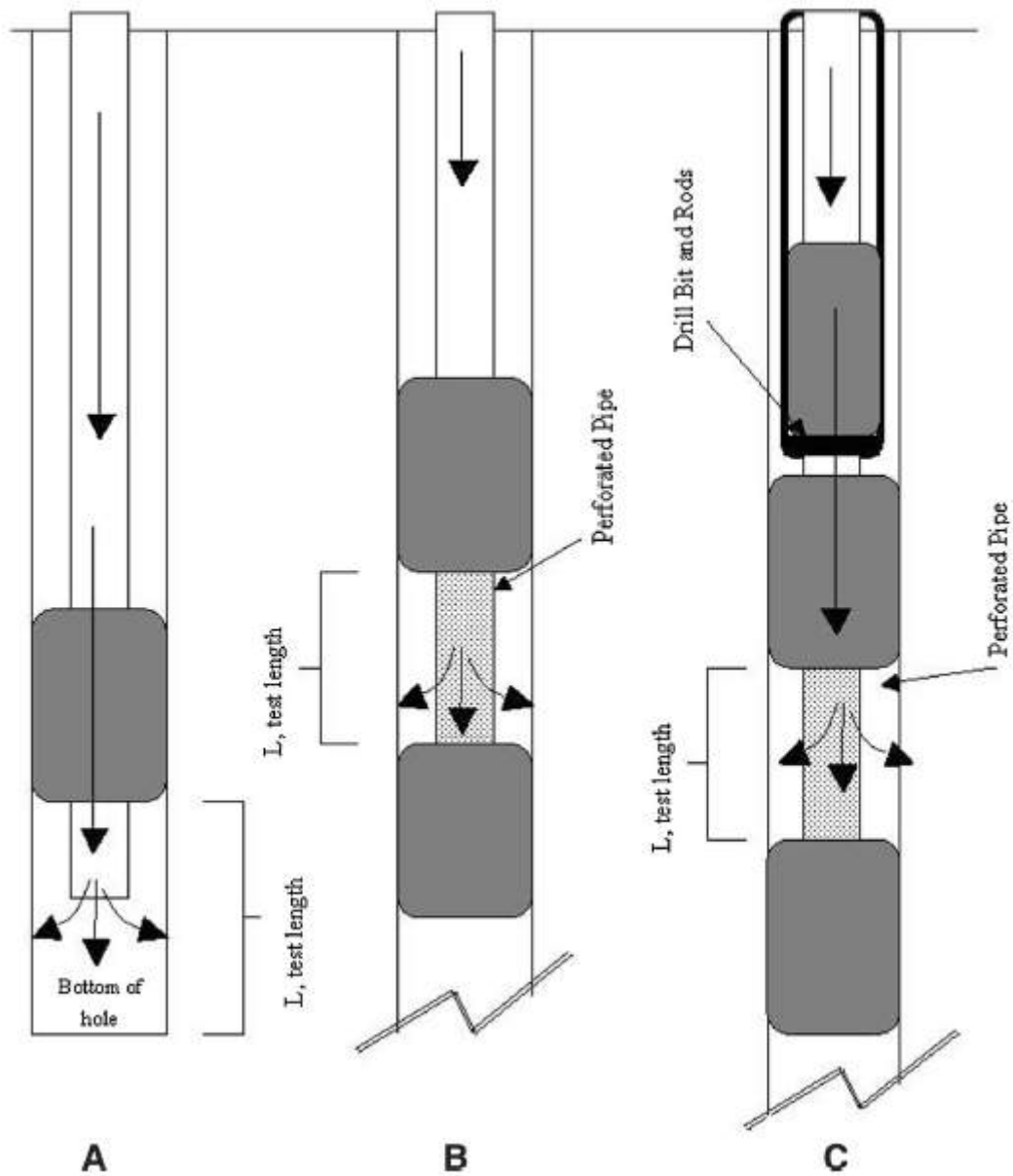


Figure 65 Illustration of packer test assemblies, a) single packer test-open borehole; b) double packer test- open borehole; c) double packer test wireline assembly (Royle, 2002; Yihdego, 2017)

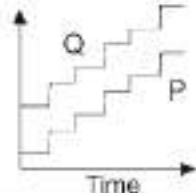
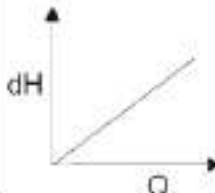

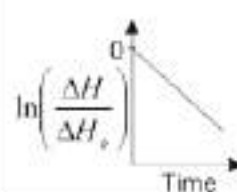
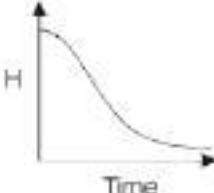
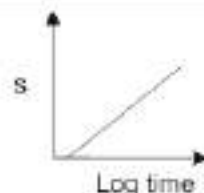


Test Type	Typical Test Results	Typical Analysis Method	Typical Analysis Graph	Head and Flow	Major Advantages	Unique Insights
Constant head step		Thiem $T = \frac{Q}{2\pi\Delta H} \ln\left(\frac{r_o}{r_w}\right)$		Head and flow are constant (for each step)	Validate Darcian flow	Identifies the onset of non-Darcian flow
Instantaneous slug		Hvorslev (Radial flow) $T = \frac{m(A_{ss})}{2\pi} \ln\left(\frac{r_o}{r_w}\right)$		Head and flow are variable	Rapid test	Identifies fracture deformation and well development effects
Constant rate pumping		Cooper-Jacob Straight Line Method $T = \frac{2.3Q}{4\pi\Delta s}$		Flow is constant but head is variable	Investigates large volumes	Identifies dual permeability effects
Recovery after constant rate pumping		Theis Recovery Method $T = \frac{2.3Q}{4\pi\Delta s'}$		Head and flow are variable	Investigates large volumes	Identifies dual permeability effects

Figure 66 Four categories of hydraulic tests commonly applied to packer tests in fractured rock (Quinn et al., 2012)

Bliss and Rushton (1984) investigated the suitability of the double packer testing technique when it is used to estimate how the hydraulic conductivity of an aquifer varies with depth, and it was shown that the typical models applied usually provided adequate estimates for zones of both high and low hydraulic conductivity. Other features that were considered, included the effect of the length of fissures, the presence of boundaries, the possibility of water flowing around the packers, the length and spacing of the packers and the influence of the free water surface (Bliss and Rushton, 1984).

Kuhlman et al. (2014) highlight that there are a number of considerations associated with packer inflation that require special attention when applied to the depths associated with a deep borehole. These relate to the method used to inflate the packer and the proper sizing of lines and pumps. The packer inflation pressure must be sufficient to expand the packer gland against the borehole wall and it must overcome hydrostatic pressure at depth. Therefore, the inflation pressure required will vary significantly over the 1.5 km of bedrock in the boreholes (Kuhlman et al., 2014).

The upper range of hydraulic conductivity that can be measured using packer systems will be limited by the hydraulics of the injection system (rate and pressure output limit of pump, supply line (friction losses), water availability, etc.). Therefore, it is important to determine before finalising equipment what the expected testing range of the zones of interest will be, before starting the testing program (Yihdego, 2017).

4.4.2 Flowing Fluid Electrical Conductivity (FFEC) logging

Flowing Fluid Electric Conductivity (FFEC) logging is a technique that uses contrasts in borehole and formation fluid salinities to identify permeable inflow zones in a borehole (Dobson et al., 2016). To perform the logging, the borehole is first flushed with a low salinity fluid, the hydraulic head is lowered by pumping to induce inward fluid flow from the formation along permeable fractures, and a conductivity log is run into the borehole to detect zones with increased conductivity (Figure 67). Runs conducted using different drawdowns and at different times can be used to determine not only where the permeable inflow zones are located, but also estimate inflow salinities and transmissivities using the relation in Equation 2.

$$A = q \cdot C \cdot \Delta t \quad \text{Equation 2}$$

where,

A is the area under the conductivity curve for a particular inflow zone,

q is the inflow rate for that zone,

C is the salinity of the inflow water (expressed as fluid electrical conductivity ($\mu\text{S}/\text{cm}$) or NaCl ionic concentration in g/ℓ), and

Δt is the elapsed time since the start of the inflow into the borehole.

In the resultant ΔFEC profile, the peaks are skewed in the direction of water flow at their locations in the borehole (Figure 67). The degree of skewness is dependent on the local flow rate along the borehole. A simple fitting code BORE-II has been developed to analyse such data to yield values of q and C of each flow zone intercepted by the borehole (Doughty and Tsang, 2000). Since, alternative analysis methods for FFEC logging data have been developed (Moir et al., 2014). From the inflow rates (q) and the pressure drawdown in the borehole due to the constant-rate pumping, transmissivity values of all inflow zones can be calculated, if assumed that they have the same initial pressure heads (Tsang et al., 2016).

The FFEC method does not require a specialised probe, only a typical EC/T probe, a pressure sensor, and a downhole pump, which are all normally available at a drill site for monitoring properties of the drilling fluid (Tsang et al., 2016).

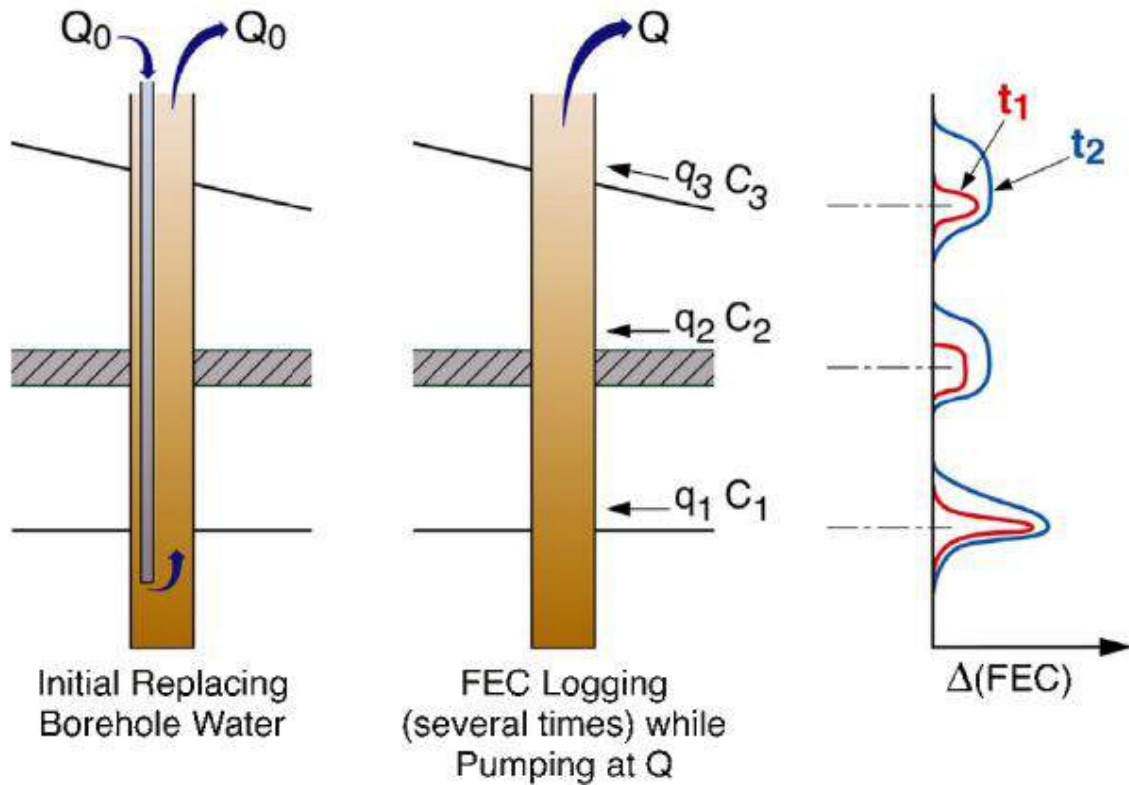


Figure 67 Illustration of the FFEC logging method. The borehole is first flushed with low-salinity fluid, water level of well is lowered to induce flow into borehole along permeable fractures, and conductivity log is run to identify regions with increased salinity corresponding to inflow zones. Q represents the pump flow rate, $\Delta(\text{FEC})$ is the change in electrical conductivity at time intervals t , q is the inflow rate, and C is the salinity of the formation water associated with each flow zone (Tsang et al., 2016).

The FFEC method can be extended, if the procedure is repeated using one (or two) higher or lower pumping rate at the top of the well, where analysis of the data would yield the initial hydraulic heads of the flow zones at the different depths, which could be different from each other (Tsang and Doughty, 2003). The occurrence of different initial or inherent pressure heads is to be expected for a fractured rock or a heterogeneous permeable medium, which under a pressure gradient, will present a heterogeneous pressure field. Thus, a borehole penetrating the medium will have pressure heads at different depths deviating from those of a normal hydrostatic pressure-depth relationship. These pressure heads add to our knowledge of the heterogeneity structure of the permeable medium (Tsang et al., 2016).

4.4.3 Combination of FFEC and packer pumping testing

It is clear that both packer pumping tests and FFEC logging have their own advantages and disadvantages. It is thus not a question of one or other, but how these two methods can be used to complement each other. Due to the cost and time of conducting packer pumping tests, it appears to be good practise to first conduct FFEC to identify which zones are most important for further analysis with specific packer pumping tests over those areas of the borehole, which in turn could be used to refine the FFEC data.

A similar synergetic relationship is described by Quinn et al. (2015) for the use of a FLUTE profiling with straddle packer testing. Quinn et al. (2015) highlights that it is most efficient to conduct straddle packer testing only in priority zones selected after the assessment prior collected borehole data. The T profile obtained from the FLUTE liner method is used in selecting high permeability zones for application of the

multiple-test method using straddle packers. The results from the packer tests then in turn refine the T estimation from the liner profile.

Doughty et al. (2017) recommends that FFEC logging be conducted during drilling whenever suitable breaks in the drilling schedule occur because the relative ease of these tests provides high value information to guide more expensive and time-consuming studies to be conducted after the drilling is completed, i.e. packer pumping tests. Doughty et al. (2017) also recommends conducting a post-drilling regular FFEC logging that includes the initial replacement of borehole water because it would improve the accuracy of hydrological data obtained from the deep borehole (Doughty et al., 2017)).

5 BVDP BOREHOLE DRILLING AND METHODOLOGY

5.1 INTRODUCTION

The methodology for the BVDP borehole drilling is presented which details the pre-drilling preparations necessary before commencing borehole drilling, including processes, protocols, and equipment requirements. This includes drilling operations, geology core processing, water and gas sampling, and microbiological sampling. Following sections outline the borehole design, specifying the drilling depths, casing installations, and logging phases. The final sections elaborate on the workflows for geological core processing, fluid sampling, online gas monitoring, and microbiological sampling, detailing the sampling procedures, equipment, and processing steps involved at various stages of the drilling process.

5.2 DRILL SITE

The borehole is located on the eastern limb of the Bushveld Igneous Complex (BIC) on the Impala Marula Mine. Figure 68 shows the position of the drill site with respect to the simplified geology on surface and neighbouring towns and roads. The borehole intersects the Critical Zone of the Rustenburg Layered Suite (RLS) on surface.

The Critical Zone is characterised by layers of cyclic chromitite, pyroxenite, norite and anorthosite and the unit has a lateral thickness of up to 1 500 m. The Lower Critical Zone contains LG1 – LG7 and MG1 – MG2 seams. The Upper Critical Zone contains the MG3 – MG5 chromitite layers, UG1 – UG3 seams and the Merensky Reef.

The underlying Lower Zone is comprised of pyroxenite, harzburgites and dunites. Three subzones are typically identified within the Lower Zone, namely an upper and lower bronzitite subzone (hard layers of orthopyroxenite) with a center harzburgites subzone (less resistant layers of olivine-rich rocks).

Geological logs from three boreholes near the drill site have been collated by Wilson (2015) for a stratigraphic column showing the Clapham section of the eastern limb of the BIC (Figure 70 and Figure 71). The boreholes are located in the Lower Zone of the RLS, and illustrate the expected lithologies to be intersected from the Lower Zone to the underlying Marginal Zone, Basal Ultramafic Sequence (BUS) and quartzite floor rocks of the Transvaal Supergroup.

The site is positioned on the surface lease area of Impala's Marula Mine within the fence boundary of the shaft area of the mine (Figure 69). Local communities are found to the north-east and south of the drill site, along with a Tailings Storage Facility (TSF) to the south-east.

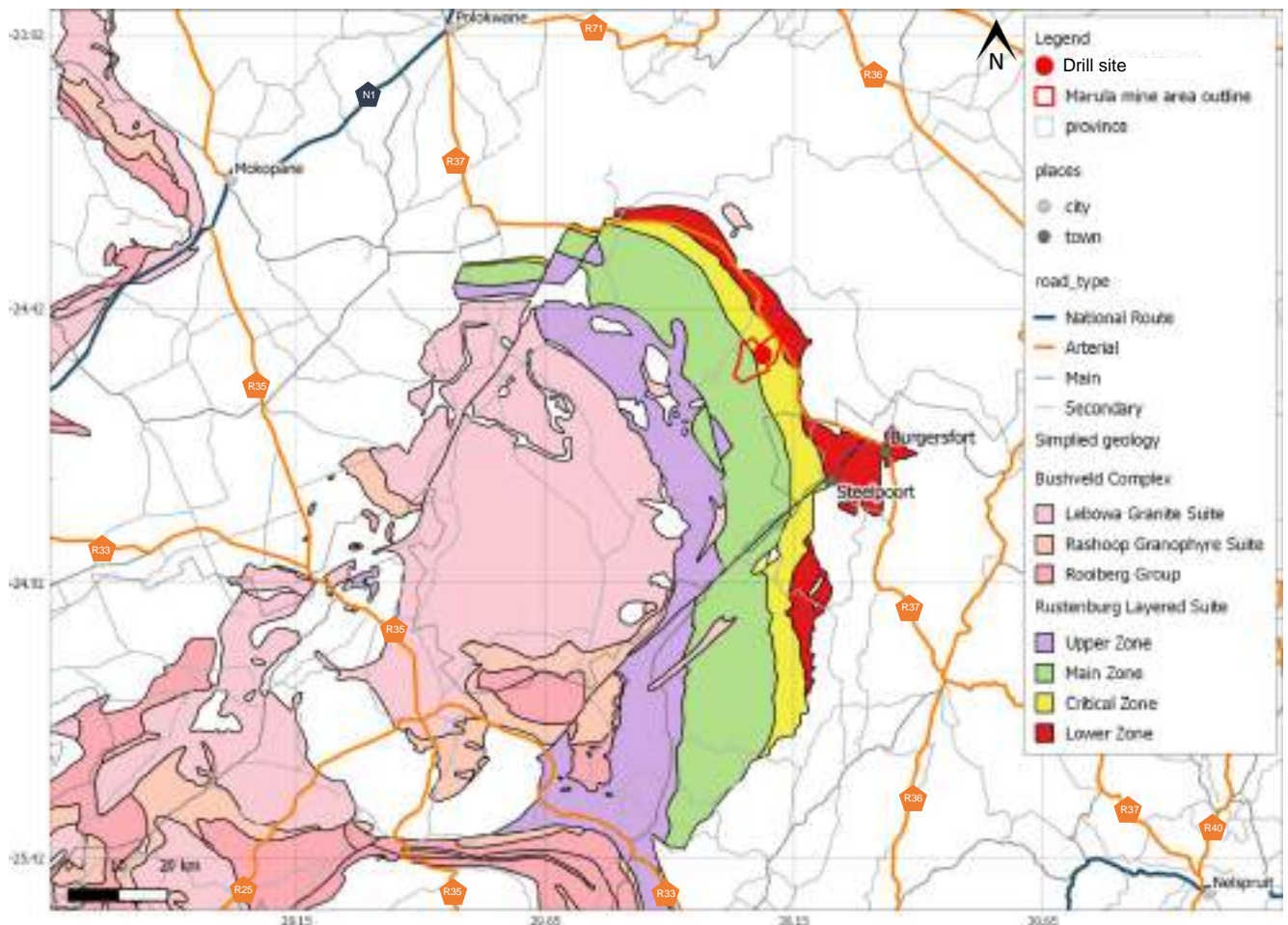


Figure 68 Location of the borehole on the Marula Mine lease area within the eastern limb of the Bushveld Igneous Complex (BIC)

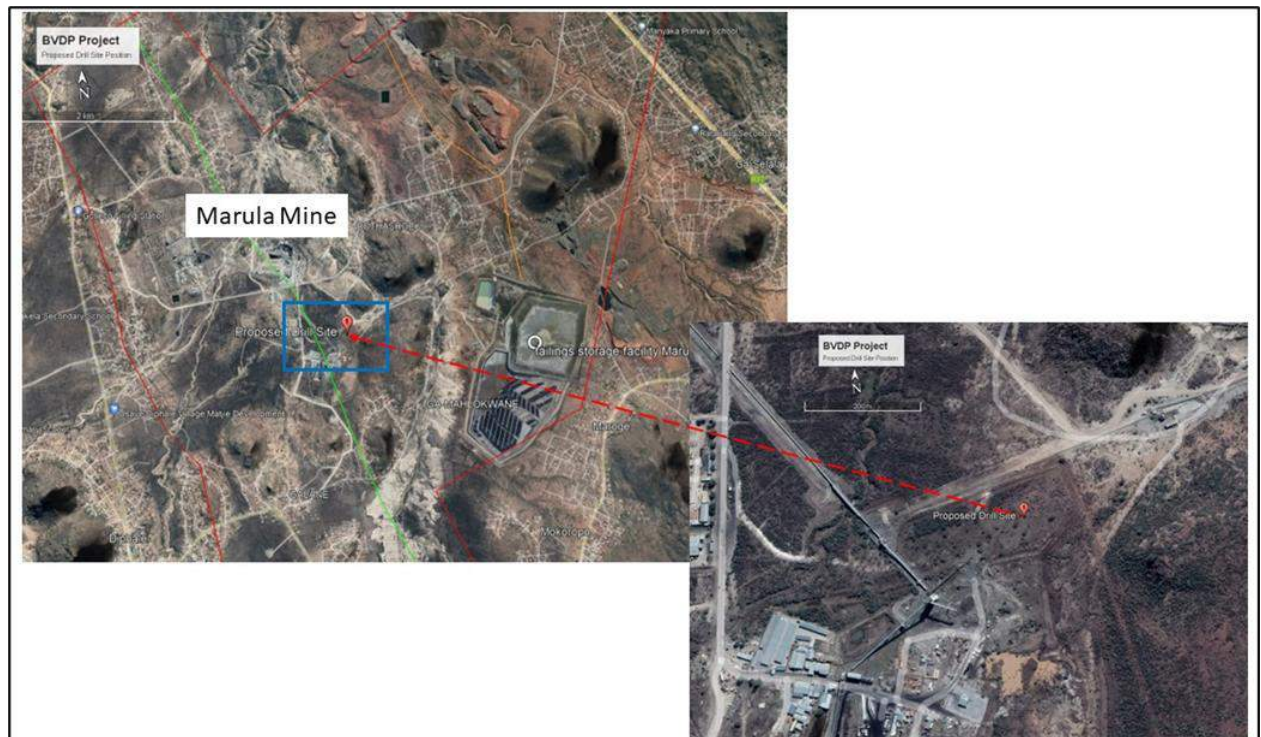
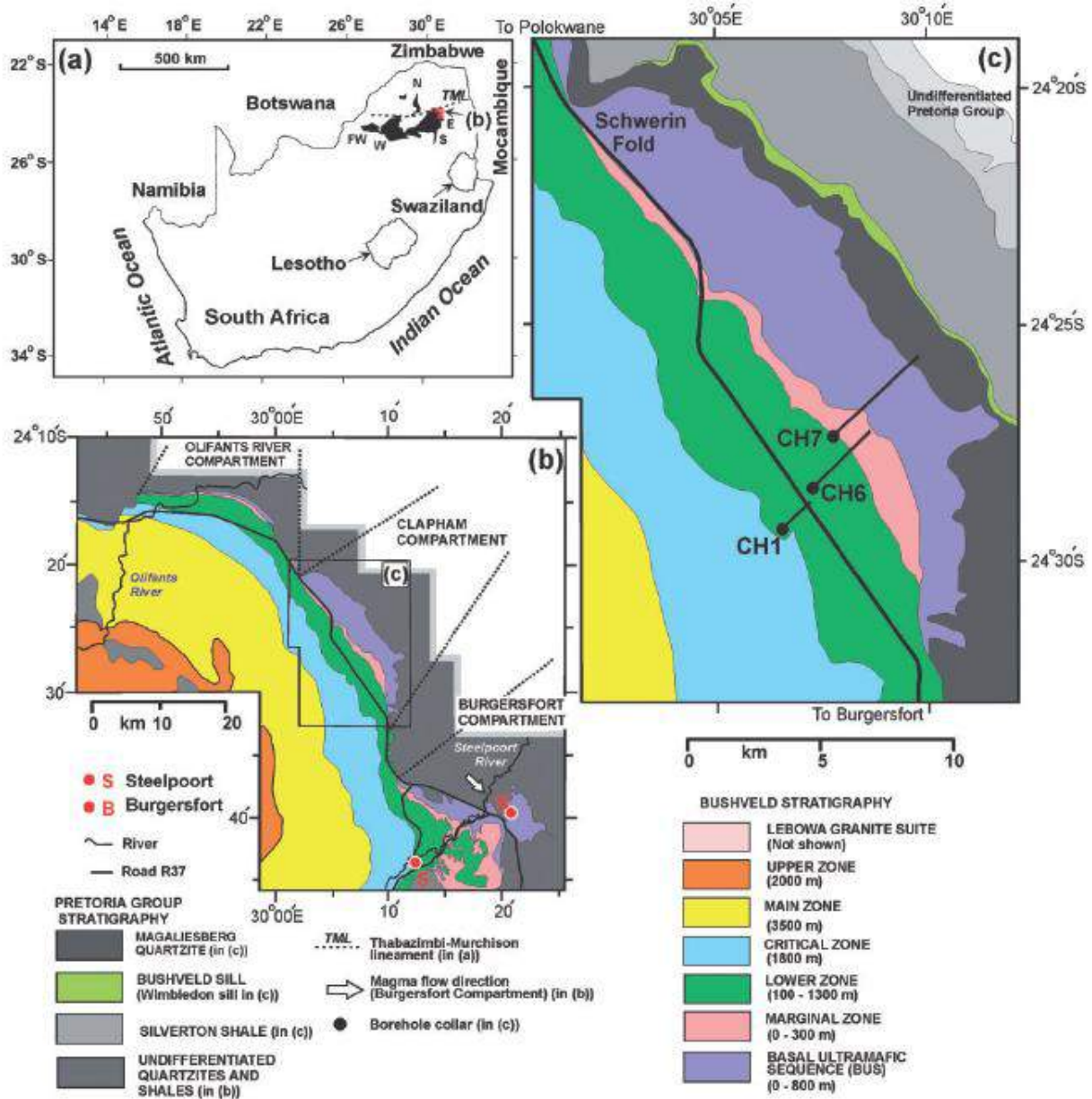


Figure 69 Borehole is located north-east from the Marula Mine operations area.



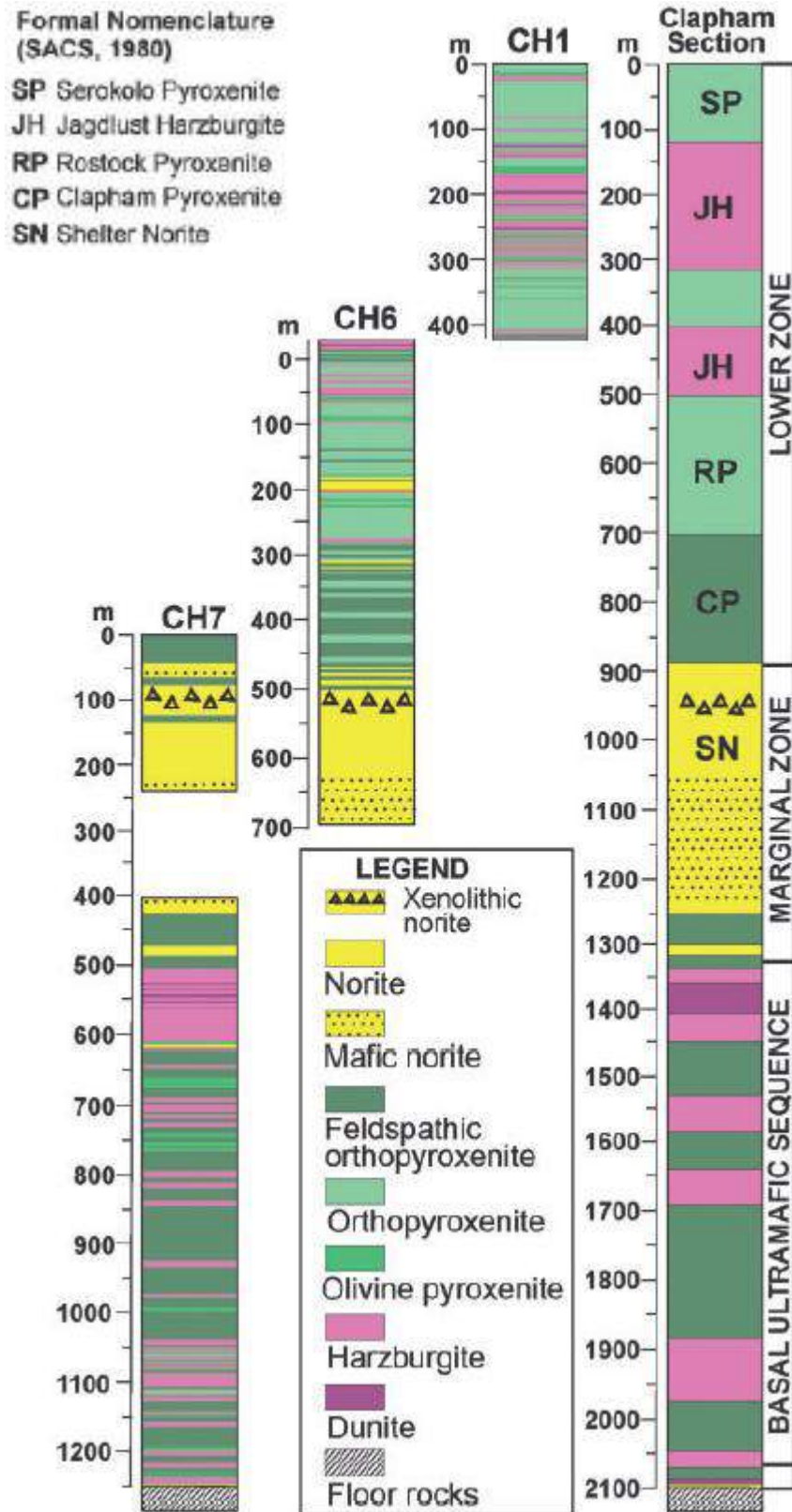


Figure 71 Stratigraphy of the Lower and Marginal Zones of the Bushveld Igneous Complex and BUS from the combined profiles derived from the drill cores CH1, CH6 and CH7 is called the Clapham section (Wilson, 2015).

5.3 PRE-DRILLING

Before drilling can commence, numerous processes and protocols need to be in place, as well as equipment and sampling supplies are required.

5.3.1 Drilling

The following outlines the pre-drilling processes and checks that are required:

- Crew onboarding
 - HR recruitment process
 - Internal training and refreshers
 - Mobilise crew to site
 - Compile safety file
 - Safety file approvals
 - Medicals (Labour crew)
 - Medicals (Supervisors)
 - Site Induction and Training (On Boarding)
- Rig Mobilisation
 - Rig preparation at workshop
 - Engineering Inspection of equipment at workshop
 - Mobilise Drill Rig to Client
 - Prepare drill pad and fencing
 - Site Set-up (includes office container, storage for samples, etc.)
 - Final Inspections and clearance of drill rigs

5.3.2 Geology – core processing

For the aspects of core-processing the following per-drilling processes are required:

1. Workflow outline – the process of how the core will be received, handled, analysed and stored
2. Core storage trays procured as per CGS standards as CGS Donkerhoek will be the core repository
3. Camera and camera stand to ensure high-quality images of the core be taken
4. Data capturing and processing methodology
5. Staff requirements and hiring of personal on-site to perform core logging
6. Transportation arrangements for core from drill site to on-site storage and final transport to CGS Donkerhoek.

5.3.3 Water sampling

The following components were considered in the planning for water sampling during drilling:

- Workflow outline/Sampling protocol – process of how and when samples will be collected
- Procurement of sampling bottles and equipment
- Storage of samples
- Transportation of samples

For research aspects on this borehole, a motivation to the hosting mine has been submitted to advocate for leaving the hole open for additional sampling and surveying of the deep section.

5.3.4 Gas analysis

For the aspects related to the online gas analysis, the following pre-drilling requirements were considered:

- Collaboration with researchers from ICDP and Eawag/University of Basel
- Planning and timeline alignment
- Importing of equipment and rental/usage agreements
 - Degasser unit from ICDP
 - Mini-Ruedi mass spectrometer from Eawag/University of Basel
- Facilitation of travel arrangements for personal for equipment training
- Ensuring on-site internet to allow for remote monitoring
- Facilitation of requirements to the drillers and drilling methodology

5.3.5 Microbiological sampling

The following components were considered in the pre-drilling planning for microbiological sampling:

- Collaboration with researchers from ICDP/GFZ, University of Tokyo and University of Free State
- Planning and timeline alignment
- Importing/purchasing of equipment and materials
 - Contamination tracer
 - Microscope and sampling materials
 - Rock-cutter
- Facilitation of travel arrangements for personal for equipment training
- Arranging on-site and off-site sampling protocols
- Advising on handling of core materials and processes for core repository requirements
- Facilitation of requirements to the drillers and drilling methodology

5.4 BOREHOLE DESIGN

The borehole has been designed as follows:

- Drilling of PQ sized core from 0 m to approximately 50 m,
- Install PW casing,
- Drilling of PQ sized core from 50 m to approximately 350 m,
- HW casing to be installed,
- Drilling from 350 m to approximately 800 m,
- NW casing to be installed,
- Drilling NQ from 800 m to EOH (maximum depth of 2 500 m).

For the first 350 m of the borehole, geophysical and hydrophysical logging will be conducted in Phase 1 before casing is installed. From 350 m to a depth of approximately 950 m, geophysical logging and hydraulic testing will be conducted in Phase 2 before casing is installed. Phase 3 entails drilling the borehole from 950 m to total depth of maximum of 2 500 m and conducting water sampling and packer testing. The borehole section from 950 m to depth will not be cased (Figure 72).



Figure 72 Borehole drilling and design, consisting of three phases, showing the Bushveld Complex lithologies and the underlying Transvaal Supergroup (*not to scale).

5.5 DRILLING AND SAMPLING WORKFLOW ON SITE

The drilling of core and the sampling that will occur on-site during the drilling phases is presented as the workflow. This includes the geological core, fluid sampling, online gas analysis and microbiological workflows. There are additional workflows for the testing/sampling periods between the drilling phases which will be presented in the following section.

5.5.1 Geological core workflow

Drill rig area:

The workflow at the drill rig itself (fenced-in drill rig site) with regards to core handling will be as follows:

- Remove fresh core run from core barrel, wash/wipe clean and place on angle-iron stand with top- and bottom plastic markers clearly labelled with core run number and driller's depths. Scientific Site Manager adds red and blue line on core (red is on the right when looking to the top of the core).
- Transfer core run to core trays using hammer breaks or natural pieces to fit the tray. Add markers for top, bottom of the core (labelled with core run number) and any gaps.
- Deliver core trays to the BVDP area, keeps a record of core trays delivered that is signed off by BVDP team. Expected daily output: 20 meters = 6-7 core trays.

Drill site research area:

The subsequent workflow at the drill site (fenced-in site for BVDP staff with office/lab containers) for core handling will be as follows:

- Check core-tray labelling and completeness, check back with drillers as needed.
- Add red and blue direction lines to the core.
- Inspect each core section (tray slot) for condition, measure section lengths, assure that markings and labels are visible, re-arrange broken pieces if necessary.
- Enter core run, section numbers, core recovery, core condition etc (see sheet), enter sections and section length, enter location of the section in core box (under Section Split and any notes into mDIS. Print labels.
- Make smartphone photographs of full core trays in dry and wet condition with colour chart, scale and core box label; upload photos to mDIS.
- Take microbiology sample as needed (every 100 m) - see microbiology workflow (Section 5.3.5).
- Close core trays with lid and carefully stack for transport to core shed.

Marula Mine core shed:

- Open core trays, transfer to the photography stand. Fill out core box number, date, operator (initials) on colour calibration card. Photograph twice, first dry, then wet.
- Log the core lithologically and enter the data into mDIS along with uploaded photos (edit if necessary)
- After photography and logging, re-lid the core trays and transfer to the storage area for transport to Donkerhoek.

Core Library in Donkerhoek:

- For each shipment from Marula, carefully unpack core-box pallets, check and confirm core box and core tray labels listed in the paper logs provided.
- Transfer core boxes to the logging station and conduct detailed lithologic logs with entry into mDIS (should be done by 2 people)
- Transfer logged core boxes to multispectral scanner and perform scanning. Transfer core boxes to the shelves provided.

5.5.2 Fluid sampling workflow

5.5.2.1 Information from drillers

Valuable groundwater information is accessible from the moment drilling begins. This information includes water intersections, drilling fluid circulation losses, basic water chemistry, and resting water levels. The drilling contractor and site geologist, supervised by project managers, can easily collect this data with minimal effort. It is crucial to optimize the information obtained from the drillhole.

During core drilling the driller monitors a minimum of three gauges on a drill rig: water pressure, feed pressure and torque pressure. It is important that the information on water strikes, circulation/water losses and water levels and must be collected and recorded correctly by the drillers.

Considerations (Morton, 2021):

1. When the water table is encountered the driller notices that water pressure will start to increase. Also, when lowering the overshot to lift the core tube there will be slack in the line, this is also the sign of a water table in front of the core bit. This should be noted and recorded by the drillers.
2. During drilling by any method, the depth of the first water strike should be recorded by the driller on daily drill logs and the drill sheets.
3. Core drilling does not enable the measurement of yield, however, if a permeable zone (possibly an aquifer or water bearing fracture) is intercepted the driller will note circulation losses and need to top up the corehole with water and drilling fluids. The more water and fluid used indicates the greater the permeability. This provides a guide for the possible groundwater characteristics and pumping yields at the corehole location.
4. During core drilling the level of drilling fluid in the core hole represents the hydraulic pressure being maintained by the driller to keep the hole open, the bit lubricated and optimise the efficiency of the drilling. If the drilling is stopped for any reason (e.g., a drillers' break weekend or at the end of the hole) the fluid level will equilibrate to the actual groundwater level. This is essential information and should be recorded with a hole depth and date.
5. As the drill hole deepens different aquifers, with different groundwater pressures may be encountered therefore the level of fluid in the corehole should be measured after any cessation of drilling over 24 hours.
6. It is possible that artesian conditions, where the fluid flows out of the core hole, may be encountered and these too should be noted on the drilling log with date and corehole depth.
7. During drilling the pH and the electrical conductivity of the water encountered may change indicating interception of different aquifers.

5.5.2.2 Monitoring and sampling circulating drill fluids

To supplement the drillers' record of water pressure, loses, strikes and levels, the circulating drill mud is going to be sampled. This is not common practice, but to optimise the groundwater collection process, it is included.

Drilling additives are required to maintain the borehole stability and ensure the borehole reaches the planned depth without failure. However, these added substances influence the groundwater and prevent representative fluid formation samples from being collected during drilling. Many standard water quality measurements are not able to be performed if the sample contains even trace amounts of the added drilling substances (typically organic in nature). For this reason, water sample are typically not collected during drilling, but only afterwards once the hole can be purged and cleaned, or expensive packer system put in place to flush the isolated zone and collect a representative sample. Yet, information is potentially being lost by not collecting samples during drilling. Thus, the rationale is to potentially use the drilling additives as a tracer itself by monitoring the circulating drill fluid itself during drilling or apply an additional method to remove drilling additives before analysis.

For monitoring the drilling fluid approach, the assumption is that the difference between the measured circulating fluid from the added drilling fluid and source water is from the groundwater intersected. Importantly, a record of when and how much drilling fluid is added to the source water will be important.

5.5.2.3 *Drilling fluid sampling protocol*

A set of fluid samples will be collected:

1. Source water
2. Additives
3. Circulating drilling fluid

The source water will be sampled initially and then again if the source is changed or of a temporal quality. The drilling additives will be constant in composition, thus only the concentrations and specific combinations will be recorded. The list of drilling additives for the drilling operations include:

1. AMC COREWELL
2. AMC EZZEE TROL
3. AMC FLOC DD
4. AMC LIQUI POL
5. AMC TORQUE GUARD

The circulating drilling fluid will then be monitored periodically to identify potential changes, and specifically when water losses or gains are noted by the drillers. How often the periodic samples of the circulating drill fluid will depend on the penetration rate and the rate at which changes can be measured. At the beginning, samples of the drilling fluid can be collected on the hour to assess changes, if changes are slow then daily samples could be taken. This also depends on how the samples will be analysed to determine a reasonable number of analyses.

Sampling procedure:

- Rinse container in collected fluid three times.
- Collect fluid in container (500 ml plastic bottle), fill to the top to ensure no head space. Close lid tightly. To be stored for analysis. Labelled and stored with appropriate record system.
- Collect an additional sample in a larger container for field measurements of pH, EC, temperature, redox, dissolved oxygen using infield probes. Record measurements, time/date, drilling depth and any other important aspects of drilling at that time.

5.5.3 **Online gas workflow**

Continuous mud gas logging during drilling is a standard technique in oil and gas exploration, where they are used to test reservoir rocks for hydrocarbons while drilling. Online gas monitoring extends this technique for scientific drilling in hydrocarbon and non-hydrocarbon formations to sample and study the composition of crustal gases (ICDP, 2024).

Online-gas monitoring is a three-step process that includes 1) gas release from the formation, 2) gas extraction at the surface and 3) real-time gas analysis.

- Gas release from the formation
Drilling mud gas that circulates in the borehole comprises air and gaseous components that are mechanically released as the drill bit, including components present in the pore space of the crushed rock and gas entering the borehole through permeable strata either as free gas or, more likely dissolved in liquids. Continuous inflow of fluids in the borehole along the entire borehole wall is hampered through the rapid formation of mud-cake that covers the borehole wall and acts as a seal (Figure 73) (ICDP, 2024).

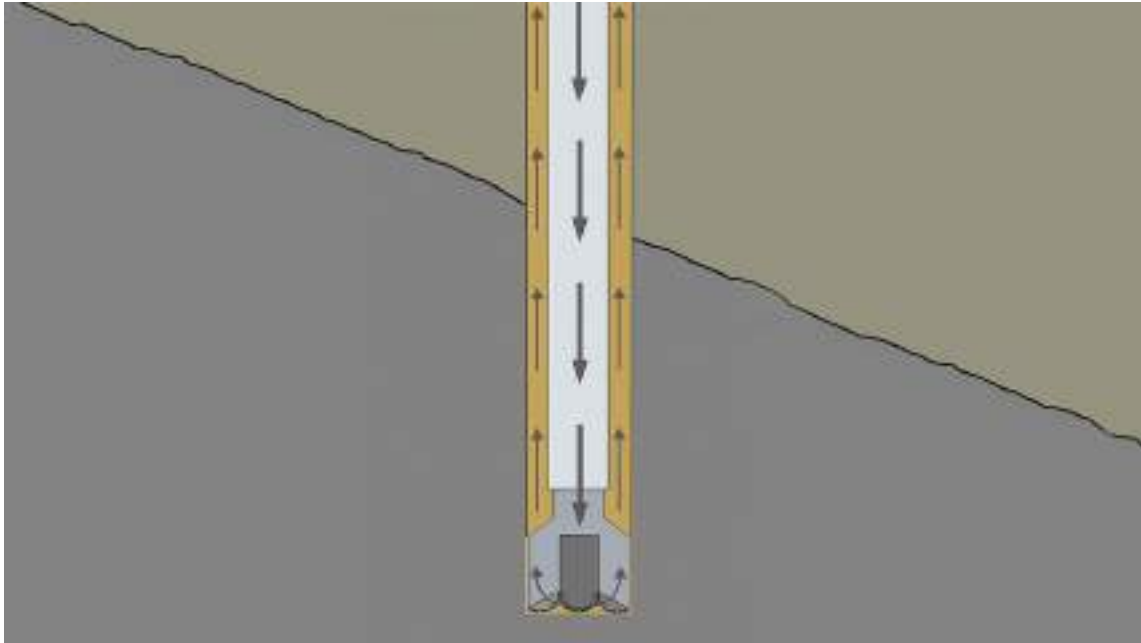


Figure 73 Illustration of the circulating drilling fluid around a drill that gas from the surrounding formations dissolve into (ICDP, 2024)

- **Gas extraction at the surface (degasser/separator)**
Back at the surface, a portion of the circulating mud is admitted to a mud gas separator and gas dissolved in the drilling mud is extracted mechanically under slight vacuum. The separator is composed of a steel cylinder with an explosion-proof electrical motor on top that drives a stirring impeller mounted inside the cylinder. The gas separator is installed as close as possible to the outlet of the mudflow line, either in the "Possum belly" above the shaker screens or in the mud ditch, to minimize air contamination and degassing of the drill mud before gas extraction (Figure 74). A small membrane pump is used to build up vacuum and to pump the extracted gas into a laboratory trailer, which should be installed not more than a few tens of meters away from the gas separator (ICDP, 2024).
- **Real-time gas analysis**
From the online gas analysis, the miniRUEDI equipment from Eawag is being utilised. The miniRUEDI is a portable mass spectrometer for quantification of He, Ne, Ar, Kr, N₂, O₂, CO₂, CH₄, H₂ and other gas species in gases and water. The miniRUEDI is designed for environmental research and allows maintenance-free on-site gas analysis during field work at remote locations (Brennwald, et al., 2016).

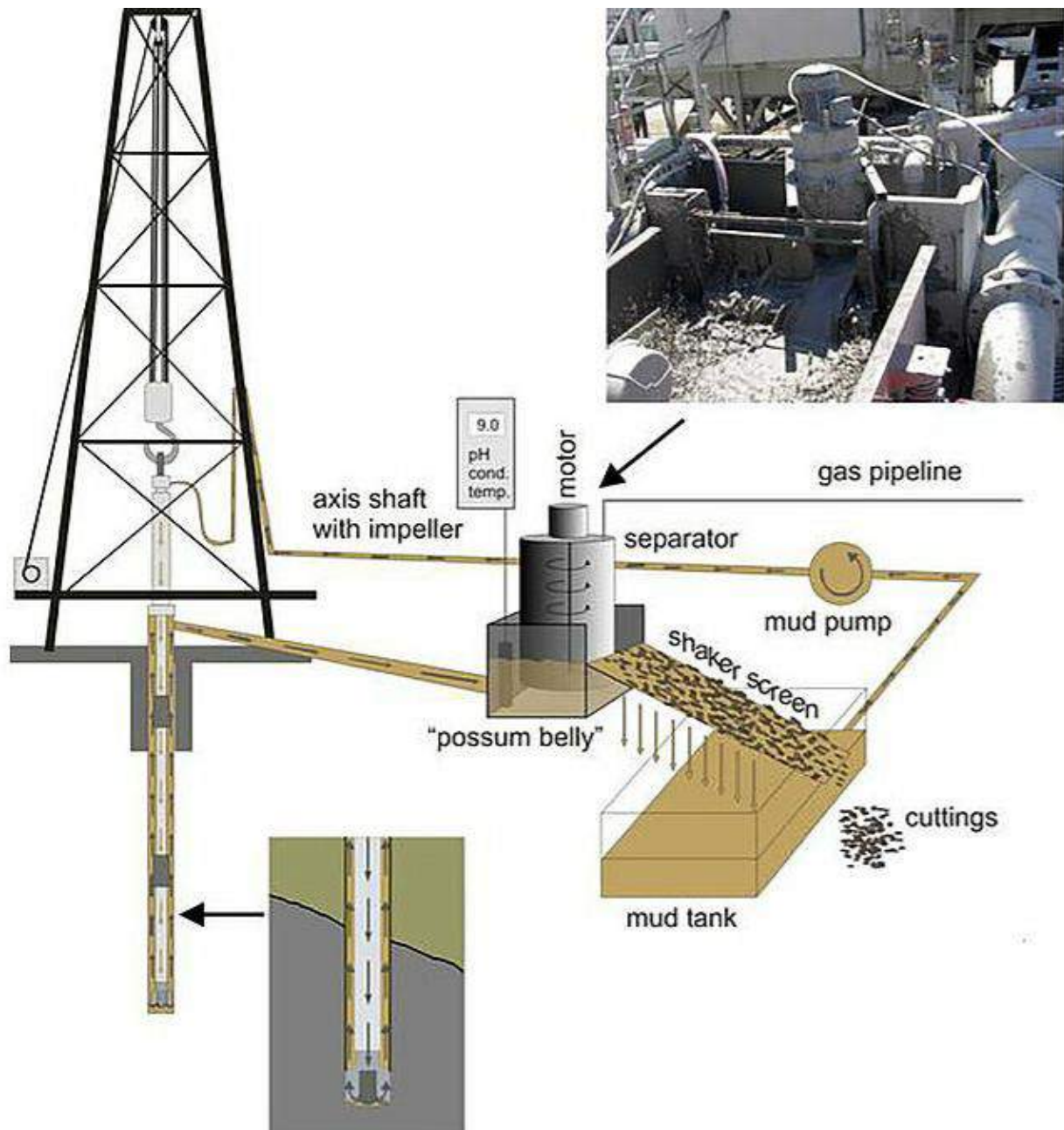


Figure 74 Illustration of the surface circulation system where the degassing unit is placed in the “Possum belly” (ICDP, 2024)

5.5.3.1 Degasser/separator

The gas dissolved in the drilling mud is extracted mechanically under slight vacuum using a custom-built water-gas separator. This is composed of a steel cylinder (30 cm diameter, variable height) with an explosion-proof electrical motor on top that drives a stirring impeller mounted inside the cylinder (Figure 75). The gas separator is installed as close as possible to the outlet of the mudflow line to minimise air contamination and degassing of the drill mud, e.g. at the mud pit above the shaker screens. A small membrane pump is used to build up vacuum and to pump the extracted gas via PTFE tubes (4 mm inner diameter) into a laboratory trailer/container, which should be installed not more than a few tens of meters away from the gas separator. Depending on the amount of dissolved mud gas, the gas flux is adjusted between 0.5 and 5 l/min, which in turn determines the pressure in the separator and the travel time to the trailer. Gas will be monitored and sampled at the outlet of the membrane pump, where the gas pressure is slightly higher than atmospheric pressure.

A. Gas-Water separator



B. Valve made of plastic tubes in steel box



C.



D.



Figure 75 Photos of the A) degasser/gas-water separator, B) photo of the degasser/gas-water-separator installed at the BVDP drill site within the circulating drilling mud system on surface, C) water safety valve installed on site, and D) closeup of gas line safety valve with water levels visible in the outer and inner tubes

5.5.3.2 miniRUEDI equipment

The miniRUEDI is a Portable and Autonomous Mass Spectrometric System for On-Site Environmental Gas Analysis. The equipment setup, gas inlet system, and data processing and calibration are discussed.

Equipment setup

The setup of the miniRUEDI system is illustrated in Figure 76. A parts list is given in Table 17. The computer-controlled valve (S) is used to select the gas inflow from different gas sources at approximately atmospheric pressure. The capillary (C) controls the gas flow from the gas inlet into the vacuum system. The continuous gas flow from the capillary into the quadrupole mass spectrometer (QMS) is balanced by the turbomolecular pump (TP), which produces a high vacuum in the QMS. The gas species in the QMS are ionized in the open, cylindrically symmetrical ion source by electron impact ionization. The resulting ion beam then passes a quadrupole mass filter set to a specific m/z ratio (m : ion mass number, z : ion charge number), and the ion beam strength at this m/z value is quantified using either a Faraday cup (F) or a secondary electron multiplier (M) detector (Brennwald, et al., 2016).

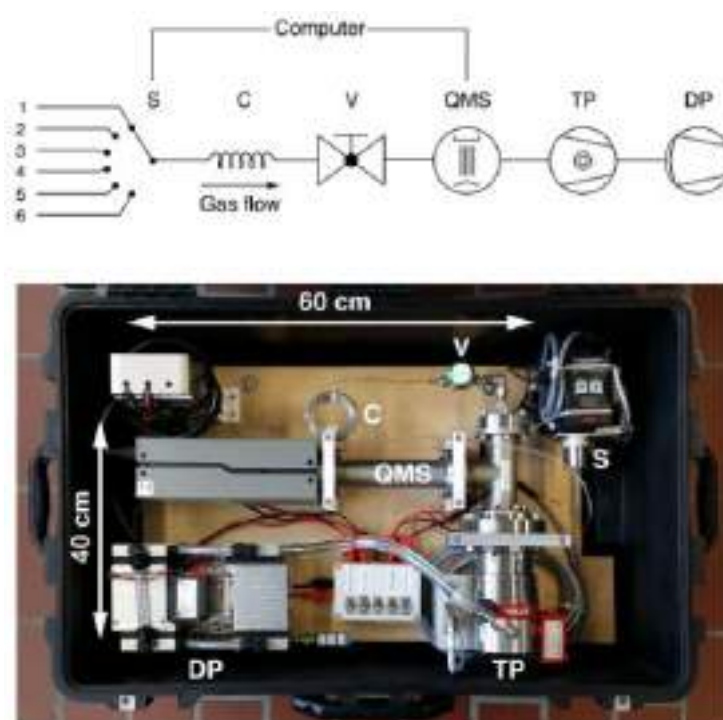


Figure 76 Schematic overview (top) and photo (bottom) of the miniRUEDI mass-spectrometer system (see also Table 17): 6-port inlet selector valve (S), capillary (C), inlet valve (V), quadrupole mass spectrometer (QMS), turbomolecular pump (TP), and diaphragm pump (DP). The inlet selector valve and the quadrupole mass spectrometer are controlled by a computer. The photo shows the miniRUEDI mounted in a wheeled hardshell suitcase for transport and protection (Brennwald, et al., 2016).

Table 17 Parts list for the miniRUEDI, depicted in Figure 76 (Brennwald, et al., 2016)

Part	Description
S	six-port inlet selector valve (VICI C5-2306EMHY)
C	10 m stainless steel tubing with 0.1 mm inner diameter (VICITSS104)
V	Inlet valve (Swagelok SS-4H)
QMS	Quadrupole mass spectrometer with Faraday cup and secondary electron multiplier detectors (Stanford Research Systems RGA-200)
TP	Turbomolecular pump with 70 L/s pumping speed (Pfeiffer HiPace 80)
DP	diaphragm pump for <20 mbar forevacuum (KNF N 813.4ANDC-B)
Power Supply	4 VDC power supply (max. 5A during turn on) for S, QMS, TP, and DP, for instance 2×12 V “car batteries” or mains voltage converter (e.g., Mean Well SP-240-24)

Gas Inlet System

The sample gas pressure is reduced from approximately atmospheric pressure to the high vacuum in the QMS using a 10 m long capillary with an inner diameter of 0.1 mm. The rugged 1/16" stainless-steel capillary tubing prevents the leakage of He and other mobile gases through the tubing walls. We empirically determined the gas flow through this capillary to 0.06 cmSTP3/min. This gas flow results in a total gas pressure of approximately 2×10^{-8} bar in the MS vacuum chamber, which yields maximum overall sensitivity of the MS while not exceeding the linear operation range of the MS. The observed travel time of the gas from the capillary inlet to the QMS is approximately 80 s. An instantaneous step-like concentration change at the capillary inlet is smeared out over approximately 10 s (50% rise time) once it reaches the QMS, resulting in an analytical time resolution of $\lesssim 1$ min (Brennwald, et al., 2016).

Compared to MS systems with a typical two-stage pressure reduction using a capillary followed by a pinhole/bypass system, the miniRUEDI gas consumption is lower by several orders of magnitude. The system is therefore most suitable for applications where low gas consumption is beneficial, such as the GE-MIMS technique. With a typical total gas concentration in air-saturated water of approximately 25 cmSTP3/L, a waterflow rate of ≥ 0.1 L/min through the membrane contactor would provide more than 100 times the gas amount consumed by the miniRUEDI. This illustrates how the miniRUEDI allows unbiased GE-MIMS analysis at low waterflow rates. Furthermore, pinhole/bypass stages or similar flow bifurcations may introduce uncontrollable fractionation of gas species in vacuum systems. Such artifacts are avoided in the miniRUEDI by the absence of a secondary pressure reduction stage (Brennwald, et al., 2016).

Data Processing and Calibration

The peak heights in the m/z spectrum are recorded in a user-defined sequence of the relevant m/z values using the F and M detectors, and repeated readings are averaged over a time interval suitable for a given application. The means ($s_{m/z}$) of the peak heights recorded during each interval at each m/z ratio are used as the raw measurement results of each measurement step. The $s_{m/z}$ values obtained from sample or standard-gas analyses are corrected for the instrument blank by subtracting the $s_{m/z}$ values obtained with the inlet valve V closed. The blank-corrected $s_{m/z}$ values are calibrated in terms of the partial pressures of the different gas species in the sampled gas by peak height comparison relative to a reference gas with well-known partial pressures of the species of interest. The mixing ratios of the different gas species in the gas are unaffected by the gas passage through the capillary because the viscous flow regime prevailing throughout most of the capillary prevents fractionation of the gas species. For a given total gas pressure at the capillary inlet, the peak height at a given m/z value is therefore linearly related to the partial pressure of the respective gas species in the sampled gas. Note, however, that the capillary gas flow approaches the molecular flow regime at the outlet to the QMS vacuum. The rate of the total gas flow through capillary is therefore not a perfectly linear function of the total gas pressure at the capillary inlet. We found this nonlinearity to be negligible for the quantification of the partial pressures (bias $< 1\%$) if the pressure difference between the sample gas and the reference gas at the capillary inlet is $\lesssim 50$ mbar. For larger pressure differences, accurate partial pressures are obtained by normalizing their sum to correspond to the true sample gas pressure at the capillary inlet (Brennwald, et al., 2016).

In many environmental applications, ambient air can be used as a well-defined and convenient gas standard for noble gases, N₂ and O₂. A dedicated standard-gas mixture is only required for species with unknown or variable atmospheric partial pressures, or if the sampled partial pressures are vastly different from those in air, for example in systems with high abundances of CO₂, CH₄ or (non-atmospheric) He (Brennwald, et al., 2016).

To account for drifts in the instrument sensitivity resulting from changes in the flow resistance of the gas inlet or the sensitivity of the mass spectrometer, the standard gas is analysed periodically in between sample gas analyses. The $s_{m/z}$ values obtained in each sample-gas analysis step are then calibrated using the $s_{m/z}$ values of the standard-gas analysis steps interpolated to the analysis time of the sample gas step. Finally, the standard error of the sample gas analyses is estimated from the standard deviation of replicate analysis results obtained from standard gases (Brennwald, et al., 2016).

5.5.4 Microbiological workflow

The microbiology sampling will have an on-site and off-site processing, where samples collected at the drill site will be transported to an off-site processing facility for final sampling procedures. This is mainly for safety concerns at the drill site as the secondary processing will require cutting of the core. The workflow processes for each will be outlined with an indication of the risks at each phase.

Our sampling strategy is two-pronged, aiming for both (1) a general overview of the distribution and changes in microbial community composition throughout the cored depth range and (2) more detailed analyses around specific intervals, e.g. Chromitite layers or fractures. To do so we envision two types of samples:

- “Standard” samples with a resolution of one sample every 100 m. This depth resolution is somewhat flexible, and sampling points can easily be moved several meters, depending on advice from the geology team. We envision a total number of 20 to 25 samples, a much lower resolution would severely hamper our chances to interpret any depth trends. A higher resolution will not be necessary as it would eventually lead to an overload in our labs, given the very time-consuming analyses.
- “Special” samples around specific intervals will have to be determined on the spot, i.e. when Chromitite layers or fractures are hit. The total number of samples taken, and their position needs to be discussed on site.

The optimal sample size would be a 10 cm whole round core for each sample, resulting in a 60 cm core section to be removed. The best possible option are whole round cores (WRC), but we are aware that this is not always an option. Splitting the core into half cores exposes the cores too much to oxygen (air), also the cutting requires water, thereby contaminating the very centre of the core, which is the most uncontaminated part. For PQ cores, a half core is sufficient for microbiology. For HQ cores, a sliver of about $\frac{1}{4}$ of the diameter could be cut off but still leaving enough material for microbiology. For NQ cores, there is too little material to cut off any slivers.

5.5.4.1 Sampling procedure

Microbiology work is currently limited to the cores. Thus, the on-site data collection is surrounded by the timely collection of core samples and their storage and on-site analysis. On-site the sampling has 3 components, 1) Core sample selection; 2) tracer added to drilling fluid; 3) collection of core and drilling fluid samples; 4) processing of the core; 5) processing of cores for storage and transport; and 6) contaminate evaluation based on tracer.

- Core sample selection

The selection of sampling spots will be guided by the on-site geologists to ensure the microbiological core samples taken do not impinge on the research aims of the BVDP.

- Tracer added to drilling fluid

The tracer procedure at the drill site is outlined in Figure 77. Tracer is added to the drilling fluid before microbiological sample is collected.

- Collection of core and drilling fluid samples

Once a sampling spot is identified, the whole core segment of the appropriate length will be cut off from the core or a piece that is naturally broken off will be removed, i.e. two 30 – 50 cm core sections. A spacer will be inserted into the core to mark the interval. See illustrated process in Figure 78, where each of the two sections are processed and stored differently. Concurrently, samples of the drilling fluids will be collected.

It is of utmost importance that the microbiological samples are taken as fast as possible after the core reaches the surface. Storing the cores in air for many hours or even days in a repository renders them completely unsuitable for microbiological analyses.

- Core processing

- One 30 – 50 cm core section will be immediately placed in a N₂-purgated bag and stored at -20°C in a freezer.
- The other 30 – 50 cm core section will be used to retrieve a surface fragment (2 – 3g) of the core sample is removed with a sterile chisel for contamination evaluation (Friese et al., 2017). See procedures below for use in contamination evaluation.
- The core will then quickly be cleaned by wiping down excess drill mud, followed by careful rinsing with sterile-filtered (0.2 µm pore size) water.
- Then the outside of the core will be flamed with a hand-held torch to kill off any microorganisms that were potentially introduced via the drill mud. The fluorescent tracer that is used to monitor infiltration.
- After cleaning and torching, the core will be placed in a N₂-purgated bag for temporal storage in a fridge at 4°C. Alternatively, stored in a vacuum-sealed sterilized plastic bag with an oxygen remover.

- Processing of cores for storage and transport

The core samples stored at the specific temperature will be transported under the same conditions or as close as possible for the physical transportation. Core samples requiring cutting will be transported to the secondary storage facility at the University of Limpopo., while core samples that do not require cutting (i.e. NQ size cores) can be transported and shipped from the site directly.

6) Drilling fluid samples and contamination evaluation

1. Add an adequate amount of fluorescent tracer reagent to a drilling fluid tank and stir vigorously. After stirring, 10 ml and 40 ml of the drilling fluid are collected in a 15 ml tube and three 50 ml tubes and stored at 4°C and -20°C, respectively.
2. Samples for contamination control will be taken alongside and analysed on site via fluorescence microscopy. A microscope will be housed in the office container for this analysis on-site.
3. Core surface fragment is washed for 5 min in sterile MilliQ water (1 ml water g⁻¹ rock) using a vortex. The liquid was filtered on a polycarbonate membrane filter and bead concentration on the core's surface was estimated by counting 30 random fields of view using fluorescent microscopy. Flame sterilization of the core surface was repeated until at least 99.9 % of the microspheres in the drilling liquid had been quenched (quenching of the microsphere fluorescence occurs upon heating above 100 °C).
4. The fluorescent tracer that is used to monitor infiltration of drill mud into the core will lose its fluorescence upon heating to >100°C. The fluorescence signal after the heat sterilization is analysed as an indicator for heat sterilization. For this, the large split aliquots after the heat sterilization are aseptically rinsed with sterile-filtered (0.2 µm pore size) water. The water is collected in a 15 ml tube from the bag and stored at +4°C.

Before drilling



Water tank from a local source



@ 10^8 to 10^9 beads ml^{-1}

Mix tank for drill mud & Tracer



Tracer container
AFN-09, Radiant
Color NV, 0.25 – 0.45
 μm in diameter



- From a tracer container, add the tracer stock sol. by a bucket or by a pump.
- After mixing, drilling fluid is stored in 1X15 ml and 3X50 ml tubes.
- 1X15 ml is stored at 4°C.
- 3X50 ml tubes are stored at -20°C ('maximum vol. = ~40ml).
- **Wear gloves!!**
- **Tracer is light-sensitive!!**



After core recovery (pictures from IODP)



- From an inner tube after core recovery, drilling fluid is collected in 1X15 ml and 3X50 ml tubes.
- 1X15 ml tube is stored at 4°C.
- 3X50 ml tubes are stored at -20°C ('maximum vol. = ~40ml).
- **Wear gloves!!**
- **Tracer is light-sensitive!!**

Figure 77 Tracer procedures at the drill site, depicting the addition of the tracer to the drill mud and periodic sampling of the drill fluid. For safety, it is recommended to wear gloves during this sampling.

After sample registration in the mDIS (Drilling Information System)

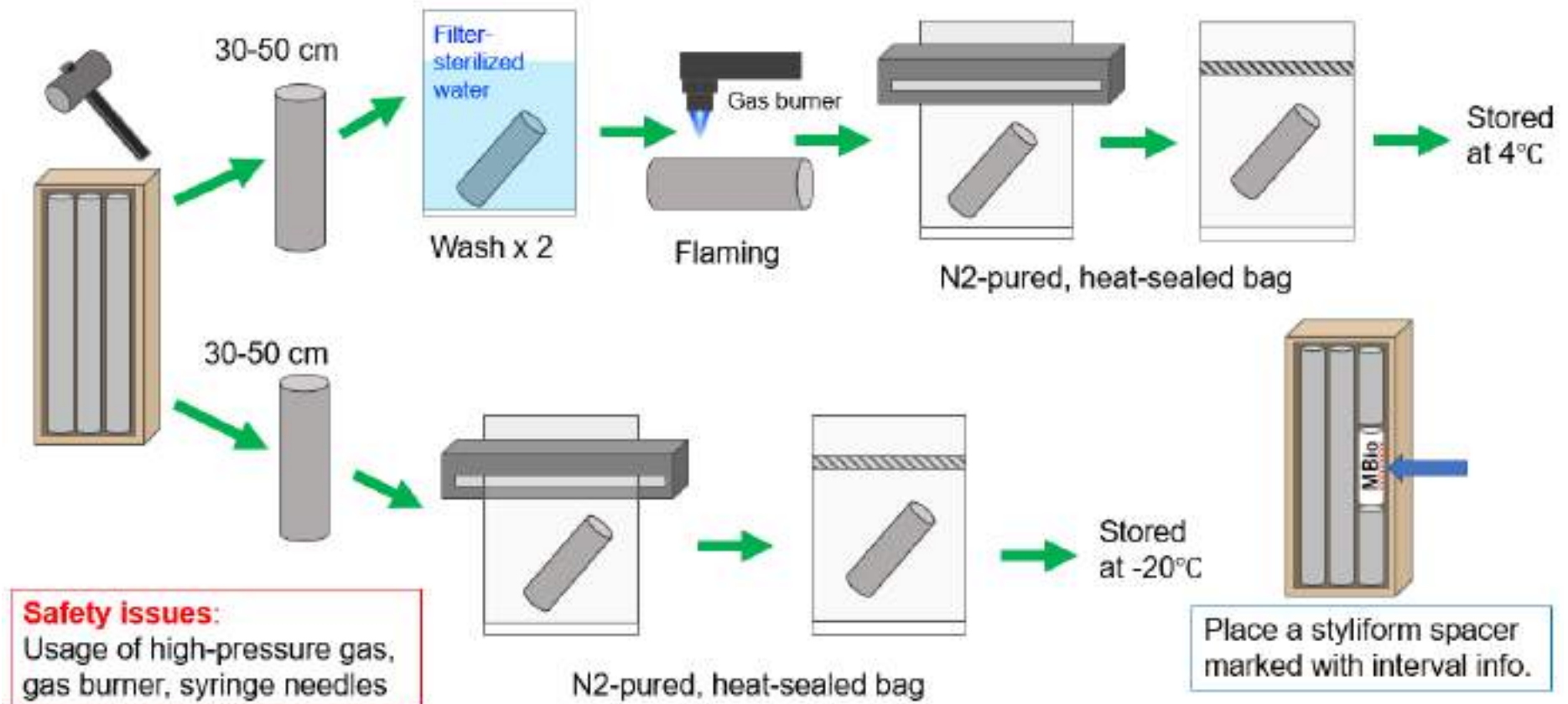


Figure 78 Core sampling procedure at the drill site, illustrating breaking 1 m core intervals from drill rig into sections for two separate processes and storage

5.6 PHASED SURVEYING AND SAMPLING

The BVDP borehole design consists of 3 phases of drilling with surveying and sampling in between each phase. Phase 1 (350 m) and phase 2 (800 m) are specifically important because the upper 800 m of the borehole will be cased and sealed, thus these are the only periods to collect information from the uncased borehole.

During these phases of surveying and sampling, the following workflow will be followed:

- Geophysical/Hydrophysical logging
- Water/Fluid sampling

Hydrophysical logging, consisting of fluid electrical conductivity and temperature, will be conducted last to try to allow the maximum period of the borehole to settle and allow formation water to enter the borehole. Due to standing time and the cost implications, the borehole will not be able to rest for as long as typically stipulated. For the same reason, the water sampling will be conducted last to try to optimise the collection of a representative sample, within the constraints of performing these tests in between drilling phases.

5.7 GEOPHYSICAL SURVEYING

Wireline Africa Pty Ltd. has been appointed as the geophysical logging company that will be responsible for:

1. Geophysical logging,
2. Hydrophysical logging (Fluid EC and temperature), and
3. Depth-specific/in-situ fluid sampling (Phase 1 and 2)

5.7.1 Tools

The planned geophysical logging tools to be used include:

- Three arm caliper/gamma/temperature (first run tool)
- Dual compensated density, gamma, caliper
- Magnetic susceptibility
- Optical and/or acoustic televiewer
- Full-wave sonic
- Neutron
- Dual Inductive tool
- Resistivity
- Dipmeter
- Induced polarization
- Flow meter
- Water sampling tool
- North Seeking gyro

5.7.2 Methodology

The logging unit and ancillary equipment (probes, generators, chains, shackles, sources, calibrators, and tripod if required etc.) are housed in a 4 x4 Toyota Land cruiser or similar vehicle, and in most cases the holes will be logged from the drill rig. However, if it is no longer available and has already moved off site a tripod or boom can be used. All measurements are recorded in 1 cm sampling increments as the tools are raised to the surface on a taut wireline. In an ideal environment the boreholes will be fluid filled.

After establishment on site, and on completion of inductions, risk assessments, toolbox talks etc. the logging operation can begin and would generally be carried out in a specific sequence after discussion with the client. A 2.5 KVA generator is used to power the equipment.

Each probe is carefully lowered into the well and run to total depth at 20/30 m/min. Once at TD it is then logged out at the recommended speed - anything from 2 to 12 m/min. It is estimated that one 400 m deep well (logged with the above tool suite) should take approx. 8 hours (1 day) to complete depending on the ATV logging requirements. (This tool is run at a maximum speed of 2 m/min).

Two staff members (minimum one engineer and one helper – both with first aid, firefighting, and radioactive certification) are required on site for every 12-hour work period – if 24-hour operations are necessary a staff compliment of 4 will be needed with a security presence throughout the night.

Calibration and logging standards are of the highest quality, whilst all work is completed methodically and safely. Strict safety and security measures are always employed to ensure that the radioactive source is always secured either to the sonde, in the truck or in the source storage area. Chains and padlocks will always be used.

5.8 FLUID SAMPLING

5.8.1 Phase 1 (350 m) and Phase 2 (800 m)

Fluid samples will be collected by the geophysical logging contractors (Wireline) for phase 1 (350 m) and phase 2 (800 m) to optimise drill rig stand-by time. The fluid sampling tool will be utilised last to allow for previous survey results to inform on the optimal location/depth for samples to be collected, typically focusing on identified zones of groundwater flow or high permeability/preferential flow.

The borehole will be flushed by the drillers with clean water to try to remove as much drilling fluid as possible, while maintaining the stability of the hole, to assist in collecting a representative sample. Drilling fluid additives even in minor concentrations can hamper quality analyses. Thus, deploying the fluid sampler tool is also an attempt to allow the borehole to settle and allow groundwater to flow back to the hole as pressure is reduced in the hole.

The Wireline sampling tool is limited to a capacity of 500 ml. Four samples have been allocated to each phase, 8 in total, which could be distributed differently depending on the identified zones of interest. The limited volume of fluid allows for (minimum required volumes for analysis):

- 125 ml cations (acidified)
- 125 ml anions
- 15 ml stable isotopes ($\delta^{18}\text{O}$, $\delta^{17}\text{O}$ and $\delta^2\text{H}$)

Sampling procedure:

1. Receive fluid sample from contractor, facilitate transfer to collected container.
2. Field measurements of pH, EC, temperature, redox, dissolved oxygen (record along with drill hole information).
3. Filter sample with a syringe and appropriate filter.
4. Test for drilling fluid additives and consider measures to remove.
5. Fill the required sampling containers.
6. All samples to be filled to the brim of the container to ensure no head space prior to capping the container. Tightly cap the containers to prevent evaporation of the sample and wrap the cap with parafilm as an extra measure.
7. Clearly label samples per laboratory requirements, and ensure record/label system that notes drill hole conditions (depth, logging details, etc.)
8. Store samples at ambient temperature.

5.8.2 Phase 3 (End of Hole - EOH)

Fluid samples for the deeper section of the hole will be collected by Solexperts. The Solexperts sampling tool is limited to a capacity of 1 L.

5.8.2.1 Equipment and preparation

As a preparation for groundwater sampling water is pumped out of the borehole with a submersible pump. The pump can be defined as soon as the depth of the water table is known. Ideally 3 times the volume of the open borehole section should be pumped. However, if the inflow into the boreholes is very low (low permeability) less than the target volume will be pumped such that the probe can be taken in a reasonable time (4.54 l/m => about 6.8 m³), e.g. maximum water table drawdown 250 m and a flow rate of 16 l/min of the high performance submersible pump result in pumping time between 7 and 8 h to pump once the entire volume of the open hole wellbore storage. In such a case the pumping operation would take about 24 h. The flow rate and the downhole pressure will be monitored online with the Solexperts data acquisition system. Subsequently to the completion of the pumping phase, the pump will be de-installed and the downhole sampling device will be lowered to the target depth using a winch system.

Pumping equipment consist of 3" submersible pump, an electrical pressure sensor installed above the pump and a control panel (flowmeter, manometers and flow board), a 300 m wireline winch system for the pump installation in the borehole and hose.

5.8.2.2 Sampling procedure

The volume of fluid from the Solexperts sampler is larger at 1 L, but still limited to this amount and allows for (minimum required volumes for analysis):

- 125 ml cations (acidified)
- 125 ml anions
- 15 ml stable isotopes ($\delta^{18}\text{O}$, $\delta^{17}\text{O}$ and $\delta^2\text{H}$)

Sampling procedure:

- Receive fluid sample from contractor, facilitate transfer to collected container.
- Field measurements of pH, EC, temperature, redox, dissolved oxygen (record along with drill hole information).
- Filter sample with a syringe and appropriate filter.
- Test for drilling fluid additives and consider measures to remove.
- Fill the required sampling containers.
- All samples to be filled to the brim of the container to ensure no head space prior to capping the container. Tightly cap the containers to prevent evaporation of the sample and wrap the cap with parafilm as an extra measure.
- Clearly label samples per laboratory requirements, and ensure record/label system that notes drill hole conditions (depth, logging details, etc.)
- Store samples at ambient temperature.

5.9 HYDRAULIC TESTING

Standard Wireline Inflatable Packer System (SWIPS) tests are frequently used in hydrogeological and geotechnical investigations to provide important information on rock formation properties such hydraulic conductivity/permeability. The information gathered through either a pressured test or falling head test is used to calibrate groundwater models and assumptions, and to provide information on depressurisation characteristics of a zone of interest for slope stability purposes. HydroGeo Services has been selected as the contractor for conducting the packer testing in the 350 m to 800 m section (phase 2). The upper 350 m hole at

size PQ is too large for hydraulic testing. Solexperts has been selected as the contractor to conduct the hydraulic testing in the 800 m to EOH section (phase 3).

5.9.1 Procedure – SWIPS Operation (HydroGeo Services – phase 2)

This operation procedure should be read in conjunction with Inflatable Packers International (IPI) SWIPS Operation Manual. For phase 2, 5 days of packer testing has been allocated, with an average of 5 or 6 tests per day, thus 25 to 30 tests in total for this section.

Procedure for SWIPS operation:

- Unpack SWIPS Gear
- Geotechnical Engineer is required to determine Test Setup
- Hole Conditioning and Drill Bit Location
- Assemble SWIPS Equipment to Test Requirements
- Insert SWIPS Tool into the Borehole
- Tank Setup and Water Quality
- Vibrating Wire Piezometer
- SWIPS Bladder Inflation
- Conduct Packer Testing

There are three commonly used methods on mining and exploration sites to conduct downhole packer aquifer testing, each suited to different aquifer situations. These three methods are known as the Pressure Test, the Falling Head Test and Airlift/Rising Head test.

- Note: The standard Elster analogue flow meters supplied with the SWIPS console are only rated to 80 Litres/minute. Flows over this rate may yield inaccurate readings and can cause the flow meters to fail mid-test. In these situations, a falling head test is recommended, as the flow meter is not utilised in this test method.

Pressure Test

- The pressure test is suited to aquifers that have moderate to low inflow rates. This test type provides an accelerated means of testing these aquifer conditions.
- Steady test pressures are required to be maintained during testing and pressure fluctuations should be minimised by the Driller wherever possible.
- The Geotechnical Engineer will determine the appropriate test pressures, the number of stages to be tested and the time taken for each stage. The flow rate per minute is then determined for a range of different test pressures which gives an indication as to the permeability of the tested zone.

Falling Head Test

- 1) The falling head test is more suited to situations where the 'water take' by the aquifer or test zone is high.
- 2) A falling head test is suited to situations where the pumped flow rates supplied by the Drill Rig at the desired test pressure will be insufficient, or where water usage at elevated test pressures will be excessive.
- 3) In the Falling Head Test, a Minitrol (data logger) or Dipper is used to measure the drop in water level, per time interval (i.e. Normally per minute) from the hole collar level to a stabilisation level (normally the natural groundwater table).
 - The pressure applied to the test zone of interest is the water head pressure only in the drill string.

6 BVDP BOREHOLE DRILLING RESULTS

The results presented provide an analysis of hydrological and geological characteristics from borehole data collected, focusing on groundwater behaviour through hydrological logging and sampling, and geological stratigraphy.

The analysis of borehole data reveals significant hydrological and geological characteristics of the subsurface environment. Open fractures were observed up to 322 metres deep, with the largest aperture measuring 40 mm at 321 mbgl, indicating high subsurface permeability. Major fractures extended to 935 mbgl, but only one had a measured aperture. Hydraulic conductivity estimates from packer tests indicated permeability variations related to pressure loss and geological composition, particularly pyroxenite and chromitite layers.

Continuous hydrological measurements showed a groundwater level at 24 mbgl and increasing total dissolved solids (TDS) with depth, peaking over 6,000 mg/l at 450 mbgl, suggesting potential saline groundwater inflow. Following phase 1 sealing, a new profile (BVDP-3-B) was established, with temperature readings peaking at 39°C after 350 m. Drilling fluid contamination posed challenges for water sample collection and analysis, limiting the effectiveness of standard flushing procedures. Stable water isotope analysis utilised Laser-Based Spectroscopy (LGR) and Isotope Ratio Mass Spectrometry (IRMS), revealing $\delta^{18}\text{O}$ and $\delta^2\text{H}$ signatures consistent with low-latitude regions and an increasing depletion trend with depth, indicating variations linked to groundwater inflow. Drilling fluid analysis indicated minimal settling, with localised concentration in shallow depths. In Phase 2, isotopic analysis with the Picarro system showed variations in contamination levels, necessitating careful interpretation of isotope ratios.

Overall, the borehole study provides crucial insights into subsurface hydrology and geology, highlighting the complexities of groundwater inflow, drilling fluid contamination, and the influence of geological structures on hydraulic conductivity. The report enhances our knowledge of groundwater systems and has the potential to contribute to informed decision-making regarding water security and sustainable development in South Africa and beyond.

6.1 LITHOLOGICAL LOGS

The geological log is presented in Figure 79, illustrating the lithological sequence encountered in the BVDP-3 borehole. The borehole intersects a range of mafic and ultramafic rock types from the surface downwards, including norite (NORIT), serpentinite (SERP), gabbro-norite (GABNR), anorthosite (ANRTS), pyroxenite (PYRXN), dolerite (DOLRT), chromite (CHR), harzburgite (HZB), dunite (DUN), olivine orthopyroxenite (OLOPX), and gabbro-norites with minor anorthosites (GABNR;ANRTS). Each rock unit is recorded by its top and bottom depths in this simplified lithological log. A detailed geological log is presented in Appendices Table A, with specific structures identified for increased groundwater flow.

The upper layers are dominated by norite, gabbro-norite, anorthosite and occasional gabbro-norites with minor anorthosites. Norite and gabbro-norite are generally dense, low-porosity rocks, limiting primary permeability. However, fracturing within these layers, particularly in gabbro-norites with anorthositic intrusions, could enhance secondary porosity, making them potential, though low-yield, aquifer zones. Furthermore, serpentinite (SERP) within this section indicates some degree of hydrothermal alteration, which may enhance fracture permeability. Fractured serpentinite could facilitate minor groundwater flow.

Deeper down, the sequence transitions into interbedded anorthosite, pyroxenite, and dolerite intrusions, with occurrences of gabbro-norites and norite below with gabbro-norites some minor anorthosites lower down again. Dolerite, known for its tendency to fracture, may act as a minor conduit for groundwater flow in otherwise impermeable zones. From about 220 mbgl, the occurrences of pyroxenite increase and thicken, with more chromite below 500 mbgl. At greater depths, ultramafic units such as harzburgite and dunite, along with

occasional chromite bands and sections of olivine orthopyroxenite, dominate the stratigraphy. These rocks typically exhibit very low primary porosity. Sections of olivine orthopyroxenite could facilitate minor groundwater flow, while harzburgite and dunite are likely to act as confining layers due to their low permeability.

The sequence of dense, largely impermeable lithologies, interrupted by fractured dolerite dykes and sections of gabbro-norites with minor anorthosites, suggests that groundwater flow may be limited to specific fracture zones. The presence of dolerite and fractured gabbro-norites with minor anorthosite inclusions may create compartmentalisation within the aquifer system, acting as barriers or conduits depending on their fracture connectivity. Fractured dolerite, serpentinite, and the more fractured norite could act as preferential pathways for any groundwater present at depth.

The simplified lithological log highlights a complex hydrogeological profile, where groundwater occurrence and movement are likely controlled by secondary porosity within fractured zones rather than primary permeability. In general, the rock units encountered are expected to have low groundwater storage capacities, with the potential for minor, localised flow through fractured dolerite, serpentinite, gabbro-norites with minor anorthosites, and possibly anorthosite layers. This would be relevant for low-yield groundwater extraction or as part of a larger, regional groundwater monitoring network.

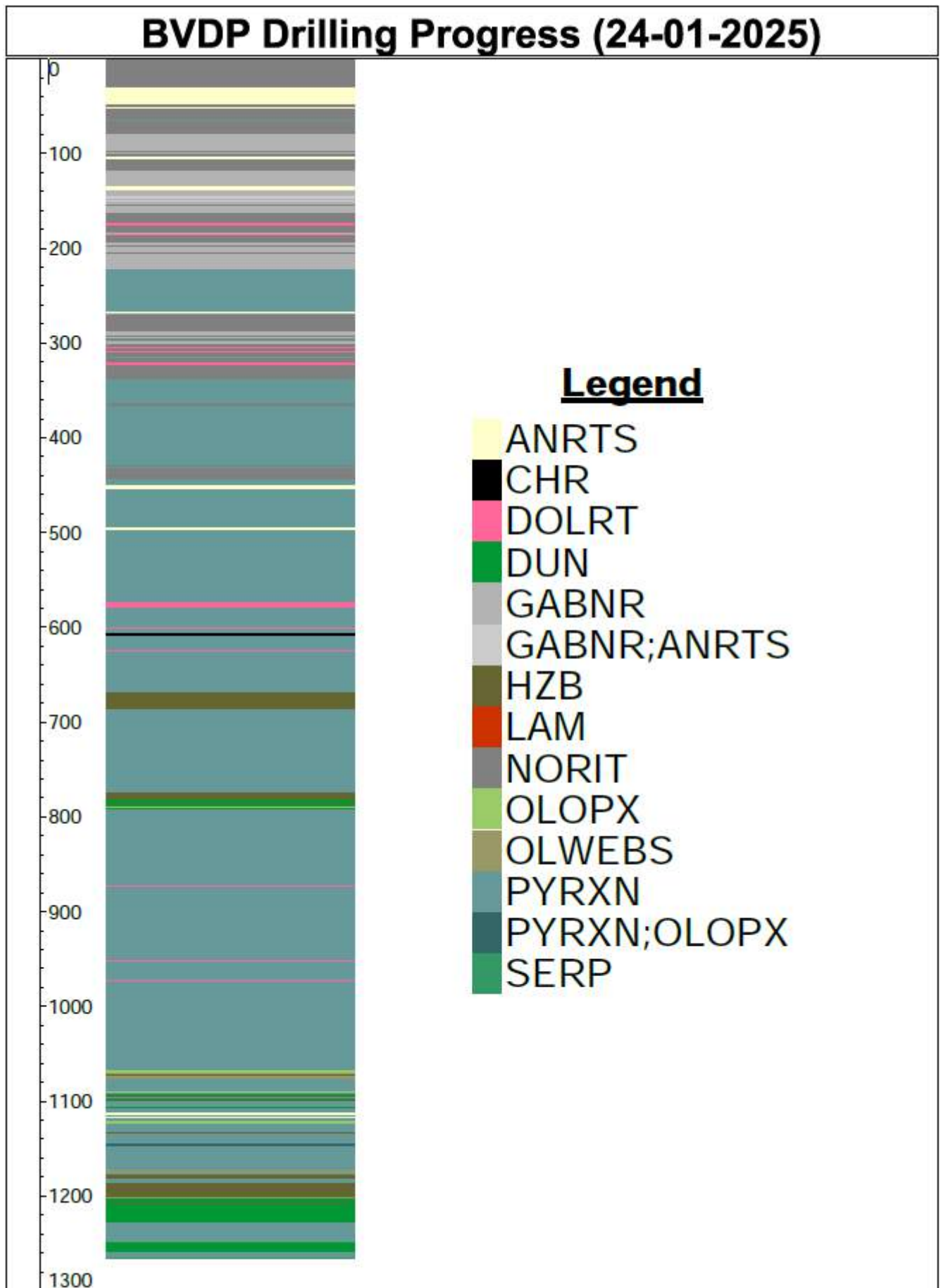


Figure 79 Simplified lithological log showing changes in lithology over the complete current depth of the BVDP hole

6.2 GEOPHYSICAL SURVEYS

The hole was surveyed using a total of nine geophysical tools plus a gyro. The geophysical logging produced a structure, lithology, geotechnical and hydrology logs.

6.2.1 Structure log summary

Structures were identified from the geophysical surveys and classified into:

- Open fracture with a measured aperture
- Major open joint/fracture
- Minor open joint/fracture
- Closed joint/fracture
- Bedding
- Drilling induced fracture

The open fractures noted in the borehole with depth are illustrated in Figure 80, these are limited to the top 322 meters of the hole. The largest open fracture aperture of 40 mm was measured at a depth of 321 mbgl. Total water loss was experienced in the hole until the first 350 m was sealed off, illustrating how permeability the subsurface at these depths is. Major open joint/fractures are also plot with depth, however only one has an associated measured aperture. Major open fractures were identified all the way along the borehole up to a depth of 935 mbgl.

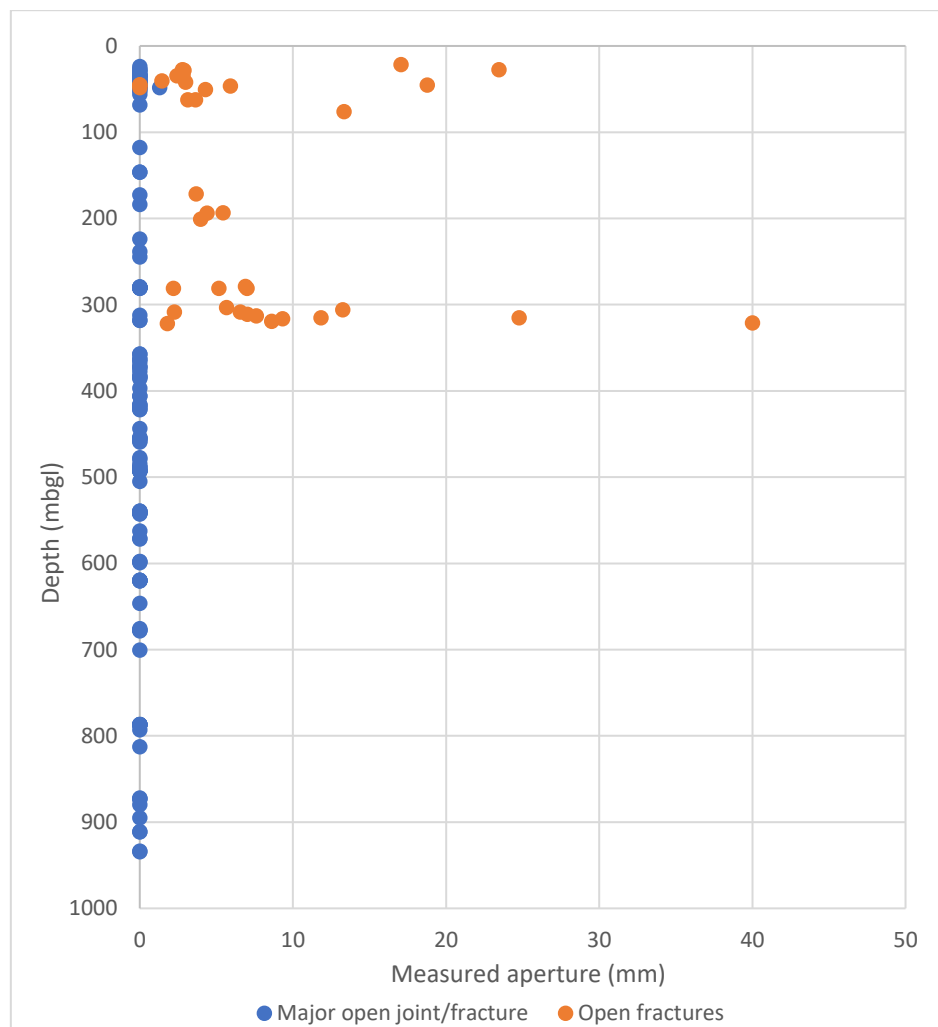


Figure 80 Depth of open fractures and major open joint/fractures identified from geophysical logging

6.2.2 Hydrological log

For the hydrological log, fluid electrical conductivity (EC) and fluid temperature were logged continuously with depth along with the calliper and flowmeter measurements. The log is displayed in Figure 83.

The TDS is calculated from the measured fluid electrical conductivity and plot in Figure 81. From the log, the groundwater level is seen at a depth of 24 mbgl. There is an overall increasing trend over the depth of the hole, as to be expected, however, series of peaks and troughs with depth could indicate groundwater inflow zones. The largest peak at a depth of 450 mbgl measures TDS values of over 6 000 mg/l, possibly indicating the inflow of highly saline groundwater.

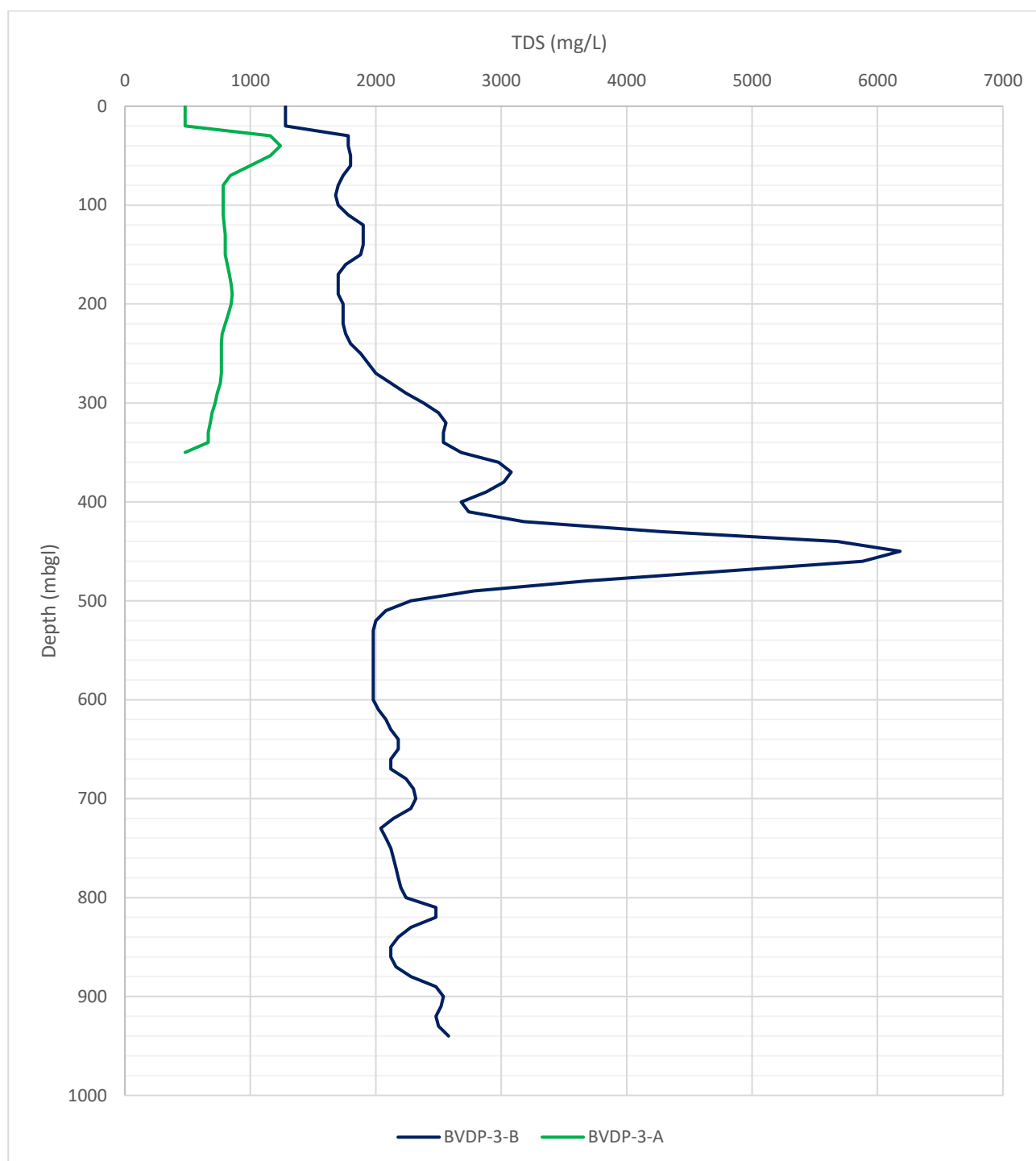


Figure 81 Total dissolved Salts (TDS) calculated from measured fluid electrical conductivity from geophysical log

After the cementing and grouting of phase 1, the re-drilled core was given a new notation, thus, why there is a BVDP-3-B and BVDP-3-A. The BVDP-3-B is thus the profile of the new hole after drilling through the cemented top section, thus the first 350 m has solid steel casing and thus the sharp increase after this depth could be a function of this (Figure 81). The temperature is plot in Figure 82, showing an increasing trend with depth to a maximum temperature of 39°C.

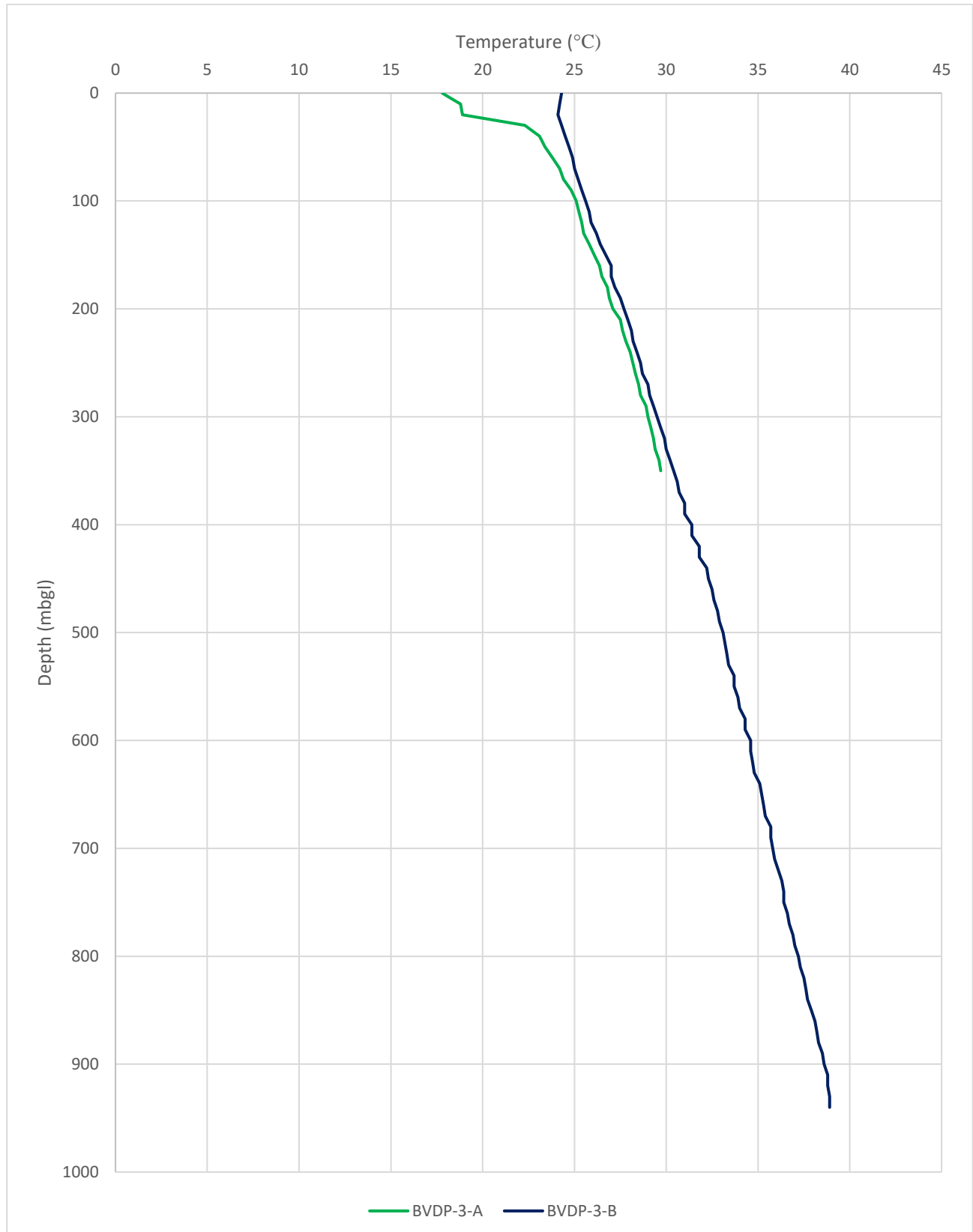
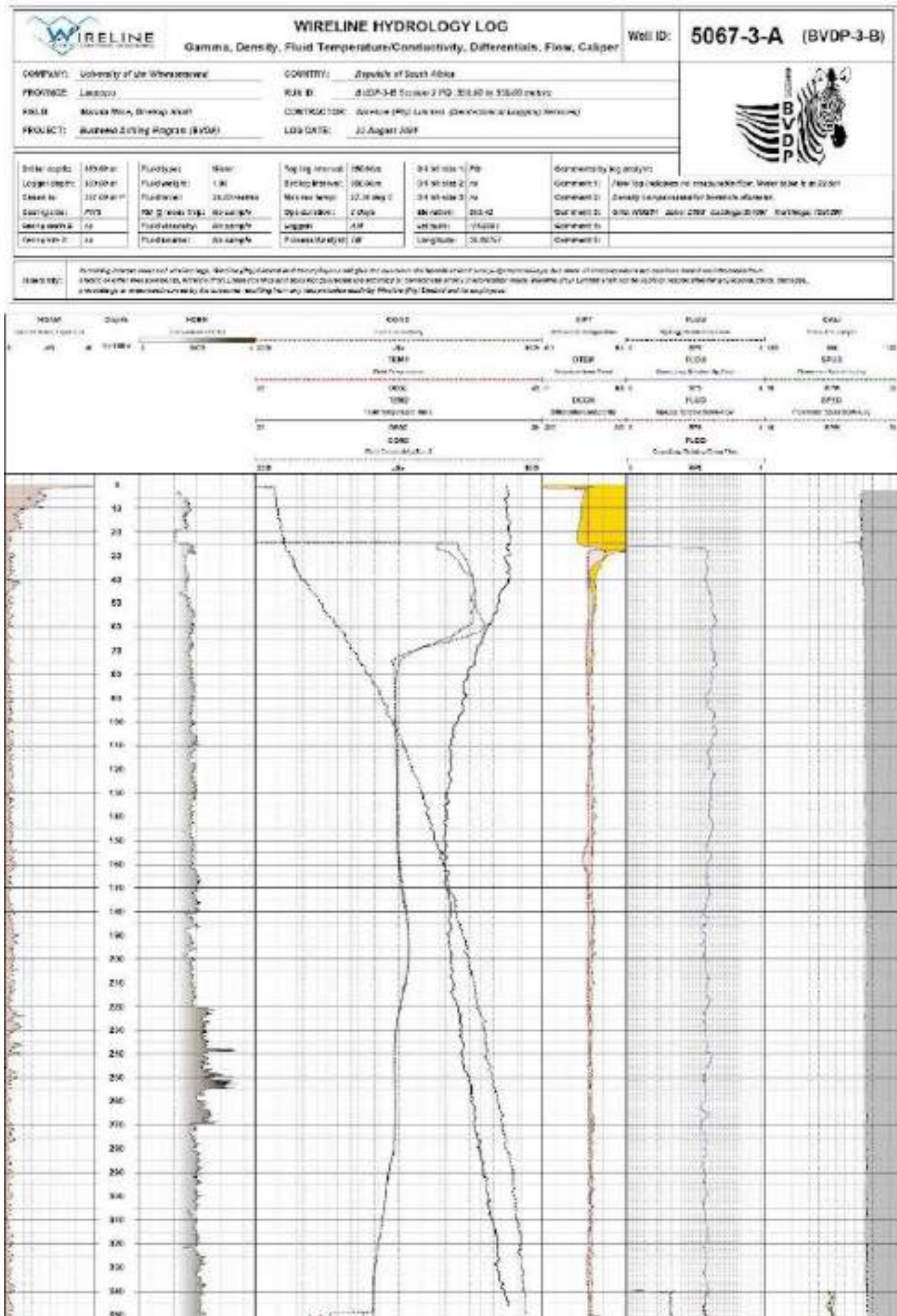
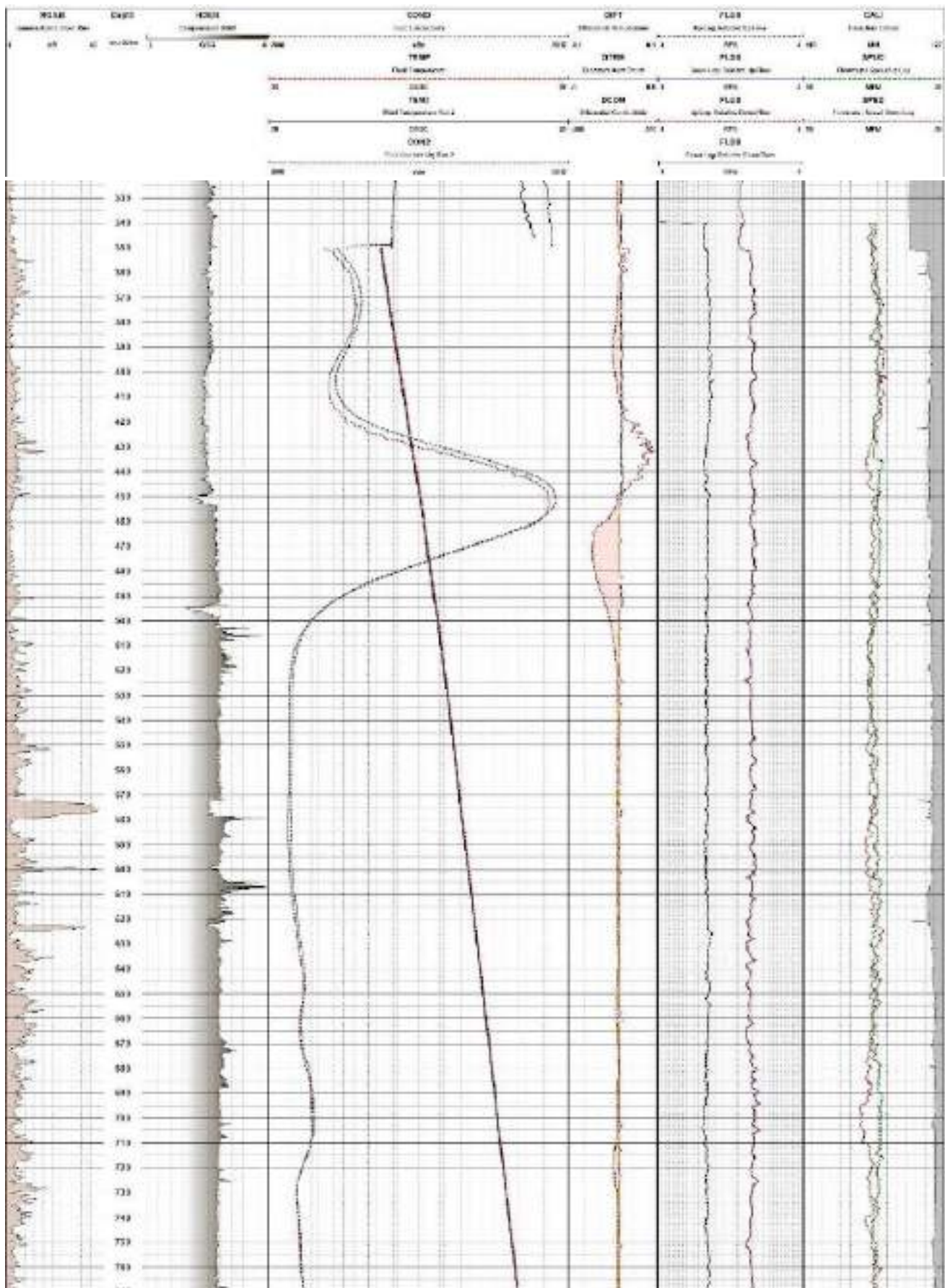


Figure 82 Fluid temperature measured from geophysical logging





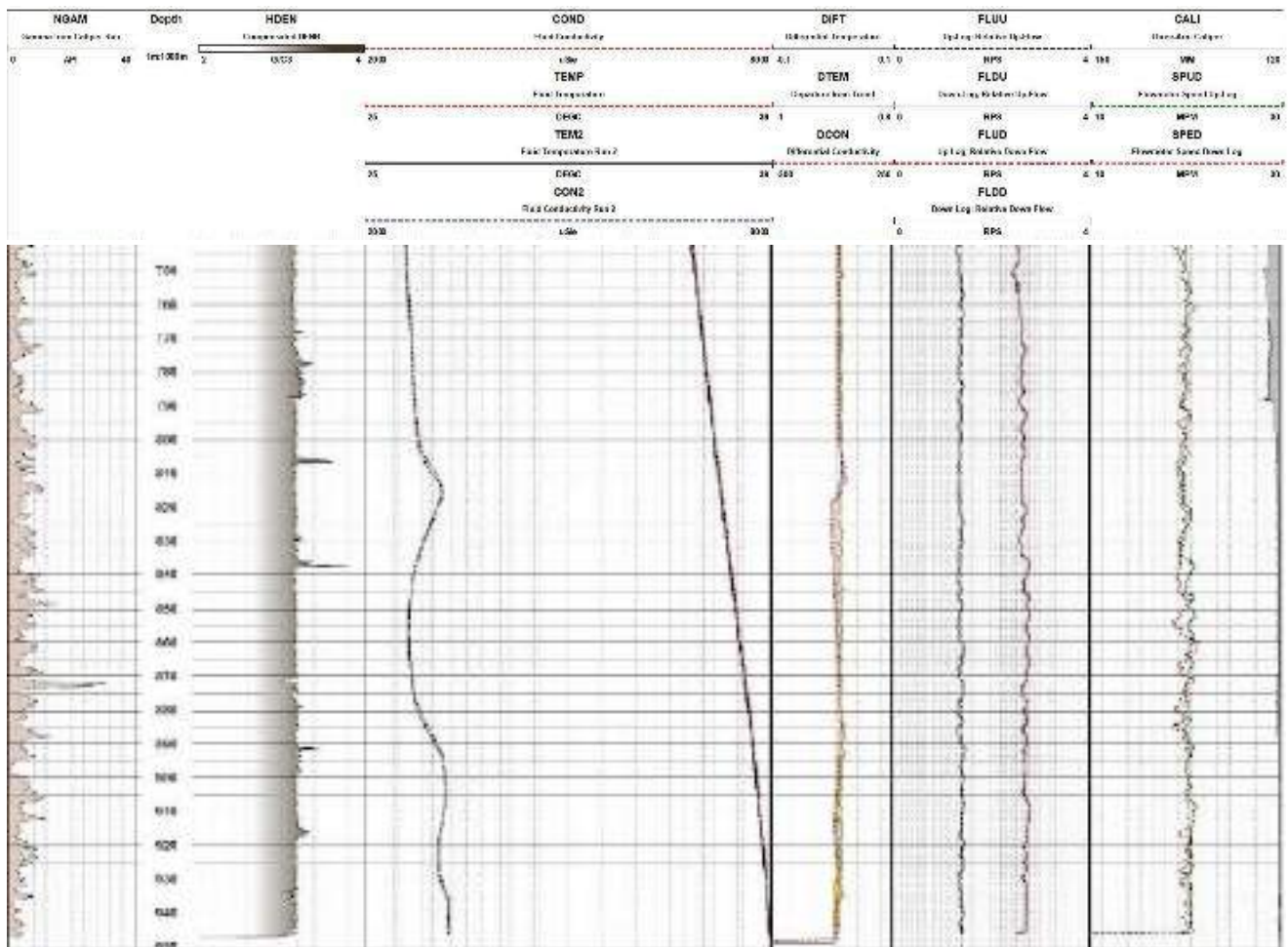


Figure 83 Hydrology log presented from the geophysical logging, including fluid electrical conductivity (EC) and fluid temperature with depth along with the calliper and flowmeter measurements

6.2.3 Borehole Radar

Borehole radar is a high-resolution geophysical logging tool employed to investigate the subsurface around boreholes by transmitting high-frequency electromagnetic waves. This method is particularly effective for identifying geological structures such as fractures, faults, voids, and lithological boundaries. The system typically comprises a transmitter and receiver, which are lowered into the borehole (Tsogtbaatar and Sato, 2024). The fundamental operating principle of borehole radar involves the transmission of electromagnetic pulses into the surrounding rock mass. When these pulses encounter interfaces between materials with contrasting electromagnetic properties—such as fractures or water-filled cavities—they are reflected to the receiver. The time delay and amplitude of these reflections are used to map subsurface features beyond the borehole wall (Liu and Sato, 2006).

In a South African context, borehole radar can be used in groundwater investigations, particularly in hard rock environments, to detect fracture networks and identify potential aquifers. This is especially valuable in hydrogeological studies where groundwater flow is influenced by structural features. However, the method's efficacy may be limited in highly conductive environments, such as those containing saline groundwater or clay-rich formations, where the radar signal is subject to significant attenuation.

The borehole radar results, performed during Phase 2 surveying, is presented in Figure 84 to Figure 87.

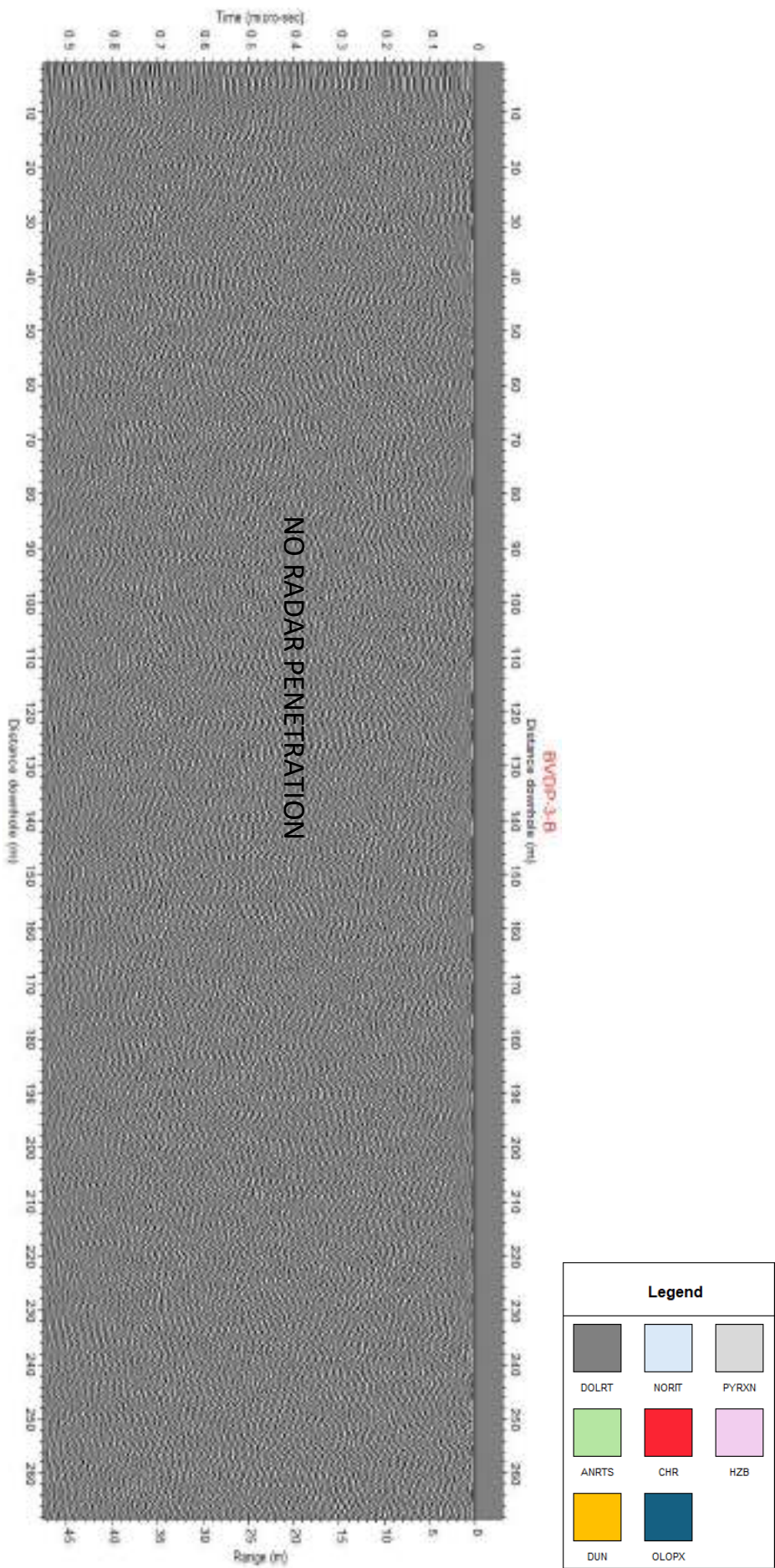


Figure 84 Borehole radar results from a depth of 0 to 260 mbgl, showing the general lithological log

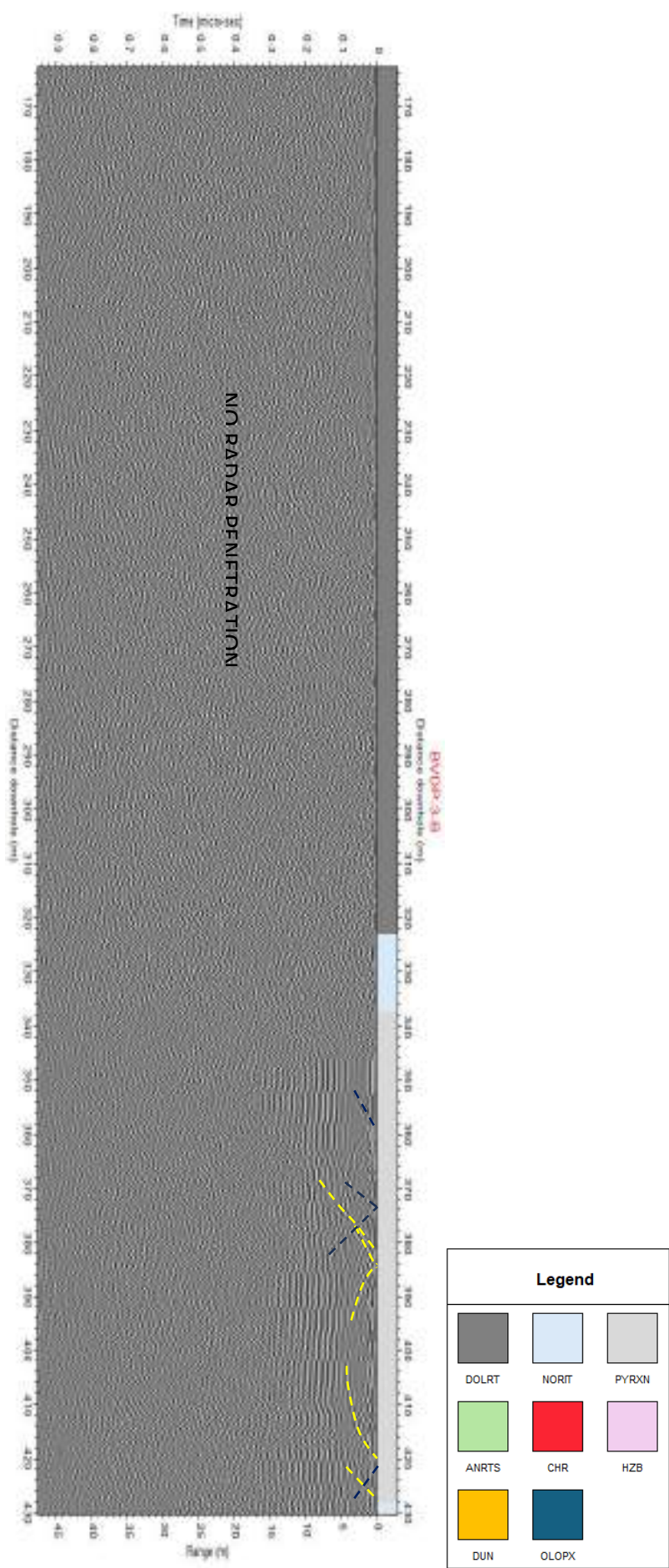


Figure 85 Borehole radar results from a depth of 160 to 430 mbgl, showing the general lithological log

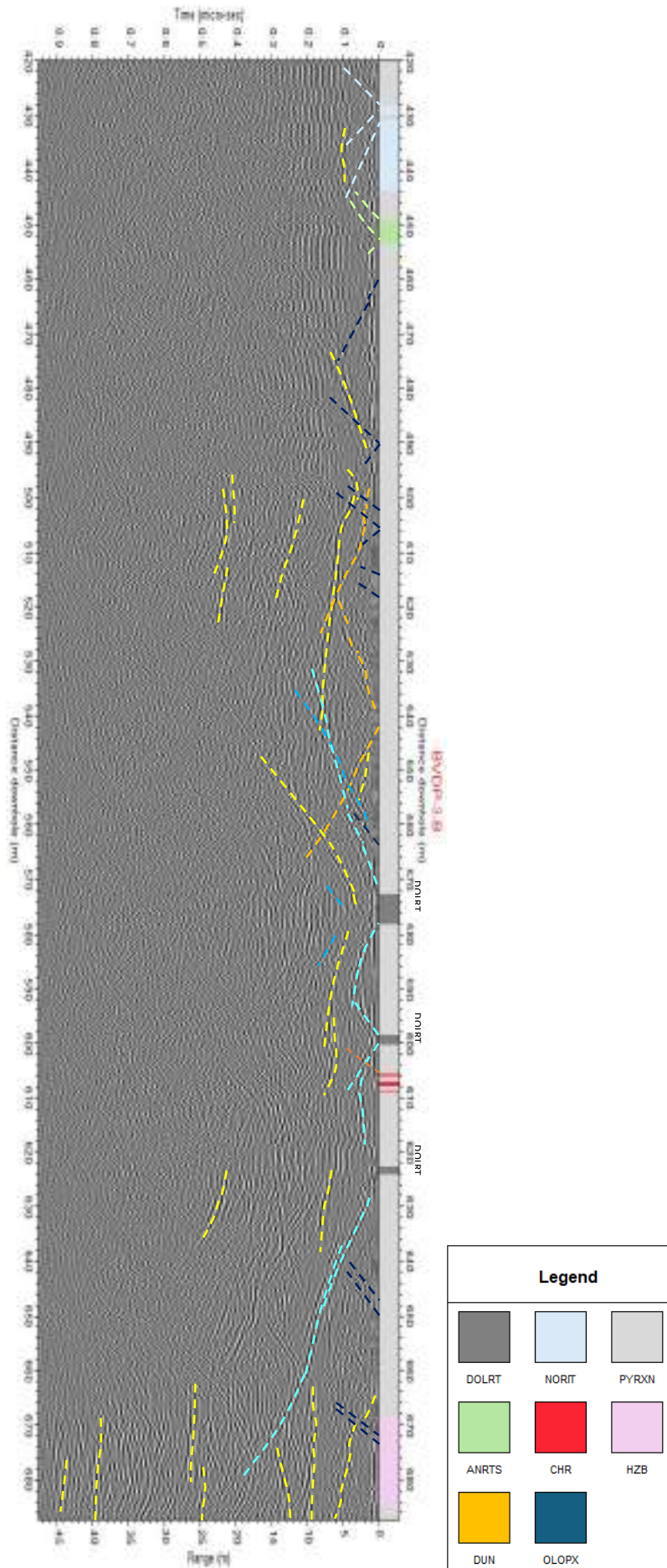


Figure 86 Borehole radar results from a depth of 420 to 680 mbgl, showing the general lithological log

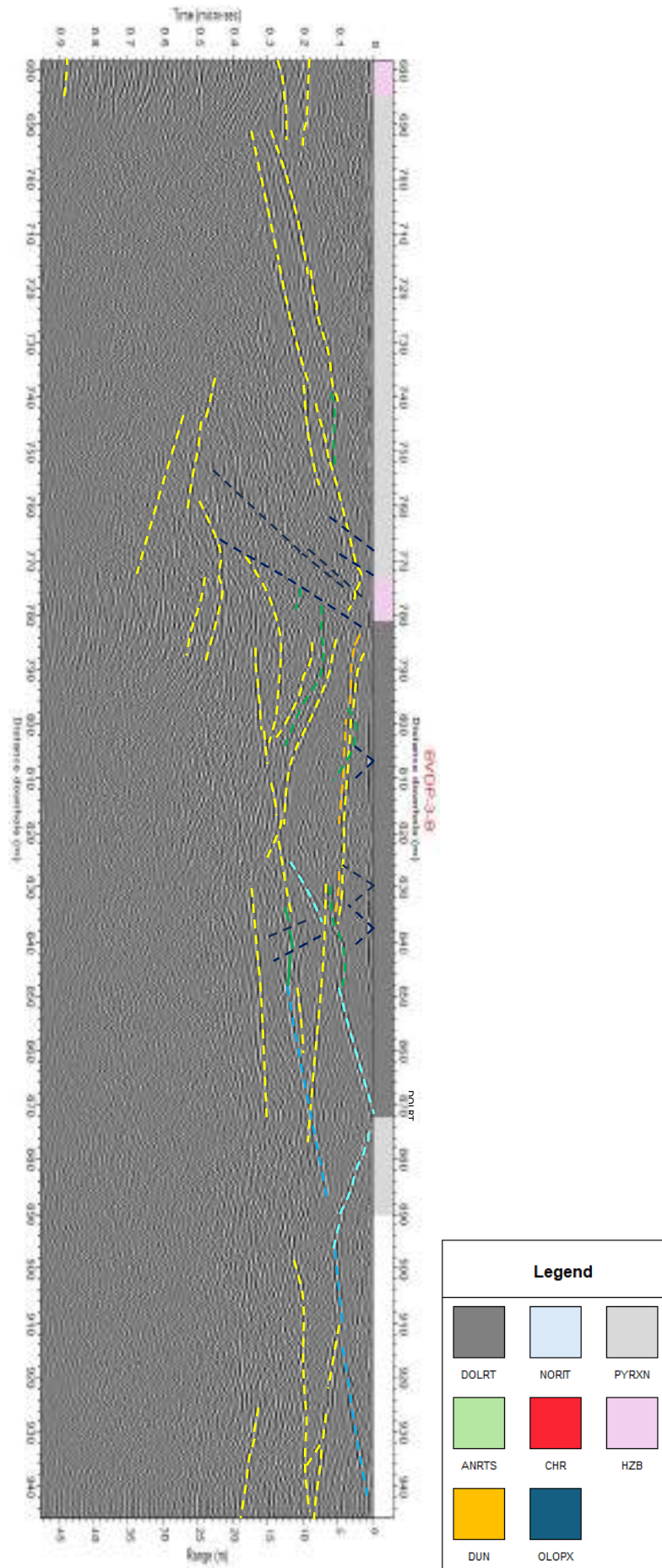


Figure 87 Borehole radar results from a depth of 680 to 940 mbgl, showing the general lithological log

BHR penetration depth of about 45 m was possible from the BVDP-3-B hole. The following observations are made from the results:

There is no radar penetration through the metal casing at the time (0 – 350 mbgl). Illustrating the loss of collecting data from these previous sections once solid casing has been installed. The BHR was only run in the hole during the phase 2 survey, and thus no information for the phase 1 section from 0 – 350 mbgl.

A radar reflection has been associated with dolerite intersections at depths of approx. 570 – 580 mbgl; 600 mbgl; 620 mbgl and 780 – 870 mbgl. Potentially, illustrating fractures at great depths which could be related to potential groundwater flow paths.

BHR detected features that could be tracked from borehole intersections.

There are several reflections in the results that may require further investigation.

6.3 PHASE 1 WATER SAMPLING AND PRELIMINARY RESULTS

After the phase 1 geophysical surveys were completed, preliminary raw survey data was provided to inform depth-specific water sampling, along with the geological logs for the hole. The raw data preview along with the depths at which sampling was selected is shown in Figure 88 to Figure 90. Six samples were taken at the following depths:

- 46 mbgl
- 62.5 mbgl
- 75.5 mbgl
- 110 mbgl
- 272 mbgl
- 292 mbgl

When collecting water samples from boreholes for analysis, the presence of drilling fluid poses a significant concern, as it can contaminate the water and alter the results of chemical and isotopic analyses. Drilling fluid, typically used to lubricate and cool the drill bit, may contain additives or chemicals that can mix with the groundwater, leading to inaccurate readings of water quality or isotope ratios. Due to this reason, it is typical procedure to flush, purge and ensure all drilling fluids have been removed before sampling is conducted. However, the BVDP drilling project, the tight drilling schedule, associated drill standing time cost implications, and a serious concern of the borehole collapse did not allow for extensive flushing and resting of the borehole before sampling was conducted, and then the borehole cased with solid casing. Thus, for research purposes samples were collected from the available window and the influence of the remaining drilling fluid is attempted to understand the implications for the results obtained. The hole was flushed with clean water for 9 hours (single driller's shift), geophysical surveys were conducted over 2 days, and then water samples were collected with a controlled depth-specific sampler.

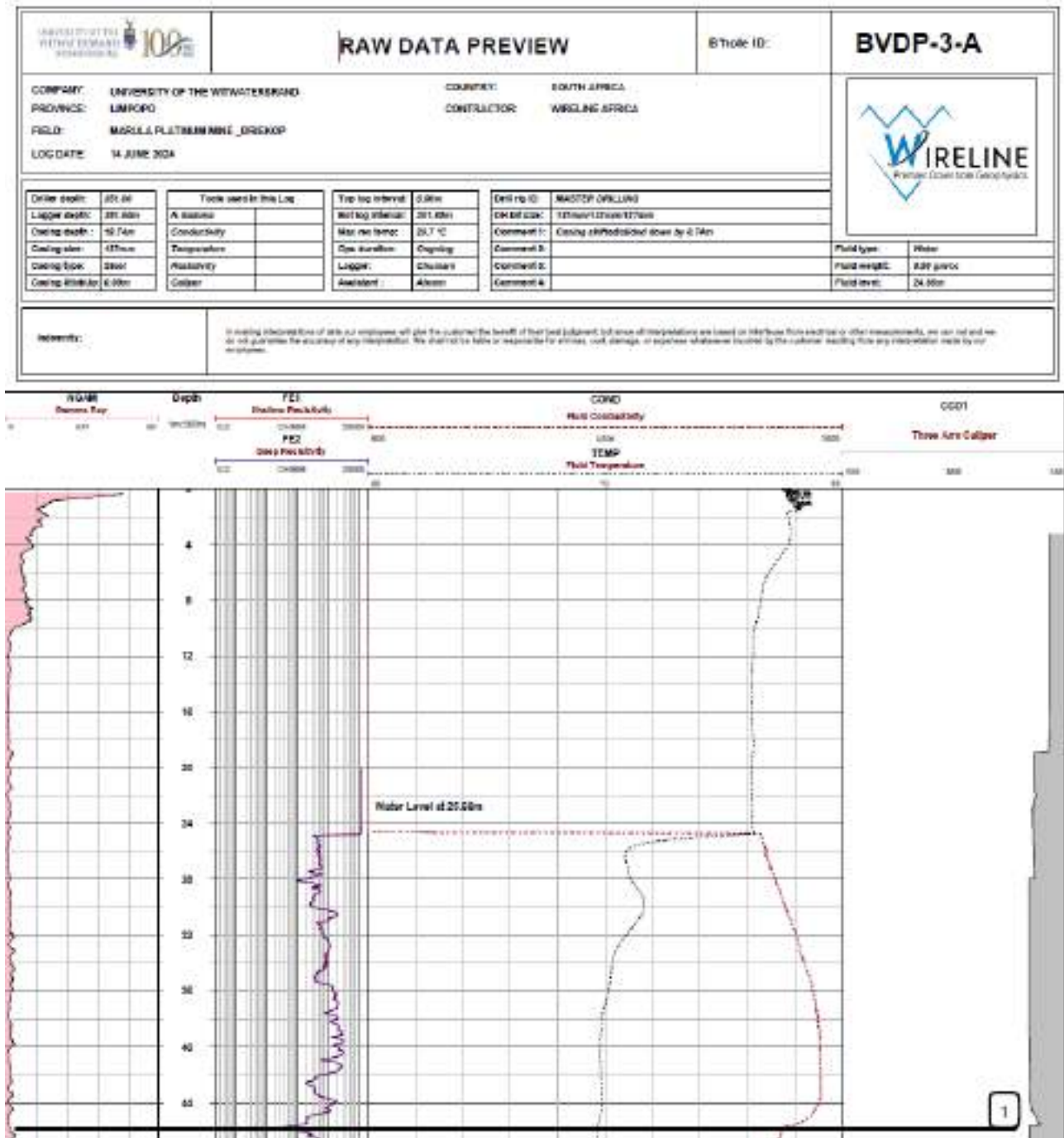


Figure 88 Raw geophysical data preview for the purpose of selecting depths for fluid sampling (depth from 0 to 47 mbgl) showing sample 1 depth at 46 mbgl.

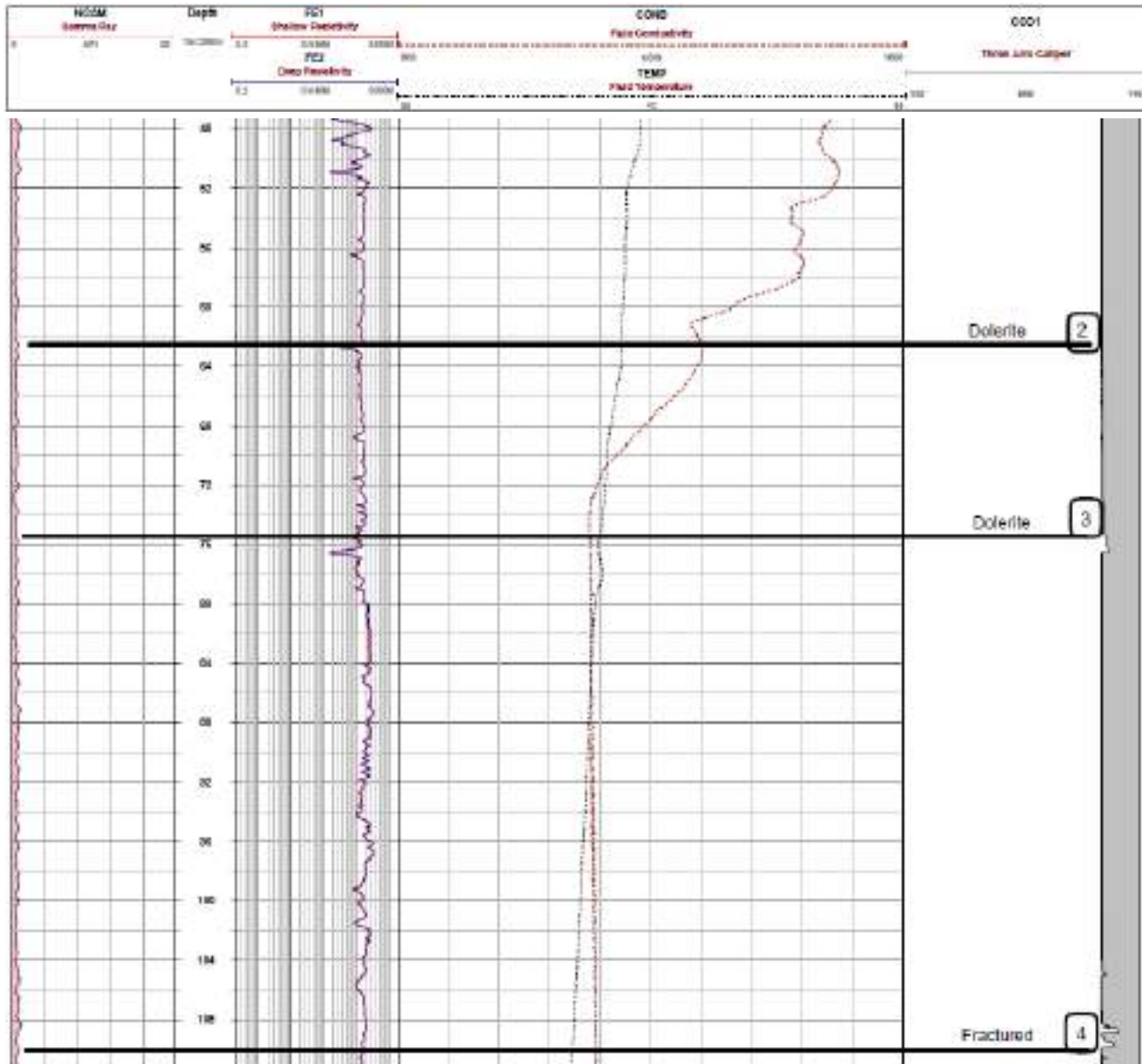


Figure 89 Raw geophysical data preview for the purpose of selecting depths for fluid sampling (depth from 46 to 109 mbgl) showing sample 2 depth at 62.5 mbgl, sample 3 at 75.5 mbgl and sample 4 at 110 mbgl.

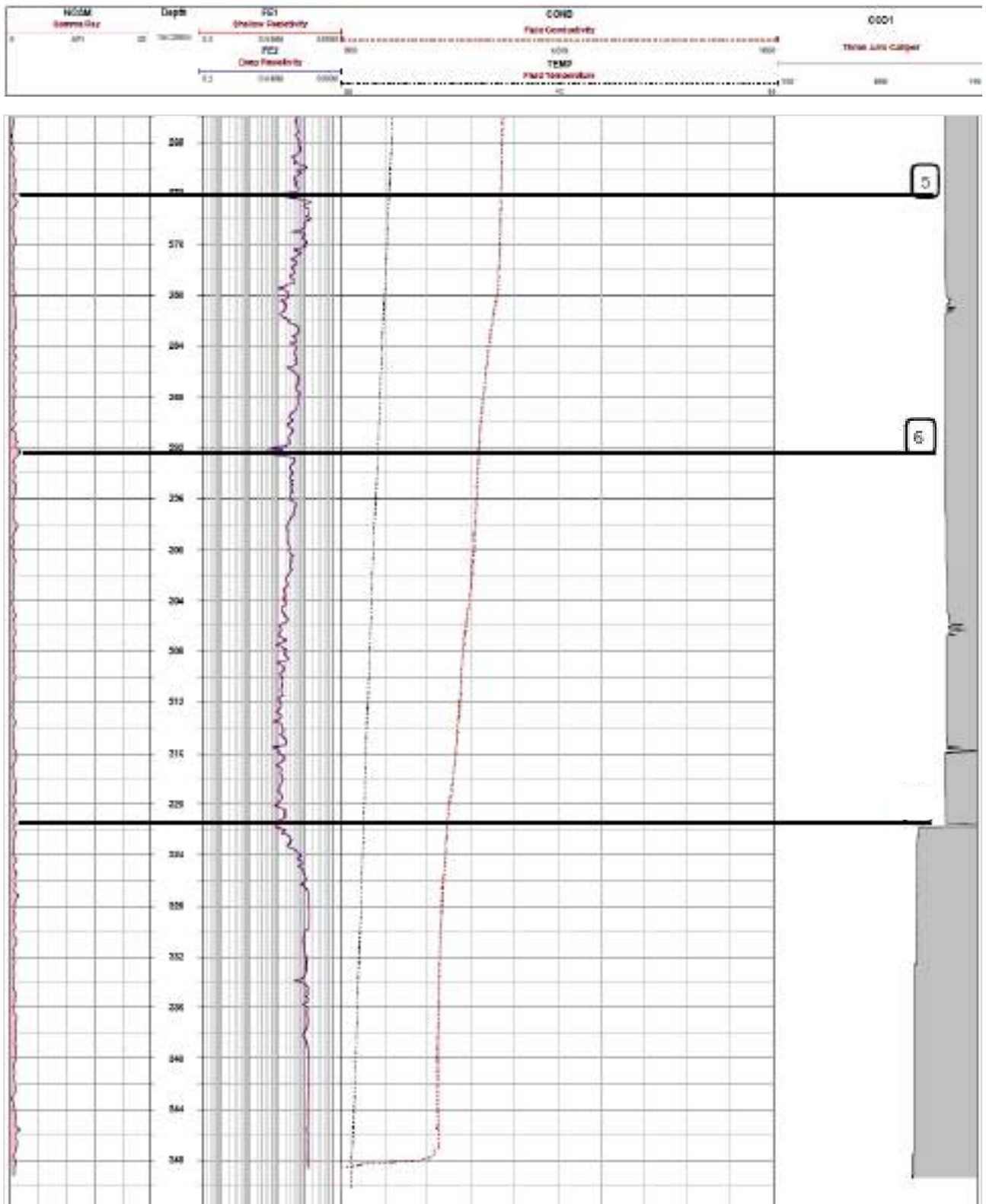


Figure 90 Raw geophysical data preview for the purpose of selecting depths for fluid sampling (depth from 266 to 352 mbgl) showing sample 5 depth at 272 mbgl and sample 6 at 292 mbgl.

6.3.1 Water quality

The six (6) groundwater samples were analysed by a SANAS accredited laboratory for the chemical compositions (anions and cations) and for dissolved micro determinants as per Table 18. The chemical composition of the groundwater samples reveals distinct groupings based on their ion concentrations, reflecting variations in water-rock interaction processes at different depths. The Piper diagram shows that samples BVDP_46, BVDP_62.5, and BVDP_75.5 share a similar chemical profile, characterised by an enrichment in magnesium (Figure 91). This results in a groundwater type with a predominant calcium-magnesium-chloride-sulphate composition (Ca-Mg-Cl-SO_4). In contrast, samples from BVDP_110, BVDP_272, and BVDP_292 display a shift towards bicarbonate enrichment, suggesting a different interaction with the surrounding geology. Sample BVDP_110 shows a mixed composition with both calcium sulphate (Ca-Mg-Cl-SO_4) and calcium bicarbonate (Ca-Mg-HCO_3) characteristics, indicating transitional water chemistry. However, the water samples plot within the sub-triangle also classified by some as a “mixed water type”. Considering the flushing of the hole and use of circulating drilling fluid, this does highlight the intricacies with interpreting these results.

The STIFF diagrams allow for a visual comparison of chemical similarities and differences between samples taken at various depths. The shape and distribution of ions on the diagrams for BVDP_46, BVDP_62.5, and BVDP_75.5 appear very similar, suggesting consistent water chemistry within this depth range. Likewise, samples BVDP_110, BVDP_272, and BVDP_292 exhibit a uniform pattern, indicating stable geochemical conditions with depth (Figure 92).

Finally, the Schoeller diagram provides an overview of the groundwater’s chemical composition trends across depths. Samples BVDP_46 and BVDP_62, as well as BVDP_75, show an overall similar trend, with only minor variations in specific ion concentrations (Figure 93). Likewise, samples BVDP_272 and BVDP_292, along with BVDP_110, display consistent chemical profiles, reinforcing the observations made from the Piper and STIFF diagrams.

The patterns observed across these diagrams highlight two main groundwater types within the study area, however the reason for these grouping is complicated by the flushing of the hole with fresh surface water to remove as much drilling fluid as possible (9 hours of flushing for a full driller’s shift, and 2 days of geophysical logging before samples were collected with depth-specific samplers. From a geological perspective, possible reasons for the shift in water quality between these groups after 110 mbgl, including the first occurrence of dolerite dykes from 62.5 mbgl and again at around 73 – 74 mbgl. With this the occurrence of pyroxenite increases from this occurrence. However, the influencing of flushing and drilling fluid might far surpass these.

Table 18 Phase 1 groundwater sampling results.

BVDP BOREHOLE (PHASE 1) SAMPLE ANALYSIS RESULTS							
Parameter	Unit	BVDP_46	BVDP_62.5	BVDP_75.5	BVDP_110	BVDP_272	BVDP_292
Sampling depth (mbgl)		46	62.5	75.5	110	272	292
Date		15/06/2024	15/06/2024	15/06/2024	15/06/2024	15/06/2024	15/06/2024
Time		07:50	08:09	08:30	08:52	09:28	10:06
Chemical determinants							
Turbidity	NTU	11.7	10.1	358	325	30	163
Colour	units Pt-Co	110	>500	>500	>500	269	327
pH		7.93	7.78	7.41	7.09	7.11	7.43
EC	mS/m	133.17	135.41	110.31	92.56	83.33	80.76
Ca	mg/L	43.51	39.78	38.46	40.83	41.82	39.45
Mg	mg/L	119.98	119.73	88.6	67.46	56.67	47.22
Na	mg/L	74.91	73.54	67.98	62.5	60.5	60.15
K	mg/L	4.35	1.64	6.09	8.08	9.27	7.6
Total Alkalinity	mg CaCO ₃ /L	327.04	312.72	259.31	254.02	218.51	206.91
F	mg/L	0.34	0.45	0.53	0.51	0.45	0.58
Cl	mg/L	171.23	178.51	129.83	82.72	81.23	80.39
NO ₂ as N	mg/L	0.914	0.906	0.729	0.007	0.041	0.029
NO ₃ as N	mg/L	1.59	6.84	3.75	0.2	0.21	0.23
SO ₄	mg/L	175.621	228.008	218.836	138.629	120.914	119.178
TDS	mg/L	943.62	1004.54	844.18	666.61	601.22	573.25
PO ₄ as P	mg/L	<0.042	<0.042	<0.042	<0.042	<0.042	<0.042
NH ₃ as N	mg/L	1.162	1.204	1.333	0.978	<0.101	0.698
Total Organic Carbon as C	mg/L	44.99	36.35	44.54	63.75	51.85	54.9
Micro determinants (dissolved)							
Al	µg/L	58.858	149.788	575.121	70.878	299.689	228.398
Sb	µg/L	1.74	<0.065	<0.065	0.086	<0.065	<0.065
As	µg/L	<0.022	<0.022	<0.022	<0.022	<0.022	<0.022
Ba	µg/L	49.562	42.15	32.577	26.299	26.533	22.851
B	mg/L	<0.040	<0.040	<0.040	<0.040	<0.040	<0.040
Cd	µg/L	<0.001	<0.001	<0.001	0.02	<0.001	<0.001
Cr	µg/L	15.486	28.502	31.938	9.801	11.785	10.662
CN	µg/L	1.41	1.19	1.11	1.06	1.21	1.14
Cu	mg/L	0.305	0.223	0.216	0.103	0.235	0.283
Fe	mg/L	0.943	0.838	1.773	1.878	3.883	2.967
Hg	µg/L	4.252	2.095	1.241	1.411	1.376	0.466
Mn	µg/L	89.345	61.549	25.716	211.32	92.591	62.92
Ni	µg/L	11.313	10.106	11.468	13.289	9.558	9.194
Pb	µg/L	2.568	1.329	1.045	0.754	1.22	1.393
Se	µg/L	0.768	0.322	0.353	0.122	0.115	0.031
U	µg/L	1.991	2.086	2.146	2.183	2.069	2.045
Zn	mg/L	0.091	0.126	0.136	0.102	0.057	0.039

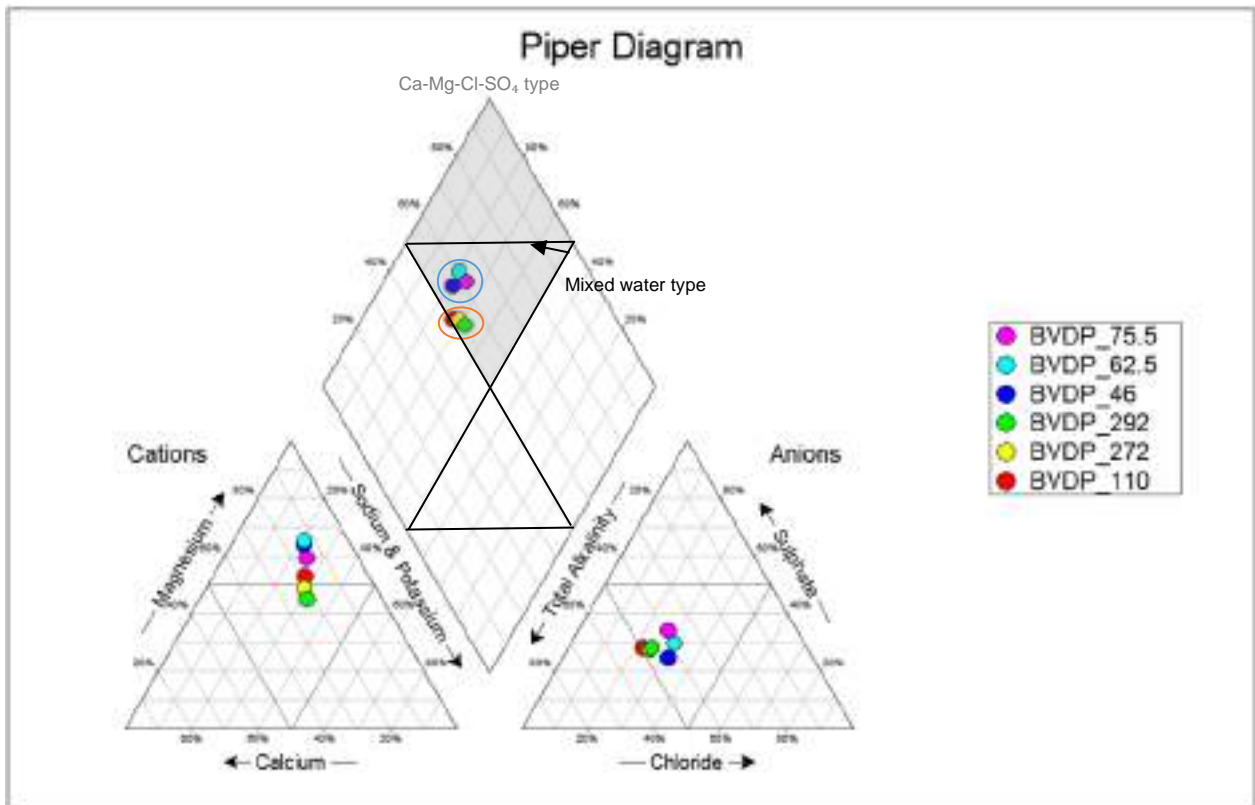


Figure 91 Piper diagram of the phase 1 groundwater samples

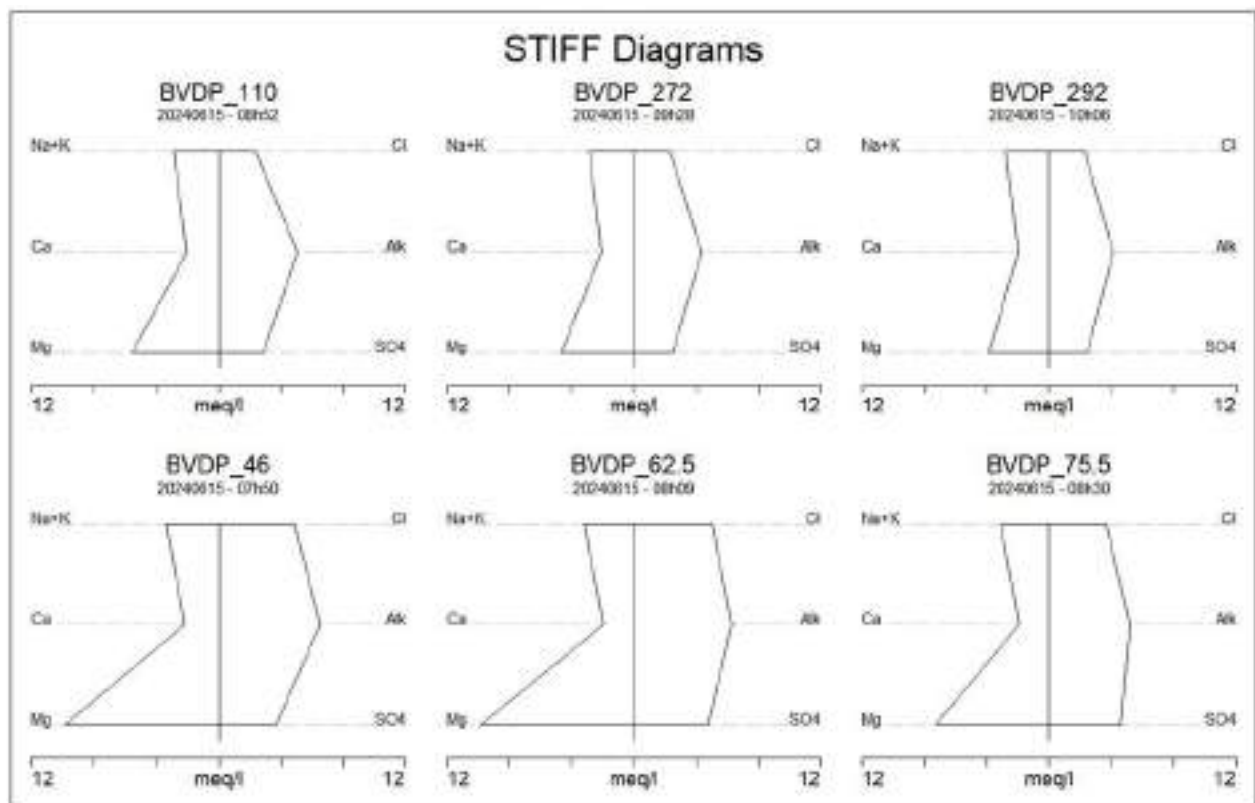


Figure 92 STIFF diagrams of the phase 1 groundwater samples.

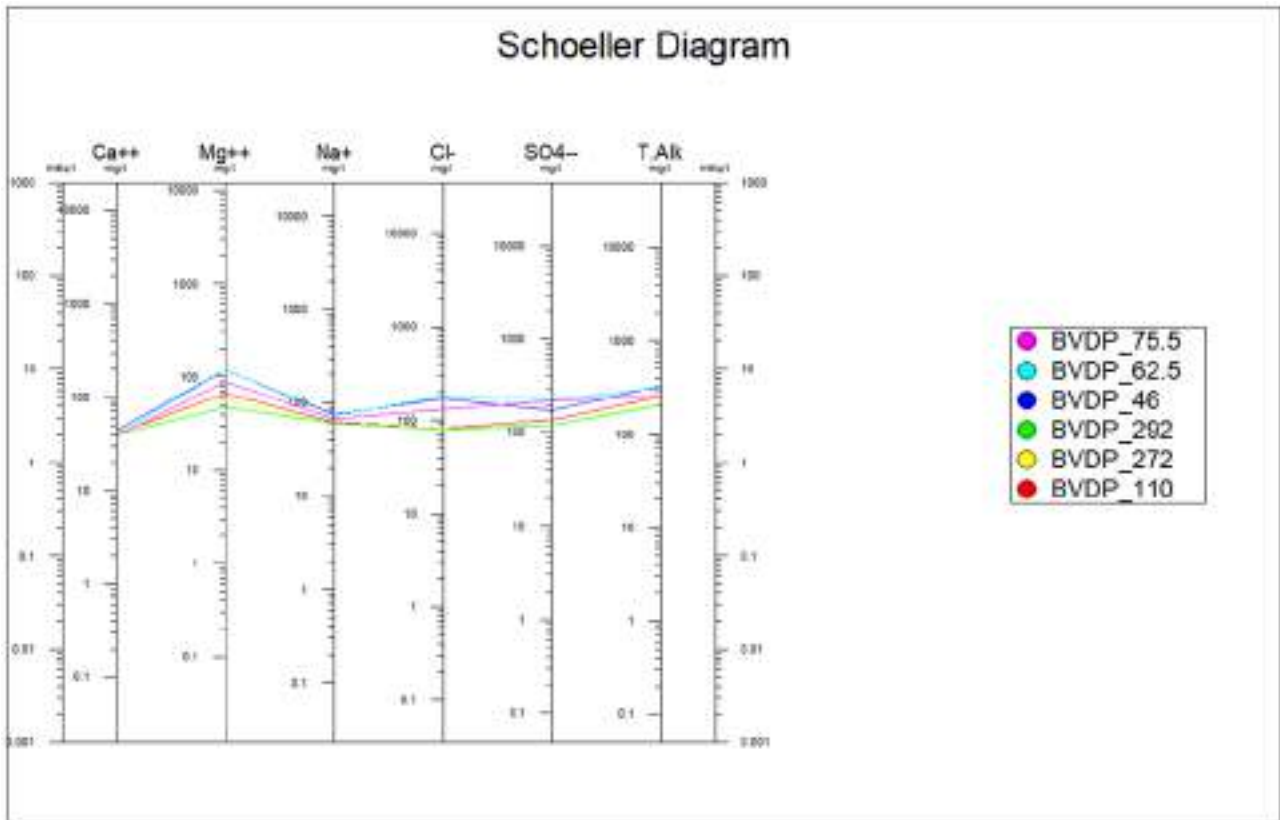


Figure 93 Schoeller diagram of the phase 1 groundwater samples.

6.3.2 Stable water isotopes

For the water samples to be sent for isotope analysis, the samples were filtered with 0,45 micron meter syringe filter (Figure 94). Due to the viscous nature of the drilling fluid, the filtering of these samples took considerable effort and pressure with at times multiple filters to be used for a single sample volume.



Figure 94 Filtering process for sample processed for isotope analysis

When it comes to stable water isotope analysis of potentially contaminated samples with organic compounds, the choice between Laser-Based Spectroscopy (LGR) and Isotope Ratio Mass Spectrometry (IRMS) is crucial due to the different ways these methods handle sample purity and potential interferences (Table 19).

LGR (Los Gatos Research) – Laser-Based Spectroscopy

LGR instruments use cavity ring-down spectroscopy (CRDS) or off-axis integrated cavity output spectroscopy (OA-ICOS) to measure water vapour directly. The laser interacts with water molecules in the vapour phase, and isotope ratios ($\delta^{18}\text{O}$ and $\delta^2\text{H}$) are determined by how much light is absorbed at specific wavelengths.

LGR instruments are more susceptible to interference from organic contaminants in the water. Compounds such as alcohols, oils, or other volatile organic compounds (VOCs) can absorb light at the same wavelengths used to measure isotopes, leading to inaccurate readings. Many organic molecules overlap with the absorption spectra of water isotopologues, causing spectral interference. This can result in incorrect isotope ratio measurements if contaminants are present in significant amounts. While LGR systems often have some ability to detect interference and apply corrections, their precision can still suffer, especially if contaminant levels are high. Techniques such as filtration and purification of samples may be necessary before measurement, but they can add complexity and are not always fully effective for all types of contaminants.

If samples are suspected to have organic contamination, LGR instruments may struggle to provide accurate results, and users would need to exercise caution when interpreting the data. This method is better suited for clean or minimally contaminated water samples.

IRMS (Isotope Ratio Mass Spectrometry)

IRMS involves converting water samples into gas phase molecules (CO_2 for oxygen isotopes and H_2 for hydrogen isotopes) before measuring isotope ratios. This conversion occurs through controlled chemical reactions (e.g., reacting water with carbon or metal catalysts).

One of the major strengths of IRMS is its lower sensitivity to organic contamination compared to laser-based systems. During sample preparation, the water is chemically transformed into gas (CO_2 or H_2), leaving many contaminants behind, which are not converted into these specific gases. The process of converting water into pure CO_2 or H_2 effectively removes organic impurities, meaning the resulting gas is much less likely to contain unwanted compounds that could affect isotope ratios. IRMS maintains its high precision and accuracy even when samples contain organic impurities. This makes it a preferred method when working with water samples from polluted or complex environments where contaminants are expected.

If the sample is from a potentially contaminated source (such as groundwater affected by pollution, wastewater, or industrial sites), IRMS is far more reliable. It provides accurate isotope ratio data even when organics are present, due to the chemical conversion process that isolates the target molecules for analysis.

Table 19 Key Differences in Handling Organic Contaminants

Aspect	LGR (Laser Spectroscopy)	IRMS (Isotope Ratio Mass Spectrometry)
Sensitivity to Organics	Highly sensitive to contamination from organics due to spectral overlap	Much less sensitive to organics; conversion process removes many contaminants
Accuracy with Contaminated Samples	Lower accuracy; contaminants may distort readings	High accuracy even with contaminated samples due to gas conversion
Mitigation of Interference	Requires pre-treatment (e.g., filtration, vapour purification), but not always effective	Organics are largely excluded during gas conversion, so interference is minimal
Best Use Case	Clean or minimally contaminated samples	Contaminated or complex samples, especially those with organics

When dealing with organically contaminated water samples, IRMS is the more robust choice due to its chemical conversion process, which isolates the isotopes of interest and minimises interference from contaminants. However, the analysis is LRMS is time-consuming, requires specific specialised instrumentation which requires maintained and upkeep thus making this method of analysis more expensive than LGR. UCT has a lab that can provide stable isotope analysis by IRMS method, however, with a small number of samples the cost of running this equipment becomes a hurdle. The BIOGRIP lab at SUN has LGR and Picaro instrumentation which is easier to run and maintain with simpler sample preparation, but as explained is specifically sensitive to contaminated samples. LGR instruments, while useful for many applications, are more prone to inaccuracies in the presence of organic compounds due to their reliance on laser absorption, which can be affected by contaminants. Thus, a method of analysing on the LGR or Picaro is suggested with additional specific samples analysed by the IRMS system for evaluation of the sensitivity of the LGR/Picaro results.

Results and interpretation

The $\delta^{18}\text{O}$ and $\delta^2\text{H}$ plot of the Phase 1 samples against the Global Meteoric Water Line (GMWL) illustrates the isotopic signatures of the samples in a broader geographical context, showing their alignment with low-latitude regions characterised by overall enriched isotopes (Figure 95). When plotted on a local scale, the same $\delta^{18}\text{O}$ and $\delta^2\text{H}$ data reveal variations in isotopic composition with depth, highlighting the potential influence of groundwater sources and recharge dynamics at different depths (Figure 97).

Trend of general increase in depletion with an increase in depth, which is a typical trend seen in groundwater samples with depth. There seems to be two group, one consisting of the shallow samples (depths of 46 and 62.5 mbgl) and deeper samples (depths 110, 272 and 292 mbgl), with an intermediate point in between representing the sample depth 75 m. These results seem to be mirrored by the d-excess (dD) measured for the samples using the LRMS instrumentation, where the shallower samples have a larger difference compared to the LGR results, the intermediate sample (75 mbgl) has no measured difference, and the deeper samples have smaller and then a negative difference (Table 20).

Since the drilling fluid used is not a particulate suspension but rather a dissolved polymer or similar additive, it is unlikely to settle significantly within the borehole. These fluids are formulated to remain evenly distributed throughout the borehole to maintain stability. However, in shallow parts of the borehole where circulation slows or ceases, the fluid could potentially concentrate, leading to more significant impacts on the isotope composition of the water samples taken from those depths.

Considering the identified fractures in the geophysical logging data, there is a substantial open fracture identified at 76 mbgl with an aperture of 13 mm (Figure 80). Additionally, the TDS profile shows a peak in TDS values around 40 mbgl and then decreases and stabilises at around 75 mbgl (Figure 83). This could explain the minimal dD value for the 75 mbgl sample specifically. There were several open fractures identified at around 200 mbgl and then again around 300 mbgl, which could be a means for deeper groundwater to be flowing into the borehole and these depth-specific samples to be more representative of the natural groundwater system as well as the drilling fluid being more diluted here due to the additional inflow of non-contaminated groundwater with respect drilling fluids.

Table 20 Calculated Deuterium excess (dD) on the phase 1 samples from the IRMS and IGR for comparison with the deviation between the measurements

Sample No.	Sample depth (mbgl)	IRMS	LGR	Deviation
		dD		
1	46 m	5,1	0,7	4,4
2	62 m	5,1	0,7	4,4
3	75 m	-0,8	-0,8	0,0
4	110 m	-1	-2,5	1,5
5	272 m	-3,3	-2,5	-0,8
6	292 m	no gas	-2,5	\

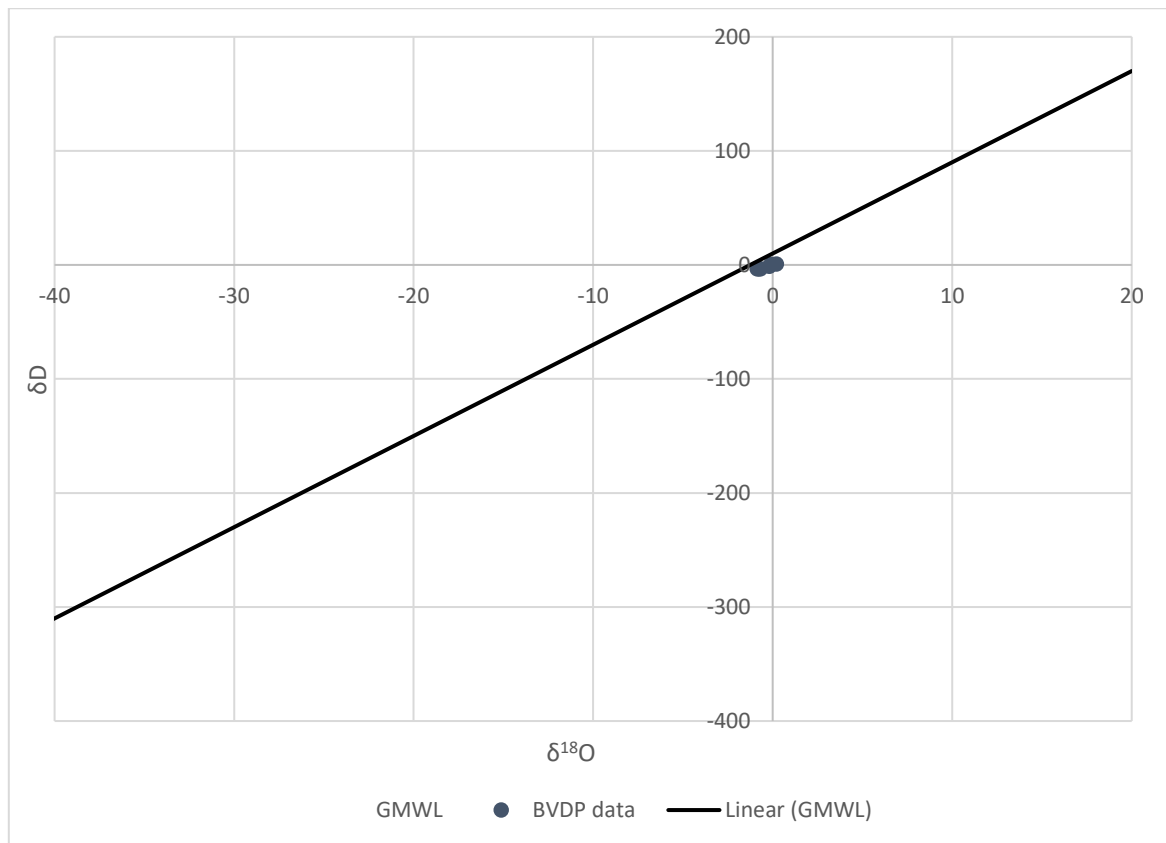


Figure 95 Delta plot of the phase 1 samples with GMWL on a global scale showing the location of the samples with respect to larger context, namely low latitude geography plotting with enriched overall isotopes

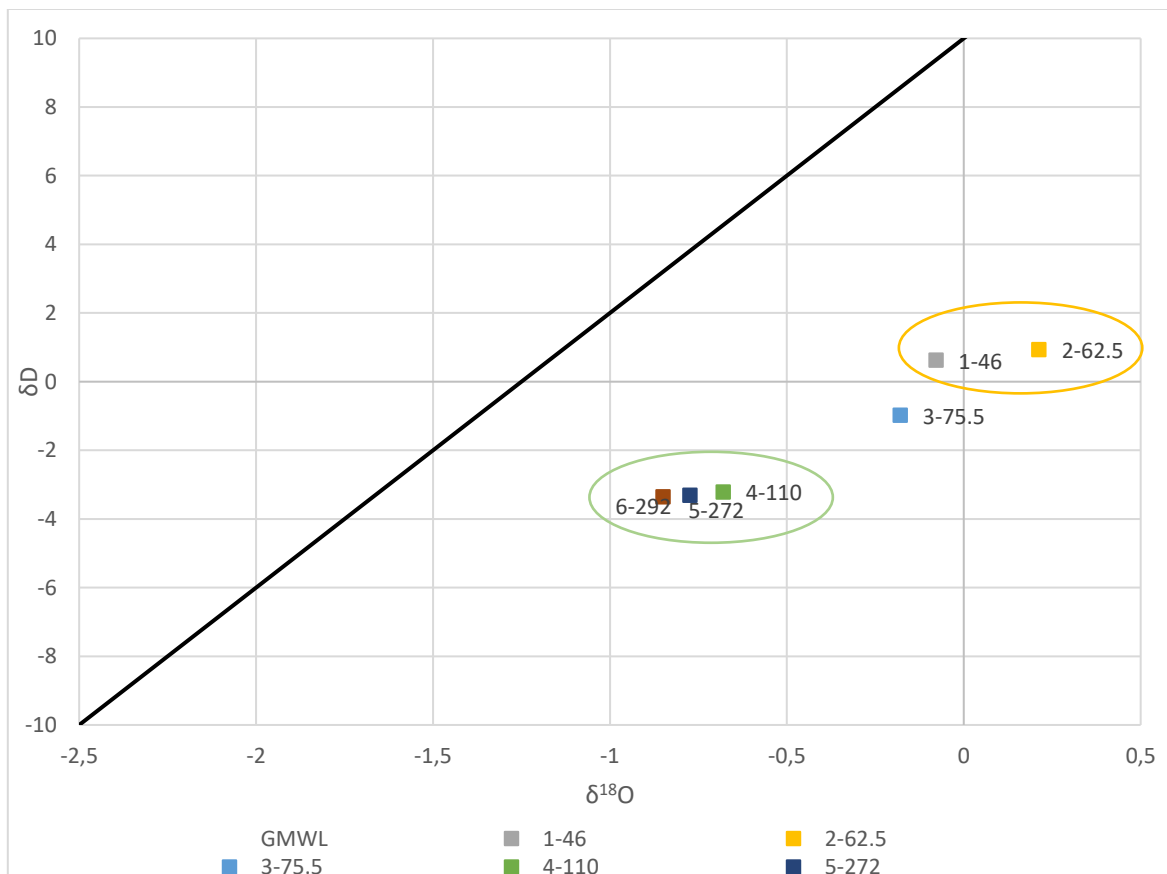


Figure 96 Delta plot of the phase 1 samples on a local scale showing the variation in isotope signatures with depth

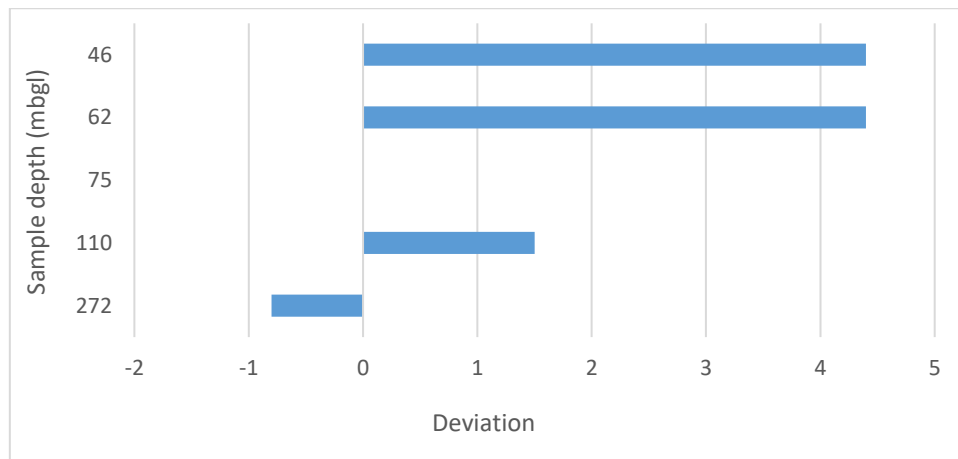


Figure 97 Illustration of the deviation between Deuterium excess for each sample

6.4 PHASE 2 WATER SAMPLING AND PRELIMINARY RESULTS

After the phase 2 drilling was completed, geophysical surveys were performed and once again preliminary raw survey data was provided to inform depth-specific water sampling, along with the geological logs for the hole. The raw data preview along with the depths at which sampling was selected is shown in Figure 98 to Figure 100.

Ten samples, numbered 7 to 16 as follow on from phase 1 samples, were taken at the following depths:

- 362 mbgl
- 383 mbgl; 389 mbgl – combined into single sample at 385 mbgl
- 450 mbgl
- 575 mbgl
- 623 mbgl
- 650 mbgl
- 695 mbgl
- 815 mbgl
- 885 mbgl
- 935 mbgl

The consideration of the remaining drilling fluid is also a concern with these collected samples, albeit that the hole was flushed for 9 hours (one drillers shift) and rested for 3 days while the geophysical surveys were conducted. The fluid profiles and water sampling were conducted last at a best attempt to collect representative samples as far as possible. While the overbalancing considerations were drill standing time costs and maintaining the open hole.

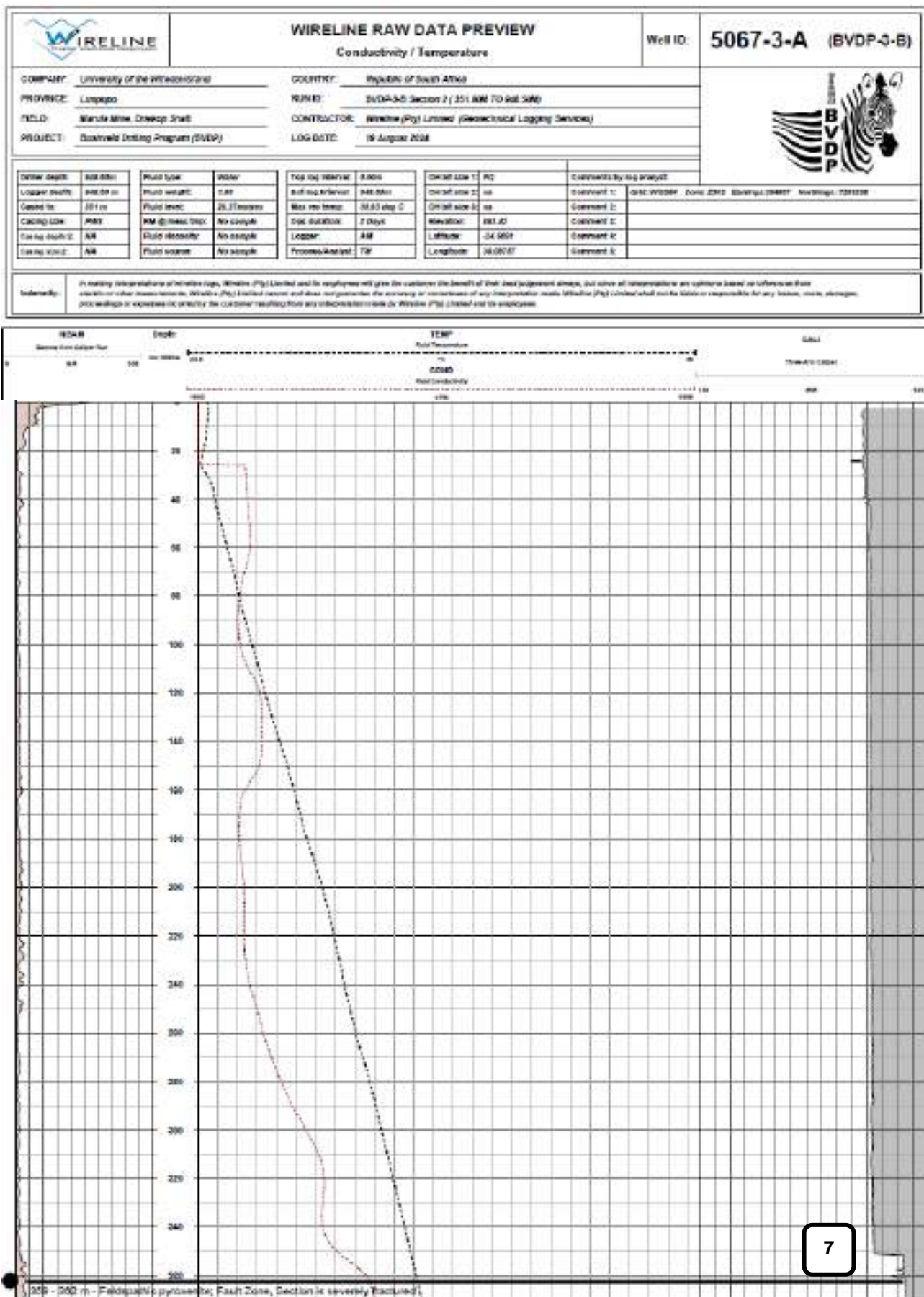


Figure 98 Raw geophysical data preview from phase 2 survey, for the purpose of selecting depths for fluid sampling (depth from 0 to 370 mbgl) showing sample 7 at a depth at 362 mbgl. Solid casing installed in phase 1 is noted to a depth of 350 mbgl

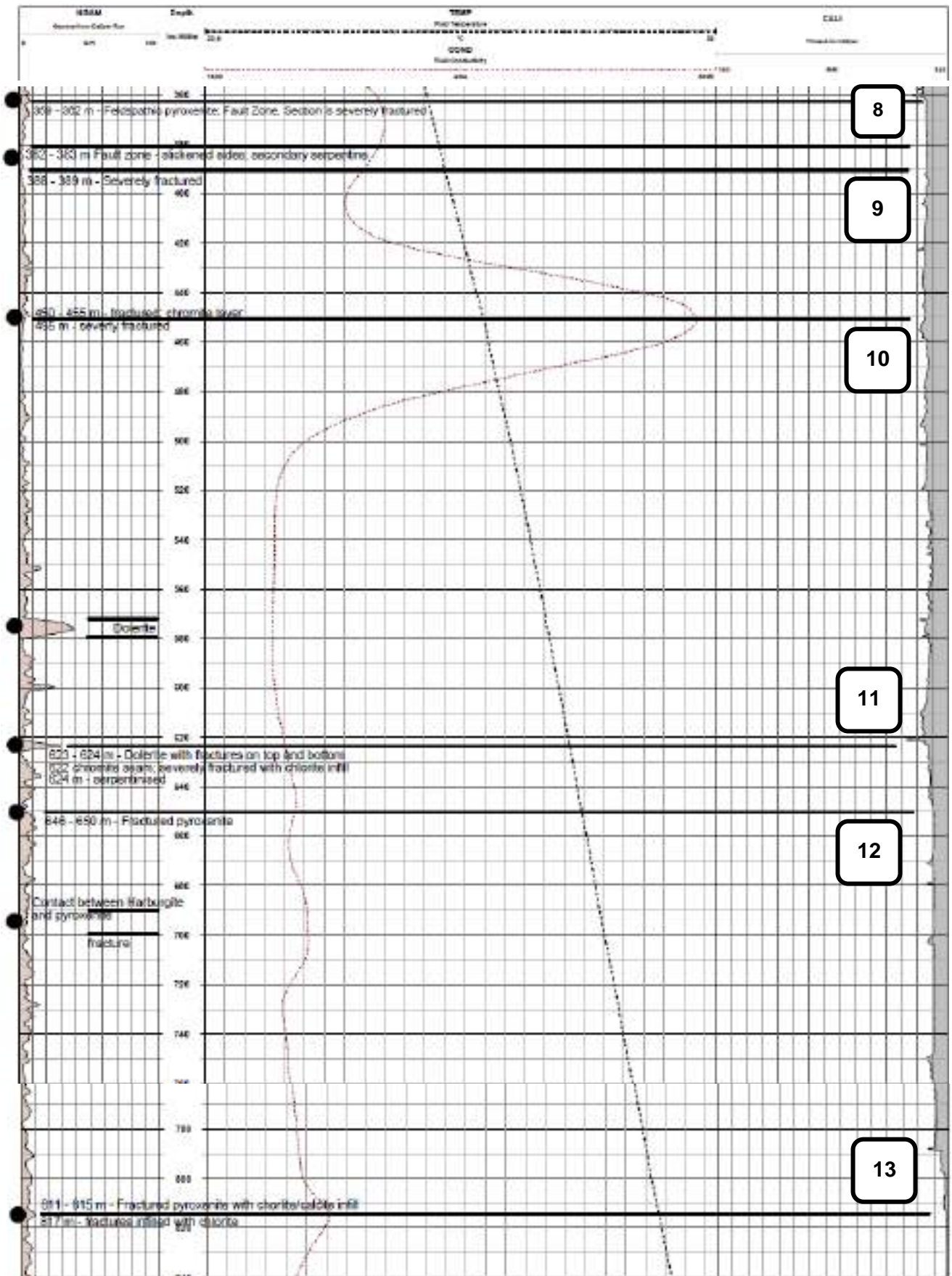


Figure 99 Raw geophysical data preview from phase 2 survey, for the purpose of selecting depths for fluid sampling (depth from 360 to 840 mbgl) showing sample 8 to 13 at a depth 383, 389, 450, 575, 623, 650 and 695 mbgl, respectively.

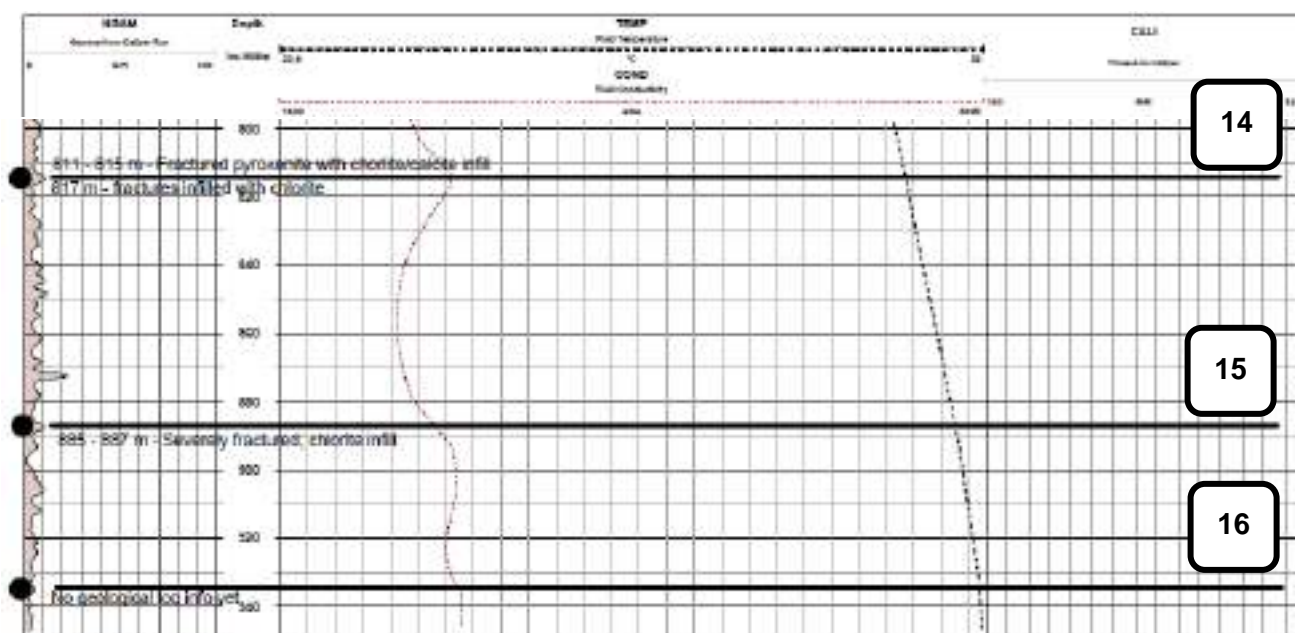


Figure 100 Raw geophysical data preview from phase 2 survey, for the purpose of selecting depths for fluid sampling (depth from 800 to 950 mbgl) showing sample 14 to 16 at a depth 815, 885 and 935 mbgl, respectively.

6.4.1 Water quality

Ten groundwater samples were analysed by a SANAS accredited laboratory for both the chemical compositions (anions and cations) as well as for dissolved micro determinants as per Table 21. From the Piper diagram (Figure 101), several interpretations can be made regarding the groundwater samples. Samples BVDP_362 and BVDP_385 cluster closely together, exhibiting a similar chemical composition characterised by an enrichment of sodium, potassium, and chloride. This grouping indicates that these samples belong to a sodium chloride (Na-K-Cl-SO_4) groundwater type. In contrast, groundwater sample BVDP_450 is completely isolated from the other two clusters, showcasing enrichment in calcium and chloride, which classifies it as a calcium sulphate (Ca-Mg-Cl-SO_4) type of groundwater. Additionally, samples BVDP_575, BVDP_623, BVDP_650, BVDP_695, BVDP_885, BVDP_935_A, and BVDP_935_B cluster together, revealing a similar chemical composition enriched with sodium and potassium. Notably, BVDP_935_A and BVDP_885 exhibit higher chloride concentrations than the other samples in this group, reinforcing the classification of this cluster as a sodium chloride (Na-K-Cl-SO_4) type.

The Durov diagram (Figure 102) provides insights into the pH and electrical conductivity (EC) of the groundwater samples. BVDP_362 and BVDP_385 show similar EC and pH values, ranging from 316 mS/m to 333 mS/m and 6.48 to 6.56, respectively. Conversely, sample BVDP_450 stands out with an isolated EC of 580.03 mS/m and a pH of 6.32, distinguishing it from the overall cluster of groundwater samples. In the cluster comprising BVDP_575, BVDP_623, BVDP_650, BVDP_695, BVDP_885, BVDP_935_A, and BVDP_935_B, the EC values are very similar, ranging from 221 mS/m to 248 mS/m, while the pH values span from 6.61 to 7.63.

The STIFF diagrams (Figure 103) further visualise the similarities and differences in chemical composition among groundwater samples taken at various depths. BVDP_362 and BVDP_385 display a nearly identical distribution of chemical components. In contrast, sample BVDP_450 presents a markedly different distribution, characterized by a notable high chloride enrichment. Meanwhile, samples BVDP_575, BVDP_623, BVDP_650, BVDP_695, BVDP_885, BVDP_935_A, and BVDP_935_B demonstrate a similar distribution of chemical components.

Lastly, the Schoeller diagram (Figure 104) highlights trends in chemical compositions across the groundwater samples. BVDP_362 and BVDP_385 exhibit a comparable trend in chemical composition distribution. In contrast, BVDP_450 shows a trend that diverges significantly from the overall chemical composition trends observed in the other samples. Finally, samples BVDP_575, BVDP_623, BVDP_650, BVDP_695, BVDP_885, BVDP_935_A, and BVDP_935_B display a generally similar trend in chemical composition, with slight variations among the samples in this cluster.

The water quality of the sample taken at 450 mbgl, does correspond the geophysical TDS profile, where an increase was seen peaking at 450 mbgl. However, the reason for this large spike in TDS is unclear yet, most probable are flushing and drilling fluid influences, with the stable isotopes to be analysed for further investigation. There is a clear trend in increasing chloride and calcium.

The samples from this phase 2 sampling also seem to plot off from the first run of sampling, plotting on the carbonate side of the Piper diagram, this is quote possible the effect of the drilling fluid and/or the flushing of the hole. For this phase, additionally a source water sample was collected and analysed for stable water isotope results. The next analysis would be to consider these end member and work toward a mixing model.

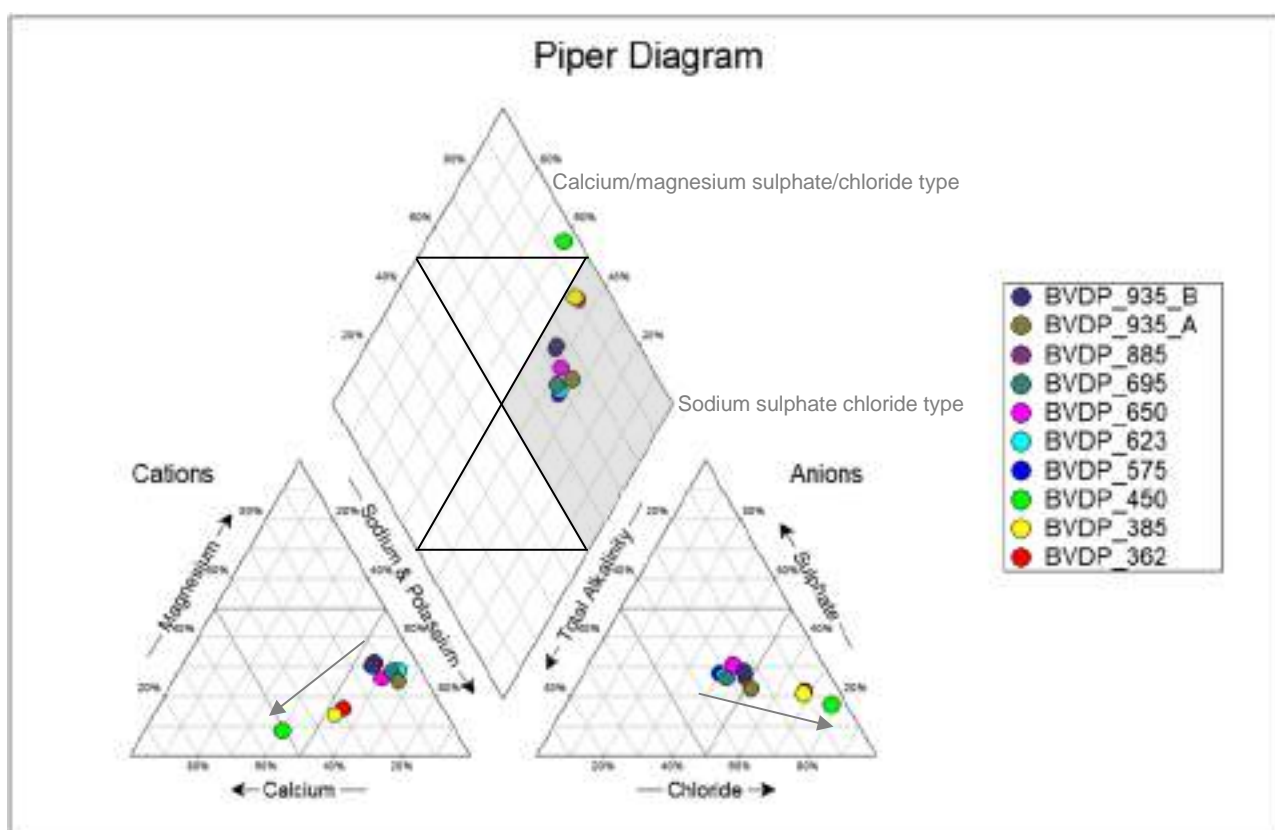


Figure 101 Piper diagram of the phase 2 groundwater samples.

Table 21 Phase 2 groundwater sampling results.

BVDP BOREHOLE (PHASE 2) SAMPLE ANALYSIS RESULTS											
Parameter	Unit	BVDP_362	BVDP_385	BVDP_450	BVDP_575	BVDP_623	BVDP_650	BVDP_695	BVDP_885	BVDP_935_A	BVDP_935_B
Sampling depth (mbgl)		362	385	450	575	623	650	695	885	935	935
Date		22/08/2024	22/08/2024	22/08/2024	22/08/2024	22/08/2024	22/08/2024	22/08/2024	22/08/2024	22/08/2024	22/08/2024
Time		09:12	09:48	10:32	11:15	11:54	12:31	13:15	15:08	14:16	15:45
Chemical determinants											
Turbidity	NTU	122	154	110	170	163	247	232	89.8	259	59.5
Colour	units Pt-Co	>500	>500	>500	>500	>500	>500	>500	268	>500	164
pH		6.48	6.56	6.32	6.67	6.61	6.66	6.69	7.59	7.2	7.63
EC	mS/m	316.21	332.32	580.03	228.86	228.86	238.75	230.75	227.05	248.02	221.56
Ca	mg/L	181.76	225.17	613.82	28.39	27.36	56.93	36.84	58.07	42.5	62.64
Mg	mg/L	59.62	57.34	61.78	70.47	73.67	70.37	74.03	89.08	76.73	85.78
Na	mg/L	378.09	408.93	543.152	293.61	299.59	298.76	292.51	287.55	370.88	284.3
K	mg/L	20.18	19.33	31.204	23.75	23.81	23.27	25.322	26.02	22.91	26.36
Total Alkalinity	mg CaCO ₃ /L	157.29	179.2	155.32	401.53	391.25	363.89	396.46	316.41	335.95	289.63
F	mg/L	0.58	0.42	1.23	2.45	1.35	2.25	2.05	0.64	0.61	0.58
Cl	mg/L	760.4	805	1948.1	356.17	376.72	412.46	393.9	431.47	488.52	398.5
NO ₂ as N	mg/L	0.013	0.01	0.011	<0.006	<0.006	0.012	0.006	0.012	0.014	2.384
NO ₃ as N	mg/L	0.33	0.3	0.31	0.33	0.32	0.32	0.3	0.86	0.3	16.22
SO ₄	mg/L	326.78	331.99	577.08	335.06	330.91	399.17	322.06	315	287.08	324.84
TDS	mg/L	1897.16	2039.33	3949.71	1523.92	1538.1	1579.88	1561.03	1564.27	1638.9	1589.74
PO ₄ as P	mg/L	<0.042	<0.042	<0.042	0.104	0.08	<0.042	0.048	<0.042	<0.042	<0.042
NH ₃ as N	mg/L	<0.101	<0.101	<0.101	<0.101	<0.101	<0.101	<0.101	19.65	<0.101	19.85
Total Organic Carbon as C	mg/L	243.45	314.55	333.01	604.72	636.49	557.37	601.86	249.24	245.53	233.54
Micro determinants (dissolved)											
Al	µg/L	3.286	<0.326	<0.326	3.737	0.367	<0.326	<0.326	1.108	<0.326	0.45
Sb	µg/L	1.745	1.796	1.24	4.486	4.44	3.878	4.202	4.078	0.336	4.304
As	µg/L	0.773	0.807	0.748	1.314	1.625	1.448	1.563	1.163	1.02	1.062
Ba	µg/L	46.979	70.129	72.187	21.756	19.991	34.458	22.641	19.879	14.417	20.217
B	mg/L	0.062	0.066	0.902	0.078	0.077	0.078	0.2	0.072	0.07	0.067
Cd	µg/L	0.173	0.168	0.093	0.283	0.193	0.15	0.082	0.093	0.015	0.056
Cr	µg/L	2.898	2.232	1.45	6.283	6.523	4.994	5.993	4.271	3.469	3.938
CN	µg/L	2.69	<0.73	<0.73	<0.73	<0.73	<0.73	0.82	0.89	0.81	0.81
Cu	mg/L	0.315	0.226	0.282	0.076	0.066	0.031	0.057	<0.010	<0.010	<0.010
Fe	mg/L	2.513	1.091	3.658	1.911	2.932	1.702	7.386	0.3	1.925	0.265
Hg	µg/L	2.234	1.363	0.794	1.86	1.409	1.303	1.323	2.283	1.352	2.429

Research-based deep drilling in the Bushveld Igneous Complex

Mn	µg/L	177.385	188.192	199.822	295.844	416.118	211.215	464.908	149.059	188.907	114.141
Ni	µg/L	24.549	27.641	29.964	47.811	46.558	43.524	46.738	40.522	37.69	38.493
Pb	µg/L	2.283	1.89	1.628	2.489	2.952	2.17	2.127	1.789	1.561	1.795
Se	µg/L	0.071	0.24	0.132	0.854	0.684	0.546	0.744	0.387	0.366	0.515
U	µg/L	1.738	1.625	1.636	2.194	1.679	1.634	1.622	1.729	1.695	1.748
Zn	mg/L	2.547	4.318	10.552	7.801	5.959	7.475	10.085	0.682	0.223	0.571

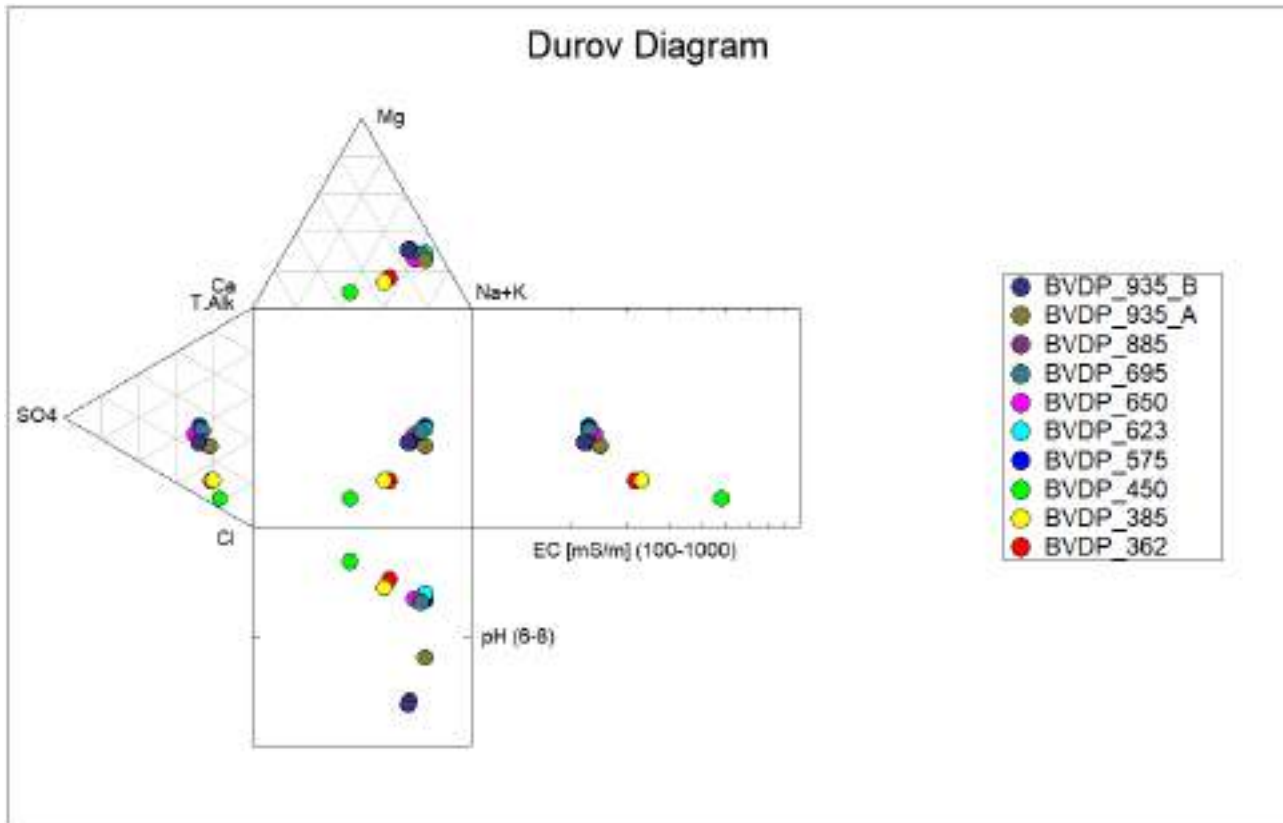


Figure 102 Durov diagram of the phase 2 groundwater samples.

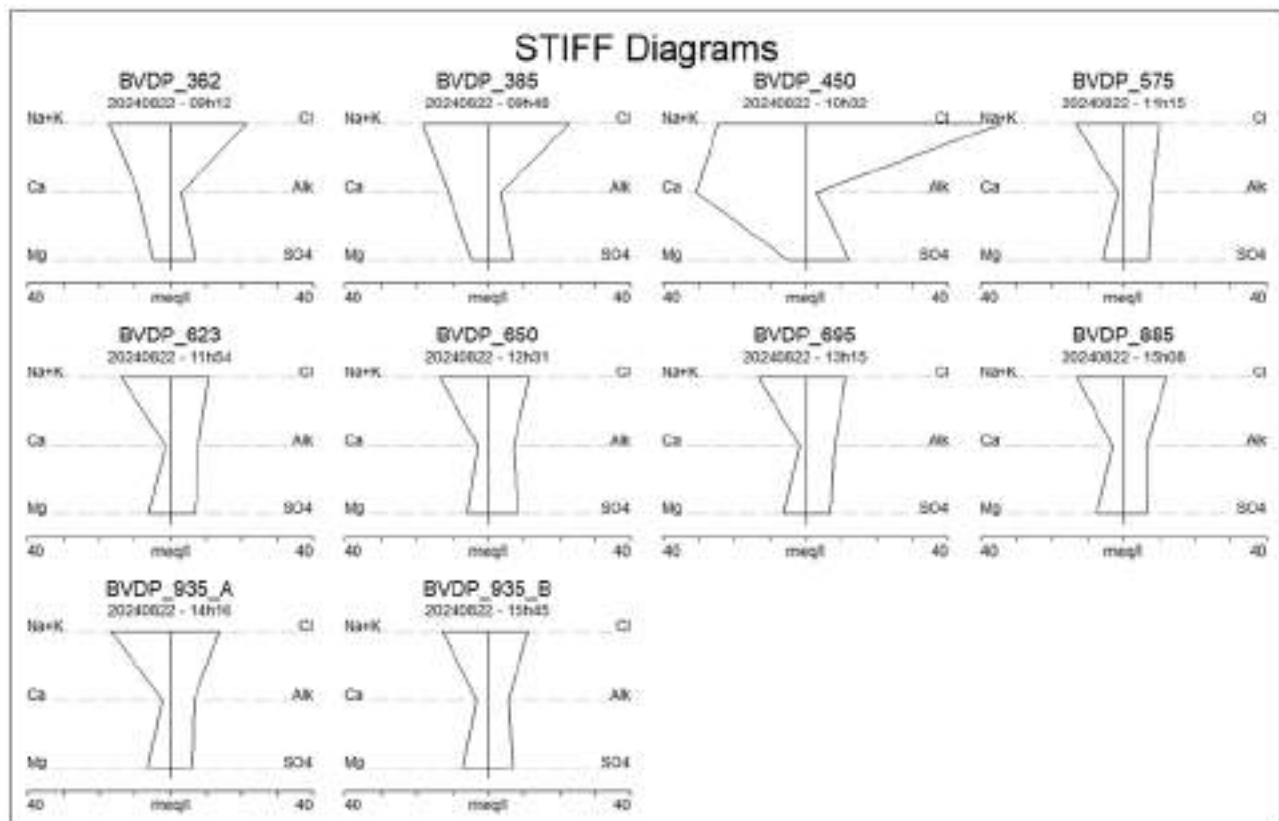


Figure 103 STIFF diagrams of the phase 2 groundwater samples.

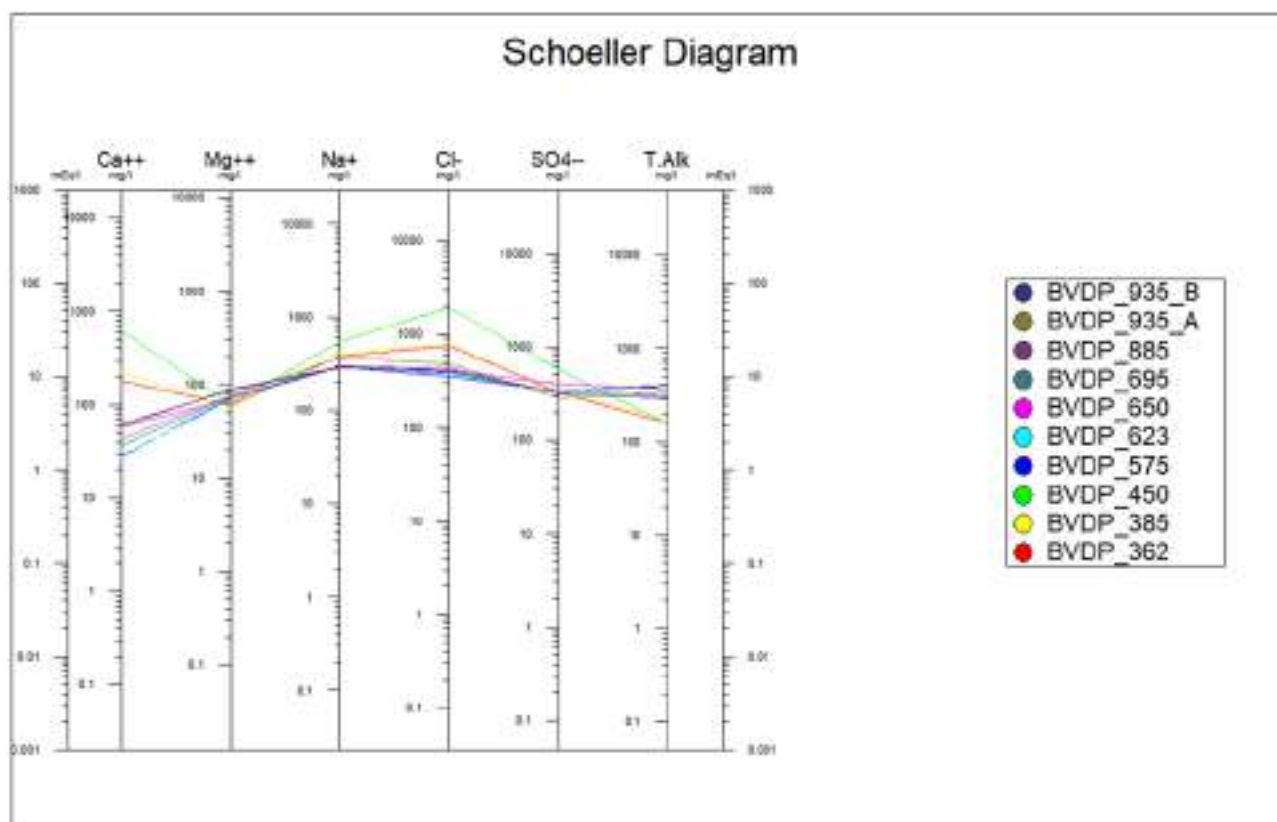


Figure 104 Schoeller diagram of the phase 2 groundwater samples.

6.4.2 Stable water isotope

The same filtering preparation was followed as described in Section 2.5.2.

For this round of analysis, the Picarro analysis system was considered because the amount of visible contamination in this round of samples posed a higher risk to the LGR instrumentation. When considering Picarro instrumentation for stable isotope analysis in water, particularly in potentially contaminated samples with organics, the approach is similar to what was described for LGR (Laser Gas Analyser) and LRMS (Laser Resonance Mass Spectrometry). Picarro instruments, like LGR, use Cavity Ring-Down Spectroscopy (CRDS) to measure isotope ratios of water. CRDS works by detecting the absorbance of laser light in a sample, where the time it takes for the light to decay inside a cavity correlates with the concentration of the target isotopes (e.g., $\delta^{18}\text{O}$ and $\delta^2\text{H}$). The technology offers high sensitivity and precision, similar to the methods used in LGR. However, as with LGR, contamination by volatile organic compounds (VOCs) or other dissolved organic materials can affect the laser absorbance or lead to spectral interferences, thereby compromising accuracy. One advantage of Picarro systems is their ability to use post-processing algorithms to identify and mitigate some interferences. However, organic contamination can still cause shifts in isotope ratios, leading to inaccurate readings unless samples are pre-treated to remove interfering compounds or carefully filtered before analysis.

In comparison to LRMS, which uses ionization of the sample and mass filtering, Picarro's CRDS technique does not involve ionization and thus avoids some of the matrix effects present in mass spectrometry. However, LRMS typically provides more detailed mass information and can be better for analysing complex mixtures where identifying the nature of contamination is critical. While the Picarro's CRDS instrumentation offers robust and precise isotope ratio measurements for uncontaminated water samples, it shares some of the same challenges as LGR when dealing with organic contamination. Pre-treatment, sample purification, or using multiple analysis methods may be necessary to ensure reliable results when organics are present in water samples. To this end, the samples were allowed time to settle and filtered for a second time to remove as much of the residual drilling fluid as possible.

With running these phase 2 samples on the Picarro system, an additional indicator was provided by the analysis software which indicates which samples showed trace contamination of organic materials. Thus, each sample is accompanied with an indication of whether that sample was clean, or trace contamination detected which may have slightly shifted for the isotope values (Figure 105).

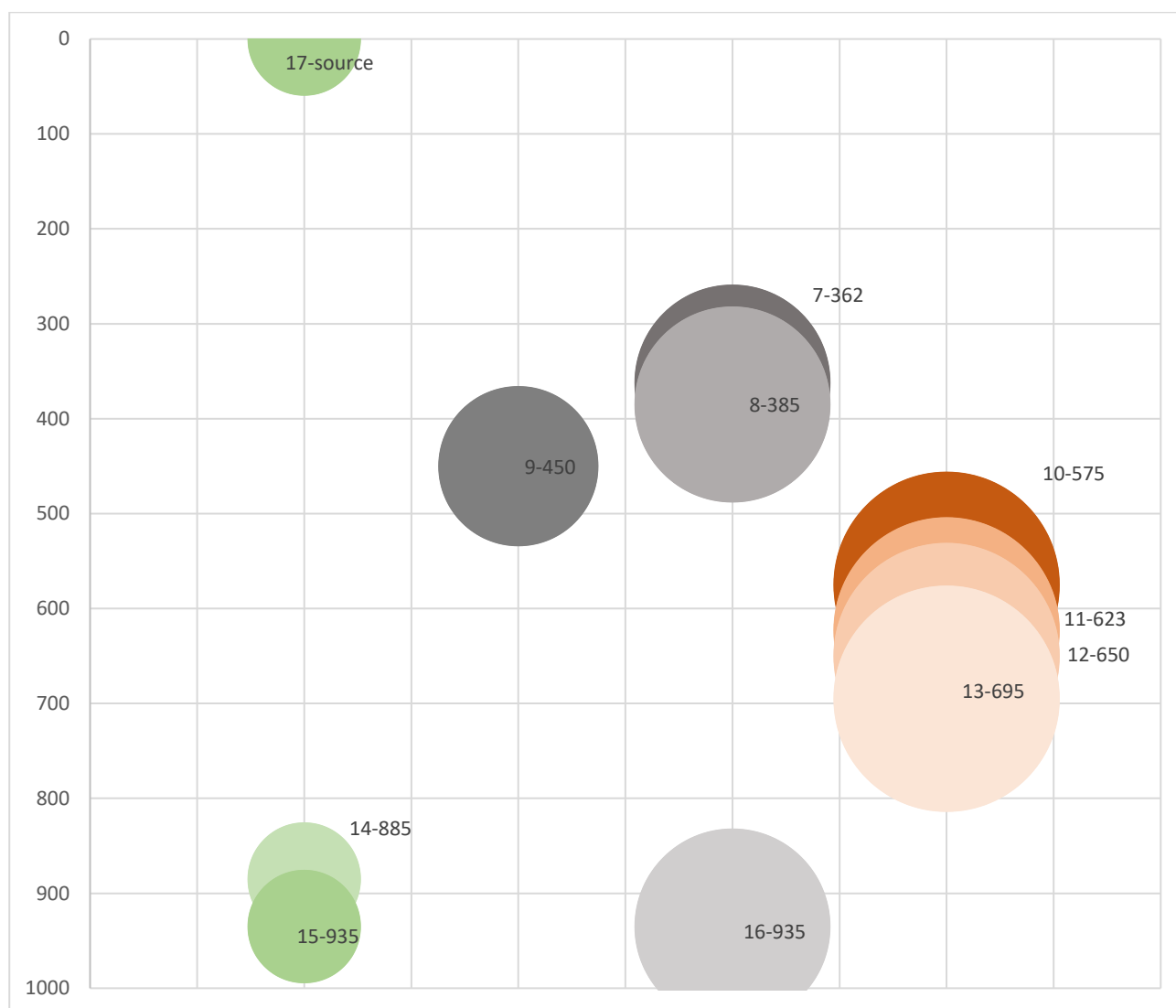


Figure 105 Illustration of which samples were flagged as having trace amounts of potential contamination (orange: both runs indicated contamination; grey: one of two runs indicated contamination (either trace and then clean, or clean and then trace detected; green: both runs were clean)

Samples indicating no trace of organic contaminants were samples 14 (885 mbgl), 15 (935 mbgl) and the source water (indicated as green zone on Figure 106). Samples indicating some trace of contamination included 7 (362 mbgl), 8 (385 mbgl), 9 (450 mbgl) and 16 (935 m) (grey on Figure 106). Samples indicating contamination at both runs were 10 (575 mbgl), 11 (623 mbgl), 12 (650 mbgl) and 13 (695 mbgl) (orange on Figure 106). From Figure 106, it might seem that the fractured zone at around 900 mbgl could have been from groundwater into the borehole and thus giving the no trace/clean indicator on the Picarro, however, the stable isotopes show that these samples have the same signature as the source water used to flush the hole before sampling. Thus, it would seem that the fresh water flushed into the hole has settled at the bottom and has little influence from the drilling fluid, albeit there is some mixing which could be from groundwater (Figure 31 – green circle). These samples have an enriched signal with both positive ratios and indicative of surface water source.

Samples indicating contamination at both runs were 10 (575 mbgl), 11 (623 mbgl), 12 (650 mbgl) and 13 (695 mbgl) (orange zone on Figure 106 and orange circle on Figure 107). These samples are also show enriched isotope signatures and plot close to the source water and associated deep samples already discussed, albeit that these plot slightly lower down the delta plot. The depth range of these samples is from 575 to 695 mbgl and indicate that this zone still has higher concentrations of drilling fluids present. There is also a large peak in the download TDS profile above this zone at approximately 450 mbgl, perhaps indicating some transition to a zone of higher drilling fluid concentrations. Alternatively, the peak in TDS could also perhaps indicate saline groundwater moving into the borehole at this depth.

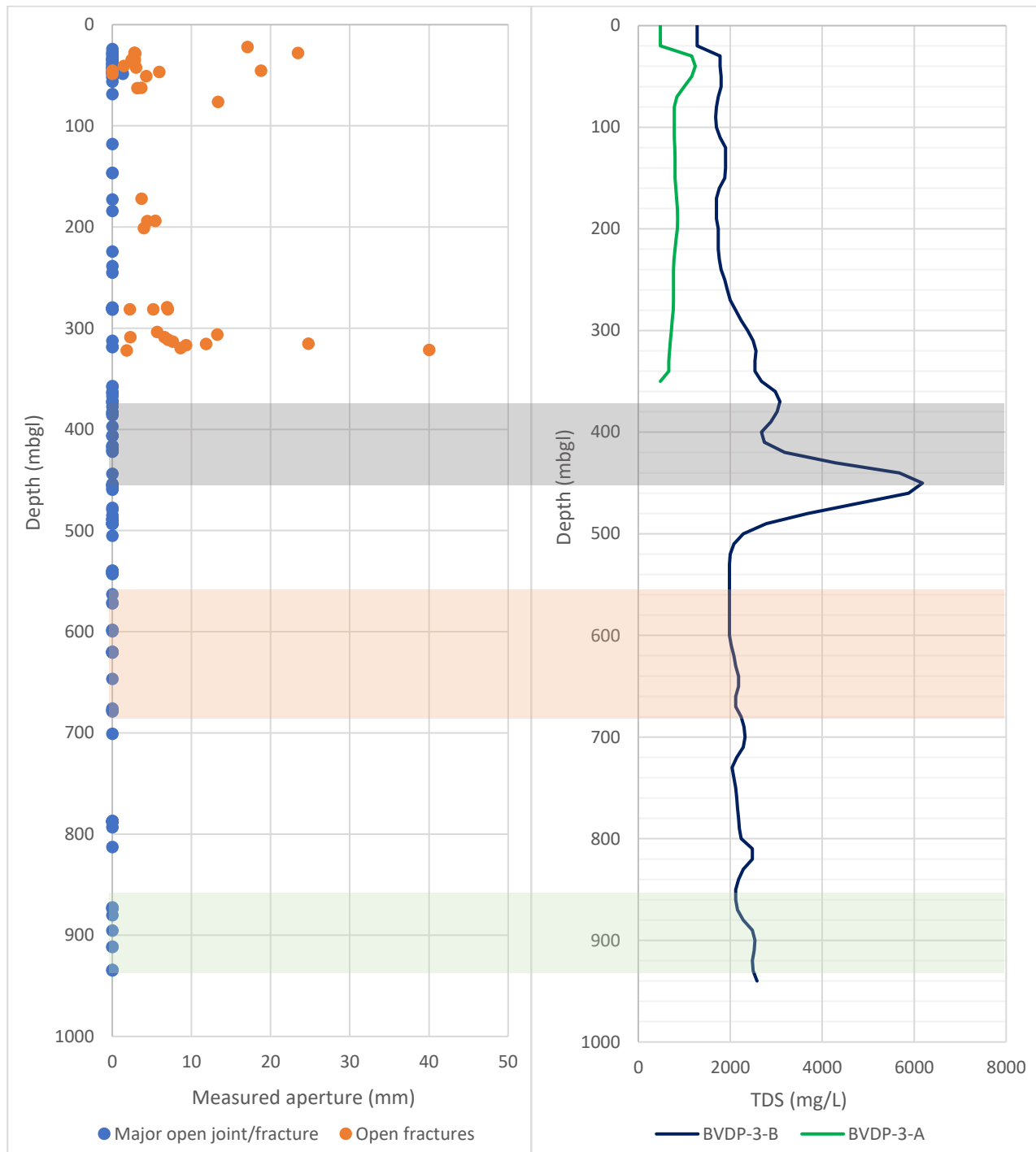


Figure 106 Zones of samples based on Picarro indication of degree of trace organic contaminants that might affect isotopes results (orange: both runs indicated contamination; grey: one of two runs indicated contamination (either trace and then clean, or clean and then trace detected; green: both runs were clean)

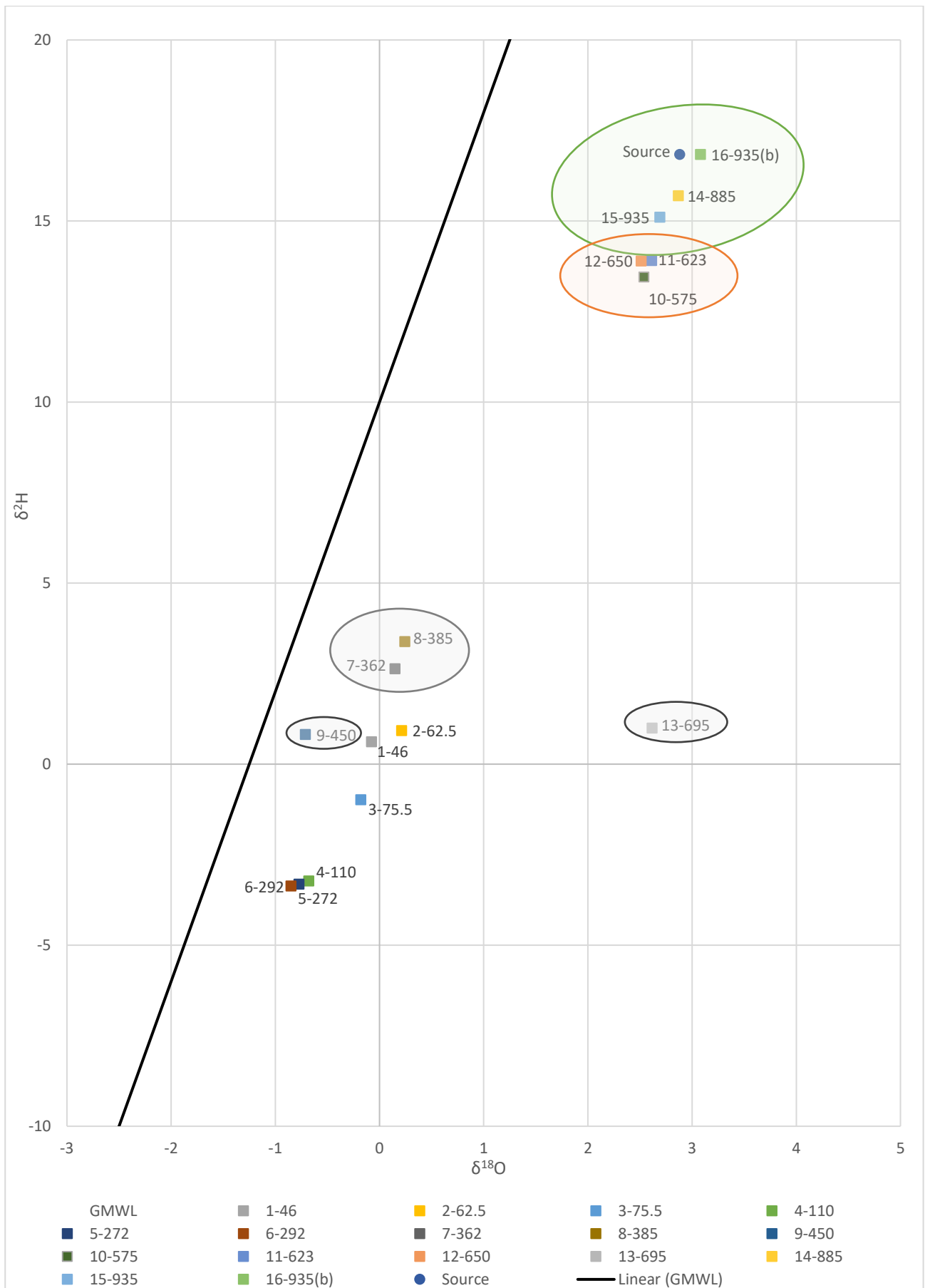


Figure 107 Delta plot of phase 1 and 2 samples on a local scale showing the variation in isotope signatures with depth. Labels denote sample number and depth at which sample was collected. Samples 1 – 6 form Phase 1 and samples 7 – 16 and source form Phase 2. The source sample is the surface clean water supply used to flush the hole.

Samples indicating some trace of contamination included 7 (362 mbgl), 8 (385 mbgl), 9 (450 mbgl) and 16 (935 m) (grey zone on Figure 106 and 3 grey circles on Figure 107). These samples showing traces of organic contaminant, but slightly less than the previous group, and include mostly the shallower samples for this phase 2 sampling except for a single deep sample. These samples are less enriched than those of the previous groups discussed yet are still considered more enriched than traditionally groundwater samples. Samples 7 (362 mbgl) and sample 8 (385 mbgl) plot above the previous phase 1 shallow samples, which is opposite to what would be traditionally expected, namely deeper groundwater samples progressively becoming more depleted in isotope ratios. Yet, considering the source water used to flush the hole, this clear trend in more depleted signatures could indicate mixing with inflowing groundwater. Sample 9 (450 mbgl) shows a distinct signature further along the increasing depletion trend, which could indicate higher groundwater mixing, especially considering the severely fractured features as well as a chromite layer were noted in the geological log at 450 – 455 mbgl. Interestingly, sample 13 (695 mbgl) also plots with a distinct signature with a clear reduction in the d-excess, which could be HCO_3 . On the geological log, a contact between Harzburgite and pyroxenite, as well as fractures are noted. Potentially, indicating mixing with a different groundwater source with a slightly different water type. There is also a slight peak in the TDS profile at this depth (Figure 81).

6.5 DRILLING FLUID SAMPLING AND PRELIMINARY ANALYSIS

Drilling fluids are primarily involved in exploration drilling as a protective measure to ensure that the structural integrity of the borehole is not compromised, thereby increasing the efficiency and success of the drilling (Bendi et al., 2024). Additionally, these drilling fluids ensure that cuttings and associated gas in the borehole are transported to the surface, prevents pressure build-up in the borehole, and enhancing drill bit performance through temperature control and lubrication (Bendi et al., 2024).

Various sources have highlighted the complexity of selecting a specific drilling fluid based on the heterogenous subsurface nature related to subsurface temperature- and pressure systems (Guancheng et al., 2022). The choice of drilling fluid is therefore not only dependent of the type of subsurface geological composition but the target drilling depth and environmental considerations (Bendi et al., 2024). The drilling muds for the BVDP borehole drilling were sourced from AMC Drilling Optimisation, which mainly focuses optimizing the performance of water-based drilling fluids which includes mostly water, clays and additives.

The drilling fluids that were used during drilling of the BVDP deep borehole are:

- AMC Corewell (produces a fluid system)
- AMC EZEE PAC L (highly dispersive low viscosity cellulose polymer)
- AMC EXEE TROL (highly dispersive, versatile blend of polymers)
- AMC FLOC DD (promotes settlement of fine to colloidal sized drill cuttings in non-dispersed, polymer and low-solids water-based drilling fluids)
- AMC LIQUI POL (rapid yielding, high molecular weight polymer in liquid)
- AMC TORQUE GUARD (extreme pressure lubricant)

According to Simona et al., (2018), drilling fluids have the ability to change the groundwater chemistry and the ion exchange ratio conditions when mixed with groundwater during drilling. Samples were collected on site as per “BVDP – Drilling Fluid Sampling Protocol”. These samples included three samples per sampling event: BVDP_Source; BVDP_In and BVDP_Out. BVDP_Source is a sample of the source water that is mixed with the drilling fluid; BVDP_In is collected at the drilling rig which is indicative of the mixed water and drilling fluids that is used for drilling; and, BVDP_Out is collected at the inflow tank of the solid-removal unit as per Figure 108.

The chemical composition of the drilling fluids on three different sampling occasions in July 2024, were analysed by an accredited laboratory to compare with the groundwater quality of the BVDP deep borehole as per Table 22. It should be noted that the groundwater samples that were analysed at specific depths, were done after the borehole was purged, thereby attempting to reduce the concentrations of drilling fluids in the

samples. This can be seen when comparing the total dissolved organic carbon as C (DOC) concentrations of the depth specific sample with the drilling fluid samples (BVDP_In and BVDP_Out). In order for the laboratory to analyse the chemical composition of the drilling fluids, dilution with a type II polisher was done x500, which may lead to inaccurate/compromised EC and pH concentrations.

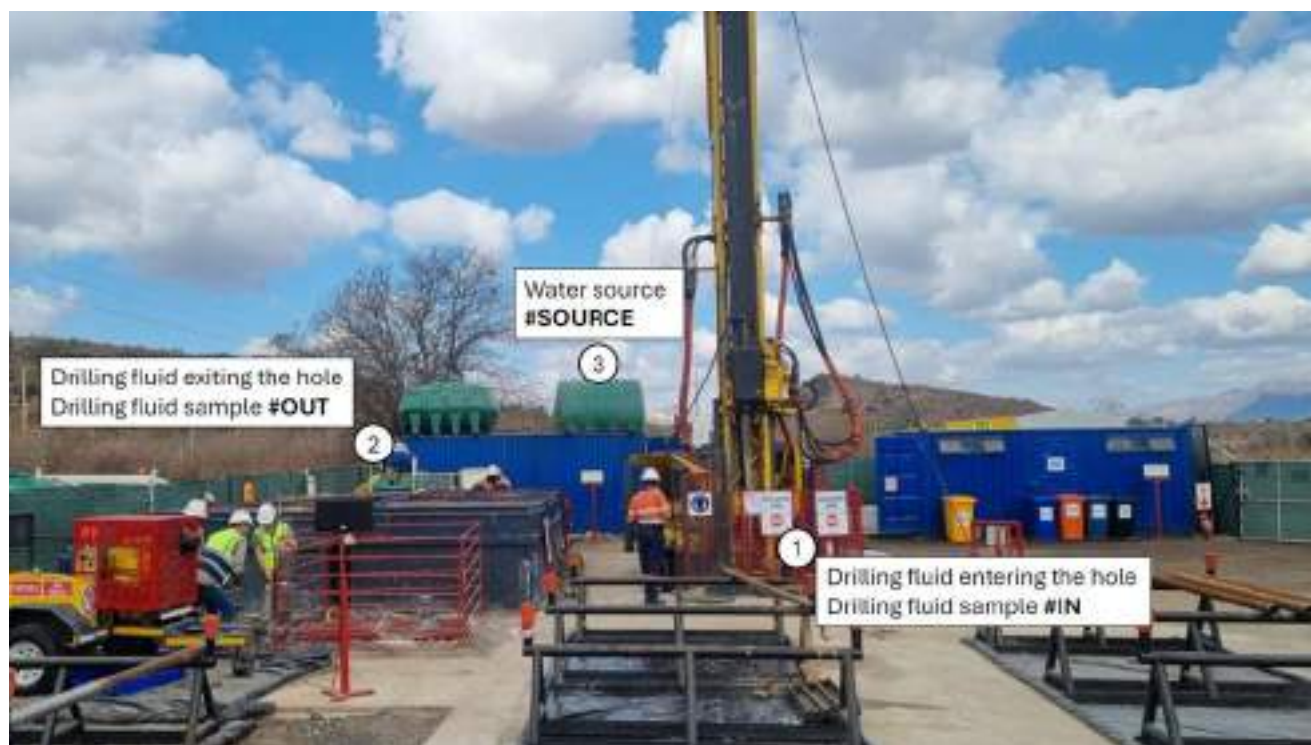


Figure 108 "BVDP- Drilling Fluid Sampling Protocol" locations.

The following can be interpreted from the chemical composition diagrams:

- 10 July 2024: The Piper, Durov and STIFF diagrams (Figure 109 to Figure 111) indicates that chemical composition of BVDP_Source_1 and BVDP_In_1 are similar being a calcium sulphate water ($\text{Ca(Mg)Cl(SO}_4\text{)}$), in comparison to BVDP_Out_1 which is also a calcium sulphate water being more enriched with bicarbonate. The Schoeller diagram (Figure 112) indicates that the chemical trend of BVDP_Source_1 and BVDP_In_1 are overall similar in comparison to BVDP_Out_1, which shows a unique chemical trend.
- 16 July 2024: The Piper, Durov and STIFF diagrams (Figure 113 to Figure 115) indicates that chemical composition of BVDP_In_2 and BVDP_Out_2 are similar being a calcium sulphate water ($\text{Ca(Mg)Cl(SO}_4\text{)}$), in comparison to BVDP_Source_2 which is a sodium chloride (Na(K)ClSO_4) water being more enriched with sodium and potassium. The Schoeller diagram (Figure 116) indicates that the chemical trend of BVDP_In_2 and BVDP_Out_2 are overall similar in comparison to BVDP_Source_2, which shows a different chemical trend.
- 23 July 2024: The Piper, Durov and STIFF diagrams (Figure 117 to Figure 119) indicates that chemical composition of BVDP_Source_3, BVDP_In_3 and BVDP_Out_3 are similar being a sodium chloride (Na(K)ClSO_4) water. The Schoeller diagram (Figure 120) indicates that the chemical trend of BVDP_In_3 and BVDP_Out_3 are overall similar in comparison to BVDP_Source_3, which shows a slight deviation from the overall chemical trend.

Table 22 Drilling fluid sample analysis results.

BVDP BOREHOLE (PHASE 2) SAMPLE ANALYSIS RESULTS										
Parameter	Unit	BVDP_Source_1	BVDP_In_1	BVDP_Out_1	BVDP_Source_2	BVDP_In_2	BVDP_Out_2	BVDP_Source_3	BVDP_In_3	BVDP_Out_3
Date		10/07/2024	10/07/2024	10/07/2024	16/07/2024	16/07/2024	16/07/2024	23/07/2024	23/07/2024	23/07/2024
Time		07:30	07:30	16:00	08:45	08:45	08:45	08:00	08:00	10:00
Current drilling depth		545.45	545.45	545.45	626	626	626	713.45	713.45	713.45
Chemical determinants										
Turbidity	NTU	2.26	483	>800	34.4	141	128	2.71	218	183
Colour	units Pt-Co	14	>500	>500	42	>500	>500	23	>500	>500
pH		6.83	6.61	6.45	6.55	6.38	6.28	6.47	6.18	6.16
EC	mS/m	103.99	<LOD	<LOD	187.15	<LOD	<LOD	192.4	<LOD	<LOD
Ca	mg/L	47.4	38.33	25	64.07	46.81	43.71	63.48	54.25	43.75
Mg	mg/L	45.27	49.95	49.55	74.63	68.01	69.84	74.5	96.25	101.27
Na	mg/L	103.02	99.24	103.56	210.27	161.19	162.85	215.85	232.11	237.59
K	mg/L	10.38	14.26	2.24	20.61	20.44	20.24	22.83	34.45	35.09
Total Alkalinity	mg CaCO ₃ /L	127.22	180.6	279.7	156.51	181.04	174.8	170.58	222.38	220.6
F	mg/L	0.5	0.52	0.5	0.39	0.53	0.43	0.45	0.4	0.42
Cl	mg/L	147.88	187.56	139.7	279.71	238.35	236.98	288.68	339.77	355.43
NO ₂ as N	mg/L	7.74	0.043	0.27	8.93	8.94	7.81	8.42	13.19	14.43
NO ₃ as N	mg/L	24.7	0.19	1.8	58.2	27.7	27.8	62.2	44.1	45.7
SO ₄	mg/L	155.91	111.24	82.86	292.16	208.64	206.54	295.87	272.68	261.66
TDS	mg/L	786.22	709.11	733.49	1418.85	1097.49	1083.82	1469.1	1518.8	1532.69
PO ₄ as P	mg/L	<0.042	<0.042	0.075	<0.042	<0.042	<0.042	<0.042	0.046	0.056
NH ₃ as N	mg/L	4.947	0.103	0.348	17.13	<0.101	<0.101	18.3	<0.101	<0.101
TOC as C	mg/L	4.83	983.72	917.03	6.4	1514.86	1025.67	6.54	1106.45	2491.92
Micro determinants (dissolved)										
Al	µg/L	6.899			3.417			2.817		
Sb	µg/L	1.905			4.442			4.377		
As	µg/L	0.56			0.944			0.898		
Ba	µg/L	27.967			18.16			17.997		
B	mg/L	0.066	<4	<0.8	0.09	<0.8	<0.8	0.093	<0.8	<0.8
Cd	µg/L	<0.001			<0.001			<0.001		
Cr	µg/L	2.088			1.357			1.096		
CN	µg/L	1.08	1.17	1.04	1.08	1.14	1.12	1.34	1.28	1.18
Cu	mg/L	<0.010	<1	<0.2	<0.010	<0.2	<0.2	<0.01	<0.2	<0.2
Fe	mg/L	0.102	12.61	18.6	0.013	8.412	8.006	0.011	10.194	9.804

Hg	µg/L	0.599			0.386			0.351		
Mn	µg/L	0.663			25.144			14.926		
Ni	µg/L	22.504			53.662			42.614		
Pb	µg/L	0.03			0.095			0.046		
Se	µg/L	0.097			0.72			1.306		
U	µg/L	1.317			0.754			0.893		
Zn	mg/L	0.018	<0.500	<0.100	0.028	<0.100	<0.100	0.063	<0.100	<0.100

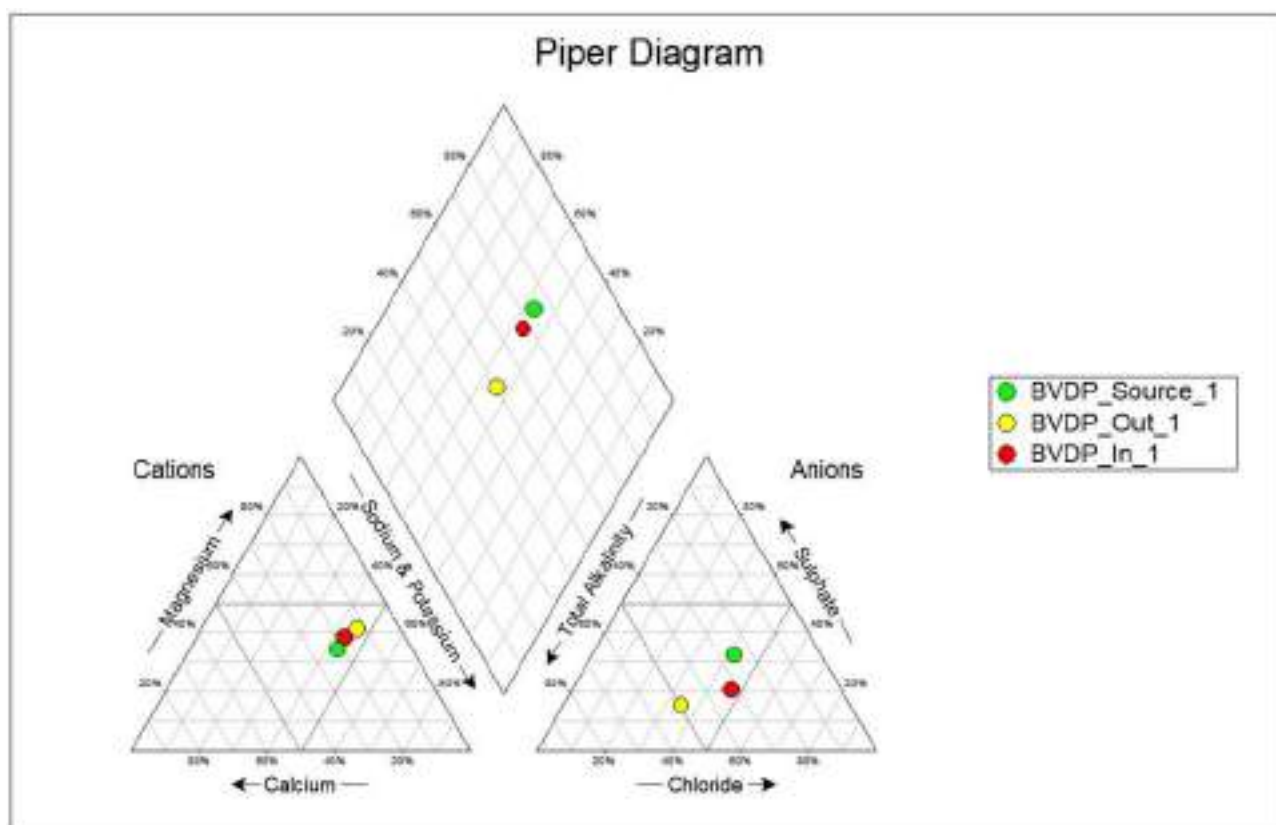


Figure 109 Piper diagram of the drilling fluid samples from 10 July 2024.

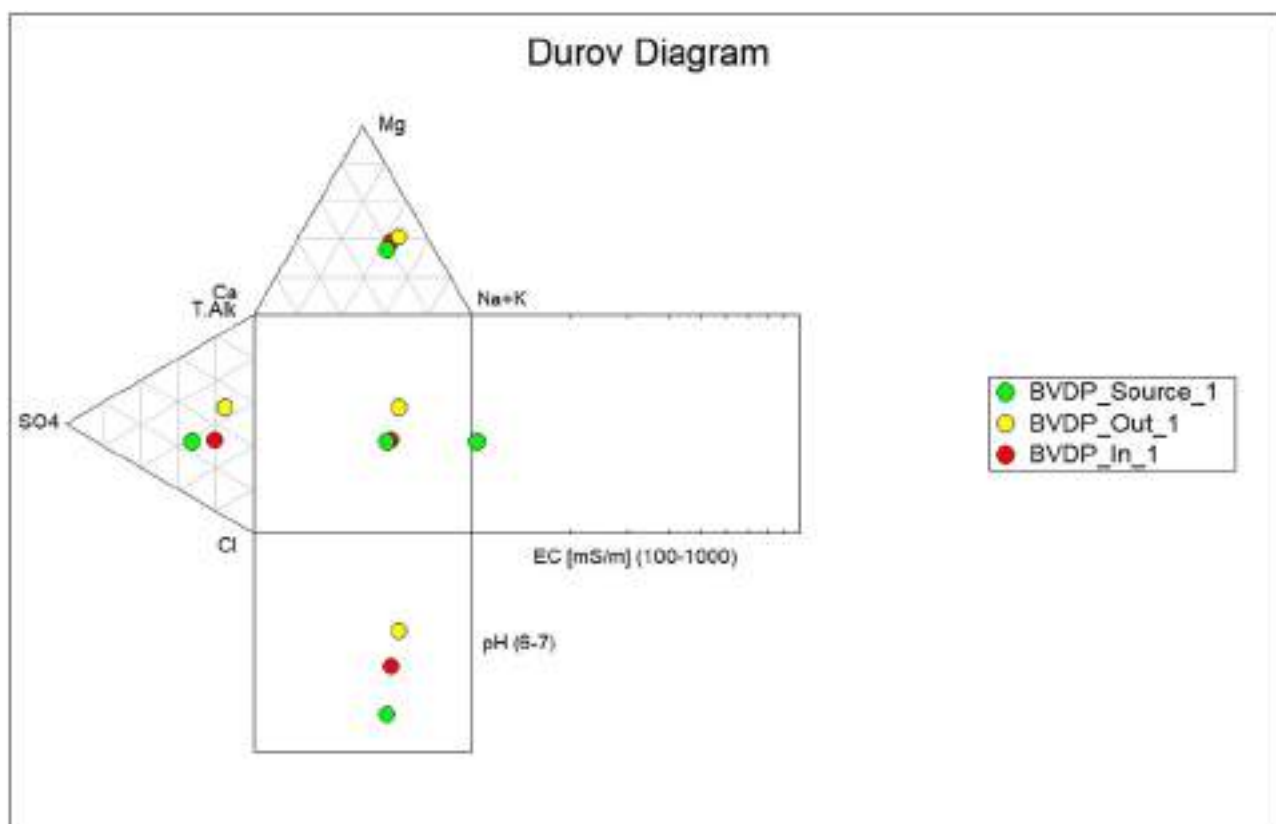


Figure 110 Durov diagram of the drilling fluid samples of 10 July 2024.

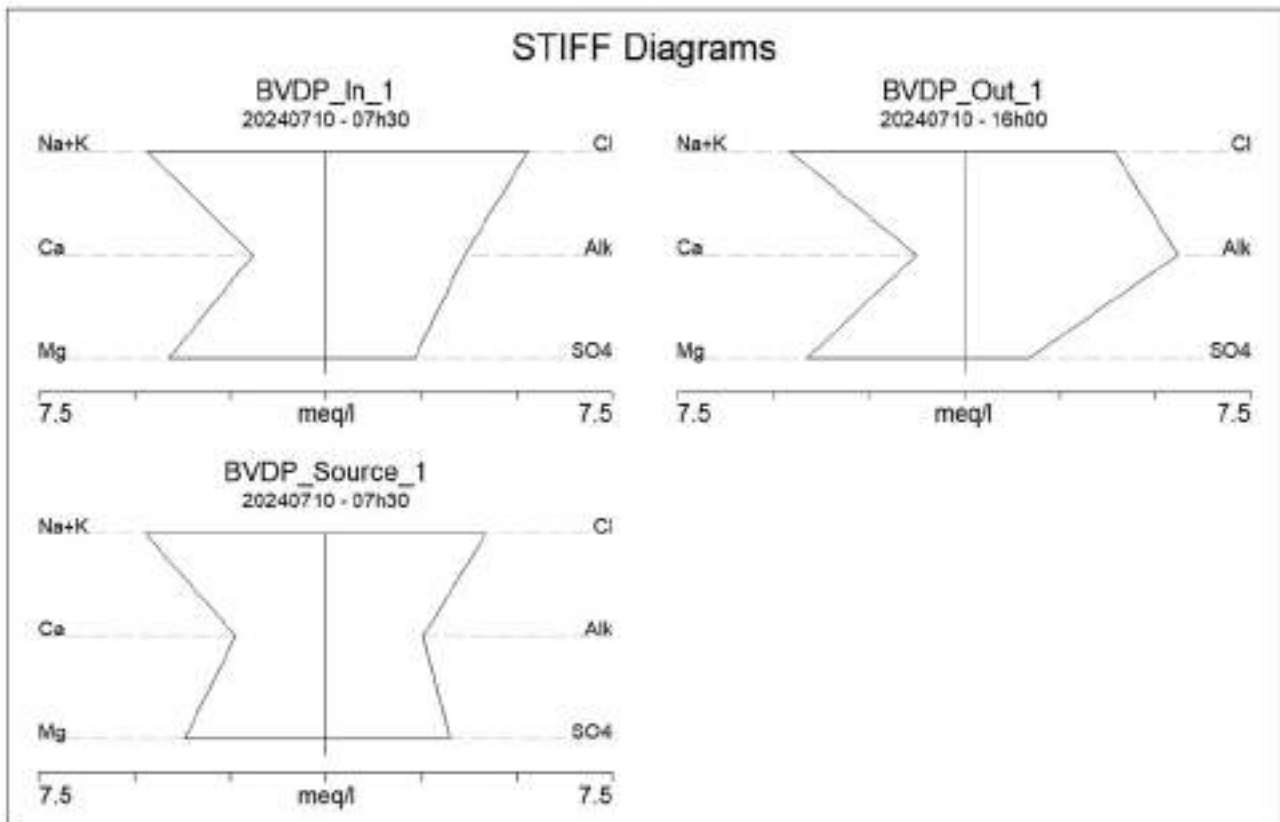


Figure 111 STIFF diagram of the drilling fluid samples of 10 July 2024.

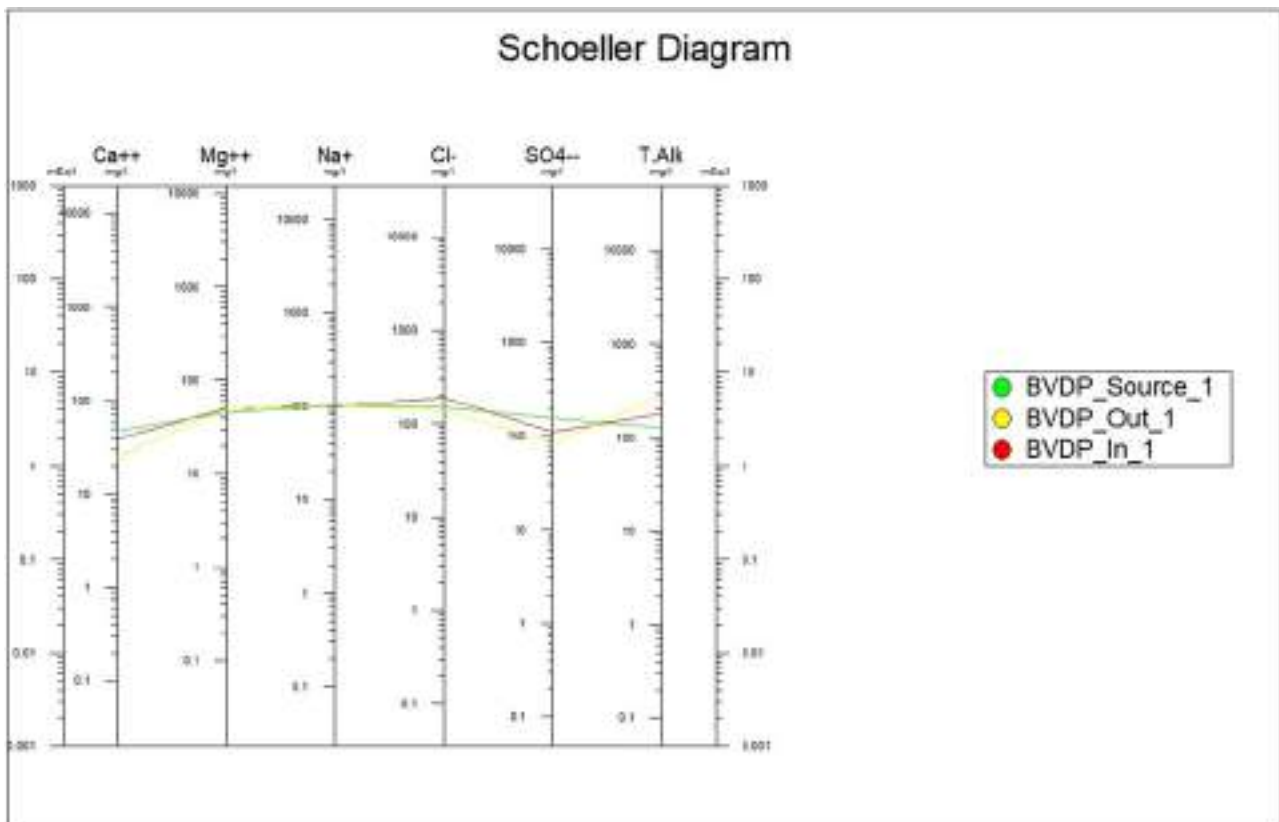


Figure 112 Schoeller diagram of the drilling fluid samples of 10 July 2024.

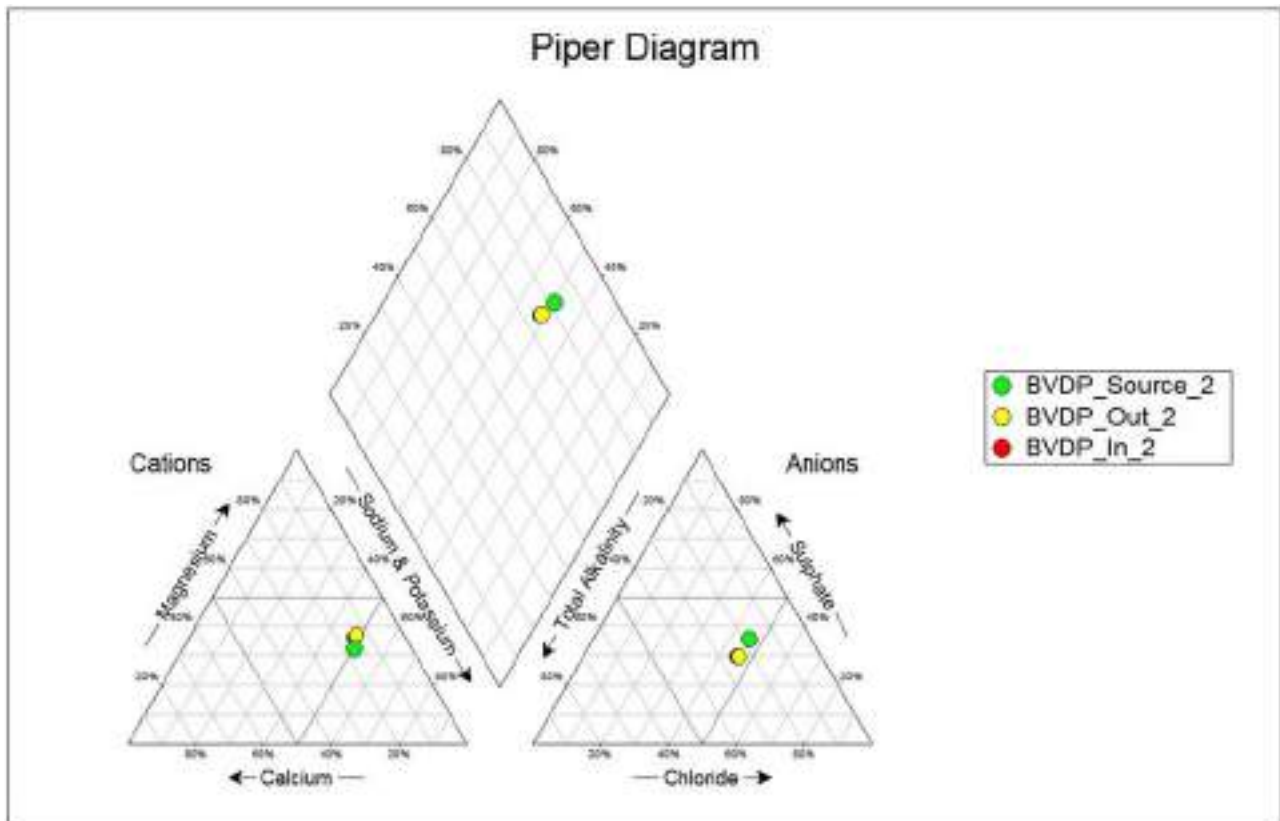


Figure 113 Piper diagram of the drilling fluid samples of 16 July 2024.

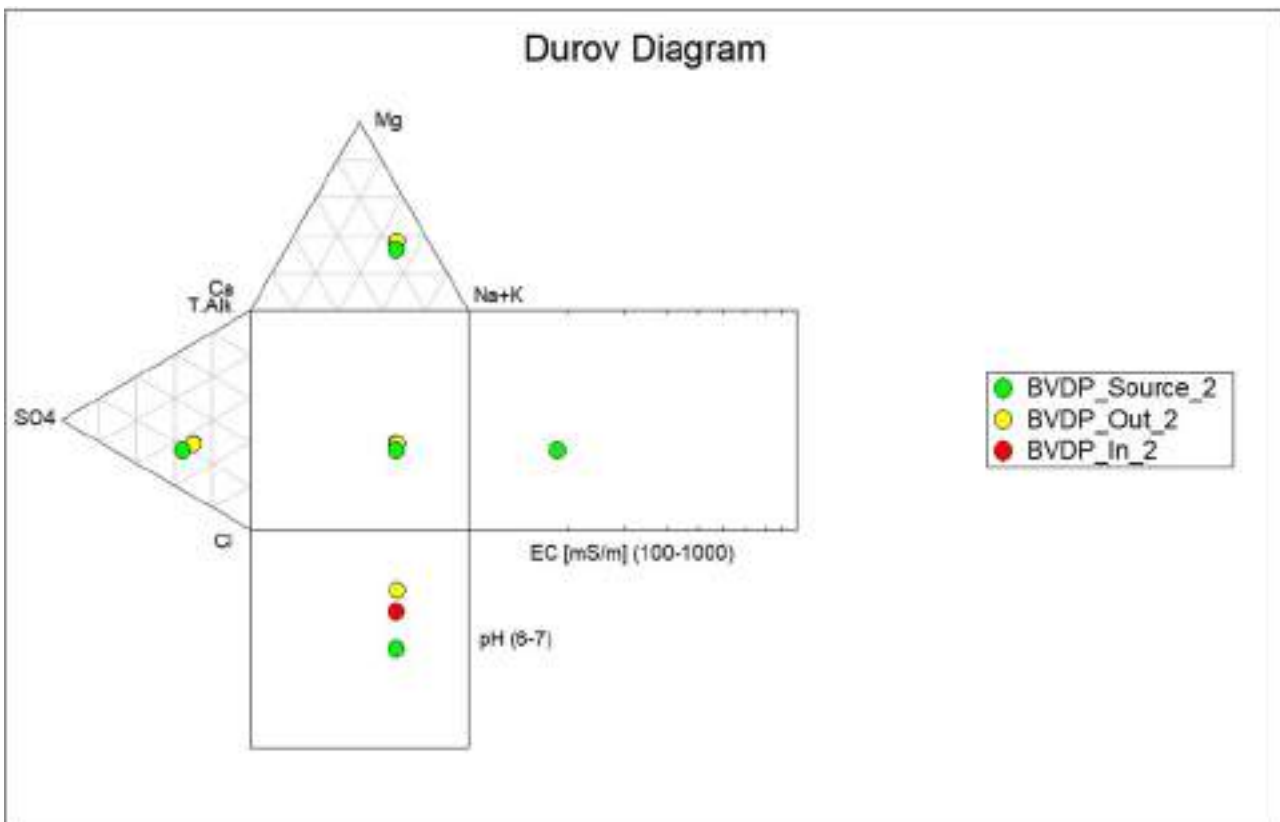


Figure 114 Durov diagram of the drilling fluid samples of 16 July 2024.

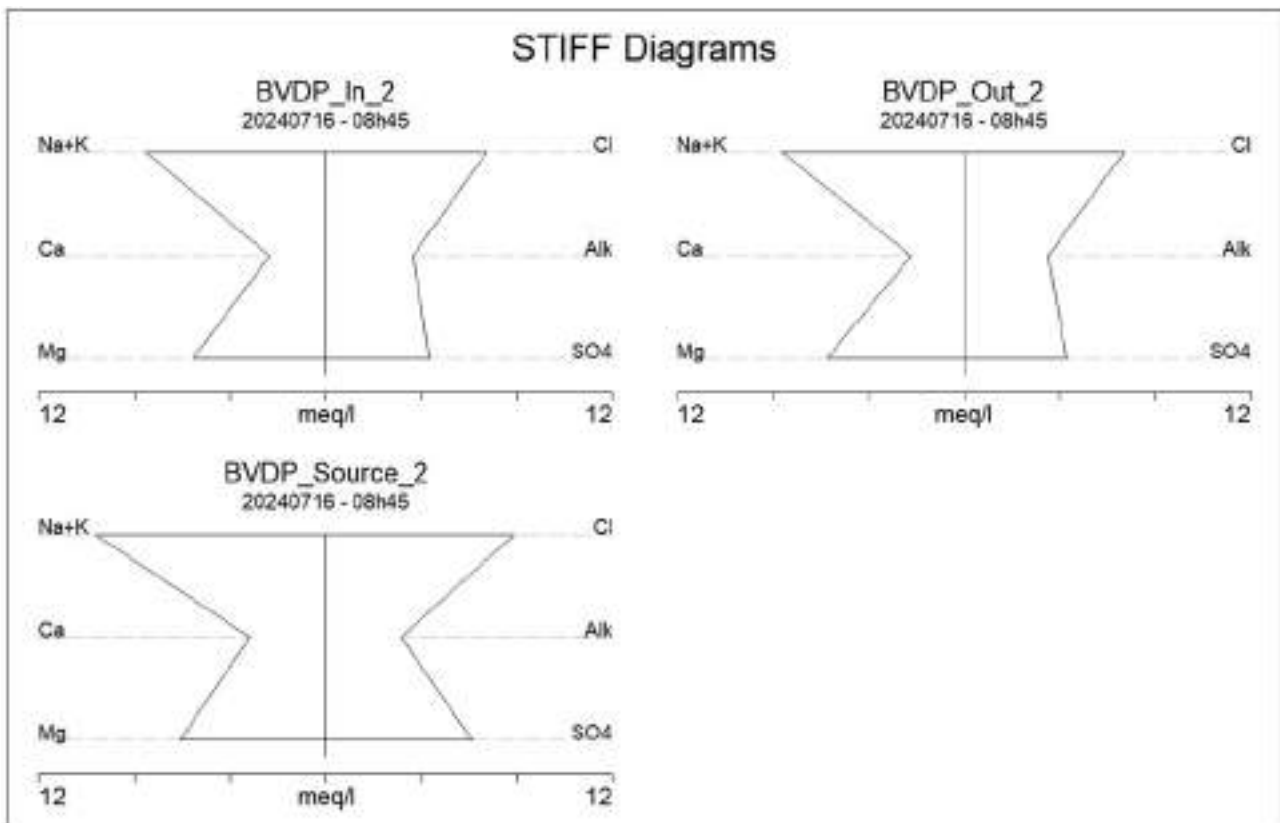


Figure 115 STIFF diagrams of the drilling fluid samples of 16 July 2024.

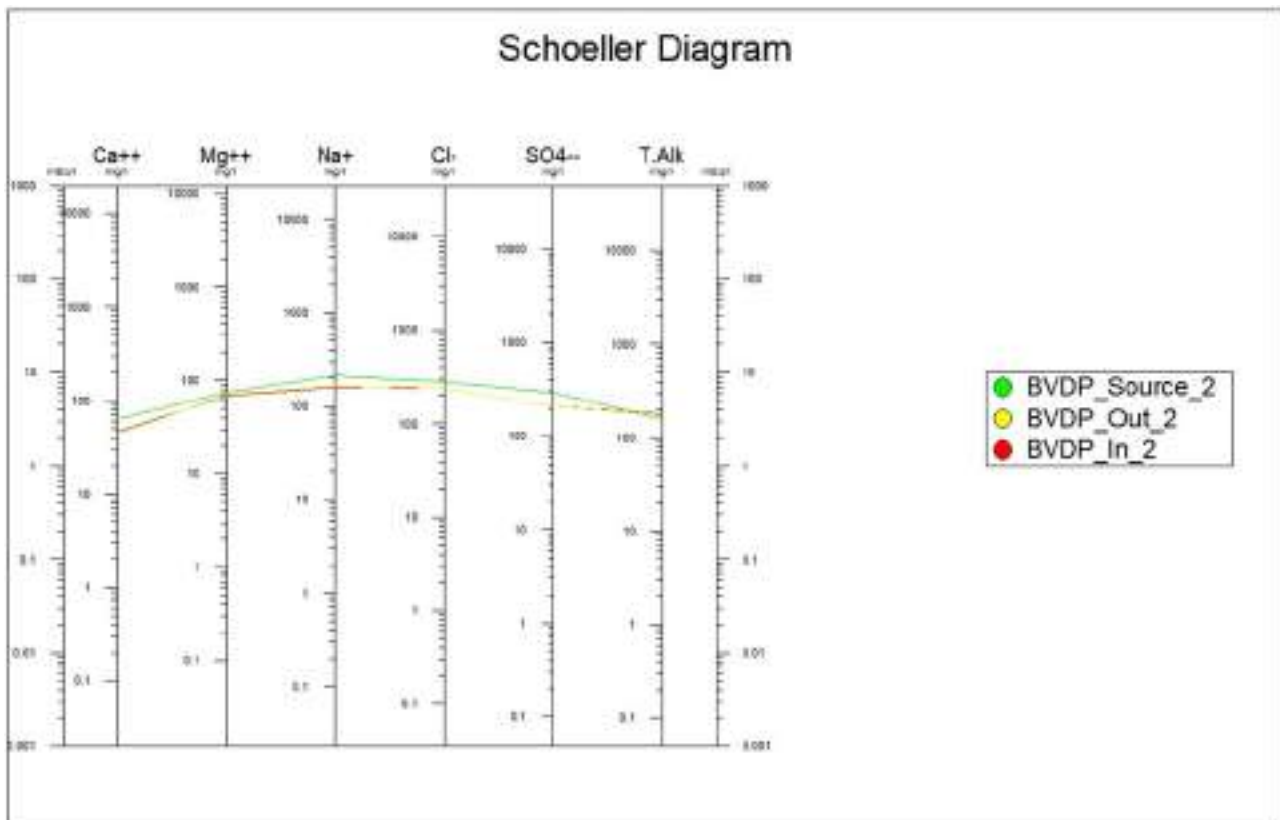


Figure 116 Schoeller diagram of the drilling fluid samples of 16 July 2024.

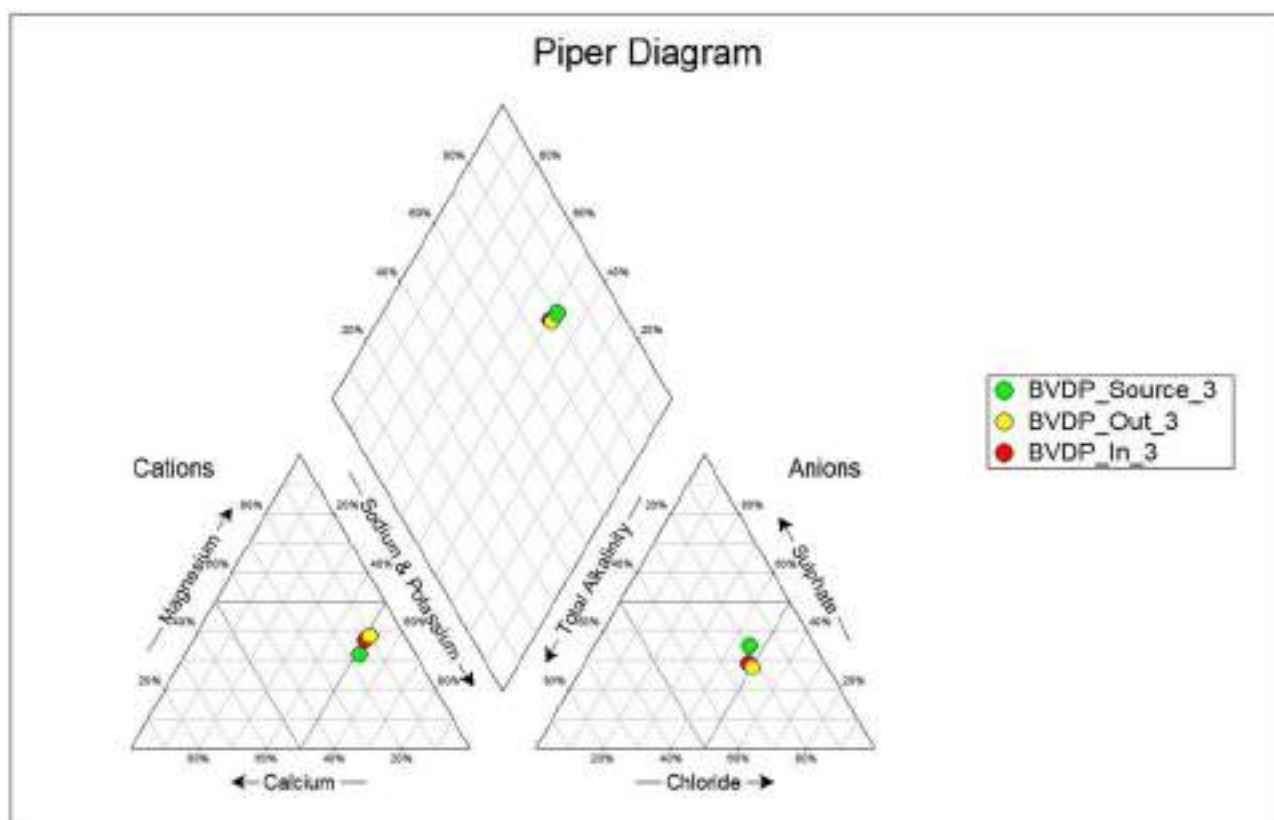


Figure 117 Piper diagram of the drilling fluid samples of 23 July 2024.

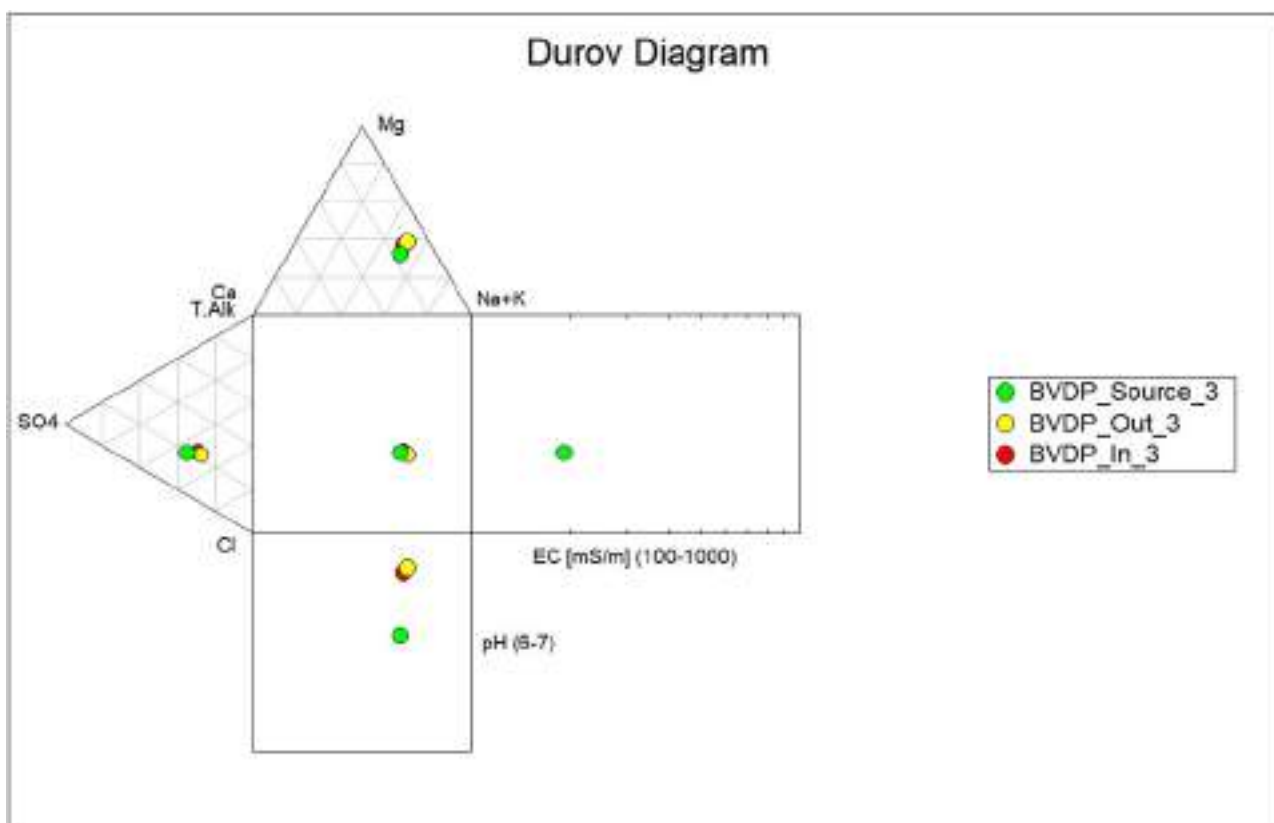


Figure 118 Durov diagram of the drilling fluid samples of 23 July 2024.

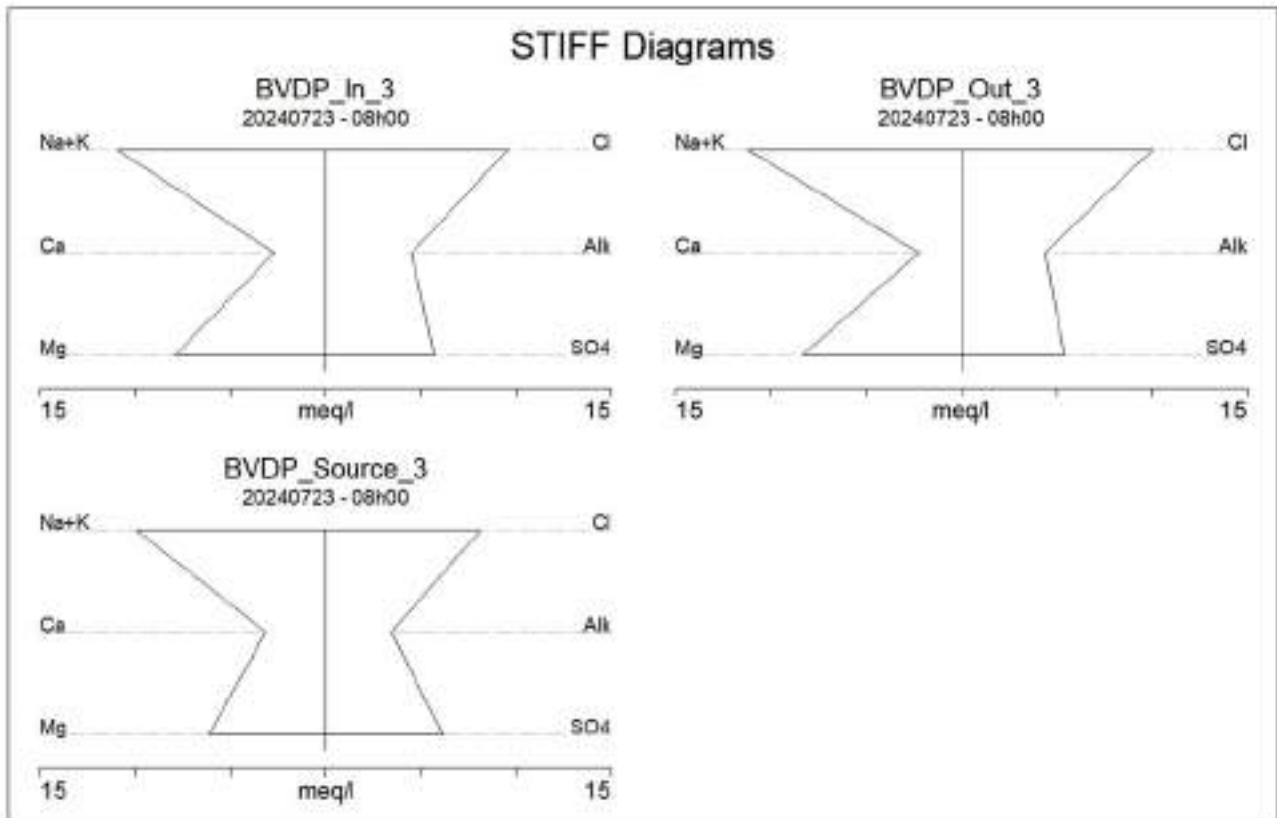


Figure 119 STIFF diagrams of the drilling fluid samples of 23 July 2024.

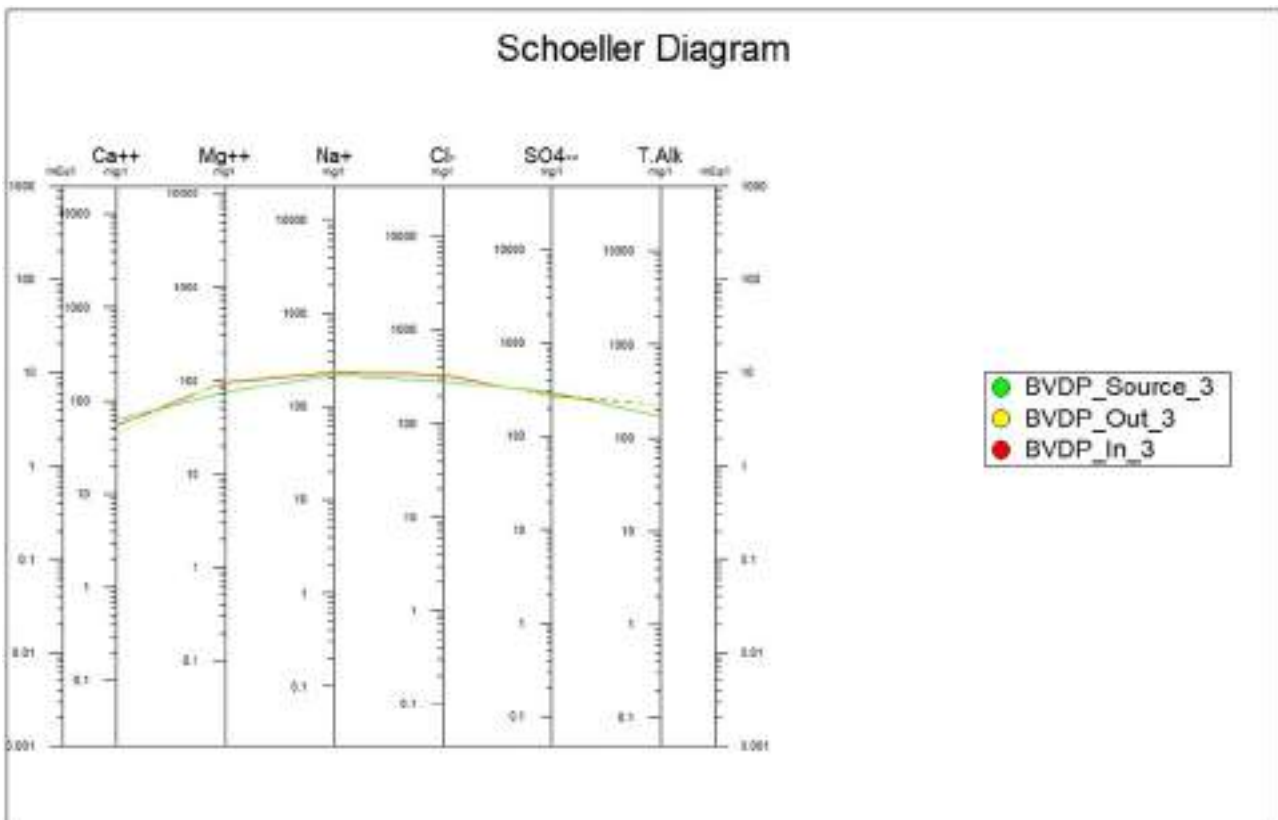


Figure 120 Schoeller diagram of the drilling fluid samples of 23 July 2024.

6.6 HYDRAULIC TESTING

The primary objectives of packer testing in mining and exploration projects are typically two-fold: to support groundwater modelling and inflow prediction for different lithologies or structures, and to identify specific features for the installation of vibrating wire piezometers for long-term pore pressure monitoring. In deep borehole testing, cumulative testing is often employed using a single packer, progressing from the bottom of the borehole upwards until high permeability zones are encountered. At this stage, it is more effective to switch to a double packer configuration to spot test specific zones of interest, particularly where geological structures suggest potential water conduits. The maximum interval that can be tested with a double packer is 6 metres, making full-hole testing with this configuration costly for the client. An alternative approach involves testing while drilling is in progress, although this method can also be expensive due to the need for continuous site presence. The following section details the methodology and findings of the packer testing performed in borehole BVDP-03, including the permeability values obtained from various test intervals and configurations. A contractor, Hydro-Geo Services (HGS), were used for the packer testing.

6.6.1 Methodology and field report

The following is a field report covering the packer testing conducted on borehole:

- The packer testing equipment was offloaded, serviced, and assembled. Equipment setup is shown in Figure 121 using a HQ SWiPS System.
- The drilling core barrel was fitted with a modified landing ring, and a surface inflation test was performed to ensure that the packer testing equipment was compatible with the core barrel configuration, confirming no leakage. All equipment was deemed to be in proper working order.
- The drilling crew then lowered the drill rods to the bottom of the borehole and commenced flushing, which took up the remainder of the shift on Friday.
- Core from the borehole was examined and used to identify potential zones of permeability. Zones earmarked for testing from inspection of the core corresponded with those recommended using raw geophysical data and geological logs.
- HGS personnel returned to the site at 07:15 on 25 August to commence packer testing, requesting that the borehole be flushed again prior to testing.
- The first packer test was conducted using a single packer configuration from 930.5 m to 948.5 m, with step tests at 200 KPa, 400 KPa, 600 KPa, 400 KPa, and 200 KPa. The permeability in this zone was found to be very low, with an average flow rate of 0.71 L/min at 600 KPa.
- Two additional tests were performed using the single packer configuration, both of which also showed very low permeability. Testing was paused on Sunday, 26 August, as it was not a working day for Master Drilling.
- Five more packer tests were conducted using the single packer configuration, with flushing between each test. All tests showed low injection flow rates. The test zones are reflected in the packer testing results.
- Four further tests were carried out using the single packer configuration, with the final test performed at 357.5 m, just below the PQ casing. As with previous tests, these zones exhibited low permeability.



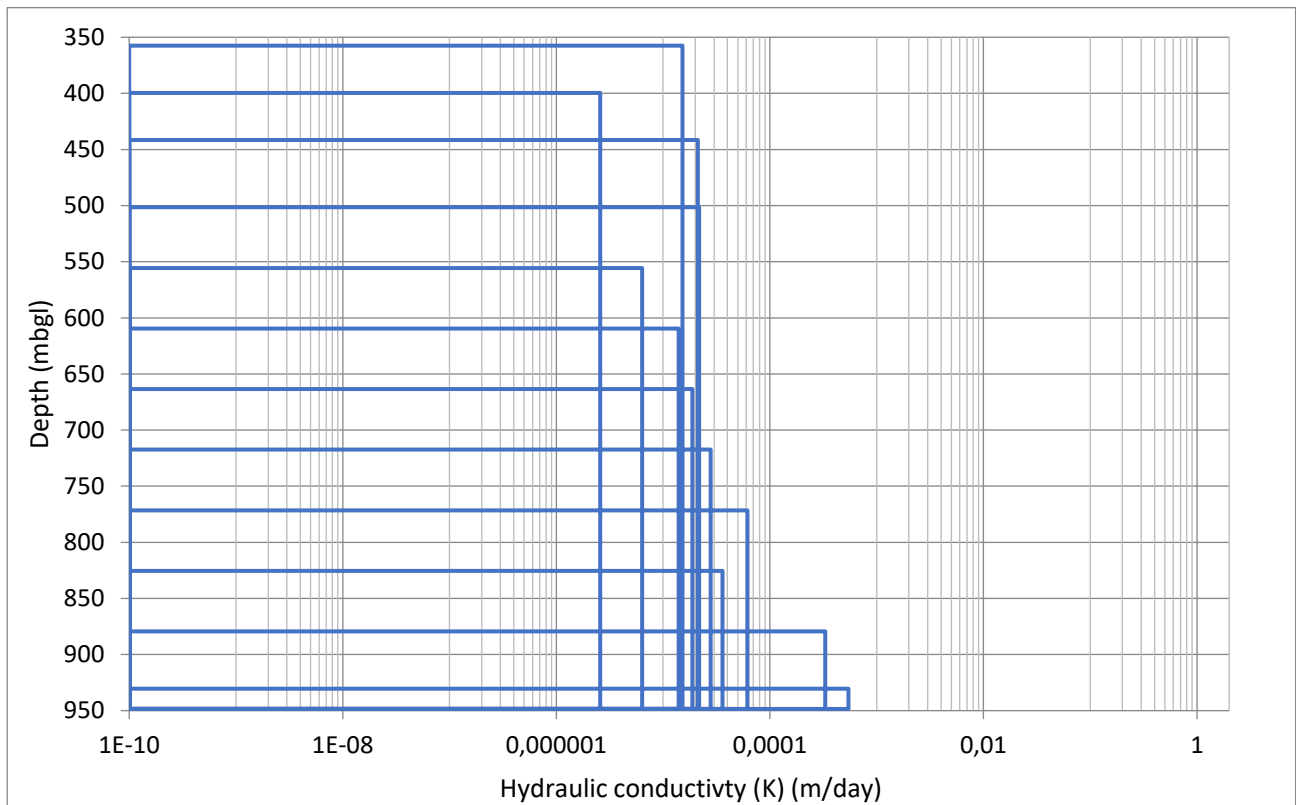
Figure 121 Hydraulic packer testing setup with HQ SWiPS System

6.6.2 Results

A summary of the estimated hydraulic conductivity for each of the 12 packer tests performed at shown in Table 23, along with a graphical representation in Figure 122. The estimated hydraulic conductivity shows a decrease in permeability between certain tests, which can be attributed to pressure loss over distance. As the test section length increases, the injection pressure becomes less direct. While cumulative testing is less accurate in terms of providing highly precise data, it does offer a permeability profile of the borehole. The large interval testing shows overall lower hydraulic conductivity zones; however, this was expected from the deep igneous lithologies. Yet, there are variations in the determined values and can be useful to better understand the system. To this end, the packer testing hydraulic conductivity values are compared to the geophysical structure log of fractures as well as details from the geological log (Figure 123). The geology intersected in the hole is mainly pyroxenite (upper and lower Critical Zone) with smaller zones of fractures and chromitite, which seem to be more permeable.

Table 23 Summary of the 12 hydraulic packer testing conducted over the Phase section of the hole

Test Number	Top of Test (m)	Bottom of Test (m)	Test Section length (m)	K (m/day)	Packer Type
1	930,5	948,5	18,0	0,0005	HQ SWiPS Single
2	879,5	948,5	69	0,0003	HQ SWiPS Single
3	825,5	948,5	123	3,6E-05	HQ SWiPS Single
4	771,5	948,5	177	6,2E-05	HQ SWiPS Single
5	717,5	948,5	231	2,8E-05	HQ SWiPS Single
6	663,5	948,5	285	1,9E-05	HQ SWiPS Single
7	609,5	948,5	339	1,4E-05	HQ SWiPS Single
8	555,5	948,5	393	6,4E-06	HQ SWiPS Single
9	501,5	948,5	447	2,2E-05	HQ SWiPS Single
10	441,5	948,5	507	2,1E-05	HQ SWiPS Single
11	399,5	948,5	549	2,6E-06	HQ SWiPS Single
12	357,5	948,5	591	1,5E-05	HQ SWiPS Single

**Figure 122 Plot of estimated hydraulic conductivity from each packer test conducted**

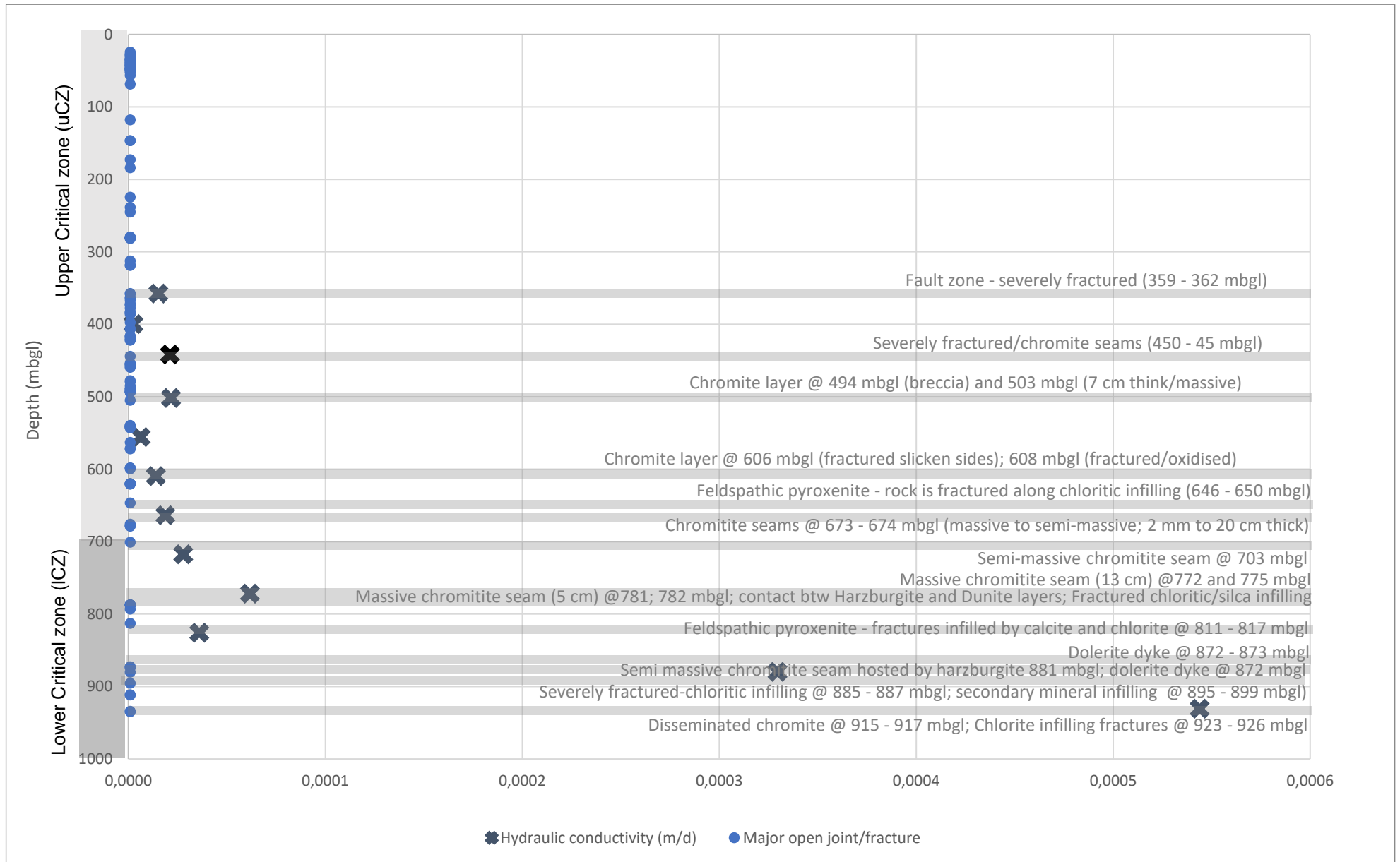


Figure 123 Correlation of hydraulic conductivity (K in m/d) against depth and results from the packer testing to the geophysical structural log and geological log details. General lithology is indicated behind the depth scale with predominantly pyroxenite of the upper and lower Critical Zone.

The determine hydraulic conductivity from the packer tests are low, yet there is variation with depth, and where there are slightly higher values estimated the depth typically correlates to specific features commented on the geological log as summarised in Table 24.

Table 24 Hydraulic test number, estimated hydraulic conductivity (K) and associated comments from the geological log approximately at the corresponding depth

Test Number	Top of Test (m)	K (m/day)	Corresponding comments in the geological log
1	930,5	0,0005	Disseminated chromite @ 915 - 917 mbgl Chlorite infilling fractures @ 923 - 926 mbgl
2	879,5	0,0003	Severely fractured-chloritic infilling @ 885 - 887 mbgl Secondary mineral infilling @ 895 - 899 mbgl) Dolerite dyke @ 872 - 873 mbgl Severely fractured-chloritic infilling @ 885 - 887 mbgl Secondary mineral infilling @ 895 - 899 mbgl)
3	825,5	3,60E-05	Feldspathic pyroxenite - fractures infilled by calcite and chlorite @ 811 - 817 mbgl
4	771,5	6,20E-05	Massive chromitite seam (5 cm) @781 and 782 mbgl Contact between Harzburgite and Dunite layers Fractured chloritic/silica infilling Massive chromitite seam (13 cm) @772 and 775 mbgl
5	717,5	2,80E-05	Semi-massive chromitite seam @ 703 mbgl
6	663,5	1,90E-05	Chromitite seams @ 673 - 674 mbgl (massive to semi-massive; 2 mm to 20 cm thick) Feldspathic pyroxenite - rock is fractured along chloritic infilling (646 - 650 mbgl)
7	609,5	1,40E-05	Chromite layer @ 606 mbgl (fractured slicken sides); 608 mbgl (fractured/oxidised)
8	555,5	6,40E-06	Reduction in K, no corresponding geological features
9	501,5	2,20E-05	Chromite layer @ 494 mbgl (breccia) and 503 mbgl (7 cm thick/massive)
10	441,5	2,10E-05	Severely fractured/chromite seams (450 - 45 mbgl)
11	399,5	2,60E-06	Reduction in K, no corresponding geological features
12	357,5	1,50E-05	Fault zone - severely fractured (359 - 362 mbgl)

The main features identified include:

Chromitite and chromite Layers

Disseminated chromite: located at 915–917 mbgl.

Massive and semi-massive chromitite seams: Found at multiple depths, including 781–782 mbgl, 772–775 mbgl, and 703 mbgl, with thicknesses ranging from a few mm to cm.

Chromite layers with fracturing and breccia: Noted at 606 mbgl, 494 mbgl (breccia), and 503 mbgl (7 cm thick, massive).

Fracturing and faults

- Severely fractured zones with chloritic infilling: Observed at depths like 885–887 mbgl and 450–455 mbgl, often associated with chloritic mineral infilling.
- Fault zone: A highly fractured section at 359–362 mbgl, likely contributing to localized permeability.

Mineral infilling in fractures

- Chlorite-infilling fractures seen in areas such as 923–926 mbgl and 646–650 mbgl, filling fractures in various lithologies.
- Secondary mineral infilling found between 895–899 mbgl, likely influencing permeability
- Calcite and chlorite infill: Located in feldspathic pyroxenite at 811–817 mbgl, contributing to structural weaknesses.

Other lithological features

Dolerite dyke: found at 872–873 mbgl, potentially affecting the surrounding rock structure and fluid flow.

Contact between harzburgite and dunite: Located near chromitite seams, possibly marking changes in geological composition and fluid pathways.

These grouped features highlight that chromitite/chromite layers, fracturing, and mineral infilling (especially with chlorite and calcite) are key factors influencing hydraulic conductivity variations in the borehole. Fractured and faulted zones with mineral infilling tend to increase permeability, while massive chromitite seams and dolerite dykes are generally less permeable due to their consolidated nature.

6.7 ONLINE GAS ANALYSIS

The KivuRUEDI is a portable mass spectrometer for quantification of He, Ne, Ar, Kr, N₂, O₂, CO₂, CH₄, H₂ and other gas species in air and water (gas partial pressures). It allows on-site gas analysis during field work. Some key information about the characteristics of the equipment is summarised below:

- The mass spectrometer has two detectors: The Faraday cup and the secondary electron multiplier. The multiplier is important for less abundant elements (4He and 84Kr).
- The instrument operates with a 24V power supply with a consumption of about 50 W under normal operation.
- The instrument has six capillary inlets which can be rotated between samples and standards.
- The gases are continuously sampled and transferred through a capillary pressure reduction system into a vacuum chamber, where they are analysed using the quadrupole mass spectrometer with a time resolution of ≤ 1 min.
- The analytical uncertainty is approximately 1% to 3%.
- Calibration is done by the ambient air or custom gas bags standards. There is no need for calibration using external water standards.
- The KivuRUEDI is composed of two pumping systems in order to achieve the high vacuum condition for the mass spectrometer which are the diaphragm pump and the turbomolecular pump. They are sensitive to shock, mostly when it is switched on.
- The KivuRUEDI can measure the following gas species according to their respective atomic masses:
 - Hydrogen (H₂) – atomic mass of 2
 - Helium (He) – atomic mass of 4
 - Methane (CH₄) – atomic mass of 15
 - Nitrogen (N₂) – atomic mass of 28
 - Oxygen (O₂) – atomic mass of 32
 - Argon (Ar) – atomic mass of 40
 - Carbon dioxide (CO₂) – atomic mass of 44
 - Krypton (Kr) – atomic mass of 84

6.7.1 Configuration

The KivuRUEDI consist of the following components as per Figure 124:

- Turbomolecular pump
- Diaphragm pump which created a vacuum
- Control switches
- Valve selector
- Quadrupole mass spectrometer
- Six-port inlet valve selector
- Inlet valve
- Six capillaries
- Standard gas bags
- KivuRUEDI laptop



Figure 124 Components of the KivuRUEDI.

6.7.2 Standard operating procedure

The degassing unit at the drilling rig ensures that the drilling fluid from the drilling rig is degassed which feeds into a safety trap that acts as a water vapour prevention control unit, to ensure that gas and not water vapour flows from the degasser into the gas line. The gas line feeds into the container where the gas pump and gas regulator control the flow rate of gas into the sample line. From the gas regulator, the gas line is connected to a water trap filled with silica gel, that acts as a secondary water vapour prevention control unit that allows water vapour to condensate and be absorbed by the silica gel; followed by a third line of prevention, which is a 0.45 μm syringe filter. The gas line (sample line) then feeds into the KivuRUEDI which is connected to a sample line capillary (capillary 3) via a swage lock, from where the quadrupole mass spectrometer will measure the

atomic masses for specific gas species in the sample line. The outlet of the sample line should feed out of the container (exhaust) to ensure that gas does not build up in the container.

The KivuRUEDI was set up in a separate container on the BVDP site, in order to keep the ambient conditions as stable as possible for calibration purposes. Capillary 4 in measures these ambient conditions in the container. Capillary 1 and capillary 2, are connected to the standard gas bags with known gas concentrations, which are used for calibration purposes of CO₂ and CH₄. Capillaries 5 and 6, are the spare and blank capillaries.

The main power supply to the KivuRUEDI is a 220V UPS (uninterruptable power supply) outlet connected to a surge protector at the outlet of the container. The UPS supplies power to the KivuRUEDI laptop, the KivuRUEDI and the gas pump.

For the start-up of the KivuRUEDI, the following procedure was followed:

- The UPS should be connected to the outlet of the container. This then supplies power to the KivuRUEDI, the KivuRUEDI laptop and the gas pump.
- The KivuRUEDI laptop should be on and connected to the WIFI (wireless fidelity) and the KivuRUEDI.
- The control switches should be switched on, starting from the left side to the right side. These switches should therefore be switched on in the following order:
 - Control switch 1 (diagram pump).
 - Control switch 2 (turbomolecular pump) – After the turbo pump has been switched on a green light will start flashing. Enough time should be given for the green light to stop flashing and turn into a solid green light before the process can be continued as this ensure that the turbo pump is working under stable conditions. If the green light is flashing and a sold orange light appears, the process should be followed to shut down the KivuRUEDI as this can be an indication that the power supply is not stable or be an indication that there might be a complication at the KivuRUEDI.
 - Once the green light on the turbomolecular pump is solid, control switch 3 (vici/inlet selector valve) can be switched on; and,
 - Control switch 4 (mass spectrometer).
- After the first 4 control switches have been switched on, then the green valve should be opened, which allows gas to flow into the capillaries.
- The RUEDI-measure software is then opened, only if when the KivuRUEDI laptop which has to be connected to the KivuRUEDI and the WIFI.
- Warm up the system. This is the pre-conditioning of the system and should be executed to prepare the instrument for analysis. It should always be run, except if the instrument is already initialised from a previous run (there is no need to do the same procedure in between a set of analysis in the same location).
- A graph is displayed, where the y scale is 100% from the initial signal. The warm up procedure should be left running until all the system is equilibrated and the detector signal stabilises. It takes approximately 15 minutes as per Figure 124. Once the system is equilibrated, the warm up procedure can be stopped.
- The system automatically starts the “peak tuning procedure”. This step enables the mass spectrometer’s mass filter to centre detected peaks at the correct m/z values. A message “Please wait tuning m/z scale” is displayed and the process stops automatically once completed.
- After the peak tuning procedure has been completed, a blank analysis is necessary to determine the “analytical zero” of the instrument. The blank analyses are used later for data processing, it is therefore important to be included at the beginning and at the end of the analysis set to ensure that the software will not be able to process the data.
- The software will ask to open/close the green inlet valve when starting and completing the blank analysis. Open/close the valve as required.
- Once a blank analysis has been done, the green inlet valve can be opened, and the sample analysis sequence can be initiated in a continuous sequence as per Figure 125.
- Once the analysis procedure is complete as per Figure 126, the KivuRUEDI measure software can be closed. It is recommended the data be processed to ensure that the analysis was successful before following the shutdown procedure.

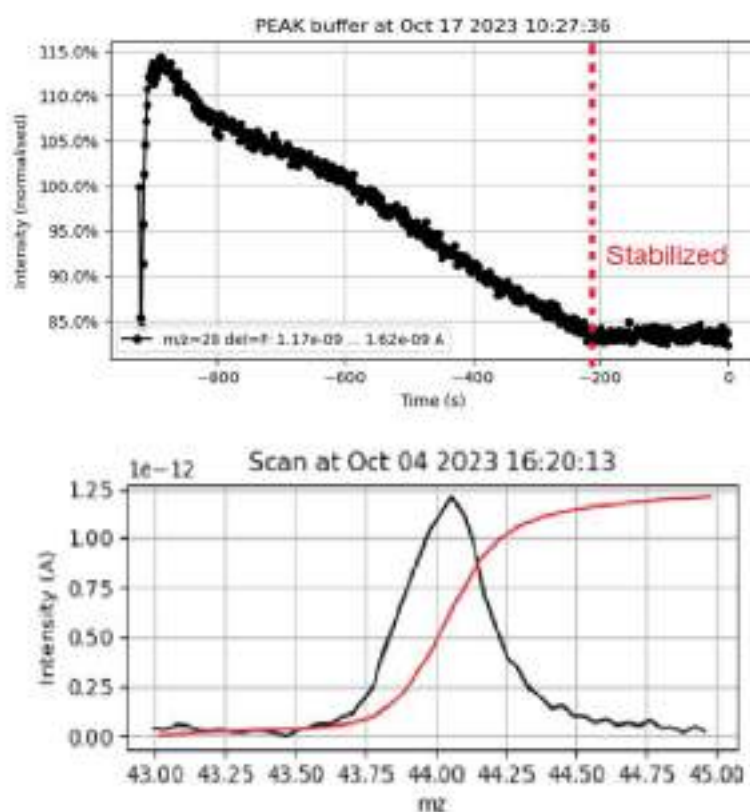


Figure 125 System equilibration (upper) and peak procedure (lower).



Figure 126 Analysis set label.



Figure 127 Example of an analysis sequence.

For the shut-down of the KivuRUEDI, the following procedure was followed:

- Ensure that the current analysis has been stopped and that the KivuRUEDI software on the laptop has been closed.
- Close the green inlet valve.
- The control switches should be switched off, starting from the right side to the left side. These switches should therefore be switched off in the following order:
 - Control switch 4 (mass spectrometer).
 - Control switch 3 (vici/inlet selector valve).
 - Control switch 2 (turbomolecular pump) – After the control switch has been switched off, enough time should be allowed for the green flashing light to stop flashing and for no lights to be on at the turbomolecular pump. This ensures that the turbomolecular pump has been winded down in order to protect the pump; and,
 - Control switch 1 (diagraph pump).
- Close the standard gas bags and disconnect the cables of the KivuRUEDI from the UPS.

The operating of the MR system has been challenging in terms of managing a remote drilling location as well as the novel application of this technology to circulating drilling fluid. An example of an analysis sequence is shown in Figure 127, albeit that due to a number of unforeseen problems on site, the relative gas data cannot be quantified. The system has now been optimised and will produce the required data for the last section of the BVDP borehole.

6.8 SUMMARY

The analysis of borehole data reveals significant hydrological and geological characteristics of the subsurface environment. Open fractures were observed up to a depth of 322 metres, with the largest aperture measuring 40 mm at 321 mbgl. These fractures contributed to total water loss until the first 350 metres were sealed, indicating high permeability in the subsurface. Major fractures were identified along the borehole, extending to a depth of 935 mbgl, although only one fracture had a measured aperture.

The hydrological log captured continuous measurements of fluid electrical conductivity (EC), temperature, and other parameters. A groundwater level was detected at 24 mbgl, showing an overall increasing trend in TDS with depth, with notable peaks suggesting groundwater inflow zones. The highest TDS values (over 6,000 mg/l) were recorded at 450 mbgl, indicating potential inflow of saline groundwater.

After sealing phase 1, a new profile was established for the re-drilled core, designated as BVDP-3-B. This section, with solid steel casing, showed a sharp increase in readings after 350 m. Temperature measurements reached a maximum of 39°C, following a consistent upward trend with depth.

Challenges in water sample collection arose due to drilling fluid contamination, which could affect chemical and isotopic analysis. While standard procedures typically involve extensive flushing and purging to eliminate drilling fluids before sampling, time constraints during the BVDP project limited this process. Consequently, samples were collected with an understanding of the potential influence of remaining drilling fluids.

In terms of stable water isotope analysis, two methods—Laser-Based Spectroscopy (LGR) and Isotope Ratio Mass Spectrometry (IRMS)—were considered, each with its advantages and limitations in handling sample purity and potential interferences. The $\delta^{18}\text{O}$ and $\delta^2\text{H}$ isotopic signatures of Phase 1 samples aligned with low-latitude regions, suggesting groundwater source and recharge dynamics. A general trend of increasing depletion with depth was observed, indicating variations in isotopic composition linked to groundwater inflow. Notable open fractures were identified, particularly at 76 mbgl, and the TDS profile exhibited peaks that may indicate saline groundwater inflow. Analysis of the drilling fluid, primarily a dissolved polymer, suggested minimal settling in the borehole, although localised concentration might occur in shallow depths where circulation slows.

For isotopic analysis, the Picarro system was chosen for Phase 2 samples due to contamination concerns. Results showed variations in contamination levels across samples, with some indicating trace contamination from organic materials. These findings highlighted the need for careful interpretation of isotope ratios, as pre-treatment and filtering were essential to mitigate contamination effects.

The hydraulic conductivity estimated from packer tests revealed variations in permeability, attributed to factors such as pressure loss over distance and the geological composition, primarily consisting of pyroxenite with zones of fractures and chromitite. The relationship between hydraulic conductivity and geological features underscored the importance of chromitite layers and mineral infilling on permeability variations within the borehole.

A summary of the findings made from phase 1 and phase 2 investigations at borehole BVDP-3 are presented in Figure 128., with the downhole TDS profile and zones of drilling fluid contamination identified from the stable isotopes along with the packer testing results analysis with geological features noted as possible locations for groundwater flow along with downhole geophysical structure information (depth major open fractures were identified).

The BVDP borehole study presents crucial insights into the subsurface hydrology and geology, emphasising the complexities of groundwater inflow, drilling fluid contamination, and the influence of geological structures on hydraulic conductivity.

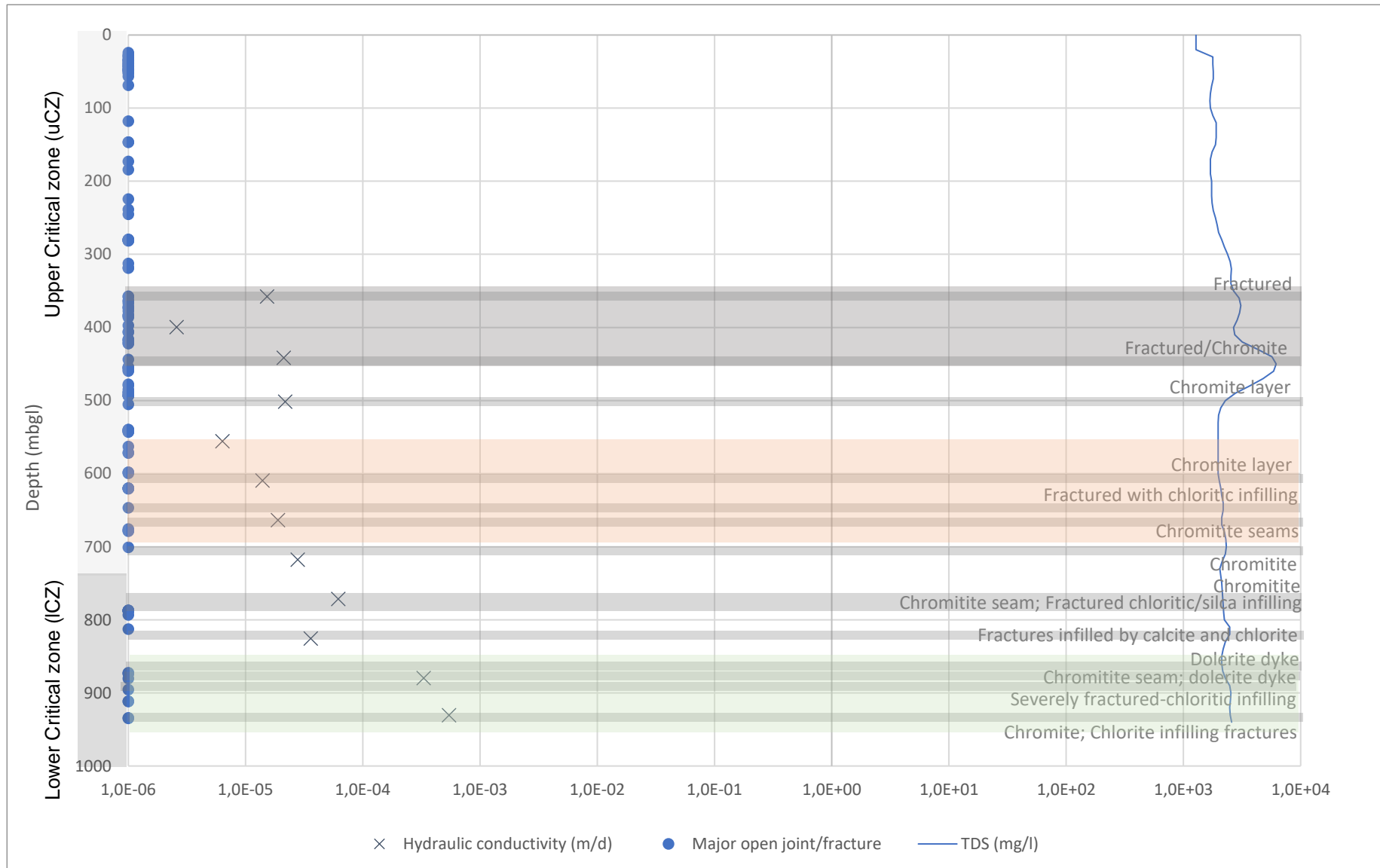


Figure 128 Visual representation of the information collected and analysed on the borehole in this report, with the downhole TDS profile and zones of drilling fluid contamination identified from the stable isotopes added to the packer testing results analysis with geological features noted as possible locations for groundwater flow along with downhole geophysical structure information (depth major open fractures were identified)

7 DEEP GROUNDWATER INSIGHTS FROM BVDP BOREHOLE

7.1 OVERVIEW

The Bushveld Igneous Complex (BIC) represents one of the world's largest layered igneous intrusions, renowned for its mineral resources. However, its potential as a groundwater resource in deep crystalline environments is underexplored. Drilling in the eastern limb has revealed significant hydrological anomalies, including substantial groundwater inflows at depths exceeding 1 150 m and the emergence of a dark, odorous fluid. These findings challenge traditional hydrogeological models and highlight the need for further investigation.

This chapter examines the data collected during drilling operations, integrating geological, hydrological, and geochemical findings to evaluate the potential of deep groundwater as a future water supply. The discussion addresses both the challenges and opportunities associated with groundwater development in crystalline rock settings, emphasising the role of fracture networks in fluid movement and storage.

7.2 GEOLOGICAL AND STRUCTURAL CONTEXT

Drilling in Hole B intersected the Rustenburg Layered Suite, characterised by norite, pyroxenite, and anorthosite, culminating in a lamprophyre dyke between 1 265 m and 1 270 m. The dyke displayed swelling behaviour when exposed to water, emphasising its potential as a key hydrological feature. The primary porosity of these lithologies is low; hence, water storage and flow are predominantly governed by fractures.

Fractures observed between 1 150 m and 1 270 m indicate significant secondary porosity and permeability, driven by brittle deformation. These features likely connect to regional fault systems, enhancing fluid movement. Similar fracture-controlled flow systems have been documented in other parts of the Bushveld, underscoring the importance of structural controls on groundwater dynamics.

7.3 HYDROLOGICAL FINDINGS

One of the most notable challenges encountered during the drilling of Hole B was the inability to successfully cement the borehole between 1 150 m and 1 270 m below ground level, despite four attempts. This issue is attributed to significant groundwater or fluid inflows at this depth, which prevented the cement from curing. Persistent groundwater inflows in this interval suggest highly transmissive zones, governed by fracture networks. This contrasts with the impermeability typically associated with crystalline rock at depth. This anomaly is particularly noteworthy as earlier sections of the borehole were cemented without issue, even in the presence of water. The drilling team, experienced in cementing boreholes under such conditions, identified this depth as exhibiting markedly different hydrological behaviour.

Visual evidence from the re-drilled section of the borehole reveals distinct flow lines where the cement did not set, indicating active water movement through fractures or permeable zones (Figure 129). These observations suggest that the hydrological characteristics at this depth differ significantly from the upper sections of the borehole. While the unaltered and unweathered nature of the igneous rock at these depths was expected to limit groundwater occurrence, the presence of inflows and the associated fluid anomaly point to the possibility of greater alteration or fracturing than previously anticipated. Structural features such as fractures, faults, or dykes may provide pathways for fluid migration, emphasising the role of secondary porosity in controlling groundwater dynamics in crystalline rock environments.

The first attempt to cement the hole that had intercepted the lamprophyre dyke and deviated, followed standard procedures, allowing sufficient time for the cement to cure. However, when the borehole was flushed with clean water, a dark, strong-smelling fluid was expelled from the hole. This fluid represents an unexpected anomaly, raising questions

about its origin and composition. A sample of the fluid was collected for analysis, though the results are still pending (Figure 129).

The emergence of a dark, strong-smelling fluid during borehole flushing raises questions about deep hydrogeological and geochemical processes. Hypotheses include:

- Hydrothermal activity: Migration of fluids enriched with minerals and gases from deep geological sources
- Brine entrapment: Trapped saline water associated with the emplacement of the BIC
- Organic interactions: Decomposition of ancient organic material or microbial activity

This unexpected hydrological behaviour highlights the complexity of deep groundwater systems in the Bushveld Complex and underscores the need for further investigation. Further geochemical and isotopic studies are essential to clarify the fluid's origin and implications for water quality and resource development. Advanced geochemical and isotopic analyses of the fluid sample, coupled with geophysical surveys to map fracture networks, are recommended to better understand the mechanisms driving these anomalies and their implications for deep groundwater resources.



Figure 129 Re-drilled cement after an attempt to cure cement in the hole at depth (1 150 m to 1 270 m **where lamprophyre dyke was intersected*); cement core shows distinct places where flow prevented curing (left); anomalous fluid sampled (right)

7.4 HYDROGEOLOGICAL IMPLICATIONS

The findings reaffirm the importance of fractures in facilitating groundwater movement in crystalline environments. These features create localised aquifers capable of storing and transmitting water, even in otherwise impermeable formations.

The analysis of drilling and geophysical data highlights significant fracture networks throughout the borehole, offering valuable insights into the structural controls on groundwater flow within the eastern limb of the Bushveld Complex. In

the shallow sections of the borehole, open fractures were observed from the surface to approximately 322 meters below ground level (mbgl). The largest measured aperture of these fractures was 40 mm at 321 mbgl, indicating high permeability and the capacity for fluid movement in this zone. The extensive fracturing resulted in total water loss during drilling until the first 350 m of the borehole was sealed with casing, underscoring the hydrological significance of these shallow fractures.

Below this shallow zone, significant fractures were encountered between 322 m and 935 mbgl, exhibiting varying aperture sizes and degrees of connectivity. Many of these deeper fractures displayed evidence of infill materials such as calcite and chlorite, indicating chemical precipitation processes that may partially obstruct fluid movement. Despite this, these fractures remain hydrologically important, as their density and connectivity suggest they act as key conduits for groundwater flow.

Of particular interest is the high-density fracture zone identified starting at approximately 800 mbgl and extending to greater depths. This interval exhibited elevated hydraulic conductivity, reflecting the presence of interconnected fractures capable of sustaining substantial fluid movement. Hydrological logging further supports the importance of this interval, with flowmeter data indicating significant groundwater inflows at multiple depths within this range. These findings highlight the presence of structurally controlled flow pathways, even in unweathered and otherwise low-permeability igneous rocks.

The observations from this study underscore the role of fractures in enhancing permeability and facilitating groundwater movement in the Bushveld Complex. The high fracture density in the 800–935 m interval suggests the potential for localised deep aquifer systems. However, the variability in fracture characteristics, such as the presence of calcite and chlorite infill in some zones, emphasises the heterogeneous nature of these systems and their capacity to store and transmit water.

While recharge mechanisms remain uncertain, fracture-controlled aquifers may store significant volumes of water. Possible recharge pathways include lateral flow from adjacent formations or slow infiltration from surface systems.

7.5 CONCEPTUALISING DEEP GROUNDWATER IN THE BUSHVELD

The findings necessitate revisions to the existing hydrogeological model for the eastern Bushveld limb (Figure 130).

Key updates include:

Upper shallow aquifer

From the analysed water quality information, there appears to be two distinct systems, a shallow and deeper system. The difference in water quality could confirm the assumption made in the western limb that shallow aquifers are generally not linked to deeper aquifers (> 300 mbgl).

Fractured aquifer (shallow to intermediate depth)

Below the weathered zone, the fractured aquifer extends between 100 m and 500 m depths, dominated by fractures and joints in the Critical Zone lithologies. Chromite seams and layers have been linked to increased preferential flow and higher hydraulic conductivity values.

High-density fracture zone (deep aquifer)

A significant high-density fracture zone is identified starting at approximately 800 m depth and extending deeper into the critical and lower zones of the Bushveld Complex. These deep fractures exhibit enhanced connectivity, creating high-yield aquifer potential and facilitating groundwater flow.

Deeper groundwater anomalies (1 150 m – 1 269 m)

The model highlights an anomaly at depths between 1 150 m and 1 270 m, where significant groundwater inflows were encountered during drilling. This zone prevented successful cementing operations due to persistent fluid movement.

The presence of a dark, strong-smelling fluid is noted in this interval, suggesting potential interactions with hydrothermal fluids, brines, or deep-seated organic processes.

Structural influences on groundwater flow

The lamprophyre dyke at greater depths (approximately 1 265 m–1 270 m) is depicted as a potential conduit or barrier for fluid migration, depending on fracture orientation and density. The connectivity of faults and fractures is shown to control localised recharge pathways and groundwater flow.

The updated model highlights the complexity of groundwater systems in the Bushveld Complex, with significant variability in hydraulic properties and flow dynamics. The integration of deep fracture-controlled aquifers into the model provides a framework for assessing groundwater potential at depth. It also identifies key zones for further investigation, particularly for geothermal energy potential, isotopic dating, and long-term monitoring of fluid dynamics.

This conceptual model serves as a tool for guiding future groundwater exploration and resource development in the region, emphasising the interplay between geology, hydrology, and geochemistry in deep igneous environments.

7.6 LONG-TERM INVESTIGATIONS AND FUTURE POTENTIAL

Looking ahead, a unique opportunity has arisen to maintain the borehole as an open scientific observation site. Following a year-long rest period to mitigate the influence of drilling fluids, more rigorous investigations will focus on the deeper sections of the hole, reaching depths of 2 to 2.5 km. These investigations will aim to enhance the understanding of deep groundwater dynamics, isotopic age dating, microbiological activity, and geothermal potential, contributing valuable data for future resource management.

These investigations will focus on the deeper sections, reaching 2 to 2.5 km in depth, and will include:

- Water sampling for isotopic age dating: Stable and radiogenic isotopes will provide insights into groundwater residence times and recharge processes, contributing to a deeper understanding of the system's sustainability
- Packer testing: To assess hydraulic properties and delineate transmissive zones
- Microbiological sampling: Long-term monitoring will target microbial communities to explore subsurface biosphere dynamics and their interactions with groundwater
- Heat flow measurements: Temperature profiling and heat flow studies will assess the geothermal potential of the system, contributing to the evaluation of low-enthalpy geothermal resources

These investigations aim to enhance understanding of deep aquifer dynamics, inform sustainable groundwater use, and evaluate the feasibility of geothermal energy production.

7.7 POTENTIAL FOR FUTURE WATER SUPPLY

For resource development, deep groundwater in the BIC holds potential as a supplementary water resource for industrial applications, particularly in mining operations. The geochemical characteristics, including salinity, may limit its direct use for drinking water but could be treated for specific needs.

The exploration of deep groundwater systems aligns with global efforts to diversify water resources in response to increasing demand and climate variability. The findings from the BIC offer valuable insights into the development of similar resources in other crystalline environments.

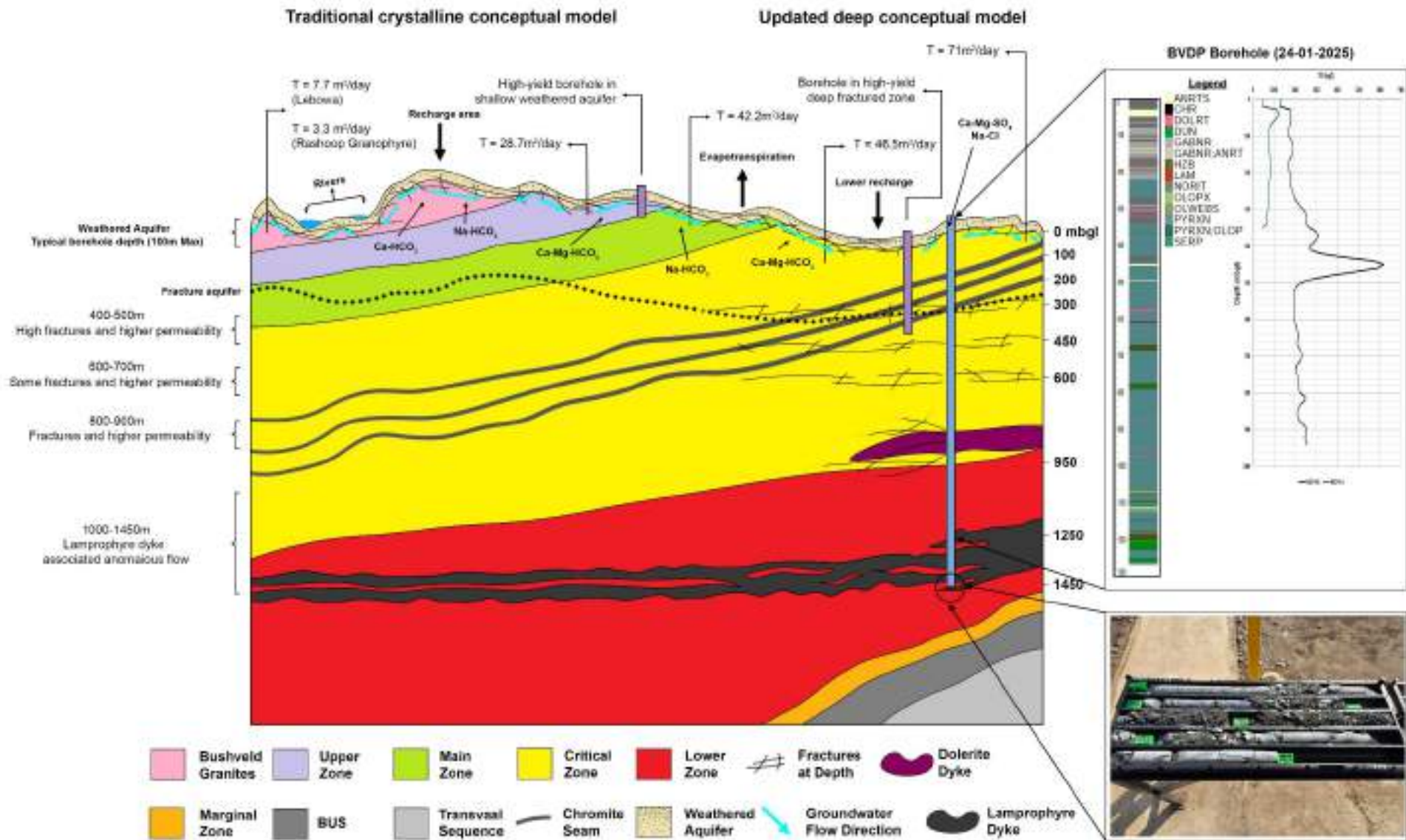


Figure 130 Updated hydrogeological conceptual model of the eastern limb of the Bushveld Igneous Complex including the insights from the deep drilling project hole up to a depth of 1 450 mbgl along with simplified geological log, hydrological log and photos of broken lamprophyre core at 1420 mbgl.

8 CONCLUSIONS AND RECOMMENDATIONS

This Water Research Commission (WRC) project has provided groundbreaking insights into deep groundwater systems within the eastern limb of the Bushveld Igneous Complex (BIC). The research represents one of the most detailed hydrogeological investigations conducted on deep fractured aquifers in South Africa, contributing significantly to the understanding of groundwater occurrence, flow, and geochemical evolution in crystalline rock environments. This project was conducted in collaboration with the Bushveld Complex Drilling Project (BVDP), which provided an opportunity to integrate geological, geophysical, and hydrogeochemical datasets for comprehensive groundwater system characterisation.

The original plan envisioned drilling two boreholes to depths of $\pm 2,500$ m to assess the extent of deep aquifers and their structural controls. However, due to logistical and funding constraints, the project ultimately focused on a single borehole, which was successfully drilled to a depth of 950 m. This borehole provided valuable insights into the hydrogeological properties of deep fractured aquifers, particularly regarding fracture-controlled flow, groundwater chemistry, and structural influences on permeability. The study confirmed that groundwater movement is primarily controlled by structural features, including faults, dykes, and joint networks, rather than primary rock porosity, which is negligible in this setting.

8.1 HYDROGEOLOGICAL AND STRUCTURAL INSIGHTS

Drilling and geophysical logging identified a high-density fracture zone starting at 800 m, which exhibited notable groundwater inflows. These results challenge conventional assumptions that unweathered igneous rock is impermeable at depth, instead demonstrating that deep-seated fractures and structural discontinuities serve as key conduits for groundwater movement. Borehole imaging and geophysical analysis further confirmed that these fractures are aligned with regional faulting patterns, suggesting structural connectivity across significant depths. These findings highlight the potential for deep groundwater resources within structurally complex settings, which had previously been underexplored due to the high costs associated with deep drilling.

8.2 HYDROCHEMICAL AND ISOTOPIC EVOLUTION

Hydrochemical and isotopic analysis revealed a clear transition in groundwater composition with depth. Shallower groundwater exhibited a Ca-Mg-HCO₃ dominated composition, while deeper groundwater evolved to a Na-Cl facies, indicating increasing mineralisation along flow paths. The isotopic signatures of $\delta^{18}\text{O}$ and $\delta^2\text{H}$ suggest that the groundwater at these depths has undergone prolonged residence times with limited modern recharge, reinforcing the hypothesis that deep groundwater systems in the BIC are largely isolated from near-surface hydrological processes. A notable anomalous groundwater inflow between 1,150 m and 1,270 m included the presence of a dark, odorous fluid, raising questions about potential deep-seated geochemical interactions. The source of this fluid remains uncertain, but its presence could indicate interactions with hydrothermal systems, organic-rich lithologies, or deep brine reservoirs. Further geochemical characterisation of this fluid is essential to determine its origins and potential implications for deep groundwater chemistry.

Another key challenge encountered was the influence of drilling fluids on sample integrity, which complicated initial geochemical and isotopic assessments. The continuous circulation of drilling fluids resulted in some contamination of water samples, making it difficult to accurately assess in-situ conditions. Despite this challenge, stable isotope analysis using Laser-Based Spectroscopy (LGR) and Isotope Ratio Mass Spectrometry (IRMS) provided valuable insights into groundwater flow dynamics and recharge processes. The future use of noble gas isotopes for groundwater dating will further refine our understanding of groundwater residence times and recharge mechanisms.

8.3 DRILLING CHALLENGES AND BOREHOLE MANAGEMENT

One of the most unexpected observations during drilling was the failure of cementing operations at depth, which allowed fluid movement to persist within the borehole. This raised concerns regarding the stability and sealing of deep fractures, further emphasizing the complex hydrogeological nature of this system. Unlike typical mining exploration boreholes, which are permanently sealed or cemented for safety reasons, this borehole has been advocated to remain open for continued scientific research. This decision allows for long-term monitoring and further sampling once hydrogeological conditions stabilise, reducing the impact of drilling-related disturbances.

8.4 IMPLICATIONS FOR WATER RESOURCE DEVELOPMENT AND GEOTHERMAL POTENTIAL

The findings of this study have practical implications for water resource management in South Africa. The confirmation of fracture-controlled groundwater flow at depth suggests that similar deep aquifers may exist elsewhere in the BIC and other crystalline basement terrains. This has potential significance for industries reliant on groundwater, particularly mining operations, where access to deep, structurally controlled groundwater could provide an alternative water source. However, the limited recharge rates observed suggest that these systems may not be suitable for large-scale abstraction without long-term sustainability assessments.

Additionally, the elevated temperatures observed during drilling, along with the detection of dissolved gases, including methane, suggest the potential for geothermal energy exploration within the Bushveld Complex. While this project did not focus explicitly on geothermal resource evaluation, the data collected supports further research into the thermal characteristics of deep groundwater systems in the BIC.

8.5 RECOMMENDATIONS

Given the significance of these findings, the following actions are strongly recommended to maximise the scientific value of this borehole and facilitate further research into deep groundwater systems:

1. Post-Drilling Sampling and Isotopic Analysis

- Allow the borehole to rest and stabilise post-drilling to eliminate the influence of drilling fluids.
- Conduct noble gas isotope studies to determine groundwater age and recharge characteristics.

2. Long-Term Monitoring Infrastructure

- Install hydrological and geochemical monitoring equipment to track changes in groundwater pressure, chemistry, and temperature over time.

3. Comprehensive Fluid Analysis

- Further analyse the dark, odorous fluid encountered at depth to assess its origins and broader hydrogeochemical implications.

4. Collaboration with Mining and Research Institutions

- Strengthen partnerships with mining operations, universities, and government agencies to integrate findings into a regional hydrogeological framework.

5. Geothermal Resource Assessment

- Investigate the thermal gradient and heat flow data collected during drilling to assess the feasibility of geothermal energy development.

6. Deep Groundwater Resource Evaluation

- Conduct additional hydraulic testing and geophysical investigations to refine the conceptual hydrogeological model for structurally controlled aquifers in the BIC.

By maintaining this borehole as a dedicated scientific observation site, this project ensures that subsequent research will continue to build on these findings, advancing knowledge of deep groundwater dynamics, hydrogeochemical evolution, and geothermal potential. The insights gained from this study contribute not only to academic research but also to practical water resource management strategies, particularly in regions where groundwater is a critical component of economic and environmental sustainability.

This WRC-funded research has laid a strong foundation for future investigations into deep groundwater systems, demonstrating the value of research-based drilling in advancing hydrogeological understanding in South Africa. Continued funding and collaboration will be essential to fully unlock the potential of deep fractured aquifers and their role in long-term water security and energy sustainability.

9 REFERENCES

- Adeola, A. M., Kruger, A., Elias Makgoale, T., and Ondego Botai, J. (2022). Observed trends and projections of temperature and precipitation in the Olifants River Catchment in South Africa. *Plos One*, 17(8), e0271974.
- Adesola, G. O., Thamaga, K. H., Gwavava, O., and Pharoe, B. K. (2023). Groundwater Potential Zones Assessment Using Geospatial Models in Semi-Arid Areas of South Africa. *Land*, 12(10), 1877.
- Agliardi, F., Sapigni, M., and Crosta, G.B. (2016). Rock mass characterization by high-resolution sonic and GSI borehole logging. *Rock Mechanics and Rock Engineering*, 49(11), 4303-4318.
- Ahokpossi, D. P., Atangana, A., and Vermeulen, P. D. (2018). Hydro-geochemical characterizations of a platinum group element groundwater system in Africa. *Journal of African Earth Sciences*, 138, 348–366.
- Altstatt, A.A., Saltus, R.W., Bruhn, R.L., and Haeussler, P.J. (2002). *Magnetic susceptibilities measured on rocks of the upper Cook Inlet, Alaska*. US Geological Survey Open-File Report, 2, 18.
- Anglo American Platinum, (2014). Operations Review. Anglo American Platinum.
- ASSORE (Pty) Ltd. (2016). *Social and Labour Plan for Dwarsriver Chrome Mine (Pty) Ltd*. ASSORE (Pty) Ltd.
- Balch, A.H., Lee, M.W., Miller, J.J., and Ryder, R.T. (1982). The use of vertical seismic profiles in seismic investigations of the earth. *Geophysics*, 47(6), 906-918.
- Basson, I. J. (2019). Cumulative deformation and original geometry of the Bushveld Complex. *Tectonophysics*, 750(November 2018), 177–202. <https://doi.org/10.1016/j.tecto.2018.11.004>
- Belkhiri, L., Boudoukha, A., Mouni, L., and Baouz, T. (2010). Application of multivariate statistical methods and inverse geochemical modeling for characterization of groundwater—a case study: Ain Azel plain (Algeria). *Geoderma*, 159(3–4), 390–398.
- BESST, 2018. Exploratory Borehole Sampling: Deep Borehole Sampling. Available at: <https://besst-inc.com/index.php/exploratory-borehole-sampling/> [Accessed 28-05-2022].
- Bliss, J.C., and Rushton, K. R. (1984). The reliability of packer tests for estimating the hydraulic conductivity of aquifers. *Quarterly Journal of Engineering Geology and Hydrogeology*, 17(1), 81-91.
- Boness, N.L., and Zoback, M.D. (2004). Stress-induced seismic velocity anisotropy and physical properties in the SAFOD Pilot hole in Parkfield, CA. In *Gulf Rocks 2004*, the 6th North America Rock Mechanics Symposium (NARMS). OnePetro.
- Botha, F. S., and Van Rooy, J. L. (2001). Affordable water resource development in the northern province, South Africa. *Journal of African Earth Sciences*, 33(3–4), 687–692.
- Brennwald, M.S., Schmidt, M., Oser, J., and Kipfer, R. (2016). A portable and autonomous mass spectrometric system for on-site environmental gas analysis. *Environmental science & technology*, 50(24), 13455-13463.
- Buchanan, P.C. (2006) The Rooiberg Group, In Johnson, M.R., Anhaeusser, C.R. and Thomas, R.J. (Eds) *The Geology of South Africa*. Geological Society of South Africa Council for Geoscience Johannesburg Pretoria.
- Burger, J., Knight, J.W., Dreyer, D.W. and Obermeyer, P.G. (2016). *A Technical Report on the Smokey Hills Platinum Mine, Limpopo Province, South Africa - Update*. Minxcon (Pty) Ltd. Roodepoort, South Africa: Aberdeen International Inc.
- Cawthorn, R.G. (2006) The Bushveld Complex, In Johnson, M.R., Anhaeusser, C.R. and Thomas, R.J. (Eds) *The Geology of South Africa*. Geological Society of South Africa Council for Geoscience Johannesburg Pretoria.
- Chan, J.S., Schmitt, D.R. and Kueck, J. (2014). *Log Analysis of Fractures in a Deep Borehole, Northeastern Alberta, Canada* [extended abstract]. CSPG/CSEG/CWLS GeoConvention 2012, (Vision) Calgary TELUS Convention

- Centre and ERCB Core Research Centre, Calgary, AB, Canada, 14-18 May 2012. Available at: https://www.searchanddiscovery.com/documents/2014/50942chan/ndx_chan.pdf [Accessed on 02-04-2022].
- Clarke, B., Uken, R. and Reinhardt, J. (2009) 'Structural and compositional constraints on the emplacement of the Bushveld Complex, South Africa', *Lithos*, 111(1–2), pp. 21–36.
- Cogswell, D. (2022). *Borehole Flowmeter*. Borehole Wireline Logging. Available at: <https://borehole-wireline.com.au/borehole-flowmeters/> [Accessed 29-04-2022].
- Council for Geoscience, (2000). Bushveld Complex South Africa.
- Dalasile, P. and Abiye, T. (2018). *Hydrogeological study of geological features in the groundwater system of Tweefontein 360KT farm, Limpopo Province*. Johannesburg: School of Geoscience, Faculty of Science, University of the Witwatersrand.
- Davraz, A., and Batur, B. (2021). Hydrogeochemistry characteristics of groundwater and health risk assessment in Yalvaç–Gelendost basin (Turkey). *Applied Water Science*, 11(4), 67.
- Department of Water and Sanitation. (2020). *Surface and Groundwater Information*.
- Dillon, P., and Arshad, M. (2016). Managed aquifer recharge in integrated water resource management. In Jakeman, A.J., Barreteau, O., Hunt, R.J., Rinaudo, J.D., and Ross, A. (Eds). *Integrated groundwater management* (p. 762). Springer Nature, Springer, Cham.
- Dippenaar, M. A. (2008). Characterisation of some fractured-rock aquifers in Limpopo province, South Africa: review and case study. University of Pretoria.
- Dlubac, K., Knight, R., Song, Y.Q., Bachman, N., Grau, B., Cannia, J., and Williams, J. (2013). Use of NMR logging to obtain estimates of hydraulic conductivity in the High Plains aquifer, Nebraska, USA. *Water Resources Research*, 49(4), 1871-1886.
- Dobson, P., Tsang, C.F., Kneafsey, T., Borglin, S., Piceno, Y., Andersen, G., Nakagawa, S., Nihei, K., Rutqvist, J., Doughty, C. and Reagan, M. (2016). *Deep Borehole Field Test Research Activities at LBNL*. Report for U.S. Department of Energy. Available at: <https://www.osti.gov/servlets/purl/1306290> [Accessed 30-04-2022].
- Douagui, A. G., Kouadio, S. K. A., Mangoua, J. O. M., Kouassi, A. K., Kouam, B. K., & Savané, I. (2019). Using specific capacity for assessing of the factors controlling borehole productivity in crystalline bedrock aquifers of N'Zi, Iffou and Moronou regions in the eastern area of côte d'Ivoire. *Groundwater for Sustainable Development*, 9, 100235.
- Doughty, C. and Tsang, C.F. (2000). BORE-II-A code to compute dynamic wellbore electrical conductivity logs with multiple inflow/outflow points including the effects of horizontal flow across the well. Available at: https://ipo.lbl.gov/wp-content/uploads/sites/8/2014/07/2014BOREII_UserGuide-1.pdf [Accessed 30-04-2022].
- Doughty, C., and Tsang, C.F. (2005). Signatures in flowing fluid electric conductivity logs. *Journal of Hydrology*, 310(1-4), 157-180.
- Doughty, C., Takeuchi, S., Amano, K., Shimo, M., and Tsang, C.F. (2005). Application of multi-rate flowing fluid electric conductivity logging method to well DH-2, Tono Site, Japan. *Water resources research*, 41(10).
- Doughty, C., Tsang, C.F., Rosberg, J.E., Juhlin, C., Dobson, P.F., and Birkholzer, J.T. (2017). Flowing fluid electrical conductivity logging of a deep borehole during and following drilling: estimation of transmissivity, water salinity and hydraulic head of conductive zones. *Hydrogeology Journal*, 25(2), 501-517.
- Doveton, J. (2017). *Geological Log Analysis*. Kansas Geological Survey, University of Kansas. Available at: https://www.kgs.ku.edu/Publications/Bulletins/LA/00_contents.html [Accessed 13-03-2022].
- Du Toit, W and Scholes, M. (2018). *Environmental Impact Assessment and Environmental Management Programme Report for the proposed extension of the Two Rivers Platinum mining right area*. Malan Scholes Consulting. Steelpoort, Limpopo Province, South Africa: Two Rivers Platinum (Pty) Ltd.

- DWA. (2011). Development of a reconciliation strategy for the Olifants River water supply system. Groundwater options report.
- DWAF (2006). GROUNDWATER RESOURCE ASSESSMENT II – TASK 3aE RECHARGE.
- Elango, L., and Kannan, R. (2007). Rock–water interaction and its control on chemical composition of groundwater. *Developments in Environmental Science*, 5, 229–243.
- Erzinger, J., Wiersberg, T., and Dahms, E. (2004). Real-time mud gas logging during drilling of the SAFOD Pilot Hole in Parkfield, CA. *Geophysical Research Letters*, 31(15).
- Erzinger, J., Wiersberg, T., and Zimmer, M. (2006). Real-time mud gas logging and sampling during drilling. *Geofluids*, 6(3), 225-233.
- Foster, S., and MacDonald, A. (2014). The ‘water security’ dialogue: Why it needs to be better informed about groundwater. *Hydrogeology Journal*, 22(7), 1489–1492.
- Fourie, F., Allwright, A., Esterhuysen, S., Govender, N., and Makiwane, N. (2020). Characterisation and protection of potential deep aquifers in South Africa (Issue 2434). www.wrc.org.za
- Freeze, R. A., and Cherry, J. A. (1979). Groundwater.
- Freifeld, B. (2009). The U-tube: a new paradigm for borehole fluid sampling. *Scientific Drilling*, 8, 41-45.
- Frignet, B.G., and Hartog, A.H. (2014). Optical vertical seismic profile on wireline cable. In *SPWLA 55th Annual Logging Symposium*. OnePetro.
- Gaillot, P., Brewer, T., Pezard, P., and Yeh, E.C. (2007). Borehole imaging tools—principles and applications. *Scientific Drilling*, 5, 1-4.
- GCS (Pty) Ltd (2020). Desktop geohydrological and preliminary risk assessment for the Proposed Vygenhoek Platinum Mine, (0).
- Gebrekrstos, R. and Cheshire, P. (2012). Hydrogeological properties of the UG2 Pyroxenite aquifers of the Bushveld Complex, in *Proceedings of the 5th Platinum Conference of the Southern African Institute of Mining and Metallurgy*, pp. 143–152.
- German Research Centre for Geosciences (GFZ) and International Continental Drilling Scientific Drilling Program (ICDP), 2020. *Online Gas Monitoring of Drilling Mud*. Available at: https://www.icdp-online.org/fileadmin/icdp/services/img/Poster_Mudgasmonitoring_web.pdf [Accessed on 05-05-2022].
- Gibbs, R. J. (1970). Mechanisms controlling world water chemistry. *Science*, 170(3962), 1088–1090.
- Glover, P. (2014a). Electrical logging In *Petrophysics MSc course notes*. University of Leeds, School of Earth and Environment. Available at: http://homepages.see.leeds.ac.uk/~earpwjg/PG_EN/CD%20Contents/_GGL-66565%20Petrophysics%20English/Chapter%2019.PDF [Accessed 15-04-2022].
- Greenbaum, D. (1992). Structural influences on the occurrence of groundwater in SE Zimbabwe. *Geological Society, London, Special Publications*, 66(1), pp. 77–85.
- Grönwall, J., and Danert, K. (2020). Regarding groundwater and drinking water access through a human rights lens: Self-supply as a norm. *Water*, 12(2), Article 419. <https://doi.org/10.3390/w12020419>
- Gude, V. G. (2018). Desalination and water reuse to address global water scarcity. *Reviews in Environmental Science and Bio/Technology*, 17(3), 173–192.
- Gyamfi, C., Ndambuki, J. M., and Salim, R. W. (2016). Hydrological responses to land use/cover changes in the Olifants Basin, South Africa. *Water*, 8(12), 588.
- Hardage, B.A. (1985). Vertical seismic profiling. *The Leading Edge*, 4(11), 59-59.
- Harms U., Tobin H.J. (2011) Deep Scientific Drilling. In: Gupta H.K. (Eds) *Encyclopedia of Solid Earth Geophysics. Encyclopedia of Earth Sciences Series*. Springer, Dordrecht. https://doi.org/10.1007/978-90-481-8702-7_195

- Holland, M. (2011). Hydrogeological characterisation of crystalline basement aquifers within the Limpopo Province, South Africa. University of Pretoria.
- Holland, M. (2012). Evaluation of factors influencing transmissivity in fractured hard-rock aquifers of the Limpopo Province. *Water SA*, 38(3), pp. 379–390.
- ICDP. (2024). ICDP Equipment, our surface instrumentation and more. International Continental Drilling Programme. <https://www.icdp-online.org/support/equipment/>
- ICRC (2010). *Technical review: borehole drilling and rehabilitation under field conditions*. Tech. Geneva, Switzerland, ICRC.
- Ivanhoe Mines, (2022). *Ivanhoe Mines, New Horizons*. Retrieved from Ivanhoe Mines: <https://www.ivanhoe-mines.com>
- Jerram, D.A., Millett, J.M., Kück, J., Thomas, D., Planke, S., Haskins, E. and Pierdominici, S. (2019). Understanding volcanic facies in the subsurface: a combined core, wireline logging and image log data set from the PTA2 and KMA1 boreholes, Big Island, Hawaii. *Scientific Drilling*, 25, 15-33. <https://doi.org/10.5194/sd-25-15-2019>
- Jones, F.H.M. and Oldenburg, D.W. (2007). *Geophysics for Practising Geoscientists: Learning Resources about Applied Geophysics. Version 1.0 (2007/11)*. University of British Columbia, Department of Earth and Ocean Sciences. Available at: <https://www.eoas.ubc.ca/courses/eosc350/content/index.htm> [Accessed 20-05-2022].
- Jones, M.Q.W. (2018). Virgin rock temperatures and geothermal gradients in the Bushveld Complex. *Journal of the Southern African Institute of Mining and Metallurgy*, 118(7), pp. 671–680.
- Karjalainen, A. (2020). *Borehole magnetic resonance method in hard rock environments: a case study from the Olkiluoto spent nuclear fuel repository site* [Master's Thesis, University of Helsinki]. Available at: https://helda.helsinki.fi/bitstream/handle/10138/324291/Karjalainen_Aino_pro_gradu_2020.pdf?sequence=2&isAllowed=y
- Kendall. (1975). Rank correlation methods. In Charles Griffin, London (4th ed., 2). Griffin.
- Keys, W.S. (1989). Borehole geophysics applied to ground-water investigations. In USGS, *Techniques of water-resources investigations of the United States Geological Survey*. Available at: https://pubs.usgs.gov/twri/twri2-e2/pdf/TWRI_2-E2.pdf [Accessed 16-04-2022].
- Kingdon, A., Fellgett, M.W., and Williams, J.D. (2016). Use of borehole imaging to improve understanding of the in-situ stress orientation of Central and Northern England and its implications for unconventional hydrocarbon resources. *Marine and Petroleum Geology*, 73, 1-20.
- Kinnaird, J.A. (2005). *The Bushveld large igneous province: Review Paper*. The University of the Witwatersrand, Johannesburg, South Africa, 39pp [Preprint].
- Koperna, G. (2020). *Geophysical Well Log Report (Deliverable 6.2.a)* (No. DOE-SSEB-0029465-61). Southern States Energy Board, Peachtree Corners, GA (United States). Available at: <https://www.osti.gov/servlets/purl/1639013> [Accessed 12-05-2022].
- Kuhlman, K.L., Arnold, B.W., Brady, P.V., Sassani, D.C., Freeze, G.A., and Hardin, E. (2014). *Site Characterization for a Deep Borehole Field Test* (No. SAND2014-19866C). Sandia National Lab.(SNL-NM), Albuquerque, NM (United States). Available at: <https://rampac.energy.gov/docs/default-source/storage/12370.pdf> [Accessed 30-04-2022].
- Kumar, P. S. (2013). Interpretation of groundwater chemistry using piper and Chadha's diagrams: a comparative study from Perambalur Taluk. *Elixir Geosci*, 54, 12208–12211.
- Lalumbe, L. *Department of Water and Sanitation (DWS) Report – GHP 1214 – Sephaku Community, C9B51B024 2529BA, H06*
- Legchenko, A., Baltassat, J.M., Beauce, A., and Bernard, J. (2002). Nuclear magnetic resonance as a geophysical tool for hydrogeologists. *Journal of Applied Geophysics*, 50(1-2), 21-46.

- Lencwane, M. (2021). Investigation of hydrogeochemical processes of groundwater at royal Bafokeng platinum mine in the Bushveld Igneous Complex, South Africa. Faculty of Science, University of the Witwatersrand, Johannesburg.
- Lenhardt, N., Masango, S. M., Jolayemi, O. O., Lenhardt, S. Z., Peeters, G. J., and Eriksson, P. G. (2017). The Palaeoproterozoic (~ 2.06 Ga) Rooiberg Group, South Africa: dominated by extremely high-grade lava-like and rheomorphic ignimbrites? New observations and lithofacies analysis. *Journal of African Earth Sciences*, 131, 213-232.
- Lenkoe-Magagula, K. (2013). *Groundwater Impact Assessment - 18 Shaft*. SLR Global Environmental Solutions. Rustenburg: Impala Platinum Mine.
- Liu, S., and Sato, M. (2006). Subsurface water-filled fracture detection by borehole radar: A case history. *Journal of Environmental & Engineering Geophysics*, 11(2), 95-101.
- Lourens, P.J.H. (2013). *The relation between South African geology and geohydrology* [Master's Thesis, University of the Free State].
- Madrucci, V., Taioli, F., and de Araújo, C. C. (2008). Groundwater favorability map using GIS multicriteria data analysis on crystalline terrain, São Paulo State, Brazil. *Journal of Hydrology - J HYDROL*, 357, 153–173. <https://doi.org/10.1016/j.jhydrol.2008.03.026>
- Mäkelä, J. (2012). Drilled well yield and hydraulic properties in the Precambrian crystalline bedrock of Central Finland.
- Malan Scholes Consulting (Pty) Ltd (MSC) (2018). Environmental Impact Assessment and Environmental Management Programme Report for The Proposed Extension of the Rivers Platinum Mining Right Area. MSC/57/18/TRP.
- Marula. (2018). *Marula*, Fact Sheet. Marula, Members of the Implats Group.
- Masindi, K., and Abiye, T. (2018). Assessment of natural and anthropogenic influences on regional groundwater chemistry in a highly industrialized and urbanized region: a case study of the Vaal River Basin, South Africa. *Environmental Earth Sciences*, 77, 1–14.
- McCaffrey, L. P. (1998). Distribution and causes of high fluoride groundwater in the western Bushveld area of South Africa.
- McCarthy, T. and Rubidge, B. (2005). *The story of Earth and Life: A southern African perspective on a 4.6-billion-year journey*. Cape Town, South Africa: Struik Nature.
- McFarlane, M. J., Chilton, P. J., and Lewis, M. A. (1992). Geomorphological controls on borehole yields: a statistical study in an area of basement rocks in central Malawi. *Geological Society, London, Special Publications*, 66(1), 131–154.
- Metago Environmental Engineers (Pty) Ltd (2016). Environmental Impact Assessment and Environmental Management Report Programme Spitzkop and Mareesburg.
- Mining Data Solutions Online (MDS) (2022). Mining Data Solutions. Retrieved from Mining Data Online: <https://miningdataonline.com>
- Moir, R.S., Parker, A.H., and Brown, R.T. (2014). A simple inverse method for the interpretation of pumped flowing fluid electrical conductivity logs. *Water Resources Research*, 50(8), 6466-6478.
- Morton, K. (2021). The Use of Mineral Exploration Drilling to Kickstart Hydrogeology Data Collection for Pre-Feasibility Mining Studies and Beyond. – In: Stanley, P. Wolkersdorfer, C. Wolkersdorfer, K. *Mine Water Management for Future Generations*. – p. 386 – 392; Cardiff, Wales, United Kingdom (Natural Resources Wales, The Coal Authority, Welsh Government, Cardiff University).
- Northam Platinum Holdings. (2021). *The new Northam: continuing to create value for all stakeholders, annual integrated report*. South Africa: Northam Platinum Holdings Limited.

- Onana, A. B. A., Ngoupayou, J. R. N., and Ondo, J. M. (2017). Analysis of crystalline bedrock aquifer productivity: Case of central region in Cameroon. *Groundwater for Sustainable Development*, 5, 66–74.
- Oristaglio, M.L. (1985). A guide to current uses of vertical seismic profiles. *Geophysics*, 50(12), 2473-2479.
- Orpen, W. R. G. (1994). Recommended map legend and mapping methodology for the compilation of regional hydrogeological maps of the Republic of South Africa at a scale of 1: 500 000.
- Paillet, F.L. (1994). *Application of borehole geophysics in the characterization of flow in fractured rocks* (Vol. 93, No. 4214). US Geological Survey.
- Peyper, L., Mathews, C., Ryan, B., Stoddard, E., Isa, M. and McKay, D. (2021). The Mining Yearbook, 2021. (E. McKay, Ed.) Cape Town: Miningmx (Pty) Ltd.
- Planke, S., Cerney, B., Bückner, C.J., and Nilsen, O. (1999). Alteration effects on petrophysical properties of subaerial flood basalts: Site 990, Southeast Greenland margin. In *Proceedings of the Ocean Drilling Program, Scientific Results* (Vol. 163, pp. 17-28). Ocean Drilling Program, College Station. <https://doi.org/10.2973/odp.proc.sr.163.105.1999>
- Prensky, S.E. (1999). Advances in borehole imaging technology and applications. *Geological Society, London, Special Publications*, 159(1), 1-43.
- Quinn, P., Cherry, J.A., and Parker, B.L. (2012). Hydraulic testing using a versatile straddle packer system for improved transmissivity estimation in fractured-rock boreholes. *Hydrogeology Journal*, 20(8), 1529-1547.
- Quinn, P., Cherry, J.A., and Parker, B.L. (2015). Combined use of straddle packer testing and FLUTE profiling for hydraulic testing in fractured rock boreholes. *Journal of Hydrology*, 524, 439-454.
- Ramushu, A., Okujeni, C., Siad, A. and Bailie, R. (2018). Geochemical and Petrographic Characterization of the Transition Boundary between the MG2 package to MG3 package at Dwarsriver Chrome Mine, Bushveld Complex, South Africa. Department of Earth Sciences, Faculty of Natural Science, University of the Western Cape.
- READ, 2020. ABI-43 *Integrity Mode: Acoustic Borehole Imager*. Technical Data Sheet. Available at: <https://readcasedhole.com/wp-content/uploads/2020/07/READ-ABI43-Integrity-Mode-TechDataSheet-V1.pdf> [Accessed at 05-05-2022].
- Rezaei, M., Nikbakht, M., and Shakeri, A. (2017). Geochemistry and sources of fluoride and nitrate contamination of groundwater in Lar area, south Iran. *Environmental Science and Pollution Research*, 24, 15471–15487.
- Rose, D., Viljoen, F., Knoper, M., and Rajesh, H. (2011). Detailed assessment of platinum-group minerals associated with chromitite stringers in the Merensky Reef of the eastern Bushveld Complex, South Africa. *The Canadian Mineralogist*, 49(6), 1385-1396.
- Royle, M. (2002). *Standard operating procedures for borehole packer testing*. Available at: <https://www.scribd.com/document/169264009/Packer-Testing> [Accessed 05-05-2022].
- Rushby, L. (2015). University of Cape Town. Retrieved from Governmental Publications.
- SADC-GMI, IGRAC, IGS (2019) *SADC Framework for Groundwater Data Collection and Data Management. SADC-GMI report*. Bloemfontein, South Africa
- Sami, K. (2009). Groundwater exploration and development. *The Basement Aquifers of Southern Africa*, p. 19.
- Schürch, M., and Vuataz, F.D. (2002). Hydrochemical multiparameter log analysis in a shallow, heterogeneous alluvial aquifer (Wallis Canton, Switzerland). *Bulletin for Applied Geology*, 7(1), 3-18.
- Scoon, R. and Viljoen, M. (2016). The Eastern Limb of the Bushveld Complex, South Africa. In *Africa's Top Geological Sites - produced for the 35th International Geological Congress in Cape Town* (pp. 55-60). Cape Town, South Africa: Struik Nature, a division of Penguin Random House (Pty) Ltd.

- Scoon, R.N. (2002). A new occurrence of Merensky Reef on the flanks of the Zaaikloof dome, northeastern Bushveld Complex: Relationship between diapirism and magma replenishment. *Economic Geology*, 97(5), pp. 1037–1049.
- Scoon, R.N. and Mitchell, A.A. (2004). The platiniferous dunite pipes in the eastern limb of the Bushveld Complex: review and comparison with unmineralized discordant ultramafic bodies. *South African Journal of Geology*, 107(4), pp. 505–520.
- Scoon, R.N. and Teigler, B. (1995). A new LG-6 chromite reserve at Eerste Geluk in the boundary zone between the central and southern sectors of the eastern Bushveld Complex. *Economic Geology*, 90(4), pp. 969–982.
- Scoon, R.N. and Viljoen, M.J. (2019). Geoheritage of the Eastern Limb of the Bushveld Igneous Complex, South Africa: a uniquely exposed layered igneous intrusion. *Geoheritage*, 11(4), pp. 1723–1748.
- Seabrook, C. L. (2005). *The Upper Critical and Lower Main Zones of the eastern Bushveld Complex* [Doctoral dissertation, University of the Witwatersrand].
- Sergeant, C. J., Starkey, E. N., Bartz, K. K., Wilson, M. H., and Mueter, F. J. (2016). A practitioner's guide for exploring water quality patterns using principal components analysis and Procrustes. *Environmental Monitoring and Assessment*, 188, 1–15.
- Serra, O.E. (1983). *Fundamentals of well-log interpretation*. Elsevier, Netherlands. ISBN 0-444-2132-7.
- Services Shangani Management (2020). *Geohydrological Impact Assessment - Hydrogeological study for Borwa and Lebowa Shafts*. Available at: http://www.shangani.co.za/wp-content/uploads/Annexure-E_Geohydrological-Assessment.pdf.
- SFA (Oxford). (2022). The Bushveld Complex, South Africa, Eastern Limb. Retrieved from SFA Oxford: <https://www.sfa-oxford.com/knowledge-and-insights/platinum-group-metals/pgm-mining/south-africa/the-bushveld-complex/eastern-limb>.
- Sheikhy Narany, T., Ramli, M. F., Aris, A. Z., Sulaiman, W. N. A., Juahir, H., and Fakharian, K. (2014). Identification of the hydrogeochemical processes in groundwater using classic integrated geochemical methods and geostatistical techniques, in Amol-Babol Plain, Iran. *The Scientific World Journal*, 2014.
- Sibanye-Stillwater. (2020). *Mineral Resources and Mineral Reserves Report*. Sibanye-Stillwater.
- Smith, M., Cross, K., Paden, M., and Laban, P. (Eds.). (2016). *Spring: Managing groundwater sustainably*. IUCN. <https://doi.org/10.2305/IUCN.CH.2016.WANI.8.en>
- Speight, J.G. (2019). Origin and Production In Speight, J.G. (Ed), *Natural gas: a basic handbook*. Gulf Professional Publishing. <https://doi.org/10.1016/B978-0-12-809570-6.00002-3>
- Steingrímsson, B. (2011). Geothermal well logging: Geological wireline logs and fracture imaging. *Short Course on Geothermal Drilling, Resource Development and Power Plants*, El Salvador.
- Stewart, R.R., Huddleston, P. D., and Kan, T. K. (1984). Seismic versus sonic velocities: A vertical seismic profiling study. *Geophysics*, 49(8), 1153-1168.
- Stoch, B., Basson, I. J., and Miller, J. A. (2020). Implicit Geomodelling of the Merensky and UG2 Reefs of the Bushveld Complex from Open-Source Data: Implications for the Complex's Structural History. *Minerals*, 10(11), 975.
- Titus, R., Witthüser, K. and Walters, B. (2009) 'Groundwater and mining in the Bushveld Complex', in Proceedings of the international mine water conference, Pretoria, South Africa. *CiteSeer*, pp. 178–184.
- Tladi, T. M., Ndambuki, J. M., Olwal, T. O., and Rwanga, S. S. (2023). Groundwater Level Trend Analysis and Prediction in the Upper Crocodile (West) Basin, South Africa.
- Tretner, A., Zimmer, M., Erzinger, J., Nakada, S., and Saito, M. (2008). Real-time drill mud gas logging at the USDP-4 drilling, Unzen volcano, Japan. *Journal of Volcanology and Geothermal Research*, 175(1-2), 28-34.

- Trumbull, R. B., Ashwal, L. D., Webb, S. J., and Veksler, I. V. (2015). Drilling through the largest magma chamber on Earth: Bushveld Igneous complex Drilling Project (BICDP). *Scientific Drilling*, 19, 33-37.
- Tsang, C.F., and Doughty, C. (2003). Multirate flowing fluid electric conductivity logging method. *Water Resources Research*, 39(12).
- Tsang, C.F., Hufschmied, P., and Hale, F.V. (1990). Determination of fracture inflow parameters with a borehole fluid conductivity logging method. *Water Resources Research*, 26(4), 561-578.
- Tsang, C.F., Rosberg, J. E., Sharma, P., Berthet, T., Juhlin, C., and Niemi, A. (2016). Hydrologic testing during drilling: application of the flowing fluid electrical conductivity (FFEC) logging method to drilling of a deep borehole. *Hydrogeology Journal*, 24(6), 1333-1341.
- Tsogtbaatar, A., and Sato, M. (2024). Characterisation of geological thin layer by borehole radar. *Exploration Geophysics*, 55(2), 182-190.
- USGS (2019). *Borehole Nuclear Magnetic Resonance (NMR)*. Available at: <https://www.usgs.gov/mission-areas/water-resources/science/borehole-nuclear-magnetic-resonance-nmr#overview> [Accessed 29-04-2022].
- USGS, 2016. *Vertical flowmeter logging*. Available at: <https://water.usgs.gov/ogw/bgas/flowmeter/> [Accessed 29-04-2022].
- van Biljon, M. (2013). *Numerical modelling and geohydrological report for the Leeuwkop project, Revision 2*. MVB Groundwater Consulting.
- Van Wyk, E., Van Tonder, G. J., and Vermeulen, D. (2012). Characteristics of local groundwater recharge cycles in South African semi-arid hard rock terrains: Rainfall–groundwater interaction. *Water SA*, 38(5), 747–754.
- Velis, M., Conti, K. I., and Biermann, F. (2017). Groundwater and human development: Synergies and trade-offs within the context of the sustainable development goals. *Sustainability Science*, 12(6), 1007–1017. <https://doi.org/10.1007/s11625-017-0490-9>
- Vetger, J. R. (1995). An explanation of a set of national groundwater maps, WRC report TT 74/95. Water Res. Comm. Pretoria, South Africa.
- Viljoen, M. and Chürmann, L. (1998). Platinum-group metals In Wilson, M.G.C. and Anhaeusser, C.R. (Eds) *The mineral resources of South Africa*, pp. 532–568.
- Vouillamoz, J.M., Descloitres, M., Toe, G., and Legchenko, A. (2005). Characterization of crystalline basement aquifers with MRS: comparison with boreholes and pumping tests data in Burkina Faso. *Near Surface Geophysics*, 3(3), 205-213.
- Wali, S. U., Umar, K. J., Abubakar, S. D., Ifabiya, I. P., Dankani, I. M., Shera, I. M., and Yauri, S. G. (2019). Hydrochemical characterization of shallow and deep groundwater in Basement Complex areas of southern Kebbi State, Sokoto Basin, Nigeria. *Applied Water Science*, 9, 1–36.
- Walsh, D., Turner, P., Grunewald, E., Zhang, H., Butler Jr, J.J., Reboulet, E. and Fitzpatrick, A. (2013). A small-diameter NMR logging tool for groundwater investigations. *Groundwater*, 51(6), 914-926.
- Water Geosciences Consulting (2007). *Groundwater Report for the Spitzkop area, Steelpoort Valley, Limpopo Province*. Published report.
- Webb, S., Ashwal, L., Roelofse, F., Khosa, D., Trumbull, R., and Klemd, R. (2019). *The Bushveld Drilling Project (BVDP): Full Proposal*. Report for the International Continental Scientific Drilling Program.
- Webb, S., Ashwal, L., Roelofse, F., Trumbull, R., and Klemd, R. (2021). *The Bushveld Drilling Project (BVDP): Executive Summary*. Report for the International Continental Scientific Drilling Program.
- West, L.J., and Odling, N.E. (2007). Characterization of a multilayer aquifer using open well dilution tests. *Groundwater*, 45(1), 74-84.

- Wiersberg, T., and Erzinger, J. (2007). A helium isotope cross-section study through the San Andreas Fault at seismogenic depths. *Geochemistry, Geophysics, Geosystems*, 8(1).
- Wiersberg, T., and Erzinger, J. (2008). Origin and spatial distribution of gas at seismogenic depths of the San Andreas Fault from drill-mud gas analysis. *Applied Geochemistry*, 23(6), 1675-1690.
- Wiersberg, T., Erzinger, J., Zimmer, M., Schicks, J., and Dahms, E. (2005). Real-time gas analysis at the Mallik 2002 gas hydrate production research well. In *Scientific Results from Mallik 2002 Gas Hydrate Production Research Well Program, Mackenzie Delta, Northwest Territories, Canada*. Geological Survey of Canada.
- Wilson, A. H. (2015). The earliest stages of emplacement of the eastern Bushveld Complex: development of the Lower Zone, Marginal Zone and Basal Ultramafic Sequence. *Journal of Petrology*, 56(2), 347-388.
- Wilson, J.T., Mandell, W.A., Paillet, F.L., Bayless, E.R., Hanson, R.T., Kearl, P.M., Kerfoot, W.B., Newhouse, M.W. and Pedler, W.H. (2001). *An evaluation of borehole flowmeters used to measure horizontal ground-water flow in limestones of Indiana, Kentucky, and Tennessee, 1999* (No. 1). US Department of the Interior, US Geological Survey. Water-Resources Investigation Report 01-4139.
- Wonik, T., (2007). Borehole Logging In Knödel, K., Lange, G., and Voigt, H.J. (Eds). *Environmental geology: handbook of field methods and case studies*. Springer Science & Business Media.
- WSM Leshika, (Pty) Ltd (2004) Deep Aquifer Drilling Program. WSM Leshika. Available at: <https://www.dws.gov.za/ghreport/Home/Download.aspx?Id=5061>.
- Xu, Y., and Beekman, H. E. (2003). Groundwater recharge estimation in Southern Africa (Vol. 64). Unesco.
- Yidana, S. M., Banoeng-Yakubo, B., Akabzaa, T., and Asiedu, D. (2011). Characterization of the groundwater flow regime and hydrochemistry of groundwater from the Buem formation, Eastern Ghana. *Hydrological Processes*, 25(14), 2288–2301.
- Yihdego, Y. (2017). Hydraulic in situ testing for mining and engineering design: packer test procedure, preparation, analysis and interpretation. *Geotechnical and Geological Engineering*, 35(1), 29-44.
- Zakaria, N., Anornu, G., Adomako, D., Owusu-Nimo, F., and Gibrilla, A. (2021). Evolution of groundwater hydrogeochemistry and assessment of groundwater quality in the Anayari catchment. *Groundwater for Sustainable Development*, 12(April 2020), 100489. <https://doi.org/10.1016/j.gsd.2020.100489>

APPENDIX A

Table A: Geological Log

Core section bottom depth (mbgl)	Lithology	CASE	Zone	Description
0,8	NORIT		uCZ	Fractured, rock altered as a result of fluid movement.
0,8	NORIT		uCZ	
0,8	NORIT		uCZ	
0,89	NORIT		uCZ	
1,86	NORIT		uCZ	
1,87	NORIT		uCZ	Fractured, path way for fluid movement.
2,11	NORIT		uCZ	Altered
2,11	NORIT		uCZ	
2,81	NORIT		uCZ	
2,9	NORIT		uCZ	Alteration of the rock- 20%
2,9	NORIT		uCZ	
3	NORIT		uCZ	
3,58	NORIT		uCZ	
3,76	NORIT		uCZ	Alteration of the rock- 20%
3,76	NORIT		uCZ	
4,55	NORIT		uCZ	
4,71	NORIT		uCZ	Alteration of the rock- 20%
4,71	NORIT		uCZ	
5,41	NORIT		uCZ	
5,66	NORIT		uCZ	With black spots that could be secondary magnetite
6	NORIT		uCZ	
6,3	NORIT		uCZ	
6,6	NORIT		uCZ	Core has fractures and the rock is slightly serpentinised; With black spots that could be secondary magnetite
6,74	NORIT		uCZ	Core is fractured and serpentinised; With black spots that could be secondary magnetite
7,29	NORIT		uCZ	
7,53	NORIT		uCZ	Core is fractured and serpentinised.
8,26	NORIT		uCZ	Core is fractured and serpentinised
8,26	SERP		uCZ	Core is fractured and highly serpentinised. Light green with dark green, greyish and brownish parts.
8,26	GABNR		uCZ	
8,27	NORIT		uCZ	Core is fractured and serpentinised.
9,04	GABNR		uCZ	
9,42	NORIT		uCZ	Core is fractured and serpentinised.
9,86	NORIT		uCZ	Core is fractured and serpentinised. Light green with dark green, greyish and brownish parts.
9,97	GABNR		uCZ	
10,27	NORIT		uCZ	Core is fractured and serpentinised. Darker green with lighter shades of green, greyish and brownish parts.
10,73	NORIT		uCZ	Core is fractured and serpentinised. Darker green with lighter shades of green, greyish and brownish parts.
10,84	GABNR		uCZ	

11,03	NORIT	u CZ	Core is fractured and serpentinised. Darker green with lighter shades of green, greyish and brownish parts.
11,44	NORIT	u CZ	Core is fractured and serpentinised. Darker green with lighter shades of green, greyish and brownish parts.
11,6026	NORIT	u CZ	Fault Zone-Core is fractured and serpentinised. Darker green with lighter shades of green, greyish and brownish parts.
11,745	GABNR	u CZ	
12,095	GABNR	u CZ	
12,11	SERP	u CZ	Serpentine after an olivine-bearing protolith; The rock is severely altered and porous
12,58	GABNR	u CZ	
12,96	NORIT	u CZ	
12,96	NORIT	u CZ	
12,96	SERP	u CZ	Fault Zone, Severely altered and porous.
12,9631	SERP	u CZ	The rock is porous. Alteration-50%. With black spots(magnetite).
13,47	GABNR	u CZ	White calcite veins
13,64	NORIT	u CZ	
13,94	NORIT	u CZ	
14,38	GABNR	u CZ	Fracture Zone with white calcite and chlorite at joints; White calcite veins
14,65	NORIT	u CZ	
14,78	NORIT	u CZ	
14,7864	SERP	u CZ	Highly altered
15,07	GABNR	u CZ	Fracture Zone with white calcite and chlorite at joints; White calcite veins
15,73	NORIT	u CZ	
16,04	GABNR	u CZ	with white calcite and chlorite
16,68	NORIT	u CZ	
16,89	GABNR	u CZ	
17,55	NORIT	u CZ	
17,6	NORIT	u CZ	
17,6	NORIT	u CZ	White silicate veins 1-2cm in size
17,6	NORIT	u CZ	Fractured
17,6	NORIT	u CZ	
17,83	GABNR	u CZ	
18,25	GABNR	u CZ	
18,55	GABNR	u CZ	
19,47	NORIT	u CZ	
19,48	GABNR	u CZ	
20,38	NORIT	u CZ	
20,47	GABNR	u CZ	
20,54	NORIT	u CZ	
21,07	GABNR	u CZ	Fractured with white calcite veins and Greyish blue green veins
21,23	NORIT	u CZ	
21,23	NORIT	u CZ	
21,23	NORIT	u CZ	
21,37	GABNR	u CZ	Greyish blue green veins
22,15	NORIT	u CZ	
22,15	NORIT	u CZ	
22,28	GABNR	u CZ	
22,2825	GABNR	u CZ	
23,22	ANRTS	u CZ	Greyish blue green chlorite and white calcite veins

23,48	NORIT		uCZ	
24,11	ANRTS		uCZ	Secondary Greyish blue green chlorite and white calcite at fracture joints
24,15	NORIT		uCZ	
24,96	ANRTS		uCZ	Secondary Greyish blue green chlorite and white calcite at fracture joints
25,11	NORIT		uCZ	
25,91	ANRTS		uCZ	
26,09	NORIT		uCZ	
26,61	NORIT		uCZ	Core is fractured
26,89	ANRTS		uCZ	Fractured with greyish blue green chlorite alteration at joints
26,94	NORIT		uCZ	Core is fractured
27,08	ANRTS		uCZ	Fractured with greyish blue green chlorite alteration at joints
27,67	NORIT		uCZ	
27,92	NORIT		uCZ	
28,58	GABNR		uCZ	
28,85	NORIT		uCZ	
28,8562	NORIT		uCZ	
29,51	GABNR		uCZ	
29,6	ANRTS		uCZ	
29,6	ANRTS		uCZ	
29,6	ANRTS		uCZ	
29,81	ANRTS		uCZ	Fractured
30,55	GABNR		uCZ	
30,77	ANRTS		uCZ	
31,52	GABNR		uCZ	
31,73	ANRTS		uCZ	
32,45	GABNR		uCZ	Fractured with calcite and chlorite alteration at joints
32,66	ANRTS		uCZ	
33	GABNR		uCZ	Fractured with calcite and chlorite alteration at joints
33,47	ANRTS		uCZ	
33,54	ANRTS		uCZ	
34,36	GABNR;ANRTS		uCZ	
34,5	ANRTS		uCZ	
35,41	ANRTS		uCZ	
35,41	GABNR;ANRTS		uCZ	
35,51	ANRTS		uCZ	
35,94	GABNR;ANRTS		uCZ	
36,18	GABNR		uCZ	With white calcite and silica veins (greyish blue green) chlorite veins; Alteration (chlorite) in fractures.
36,4	ANRTS		uCZ	
37,21	GABNR		uCZ	With white calcite and silica veins (greyish blue green) chlorite veins; Alteration (chlorite) in fractures.
37,31	ANRTS		uCZ	
38,13	GABNR		uCZ	
38,26	ANRTS		uCZ	
38,64	ANRTS		uCZ	
39,06	GABNR;ANRTS		uCZ	
39,11	ANRTS		uCZ	
39,12	GABNR;ANRTS		uCZ	

39,82	GABNR	uCZ	
40,11	ANRTS	uCZ	
40,75	GABNR	uCZ	
41,11	ANRTS	uCZ	
41,61	ANRTS	uCZ	
41,73	GABNR	uCZ	
41,94	ANRTS	uCZ	
41,94	ANRTS	uCZ	
41,94	ANRTS	uCZ	The core is altered as a result of fluids infiltrating the fractures (Oxidised clay minerals)
42	GABNR	uCZ	
42,6	GABNR	uCZ	
43,5	GABNR;NORIT	uCZ	
43,86	ANRTS	uCZ	
44,46	GABNR;NORIT	uCZ	
44,57	ANRTS	uCZ	
44,6	ANRTS	uCZ	
44,6	ANRTS	uCZ	
45,1	GABNR	uCZ	
45,25	GABNR	uCZ	
45,76	ANRTS	uCZ	Fault zone, the rock is semi-porous with secondary clay minerals forming within the fractures (Rock alteration - 30%)
46,185	GABNR	uCZ	
46,72	ANRTS	uCZ	Fault zone, the rock is semi-porous with secondary clay minerals forming within the fractures (Rock alteration - 30%)-due to Hydrothermal fluid movement
47,105	GABNR	uCZ	
47,56	ANRTS	uCZ	
48	GABNR	uCZ	
48,5	NORIT	uCZ	
48,94	GABNR	uCZ	
49,47	NORIT	uCZ	
49,66	GABNR	uCZ	
50,44	NORIT	uCZ	
50,53	GABNR	uCZ	Section is highly fractured (Fault Zone)
50,6042	NORIT	uCZ	
50,66	NORIT	uCZ	
51,07	GABNR	uCZ	
51,26	ANRTS	uCZ	
51,2683	ANRTS	uCZ	
51,41	GABNR	uCZ	
51,413	GABNR	uCZ	With greyish blue green chloritic veins
52,22	NORIT	uCZ	
52,39	NORIT	uCZ	With greyish blue green chloritic veins
53,18	NORIT	uCZ	
53,29	NORIT	uCZ	With greyish blue green chloritic veins
53,66	NORIT	uCZ	
53,97	NORIT	uCZ	
53,97	NORIT	uCZ	With greyish blue green chloritic veins
54,18	NORIT	uCZ	With greyish blue green chloritic veins

54,98	NORIT		uCZ	
55,08	NORIT		uCZ	With greyish blue green chloritic veins
55,95	NORIT		uCZ	
56	NORIT		uCZ	With greyish blue green chloritic veins
56,58	NORIT		uCZ	
56,6	ANRTS		uCZ	
56,6	NORIT		uCZ	
56,94	NORIT		uCZ	
57,02	NORIT		uCZ	
57,65	NORIT		uCZ	
57,65	NORIT		uCZ	
57,65	NORIT		uCZ	
57,775	NORIT		uCZ	
58,62	NORIT		uCZ	
58,68	NORIT		uCZ	
59,59	NORIT		uCZ	
59,62	NORIT		uCZ	
60,055	NORIT		uCZ	
60,5	NORIT		uCZ	
60,6	NORIT		uCZ	
61,55	NORIT		uCZ	With a network of greyish blue green chlorite veins
61,59	NORIT		uCZ	
62,45	NORIT		uCZ	
62,55	DOLRT		uCZ	Dolerite dyke
62,68	NORIT		uCZ	
63,05	DOLRT		uCZ	Dolerite dyke
63,23	NORIT		uCZ	
63,2312	NORIT		uCZ	
63,2326	ANRTS		uCZ	
63,25	DOLRT		uCZ	Dolerite dyke
64,15	PYRXN		uCZ	
64,23	DOLRT		uCZ	Dolerite dyke
65,02	PYRXN		uCZ	
65,16	NORIT		uCZ	
65,5	PYRXN		uCZ	
66,02	NORIT		uCZ	
66,05	NORIT		uCZ	
66,9	NORIT		uCZ	
67,02	NORIT		uCZ	
67,82	NORIT		uCZ	
67,97	NORIT		uCZ	
68,55	NORIT		uCZ	
68,83	NORIT		uCZ	
68,93	NORIT		uCZ	
68,94	NORIT		uCZ	
69,745	NORIT		uCZ	

69,754	NORIT	uCZ	With chloritic veins
69,89	NORIT	uCZ	
70,7	NORIT	uCZ	With chloritic veins
70,82	NORIT	uCZ	
70,8239	NORIT	uCZ	
71,59	ANRTS	uCZ	
71,65	NORIT	uCZ	With chloritic veins
71,74	ANRTS	uCZ	
71,995	NORIT	uCZ	With chloritic veins
72,41	GABNR	uCZ	With chloritic veins
72,67	NORIT	uCZ	
73,4	GABNR	uCZ	With chloritic veins
73,403	GABNR	uCZ	With chloritic veins
73,65	NORIT	uCZ	
74,35	DOLRT	uCZ	With chloritic veins
74,353	DOLRT	uCZ	Dolerite intrusion
74,51	NORIT	uCZ	
74,68	NORIT	uCZ	
75,1	DOLRT;NORIT	uCZ	Dolerite intrusion
75,37	NORIT	uCZ	
75,98	NORIT	uCZ	
76,16	NORIT	uCZ	
76,93	NORIT	uCZ	
77,12	NORIT	uCZ	
77,67	NORIT	uCZ	
77,87	NORIT	uCZ	
77,99	NORIT	uCZ	
78	ANRTS	uCZ	
78,81	ANRTS	uCZ	
78,96	GABNR	uCZ	fractured and altered; -Silicate vein 0-0.16-white pale green
79,76	NORIT	uCZ	
79,83	GABNR	uCZ	
80,6	GABNR	uCZ	
80,75	NORIT	uCZ	-With greyish blue green chlorite veins
81	NORIT	uCZ	-With fractures and greyish blue green chlorite veins
81,48	NORIT	uCZ	-With fractures and greyish blue green chlorite veins
81,51	GABNR	uCZ	
82,38	NORIT	uCZ	-With fractures and greyish blue green chlorite veins
82,44	GABNR	uCZ	
83,37	NORIT	uCZ	-With fractures and greyish blue green chlorite veins
83,38	GABNR	uCZ	
83,62	GABNR	uCZ	
84,15	GABNR	uCZ	Fault Zone (highly fractured)
84,33	GABNR	uCZ	
84,96	GABNR	uCZ	Fault Zone (highly fractured); Chloritic veins

85,33	GABNR	uCZ	
85,93	GABNR	uCZ	Fault Zone (highly fractured); Chloritic veins
86,33	GABNR	uCZ	
86,6	GABNR	uCZ	
86,85	NORIT	uCZ	Fault Zone (highly fractured); Chloritic veins; With silica stalkwork
87,1	GABNR	uCZ	
87,85	NORIT	uCZ	Fault Zone (highly fractured); Chloritic veins-greyish blue green; With silica stalkwork
88	GABNR	uCZ	
88,8	GABNR	uCZ	with chlorite veins
88,92	GABNR	uCZ	
89,59	GABNR	uCZ	
89,75	GABNR	uCZ	with chlorite veins
89,9	GABNR	uCZ	
90,1	GABNR	uCZ	with chlorite and silica veins
90,42	GABNR	uCZ	with chlorite veins
90,81	GABNR	uCZ	
91,33	GABNR	uCZ	with chlorite veins
91,77	GABNR	uCZ	
92,3	GABNR	uCZ	Fractured; with chlorite veins
92,61	GABNR	uCZ	
93,03	GABNR	uCZ	with chlorite veins
93,19	GABNR	uCZ	with chlorite veins
93,53	GABNR	uCZ	with silica and Opx veins
94,05	NORIT	uCZ	with chlorite veins
95,01	NORIT	uCZ	with chlorite veins
95,52	NORIT	uCZ	
95,86	GABNR	uCZ	with chlorite veins
96,02	GABNR	uCZ	with chlorite veins
96,33	GABNR	uCZ	
96,68	GABNR	uCZ	with greyish blue green chlorite veins
97,28	GABNR	uCZ	
97,286	NORIT	uCZ	
97,68	GABNR	uCZ	with greyish blue green chlorite veins
98,28	GABNR	uCZ	
98,55	GABNR	uCZ	with greyish blue green chlorite veins
98,64	GABNR	uCZ	
98,98	GABNR	uCZ	With greyish blue green chlorite veins
99,13	GABNR	uCZ	
99,52	GABNR	uCZ	With greyish blue green chlorite veins
100,06	NORIT	uCZ	
100,51	GABNR	uCZ	With greyish blue green chlorite veins
100,95	NORIT	uCZ	
101,46	GABNR	uCZ	With greyish blue green chlorite veins and alternating, thin anorthosite layers
101,62	NORIT	uCZ	
101,77	NORIT	uCZ	

102,05	GABNR		uCZ	With greyish blue green chlorite veins
102,28	GABNR		uCZ	With greyish blue green chlorite veins
102,575	NORIT		uCZ	
102,5864	NORIT		uCZ	
103,25	GABNR		uCZ	With greyish blue green chlorite veins
103,52	ANRTS		uCZ	
104,18	GABNR		uCZ	With greyish blue green chlorite veins
104,36	NORIT		uCZ	
104,605	NORIT		uCZ	
104,97	GABNR		uCZ	With greyish blue green chlorite veins
105,26	ANRTS		uCZ	
105,89	GABNR		uCZ	With greyish blue green chlorite veins
106,14	NORIT		uCZ	
106,79	GABNR		uCZ	With greyish blue green chlorite veins
107,01	NORIT		uCZ	With silica veins
107,63	NORIT		uCZ	
107,76	GABNR		uCZ	With greyish blue green chlorite veins
107,85	NORIT		uCZ	
108	GABNR		uCZ	With greyish blue green chlorite veins
108	GABNR		uCZ	With greyish blue green chlorite veins
108	GABNR		uCZ	
108,76	ANRTS		uCZ	
108,766	NORIT		uCZ	
109,49	GABNR		uCZ	
109,498	GABNR		uCZ	Fractured with chlorite alteration at joints
109,65	ANRTS		uCZ	
110,49	PYRXN		uCZ	Fractured
110,54	NORIT		uCZ	Leuconorite with white silica and green chlorite veins
110,97	PYRXN		uCZ	Fractured with chlorite alteration at joints
111,34	PYRXN		uCZ	Fractured with greyish blue green chlorite alteration at joints
112,25	PYRXN		uCZ	Fractured- with chloritic alteration at joints.
113,16	PYRXN		uCZ	Fractured with greyish blue green chlorite alteration at joints
114	PYRXN		uCZ	Fractured with greyish blue green chlorite alteration at joints
114,86	PYRXN		uCZ	Fractured with greyish blue green chlorite alteration at joints
115,71	PYRXN		uCZ	
116,71	PYRXN		uCZ	
117	PYRXN		uCZ	
117,6	PYRXN		uCZ	
118,45	PYRXN		uCZ	
119,39	PYRXN		uCZ	Fractured
120	PYRXN		uCZ	
120,28	PYRXN		uCZ	
121,23	PYRXN		uCZ	
122,19	PYRXN		uCZ	
123,1	PYRXN		uCZ	
123,99	PYRXN		uCZ	

124,92	PYRXN		uCZ	
125,95	PYRXN		uCZ	Chlorite veins
126,81	PYRXN		uCZ	Chlorite veins
127,725	PYRXN		uCZ	Chromite mineralization-disseminated + seams (1mm - 3mm in size, 40vol.% Chr) over 0.8m of the section
128,705	PYRXN		uCZ	Chromite mineralization-disseminated (>10 vol.%) + seams (0.5-10cm in size, 40-50vol.% Chr) over 0.8m of the section
129,02	PYRXN		uCZ	
129,63	PYRXN		uCZ	
130,59	PYRXN		uCZ	
131,6	PYRXN		uCZ	
132	PYRXN		uCZ	Fractured
132,39	PYRXN		uCZ	Fractured
133,38	PYRXN		uCZ	Fractured
133,82	ANRTS		uCZ	Greyish blue green chlorite and white calcite veins
134,71	ANRTS		uCZ	Secondary Greyish blue green chlorite and white calcite at fracture joints
135,56	ANRTS		uCZ	Secondary Greyish blue green chlorite and white calcite at fracture joints
136,51	ANRTS		uCZ	
				Fractured with greyish blue green chlorite alteration at joints
137,49	ANRTS		uCZ	
				Fractured with greyish blue green chlorite alteration at joints
137,68	ANRTS		uCZ	
138,27	NORIT		uCZ	
139,18	GABNR		uCZ	
140,11	GABNR		uCZ	
				Fractured
140,41	ANRTS		uCZ	
141,15	GABNR		uCZ	
142,12	GABNR		uCZ	
				Fractured with calcite and chlorite alteration at joints
143,05	GABNR		uCZ	
				Fractured with calcite and chlorite alteration at joints
143,6	GABNR		uCZ	
144,07	ANRTS		uCZ	
144,96	GABNR;ANRTS		uCZ	
146,01	GABNR;ANRTS		uCZ	
146,54	GABNR;ANRTS		uCZ	
146,78	GABNR		uCZ	With white calcite and silica veins (greyish blue green) chlorite veins; Alteration (chlorite) in fractures.
147,81	GABNR		uCZ	With white calcite and silica veins (greyish blue green) chlorite veins; Alteration (chlorite) in fractures.
148,73	GABNR		uCZ	
149,66	GABNR;ANRTS		uCZ	
149,72	GABNR;ANRTS		uCZ	
150,42	GABNR		uCZ	
151,35	GABNR		uCZ	
152,33	GABNR		uCZ	
152,6	GABNR		uCZ	

153,2	GABNR		uCZ	
154,1	NORIT		uCZ	
155,06	NORIT		uCZ	
155,7	GABNR		uCZ	
155,85	GABNR		uCZ	
156,785	GABNR		uCZ	
157,705	GABNR		uCZ	
158,6	GABNR		uCZ	
159,54	GABNR		uCZ	
160,26	GABNR		uCZ	
				Feldspar<40% Pyroxene>60% Section is highly fractured (Fault Zone)
161,13	GABNR		uCZ	
161,67	GABNR		uCZ	
162,01	GABNR		uCZ	
162,31	GABNR		uCZ	
162,99	NORIT		uCZ	
163,89	NORIT		uCZ	
164,57	NORIT		uCZ	
164,78	NORIT		uCZ	
165,68	NORIT		uCZ	
166,6	NORIT		uCZ	
167,54	NORIT		uCZ	
167,62	NORIT		uCZ	
168,375	NORIT		uCZ	
169,28	NORIT		uCZ	
170,22	NORIT		uCZ	
170,655	NORIT		uCZ	
171,1	NORIT		uCZ	
172,15	NORIT		uCZ	With a network of greyish blue green chlorite veins
173,15	DOLRT		uCZ	
173,65	DOLRT		uCZ	
173,85	DOLRT		uCZ	
174,83	DOLRT		uCZ	
175,76	NORIT		uCZ	
176,62	NORIT		uCZ	
177,5	NORIT		uCZ	
178,42	NORIT		uCZ	
179,43	NORIT		uCZ	
179,54	NORIT		uCZ	
180,345	NORIT		uCZ	
180,75	NORIT		uCZ	With chloritic veins
181,3	NORIT		uCZ	With chloritic veins
182,25	NORIT		uCZ	With chloritic veins

182,595	NORIT		uCZ	With chloritic veins
183,01	NORIT		uCZ	With chloritic veins
184	GABNR		uCZ	With chloritic veins
184,3	GABNR		uCZ	With chloritic veins
184,95	DOLRT		uCZ	Dolerite dyke
185,25	DOLRT		uCZ	Dolerite dyke
185,7	NORIT		uCZ	
186,58	NORIT		uCZ	
187,53	NORIT		uCZ	
188,47	NORIT		uCZ	
188,6	NORIT		uCZ	
189,41	ANRTS		uCZ	
190,36	NORIT		uCZ	
191,35	NORIT		uCZ	
191,6	NORIT		uCZ	With fractures and greyish blue green chlorite veins
192,08	NORIT		uCZ	With fractures and greyish blue green chlorite veins
192,98	NORIT		uCZ	With fractures and greyish blue green chlorite veins
193,97	NORIT		uCZ	With fractures and greyish blue green chlorite veins
194,75	GABNR		uCZ	Fault Zone (highly fractured); chloritic veins
195,56	GABNR		uCZ	Fault Zone (highly fractured); chloritic veins
196,53	GABNR		uCZ	Fault Zone (highly fractured); chloritic veins
197,45	NORIT		uCZ	Fault Zone (highly fractured); chloritic veins
198,45	NORIT		uCZ	Fault Zone (highly fractured); chloritic veins
199,4	GABNR		uCZ	With chloritic veins
200,35	GABNR		uCZ	With chloritic veins
200,7	GABNR		uCZ	With chloritic veins
201,02	GABNR		uCZ	With chloritic veins
201,93	GABNR		uCZ	With chloritic veins
202,9	GABNR		uCZ	With chloritic veins
203,63	GABNR		uCZ	With chloritic veins
203,79	GABNR		uCZ	With chloritic veins
204,65	NORIT		uCZ	With chloritic veins
205,61	NORIT		uCZ	With chloritic veins
206,46	GABNR		uCZ	With chloritic veins
206,62	GABNR		uCZ	With chloritic veins
207,28	GABNR		uCZ	With chloritic veins
208,28	GABNR		uCZ	With chloritic veins
209,15	GABNR		uCZ	With chloritic veins
209,58	GABNR		uCZ	
210,12	GABNR		uCZ	
211,11	GABNR		uCZ	
212,06	GABNR		uCZ	With greyish blue green chlorite veins
212,65	GABNR		uCZ	With greyish blue green chlorite veins
212,88	GABNR		uCZ	With greyish blue green chlorite veins
213,85	GABNR		uCZ	With greyish blue green chlorite veins
214,78	GABNR		uCZ	With greyish blue green chlorite veins

215,57	GABNR	uCZ	With greyish blue green chlorite veins
216,49	GABNR	uCZ	With greyish blue green chlorite veins
217,39	GABNR	uCZ	With greyish blue green chlorite veins
218,36	GABNR	uCZ	With greyish blue green chlorite veins
218,6	GABNR	uCZ	With greyish blue green chlorite veins
219,17	GABNR	uCZ	With greyish blue green chlorite veins
220,09	GABNR	uCZ	
220,89	GABNR	uCZ	Fractured with chlorite alteration at joints
221,09	PYRXN	uCZ	Fractured
221,57	PYRXN	uCZ	Fractured with chlorite alteration at joints
221,94	PYRXN	uCZ	Fractured with greyish blue green chlorite alteration at joints
222,85	PYRXN	uCZ	Fractured with greyish blue green chlorite alteration at joints
223,76	PYRXN	uCZ	Fractured with greyish blue green chlorite alteration at joints
224,6	PYRXN	uCZ	Fractured with greyish blue green chlorite alteration at joints
225,46	PYRXN	uCZ	Fractured with greyish blue green chlorite alteration at joints
226,31	PYRXN	uCZ	
227,31	PYRXN	uCZ	
227,6	PYRXN	uCZ	
228,2	PYRXN	uCZ	
229,05	PYRXN	uCZ	
229,99	PYRXN	uCZ	Fractured
230,6	PYRXN	uCZ	
230,88	PYRXN	uCZ	
231,83	PYRXN	uCZ	
232,79	PYRXN	uCZ	
233,7	PYRXN	uCZ	
234,59	PYRXN	uCZ	
235,52	PYRXN	uCZ	
236,55	PYRXN	uCZ	With chloritic veins
237,41	PYRXN	uCZ	With chloritic veins
238,325	PYRXN	uCZ	Chromite mineralization-disseminated + seams
239,305	PYRXN	uCZ	Chromite mineralization-disseminated + seams
239,62	PYRXN	uCZ	
240,23	PYRXN	uCZ	
241,19	PYRXN	uCZ	
242,2	PYRXN	uCZ	Fractured
242,6	PYRXN	uCZ	Fractured
242,99	PYRXN	uCZ	Fractured
243,98	PYRXN	uCZ	Fractured
244,84	PYRXN	uCZ	Fractured; Chlorite veins
245,6	PYRXN	uCZ	Fractured; Chlorite veins
245,76	PYRXN	uCZ	Fractured; Chlorite veins

246,69	PYRXN		uCZ	Fractured; Chlorite veins
247,605	PYRXN		uCZ	Fractured; Chlorite veins
248,525	PYRXN		uCZ	Fractured; Chlorite alteration; Disseminated chromite
248,66	PYRXN		uCZ	Fractured; Chlorite alteration; Disseminated chromite
249,33	PYRXN		uCZ	Fractured; Chlorite alteration; Disseminated chromite
250,28	PYRXN		uCZ	Fractured; Chlorite alteration; Disseminated chromite
251,23	PYRXN		uCZ	Fractured; Chlorite alteration; Disseminated chromite
251,65	PYRXN		uCZ	Fractured; Chlorite alteration; Disseminated chromite
252,06	PYRXN		uCZ	
252,95	PYRXN		uCZ	
253,78	PYRXN		uCZ	
254,6	PYRXN		uCZ	
255,48	PYRXN		uCZ	
256,4	PYRXN		uCZ	
257,33	PYRXN		uCZ	
257,65	PYRXN		uCZ	
258,17	PYRXN		uCZ	
259,16	PYRXN		uCZ	
260,11	PYRXN		uCZ	
260,54	PYRXN		uCZ	
261,05	PYRXN		uCZ	
261,95	PYRXN		uCZ	
262,82	PYRXN		uCZ	
263,7	PYRXN		uCZ	3 chromitite seams
264,48	PYRXN		uCZ	
265,43	PYRXN		uCZ	
266,36	PYRXN		uCZ	
266,6	PYRXN		uCZ	3 chromitite seams
267,18	ANRTS		uCZ	
268,16	NORIT		uCZ	
268,96	GABNR		uCZ	5cm thick semi-massive chromitite seam-50vol% fine grained chr
269,59	PYRXN		uCZ	disseminated 10vol% fine grained chromite; Chlorite veins; 5 to 10 cm thick dyke
269,84	ANRTS		uCZ	host disseminated chromite; Chlorite veins
270,8	NORIT		uCZ	host disseminated chromite; Chlorite veins
271,79	NORIT		uCZ	host disseminated chromite; Chlorite veins
272,53	NORIT		uCZ	host disseminated chromite; Chlorite veins
272,82	NORIT		uCZ	disseminated chromite; Chlorite veins; Fractures associated with a Shear Zone
273,75	NORIT		uCZ	host disseminated chromite; Chlorite veins
274,7	NORIT		uCZ	Chlorite veins
275,68	NORIT		uCZ	
276,46	NORIT		uCZ	
277,38	NORIT		uCZ	Chlorite veins
278,32	NORIT		uCZ	Chlorite veins
278,55	NORIT		uCZ	Shear Zone (Section very fractured); Chlorite veins; rock is severely altered and porous
279,22	NORIT		uCZ	Chlorite veins
280,17	NORIT		uCZ	Chlorite veins; Shear Zone (Section very fractured)

281,02	NORIT		uCZ	Chlorite veins
281,65	NORIT		uCZ	Chlorite veins
281,79	NORIT		uCZ	Chlorite veins
282,7	NORIT		uCZ	Chlorite veins; chromite lens
283,66	NORIT		uCZ	Chlorite veins
284,6	NORIT		uCZ	Chlorite veins
285,53	NORIT		uCZ	Chlorite veins
286,51	NORIT		uCZ	Chlorite veins
287,46	NORIT		uCZ	Chlorite veins
287,62	NORIT		uCZ	Chlorite veins
288,28	GABNR		uCZ	Chlorite veins
289,26	GABNR		uCZ	Chlorite veins Chlorite veins; 10cm thick dolerite dyke
290,15	GABNR		uCZ	
290,63	GABNR		uCZ	Chlorite veins
291,04	GABNR		uCZ	Chlorite veins Chlorite alteration along fractures
291,89	NORIT		uCZ	Disseminated chromite
292,78	NORIT		uCZ	
293,53	GABNR		uCZ	
293,75	GABNR		uCZ	
294,74	NORIT		uCZ	fractured disseminated chr
295,53	NORIT		uCZ	
296,47	GABNR		uCZ	
296,65	GABNR		uCZ	disseminated chr
297,31	PYRXN		uCZ	Chromitite lenses; Secondary calcite and serpentine in fractures
298,09	GABNR		uCZ	
299,02	GABNR		uCZ	
299,6	GABNR		uCZ	disseminated chr
299,86	GABNR		uCZ	
300,76	GABNR		uCZ	Chromitite lenses at 0.7m of the section
301,61	NORIT		uCZ	Fault Zone; Slicken sides + Chlorite alteration
302,38	NORIT		uCZ	
302,7	NORIT		uCZ	
303,2	PYRXN		uCZ	
304,12	PYRXN		uCZ	Fault Zone
305,03	DOLRT		uCZ	
305,23	DOLRT		uCZ	
305,7	NORIT		uCZ	
305,85	NORIT		uCZ	
306,74	DOLRT		uCZ	Dolerite dyke; Calcite and chlorite alteration

307,7	NORIT		uCZ	Calcite and chlorite alteration
308,6	PYRXN		uCZ	Calcite and chlorite alteration
309,54	DOLRT		uCZ	chlorite alteration
309,84	DOLRT		uCZ	chlorite alteration
310,47	NORIT		uCZ	chlorite alteration
311,32	NORIT		uCZ	chlorite alteration
311,57	NORIT		uCZ	chlorite alteration
312,21	NORIT		uCZ	chlorite alteration
313,11	NORIT		uCZ	chlorite alteration
314,08	NORIT		uCZ	chlorite alteration; Fault Zone; chlorite alteration at fractures
314,68	PYRXN		uCZ	chlorite alteration; Fault Zone; chlorite alteration at fractures
314,96	PYRXN		uCZ	chlorite alteration
315,76	NORIT		uCZ	Fault Zone, Severely fractured; chlorite alteration
316,49	NORIT		uCZ	Fault Zone, slicken sides; chlorite alteration
317,35	NORIT		uCZ	Fault Zone, slicken sides; chlorite alteration
318,21	NORIT		uCZ	Fault Zone, slicken sides; chlorite alteration
318,24	NORIT		uCZ	Fault Zone, slicken sides; chlorite alteration
319,2	NORIT		uCZ	Fault Zone, slicken sides; chlorite alteration
320,08	NORIT		uCZ	Fault Zone, slicken sides; chlorite alteration
320,6	DOLRT		uCZ	Dolerite dyke
320,93	DOLRT		uCZ	Dolerite dyke; Fault Zone
323,45	NORIT		uCZ	
323,6	NORIT		uCZ	
323,3	DOLRT		uCZ	Dolerite dyke; Fault Zone; -Severely fractured section
323,5	NORIT		uCZ	
323,6	NORIT		uCZ	
324,3	NORIT		uCZ	
325,1	NORIT		uCZ	
326,0	NORIT		uCZ	
326,6	NORIT		uCZ	
326,9	NORIT		uCZ	
327,7	NORIT		uCZ	
328,7	NORIT		uCZ	
329,6	NORIT		uCZ	
330,5	NORIT		uCZ	
331,4	NORIT		uCZ	
332,3	NORIT		uCZ	
332,8	NORIT		uCZ	
333,0	NORIT		uCZ	
334,0	NORIT		uCZ	
334,9	NORIT		uCZ	
335,6	NORIT		uCZ	
335,7	NORIT		uCZ	
336,6	NORIT		uCZ	
337,6	NORIT		uCZ	
338,5	PYRXN		uCZ	
338,6	PYRXN		uCZ	

339,3	PYRXN		uCZ	
340,3	PYRXN		uCZ	
341,3	PYRXN		uCZ	
341,7	PYRXN		uCZ	
342,1	PYRXN		uCZ	
343,0	PYRXN		uCZ	
343,9	PYRXN		uCZ	
344,6	PYRXN		uCZ	
344,8	PYRXN		uCZ	
345,8	PYRXN		uCZ	
346,7	PYRXN		uCZ	
347,6	PYRXN		uCZ	
348,6	PYRXN		uCZ	
349,5	PYRXN		uCZ	
350,5	PYRXN		uCZ	Phase 1 depth (PQ)
351,4	PYRXN		uCZ	
351,6	PYRXN		uCZ	
352,8	PYRXN		uCZ	
353,7	PYRXN		uCZ	
357,1	PYRXN		uCZ	
358,1	PYRXN		uCZ	
359,1	PYRXN		uCZ	
359,5	PYRXN		uCZ	Fault Zone, Section is severely fractured
359,9	PYRXN		uCZ	Chlorite + Calcite veins
360,8	PYRXN		uCZ	Chlorite + Calcite + serpentine associated with fractures
361,7	PYRXN		uCZ	
362,4	PYRXN		uCZ	
362,6	PYRXN		uCZ	
363,6	NORIT		uCZ	
364,5	NORIT		uCZ	
366,3	PYRXN		uCZ	
367,3	PYRXN		uCZ	
368,3	PYRXN		uCZ	
368,5	PYRXN		uCZ	
369,2	PYRXN		uCZ	
370,1	PYRXN		uCZ	
371,1	PYRXN		uCZ	
371,5	PYRXN		uCZ	
354,3	PYRXN		uCZ	
355,3	PYRXN		uCZ	
356,2	PYRXN		uCZ	
356,5	PYRXN		uCZ	
372,0	PYRXN		uCZ	
372,9	PYRXN		uCZ	
373,8	PYRXN		uCZ	
374,5	PYRXN		uCZ	
374,6	PYRXN		uCZ	

375,6	PYRXN		uCZ	
376,5	PYRXN		uCZ	
377,4	PYRXN		uCZ	
378,4	PYRXN		uCZ	
379,4	PYRXN		uCZ	
380,4	PYRXN		uCZ	
380,5	PYRXN		uCZ	
381,3	PYRXN		uCZ	
382,2	PYRXN		uCZ	Fault Zone (Slicken sides); Fractures associated with secondary serpentine and chlorite
383,1	PYRXN		uCZ	
383,5	PYRXN		uCZ	Fractures filled with chlorite and serpentine
383,9	PYRXN		uCZ	
384,9	PYRXN		uCZ	
385,9	PYRXN		uCZ	
386,5	PYRXN		uCZ	
386,7	PYRXN		uCZ	Fractures filled with calcite and chlorite
387,6	PYRXN		uCZ	
388,5	PYRXN		uCZ	Severely fractured
389,5	PYRXN		uCZ	
390,3	PYRXN		uCZ	
391,2	PYRXN		uCZ	
392,1	PYRXN		uCZ	
392,5	PYRXN		uCZ	Fractures filled with chlorite and calcite
393,1	PYRXN		uCZ	
394,0	PYRXN		uCZ	
395,0	PYRXN		uCZ	
395,4	PYRXN		uCZ	
395,9	PYRXN		uCZ	Section severely fractured (brittle vertical fractures); Chlorite infilling'; Microbiology sample taken at 394.52 to 395.15 (60 cm)
396,9	PYRXN		uCZ	
397,8	PYRXN		uCZ	
398,4	PYRXN		uCZ	
398,7	PYRXN		uCZ	
399,7	PYRXN		uCZ	
400,7	PYRXN		uCZ	
401,5	PYRXN		uCZ	
401,6	PYRXN		uCZ	
402,6	PYRXN		uCZ	
403,4	PYRXN		uCZ	Fractures filled with calcite and chlorite
404,4	PYRXN		uCZ	
404,4	PYRXN		uCZ	Fractures filled greyish blue green chlorite
405,3	PYRXN		uCZ	
406,3	PYRXN		uCZ	
407,2	PYRXN		uCZ	
407,6	PYRXN		uCZ	
408,0	PYRXN		uCZ	

408,9	PYRXN		uCZ	
409,9	PYRXN		uCZ	
410,4	PYRXN		uCZ	
410,8	PYRXN		uCZ	
411,8	PYRXN		uCZ	
412,8	PYRXN		uCZ	
413,6	PYRXN		uCZ	
414,4	PYRXN		uCZ	
415,4	PYRXN		uCZ	
416,3	PYRXN		uCZ	
416,4	PYRXN		uCZ	
417,3	PYRXN		uCZ	With leucocratic lenses; Chloritic alteration along fractures
418,2	PYRXN		uCZ	
419,1	PYRXN		uCZ	Fractures filled with chlorite and calcite
419,5	PYRXN		uCZ	
420,0	PYRXN		uCZ	
420,9	PYRXN		uCZ	
421,9	PYRXN		uCZ	
422,5	PYRXN		uCZ	
422,7	PYRXN		uCZ	
423,6	PYRXN		uCZ	
424,6	PYRXN		uCZ	
425,4	PYRXN		uCZ	
426,4	PYRXN		uCZ	
427,3	PYRXN		uCZ	
428,2	PYRXN		uCZ	
428,4	PYRXN		uCZ	
429,2	NORIT		uCZ	With chlorite and calcite alteration
430,2	NORIT		uCZ	With chlorite and calcite veins
431,1	PYRXN		uCZ	Disseminated Chr; with silica veins
431,5	NORIT		uCZ	Fractured with silica veins; With leucocratic lenses; Disseminated Chr
431,9	NORIT		uCZ	
432,9	NORIT		uCZ	With alternating leucocratic (Anorthosite) intervals that host phlogopite laths
433,8	NORIT		uCZ	With silica veins
434,5	NORIT		uCZ	
434,6	NORIT		uCZ	
435,5	NORIT		uCZ	
436,5	NORIT		uCZ	
437,4	NORIT		uCZ	
438,4	NORIT		uCZ	
439,3	NORIT		uCZ	
440,3	NORIT		uCZ	
440,5	NORIT		uCZ	
441,1	NORIT		uCZ	
442,1	NORIT		uCZ	
443,1	NORIT		uCZ	

443,5	NORIT	uCZ	With fractures associated with chloritic alteration
444,0	NORIT	uCZ	Disseminated chromite
444,8	PYRXN	uCZ	
445,8	PYRXN	uCZ	Fractured filled with chlorite
446,5	PYRXN	uCZ	
446,7	PYRXN	uCZ	
447,6	PYRXN	uCZ	Secondary calcite and chlorite in fractures; Chromitite lenses ; Disseminated chromite at about 0.75m within the pyroxenite
448,5	PYRXN	uCZ	Fractures filled by calcite and chlorite; Oxidation at 0.6m of the section
449,5	PYRXN	uCZ	The anorthositic intervals host chromite lense (0.5cm), disturbed chromitite seams (0.5-2mm thick) disseminated chromite which give the rock a greyish purple hue
450,3	ANRTS	uCZ	Disseminated chromite; Fractures filled with calcite and chlorite
451,3	ANRTS	uCZ	Disseminated Chromite; Fractures infilled by calcite; Silica veins
452,1	ANRTS	uCZ	Fractures infilled by calcite; Silica veins
452,4	ANRTS	uCZ	Fractures infilled by calcite; Silica veins
453,1	ANRTS	uCZ	Finely disseminated chromite (30 vol%); Hosts multiple chromitite seams (0.5-1.5cm thick)
453,8	ANRTS	uCZ	-Hosts a semi massive chromites seams (50 vol%) and dense disseminations of chromite (10-20 vol%) over 0.7 m of the section.
454,9	PYRXN	uCZ	Chlorite infilling fractures
455,5	PYRXN	uCZ	-Severely fractured
455,8	PYRXN	uCZ	Hosts a 0.5 cm thick semi massive chromitite seam at 0.15 m of the section
456,6	PYRXN	uCZ	Hosts three semi massive chromitite seams; Disseminated fine grained chromite throughout the section; Chlorite infilling fractures
457,6	PYRXN	uCZ	Chlorite infilling fractures
458,5	PYRXN	uCZ	Chlorite infilling fractures
459,4	PYRXN	uCZ	Chlorite infilling fractures
460,3	PYRXN	uCZ	Chlorite infilling fractures
461,2	PYRXN	uCZ	Chlorite infilling fractures
461,4	PYRXN	uCZ	Chlorite infilling fractures
462,1	PYRXN	uCZ	Chlorite infilling fractures
463,0	PYRXN	uCZ	Chlorite infilling fractures
463,9	PYRXN	uCZ	
464,5	PYRXN	uCZ	
464,7	PYRXN	uCZ	
465,6	PYRXN	uCZ	Chlorite infilling fractures
466,6	PYRXN	uCZ	
467,4	PYRXN	uCZ	Fault Zone-Section severely fractured
468,4	PYRXN	uCZ	Chlorite infilling fractures
469,2	PYRXN	uCZ	Chlorite infilling fractures
470,2	PYRXN	uCZ	Chlorite infilling fractures
470,4	PYRXN	uCZ	Fractures filled with calcite and chlorite
471,2	PYRXN	uCZ	Fractures filled with calcite and chlorite
472,0	PYRXN	uCZ	
472,9	PYRXN	uCZ	Secondary calcite and chlorite associated with fractures; Severely fractured
473,5	PYRXN	uCZ	
473,7	PYRXN	uCZ	
474,7	PYRXN	uCZ	Chlorite infilling fractures
475,5	PYRXN	uCZ	Fractures filled by chlorite; Severely fractured section
476,5	PYRXN	uCZ	Chlorite infilling fractures
477,4	PYRXN	uCZ	Chlorite infilling fractures

478,3	PYRXN	uCZ	Chlorite infilling fractures
479,2	PYRXN	uCZ	Fractures filled by chlorite; Section severely fractured from 0.6 m to the end of the section
479,4	PYRXN	uCZ	Fractures filled by chlorite; With anorthosite vein (3cm wide)
480,0	PYRXN	uCZ	
480,9	PYRXN	uCZ	
481,9	PYRXN	uCZ	
482,5	PYRXN	uCZ	Chlorite infilling fractures
482,6	PYRXN	uCZ	Chlorite infilling fractures
483,6	PYRXN	uCZ	Chlorite infilling fractures
484,4	PYRXN	uCZ	Fractures filled by chlorite; Severely fractured section
485,4	PYRXN	uCZ	Fractures filled by chlorite; Severely fractured section
485,5	PYRXN	uCZ	Fractures filled by chlorite; Severely fractured section
486,3	PYRXN	uCZ	Chlorite infilling fractures
487,2	PYRXN	uCZ	Chlorite infilling fractures
488,2	PYRXN	uCZ	
488,5	PYRXN	uCZ	Hosts a greyish black dolerite dyke that is about 2.5 cm wide.
			Hosts a greyish black dolerite dyke that is about 3 cm wide.
489,1	PYRXN	uCZ	
490,0	PYRXN	uCZ	Chlorite infilling fractures
			Hosts a 15 cm wide greyish black dolerite dyke; Chlorite infilling fractures
490,9	PYRXN	uCZ	
491,5	PYRXN	uCZ	
491,7	PYRXN	uCZ	
492,6	PYRXN	uCZ	
493,6	PYRXN	uCZ	Chlorite infilling a network of fractures.
494,2	PYRXN	uCZ	Chlorite and calcite infilling fractures; 1 cm thick dolerite dyke
495,4	ANRTS	uCZ	With multiple thin chromitite seams (1-2 cm) and multiple 1mm stringers as well as chromite disseminations throughout the section.
496,3	ANRTS	uCZ	With multiple thin chromitite seams (1-2 cm) and multiple 1mm stringers as well as chromite disseminations throughout the section.
497,0	ANRTS	uCZ	With multiple thin chromitite seams (1-2 cm) and multiple 1mm stringers as well as chromite disseminations throughout the section.
497,3	NORIT	uCZ	Light chromite disseminations
497,4	NORIT	uCZ	Light chromite disseminations
494,4	CHR	uCZ	100% chromite; Chlorite infilling fractures; Very fine grained
498,2	PYRXN	uCZ	Chlorite infilling fractures
499,2	PYRXN	uCZ	Chlorite infilling fractures
500,2	PYRXN	uCZ	Chlorite infilling fractures
500,4	PYRXN	uCZ	
501,2	PYRXN	uCZ	
502,1	PYRXN	uCZ	
503,1	PYRXN	uCZ	Black massive chromitite-about 2cm thick, coarse grained, 100% chromite
503,2	CHR	uCZ	Chromite-100%; 7cm thick; Massive
503,6	PYRXN	uCZ	
503,9	PYRXN	uCZ	
504,9	PYRXN	uCZ	Lightly disseminated Chromite; Disturbed chromitite stringer (1-2mm thick) at 0.68m
505,8	PYRXN	uCZ	Lightly disseminated Chromite; 3 chromitite seams; 7cm thick, semi-massive (60-90% chromite); 3cm-semi massive to massive (40-50% chromite); 0.5 cm massive
506,4	PYRXN	uCZ	Hosts 3 massive chromitite seams separated by pyroxenite.

506,8	PYRXN		uCZ	
507,7	PYRXN		uCZ	A broken chromitite seam at end of the section-thickness no clear; With trace amounts of sulphides and phlogopite
508,7	PYRXN		uCZ	Semi massive chromitite seam 0.15m; Chromite-50%; Fills interstitial spaces between large pyroxenite grains
509,5	PYRXN		uCZ	
510,4	PYRXN		uCZ	
511,3	PYRXN		uCZ	
512,3	PYRXN		uCZ	
512,4	PYRXN		uCZ	
513,2	PYRXN		uCZ	
514,1	PYRXN		uCZ	
515,0	PYRXN		uCZ	Densely disseminated chromite from 0.5 - 0.65m of the section;
515,5	PYRXN		uCZ	Lightly disseminated chromite
515,9	PYRXN		uCZ	Lightly disseminated chromite
516,8	PYRXN		uCZ	Lightly disseminated chromite
517,8	PYRXN		uCZ	
518,5	PYRXN		uCZ	Lightly disseminated chromite
518,7	PYRXN		uCZ	Densely disseminated chromite
519,7	PYRXN		uCZ	Semi massive chromitite seam (10cm tick) at 0.3m of the section
520,7	PYRXN		uCZ	
521,5	PYRXN		uCZ	Semi massive chromitite seam (about 7cm thick) at 0.3 m of the section
522,4	PYRXN		uCZ	
523,4	PYRXN		uCZ	
524,4	PYRXN		uCZ	
524,4	PYRXN		uCZ	
525,3	PYRXN		uCZ	
526,2	PYRXN		uCZ	
527,2	PYRXN		uCZ	
527,5	PYRXN		uCZ	
528,1	PYRXN		uCZ	
529,0	PYRXN		uCZ	
530,0	PYRXN		uCZ	
530,4	PYRXN		uCZ	
531,0	PYRXN		uCZ	
531,9	PYRXN		uCZ	
532,9	PYRXN		uCZ	
533,4	PYRXN		uCZ	
533,8	PYRXN		uCZ	
534,8	PYRXN		uCZ	
535,8	PYRXN		uCZ	
536,5	PYRXN		uCZ	
536,6	PYRXN		uCZ	
537,6	PYRXN		uCZ	
538,6	PYRXN		uCZ	
539,5	PYRXN		uCZ	
540,4	PYRXN		uCZ	
541,3	PYRXN		uCZ	Fractures filled with secondary chlorite and silica

542,3	PYRXN		uCZ	Fractures filled with secondary chlorite and silica
542,5	PYRXN		uCZ	Section is severely broken.
543,2	PYRXN		uCZ	
544,2	PYRXN		uCZ	Chlorite fills fractures.
545,2	PYRXN		uCZ	
545,5	PYRXN		uCZ	
546,1	PYRXN		uCZ	
547,0	PYRXN		uCZ	Chlorite filling fractures; 0.45 of section severely fractured due to alteration
548,0	PYRXN		uCZ	
548,4	PYRXN		uCZ	
548,9	PYRXN		uCZ	
549,9	PYRXN		uCZ	
550,8	PYRXN		uCZ	
551,6	PYRXN		uCZ	
551,6	PYRXN		uCZ	
552,5	PYRXN		uCZ	
553,5	PYRXN		uCZ	
554,4	PYRXN		uCZ	
555,4	PYRXN		uCZ	
556,4	PYRXN		uCZ	
557,4	PYRXN		uCZ	
557,5	PYRXN		uCZ	
558,3	PYRXN		uCZ	
559,2	PYRXN		uCZ	
560,2	PYRXN		uCZ	
560,5	PYRXN		uCZ	
561,1	PYRXN		uCZ	
561,9	PYRXN		uCZ	
562,9	PYRXN		uCZ	
563,5	PYRXN		uCZ	Chlorite infilling fractures
563,8	PYRXN		uCZ	
564,8	PYRXN		uCZ	
565,7	PYRXN		uCZ	
566,5	PYRXN		uCZ	Rock is fractured along the chlorite infilling.
566,7	PYRXN		uCZ	
567,6	PYRXN		uCZ	
568,5	PYRXN		uCZ	Chlorite infilling fractures
569,5	PYRXN		uCZ	
570,2	PYRXN		uCZ	
571,2	PYRXN		uCZ	
572,1	PYRXN		uCZ	Rock is fractured along the chlorite infilling
572,5	PYRXN		uCZ	Chlorite infilling fractures
573,0	PYRXN		uCZ	
573,9	DOLRT		uCZ	Dolerite dyke; whitish secondary mineral infilling fractures
574,8	DOLRT		uCZ	Dolerite dyke; whitish secondary mineral infilling fractures
575,5	DOLRT		uCZ	Dolerite dyke; whitish secondary mineral infilling fractures

575,7	DOLRT	uCZ	Dolerite dyke; whitish secondary mineral infilling fractures
576,7	DOLRT	uCZ	Dolerite dyke; whitish secondary mineral infilling fractures
577,6	DOLRT	uCZ	Dolerite dyke; whitish secondary mineral infilling fractures
578,5	DOLRT	uCZ	Contact between the dolerite dyke and pyroxenite; Rock is fractured along the chlorite infilling.
579,3	PYRXN	uCZ	Pyroxenite intruded by a dolerite dyke; Rock is fractured along the chlorite infilling.
580,3	PYRXN	uCZ	Pyroxenite intruded by a dolerite dyke; Rock is fractured along the chlorite infilling.
581,2	PYRXN	uCZ	Hosts 2 semi-massive; chromitite seams; Disseminated chromite
581,5	PYRXN	uCZ	Chlorite infilling fractures
582,0	PYRXN	uCZ	Chlorite infilling fractures
583,0	PYRXN	uCZ	Chlorite infilling fractures
583,9	PYRXN	uCZ	Chlorite infilling fractures
584,5	PYRXN	uCZ	
584,7	PYRXN	uCZ	
585,6	PYRXN	uCZ	Chlorite infilling fractures
586,6	PYRXN	uCZ	Chlorite infilling fractures
587,3	PYRXN	uCZ	
588,4	PYRXN	uCZ	
589,4	PYRXN	uCZ	
590,3	PYRXN	uCZ	
590,4	PYRXN	uCZ	
591,2	PYRXN	uCZ	
592,2	PYRXN	uCZ	
593,2	PYRXN	uCZ	
593,6	PYRXN	uCZ	
593,9	PYRXN	uCZ	
594,9	PYRXN	uCZ	
595,9	PYRXN	uCZ	
596,5	PYRXN	uCZ	
596,8	PYRXN	uCZ	
597,7	PYRXN	uCZ	
598,7	PYRXN	uCZ	
599,4	DOLRT	uCZ	Dolerite dyke
600,3	DOLRT	uCZ	Dolerite dyke
600,5	DOLRT	uCZ	Dolerite dyke
601,2	PYRXN	uCZ	Chlorite infilling fractures
602,1	PYRXN	uCZ	
602,5	PYRXN	uCZ	
603,0	PYRXN	uCZ	
603,9	PYRXN	uCZ	
604,9	PYRXN	uCZ	
605,4	PYRXN	uCZ	
605,9	PYRXN	uCZ	
606,3	CHR	uCZ	Chromite-100%; The seam (0.46m thick) is fractured with the fracture surfaces are smooth (slickensides)
606,4	PYRXN	uCZ	
607,2	PYRXN	uCZ	Fractured along the chlorite infilling
607,4	PYRXN	uCZ	Fractured along the chlorite infilling

608,4	CHR	uCZ	LG-6 chromitite seam; Severely fractured-altered along the fractures due to fluid movement; Oxidised (small whitish spots;
608,1	CHR	uCZ	
608,9	PYRXN	uCZ	Semi-massive seam hosted by pyroxenite
609,1	CHR	uCZ	
610,0	PYRXN	uCZ	
611,0	PYRXN	uCZ	
611,5	PYRXN	uCZ	
611,9	PYRXN	uCZ	
612,8	PYRXN	uCZ	
613,8	PYRXN	uCZ	
614,4	PYRXN	uCZ	
614,8	PYRXN	uCZ	
615,7	PYRXN	uCZ	Lightly disseminated chromite
616,7	PYRXN	uCZ	
617,5	PYRXN	uCZ	semi massive seams (Chr 40%), fine grained Chr
618,4	PYRXN	uCZ	
619,3	PYRXN	uCZ	
620,3	PYRXN	uCZ	
620,4	PYRXN	uCZ	Serpentinised pyroxenite; lightly porous; Alteration (a network of secondary chlorite veins); Massive chromitite seam (very coarse grained) 1.5cm thick; Microbiology sample-
621,2	PYRXN	uCZ	
622,0	PYRXN	uCZ	
622,8	PYRXN	uCZ	Severely fractured, particularly along chlorite infilling
623,6	DOLRT	uCZ	Dolerite dyke; Fractures with chlorite infilling
622,9	DOLRT	uCZ	Dolerite dyke;
623,7	DOLRT	uCZ	Dolerite dyke
624,3	DOLRT	uCZ	Dolerite dyke
624,6	PYRXN	uCZ	Serpentinised; Traces of Phlogopite
625,6	PYRXN	uCZ	Serpentinised
626,4	PYRXN	uCZ	fractured along chlorite infilling
627,3	PYRXN	uCZ	fractured along chlorite infilling
628,1	PYRXN	uCZ	fractured along chlorite infilling
629,0	PYRXN	uCZ	fractured along chlorite infilling
629,5	PYRXN	uCZ	Disseminated Chr throughout the section; Semi massive chr seam at the end of the section (7cm thick)
629,9	PYRXN	uCZ	Disseminated Chr throughout the section; Semi massive chr seam
630,8	PYRXN	uCZ	
631,8	PYRXN	uCZ	
632,4	PYRXN	uCZ	
632,7	PYRXN	uCZ	
633,7	PYRXN	uCZ	
634,7	PYRXN	uCZ	
635,4	PYRXN	uCZ	
635,6	PYRXN	uCZ	
636,6	PYRXN	uCZ	
637,5	PYRXN	uCZ	

638,5	PYRXN		uCZ	
639,4	PYRXN		uCZ	
640,3	PYRXN		uCZ	
641,2	PYRXN		uCZ	
641,4	PYRXN		uCZ	
642,2	PYRXN		uCZ	
643,1	PYRXN		uCZ	
644,1	PYRXN		uCZ	
644,5	PYRXN		uCZ	
644,9	PYRXN		uCZ	
645,8	PYRXN		uCZ	
646,7	PYRXN		uCZ	
647,5	PYRXN		uCZ	
648,4	PYRXN		uCZ	Rock is fractured along chloritic infilling
649,3	PYRXN		uCZ	
650,2	PYRXN		uCZ	
650,5	PYRXN		uCZ	
651,1	PYRXN		uCZ	
652,0	PYRXN		uCZ	
652,9	PYRXN		uCZ	
653,4	PYRXN		uCZ	
653,8	PYRXN		uCZ	
654,8	PYRXN		uCZ	
655,7	PYRXN		uCZ	
656,5	PYRXN		uCZ	
656,6	PYRXN		uCZ	
657,6	PYRXN		uCZ	
658,5	PYRXN		uCZ	
659,5	PYRXN		uCZ	
660,4	PYRXN		uCZ	
661,3	PYRXN		uCZ	
662,3	PYRXN		uCZ	
662,4	PYRXN		uCZ	
663,1	PYRXN		uCZ	
664,1	PYRXN		uCZ	
665,0	PYRXN		uCZ	
665,5	PYRXN		uCZ	
665,9	PYRXN		uCZ	
666,8	PYRXN		uCZ	
667,8	PYRXN		uCZ	
668,4	PYRXN		uCZ	
668,8	HZB		uCZ	
669,8	HZB		uCZ	
670,7	HZB		uCZ	Densely disseminated, interstitial chromite, forming a 'chicken wire' texture around Olivine crystals; Section is grinded
671,3	HZB		uCZ	
671,8	HZB		uCZ	

672,7	HZB	uCZ	with traces of Phlogopite; Disseminated chromite
673,7	HZB	uCZ	traces of phlogopite'; Chromitite seams -Massive to semi-massive that are about 2 mm to 20 cm thick.
674,5	HZB	uCZ	
674,5	HZB	uCZ	
675,5	HZB	uCZ	traces of phlogopite; disseminated chromite
676,5	HZB	uCZ	
677,5	HZB	uCZ	
678,4	HZB	uCZ	Disseminated chromite
679,3	HZB	uCZ	Disseminated chromite
680,3	HZB	uCZ	
680,4	HZB	uCZ	
681,2	HZB	uCZ	
682,1	HZB	uCZ	
683,0	HZB	uCZ	
683,5	HZB	uCZ	
684,0	HZB	uCZ	
684,9	HZB	uCZ	
685,9	PYRXN	uCZ	Disseminated chromite
686,5	PYRXN	uCZ	Disseminated chromite
686,8	PYRXN	uCZ	Disseminated chromite
687,8	PYRXN	uCZ	Chromitite seam 1: semi massive at 0.4 m of the section (8 cm); seam 2: Semi massive at 0.6 m of the section at 10 cm; Disseminated chromite (fine grained
688,7	PYRXN	uCZ	Chromitite semi massive seams (30vol% Chr) at 1) at 0.3 m of the section (10 cm); 2) 0.7 m of the section at 30 cm; fine grained chromite
689,5	PYRXN	uCZ	Heavy chromite disseminations-interstitial- forming a 'chicken wire' texture around Opx
690,4	PYRXN	uCZ	
691,3	PYRXN	uCZ	
692,3	PYRXN	uCZ	Section is fractured
692,5	PYRXN	uCZ	
693,1	PYRXN	uCZ	Microbiology sample (0 - 0.7 m)
694,1	PYRXN	uCZ	Microbiology sample 0 - 0.5 m
695,1	PYRXN	uCZ	
695,5	PYRXN	uCZ	
696,0	PYRXN	ICZ	Microbiology sample taken at 0.5 m.
697,0	PYRXN	ICZ	
698,0	PYRXN	ICZ	
698,4	PYRXN	ICZ	
698,9	PYRXN	ICZ	
699,8	PYRXN	ICZ	
700,8	PYRXN	ICZ	
701,4	PYRXN	ICZ	
701,7	PYRXN	ICZ	
702,7	PYRXN	ICZ	
703,7	PYRXN	ICZ	Semi massive chromitite seam at 0.8 m of section; Fine grained Chr
704,7	PYRXN	ICZ	
705,3	PYRXN	ICZ	
706,3	PYRXN	ICZ	

707,3	PYRXN		ICZ	
707,5	PYRXN		ICZ	
708,2	PYRXN		ICZ	
709,1	PYRXN		ICZ	Disseminated chromite
710,1	PYRXN		ICZ	
710,4	PYRXN		ICZ	
711,1	PYRXN		ICZ	
712,1	PYRXN		ICZ	
713,1	PYRXN		ICZ	
713,6	PYRXN		ICZ	
713,9	PYRXN		ICZ	
714,8	PYRXN		ICZ	
715,8	PYRXN		ICZ	
716,5	PYRXN		ICZ	
716,7	PYRXN		ICZ	
717,7	PYRXN		ICZ	
718,7	PYRXN		ICZ	
719,5	PYRXN		ICZ	
720,4	PYRXN		ICZ	
721,4	PYRXN		ICZ	
722,3	PYRXN		ICZ	
722,5	PYRXN		ICZ	
723,2	PYRXN		ICZ	
724,1	PYRXN		ICZ	
725,1	PYRXN		ICZ	
725,4	PYRXN		ICZ	
726,1	PYRXN		ICZ	Densely disseminated chromite forming a 'chicken wire' / network texture around Opx crystals
727,1	PYRXN		ICZ	Densely disseminated chromite forming a 'chicken wire' / network texture around Opx crystals (0 - 0.3 m of section)
728,0	PYRXN		ICZ	
728,4	PYRXN		ICZ	
729,0	PYRXN		ICZ	
729,9	PYRXN		ICZ	
730,9	PYRXN		ICZ	
731,5	PYRXN		ICZ	
731,8	PYRXN		ICZ	
732,7	PYRXN		ICZ	
733,6	PYRXN		ICZ	
734,5	PYRXN		ICZ	
736,3	PYRXN		ICZ	
737,3	PYRXN		ICZ	
737,4	PYRXN		ICZ	
738,3	PYRXN		ICZ	
739,2	PYRXN		ICZ	
740,2	PYRXN		ICZ	
740,5	PYRXN		ICZ	
741,0	PYRXN		ICZ	

742,0	PYRXN		ICZ	
743,0	PYRXN		ICZ	
743,4	PYRXN		ICZ	
743,9	PYRXN		ICZ	
744,9	PYRXN		ICZ	
745,9	PYRXN		ICZ	
746,6	PYRXN		ICZ	
746,7	PYRXN		ICZ	
747,7	PYRXN		ICZ	
748,6	PYRXN		ICZ	
749,3	PYRXN		ICZ	
749,6	PYRXN		ICZ	
750,6	PYRXN		ICZ	
751,4	PYRXN		ICZ	
752,5	PYRXN		ICZ	
753,4	PYRXN		ICZ	
754,4	PYRXN		ICZ	
755,3	PYRXN		ICZ	
755,5	PYRXN		ICZ	
756,2	PYRXN		ICZ	
757,2	PYRXN		ICZ	
758,1	PYRXN		ICZ	
758,5	PYRXN		ICZ	
759,1	PYRXN		ICZ	
760,0	PYRXN		ICZ	
761,0	PYRXN		ICZ	
761,5	PYRXN		ICZ	
761,9	PYRXN		ICZ	
762,9	PYRXN		ICZ	
763,8	PYRXN		ICZ	
764,4	PYRXN		ICZ	
764,7	PYRXN		ICZ	
765,7	PYRXN		ICZ	
766,6	PYRXN		ICZ	
767,5	PYRXN		ICZ	
768,5	PYRXN		ICZ	
769,4	PYRXN		ICZ	
770,3	PYRXN		ICZ	
770,4	PYRXN		ICZ	
771,2	PYRXN		ICZ	
772,2	PYRXN		ICZ	Massive chromitite seams at 0.7 m of the section; 13 cm thick; Fine grained chromite
773,2	PYRXN		ICZ	
773,4	PYRXN		ICZ	
774,1	HZB		ICZ	
775,0	HZB		ICZ	Massive chromitite seams at 0.7m of the section-13 cm thick
776,0	HZB		ICZ	
776,5	HZB		ICZ	

776,9	HZB		ICZ	
777,9	HZB		ICZ	
778,9	HZB		ICZ	
779,5	HZB		ICZ	
779,7	HZB		ICZ	
780,6	HZB		ICZ	
781,4	HZB		ICZ	Interstitial chromite -Densely disseminated with 'chicken wire' texture
782,5	DUN		ICZ	Densely disseminated chromite forming 'chicken wire' texture around olivine grains; Semi massive chromitite seam at 0.15m of the section; 5cm thick;
783,4	DUN		ICZ	Densely disseminated chromite
784,4	DUN		ICZ	Densely disseminated chromite
785,3	DUN		ICZ	Densely disseminated chromite; Section is fractured
785,5	DUN		ICZ	Disseminated chromite
786,2	HZB		ICZ	Section is fractured chloritic and silica infilling
787,1	DUN		ICZ	Disseminated chromite
788,1	DUN		ICZ	Disseminated Chromite
788,5	DUN		ICZ	
789,0	DUN		ICZ	
790,0	OLOPX		ICZ	
790,9	DUN		ICZ	Top of the section is severely fractured
791,3	DUN		ICZ	Section is highly fractured
792,0	PYRXN		ICZ	
793,0	PYRXN		ICZ	
793,9	PYRXN		ICZ	
794,6	PYRXN		ICZ	
794,7	PYRXN		ICZ	
795,6	PYRXN		ICZ	
796,6	PYRXN		ICZ	
797,5	PYRXN		ICZ	Fractures filled with calcite and serpentine
798,4	PYRXN		ICZ	
799,4	PYRXN		ICZ	
800,4	PYRXN		ICZ	Microbiology sample (0-0.4m)
801,4	PYRXN		ICZ	
802,3	PYRXN		ICZ	
803,3	PYRXN		ICZ	
803,5	PYRXN		ICZ	
804,1	PYRXN		ICZ	
805,1	PYRXN		ICZ	
806,1	PYRXN		ICZ	
806,4	PYRXN		ICZ	
807,0	PYRXN		ICZ	
808,0	PYRXN		ICZ	
808,9	PYRXN		ICZ	
809,5	PYRXN		ICZ	
809,8	PYRXN		ICZ	Densely disseminated chromite forming 'chicken wire' texture around pyx grains (Chr-30vol%). Fine grained chr; Section is fractured and slightly altered
810,5	PYRXN		ICZ	Semi massive chromitite hosted by pyroxenite; Fine grained chromite; 50vol% chromite; 0-0.7m of the section
810,8	PYRXN		ICZ	Slightly altered

811,7	PYRXN		ICZ	Fractured
812,5	PYRXN		ICZ	Fractures infilled by calcite and chlorite
813,4	PYRXN		ICZ	Fractures infilled by calcite and chlorite; Densely disseminated chromite forming a 'chicken wire' texture around Pyx grains. Chr is fine grained
814,3	PYRXN		ICZ	Fractures infilled by calcite and chlorite; Hosts a semi massive chromitite seam from 0 - 0,7m of the section.
815,3	PYRXN		ICZ	Fractured
815,5	PYRXN		ICZ	
816,1	PYRXN		ICZ	
817,1	PYRXN		ICZ	
817,9	PYRXN		ICZ	
818,3	PYRXN		ICZ	
819,0	PYRXN		ICZ	
820,0	PYRXN		ICZ	
820,9	PYRXN		ICZ	
821,5	PYRXN		ICZ	
821,9	PYRXN		ICZ	
822,8	PYRXN		ICZ	
823,8	PYRXN		ICZ	
824,5	PYRXN		ICZ	
824,6	PYRXN		ICZ	
825,6	PYRXN		ICZ	
826,5	PYRXN		ICZ	
827,5	PYRXN		ICZ	Chlorite infilling fractures
828,4	PYRXN		ICZ	
829,4	PYRXN		ICZ	
830,4	PYRXN		ICZ	
830,5	PYRXN		ICZ	Chlorite infilling fractures
831,3	PYRXN		ICZ	Chromitite seams 1) at 0.5 m-massive, 1cm thick; 2) at 0.53 - 4cm - massive. These are separated by pyroxenite
832,3	PYRXN		ICZ	
833,2	PYRXN		ICZ	
833,4	PYRXN		ICZ	
834,1	PYRXN		ICZ	
835,1	PYRXN		ICZ	
836,0	PYRXN		ICZ	
836,4	PYRXN		ICZ	
837,0	PYRXN		ICZ	Chromitite seams 1) 1 cm massive seam - fine grained chromite 2) 4cm thick massive chromitite seam. These seams are separated by feldspathic pyroxenite which hosts disseminated
837,9	PYRXN		ICZ	Densely disseminated chromite over the entire section forming a 'chicken wire texture around pyroxene grains
838,9	PYRXN		ICZ	Disseminated chromite over 0-0.4 m and 0.7-end of the section; Massive chromitite seam at 0.4-0.7 m, chr=98 vol%
839,6	PYRXN		ICZ	
839,7	PYRXN		ICZ	
840,6	PYRXN		ICZ	
841,6	PYRXN		ICZ	
842,3	PYRXN		ICZ	
842,7	PYRXN		ICZ	
843,7	PYRXN		ICZ	
844,6	PYRXN		ICZ	

845,6	PYRXN		ICZ	
846,4	PYRXN		ICZ	
847,4	PYRXN		ICZ	
848,2	PYRXN		ICZ	
848,5	PYRXN		ICZ	
849,1	PYRXN		ICZ	
850,0	PYRXN		ICZ	
851,0	PYRXN		ICZ	
851,5	PYRXN		ICZ	
851,9	PYRXN		ICZ	
852,9	PYRXN		ICZ	
853,8	PYRXN		ICZ	
854,3	PYRXN		ICZ	Bottom of the section is highly fractured.
854,9	PYRXN		ICZ	
855,9	PYRXN		ICZ	
856,8	PYRXN		ICZ	
857,5	PYRXN		ICZ	
857,7	PYRXN		ICZ	
858,7	PYRXN		ICZ	
859,7	PYRXN		ICZ	
860,6	PYRXN		ICZ	Bottom of the section is highly fractured.
861,5	PYRXN		ICZ	
862,4	PYRXN		ICZ	
863,4	PYRXN		ICZ	
863,5	PYRXN		ICZ	
864,2	PYRXN		ICZ	
865,2	PYRXN		ICZ	
866,1	PYRXN		ICZ	
866,5	PYRXN		ICZ	
867,0	PYRXN		ICZ	
868,0	PYRXN		ICZ	
868,9	PYRXN		ICZ	
869,5	PYRXN		ICZ	
869,8	PYRXN		ICZ	
870,8	PYRXN		ICZ	
871,8	PYRXN		ICZ	
872,1	PYRXN		ICZ	
872,7	DOLRT		ICZ	Dolerite dyke
873,2	DOLRT		ICZ	Dolerite dyke
874,5	PYRXN		ICZ	
875,5	PYRXN		ICZ	
876,4	PYRXN		ICZ	
877,3	PYRXN		ICZ	Fractured
878,3	PYRXN		ICZ	Fractured
878,5	PYRXN		ICZ	
879,2	PYRXN		ICZ	

879,7	PYRXN		ICZ	Fractured
880,1	PYRXN		ICZ	
881,1	PYRXN		ICZ	
781,4	HZB		ICZ	Semi massive chromitite seam hosted by harzburgite
781,4	HZB		ICZ	Dunite with a 10cm thick chromitite seam.
872,4	DOLRT		ICZ	Dolerite dyke
873,6	PYRXN		ICZ	
882,0	PYRXN		ICZ	
882,9	PYRXN		ICZ	Fractured
883,9	PYRXN		ICZ	
884,5	PYRXN		ICZ	
884,8	PYRXN		ICZ	
885,7	PYRXN		ICZ	Severely fractured-chloritic infilling
886,7	PYRXN		ICZ	Severely fractured-chloritic infilling
887,5	PYRXN		ICZ	Severely fractured-chloritic infilling
888,4	PYRXN		ICZ	
889,4	PYRXN		ICZ	
890,3	PYRXN		ICZ	
890,5	PYRXN		ICZ	
891,2	PYRXN		ICZ	
892,2	PYRXN		ICZ	Hosts a semi massive chromitite seam; 20cm thick; Fine grained; Displays a chicken wire texture
893,2	PYRXN		ICZ	
893,5	PYRXN		ICZ	Secondary mineral infilling fractures
894,2	PYRXN		ICZ	
895,2	PYRXN		ICZ	Secondary mineral infilling fractures.
896,2	PYRXN		ICZ	Secondary mineral infilling fractures.
896,5	PYRXN		ICZ	Secondary mineral infilling fractures.
897,0	PYRXN		ICZ	Secondary mineral infilling fractures.
897,9	PYRXN		ICZ	Secondary mineral infilling fractures.
898,9	PYRXN		ICZ	Secondary mineral infilling fractures.
899,5	PYRXN		ICZ	Secondary mineral infilling fractures.
899,8	PYRXN		ICZ	
900,8	PYRXN		ICZ	
901,8	PYRXN		ICZ	
902,5	PYRXN		ICZ	
902,6	PYRXN		ICZ	
903,5	PYRXN		ICZ	
904,3	PYRXN		ICZ	
905,2	PYRXN		ICZ	
905,5	PYRXN		ICZ	
906,1	PYRXN		ICZ	
907,1	PYRXN		ICZ	
908,1	PYRXN		ICZ	
908,5	PYRXN		ICZ	
909,1	PYRXN		ICZ	
910,0	PYRXN		ICZ	

911,0	PYRXN		ICZ	
911,5	PYRXN		ICZ	
911,8	PYRXN		ICZ	
912,8	PYRXN		ICZ	
913,8	PYRXN		ICZ	
914,5	PYRXN		ICZ	
914,7	PYRXN		ICZ	
915,7	PYRXN		ICZ	Disseminated chromite
916,6	PYRXN		ICZ	Disseminated chromite from 0.6 m to end of the section; Fractures infilled by chlorite
917,5	PYRXN		ICZ	Disseminated chromite throughout the section
918,4	PYRXN		ICZ	Chlorite infilling fractures
919,4	PYRXN		ICZ	
920,5	PYRXN		ICZ	
921,4	PYRXN		ICZ	
922,4	PYRXN		ICZ	
923,3	PYRXN		ICZ	
923,5	PYRXN		ICZ	Fractures infilled by chlorite
924,1	PYRXN		ICZ	Fractures infilled by chlorite
925,1	PYRXN		ICZ	Fractures infilled by chlorite
926,0	PYRXN		ICZ	Fractures infilled by chlorite
926,5	PYRXN		ICZ	Fractures infilled by chlorite
926,9	PYRXN		ICZ	Fractures infilled by chlorite

End of Phase 2 at 950 mbgl *logs not available at the time of report